Structural Performance of Post-tensioned Timber Frames under Gravity Loading

---

A thesis submitted in partial fulfilment
of the requirements for the Degree of
Doctor of Philosophy
by

Wouter Adrian van Beerschoten

Department of Civil and Natural Resources Engineering
University of Canterbury
Christchurch, New Zealand
2013

Abstract

A new structural system for multi-storey timber buildings has been developed over the last seven years at the University of Canterbury in collaboration with the Structural Timber Innovation Company Ltd (STIC). The system incorporates large timber structural frames or walls, connected using post-tensioning (PT) tendons, which can create large open floor plans required for office and commercial buildings. The system, initially developed as a lateral load resisting system using straight unbonded tendons, also has a significant potential for frames under gravity loading where draped PT tendons run through frames made of laminated veneer lumber (LVL) box beams. This reduces deflections and increases load carrying capacity of the beams as moment-resisting beam-column connections are created by the PT force. But compression strength of the columns perpendicular to the grain is limited and local reinforcement is needed.

The main objectives of this research were to analyse the performance of post-tensioned timber frames under gravity loading and to provide design guidance. Research was performed in four areas: material properties of LVL, beams, connections and frames.

Design of PT timber constructions requires more material properties than those provided by LVL manufacturers. Examples are the perpendicular to grain stiffness for connection design and rolling shear strength for deviator design. Experimental testing of Radiata Pine LVL has resulted in a greater understanding of the compression and shear strengths and stiffnesses in three different material orientations. Furthermore, the Poisson's ratios of LVL have been evaluated using digital image correlation techniques, which made it possible to create a 3D constitutive model of LVL.

The effect of PT on the deflections and failure strength of timber box beams was evaluated by experimental testing of four full-scale box beams loaded until failure. Post-tensioning increased the load-carrying capacity at the serviceability design limit up to 50%. A mixture of failure mechanisms (tension, compression and shear) was found and analysis showed that in a design the compression and tensile capacity of top and bottom flanges should be checked as well as the shear strength of the webs. Numerical and analytical models were developped to predict the performance of PT beams. The analytical model was used for a parameter

study on a range of beam lengths and PT forces. For box beams without PT the span length over beam depth (L/h) ratio was 8 whereas for PT beams this was 12. For all considered geometeries the design is governed by long-term deflections. This outcome was used for the implementation of a simplified design method for PT timber box beams.

Experimental testing of PT beam-column connections found that timber reinforcement as well as long fully threaded screws placed at the column interface were effective ways to increase the connection stiffness and minimize permanent rotations due to plastic deformation of the timber in compression perpendicular to grain. Four deformation components were identified: column rotation, joint panel shear deformation, interface compression and gap opening. The moment-rotation behaviour of every component was analysed and analytical design equations and design charts were presented. It was concluded that the monolithic beam analogy (MBA) design procedure, which is already implemented for concrete, can also be applied to timber rocking connections, but the shear stiffness of timber should be taken into account. A new MBA for frames under vertical loading was developed and partially validated with experimental testing results.

Experimental testing and analysis of PT timber frames made it possible to validate the analytical design equations for connection behaviour. It also showed that internal connections were stiffer and thus reached decompression before external connections did. Two modelling approaches were presented, one for a full frame model and one for a simplified beam model. For the beam model an analytical solution for bending moment distributions and deflections was derived and used for a parameter study. It was found that long-term deflections also govern the design of frames and that the compressive strength of the bottom flange of the beam (at the connection after gap opening) limited the amount of post-tensioning that could be applied to the frame. A comparison between post-tensioned timber beams and frames showed that the maximum span for a given section is very similar, but frames need less post-tensioning stress to achieve the same performance as simply supported beams.

This thesis presents the performance of long-span post-tensioned timber frames under gravity loading, which has been proven by experimental testing and detailed analysis. Design guidance is given for practising engineers to apply this technology in the real world.

Acknowledgements

I would like to acknowledge the following people and organizations for their support of this doctoral research project.

- University of Canterbury for their doctoral scholarship which covered living expenses and tuition fees for the duration of the research.

- Structural Timber Innovation Company (STIC) and their CEO Robert Finch for the financial support of experimental testing, research meetings within Australia and New Zealand, an Abaqus trainings course, student service levy, visa costs and numerous conference visits in New Zealand and abroad. Also the strong connection between STIC and the Australian and New Zealand timber industry increased my enthusiasm for the research project as it added a strong practical side to it. The recently published STIC design guidelines on post-tensioned timber frames, in particular the gravity design part, are a great output of my research and can be used by the structural engineering industry to implement a large part of my research into construction practice.

- The STIC research committee consisting of Andy Buchanan, Stefano Pampanin, Pierre Quenneville and Keith Crews, initiated a large timber research program. It was a unique opportunity and valuable experience to have been part of this program.

- The Dutch Prins Bernard Cultuurfonds for their financial support with moving to New Zealand and during the first year of this research.

- Alessandro Palermo for his supervision during the entire length of my research project. His guidance and input was very useful to keep my research on track. And his review of my thesis provided very useful comments and significantly improved the quality of this thesis.

- David Carradine for his supervision and assistance with laboratory work. Also his feedback on my publications and this thesis has strongly improved my academic writing skills.

- Athol Carr for his supervision and his involvement in the development of a material model for LVL.

- Andy Buchanan for leading and organizing a great timber research group. He was also fundamental in getting me convinced to do this PhD research here at the University of Canterbury.

- The civil engineering department for providing the research facilities and all the staff for helping out with a wide range of questions related to my research. Also their support for tutoring work and lecturing under graduate courses was much appreciated.

- My fellow timber research students; Tobias Smith, Francesco Sarti, Daniel Moroder, James O'Neill, Chris Watson, Andrew Dunbar, Tom Armstrong, Phillip Spellman, Reuben Costello, Manoochehr Ardalany, David Yeoh and Michael Newcombe. It was a pleasure to work together with so many others on this project.

- My office mates Catherine Tatarniuk and Kevin Frank for the good times spend in the office. And the suggestion of Kevin to write this thesis in LaTeXwhich, although it caused some frustration in the start, turned out to be a great tool for writing and formatting.

- Elizabeth Ackermann, Louise Barton and Alan Jolliffe for their administrative support and assisting with travel arrangements for the numerous trips.

- Brandon Hutchison for supplying a computer and providing IT support which was required for the finite element modelling and digital image correlation (DIC).

- C. Erbel and his team from Karlsruhe Institute of Technology in Germany for providing the Matlab DIC software freely available on Matlab Central and for taking the time to assist me with initial problems to get the software working.

- The technicians Shaun Cosgrove, Peter Coursey, Gavin Keats, Russell McConchie, John Maley, Alan Poynter, Stuart Toase and Michael Weavers for their support of all experimental testing. An extended gratitude to Gavin and Russell for their running of the extension lab where the beam and frame testing took place, and to Peter and Shaun for their help with implementing the digital cameras into the existing instrumentation setup.

- The laminated veneer lumber (LVL) manufacturer Nelson Pine Industries Limited. and in particular Andy van Houtte for supplying materials for experimental testing.

- Hunter Laminates Nelson Ltd, in particular Jason Guiver and Neil Dodunski, for manufacturing the beams and columns to tight specifications out of the LVL billets.

- BBR Contech, in particular Paul Blundell, for supplying post-tensioning material and equipment used for experimental testing. Even damaging their hydraulic post-tensioning jack did not lessen their cooperation.

- The CUTC for providing a great group of friends to explore the great New Zealand outdoors with. This was a great distraction from my research and made my time here all the more memorable.

- My family, especially my mother and father, for supporting me in my decision to travel to New Zealand for my research.

- My partner Zsòfi for her care and understanding during my research, especially during the final stages of thesis writing and overseas travel to attend conferences.

Table of Contents

List of Figures

List of Tables

Part I

Preface

Chapter I

Introduction

1.1 Background

A global focus on sustainability has resulted in a renewed interest in timber as a construction material. The development of engineered wood products with high strength characteristics and large dimensions, such as glue laminated timber (Glulam), cross-laminated timber (CLT) and laminated veneer lumber (LVL), have created new opportunities for timber construction. One of these opportunities is a new structural system for multi-storey timber buildings, which has been developed at the University of Canterbury in collaboration with the Structural Timber Innovation Company Ltd (STIC). This system is suitable for a wide range of building types, including commercial structures. It has the potential to compete with existing forms of construction (concrete and steel) in Australia and New Zealand in terms of cost, flexibility of structural form and structural performance (Palermo et al., 2005; Buchanan et al., 2011). The system, called Pres-Lam, incorporates large timber structural frames or walls, constructed of LVL and connected using post-tensioning tendons.

Post-tensioning is a common technique in concrete construction developed in the early 20th century, but only recently, within the PRESSS (PREcast Seismic Structural System) research program at the University of California, San Diego (Priestley et al., 1999), the application of unbonded post-tensioning in frames for buildings in seismic areas has been developed. This structural concept has been expanded to steel frames and lately also to timber frames where it has been called the Pres-Lam system. The concept of post-tensioned frames has been further developed for concrete frames in non-seismic areas, as the Brooklyn System (Pampanin et al., 2004). This system uses unbonded draped tendons to resist the vertical gravity loading.

Timber frames in non-seismic areas could also benefit from the use of unbonded post-tensioned cables. The three main benefits are the possibility to create a precamber, the possibility to connect large member sizes and the increase in load-carrying capacity. A precamber can be created during the manufacturing of a glulam beam, but for LVL this is not possible. As timber beam design is often governed by deflections, the precamber helps to satisfy the Serviceability Limit State (SLS) deflection criteria. Initial research on a nine meter post-tensioned beam has proven this (Lago and Dibenedetto, 2009). Post-tensioning can also help to create simple connections between large timber members without the need of many fasteners and steel components. One stressing operation can make multiple connections, speeding up the construction process. But more research is needed to investigate the effects of the beam-column connections, the detailing of the post-tensioning and to optimize and simplify design procedures. As the compressive strength of timber is larger than the tensile strength, for LVL11 this is 45MPa versus 30MPa, the application of post-tensioning results in an initial compressive stress in the timber which reduces tensile stresses at the bottom of the beam, very similar to the reason why post-tensioning is applied in concrete structures.

When designing a timber frame, different structural configurations are possible. Five main frame configurations (Figure 1.1) have been identified:

1. Simply supported timber beams
2. Continuous timber beams
3. Simply supported timber beams with straight post-tensioning
4. Simply supported timber beams with draped post-tensioning
5. Continuous post-tensioned timber frame

Configurations 1 and 2 do not have post-tensioning. The design of these beams is based on basic mechanical equations and prescribed by timber design standards. Design of simply supported beams is mainly governed by long-term deflections and design of continuous beams is often governed by bending strength above the mid-supports.

Two options are possible when applying post-tensioning to a frame. Firstly only the beams can be post-tensioned, with straight or draped tendons, and secondly the full frame can be post-tensioned. Post-tensioned beams have the

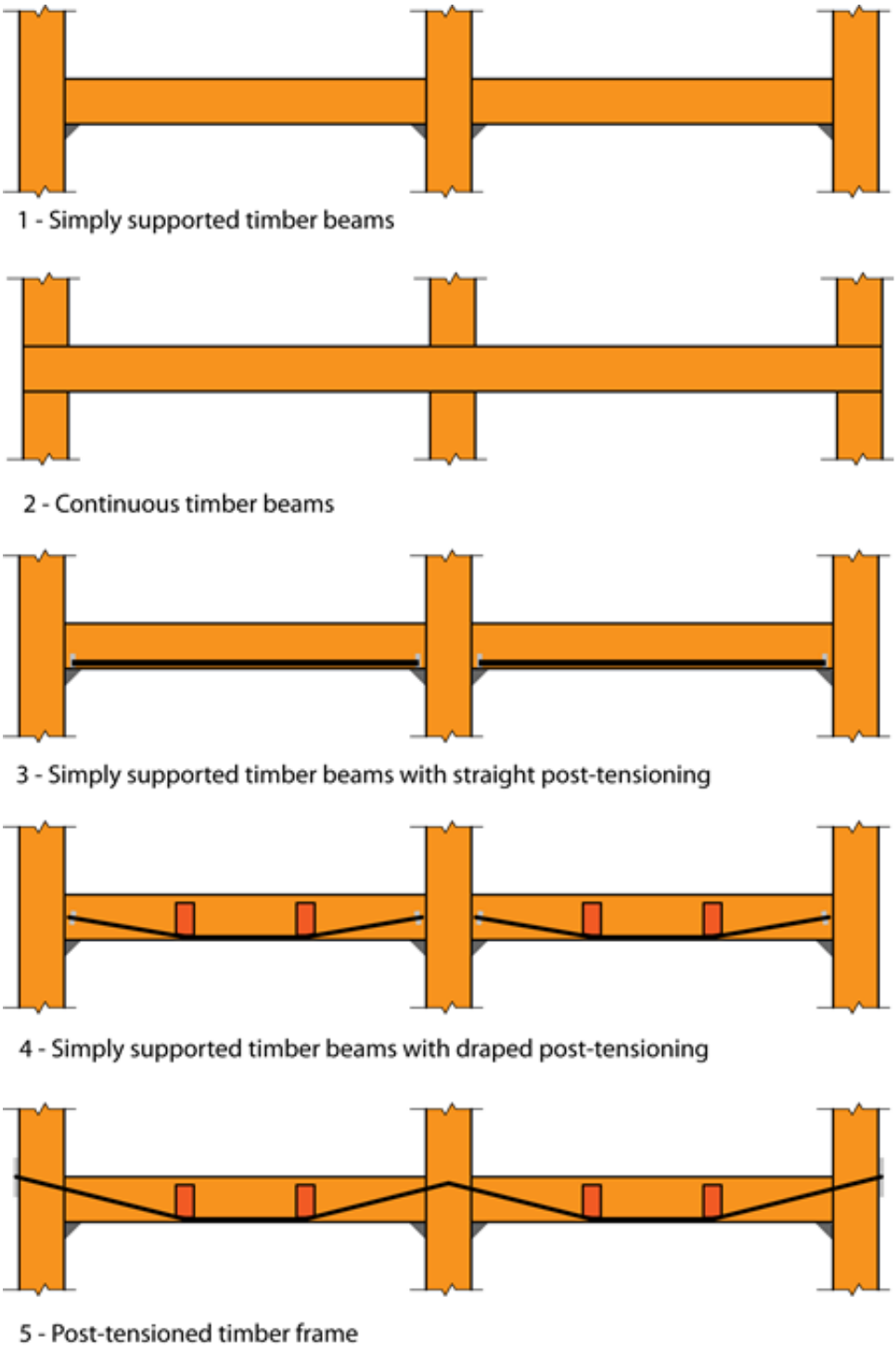

Figure 1.1: Five different frame configurations

advantage that all the manufacturing and stressing can be performed off-site. Furthermore timber is only stressed parallel to grain, which is beneficial in reducing post-tensioning losses (which mainly occur in timber loaded perpendicular to grain). Post-tensioned frames have the benefit that with one stressing operation several moment-resisting beam-column connections are created. These connections further reduce deflections and stresses in the beams. A disadvantage is that high stresses perpendicular to grain are introduced into the columns. This is a weak property of timber and some form of reinforcement in the column interface is needed.

Application of post-tensioning can significantly improve the structural performance of simply supported beams. Only a limited benefit is achieved for continuous beams, as deflections are less critical in the design and there is already the benefit of moment transfer at the supports. Furthermore, when aiming for long-span beams, within the range of 9m to 12m, creating continuous sections can become problematic from a manufacturing and construction perspective. Therefore this research does not focus on the application of post-tensioning to continuous beams.

1.2 Scope and objectives

The main objectives are to analyse the structural performance of post-tensioned timber frames under gravity loading and to provide guidance for the design of these frames. This work will aid engineers and designers in the process of designing Pres-Lam buildings. Research scope and objectives have been split in the following four areas: material properties, beams, connections and frames. A selection of the scope can be seen in Figure 1.2.

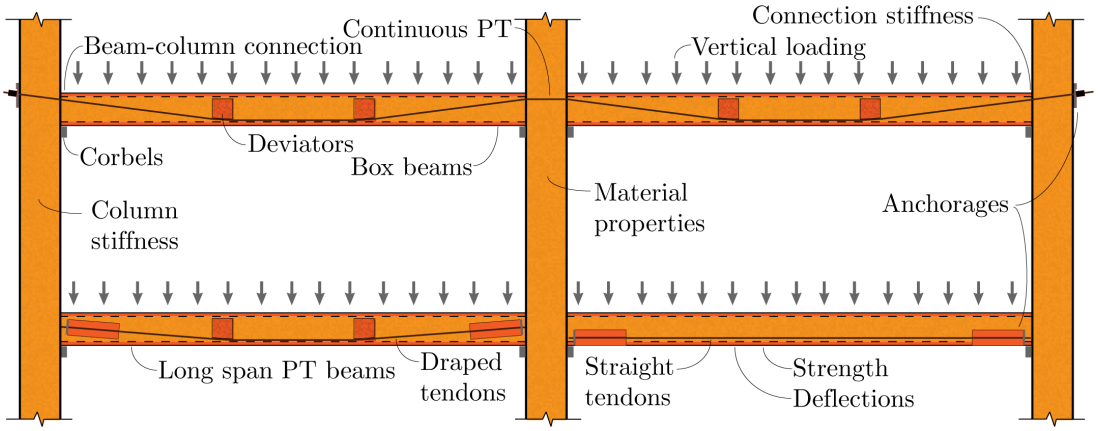

Figure 1.2: Overview of research areas

Material properties For any research using a structural material, the material properties are of fundamental importance. Several characteristic values of mechanical properties commonly used in engineering practice are supplied by New Zealand and Australian manufacturers (Wesbeam, 2005; Carter Holt Harvey, 2008; Nelson Pine Industries Limited, 2010). But post-tensioned timber construction requires more material properties than those provided by manufacturers. Examples are the perpendicular to grain stiffness for connection design and rolling shear strength for deviator design. Therefore extensive material testing of LVL has been performed in order to determine the compression strength and shear strength in different material directions. Further testing has resulted in the moduli of elasticity in compression, the Poisson's ratios and shear moduli in three different material directions. This work made it possible to develop a 3D finite

element material model of LVL. Digital image correlation techniques were used for the analysis of displacements and strains.

Experimental testing of LVL material properties has the following objectives:

- Determine the strength and stiffness of LVL under compression in different orientations.
- Determine the strength and stiffness of LVL in shear.
- Develop a three-dimensional material model for LVL for the use in FEM.
- Define non-linear stress-strain curves for LVL in compression that can be used for FEM.
- Give guidance on characteristic strength and stiffness values that can be used for timber design.

Beams Beams need to create long spans in order to achieve large open floor plans required for commercial and office buildings. Design of long-span timber beam is usually governed by deflections, therefore post-tensioning is used to create a precamber which reduces deflection. As timber has a low shear modulus, not only bending deflections are of importance, but also shear deflections become important in the deflection design of box beams. Initial testing of beams showed that post-tensioning created a precamber which helped to satisfy the serviceability limit states design requirements Lago and Dibenedetto (2009), but ultimate load carrying capacity was not tested. Therefore further experimental testing and analysis is performed in order to determine the ultimate load carrying capacity and failure mechanisms.

Beam precamber and deflections, ultimate strength, instantaneous post-tensioning losses, tendon elongation are part of the research. The design of deviators and post-tensioning anchorages is touched upon as they were needed for experimental testing. A solution using timber blocks as deviators is proposed, and thick steel plates are used as part of the anchorage system. Many different designs are possible and the viability depends largely on ease and cost of manufacturing, making in-depth research into one particular solution not very useful. However some design recommendations are given in the Appendix of this thesis.

Experimental testing of post-tensioned timber beams has the following objectives:

- Determine effects of post-tensioning on the failure strength of timber box beams.
- Evaluate effects of post-tensioning on instantaneous precamber and beam shortening.
- Assess short-term deflection behaviour of post-tensioned timber box beams.
- Determine global material properties for timber box beams

Analysis of post-tensioned timber beams has the following objectives:

- Develop numerical and analytical models to describe behaviour of post-tensioned timber beams.
- Evaluate applicability of current timber design code procedures to predict the failure load of post-tensioned timber beams.
- Perform a parameter study on the design of post-tensioned timber beams to identify critical design parameters.
- Propose a simplified design for post-tensioned timber beams.

Connections The beam-column connection stiffness influences bending moment distribution in the frames and deflections of the beams, therefore it is essential to include it in a design. Full-scale connections have been tested and analysis has identified different deformation components. Several rotation components, which contribute to the connection stiffness, are identified and analysed. Design methods for the connection behaviour form a major output of this thesis.

Previous research (Iqbal et al., 2010b) identified a reduced connection performance due to the limited strength of the column perpendicular to grain. Therefore reinforcement of the column interface is needed and different types of timber and steel reinforcement are analysed in experimental testing. Analysis of testing results and numerical modelling is performed and design equations for the different deformation components which contribute to the rotational stiffness of beam-column connections are presented.

Experimental testing of post-tensioned timber beam-column connections has the following objectives:

- Test the stiffness of post-tensioned timber beam-column connections.
- Evaluate the effectiveness of several different column reinforcement methods to reduce plastic deformations.

- Evaluate the effects of plastic deformations on the connection stiffness.
- Evaluate the applicability of proposed design methods for seismic frames.
- Analyse the design implications of a post-tensioned connection on the moment distribution in a post-tensioned timber frame.

Analysis of post-tensioned timber beam-column connections has the following objectives:

- Analyse the deformation components of post-tensioned timber connections.
- Develop and validate equations to predict the stiffness of post-tensioned timber beam-column connections.
- Adapt the seismic design method using the MMBA to gravity frames.
- Develop design charts for easy estimation of connection stiffness.

Frames Frames with straight tendons are used for seismic research and can potentially also be used for gravity dominated frames. But frames with draped tendons have the extra benefit of the uplift forces at the deviators, making the solution preferable over straight tendons. With the information about the beams and the connections it is possible to investigate the global behaviour of post-tensioned timber frames. Experimental testing on one-bay and two-bay post-tensioned timber frames is performed to evaluate deflections, rotations and bending moment distributions. The testing results are used to validate connection models. Analysis of frames focusses on the effect of different connection models and compares the performance of frames with simply supported post-tensioned beams.

Experimental testing of post-tensioned timber frames has the following objectives:

- Evaluate connection behaviour of internal and external connections in post-tensioned timber gravity frames.
- Determine effectiveness of screw reinforcement in column interface.
- Gather data to validate connection models and frame models.
- Use Digital Image Correlation (DIC) techniques to verify measurement of deformation components and to acquire full displacement fields.

Analysis of post-tensioned timber frames has the following objectives:

- Develop a modelling approach for post-tensioned timber frames.
- Evaluate the effects of tendon elongation on the design of post-tensioned timber frames.
- Develop an analytical model for analysis of bending moments and deflections in post-tensioned timber frames.
- Evaluate the effects of different connection models on bending moments and deflections of post-tensioned timber frames.
- Perform a parameter study on the design of post-tensioned timber beams to identify critical design parameters.
- Compare the performance of simply supported post-tensioned beams with post-tensioned timber frames.

1.3 Limitations

The following limitations have been identified for the work in this thesis.

- All beam designs are based on box-sections, as they make for efficient cross sections and allow for draped tendons. Different geometries are possible and the design approach as presented in this thesis can be applied to different cross-sections.

- Nearly all work in this thesis is based on the material *LVL11*, which is the most common grade of LVL available in Australia and New Zealand. The presented methodology and design procedures can be used for different grades of LVL or different engineered timber products. But presented design tables might no longer be usable, and different factors might govern the design.

- Several of the material properties which are presented in this thesis are based on a small number of tests on a single batch of LVL. Therefore these numbers might not be fully representative for the variation between different batches. When designing structures the latest material properties should always be obtained from the manufacturer of the material.

- Calculation of long-term deflections of timber beams due to creep and post-tensioning losses are still part of on-going research and fall outside the scope of this research. As these values need to be calculated for design of beams and frames, the simplified design approach based on the New Zealand timber design standard (NZS 3603:1993) have been followed. In these calculations the assumption is made that the timber is in an indoor environment and thus a creep-factor (k_2) of 2 is applied. Post-tensioning losses have been estimated based on initial research (Davies and Fragiacomo, 2007; Giorgini, 2010) as 15% for beams and 25% for frames.

- Hybrid solutions, i.e. timber beams with concrete or steel columns, have not been considered in this research. But analysis of beams and connections for these systems is very similar and joint deformation components like

interface compression deformation and joint panel shear deformation will be less significant in the design.

1.4 STIC Research project at University of Canterbury

This research forms part of a larger project on multi-storey post-tensioned timber buildings at the University of Canterbury (Buchanan et al., 2011). Figure 1.3 shows several aspects of this project. The main scope of this research project is highlighted in green. Aspects marked in orange are touched upon in this research, but not explored in full depth. Aspects in red are analysed by other researchers and are not included in this research. A separate document, the *Post-Tensioned Timber Building - Design Guide* has been prepared and published by STIC. This design guide covers several aspects which are reported on in this thesis.

Multi-storey timber building can have different structural systems to resist vertical and lateral loading like frames (beams and columns), walls and floors. Of these three major components this research focusses on the frames. Walls and floors are included in the scope of other researchers within the larger STIC project (Sarti et al., 2012; Moroder et al., 2013).

Since the start of the research project on multi-storey post-tensioned timber buildings in 2005 the main focus has been on the seismic performance (Palermo et al., 2005). Extensive experimental testing and analysis of post-tensioned timber frames and walls under lateral loading was performed (Iqbal, 2010; Newcombe, 2011), and continues to be performed (Smith et al., 2012).

For any multi-storey building the fire performance is of importance. This aspect has been addressed by other researchers for beams (Spellman et al., 2012) and for floors (O'Neill et al., 2012). Constructibility and costs of any new construction system needs to be comparable, if not better, than existing technologies in order to be taken up by the building industry. This aspect has received the attention of several researchers over the last few years (John et al., 2011; Holmes et al., 2012; Wong, 2010; Amigo, 2010) and is left out of the scope of this research. Sustainability and thermal performance have been researched by Perez et al. (2008); Perez (2012) and are not included in this work.

Long-term post-tensioning losses in post-tensioned timber frames have been the focus of other researchers (Davies and Fragiacomo, 2007; Giorgini, 2010) and this is still a topic of on-going research. Friction of post-tensioning tendons is well researched in concrete structures and design data is readily available in design codes (Standards New Zealand, 2006c). Durability of tendons has long been a

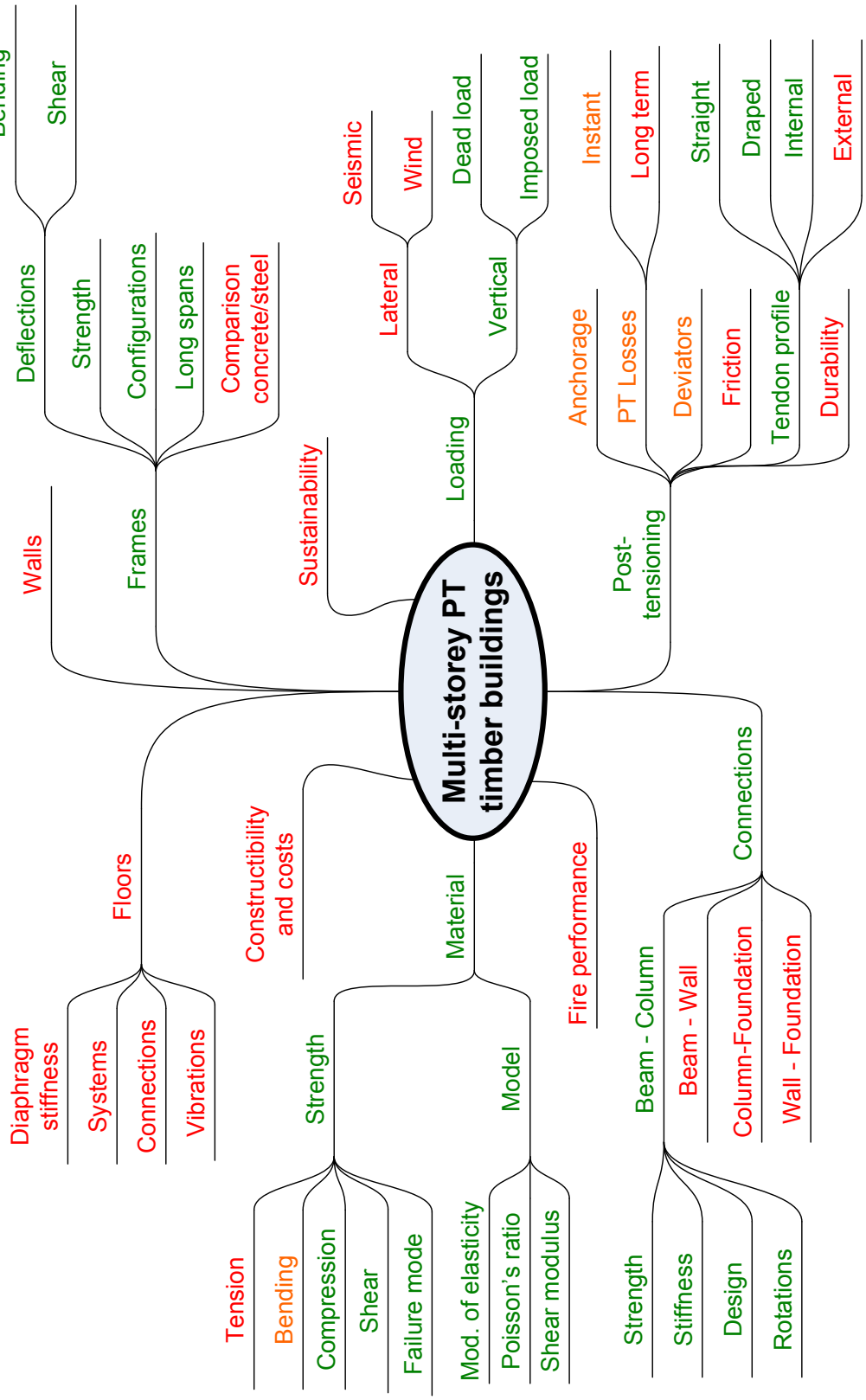

Figure 1.3: Full scope of multi-storey post-tensioned timber buildings project, in green are aspects on which this research focusses, in orange aspects which are touched upon and in red aspects which are outside the scope of this research

concern for concrete structures and design information (FIB, 2005a) and several commercial solutions are available (DYWIDAG, 2009; BBR VT International Ltd, 2010).

1.5 Thesis outline

The thesis is split in two main parts. Firstly experimental testing of material properties, beams, beam-column connections and frames. After the results of the experimental testing are presented, the focus shifts to analysis of the different components, including feasibility study and development of design methods.

Chapter 2 presents a literature review on the renewed interest in timber construction and current multi-storey timber buildings. The review extends also to post-tensioned concrete frames where the technology was developed. A separate literature study on LVL and its material properties is presented in the start of Chapter 3.

Experimental testing Chapter 3 presents a detailed study on several material characteristics of LVL. These material properties have been used to evaluate experimental testing data and for numerical modelling. It presents a literature overview of research into material properties of LVL and elastic properties of timber in general. Then it describes experimental testing and analyses on the compressive strength and stiffness of New Zealand Radiata Pine LVL in three different material directions (van Beerschoten et al., 2013b). Strength results from different loading configurations are compared with predictions based on analytical models and current design procedures. Analysis of the Poisson's ratios in the six different material directions, based on block compression testing, is presented. Experimental results of shear strength testing is described and digital image correlation (DIC) techniques have been used to determine the shear stiffness. Finally the experimental results are used to create a constitutive model for LVL (van Beerschoten et al., 2013a).

Chapter 4 describes experimental testing of four timber box beams. Firstly a summary of the designs is presented, then the test setup is described. Testing results of stiffness testing (without post-tensioning) are evaluated and material properties are derived from these tests. Next the results of stressing the beams is shown, followed by results of testing until failure. Digital Image Correlation (DIC) techniques have been used to measure displacements and strains. Results of this and comparisons with traditional instrumentation are shown at the end of the results section. The chapter finishes with conclusions which can be drawn

from the experimental testing.

Chapter 5 first describes a summary of the design of a prototype building and column reinforcements. Next, the experimental test setup is described in more detail, including instrumentation and loading protocol. Test results are presented and focus on connection stiffness and joint panel shear deformations. Implications of connection stiffness on the design of post-tensioned timber box beams are presented in the final section.

Chapter 6 describes the experimental testing campaign on a one-bay and two-bay post-tensioned timber gravity frame. The frame has draped tendons and the beam-column connection is made by the compression due to post-tensioning. Testing has been performed without post-tensioning and with different levels of post-tensioning force. The different deformation components of the beam-column connection have been investigated. Digital image correlation techniques are used to verify the deformation components.

Analysis Chapter 7 presents an analysis of post-tensioned timber beams. Four beams which were used for experimental testing have been modelled in a finite element program. Two analytical models are also presented, one for beams with straight tendons and one for beams with draped tendons. The analytical model and finite element model (FEM) results are verified against the experimental testing results. Comparisons of the failure loads with predictions based on the New Zealand timber design standard, NZS 3603:1993 (Standards New Zealand, 1993), and European timber design standard, EN 1995:2004 (CEN, 2004b), are presented. The analytical models were used to perform a parameter study on a range of post-tensioning forces and beam length for four different cross-sections. The main outcomes of the parameter study were used to develop a quick design procedure.

Chapter 8 looks in more detail into the deformation components of post-tensioned timber beam-column connections. The stiffness of these connections is of importance when modelling post-tensioned timber frames, as it influences deflections and moment distributions. The different stiffness contributions are presented; column rotation, joint panel rotation, interface compression and gap opening. Each component is analysed and analytical design equations are presented. The analysis is performed for full contact beam-column connections

and partial contact connections, whereby only the top and bottom flanges are in contact with the column. Design charts are presented for quick estimation of column rotational stiffness, joint panel shear stiffness and interface compression stiffness. Also shown is the procedure which combines the different deformation components for the use in a single rotational spring.

Chapter 9 presents the analysis of post-tensioned timber frames. Two different models are used for the analysis, a full frame model and a beam model. The full frame model requires the use of software programs to evaluate deflections, shear forces and bending moments, where the beam model can be evaluated using software programs or using analytical equations when applying a simplified connection behaviour. For the connection behaviour, the partial contact connection is used as this was proven to be more effective. For the detailed designs the non-linear connection behaviour is used, whereas for the simplified design an elasto-plastic connection behaviour is assumed. This makes it possible to create an analytical model for calculation of bending moments and deflections. The final part of the chapter presents a parameter study on a range of post-tensioning forces and beam lengths. This parameter study follows a very similar format as the parameter study on post-tensioned beams. After the parameter study, the performance of post-tensioned beams and frames is compared.

1.6 Glossary

Below is a list with abbreviations and terminology which is used throughout this thesis.

- CLT = Cross-laminated timber
- Continuous post-tensioning = post-tensioning tendons which run through the full length of a frame and are anchored at exterior columns, after stressing these tendons clamp the frame together
- Deviator = Component to allow tendons to change angle, in this thesis timber blocks are used
- DIC = Digital image correlation, technique to track a group of pixels through a series of images
- FEM = Finite element model
- Gap opening = Formation of a gap between beam and column in a post-tensioned connection
- Interface compression = Deformation of column interface under perpendicular to grain compression stresses
- Joint panel = Area of column which has a disturbed stress state due to the connection
- Joint panel shear deformation = Deformation in the joint panel due to shear stresses resulting from post-tensioning
- LVL = Laminated veneer lumber
- LVL11 = Standard LVL product available in New Zealand and Australia
- MBA = Monolithic Beam Analogy, calculation procedure to predict the performance of rocking connections
- MMBA = Modified Monolithic Beam Analogy, extension on the MBA procedure to include behaviour before decompression and after yielding of section
- PT = Post-tensioning
- STIC = Structural timber innovation company, joint Australian and New Zealand timber research organization to facilitate timber research
- UC = Unity check, design action (load, bending moment, deflection) divided by design limit (strength capacity, deflection limit)

1.7 Nomenclature

Greek symbols

α	=	Factor to account for shear area (-) ;
α	=	Angle of post-tensioning tendon at deviator (mrad) ;
β	=	Factor to calculate effective height of joint-panel zone (-) ;
χ	=	Factor to convert col. centreline moment to conn. moment;
δ_{int}	=	Displacement of column interface (mm) ;
ϵ	=	Strain (-) ;
ϵ_{pt}	=	Strain in post-tensioning tendons (-) ;
ϕ	=	Strength reduction factor from NZS 3063:1993 (-) ;
ϕ	=	Curvature of section (m^{-1}) ;
ϕ_{dec}	=	Curvature at decompression (m^{-1}) ;
ϕ_y	=	Yield curvature (m^{-1}) ;
γ_{shear}	=	Shear deformation (mrad) ;
η	=	Factor in MMBA procedure (-) ;
η	=	Beam deflection limit (-) ;
ν	=	Poisson's ratio (-) ;
ν_{ij}	=	Poisson's ratio for load in dir. i and extension in dir. j (-) ;
θ_b	=	Rotation due to bending deformation (mrad) ;
θ_{col}	=	Column rotation (mrad) ;
θ_{end}	=	Total beam rotation at end of beam (mrad) ;
θ_{imp}	=	Imposed connection rotation (mrad) ;
θ_{int}	=	Interface rotation (mrad) ;
θ_{jp}	=	Joint panel shear deformation (mrad) ;
θ_{perm}	=	Perm. conn. rotation due to plastic deformation (mrad) ;
θ_{pt}	=	Beam rotation due to post-tensioning (mrad) ;
θ_s	=	Rotation due to shear deformation (mrad) ;
θ_{sec}	=	Beam rotation due to second order effects (mrad) ;
θ_v	=	Beam rotation due to vertical loading (mrad) ;
σ	=	Stress (MPa) ;
σ_b	=	Bending stress (MPa) ;
σ_c	=	Compressive stress (MPa) ;

$\sigma_{c,90}$ = Compressive stress perpendicular to grain (MPa) ;
$\sigma_{f,c}$ = Average compressive stress of flange (MPa) ;
$\sigma_{f,c,max}$ = Maximum compressive stress of flange (MPa) ;
$\sigma_{f,t}$ = Average tensile stress of flange (MPa) ;
$\sigma_{f,t,max}$ = Maximum tensile stress of flange (MPa) ;
τ = Shear stress (MPa) ;
τ_{jp} = Shear stress in joint panel (MPa) ;
ω_{beam} = Reduction factor for beam shortening (-) ;
ω_{col} = Reduction factor for column shortening (-) ;
ω_{dev} = Reduction factor for deviator uplift (-) ;
ψ_{tl} = Factor for long-term post-tensioning losses (-) ;
Δ = Beam deflection (mm) ;
Δ_{dec} = Beam deflection at decompression (mm) ;
Δ_{dev} = Deviator deflection (mm) ;
$\Delta_{dev,dec}$ = Deviator deflection at decompression (mm) ;
ΔF_{pt} = Change in post-tensioning force (kN) ;
Δ_{imp} = Beam deflection after decompression (mm) ;
$\Delta_{imp,dev}$ = Deviator deflection after decompression (mm) ;
Δl = Change in length (mm) ;
Δl_{beam} = Shortening of beam (mm) ;
Δl_f = Shortening of frame (mm) ;
Δl_i = Initial shortening of beam (mm) ;
Δl_{pt} = Change in tendon length (mm) ;
$\Delta l_{pt,dev}$ = Tendon elongation due to deviator deflections (mm) ;
$\Delta l_{pt,gap}$ = Tendon elongation due to gap opening (mm) ;
Δ_{mon} = Deflection of beam with monolithic connections (mm) ;
Δ_y = Beam deflection at connection yield (mm).

Small Roman letters

b = Width of specimen (mm) ;
c = Neutral axis depth (mm) ;
d = Beam depth (mm) ;
e = Eccentricity of tendon within beam (mm) ;
$\overline{f}$ = Average strength value (MPa) ;
f_{05} = Fifth percentile strength value (MPa) ;
f_b = Bending strength (MPa) ;
f_c = Compressive strength (MPa) ;
$f_{c,1}$ = Char. compression strength in longitudinal direction (MPa) ;
$f_{c,2}$ = Char. compression strength in tangential direction (MPa) ;
$f_{c,3}$ = Char. compression strength in radial direction (MPa) ;
$f_{c,90}$ = Block compressive strength (MPa) ;
$f_{c,s}$ = Compressive strength incl. spreading effects (MPa) ;
f_k = Characteristic strength value (MPa) ;
f_m = Bending strength (EC5) (MPa) ;
f_s = Shear strength (MPa) ;
f_t = Tensile strength (MPa) ;
$f_{t,0}$ = Tensile strength parallel to grain (MPa) ;
f_v = Shear strength (MPa) ;
h = Height of specimen (mm) ;
h_b = Height of beam (mm) ;
k = Stiffness (kNm/mrad or kN/mm) ;
k_1 = Stiffness before decompression (kNm/mrad or kN/mm) ;
k_1 = Load duration factor for strength (NZS 3603:1993) (-) ;
k_2 = Stiffness after decompression (kNm/mrad or kN/mm) ;
k_2 = Duration of load factor (NZS 3603:1993) (-) ;
k_{24} = Size factor for timber (-) ;
k_{beam} = Vertical stiffness of beam (kN/mm) ;
k_c = Factor for increase in strength due to stress spreading (-) ;
k_c = Size effect factor in EC5 (-) ;
$k_{c,90}$ = EC5-factor based on loading config. and type of wood (-) ;
$k_{c,beam}$ = Compressive stiffness of beam (kN/mm) ;

$k_{c,col}$ = Compressive stiffness of column (kN/mm) ;
$k_{c,frame}$ = Compressive stiffness of frame (kN/mm) ;
k_{col} = Column rotational stiffness (kNm/mrad) ;
k_{eq} = Equivalent stiffness of frame and tendons (kN/mm) ;
k_{int} = Interface rotational stiffness (kNm/mrad) ;
k_{jp} = Joint panel shear stiffness (kNm/mrad) ;
k_{perp} = Perp. to grain stiffness of column interface (kN/mm) ;
k_{pt} = Stiffness of post-tensioning (kN/mm) ;
k_{scr} = Screw reinforcing stiffness factor (-) ;
l = Length of specimen (mm) ;
l_s = Length of screw (mm) ;
n = Number of beams in frame (-) ;
q = Distributed load (kN/m) ;
q_{long} = Long-term distributed load (kN/m) ;
s = Contact length in the grain direction (mm) ;
t_f = Flange thickness (mm^2) ;
t_i = Section thickness at location i (mm^2) ;
u_{con} = Beam deflections due to connection moment (mm) ;
$u_{dev,pt}$ = Deviator deflections due to post-tensioning (mm) ;
$u_{dev,sec}$ = Deviator deflections due to second order effects (mm) ;
$u_{dev,tot}$ = Total deviator deflections (mm) ;
$u_{dev,v}$ = Deviator deflections due to vertical loading (mm) ;
u_{long} = Long-term beam deflections (mm) ;
u_{pt} = Beam deflections due to post-tensioning (mm) ;
$u_{pt,long}$ = Long-term beam deflections due to post-tensioning (mm) ;
u_q = Beam deflections due to distributed load (mm) ;
$u_{q,long}$ = Beam deflections due to long-term distributed load (mm) ;
u_{sec} = Beam deflections due to second order effects (mm) ;
u_{tot} = Total beam deflections (mm) ;
u_v = Beam deflections due to vertical loading (mm) ;
w_c = Width of column (mm) ;
x = Distance from column interface (mm) ;
x_{pt} = Location of PT tendon rel. to bottom of connection (mm) ;
z = Distance to neutral axis (mm).

Capital Roman letters

A = Cross-sectional area (mm^2) ;
A_b = Cross-sectional area of beam (mm^2) ;
A_{col} = Column cross-sectional area (mm^2) ;
A_{eff} = Effective contact area (mm^2) ;
A_{pt} = Area of post-tensioning tendons (mm^2) ;
A_s = Shear area (mm^2) ;
A_{scr} = Area of screw (mm^2) ;
C = Compressive force (kN) ;
E = Modulus of elasticity (MPa) ;
$\overline{E}$ = Average modulus of elasticity (MPa) ;
E_{05} = Fifth percentile modulus of elasticity (MPa) ;
E_1/E_L = Modulus of elasticity in longitudinal direction (MPa) ;
$E_2/E_T/E_{90}$ = Modulus of elasticity in tangential direction (MPa) ;
E_3/E_R = Modulus of elasticity in radial direction (MPa) ;
$E_{k,mean}$ = Char. mean stiffness of modulus of elasticity (MPa) ;
E_{pt} = Modulus of elasticity of post-tensioning steel (MPa) ;
$F_{c,90}$ = Compressive force perpendicular to grain (N) ;
F_{dev} = Uplift force at deviator (kN) ;
F_i = Force in interface spring i (kN) ;
F_{int} = Comp. force at beam-column conn. interface (kN) ;
F_{max} = Max. force on specimen during exp. testing (kN) ;
F_{pt} = Post-tensioning force (kN) ;
$F_{pt,dec}$ = Post-tensioning force at decompression (kN) ;
$F_{pt,h}$ = Horizontal component of post-tensioning force (kN) ;
$F_{pt,i}$ = Initial post-tensioning force during testing (kN) ;
$F_{pt,max}$ = Maximum post-tensioning force during testing (kN) ;
$F_{pt,v}$ = Vertical component of post-tensioning force (kN) ;
F_v = Vertical point-load on beams (kN) ;
$F_{vertical}$ = Total vertical load on beams (kN) ;
G = Shear modulus (MPa) ;
G = Permanent loading (NZS 1170) (kPa) ;
G_{ij} = Shear modulus on i-plane for load in direction j (-);

H = Column height / inter-storey height (mm) ;
I = Second moment of inertia (mm^4) ;
I_{col} = Second moment of inertia of column (mm^4) ;
L_{eff} = Effective length (mm) ;
L_b = Beam length (mm) ;
L_{cant} = Cantilever length for seismic frame (mm) ;
L_p = Length of plastic hinge zone (mm) ;
L_{pt} = Length of post-tensioning tendons (mm) ;
M = Bending moment (kNm) ;
M^* = Design bending moment (kNm) ;
M_{con} = Connection bending moment (kNm) ;
$M_{con,max}$ = Max. connection bending moment during testing (kNm) ;
M_{cl} = Bending moment at centreline of column (kNm) ;
M_{dec} = Connection moment at decompression (kNm) ;
M_{max} = Maximum bending moment in beam (kNm) ;
M_{mid} = Mid-span bending moment (kNm) ;
M_n = Design bending moment capacity (kNm) ;
M_{pt} = Bending moment due to post-tensioning (kNm) ;
M_{sec} = Bending moment due to second order effects (kNm) ;
M_v = Bending moment due to vertical loading (kNm) ;
N = Normal force (kN) ;
N^* = Design compression force (kN) ;
N_n = Design compression capacity (kN) ;
Q = Imposed loading (NZS 1170) (kPa) ;
V = Shear force (kN) ;
V_{col} = Shear force in column (kN) ;
V_{jp} = Total shear force in joint panel (kN) ;
$V_{jp,con}$ = Shear force in joint panel due to conn. moment (kN) ;
N^* = Design shear force (kN) ;
N_n = Design shear capacity (kN) ;
Z = Section modulus (mm^3) ;
Z_h = Section modulus for half the section (mm^3) ;
Z_i = Section modulus for area above location i (mm^3).

Chapter II

Literature review

2.1 Renewed interest in timber construction

There is a renewed interest intimber as a construction material due to a current global focus on sustainability. Timber, as a material, has very good sustainable properties. For instance, the energy requirements for a timber column are much less compared to a similar steel or concrete column. Timber also functions as CO_2-storage during its lifetime, where for other products CO_2 is produced for making the construction material (Kolb, 2008).

Timber stores carbon and has much less embodied energy compared to other materials. But the biggest advantage of using timber is the opportunity for recovering energy from wood waste. This energy can be used instead of fossil fuel energy, hence reducing CO_2 emissions. Wood waste can come from all stages of harvesting and processing, and construction and demolition of timber buildings (Buchanan, 2007a).

The renewed interest has resulted in a 5-year timber research programme being funded and developed in order to increase the market share of timber buildings. In 2008, a research consortium named Structural Timber Innovation Company (STIC) was founded as a collective of major participants in the Australian and New Zealand timber industries and leading research organisations. The aim of this organization was to develop different timber engineering solutions involving innovative large-span timber building technologies primarily for use in non-residential buildings.

A survey by BRANZ (2007) has shown that commercial buildings are widely regarded as a huge opportunity area for wood. Calculations show that the volume of timber used in non-residential buildings can be increased by approximately 20%. The largest opportunities are in retail, industrial and education buildings.

Also market research in Australia has shown that there is a large opportunity for timber construction in non-traditional sectors. The biggest gains for timber framing are in medium to high rise residential buildings and in non-residential (commercial) buildings (FWPA, 2009).

2.2 High-rise timber construction

Large city fires during the late nineteenth century led to the introduction of fire protection measures, including legislative measures in several European countries, which discouraged or prohibited the use of wood frames in multi-story buildings (Mahapatra and Gustavsson, 2012). In 1991, the UK Building Regulations lifted the restrictions on the use of wood frames for multi-storey construction of more than three floors. Under current regulations, such constructions can go up to 18 meters (Mahapatra and Gustavsson, 2012) which allows for 5 stories. The Swedish legal restriction on construction of multi-storey timber buildings was repealed in 1994 (Mahapatra and Gustavsson, 2008); now there is no restriction on height of a wooden building except for that buildings with wood frames cannot be more than two floors if no sprinkler system is installed. In Germany federal regulations were revised in 2002 to allow construction of wood-framed buildings up to five storeys. The Swiss fire regulations of 2005 allow the use of timber structures in multi-storey medium-rise residential buildings with up to six storeys (Frangi and Fontana, 2010).

The Building Standard Law of Japan was revised in June 1998 and the potential to accept large-scale and high-rise timber buildings was added with provisions of the performance-based code (Sakamoto et al., 2004). In New Zealand multi-storey timber construction took a leap forward post 1992. This was when the New Zealand Building Code was introduced with the removal of the restriction on the number of storeys (then 3 stories) which could be built in timber. Since then, several buildings (mainly apartment buildings) have been built up to 5 storeys in height, but construction of buildings beyond this size has not been forthcoming (Banks, 1999). In Australia the building code was updated in 1997 whereby performance based alternatives were introduced, opening up the possibility of multi-storey timber buildings (Holmes et al., 2011).

A few countries, including the UK, Norway and New Zealand, put no automatic

limit on wood structures, instead relying on performance-based criteria that do not discriminate between materials. In the US however, building codes specify that all skyscrapers must be made from steel and concrete (Harris, 2012).

Many forms of timber buildings have been developed over the years. Figure 2.1 shows common structural forms for low- and medium-rise timber buildings. It can be seen that traditional timber buildings are mostly 2 to 3 storeys, although up to 6 stories is possible. Even modern platform buildings are unusual to reach more than 4 stories, although nowadays 10 storey buildings have been constructed, as is shown in the next section. But these platform buildings are mainly suitable for residential occupancies due to the large number of walls which limit open floor plans.

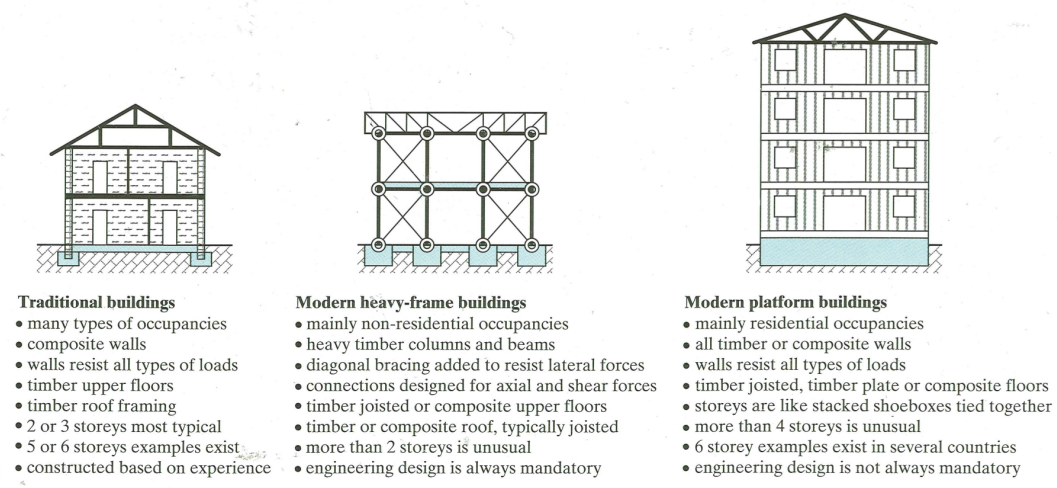

Figure 2.1: Common structural forms for low- and medium-rise timber buildings (Smith and Frangi, 2008)

Heavy-frame buildings for non-residential occupancies are usually not more than two stories. It can be seen that there is room for the development of a multi-storey timber construction system for non-residential occupancies which provides large open floor spaces. Compared to other construction systems frame construction permits longer spans with fewer internal columns. This system is appealing due to the clarity of the construction system and the open plans which give architectural freedom. This results in flexibility and adaptability in the design of the interior layout (Kolb, 2008).

Good ultimate limit state performance of timber buildings is often attributed to the high strength of timber, inherent robustness and the ability of connections to deform prior to failure. During seismic events good performance is also attributed to the high strength to mass ratio of timber which results in relatively low inertia forces. Serviceability limit state design is often governed by deflection and vibration criteria. The common method of using large continuous panellized wall and flooring systems create ideal transmission paths for vibration and sound waves (Smith and Frangi, 2008). Post-tensioned timber frames have the potential to create large open spaces without using continuous members whilst still having an efficient structural system due to moment resisting connections.

Analysis of low-rise buildings after extreme loading events has shown that connection failure and poor quality constructions are the primary causes of building damage (Foliente, 1998). Large prefabricated timber members are nowadays possible due to the development of engineered wood products such as glue laminated timber (Glulam), cross-laminated timber (CLT) and laminated veneer lumber (LVL). These prefabricated members reduce the amount of on-site construction. Post-tensioned timber connections, which can connect the large pre-fabricated elements, have a very predictable moment-rotation behaviour capable of large rotations. This system can resolve the problems of connection failure and poor quality construction and result in better structural performance under extreme loading.

2.2.1 Multi-storey timber buildings

The development of CLT made it possible to construct large timber panels, which can be used for floor and wall units. This material combined with the new fire regulations has opened up the way for tall timber buildings. Currently the tallest timber building is the ten-storey, 32m tall, Forte Building in Melbourne, Australia as shown in Figure 2.2a (Smith, 2012). Though the apartment building looks completely conventional inside and out, its structure is made from cross-laminated timber (CLT). The building will offer 23 boutique residential apartments and four townhouses.

This building took the title of tallest residential timber building from the nine-storey Stadthaus building in Murray grove, London (Figure 2.2b). That was

(a) Forte Building, Melbourne (c/o www.forteliving.com.au)

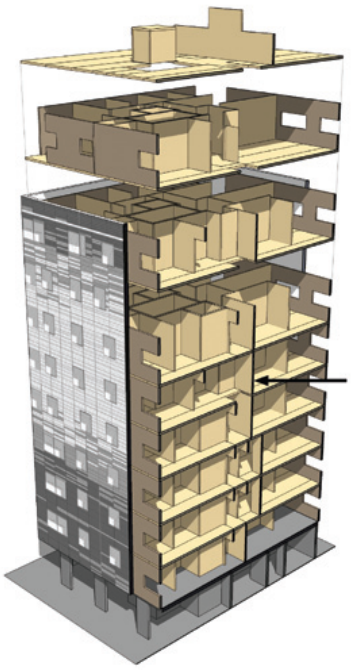

(b) Stadthaus building, London (Wells, 2011)

(c) Life Cycle Tower, Austria (Professner and Mathis, 2012)

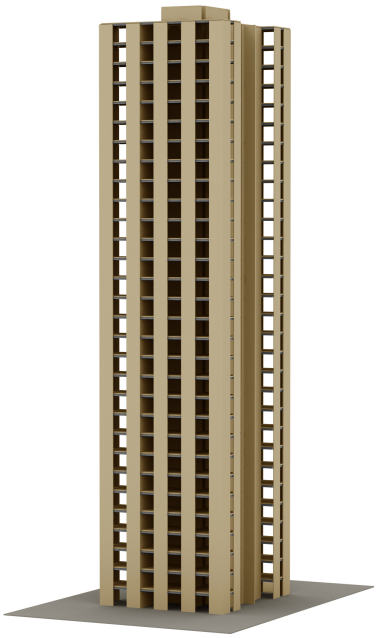

(d) Tall Wood Project, Canada (Green, 2012)

Figure 2.2: Examples of recent multi-storey timber buildings (a and b) and concepts for future buildings (c and d)

the first building of its height to have load-bearing walls and floor slabs as well as stair and lift cores constructed entirely from cross-laminated wooden panels (Wells, 2011). The tower houses twenty-nine apartments with a neighbourhood office on the ground floor. Stadthaus was assembled using a structural CLT panel system produced in Austria. As the prefabricated panels arrived on site they were immediately craned into position and fixed in place. Four carpenters assembled the eight-storey structure in twenty-seven days (Waugh et al., 2010). An overview of several more multi-storey buildings constructed with CLT can be found in a publication by Lehmann (2012).

Another recent developments is the LifeCycle Tower in Austria as shown in Figure 2.2c (Professner and Mathis, 2012), which is the concept of a new kind of urban construction: a hybrid timber high-rise building with up to 30 storeys and 100m in height. LCT ONE was constructed in 2012 as an eight-storey demonstration building in the form of an office block in Dornbirn, Austria. The structure has a concrete core, structural timber façade panels and timber-concrete composite floor panels spanning between 8 and 10 meters. The structural timber system was constructed at a rate of 1 storey per day due to a very high level of prefabrication of façade and floor panels.

New developments in Canada have led to plans for even taller timber buildings, up to 30 stories as shown in Figure 2.2d (Green, 2012). Their structural concept is based on the 'strong column - weak beam' balloon-frame approach using large timber panels as the vertical structure and floors, but using steel as material for the weak beams. Another concept for tall timber buildings is presented by van de Kuilen et al. (2011). This concept is based on CLT panels combined with a concrete core with structural outriggers. The outriggers are placed about every 10 stories and CLT panels are used for the storeys in between the outriggers. In this way buildings up to 150m tall can be constructed with up to 80% timber.

Nearly all of the above mentioned multi-storey timber buildings house apartments. This type of building allows for short floor spans and numerous walls, making it very suitable for CLT panels. Office and commercial buildings require large open floor spans. For this, a structurally efficient beam-column system is needed. Applying post-tensioning to beams can create long spans, as has been proven for many years in concrete.

2.3 Unbonded post-tensioning of concrete

Post-tensioning of concrete structures is a well developed technique. It was developed in the early 20th century with the intent to improve the overall structural performance of long-span beams and/or bridges. Nowadays it has been applied in a wide variety of structures like bridges, towers, silos and buildings (FIB, 2005b). A relatively new technique is the use of post-tensioning for moment resisting seismic frames. The technique has been developed during the PRESSS (PREcast Seismic Structural Systems) Program at the University of California, San Diego (Priestley et al., 1999). A particular connection named "hybrid" combines unbonded post-tensioning cables for self-centering with mild steel reinforcement bars for energy dissipation, as can be seen in Figure 2.3. This type of connection, called jointed ductile connection, relies on a controlled rocking motion between the structural members which has proven to have an excellent seismic performance, i.e. dissipation (mild steel) and self-centering (post-tensioned tendons) capacity. The concept has been successfully expanded to bridges (Palermo, 2004) and also to steel frames (Christopoulos et al., 2002).

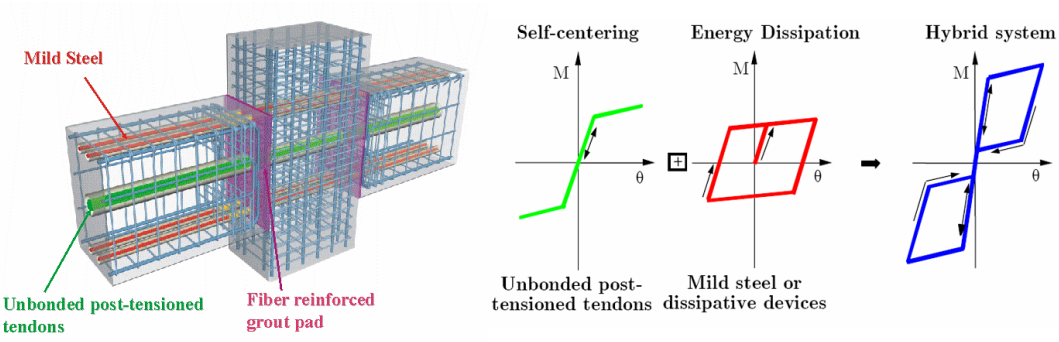

Figure 2.3: Precast concrete hybrid connection from PRESSS-Program (c/o S. Nakaki)

2.3.1 Post-tensioning using draped tendons

The unbonded post-tensioning technology for seismic frames has been extended to gravity dominated frames. This system, called the 'Brooklyn system', incorporates the structural system of a suspended bridge into a multi-storey building (Pampanin et al., 2004). Two alternatives were developed, one for small-medium span length

buildings with inclined bars (Figure 2.4a) and one for medium-large span length buildings with draped unbonded post-tensioning tendons (Figure 2.4b) to resist part of the gravity load. The technology has been tested on a 9m (centre to centre of column) one-bay specimen (Figure 2.4c) with an inter-storey height of 3.6m, based on a four storey office building prototype. The specimen was tested under monotonic cyclic loading up to 130mm vertical mid-span displacement (Figure 2.4d). It was found that the combined effect of prestress state within the member (i.e. uncracked section stiffness) and of the rigid joint condition (boundary condition for the beam similar to a fixed-end situation) resulted in significant reduction of vertical deformation/deflection under service loads.

(a) Cable stayed solution

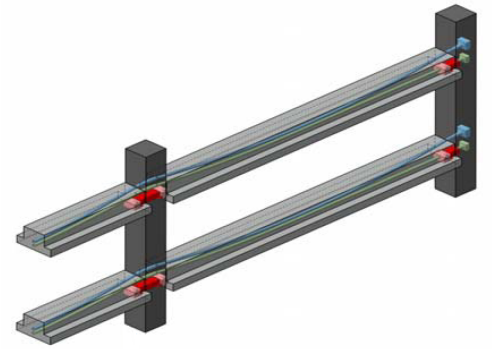

(b) Suspended solution

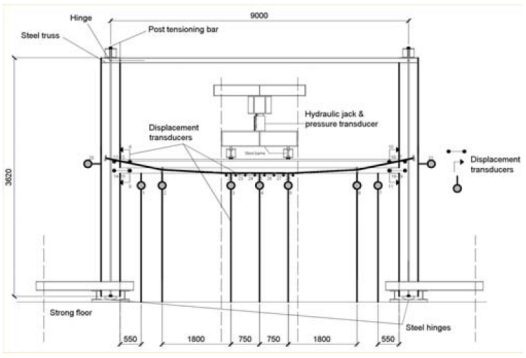

(c) Experimental testing layout

(d) Image of experimental testing

Figure 2.4: Development of the Brooklyn system (Pampanin et al., 2004)

At the time of publication in 2004, ten buildings with different use (commercial, offices, exposition, industrial, hospital), plan configurations, beam bay and floor

span length as well as storey height (up to six), had been designed and constructed in regions of low seismicity (gravity-load dominated frames) in Italy using the Brooklyn system (Figure 2.5) (Pampanin et al., 2004).

Figure 2.5: Example of concrete building with unbonded draped post-tensioning tendons (Pampanin et al., 2004)

Further experimental investigations using draped tendons under a combination of gravity and lateral loading on beam column joints have been carried out (Arnold, 2004). An internal beam-column joint was tested using draped tendons, as shown in Figure 2.6. Initially the specimen was loaded vertically with two times 130kN by two hydraulic actuators and subsequently lateral load was applied. A post-tensioning force of 550kN was applied to the specimen. The experimental testing results without additional energy dissipaters show a clear bilinear behaviour. The results are symmetric for positive and negative column drifts. Even though the tendons are eccentric at the connection, the combined effect of both connections results in a symmetric response. A larger amount of tendon elongation will occur at the side where gap opening is at the top and a lower amount of gap opening will occur at the side where gap opening is at the bottom. The combined effect will be the same as for a specimen with straight tendons.

After satisfactory joint behaviour was achieved research efforts moved to the flooring system, as it was found that gap opening can cause undesirable stresses and damage in concrete flooring systems (Muir et al., 2012). Experimental and

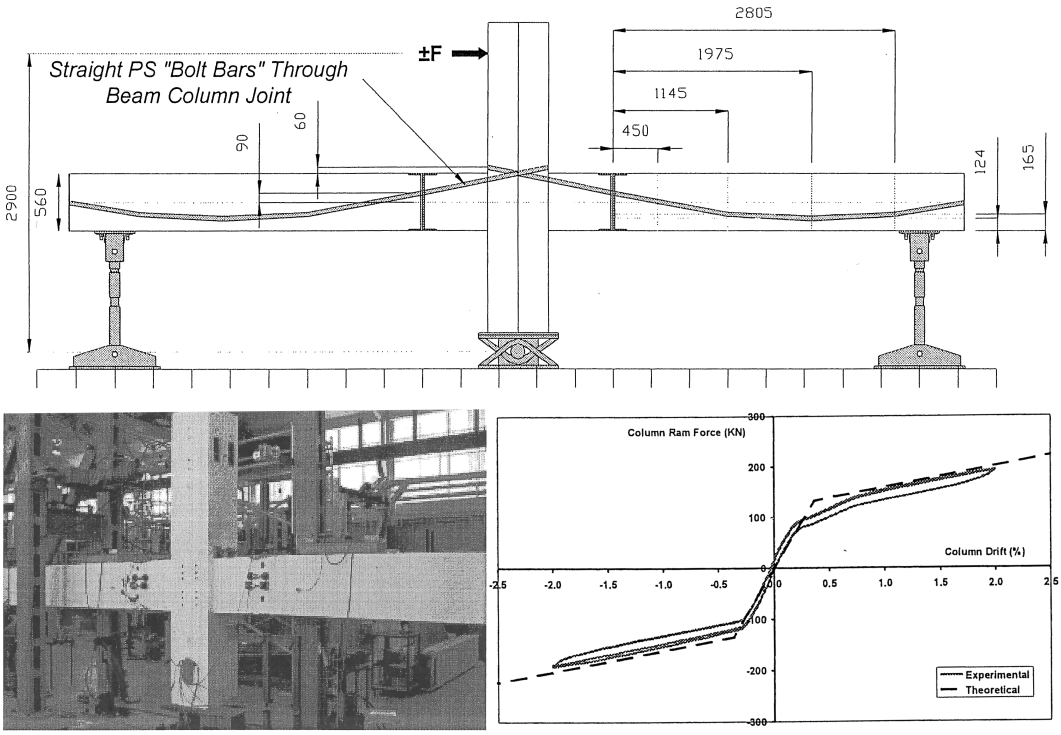

Figure 2.6: Experimental testing of concrete internal beam-column connection using draped post-tensioning tendons (Arnold, 2004)

analytical studies were performed on a 2 dimensional frame incorporating different beam-to-column connection details to minimise damage to the structural system of the floor by creating a "Non-Tearing (of the floor)" beam-to-column connection (Leslie, 2012; Muir et al., 2012).

The continuous and rapid development of jointed ductile connections for seismic resisting systems has resulted in the validation of a wide range of alternative arrangements, encompassed under the general umbrella of "hybrid" systems. A comprehensive experimental and analytical investigation into the behaviour of new connection arrangements of 2- and 3-dimensional, exterior beam-column joints was performed by Mesa (2012). Three main parameters were experimentally investigated: shear transfer mechanism, the sources and location of energy dissipation, and the longitudinal profile of post-tensioning tendons. Of specific interest was specimen HJ2, which incorporated a parabolic tendon profile and a double hinge solution at the interface, as shown in Figure 2.7. Again a very bi-linear force-displacement relationship was found, but this time the behaviour

was not symmetric as only an external connection was tested. Also the lateral force versus drift figure does not relate directly to a connection moment-rotation plot as the draped post-tensioning tendons create an initial connection moment at 0% drift. In the graph with the tendon force it can be seen that there is significant tendon elongation for positive drifts whilst there is much less tendon elongation for negative drifts.

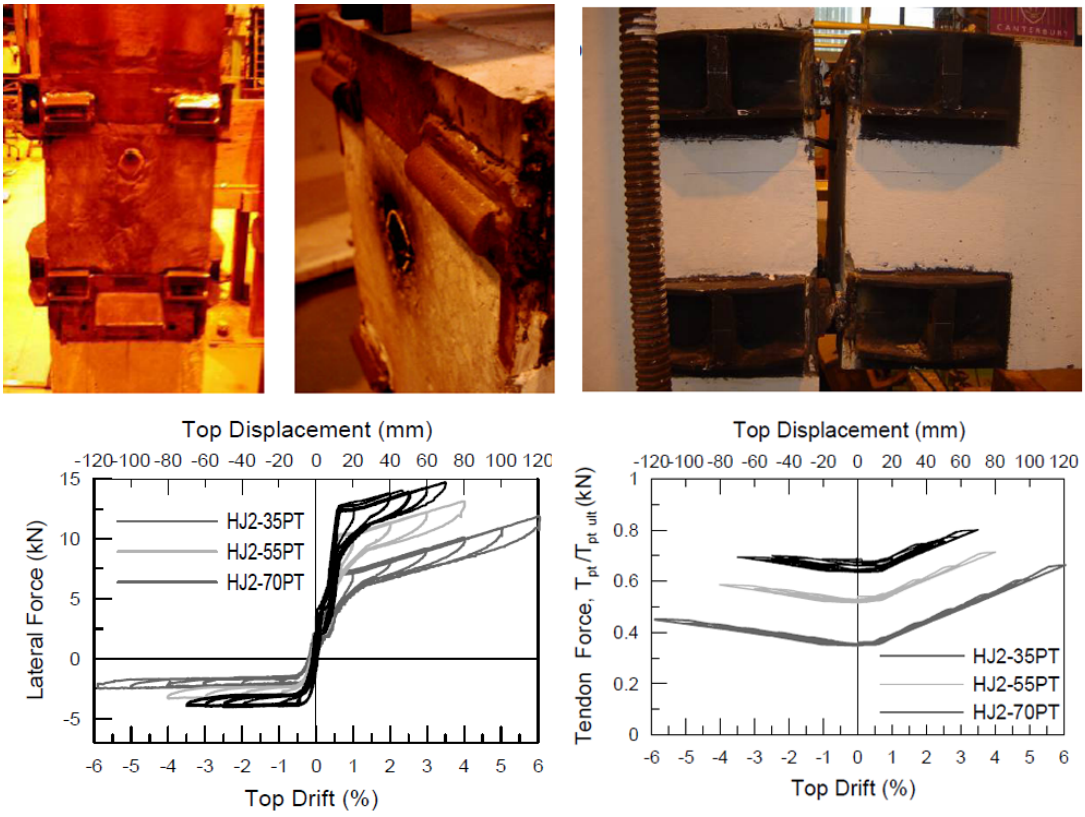

Figure 2.7: Experimental testing of double hinge solution with draped tendon placed eccentrically at the connection (Mesa, 2012)

The previously described technology is material independent, therefore recent developments in the concrete technology can also be applied to timber. There is especially the potential for further development of timber frames with draped post-tensioning tendons. The development of a double hinge solution can be used with timber box beams, where the main contribution in the compression zone is of the flange of the beam and only a very minor contribution comes from the webs.

2.3.2 Design procedures

The first application of unbonded post-tensioning was developed in the early 1990's at the University of California in San Diego. Partially debonded tendons were used in concrete beam-column joints (Figure 2.8a). Several benefits over more traditional joints were observed, namely keeping the post-tensioning tendons in the linear-elastic range, recentering capability, transfer of shear force through friction and ease of design. Limitations of the system were also identified, namely little energy dissipation, wide crack formation and large strains in the beam (Priestley and Tao, 1993).

A geometric non-linear force deformation plot was found and three points of interest were noted (Figure 2.8b), (1) decompression point where compression in the extreme fibre is lost, (2) point where the centroid of the beam reaches decompression and (3) point where the prestress steel yields and the bending moment is given as the post-tensioning force multiplied by the distance of the centre of the compression stress block to the centroid of the beam. Design equations for each of these points were presented and an equivalent bilinear relationship (Figure 2.8c) was used for non-linear time-history analysis of these joints under seismic loading.

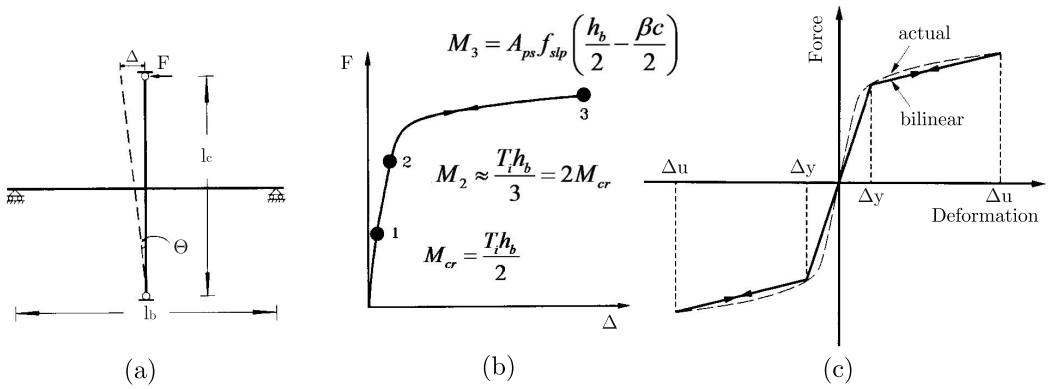

Figure 2.8: Design procedure for post-tensioned rocking connections as proposed by Priestley and Tao (1993), (a) schematics of internal post-tensioned concrete beam-column joint, (b) lateral force - deflection curve, (c) bi-linear approximation of load-deflection curve

Subsequently, for hybrid solutions a procedure named the monolithic beam analogy (MBA), was introduced as a member compatibility condition for design

of the moment-rotation behaviour of post-tensioned concrete joints (Pampanin et al., 2001). This consists of an iterative design procedure (Figure 2.9a) where a rotation at the connection is imposed, followed by an estimation of the neutral axis depth. The MBA equation (Figure 2.9b) is applied to calculate the concrete strain which can be used to calculate the concrete compressive force. Using geometric equations the elongation of post-tensioning steel can be calculated. The section equilibrium needs to be checked in order to verify if the correct neutral axis depth was guessed. Once equilibrium is satisfied the moment capacity belonging to the imposed rotation can be calculated.

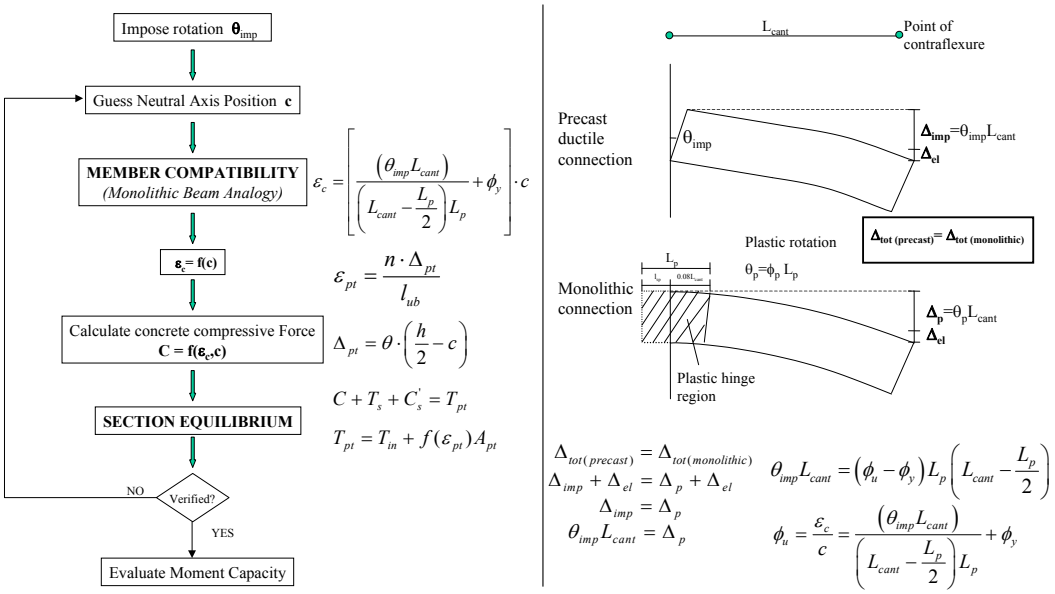

Figure 2.9: Development of MBA procedure (Pampanin et al., 2001), (a) moment-rotation analysis of ductile connection and (b) derivation of member compatibility

This MBA procedure was further developed and modified to include three different stages of connection behaviour, (1) before decompression, (2) between decompression and yielding of mild steel and (3) between yielding of steel and ultimate failure (Palermo, 2004). These three stages and main equations can be seen in Figure 2.10.

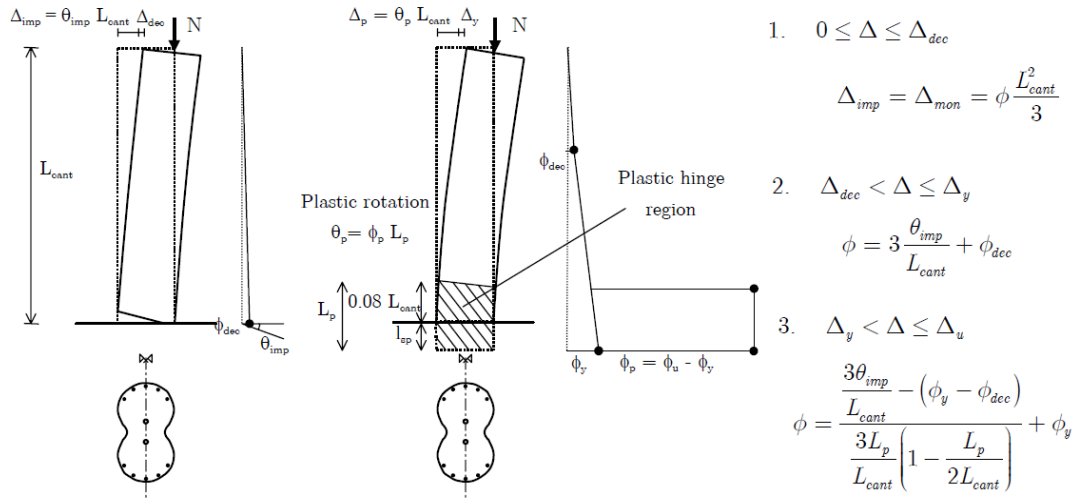

Figure 2.10: Development of modified MBA procedure (Palermo, 2004)

2.3.3 Unbonded post-tensioned concrete buildings

The development of post-tensioned concrete buildings has been applied in seismic areas around the world. An example is the 39 story, 128m high, Paramount building in San Francisco (Figure 2.11a) constructed in 2000-2001. This building consists mainly of apartments, although lower floors accommodate retail space and parking. The structure was the first major high rise building to use unbonded prestressed concrete frames (Englekirk, 2002).

Also in New Zealand buildings have been constructed with this technology. The first one was the Alan MacDiarmid building at Victoria University in Wellington, which was constructed in 2010 (Figure 2.11b). The building consists of six three-bay concrete frames, spanning 8.4m, which carry concrete double-T flooring units that span 9.9m. The beams were pretensioned off-site for gravity loads and to ensure dead load/erection sag was minimised. The beams were then centrally post-tensioned through the columns to provide the rocking mechanism. The external columns were also vertically post-tensioned to resist overturning loads and to assist with the rocking mechanism and re-centering capability at their base.

Unbonded post-tensioning technology was chosen because Victoria University, as a long-term building owner, considered the impacts of cost and benefits over

Figure 2.11: Examples of unbonded post-tensioned concrete and steel buildings, (a) Paramount building in San Francisco (Englekirk, 2002), (b) the Alan MacDiarmid Building in Wellington (c/o `http://www.victoria.ac.nz`), (c) Southern Cross Hospital in Christchurch (c/o `http://hospitals.southerncross.co.nz`), (d) Kilmore Street Medical Centre in Christchurch (Latham et al., 2013)

a longer period than a conventional developer. The results of a seismic loss assessment (for bridges) confirmed that a hybrid system provides a significant financial benefit when compared to a monolithic precast system (Marriott et al., 2009). Furthermore minimising seismic accelerations on the contents of this building was paramount when the research fit out and equipment cost far exceeded the cost of the building's structure and its fabric. And by post-tensioning the concrete frame, smaller sizes on the large spans could be achieved to allow more flexible services distribution (Cattanach and Pampanin, 2008).

New Zealand South Island's first PRESSS building, completed in 2010, is the Southern Cross Hospital in Christchurch (Figure 2.11c). This is a four storey (plus basement parking) concrete building with post-tensioned coupled walls in one direction and post-tensioned frames in the other. The hospital building sustained the very severe, beyond design level, sequence of earthquakes in September 2010 and February 2011, with no evident structural damage (Pampanin et al., 2011; Kam and Pampanin, 2011).

Not only is the unbonded post-tensioning technology used for concrete buildings, it has also been applied to steel structures. One example is the Kilmore Street Medical Centre, which is a new building located in the Christchurch central business district (Figure 2.11d). The building is three stories with over 5000m^2 of specialist medical facilities (Latham et al., 2013). Coupled braced steel frames provide the lateral-load resistance and the first application High Force-to-Volume lead extrusion devices, which provide viscous damping in parallel with replaceable yielding mild steel fuse-bars.

2.4 Post-tensioning of timber

2.4.1 Stress-lam bridges

The application of post-tensioning to timber structures is not new. A common application is transversely post-tensioned timber bridge decks. The post-tensioning force is used to clamp the laminates of the bridge deck together. This system has proven to be much more durable than the traditional nailed bridge decks and is widely used in North America (Ritter et al., 1995) and Australia (Crews, 2001). Longitudinal post-tensioning has also been identified as a possibility for for short-to-medium span timber bridges, possibly supplemented by transversely post-tensioning (Figure 2.12) (Palermo et al., 2011).

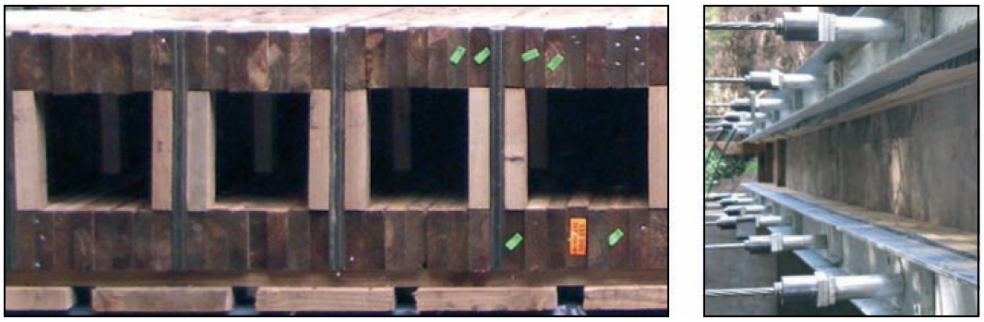

Figure 2.12: Example of transversely post-tensioned timber bridge deck (Palermo et al., 2011)

2.4.2 Prestressed beams with bond

Reinforcement of timber beams by means of prestressing with bonded tension elements has been researched as it can be easily incorporated in the manufacturing of glulam beams. The bonded tension elements can be prestressed (Figure 2.13) in order to create a precamber or not prestressed, in which case they only increase the ultimate strength of the beam. The tension elements can be made of Kevlar yarns (Galloway et al., 1996), fibre-reinforced plastics (FRP) (Triantafillou and Deskovic, 1991) or carbon fibres (Luggin and Bergmeister, 2001). These papers focus mainly on the performance of the adhesive to connect the tension members to the glulam beams and present experimental testing on specimens with spans

up to 2m. Therefore the technique seems suitable for short span beams, but the limited strength of the glue line prevents the application for larger spans.

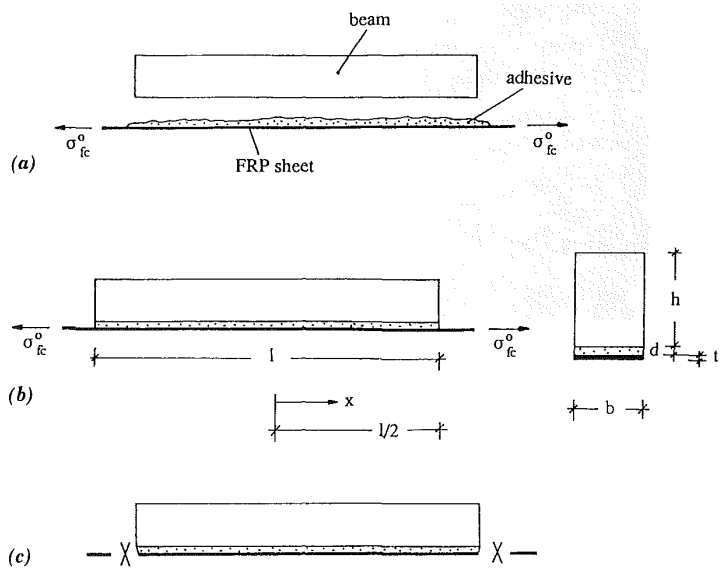

Figure 2.13: Post-Reinforcing with Pretensioned FRP Sheets: (a) FRP prestressing; (b) Curing of adhesive; (c) FRP ends released (Triantafillou and Deskovic, 1991)

2.4.3 Research into post-tensioned timber under lateral loading

The application of longitudinal post-tensioning in timber frames and walls is a relatively new technology. Over the past seven years Pres-Lam post-tensioned timber frames have been developed at the University of Canterbury (Buchanan et al., 2011) in collaboration with the international research consortium Structural Timber Innovation Company, STIC Ltd. The idea for the Pres-Lam system originated from the U.S. PRESSS research campaign. Historically seismic design of multi-story timber buildings was hindered by the limited strength and ductility of the connections (Buchanan and Fairweather, 1993), but the new Pres-Lam system resolves these limitations.

The development of engineered wood products, like laminated veneer lumber (LVL) and glulam, has made it possible to create large timber members with low variability and high design strength (Buchanan, 2007b). These materials make it

possible to manufacture large hollow core sections (beams and walls), which can be used in combination with post-tensioning technology. The so called 'Pres-Lam' system is a form of timber construction in which the timber members (frames and walls) are longitudinally post-tensioned in order to create jointed ductile connections (Palermo et al., 2005). Walls are post-tensioned to the foundation of a building, creating a rocking connection with a large compressive force, very similar to old Greek temples. In frames, continuous unbonded post-tensioning cables, anchored at exterior columns, clamp beams and columns together, creating semi-rigid moment resisting connections.

In 2005 a first experimental study was performed on the seismic performance of post-tensioned timber structures. An external beam-column connection, a wall-to-foundation and a column-to-foundation connection were tested (Figure 2.14 a-c). This testing was aimed at the ability to predict and understand the behaviour of the jointed systems to enable adequate design and detailing (Palermo et al., 2006). The study was a first step investigating the feasibility of using LVL as a multi-storey construction material. These initial tests have shown that the system provided excellent seismic behaviour (Newcombe et al., 2008). LVL is used as it is widely available in New Zealand, but research with glulam is also performed (Smith et al., 2012).

In 2008 a full-scale seismic connection test was performed on external and internal beam-column joints. This testing was performed to investigate additional complexities, such as high joint deformation and local damage mechanisms, when moving from small-scale to full-scale testing (Iqbal et al., 2010a). Also the prefabrication process was assessed. The column was tested with different reinforcing techniques. One was a large steel armouring plate, the other long, fully threaded screws. Also an unreinforced connection was tested. All tests were performed at different levels of post-tensioning.

The testing on small-scale post-tensioned beam-column connections identified that compression perpendicular to the grain in the column at the connection interface limited the connection moment capacity. The compression due to the post-tensioning force combined with the compression due to the connection moment created large localized stresses. The strength of LVL perpendicular to grain is about 25% of the strength parallel to grain, and the stiffness only 5%. This issue was more apparent in the full-scale testing, where a significant

Figure 2.14: Experimental testing of post-tensioned timber constructions at the University of Canterbury of (a) Beam-Column joint, (b) Wall-Foundation connection, (c) Column-Foundation connection, (d-e) two story building, (f-g) long span gravity beams

reduction in stiffness and post-tensioning forces was observed for unarmoured beam-column connections. A 30mm thick steel armouring plate at the connection interface was introduced and eliminated both problems (Figure 2.15). Long, fully threaded screws inserted as column reinforcement provided a reduction in post-tensioning losses but did not affect the reduction in stiffness. It should be noted that only a few screws were added to the joint and experimental testing with more screws might result in different findings.

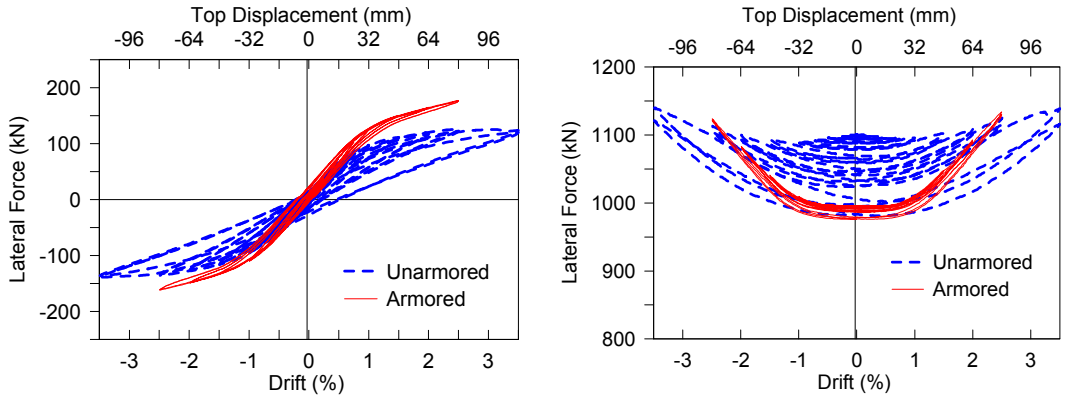

Figure 2.15: Comparison of load-drift and tendon force-drift figures for armoured and unarmoured beam-column connections (Iqbal et al., 2010b)

Further research resulted in a 2/3-scale test of a two story building (Newcombe et al., 2010c) (Figure 2.14 d-e). This testing has shown that the system was fully re-centering and had no significant damage at 2% drift. But additional mild steel reinforcement at the beam-column connections in the frame was found to be essentially ineffective at increasing the stiffness and energy dissipation due to significant elastic deformations. For different frame geometries, where the elastic deformation of the members is less, the additional mild steel reinforcement may be more effective.

Not only in New Zealand, but also at the ETH in Zurich (Switzerland) is research being performed on post-tensioned timber structures (Wanninger and Frangi, 2013). A post-tensioned beam-column timber joint has been developed using glued laminated timber (Spruce, GL24h) with local strengthening of the joint using hardwood (Ash, D40). This hardwood is placed at the at the bottom of the beam and in the joint panel zone in the column (Figure 2.16a). Shear

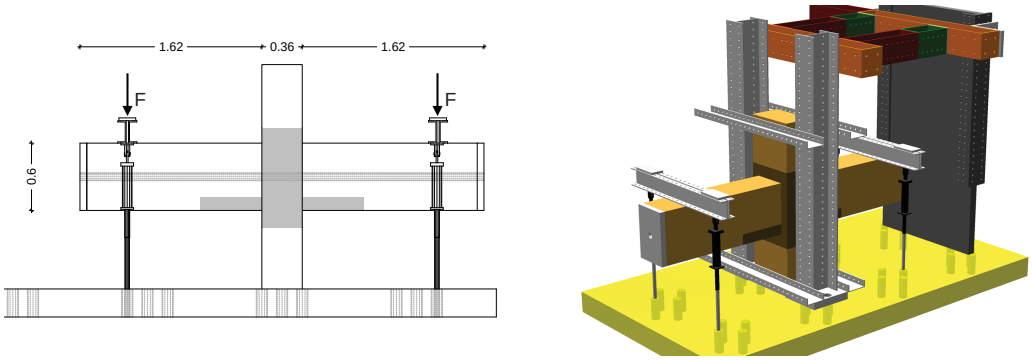

(a) Experimental testing setup

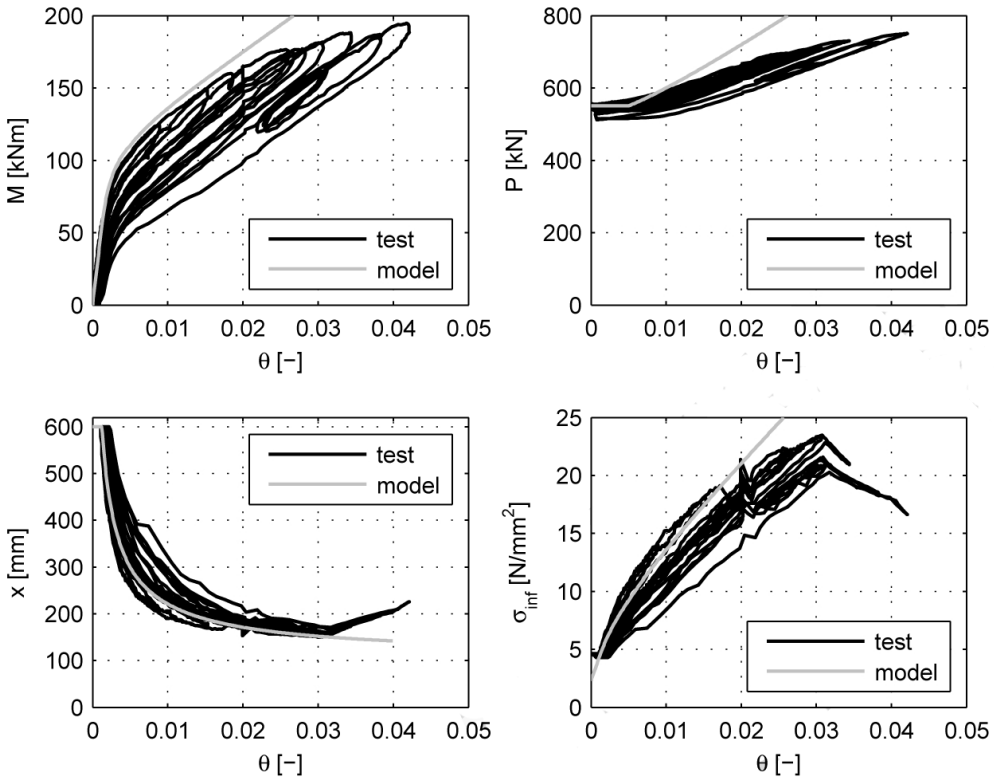

(b) Testing results

Figure 2.16: Experimental testing of post-tensioned timber connection using hardwood strengthening in the joint region (Wanninger and Frangi, 2013)

transfer at the connection was realized by friction and by creating notches into the column. Experimental testing has been performed on an internal beam-column joint with various levels of post-tensioning force, ranging from 300kN to 700kN. Testing showed a stable flag-shaped moment-rotation curve, except for a loss in post-tensioning due to hydraulic leakage. An analytical model has been developed which fits the experimental testing moment-rotation performance well, but over predicts the increase in post-tensioning force (Figure 2.16b).

2.4.4 Research into post-tensioned timber under gravity loading

The first application of longitudinal post-tensioning of timber beams was reported by Riedlbauer (1978). He showed structural schemes for thin web box beams and T-shaped beams with straight and draped tendons. His drawings show beams with a length of upto 10m and a section height of 1.3m.

At the University of Canterbury, the use of longitudinal post-tensioning was first applied to beams intended for use in long-span flooring systems. The stiffness and strength of composite laminated veneer lumber (LVL) and concrete beams was tested. Quasi-static bending tests and impact tests were conducted on four, 6m long specimens to observe the failure mechanisms and to estimate the static and dynamic properties of the systems. Specimens had a T-shape cross-section and used straight or draped tendons (Deam et al., 2008). Although the specimens were post-tensioned the main focus was on the shear connectors between the LVL beam and concrete topping.

In 2009 research was performed on the design of timber beams with draped post-tensioning tendons under gravity loading (Palermo et al., 2010). A nine meter simply supported beam and a half-scale continuous beam have been tested for serviceability loads (Figure 2.14 f-g). Testing was performed on beams with straight, internally draped and externally draped tendons (Figure 2.17). For draped tendons timber blocks were used as deviators. For testing with straight and draped tendons 6 strands (12.7mm diameter) each stressed up to 130kN were used and for the external tendons only 2 strands were used due to the increased eccentricity.

The results of these tests have shown that although the tendons do not increase the stiffness of the beam, they do create a precamber which helps to satisfy the

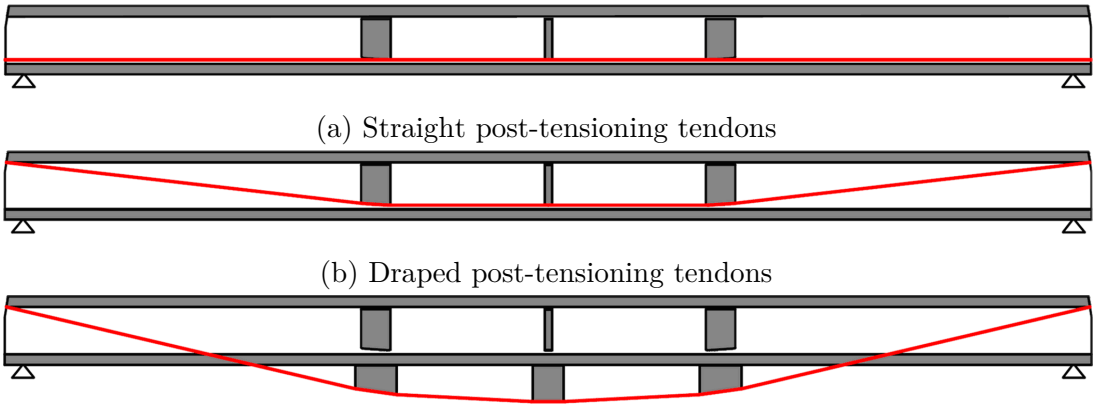

(a) Straight post-tensioning tendons

(b) Draped post-tensioning tendons

(c) External post-tensioning tendons

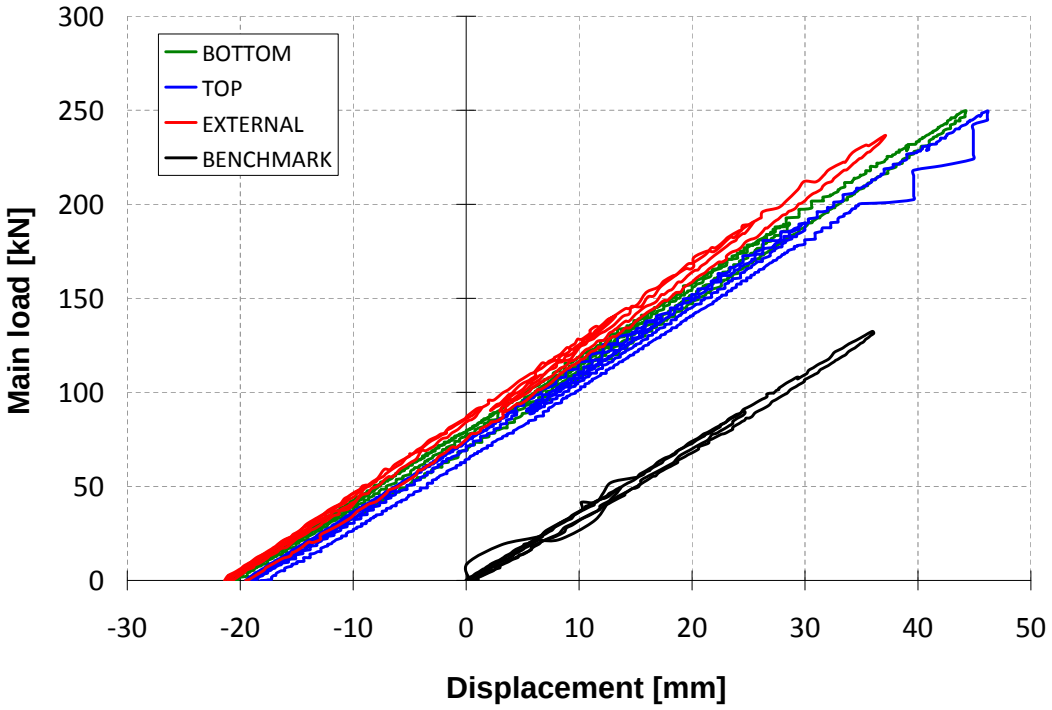

(d) Load-deflection results

Figure 2.17: Experimental testing of timber box beams with different tendon profiles under vertical loading (Lago and Dibenedetto, 2009)

serviceability limit states . It was identified that further research was needed for the possibility of using continuous post-tensioning tendons which run through the column in gravity frames.

The design of beams with draped post-tensioning tendons is complicated due to geometric non-linearities. As the beam deflects the unbonded tendons elongate and their post-tensioning stress increases. This stress increase creates a larger upwards force (due to the draped profile) and reduces the deformation. Therefore an iterative design procedure is needed as presented by Palermo et al. (2010).

2.4.5 Other post-tensioned timber research

Constructibility For any new building system to find a place in the market it has to be cost effective and have a fast construction time. Both aspects have been researched and recently published (John et al., 2011). It has been shown that the construction of the NMIT building in Nelson was similar in construction cost and time as a steel alternative. A concrete alternative would have been slightly cheaper, but would take longer to construct. It should be noted that at the time of this publication the post-tensioned timber system is still new to the market and cost improvements are expected once more similar buildings will be constructed. Similar results have been found by other research (Smith, 2008; Amigo, 2010; Newcombe et al., 2010b).

Screw reinforcement Research indicated that screw reinforcement can effectively reinforce timber in compression perpendicular to grain (Bejtka and Blass, 2006). Screw manufacturers have already published methods to calculate the strength of timber reinforce with screws (Deutsches Instutut fur Bautechnik, 2011). But very limited information is available for the strength of screws in LVL and no guidance is given to calculate the compressive stiffness.

Long, fully-threaded screws can also be used effectively as fasteners, e.g. for construction of timber corbels (Carradine et al., 2009). A significant increase in strength and stiffness can be obtained when installing the screws at a 45 degree angle (Bejtka and Blass, 2002). This technique can be used to improve design of timber corbels (Carradine et al., 2010). Recently the effect of screw reinforcement on the compressive stiffness of timber in compression perpendicular to grain was

tested (Watson et al., 2013). Experimental testing showed an increase in stiffness of up to 2.5 times.

Fire performance For any multi-storey building the fire performance is of importance. This aspect has been addressed by other researchers for floors (O'Neill et al., 2012) and for beams (Spellman et al., 2012). Three 4.36m span post-tensioned timber beams were exposed to standard fire loading (Figure 2.18). Each of the test beams were glued box beams made from 63mm LVL and were of varying external dimensions. Each beam was intended to demonstrate a specific failure mechanism at approximately 60 minutes of fire exposure. The failure mechanisms demonstrated were a shear failure in the lower corner of due to corner rounding, and a combined bending and compression failure at the end of the beam. Also tested during the full-scale testing were five different forms of anchorage fire protection.

Long-term performance The long-term behaviour is an important aspect of post-tensioned timber building design. The creep behaviour of timber could result in a significant reduction of the initial post-tensioning force. A first study has shown that losses of up to 34% could occur, especially due to the compressive stresses in the perpendicular to grain direction, which is the case in the columns (Davies and Fragiacomo, 2007). Another study has shown that screw reinforcement can be used to reduce the long-term losses due to compression perpendicular to grain stresses (Crocetti and Kliger, 2010). An analytical approach has been formulated for prediction of post-tensioning losses (Giorgini, 2010). It has been calculated that the elastic losses can be up to 22% and the time dependent losses up to 28%. A long-term experimental test has been setup and is currently being monitored.

2.4.6 Design procedures

Initially a design procedure for post-tensioned timber connections was presented (Newcombe et al., 2008) based on the Monolithic Beam Analogy (MBA) procedure developed for concrete (Pampanin et al., 2001; Palermo, 2004). But where the initial stiffness of a pre-cast post-tensioned concrete frame is effectively infinite,

Figure 2.18: Fire performance of three post-tensioned timber box beams (Spellman et al., 2012)

for timber connections there is a clear initial stiffness due to perpendicular-to-grain deformation in timber columns. This results in a connection rotation before decompression. Therefore the timber design procedure introduced an effective modulus of elasticity to account for the soft behaviour of the column under compression perpendicular to grain.

Two years later, it was concluded that while the MBA may be appropriate for concrete or steel structures, where the initial stiffness of the rocking connections is effectively infinite, they can lead to inaccurate predictions of the initial strength of softer (perpendicular-to-grain) timber connections at small rotations (Newcombe et al., 2010a). A simplified design procedure was presented based on an empirical relationship for the neutral axis depth, as shown in Figure 2.19.

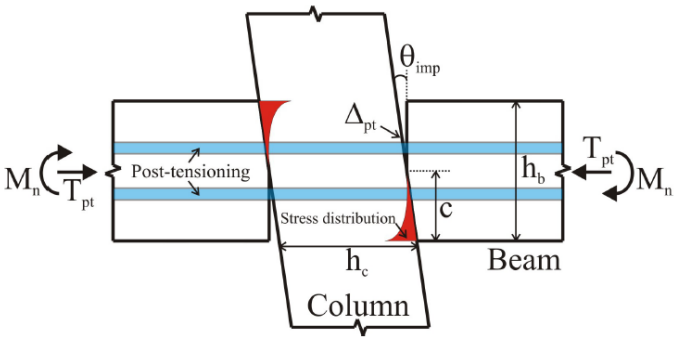

$$c = \alpha\beta h_b \left(\frac{0.054}{\sqrt{\theta_{imp}}} - 0.12 \right)$$

$$\alpha = \frac{390}{E_{perp}} + 0.42$$

$$\beta = \frac{f_i}{4.5}$$

Figure 2.19: Simplified empirical design procedure for timber rocking connections (Newcombe et al., 2010a)

Further research raised several points which questioned the accuracy of the MBA procedure (Newcombe, 2011). This included the larger neutral axis depth, the introduced effective modulus of elasticity and the linear strain profile. Therefore, a new empirical design procedure was development, based on the Pasternak Model (Pasternak, 1954) which is usually applied for modelling foundations on a semi-infinite soil continuum. In this model the perpendicular-to-grain stiffness of the timber is represented by axial springs, while the shear stiffness of the timber is represented using a constrained displacement profile. The design procedure, shown in Figure 2.20, has been adapted for timber parallel to grain reinforcement and steel plate reinforcement, but could not be validated due to lack of appro-

priate experimental testing data. It was concluded that the Pasternak Model sets a sound basis for deeper understanding of the response of rocking timber connections but further refinement is necessary.

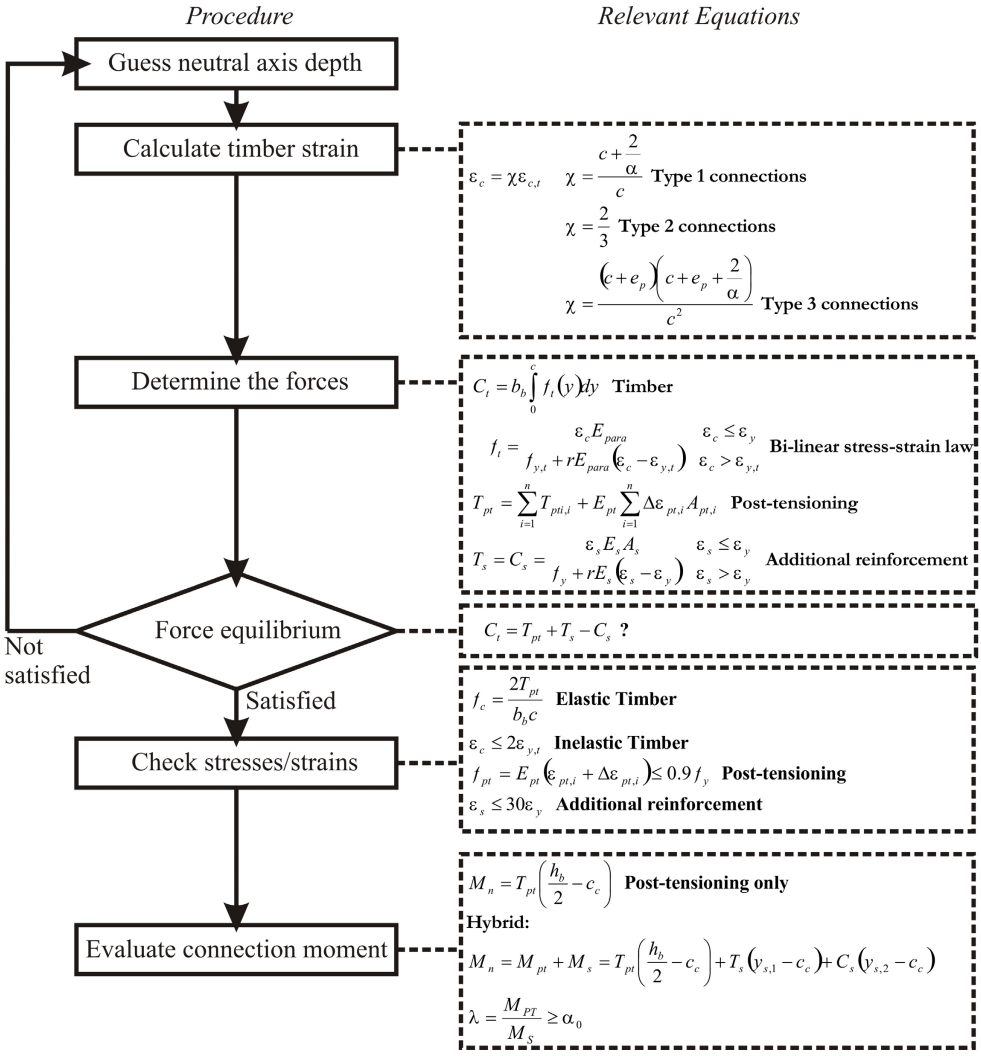

Figure 2.20: Empirical design method based on Pasternak Model (Newcombe, 2011)

This research project performed additional testing on post-tensioned timber connections and used new testing results to verify proposed design procedures. The applicability of the MBA procedure to gravity frames is also explored.

2.4.7 Post-tensioned timber buildings

Several multi-storey timber buildings have been constructed in recent years in New Zealand. The first building was a three storey Pres-Lam building in Nelson (Figure 2.21a). The seismic resisting system of the building relies on several pairs of coupled LVL shear walls (189mm thick x 3m wide x 12m tall) that incorporate four 32mm diameter post-tensioned steel bars through a central duct. A series of U-shaped steel plates placed between the walls form a coupling mechanism, and act as dissipaters to absorb seismic energy (Devereux et al., 2011). This building has been extensively monitored to measure seismic performance (Gaul et al., 2012) and long-term performance of the post-tensioned shear walls (Morris et al., 2012). A study on initial cost, life cycle cost, time of construction and comparisons with similar concrete and steel buildings show that the building was cost competitive and at least as fast to construct (John and Buchanan, 2012). A further study performing a life cycle assessment and carbon footprint analysis reported that the operation of the building is the dominant contributor to lifetime energy consumption and that operational energy is almost independent of structural material (Buchanan et al., 2012).

The Carterton Events Centre (Figure 2.21b), constructed in 2011, includes a 300-seat main auditorium using the post-tensioned timber wall as the main structural seismic system. The auditorium features 11 LVL shear walls, each 6.7 metres high, 2.4 metres wide and 180 millimetres thick. MacAlloy bars were used to apply the post-tensioning and internally epoxied mild steel bars were installed to provide energy dissipation (Curtain et al., 2012).

The Massey's College of Creative Arts (CoCA) building was constructed in 2011 using post-tensioned timber seismic frames (Figure 2.21c). On top of a concrete plinth, two storey post-tensioned timber frames were designed to resist seismic loading (Cattanach and Davies, 2013). The bays spanned 9m and 6.5m and featured draped tendons to balance part of the dead load of the flooring system. Two steel deviator pins were placed in the 9m bay and a single deviator pin was placed in the 6.5m bay. Tendons were fully exposed and in case of fire the timber structure itself was sufficiently strong. Timber blocks were glued onto the outside of the columns in order to transfer the post-tensioning force from one beam to the next in compression parallel to grain. This was done to minimize

(a) NMIT building, Nelson, NZ (c/o `http://www.isjarchitects.co.nz`)

(b) Carterton Events Centre, Carterton, NZ (c/o `http://www.cartertonec.co.nz`)

(c) Massey University Building, Wellington, NZ (c/o `http://www.massey.ac.nz`)

Figure 2.21: Examples of recently constructed/designed multi-storey post-tensioned timber buildings

the long-term post-tensioning losses.

With the redevelopment of the Christchurch central business district, several engineering companies are looking at incorporating post-tensioned timber frame and wall systems. The first buildings to use this technology in Christchurch is the Merritt Building (Figure 2.22a) which started construction in late 2012. This three storey building features one-bay post-tensioned frames in one direction and a concrete shear wall in the lengthwise direction. Each frame incorporates seven 15.2mm diameter post-tensioning strands, stressed up to 55% of the ultimate load, and four energy dissipators per beam-column connection. The frames were stressed whilst lying flat on the ground and lifted in place after stressing.

Opus International Consultants has designed a new Pres-Lam structure to replace Trimble Navigation's Christchurch office and warehouse (Figure 2.22b), which was destroyed by a fire in 2011. This building is currently under construction and upon completion, it will be the first building in New Zealand to use both post-tensioned LVL frames and post-tensioned LVL walls with energy dissipating devices for the load resisting system.

Also in Zurich, Switzerland, is a post-tensioned timber building under design. A two-storey building for the ETH House of Natural Resources will soon start construction (Figure 2.22c). This building incorporates technology developed at the Swiss Federal Institute of Technology in Zurich and incorporates hardwood in the joint region for local strengthening.

The construction of these buildings show that post-tensioning of timber buildings is a viable technology and opens up the way for multi-storey timber buildings for office and commercial use. Most of these buildings use post-tensioning only to resist lateral loads. The exceptions being the Massey University building which uses draped tendons and the Merritt building and ETH House of Natural Resources which use straight tendons to resist lateral and gravity loading. There is still the potential to improve the concept of post-tensioned timber buildings to gravity dominated frames.

(a) Merritt Building, Christchurch, NZ (c/o `http://www.sheprout.com`)

(b) Trimble navigation office, Christchurch, NZ (c/o A. Buchanan)

(c) ETH House of Natural Resources, Zurich, Switzerland (c/o mml architekten)

Figure 2.22: Examples of recently constructed/designed multi-storey post-tensioned timber buildings (continued)

Part II

Experimental testing

Chapter III

Material properties of LVL

3.1 Introduction

Several characteristic values of mechanical properties commonly used in engineering practice are supplied by New Zealand and Australian manufacturers. But post-tensioned timber construction with complex connection behaviour require more material properties than those provided by manufacturers. For column design, the strength and stiffness perpendicular to grain is essential, and for deviators and anchorages the shear strength and tensile strength perpendicular to grain are needed. Furthermore, finite element modelling (FEM) requires specific material properties to define the constitutive matrix.

Experimental testing of LVL material properties has the following objectives:

- Determine the strength and stiffness of LVL under compression in different orientations.
- Determine the strength and stiffness of LVL in shear.
- Develop a three-dimensional material model for LVL for the use in FEM.
- Define non-linear stress-strain curves curves for LVL in compression that can be used for FEM.
- Give guidance on characteristic strength and stiffness values that can be used for timber design.

This chapter presents a detailed study on several material characteristics of LVL. These material properties have been used to evaluate experimental testing data (Chapters 4 to 6) and for numerical modelling (Chapter 7). Section 3.2 presents a literature overview of research into material properties of LVL and elastic properties of timber in general. Section 3.3 describes experimental testing and analyses on the compressive strength and stiffness of New Zealand Radiata

Pine LVL in three different material directions. The properties of 45mm thick LVL, 63mm thick LVL and 36mm thick cross-banded LVL are evaluated. Strength results from different loading configurations are compared with predictions based on the model proposed by van der Put (2008) and by EN 1995:2004 (EC5) (CEN, 2004b) design procedures.

In Section 3.4 the evaluation of Poisson's ratios is presented in the six different material directions. The analysis is based on block compression testing. Section 3.5 presents experimental results of shear testing on Radiata Pine LVL, performed according to European standards EN14374 (CEN, 2004a) and EN408 (CEN, 2010) as they specify shear tests with a relatively uniform shear distribution. The shear strength has been evaluated and digital image correlation (DIC) techniques have been used to determine the shear stiffness. Section 3.6 uses data from compression and shear testing and derives a constitutive model for LVL, needed for the formation of a 3D elastic material model.

3.2 Literature study

3.2.1 LVL as a material

For engineering purposes timber can be regarded as an orthotropic material, which means that material properties vary depending upon the orientation. Being a naturally grown product, there are numerous factors which influence the strength and stiffness, resulting in significant variability of material properties. Laminated Veneer Lumber (LVL), made from rotary peeled veneers glued together using Phenol Resorcinol Formaldehyde resin, has the advantage that defects are distributed, making the material properties relatively homogeneous compared to sawn timber (Buchanan, 2007b). Within LVL there is still variability, caused by factors such as layer property manipulation, peeling methods, veneer thickness, densification and moisture content.

For LVL, three clearly defined material directions can be assigned, as there is no growth ring angle influence. These are shown in Figure 3.1: 1) longitudinal - parallel to grain; 2) tangential - perpendicular to grain and parallel to glue lines; and 3) radial - perpendicular to grain and perpendicular to glue lines.

Several characteristic values of mechanical properties commonly used in engineering practice are supplied by New Zealand and Australian manufacturers

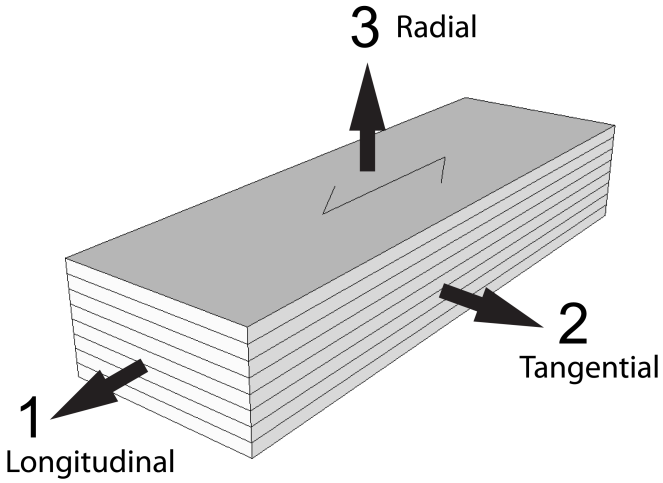

Figure 3.1: LVL material directions

Table 3.1: Comparison of LVL characteristic compression strength (f_c) and stiffness (E) as specified by several manufacturers. All values in MPa.

Material	Timber species	$f_{c,1}$	$f_{c,2}$	$f_{c,3}$	E_1[(a)]	E_2	E_3
NPIL LVL11	Radiata Pine	45	12	-	11000	-	-
NPIL Cross-banded LVL	Radiata Pine	no values specified					
CHH hySPAN	Radiata Pine	45	12	-	13200	-	-
Wesbeam e-beam E13	Maritime Pine	47	12	-	13200	-	-
Kerto-S (parallel)	Spruce	35	6.0	1.8	13800	430	130
Kerto-Q (cross-banded)	Spruce	26	9.0	2.2	10500	2400	130

(a) Characteristic values for E_1 are based on four-point bending tests

(Carter Holt Harvey, 2008; Nelson Pine Industries Limited, 2010; Wesbeam, 2005) as shown in Table 3.1. European LVL producer MetsäWood (2009) supplies a much wider range of strength and stiffness values for their normal LVL (Kerto-S) and cross-banded LVL (Kerto-Q).

There have been several studies on mechanical properties of LVL, but many of these were targeting factors during the production process, such as applied pressure (Shukla and Kamdem, 2008), layer composition (Burdurlu et al., 2007) and different adhesives (Uysal, 2005). Other research provided data comparing strength properties for different timber species (Ayd n et al., 2004). Tensile strength perpendicular to grain of LVL was investigated by Ardalany et al. (2010). Furthermore a recent study (Franke and Quenneville, 2010a) presented

compression strength and stiffness values for solid New Zealand Radiata Pine and discussed the influence of different testing standards. Another publication by Franke and Quenneville (2010b) presented the material behaviour of Radiata Pine under compression which included LVL, but cross-banded LVL was not included and strength increase due to spreading of stresses was not further evaluated.

New developments in the field of structural timber engineering, such as post-tensioned timber construction (Palermo et al., 2005; Buchanan et al., 2011) with complex connection behaviour (van Beerschoten et al., 2011a,b), require more material properties than those provided by manufacturers in New Zealand and Australia (3.1). For column design the strength and stiffness perpendicular to grain is essential, and for deviators the rolling shear strength and tensile strength perpendicular to grain are needed. Furthermore, three dimensional (3D) finite element modelling (FEM) requires specific material properties. To get reliable results from these models it is necessary to have an accurate material definition to form the constitutive matrix. This material model consists of three moduli of elasticity (E), three Poisson's ratios (ν) and three shear moduli (G). Furthermore, characteristic values are not always useful for research purposes, where average values and variations are of interest for evaluation of laboratory testing data.

3.2.2 Testing standards

Worldwide there are several different testing standards to determine mechanical properties of timber. These standards usually specify bending or compression tests for evaluation of modulus of elasticity, but different test configurations lead to different results (Leijten and Jorissen, 2010). The experimental testing presented in this chapter is focused on Radiata Pine LVL, available on the Australian and New Zealand markets, and therefore testing was based on the joint Australian & New Zealand Standards for LVL, AS/NZS 4357.2:2006 (Standards New Zealand, 2006a) and structural timber, AS/NZS 4063.1:2010 (Standards New Zealand, 2010a). Testing has also been performed according to the European standards for LVL, EN 14374:2004 (CEN, 2004a), and for structural timber, EN 408:2010 (CEN, 2010), in order to compare different test configurations.

Shear modulus is often specified based on bending tests (single span or variable span), torsion tests and more recently shear field tests (CEN, 2010). No

timber testing standard specifies tests for Poisson's ratio, but ASTM E132-04 (2010) specifies a general test method for determination of Poisson's ratio using extensometers during tension tests of structural materials.

3.2.3 Elastic properties

The first publications on elastic properties in timber date back to the early twentieth century, of which an overview table is published in Hearmon (1948). Other publications on elastic constants of wood from a similar time refer to these initial tests (U.S. Department of Agriculture Forest Products Laboratory, 1955; Wangaard, 1950). Later publications introduce different test methods for determination of elastic properties. Gunnerson et al. (1973) described a plate testing method using two way bending, which is concluded to be a good technique to determinate elastic properties but problems arise in calculation of Poisson's ratios as small deflections can not be measured accurately enough. Bodig and Goodman (1973) used this technique and compression testing. Their publication contains an extensive list of elastic properties of different timber species, including numerous pine species. A more recent publication (Bucur, 2006) describes ultrasonic techniques which can be used in non-destructive testing. This method is compared with static compression testing by Goncalves et al. (2011). The only values for LVL have been found in a publication by Janowiak et al. (2001), where several elastic properties of three types of LVL have been evaluated. An overview of elastic properties found in literature is provided in Table 3.14.

Compression Compressive behaviour of timber has been a topic of significant research (Hoffmeyer et al., 2000; Korin, 1990; Thelandersson and Mårtensson, 1997). In recent years compression perpendicular to grain has been the focus of publications (Blass and Görlacher, 2004) due to changes in EN 1995-1-1:2004+AC+A1 (EC5) (CEN, 2004b). A theoretical explanation of bearing strength, based on the equilibrium method of plasticity, is presented by van der Put (2008) and it is claimed to accurately predict the compressive strength of different loading configurations (Leijten et al., 2010).

Poisson's ratio In literature several methods for determining Poisson's ratios can be found. Early publications on Poisson's ratios in timber (Hearmon, 1948)

do not describe exact testing procedures except that testing was carried out using large-scale testing machinery. Sliker (1972) described a method using small strips of timber (32in. x 3.5in. x 0.25in. or 813mm x 89mm x 6.3mm) in a testing machine with bonded electrical-resistance strain gages mounted in a rectangular pattern in the centre of the specimen. Results were consistent with a small variation, but only two material directions have been tested. Zink et al. (1997) published the use of DIC techniques using white light speckle technique on compression specimens. This technique allowed multiple measurements spanning the entire specimen rather than from one or two points per specimen. This technique proved successful and the authors discovered that the Poisson's ratios are not constant during testing, but decrease with increasing load. A similar technique was used by Ling et al. (2009), whereby stochastic neural networks were used to to approximate the displacement profiles. Niemz and Caduff (2008) have determined the Poisson's ratios of spruce using a special fabricated testing machine, capable of measuring transversal deformations with an accuracy of 0.0015mm. Results were in line with literature values and variations between 17% and 62% were found between measurements. Another publication (Garab et al., 2010) used DIC for determining the Poisson's ratios under different growth ring angles. A video system recorded a 10 x 10 mm section with a resolution of 950 x 950 pixels and used this to create full-field displacement profiles, resulting in low coefficient of variations (7% - 19%).

Shear There have been numerous publications on shear tests focussing on shear strength of timber, i.e. Denzler and Glos (2007). The number of papers focussing on shear stiffness is limited, although several testing methods are published. Vibration time measurements have been used to determine the shear modulus of glulam beams (Görlacher and Kürth, 1994). Divos et al. (1998) compared a static three-point deflection method with vibrational methods and concluded that static and torsional vibration methods are good but the vibration method is more precise. A new block shear test (Sretenovic et al., 2004), whereby the specimen was glued between two sections of beech, gave promising results and, in comparison with ASTM D143 (2009) block test, showed a more uniform shear field. Another method, similar to the ASTM test setup, is proposed by Ukyo et al. (2010) and the DIC technique has been used to evaluate the shear modulus.

A similar technique (digital speckle photography) has been used by Hassel et al. (2009), but this time on small square blocks, making it possible to test different material orientations, although only the rolling shear modulus has been tested. Brandner et al. (2008) used shear field measurements during standard four-point bending tests. This procedure integrates determination of shear modulus with standard testing methods. For this test method large specimen sizes are needed, which is not a problem when glulam is used, but is problematic when analysing shear moduli in different material orientations. The method published in this chapter combines a standard testing method using small specimens with the use of the DIC technique to provide an easy way to measure the shear modulus in different material orientations.

3.2.4 Digital Image Correlation

DIC is a technique for measuring deformations and strains (Pan et al., 2009). Software allows users to track displacements of points through a series of images taken during the experimental testing. This technique provides full-field displacements and strains, whereas traditionally used potentiometers and strain gauges only give point wise measurements. Although DIC is widely used in the field of experimental mechanics, there is still a great potential for this technique in the field of timber testing. A good example is the determination of the shear modulus Ukyo et al. (2010) and the determination of fracture properties Franke et al. (2007).

During compression and shear testing 18MegaPixel (5184 x 3456 pixels) RAW-images of the specimen have been taken at intervals of 5 seconds using Digital SLR cameras, as shown in Figure 3.2. These images have been analysed using software, a Matlab script[1], which was used to generated a grid of markers which were tracked through the series of images. For compression testing 40 to 70 markers were placed between 20% and 80% of the specimen height. Vertical and horizontal displacements were converted to strains and averaged for all markers. For shear testing grids of up to 280 markers have been used.

[1] Developed by C. Eberl from Karlsruhe Institute of Technology, freely available for download from Matlab Central

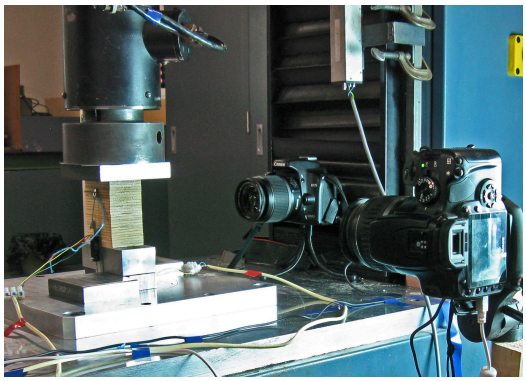

(a) Compression test

(b) Shear test

Figure 3.2: Camera setup during experimental testing

3.3 Compression strength and stiffness

This section describes experimental testing and analyses on the compressive strength and stiffness of New Zealand Radiata Pine LVL in three different material directions. It provides descriptions of the evaluation of properties of 45mm thick LVL, 63mm thick LVL and 36mm thick cross-banded LVL. Strength results from different loading configurations are compared with predictions based on the model proposed by van der Put (2008) and by EC5 (CEN, 2004b) design procedures.

3.3.1 Experimental testing

Specimens Testing was performed using five or six replicates (dependent on material availability) in the three different material directions for 45mm thick LVL, 63mm thick LVL and 36mm thick cross-banded (CB) LVL (having 2 out of 10 veneers as cross-layers) according to Australian/New Zealand and European Standards (as described in the next paragraph). Specimens were taken from LVL11 and cross-banded LVL manufactured by Nelson Pine Ltd. LVL11 has been chosen as all manufacturers in Australia and New Zealand can supply this material. Specimens were labelled as Direction-Standard-Material-Number, i.e. E1-EN-45-1 for testing in the longitudinal direction, according to the European Standard for 45mm LVL of specimen Number 1. Specimen dimensions were as close as possible to values described in the standards, but because of material dimensions, not all

dimensional requirements could be fulfilled. In total, 81 specimens were tested with dimensions as shown in Table 3.2. Density of specimens ranged between 575 and 588kg/m^3 with an average of 581kg/m^3. This was slightly above the average published density of 570kg/m^3 for Nelson Pine LVL11.

Table 3.2: Specimen description and dimensions for compression testing

Loading Direction	Material	Standard	Name	No. of tests	Length (mm)	Depth (mm)	Height (mm)
Longitudinal	LVL11 45mm	NZS4357	E1-NZS-45	6	45	45	270
	LVL11 63mm	NZS4357	E1-NZS-63	5	63	63	378
	Cross-banded	NZS4357	E1-NZS-CB	6	36	36	216
Tangential	LVL11 45mm	NZS4063	E2-NZS-45	6	270	45	45
		EN408	E2-EN-45	5	70	45	90
	LVL11 63mm	NZS4063	E2-NZS-63	5	378	63	63
		EN408	E2-EN-63	5	70	63	90
	Cross-banded	NZS4063	E2-NZS-CB	6	216	36	36
		EN408	E2-EN-CB	5	70	36	90
Radial	LVL11 45mm	NZS4063	E3-NZS-45	6	270	45	45
		EN408	E3-EN-45	5	70	45	90
	LVL11 63mm	NZS4063	E3-NZS-63	5	378	63	63
		EN408	E3-EN-63	5	70	63	126
	Cross-banded	NZS4063	E3-NZS-CB	6	216	36	36
		EN408	E3-EN-CB	5	70	36	98

Testing Standards The AS/NZS 4357.2:2006 (Standards New Zealand, 2006a) for determination of structural properties of LVL was used for testing of strength and stiffness parallel to grain, but this standard does not provide any test methods for properties perpendicular to grain. Therefore the rail test in Appendix A3 of AS/NZS 4063.1:2010 (Standards New Zealand, 2010a) for structural timber was also used. In this test only the mid-section of the specimen is loaded and strength increase due to spreading of stresses can take place. Maximum strength values are the lesser of F_{ult} and $F_{0.1d}$, where the latter is based on a constant '0.1 x d' (d = depth of cross-section in mm) offset intercept as shown in Figure 3.3a. The stiffness is based on a linear deformation offset of 2mm, regardless of specimen size. The intersection of this offset with the load-displacement curve gives the yield strength. No specification is given for derivation of the slope (stiffness) of the load-displacement curve. Therefore the measurements at 10% and 40% of

yield strength have been used to evaluate stiffness, similar to the method of the European Standard.

European Standards have also been used for compression testing. The EN 14374:2004 (CEN, 2004a) specifies requirements for LVL, although for testing it refers to methods outlined in EN 408:2010 (CEN, 2010) for determination of mechanical properties of structural timber. For parallel to grain strength and stiffness the standard is identical to the New Zealand standard, therefore these tests were not repeated. For compression perpendicular to grain a block compression test is specified. Maximum strength is based on the intersection of the load-deformation curve with a '0.01 x h' (h = height of specimen in mm) linear offset from the initial stiffness, as is illustrated in Figure 3.3b. The initial stiffness is defined as the slope of the load-deformation curve between 10% and 40% of the maximum load.

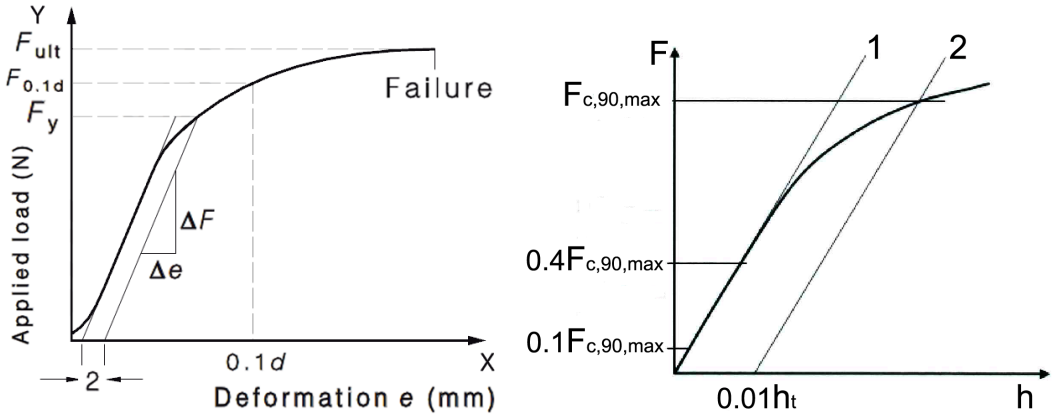

(a) AS/NZS4063 (b) EN408

Figure 3.3: Derivation of strength and stiffness based on AS/NZS4063 and EN408 (d = specimen depth, h = specimen height)

Statistical analysis of the AS/NZS testing has been performed according to AS/NZS 4357.3:2006 (Standards New Zealand, 2006b) for evaluation of structural properties of LVL and AS/NZS 4063.2:2010 (Standards New Zealand, 2010b) for evaluation methods for structural timber, where a log-normal distribution of the test results has been assumed and statistical evaluation Method 1 (Appendix B2.2) from the standard has been followed. It should be noted that the standard

assumes a sample size of 30 or more, which is not the case for this work as is explained in the next paragraph. Statistical analysis was performed according to European standard EN 14358:2006 (CEN, 2006) for calculation of characteristic values for timber structures, based on an assumed logarithmic normal distribution. Both evaluation methods are very similar, although the Australian/New Zealand standard specifies a minimum coefficient of variation of 10%, whereas the European standard specifies a minimum of 5%.

A limitation of this work is that it is based on one batch of LVL from one manufacturer. AS/NZS 4063.2:2010 requires a minimal sample size of 30 specimens for determination of characteristic values. Therefore values published in this chapter should not be used directly for design purposes, but they do give an indication for preliminary design and research purposes. Timber manufacturers should perform testing on larger sample sizes in order to supply design values.

Test setup The compression testing was performed using an Instron testing frame with an in-line 150kN load cell. A linear displacement potentiometer (50mm travel) was attached to measure crosshead movement, required for the AS/NZS testing. Two small linear displacement potentiometers (10mm travel) were attached to specimens tested to the EN Standard. These potentiometers were fixed to nails which were placed at 20% and 80% of the specimen height. Testing was stopped at 10% strain deformation, as further deformation was deemed unrealistic.

Failure mechanisms Failure mechanisms were relatively consistent among groups of test specimens and are shown in Figure 3.4. Longitudinally loaded specimens (Figure 3.4a) generally started to fail in compression, after which they buckled to one side. Tangentially loaded block specimens (Figure 3.4b) failed due to crushing, whereby the outer veneers sometimes peeled off. Radially loaded block specimens (Figure 3.4c) showed a high amount of crushing, with some of the layers crushing significantly more than others. Tangentially loaded rail specimens (Figure 3.4d) failed when the specimen started bulging outwards and outer veneers peeled off. Radially loaded rail specimens (Figure 3.4e) started failing around the edges of the load block and eventually tensile failure at the ends occurred.

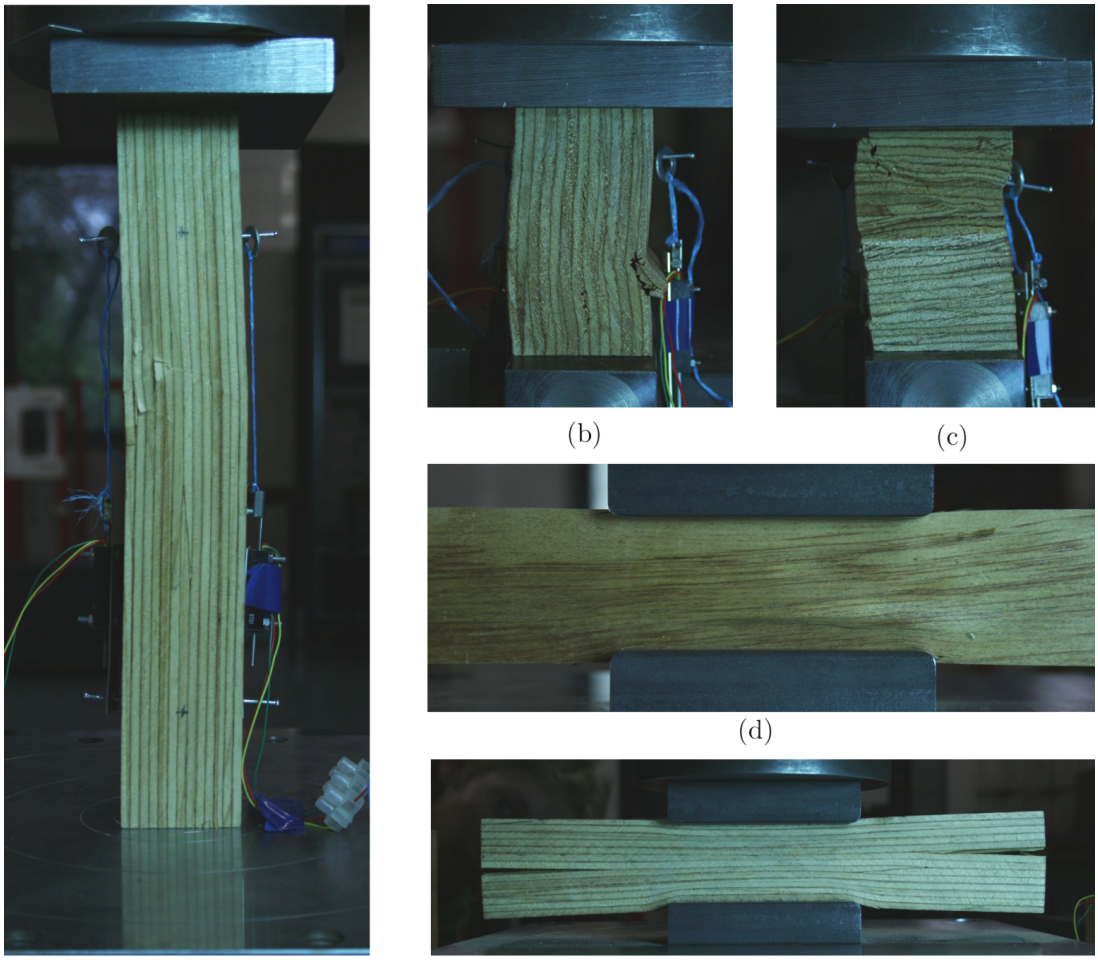

Figure 3.4: Typical failures of (a) longitudinally loaded specimen, E1-NZS; (b) tangentially loaded block specimen, E2-EN; (c) radially loaded block specimen, E3-EN; (d) tangentially loaded rail specimen, E2-NZS; (e) radially loaded rail specimen, E3-NZS

3.3.2 Compression strength results

Table 3.3 shows the average strength, coefficient of variation, fifth percentile and characteristic strength values (including the sampling factor) for the two different test setups for the three different materials and in the three different orientations.

Table 3.3: Compression test results including average strength ($\overline{f}$), coefficient of variation (CoV) / standard deviator (St.Dev.), fifth percentile (f_{05}) and characteristic strength (f_k) values (MPa) for the different materials, orientations and testing standards.

Standard	Result	45mm LVL			63mm LVL			36mm CB LVL		
		$f_{c,1}$	$f_{c,2}$	$f_{c,3}$	$f_{c,1}$	$f_{c,2}$	$f_{c,3}$	$f_{c,1}$	$f_{c,2}$	$f_{c,3}$
AS/NZS	$\overline{f}$ (MPa)	47.4	13.4	10.0	47.8	15.2	12.3	25.3	19.1	10.6
	CoV (%)	4.1	5.0	3.9	4.8	3.5	5.0	4.4	9.4	5.8
	f_{05} (MPa)	44.3			44.1			23.6		
	f_k (MPa)	42.2	13.1	9.7	41.8	14.7	11.9	22.4	18.6	10.3
EN	$\overline{f}$ (MPa)	47.4	8.2	7.5	47.8	9.1	7.9	25.3	16.8	7.3
	St.Dev. (%)	4.1	4.1	5.4	4.8	2.5	2.7	4.4	3.1	5.7
	f_k (MPa)	42.0	7.3	6.6	42.2	8.1	7.0	22.5	14.9	6.3

As expected, a clear distinction between parallel ($f_{c,1}$) and perpendicular ($f_{c,2}$ and $f_{c,3}$) to grain strength was observed. Perpendicular to grain strength of 45mm and 63mm LVL showed a small reduction in strength for radially loaded specimens ($f_{c,3}$) compared to tangential loaded ones ($f_{c,2}$). This was most likely due to all veneers sharing the load under tangential loading, but under radial loading there was no load sharing and the weakest veneers governed strength.

It can be seen that 45mm LVL and 63mm LVL had a low variability, ranging between 2.5% to 5.4%. 36mm cross-banded LVL had a slightly higher variability, up to 9.4%. It should be kept in mind that this was only the variability within one batch of LVL and does not represent the variability between different batches.

When comparing 45mm LVL and 63mm LVL, reasonably similar strength values for all three directions were found. Cross-banded LVL is made from lower grade veneers, which manifested in a reduced compression strength parallel to grain ($f_{c,1}$) which was almost half compared to the other types of LVL. The two cross layers significantly increased the tangential strength ($f_{c,2}$). The compressive strength in the radial direction ($f_{c,3}$) was similar to other types of LVL.

When comparing the compressive strength of EN test results with the AS/NZS test results, it can be seen that the compressive strength parallel to grain was the same because both standards specify the same test setup and therefore the testing was performed only once. There is a minor difference in characteristic strength, due to differences in the statistical analysis procedure. For analysis of tangential and radial strength of the AS/NZS testing a fixed '0.1 x h' deformation offset based on crosshead movement was used, whereas for the EN testing a 1% strain offset, based on the average of two potentiometers, parallel to the initial stiffness was used, as shown in Figure 3.3b. The different measurements and analysis procedures made for an unequal comparison. In general a clear reduction in compressive strength perpendicular to grain can be seen (both tangential and radial) as sideways spreading of stresses was not possible in the block test.

3.3.3 Stress spreading

It is not practical to give different strength values for every possible loading scenario. Therefore predictive methods are necessary in order to predict compressive strength under different loading scenarios.

Van der Put (2008) proposes a theoretical model to take strength increase due to stress spreading into account based on the equilibrium method of plasticity. This method leads to Equation 3.1 for the calculation of compressive strength perpendicular to grain when spreading of stresses can take place ($f_{c,s}$). This function can be rewritten to find the increase in strength due to stress spreading (k_c), as is given by Equation 3.2.

$$f_{c,s} = f_{c,90}\sqrt{\frac{L_{eff}}{s}} \tag{3.1}$$

$$k_c = \frac{f_{c,s}}{f_{c,90}} = \sqrt{\frac{L_{eff}}{s}} \tag{3.2}$$

Where:

- $f_{c,90}$ = Block compressive strength (MPa)
- $f_{c,s}$ = Compressive strength incl. spreading effects (MPa)
- L_{eff} = Effective length (mm)
- s = Contact length in the grain direction (mm)

- k_c = Factor for increase in strength due to stress spreading (-)

A stress dispersion angle ratio of 1:1 is suggested for elastic stress distribution, at small strains or at serviceability limit state (SLS) conditions, and the maximum spreading angle at higher strains, or ultimate limit state (ULS) conditions, 1:1.5. The distinction in compressive strength at SLS and ULS limit was previously proposed by Thelandersson and Mårtensson (1997) and Gehri (1997). This leads to an effective length for rail tests of $L_{eff,sls}$ = s + h and $L_{eff,uls}$ = s + 1.5h, as shown in Figure 3.5.

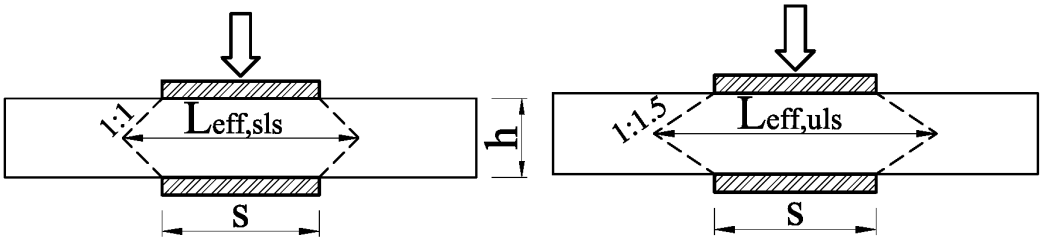

(a) SLS (b) ULS

Figure 3.5: Stress dispersion angles for testing according to AS/NZS 4063.1:2010 in SLS and ULS conditions

Another model to take different loading scenarios into account is currently in EC5 (CEN, 2004b) for design of compression perpendicular to grain (Section 6.1.5). This design procedure is based on a block compressive strength ($f_{c,90}$) multiplied by a factor ($k_{c,90}$) which depends on the loading configuration and type of timber. This is shown in Equation 3.3. Furthermore the design stress is based on effective area (A_{eff}) which increases the contact length, as is shown in Equation 3.4.

$$\sigma_{c,90} \leq k_{c,90} f_{c,90} \tag{3.3}$$

$$\sigma_{c,90} = \frac{F_{c,90}}{A_{ef}} \tag{3.4}$$

Where:

- $f_{c,90}$ = Block compressive strength (MPa)

- $k_{c,90}$ = Factor based on loading configuration and type of timber (-)
- $\sigma_{c,90}$ = Compressive stress perpendicular to grain (MPa)
- $F_{c,90}$ = Compressive force perpendicular to grain (N)
- A_{eff} = Effective contact area (mm^2)

MetsäWood (2009) has published design information for their Kerto LVL products, as EC5 only gives values for solid timber and glue-laminated timber. In this document, several values for the increase in contact length and $k_{c,90}$ factor are given, depending on the material and loading orientation. These values are shown in Table 3.4. Kerto-S has all laminates in one direction whereas Kerto-Q is cross-banded LVL.

Table 3.4: Contact length and $k_{c,90}$ factor (based on continuous supports) for Kerto LVL (MetsäWood, 2009)

Material	Increase of contact length	$k_{c,90}$
Kerto-S, edgewise	30mm along	1.0
Kerto-S, flatwise	30mm along 15mm across	1.4
Kerto-Q, edgewise	0mm along	1.3
Kerto-Q, flatwise	30mm along 15mm across	1.4

edgewise = tangential, flatwise = radial

Table 3.5 shows compressive strength ratios of rail test over the block test. This ratio has been analysed for three types of LVL at SLS and ULS design limits. Compressive strength tangentially ($f_{c,2}$) and radially ($f_{c,3}$) have been evaluated separately. A total of three ratios are shown for each material; one based on experimental testing; one based on the van der Put model and one based on EC5 design rules.

For experimental testing, SLS stresses have been evaluated based on the 1% offset method, as outlined in EN 408:2010 (CEN, 2010). ULS stresses have been taken as the highest of the maximum stress during testing or the stress at 10% strain, based on AS/NZS 4063.1:2010 (Standards New Zealand, 2010a). All values are average strength values based on strain measurement using the crosshead displacement. The full stress vs. strain curves for tangential loading

Table 3.5: Comparison of experimental and predicted (van der Put model (2008) and Eurocode 5 (CEN, 2004b)) compressive strength ratios for LVL at SLS and ULS design limits

Design limit	Method		45 mm LVL		63mm LVL		36mm CB LVL	
			$f_{c,2}$	$f_{c,3}$	$f_{c,2}$	$f_{c,3}$	$f_{c,2}$	$f_{c,3}$
SLS	Experimental	Block (EN)	8.7MPa	7.8MPa	9.7MPa	7.9MPa	17.6MPa	7.5MPa
		Rail (AS/NZS)	10.6MPa	8.2MPa	11.8MPa	9.3MPa	17.8MPa	8.3MPa
		ratio (rail/block)	*1.23*	*1.06*	*1.21*	*1.18*	*1.01*	*1.10*
	van der Put	L_{eff}	135mm	135mm	153mm	153mm	126mm	126mm
		k_c-factor	*1.22*	*1.22*	*1.30*	*1.30*	*1.18*	*1.18*
	EC5 & Kerto	L_{eff}	150mm	150mm	150mm	150mm	90mm	150mm
		$k_{c,90}$	1.0	1.4	1.0	1.4	1.3	1.4
		*EC5-factor $k_{c,90}$ * (L_{eff}/L)*	*1.67*	*2.33*	*1.67*	*2.33*	*1.30*	*2.33*
ULS	Experimental	Block (EN)	10.2MPa	9.5MPa	11.4MPa	9.7MPa	18.4MPa	9.0MPa
		Rail (AS/NZS)	13.4MPa	10.0MPa	15.2MPa	12.3MPa	19.1MPa	10.6MPa
		ratio (rail/block)	*1.32*	*1.05*	*1.33*	*1.26*	*1.04*	*1.18*
	van der Put	L_{eff}	157.5mm	157.5mm	184.5mm	184.5mm	144mm	144mm
		k_c-factor	*1.32*	*1.32*	*1.43*	*1.43*	*1.27*	*1.27*
	EC5 & Kerto	L_{eff}	150mm	150mm	150mm	150mm	90mm	150mm
		$k_{c,90}$	1.0	1.4	1.0	1.4	1.3	1.4
		*EC5-factor $k_{c,90}$ * (L_{eff}/L)*	*1.67*	*2.33*	*1.67*	*2.33*	*1.30*	*2.33*

are shown in Figure 3.6. From these graphs it can be seen that rail tests result in higher strengths compared to block tests for 45mm and 63mm LVL but not for cross-banded LVL. It can also be seen that even at 10% strain the rail test strength is still increasing, whereas the block test reaches a maximum strength around 7% strain.

Also shown in Table 3.5 are the effective length and k_c-factor according to the van der Put model. Furthermore, the effective length and increase in strength ratio based on EC5 and the Kerto design information are included. The EC5 factor is a multiplication of $k_{c,90}$ factor and effective length over contact length. These two factors are both predictions of the increase in strength of the rail test in comparison to the block test. These values can therefore be compared with the experimental ratio.

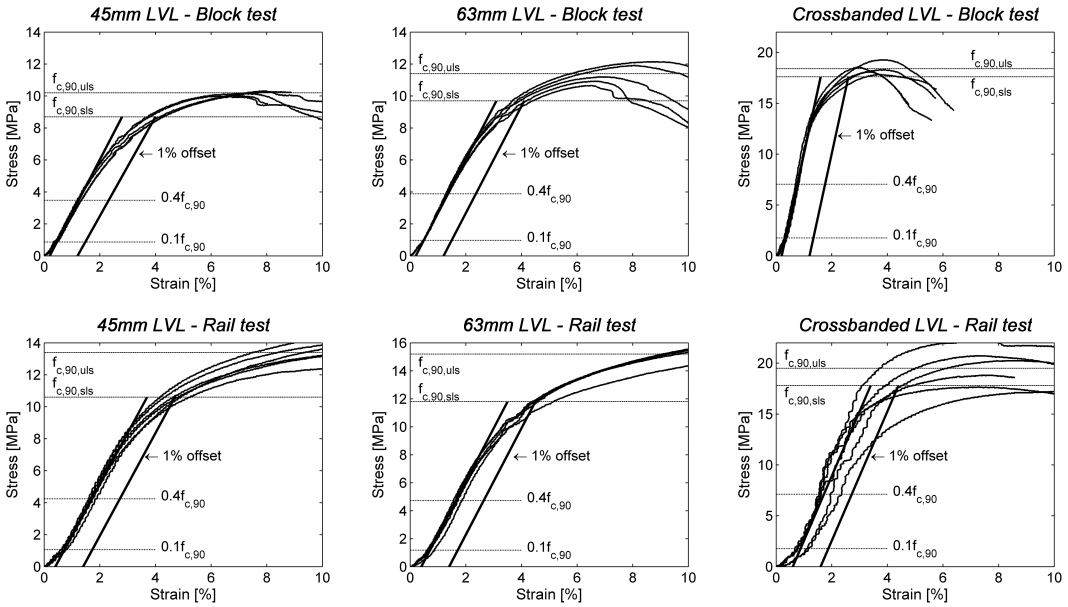

Figure 3.6: Stress-strain plots for compressive block and rail tests loaded in the tangential direction

It can be seen that the van der Put model gives excellent results for the compressive strength perpendicular to grain (E2) of 45mm LVL at SLS and ULS levels. It also gives good results for 63mm LVL. Radially loaded (E3) specimens showed a very small amount of stress spreading (6% and 5%) for 45mm LVL. For 63mm LVL there was some spreading of stresses (18% and 26%), but less

than perpendicular to grain. This suggests stress spreading should not (or only partially) be taken into account for radially loaded specimens.

Cross-banded LVL had almost no increase in strength in the rail test compared to the block test in SLS or in ULS (1% and 4%, respectively). Therefore spreading of stresses should not be included in the design of cross-banded LVL. Some stress spreading occurred in the radial direction, but this was still less than predicted by the van der Put model.

The effective length based on EC5 strongly overestimated the compressive strength of all rail specimens as tested according to AS/NZS standards. Also the $k_{c,90}$ factors as specified for Kerto LVL do not match up with experimental results. Therefore this design method is not able to predict the compressive strength of New Zealand Radiata Pine LVL.

3.3.4 Compression stiffness results

The average, 5th percentile and characteristic stiffness values are shown in Table 3.6 in the three material orientations for the three different materials. A differentiation is made between rail testing according to AS/NZS and block testing according to the EN Standard. The statistical analysis of test data has been performed according to AS/NZS 4357.3:2006 (Standards New Zealand, 2006b) and AS/NZS 4063.2:2010 (Standards New Zealand, 2010b). A log-normal distribution of the test results has been assumed and Appendices B3 and B5 from the standard have been followed.

Table 3.6: Experimental compressive stiffness results including average ($\overline{E}$), coefficient of variation (CoV), fifth percentile (E_{05}) and characteristic stiffness ($E_{k,mean}$) values (MPa) for the different materials, orientations and testing standards

Standard	Test	*45mm LVL*			*63mm LVL*			*36mm CB LVL*		
		E_1	E_2	E_3	E_1	E_2	E_3	E_1	E_2	E_3
AS/NZS	$\overline{E}$ (MPa)	12200	319	241	12500	379	371	8370	622	361
	CoV (%)	7.3	4.4	6.3	1.7	2.7	5.7	13.3	16.3	6.0
	E_{05} (MPa)	10800	297	217	12200	362	337	6670	470	327
	$E_{k,mean}$	12100	328	243	13200	394	374	8050	585	365
EN	$\overline{E}$ (MPa)	12200	426	371	12500	527	541	8370	2460	564
	CoV (%)	7.3	5.0	8.6	1.7	11.7	15.9	13.2	9.6	7.2
	E_{05} (MPa)	10800	392	321	12200	432	411	6670	2090	499

The stiffness values parallel to grain were much higher than stiffness perpendicular to grain. The tangential stiffness (E_2) was slightly higher than the radial stiffness (E_3). This was most likely due to stiffer and weaker layers sharing the load perpendicular to grain, whereas the weakest layers are governing the stiffness in the radial direction. Gluelines are not expected to influence stiffness in tangential direction due to the brittle nature of the glue and the very small volume ratio of glue to veneers. Stiffness values of 45mm LVL and 63mm LVL exhibited some differences, but for design practice they can be assumed to be the same. Cross-banded LVL had a lower stiffness parallel to grain (E_1) than the other materials, but an increase in stiffness perpendicular to grain (E_2), as would be expected from the cross-layers. The variability in stiffness of cross-banded LVL (E_1 and E_2) was almost twice that of 45mm and 63mm LVL.

Stiffness perpendicular to grain (E_2 and E_3) for the EN block tests were on average 1.4 times higher than stiffness based on AS/NZS rail tests for 45mm and 63mm LVL. The stiffness perpendicular to grain (E2) of cross-banded LVL was 4 times higher for the block test compared to the rail test. These seemingly contradictory results were likely due to differences in methods of measuring displacements. The results of the AS/NZS tests were calculated from crosshead movement, whereas results of the EN testing were based on potentiometers attached to the sides of specimens. Previous research concluded that modulus of elasticity strongly depends on gauge length. Hoffmeyer et al. (2000) found that crosshead movement gives a stiffness value of only 69% (structural timber) to 75% (glulam) compared to stiffness values based on 50mm or 100mm gauge length extensometers. For EN testing, a ratio of 70% was found for average stiffness of 45mm and 63mm thick LVL when comparing strains based on crosshead movement with strains based on the potentiometers.

3.3.5 Design values

Compression testing showed only minor variations in properties between 45mm and 63mm LVL, therefore for design purposes these materials can be considered identical. An overview of recommended design values is given in Table 3.7.

The calculated characteristic strength of LVL parallel to grain of 42MPa is lower than the specified characteristic compressive strength of 45MPa, but that

Table 3.7: Recommended preliminary design characteristic values for compression strength and stiffness, all values in MPa

Material	$f_{c,1}$	$f_{c,2,sls}$	$f_{c,2,uls}$	$f_{c,3,sls}$	$f_{c,3,uls}$	E_1	E_2	E_3
45mm / 63mm LVL11	44	8	10	7 *	9 *	12000	500	500
36mm cross-banded LVL	24	16 *	18 *	7 *	9 *	8400	2500	500

** No stress spreading allowed*

is possibly due to the small sample size. The experimental 5^{th} percentile strength of 44MPa corresponds well with the specified value of 45MPa. For tangential to grain strength ($f_{c,2}$), the manufacturers specified value of 12MPa is only valid for small connections with a similar configuration to the rail test, where stress spreading can take place and plastic deformations are allowed. A better design approach is to use a compressive strength of 8MPa for SLS design, based on the characteristic strength of EN block testing. At this level material behaviour is still largely linear elastic. For ULS design a value of 10MPa can be used if plastic deformation is accepted. For radial load ($f_{c,3}$) a design strength of 7MPa can be used, based on the characteristic strength value of EN block testing. If plastic deformation of the timber is allowed, this value can be increased to 9MPa.

When having different loading configurations than pure compression, an increase in compression strength due to spreading of stresses can be taken into account. This can be done using the proposed plasticity model of van der Put (2008). Stress spreading is only occurring for compression in the tangential direction, for radial direction stress spreading should not be allowed for.

Based on experimental testing of cross-banded LVL, the recommended design strength parallel to grain is 24MPa. Perpendicular to grain, a compressive strength of 16MPa for linear elastic behaviour and 18MPa for plastic behaviour are suggested. No stress spreading should be allowed for cross-banded LVL.

Recommended compressive stiffness for 45mm and 63mm LVL parallel to grain is the average experimental result of 12000MPa. This is slightly higher compared with the 11000MPa value specified by the manufacturer, which is based on a four-point bending test and includes some shear deformation. Stiffness perpendicular to grain (E_2, tangentially) should be based on average values from EN testing and can be taken as 500MPa. Stiffness in the radial direction (E_3) is very similar as

tangentially and can therefore also be taken as 500MPa. Suggested stiffness values for cross-banded LVL are 8400MPa parallel to grain (E_1), 2500MPa perpendicular to grain (E_2) and in the radial direction (E_3) 500MPa.

3.3.6 Non-linear behaviour

For detailed numerical modelling the non-linear behaviour of LVL is of interest. This behaviour can be extracted from the stress-strain plots as presented in Figure 3.6. Data from block testing according to EN 408:2010 CEN (2010) has been used as these specimens had a constant stress and strain field along the depth of the specimen. In finite element programs, the user can input non-linear data in a tabular form. For this stress and plastic strain are needed, which is presented in Table 3.8.

A comparison between experimental test data and the non-linear curves can be seen in Figure 3.7. When fitting a non-linear curve to experimental data, the initial stiffness was kept as close as possible to the values determined in Section 3.3.4. In the longitudinal direction, the increase in strength and stiffness of LVL11 versus cross-banded LVL can clearly be seen. In the tangential direction cross-banded LVL is clearly stronger and stiffer than LVL11, in the radial direction the behaviour is very similar.

For parallel to grain loading a softening behaviour can be seen after the maximum strength is reached. This is caused by buckling of the wood fibres and eventually buckling of the full specimen. Cross-banded LVL loaded in the tangential direction also shows some softening behaviour, whereas LVL11 shows an almost perfectly plastic behaviour up to 8% strain. For loading in the radial direction there is an gradual increase in strength up to 10% strain (at which testing was stopped). The wood fibres get compressed but they do not loose their strength.

Table 3.8: Non-linear stress strain data for LVL11 and cross-banded LVL

Material	Direction	Stress (MPa)	Strain (%)	Plastic strain (-)
LVL 11	Longitudinal	0	0.00%	0
		35	0.29%	0
		47	0.45%	0.0006
		47	0.60%	0.0021
	Tangential	0	0.0%	0
		6	1.4%	0
		9	3.5%	0.014
		10	5.0%	0.027
		10	7.0%	0.047
	Radial	0	0.0%	0
		6	1.6%	0
		8	3.5%	0.014
		9.5	10.0%	0.075
Cross-banded	Longitudinal	0	0.00%	0
		20	0.24%	0
		25	0.40%	0.0010
		25	0.60%	0.0030
	Tangential	0	0.0%	0
		14	0.6%	0
		18	2.2%	0.014
		18	3.5%	0.027
	Radial	0	0.0%	0
		6	1.2%	0
		7.5	2.5%	0.010
		9.5	10.0%	0.081

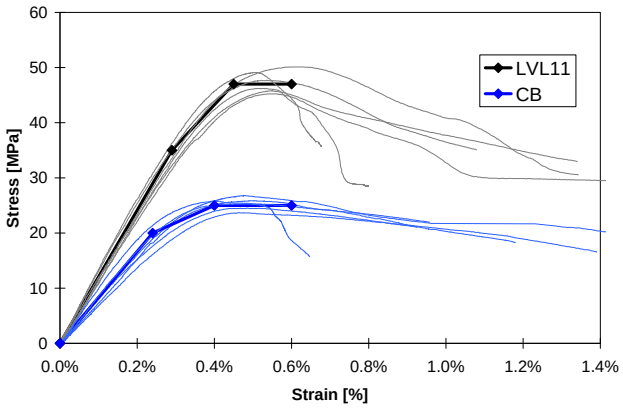

(a) Longitudinal

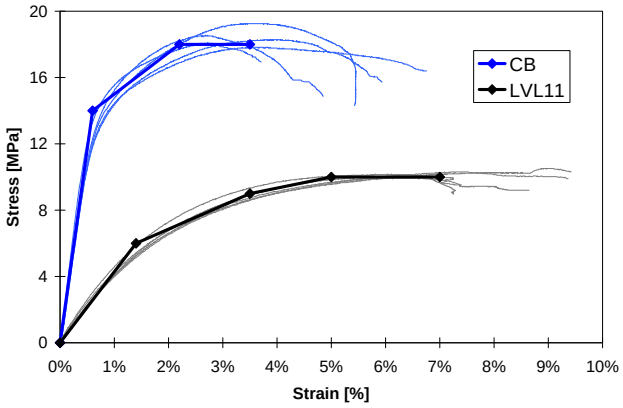

(b) Tangential

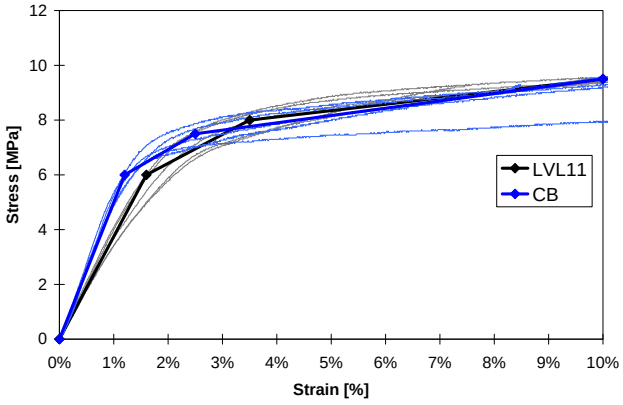

(c) Radial

Figure 3.7: Non-linear stress-strain behaviour of LVL11 and cross-banded LVL

3.4 Poisson's ratios

The Poisson's ratios (Figure 3.8a) of LVL have been evaluated using strain fields generated using DIC software. For each test two series of images, one for each side, were taken using DSLR cameras. A virtual grid of markers was generated, as is shown in Figure 3.8b. Each marker represents a square of 50 x 50 pixels which are tracked through the series of images. The coordinate of each marker is stored and the displacement relative to the first image is calculated.

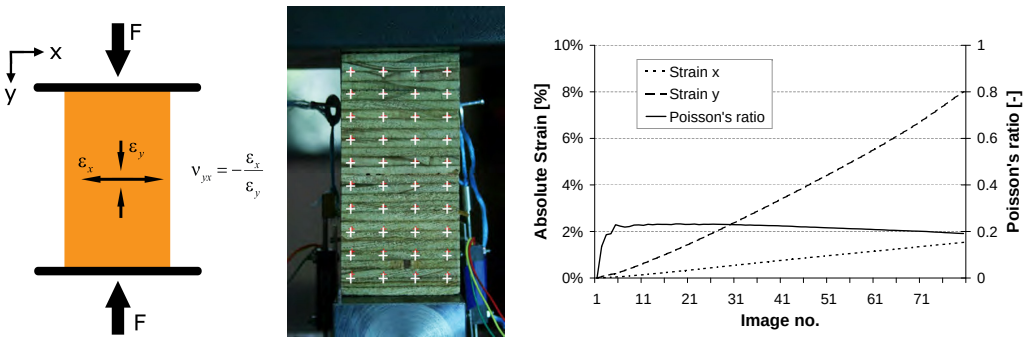

(a) Definition of Poisson's Ratio (b) Grid on specimen (c) Horizontal and vertical strain and Poisson's ratio

Figure 3.8: Evaluation of Poisson's Ratio

Average vertical and horizontal strains, calculated from displacements, during testing are shown in Figure 3.8c. Also shown in the same figure is the Poisson's Ratio, with almost perfect linear behaviour after the first 5 images. The Poisson's ratio was based on an average value between image number 30 and 60. During the first stage of testing strains were too small to give reliable results and close to failure the material behaviour was no longer linear elastic. Poisson's ratios for all tests are shown in Figure 3.9. It can be seen that the for certain directions, especially when evaluating very small strains in longitudinal direction (due to high E), there is a large spread in results. In several of these cases measured displacements were less than 5 pixels, and although the software applies sub-pixel analysis techniques, this gave issues with accuracy.

From each series of six tests the average and coefficient of variation could be calculated. The resulting values are shown in Table 3.9. The Poisson's ratio is strongly dependent on the direction, as is common for an orthotropic

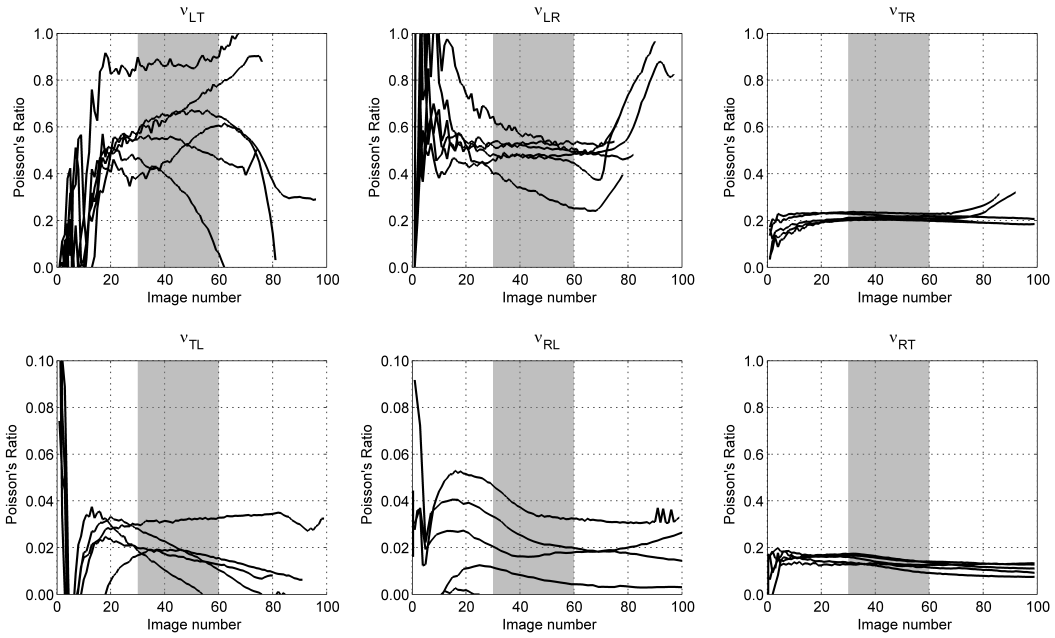

Figure 3.9: Evaluation of the six Poisson's ratios of LVL using Digital Image Correlation software

material. It can be seen that specimens loaded in longitudinal directions have a large Poisson's ratio of 0.59 and 0.48 for tangential and radial extension, respectively. For extension in longitudinal direction the Poisson's ratios are very small, approximately 0.02, and accuracy of measurements resulted in a large coefficient of variation, between 38 and 70%.

Table 3.9: Experimental average values and coefficient of variations (CoV) of Poisson's ratio

Direction	Average	CoV (%)
ν_{LT}	0.59	32.4
ν_{TL}	0.02	38.0
ν_{LR}	0.48	17.6
ν_{RL}	0.02	70.3
ν_{TR}	0.22	5.4
ν_{RT}	0.14	12.8

3.5 Shear strength and stiffness

3.5.1 Experimental testing

Shear testing was performed according to EN408 with six specimens for each shear direction as shown in Figure 3.10. Testing was performed in an Avery test frame with a capacity of 100kN whereby specimens were loaded until failure. Specimen dimensions are given in Table 3.10. Due to material dimensions, specimens had a depth of 45mm instead of 55mm as specified in EN408. Therefore steel side plates were manufactured with a thickness of 15mm, 5mm thicker than specified by the standard, in order to keep the 14° angle of the specimen. Further details of the shear testing can be found in (Dunbar et al., 2011).

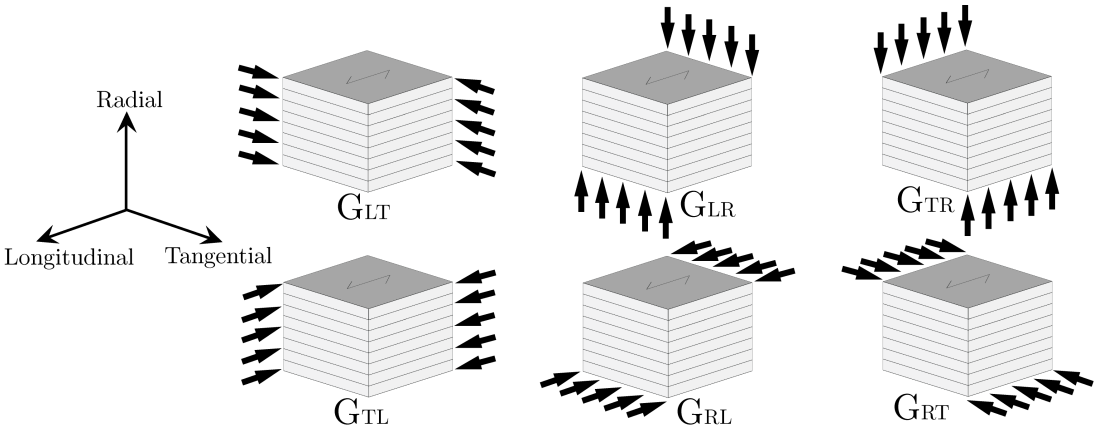

Figure 3.10: Overview of six different shear directions

Table 3.10: Specimen description and average dimensions for shear specimens

Test	Parameters	No. of tests	Length (mm)	Depth (mm)	Height (mm)
Shear 1	G_{LT}	6	295.0	45.3	44.9
Shear 2	G_{LR}	6	272.7	29.9	44.8
Shear 3	G_{TL}	6	296.8	45.4	45.3
Shear 4	G_{TR}	6	272.9	31.9	42.6
Shear 5	G_{RL}	6	295.3	31.7	43.9
Shear 6	G_{RT}	6	295.7	31.8	45.2

For calculation of the shear stress EN408 specifies Equation 3.5.

$$f_v = \frac{F_{max} \cdot cos14^o}{lb} \tag{3.5}$$

This equation calculates the shear force and divides this over the full cross-sectional area of the specimen (lb, where l = length of specimen and b is width of specimen), assuming a constant shear distribution. This assumption has been checked using two dimensional and three dimensional FEM modelling. As there were only minor differences between 3D and 2D models, the 2D model (Figure 3.11) is described here.

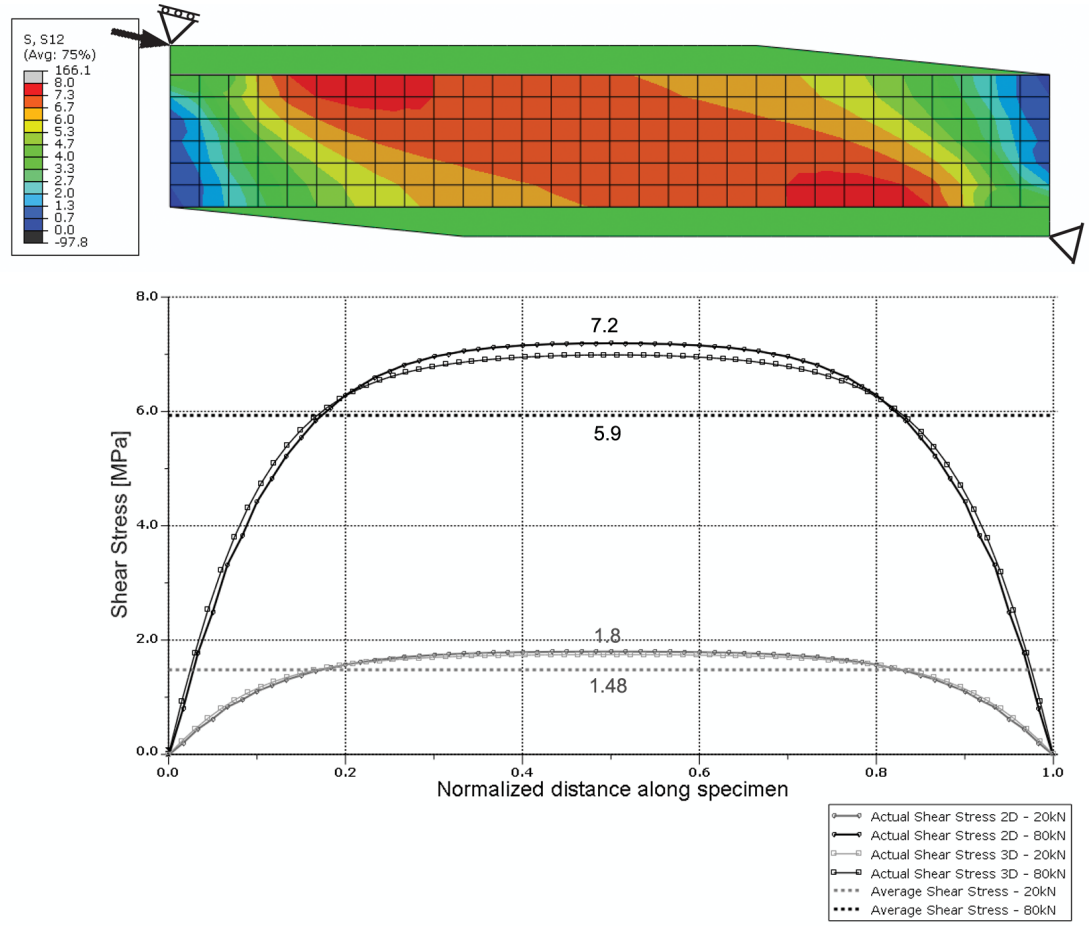

Figure 3.11: FEM model of shear test. Graph shows shear stresses along centre of the specimen.

For this model steel support plates and timber have been modelled as general-

ized plain-strain elements. The epoxy connection between steel and timber has been modelled using tie constraints. Four node quadratic elements (CPEG8) have been used. Reduced integration elements (CPEG8R) were also tried and gave the same results as fully integrated elements. One edge of the steel plate was loaded with a concentrated force under an angle of 14 degrees. This edge was restrained against movement perpendicular to direction of loading. The opposite steel plate had one restraint in direction of load and one perpendicular to direction of load. The analysis was performed under a load of 20kN and again under a load of 80kN.

Figure 3.11 shows that shear stress distribution along the centre cross-section is not constant, but is highest in the middle 60% of the length of the specimen and drops to zero at both ends, which should be the case as there cannot be shear stresses at outside faces. From this model it follows that maximum actual shear stress in the specimen is 1.22 times the average shear stress. Therefore when calculating the shear stress based on experimental testing this should be multiplied by a correction factor of 1.22, as shown in Equation 3.6. A very similar shear distribution has been found by Hassel et al. (2009). The almost uniform shear stress distribution found by Sretenovic et al. (2004) could not be reproduced.

$$f_v = 1.22 \cdot \frac{F_{max} \cdot cos14^o}{lb} \tag{3.6}$$

3.5.2 Shear strength

Failure images of shear testing can be seen in Figure 3.12. For specimens loaded as a beam (G_{TL}), specimen showed a shear failure through all layers of LVL. For specimens loaded as a plank (G_{RL}), specimens showed a failure through one of the LVL layers. Specimens loaded under rolling shear (G_{RT}) showed a peeling failure through multiple layers.

Failure loads were converted to failure stress using Equation 3.6. For each material direction six tests were performed and the average failure stress, variation, 5^{th} percentile and characteristic shear strength were calculated using EN 14358:2006 CEN (2006). The characteristic shear strength was calculated with and without the correction factor of 1.22. The results are shown in Table 3.11. From this table it can be seen that shear strength of 6MPa, as specified by the

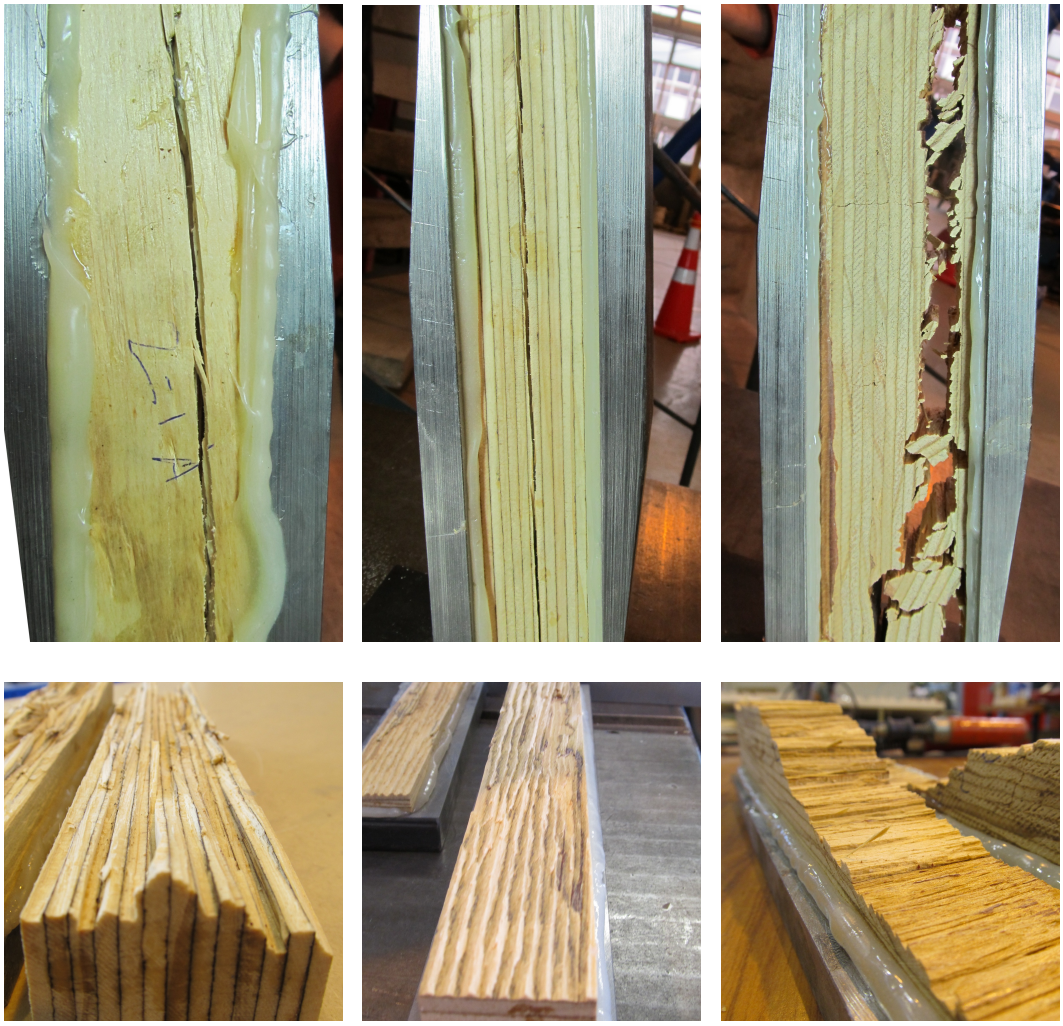

(a) Shear as beam (G_{TL}) (b) Shear as plank (G_{RL}) (c) Rolling shear (G_{RT})

Figure 3.12: Typical failures for shear testing

manufacturer for loading as a beam (G_{TL}), corresponds well with experimental testing results. Surprisingly the shear modulus in the orthogonal direction, G_{LT} was much lower than G_{TL}, even though both had shear stresses in the same orientations. It is unclear where this difference came from. Specimens loaded as a plank, G_{LR} and G_{RL}, both had very similar characteristic shear strength values of about 4.4MPa (or 3.5MPa without correction factor). The rolling shear strength, G_{RT}, had a characteristic value of about 1MPa. Again, for loading in the orthogonal direction, G_{TR} the shear strength was almost twice as high. Recommended shear strength values for design are 6MPa for loading as a beam, 3.5MPa for loading as a plank and 1MPa for rolling shear.

Table 3.11: Results of shear strength testing

Direction	Avg. failure stress (MPa)	Variation (%)	5^{th} percentile (MPa)	Char.[1] (MPa)	Char.[2] (MPa)
G_{LT}	5.52	17.1	4.11	3.65	2.99
G_{TL}	8.42	5.5	7.68	7.39	6.06
G_{LR}	5.33	8.0	4.66	4.40	3.61
G_{RL}	5.50	10.1	4.64	4.32	3.54
G_{TR}	3.01	5.5	2.75	2.64	2.17
G_{RT}	1.68	14.5	1.31	1.18	0.97

[1] Values included the correction factor of 1.22
[2] Values excluded the correction factor of 1.22

3.5.3 Shear stiffness

The shear strain has been obtained using the DIC technique. Images were taken of each specimen at 5 second intervals until failure of the specimen. Using software, a grid of markers was placed over the centre section of the specimen (Figure 3.13a) and markers were tracked through the series of images. An example of the displaced shape, multiplied with a factor 20, is shown in Figure 3.13b. For each of the images the horizontal and vertical shear deformations have been analysed. These deformations have been added to get the total shear deformation (Figure 3.13c), and rigid body rotation has been removed.

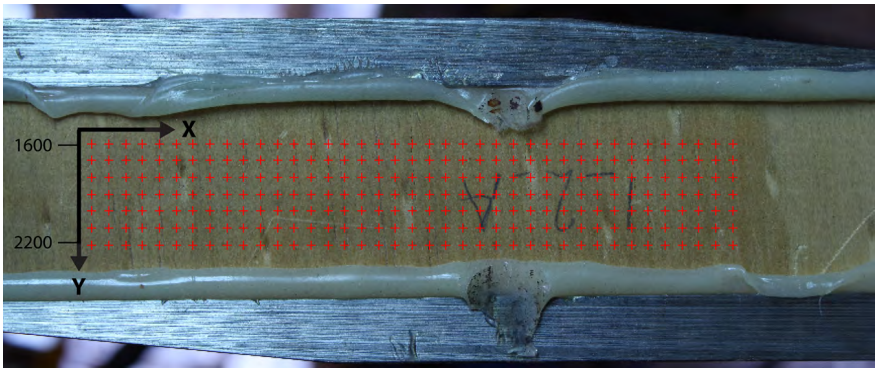

(a) Specimen (G_{LT}) with generated grid

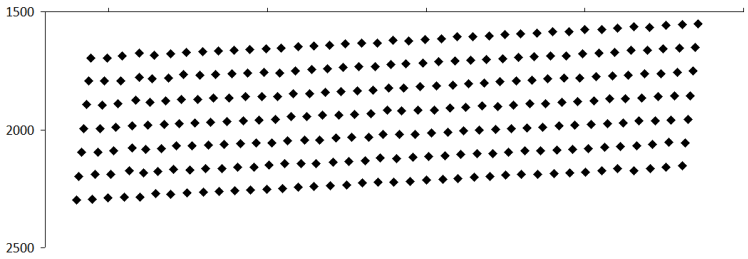

(b) Deformed grid (deformations multiplied by 20)

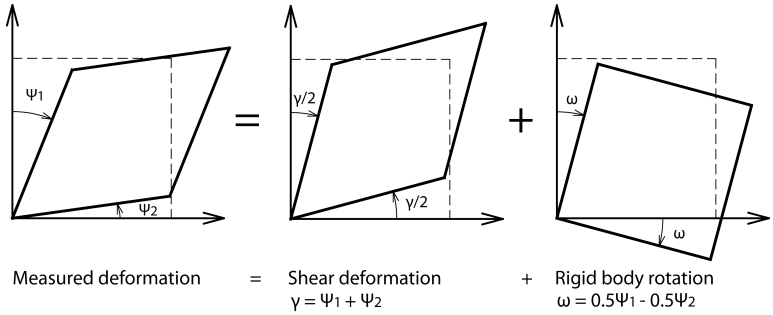

(c) Converting measured values into shear deformation and rigid body rotation

Figure 3.13: Evaluation of shear strain using Digital Image Correlation

When analysing this for all images the shear strain during testing can be found. Using corresponding timestamps from images and loading data, a stress-strain graph can be plotted. The slope of this graph, taken between 10% and 40% of maximum shear stress, gives the shear modulus. This procedure has been performed for all 36 shear tests, the result of which can be seen in Figure 3.14.

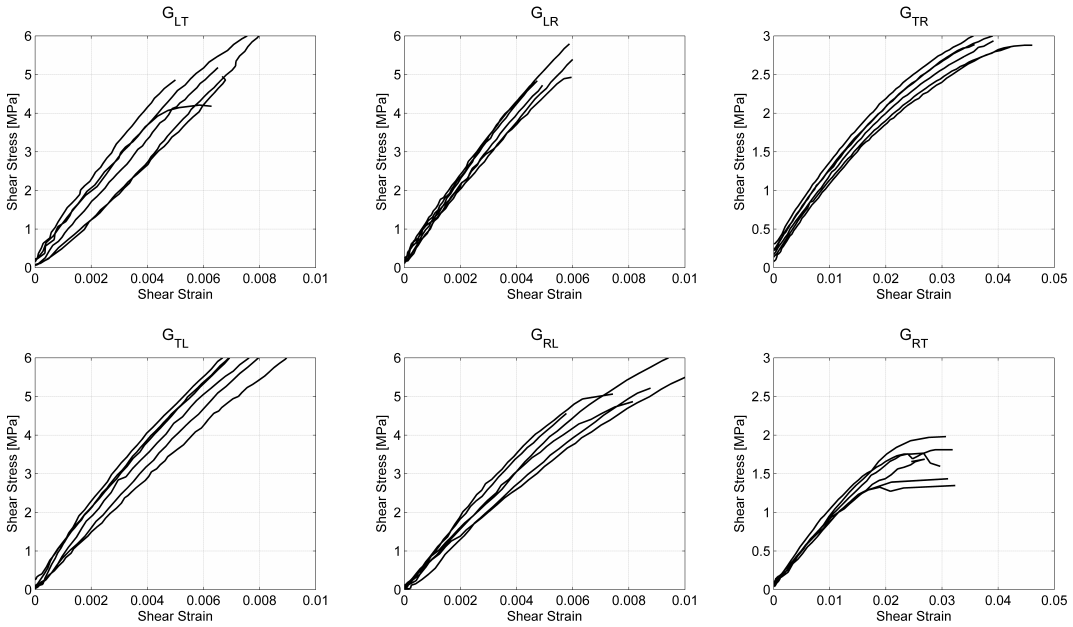

Figure 3.14: Shear stress-strain figures for six different directions

The average shear stiffness values and coefficient of variation is shown in Table 3.12. It can be seen that there is a very good correspondence between G_{LT} and G_{TL}. This should be the case as they correspond to loading in orthogonal plains which result in the same shear stress distribution and thus should result in the same shear stiffness. Also the rolling shear moduli, G_{TR} and G_{RT}, are very similar. Only G_{LR} and G_{RL} show a larger difference. Coefficients of variations between 4% and 16% were found.

Table 3.12: Experimental average values and coefficient of variations (CoV) for shear modulus

Property	Average (MPa)	CoV (%)
G_{LT}	842	15.4
G_{TL}	870	13.0
G_{LR}	1015	8.8
G_{RL}	786	16.2
G_{TR}	103	4.4
G_{RT}	89	11.5

3.6 Constitutive model

3.6.1 Theory

For the development of a 3D linear finite element material model a total of nine material properties are needed for the constitutive equations; three moduli of elasticity (E), three Poisson's ratios (ν) and three shear moduli (G). These equations are shown in the form of the compliance matrix in Equation 3.7. For LVL, having veneers rotary peeled and glued back together, there is no influence of growth rings and a clearly defined rectangular coordinate system can be used as shown in Figure 3.15. The three material directions are 1) Longitudinal - parallel to grain; 2) Tangential - perpendicular to grain and parallel to glue lines; and 3) Radial - perpendicular to grain and perpendicular to glue lines.

$$\begin{Bmatrix} \epsilon_{11} \\ \epsilon_{22} \\ \epsilon_{33} \\ \gamma_{12} \\ \gamma_{13} \\ \gamma_{23} \end{Bmatrix} = \begin{bmatrix} 1/E_1 & -\nu_{21}/E_2 & -\nu_{31}/E_3 & 0 & 0 & 0 \\ -\nu_{12}/E_1 & 1/E_2 & -\nu_{32}/E_3 & 0 & 0 & 0 \\ -\nu_{13}/E_1 & -\nu_{23}/E_2 & 1/E_3 & 0 & 0 & 0 \\ 0 & 0 & 0 & 1/G_{12} & 0 & 0 \\ 0 & 0 & 0 & 0 & 1/G_{13} & 0 \\ 0 & 0 & 0 & 0 & 0 & 1/G_{23} \end{bmatrix} \begin{Bmatrix} \sigma_{11} \\ \sigma_{22} \\ \sigma_{33} \\ \sigma_{12} \\ \sigma_{13} \\ \sigma_{23} \end{Bmatrix} \quad (3.7)$$

For an orthotropic material like timber, there are a total of six Poisson's ratios: ν_{12}, ν_{13}, ν_{21}, ν_{23}, ν_{31}, ν_{32}. Although it is commonly assumed that only three of these values are independent and that the compliance matrix is symmetrical (Maxwell's reciprocity principle). This means that off-diagonal terms have to be

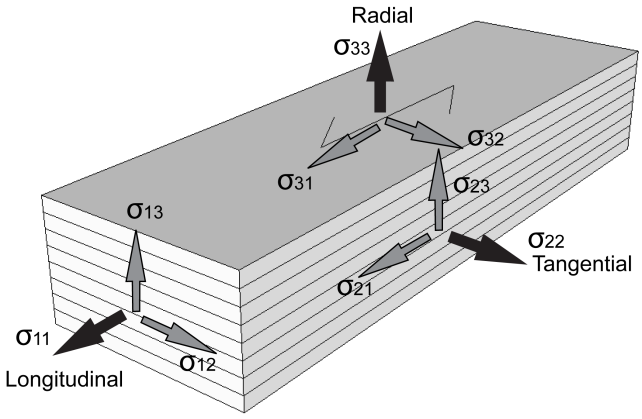

Figure 3.15: Coordinate system and stress directions in LVL

equal, which leads to relationships in Equation 3.8. Validity of this assumption is evaluated in the discussion section of this section. which results in a symmetrical compliance matrix.

$$\frac{\nu_{12}}{E_1} = \frac{\nu_{21}}{E_2}; \quad \frac{\nu_{13}}{E_1} = \frac{\nu_{31}}{E_3}; \quad \frac{\nu_{23}}{E_2} = \frac{\nu_{32}}{E_3} \tag{3.8}$$

3.6.2 Testing results

The average and coefficient of variation values for the moduli of elasticity (E), Poisson's ratios (ν) and shear moduli (G) in the three material orientations are shown in Table 3.13.

As expected for timber, the stiffness values parallel to grain were much higher than the stiffness perpendicular to grain. The stiffness in the tangential direction was slightly higher than in the radial direction. Variations in stiffness were less than 10% for all three directions. It should be kept in mind that this is the material variability of a small set of samples within one batch of LVL and is not representive of the variability within the LVL product.

The Poisson's ratio is strongly dependent on the direction, as is common for an orthotropic material. The variation in measurements is highest when extension happens in the longitudinal direction, ν_{TL} and ν_{RL}. This is due to small stresses in this direction and a high modulus of elasticity, resulting in very small strains. The second part of Table 3.13 shows average and coefficient of

Table 3.13: Experimental and computed average values and coefficient of variations (CoV) for E, ν and G. Bold values are recommended for use in FEM software.

Property	Average	CoV (%)
$\mathbf{E_L}$	**12157 MPa**	7.3
$\mathbf{E_T}$	**426 MPa**	5.0
$\mathbf{E_R}$	**371 MPa**	8.6
$\boldsymbol{\nu_{LT}}$	**0.59**	32.4
ν_{TL}	0.02	38.0
$\boldsymbol{\nu_{LR}}$	**0.48**	17.6
ν_{RL}	0.02	70.3
$\boldsymbol{\nu_{TR}}$	**0.22**	5.4
ν_{RT}	0.14	12.8
G_{LT}	842 MPa	15.4
G_{TL}	870 MPa	13.0
G_{LR}	1015 MPa	8.8
G_{RL}	786 MPa	16.2
G_{TR}	103 MPa	4.4
G_{RT}	89 MPa	11.5
ν_{LT}/E_L	48x10^{-6}	29.4
ν_{TL}/E_T	47x10^{-6}	40.6
ν_{LR}/E_L	39x10^{-6}	16.3
ν_{RL}/E_R	54x10^{-6}	70.9
ν_{TR}/E_T	516x10^{-6}	2.6
ν_{RT}/E_R	377x10^{-6}	10.8
$\mathbf{G_{LT+TL}}$	**856 MPa**	13.7
$\mathbf{G_{LR+RL}}$	**901 MPa**	17.7
$\mathbf{G_{TR+RT}}$	**96 MPa**	10.7

variation for off-diagonal terms in the compliance matrix. Normally this matrix is assumed symmetric, something which can now be verified. When comparing ν_{LT}/E_L and ν_{TL}/E_T very similar values can be seen. For ν_{LR}/E_L and ν_{RL}/E_R there is a larger difference, but this can be explained by the large coefficient of variation in the later measurement. For ν_{TR}/E_T and ν_{RT}/E_R the differences are significant and only small coefficient of variations are shown. Bodig and Jayne (1982) have also verified symmetry of the compliance matrix. Their conclusion was that although deviations exists the assumption of symmetry holds reasonably well. Furthermore they note that ν_{TL} and ν_{RL} are nearly always quite small and

may be subject to large experimental error, which has also been the case here. Although some difference between non-diagonal terms was measured, it would have large implications when implementing this in FEM software as it assumes a symmetrical constitutive matrix. Therefore it is suggested to use Poisson's ratios with the lowest variation: ν_{LT}, ν_{LR} and ν_{TR}.

The shear moduli found under six different loading orientations are listed in the top part of Table 3.13. It can be seen that there is a very good correspondence between G_{LT} and G_{TL}. This should be the case as they correspond to loading in orthogonal plains which result in the same shear stress distribution and thus should result in the same shear stiffness. Also the rolling shear moduli, G_{TR} and G_{RT}, are very similar. Only G_{LR} and G_{RL} show a larger difference. In the final part of Table 3.13 experimental results of orthogonal plains have been averaged. These values show a variation between 10% and 18%, indicating good repeatability in testing and analysis procedures.

3.6.3 Literature comparison

When comparing experimental results with literature values, shown in Table 3.14, several conclusions can be drawn. The modulus of elasticity in the longitudinal and the tangential direction(E_L and E_T) are within range of literature data. In the radial direction (E_R) the value is lower than all literature values. For sawn timber the modulus of elasticity in the radial direction is always larger than in the tangential directions, but this does not seem to be the case for LVL. This was most likely due to stiffer and weaker layers sharing the load perpendicular to grain, whereas the weakest layers are governing the stiffness in the radial direction. On the contrary, for sawn timber stiffness in the radial direction is higher than stiffness in the tangential direction due to wood rays, which act as reinforcing rods in the radial direction (Forest Products Laboratory, 1979). Due to peeling and glueing of LVL these rays are most likely damaged and do not contribute to the increased strength and stiffness in the radial direction. Comparison of E_R with other LVL products is not possible as Janowiak et al. (2001) based modulus of elasticity values on five point bending tests and thus could not evaluate the radial direction.

The Poisson's ratio ν_{LT} found by experimental testing of 0.59 corresponds

well with values for other LVL products found by Janowiak et al. (2001), but within the literature data there is a large spread in this Poisson's ratio. The Poisson's ratios ν_{LT} and ν_{LR} of Radiata Pine LVL are larger than of sawn pine species. The two small Poisson's ratios, ν_{TL} and ν_{RL}, of 0.02 are within range of literature data. The values of ν_{TR} and especially ν_{RT} are below values mentioned in literature. This can be due to influence of gluelines which add stiffness and reduce strains in the tangential direction.

The shear moduli G_{LT} and G_{LR}, of 856MPa and 901MPa respectively, are similar to values found in literature for softwoods. Shear stiffness values of different types of LVL, published by Janowiak et al. (2001), are lower than values found for Radiata Pine LVL and also mostly lower than other published values. For most species G_{LR} is slightly higher than G_{LT}, which is also found for Radiata Pine LVL. The rolling shear modulus, G_{TR}, of 96MPa is within range of values reported in literature.

Table 3.14: Overview of timber material properties from literature and experimental testing (values of E and G are in MPa)

Source	Timber species	E_L	E_T	E_R	ν_{LT}	ν_{TL}	ν_{LR}	ν_{RL}	ν_{TR}	ν_{RT}	G_{LT}	G_{LR}	G_{TR}
Experimental testing	Radiata Pine LVL	12157	426	371	0.59	0.02	0.48	0.02	0.22	0.14	856	901	96
Hearmon (1948)	Scots Pine	16300	570	1100	0.51	0.015	0.42	0.038	0.31	0.68	680	1160	66
	Softwoods (min.)	10700	430	710	0.37	0.015	0.37	0.028	0.25	0.43	620	500	23
	Softwoord (max.)	16400	900	1300	0.51	0.025	0.43	0.038	0.40	0.68	910	1180	79
	Hardwoods (min.)	10200	510	1130	0.43	0.009	0.23	0.018	0.24	0.60	600	900	190
	Hardwoods (max.)	16300	1140	2240	0.64	0.044	0.49	0.073	0.38	0.78	1060	1610	460
U.S. Dep. of Agriculture	Walnut	12741	714	1351	0.632	0.036	0.495	0.052	0.367	0.718	790	1083	266
Forest Prod. Lab. (1955)	Yellow-Poplar	11983	515	1102	0.392	0.019	0.318	0.03	0.329	0.703	827	899	132
Bodig and Goodman (1973)[1]	Sugar Pine	6743	588	884	0.349	–	0.356	–	0.358	0.428	763	836	96
	West. white Pine	9273	352	728	0.344	–	0.329	–	0.334	0.410	443	478	49
	Ponderosa Pine	7729	642	946	0.400	–	0.337	–	0.359	0.426	887	1069	117
	Lodgepole Pine	6557	447	666	0.347	–	0.316	–	0.381	0.469	301	322	32
	Red Pine	9873	430	867	0.315	–	0.347	–	0.308	0.408	800	945	114
	Loblolly Pine	11087	871	1253	0.292	–	0.328	–	0.362	0.382	898	903	142
	Pond Pine	19036	781	1356	0.364	–	0.280	–	0.320	0.389	862	958	173
	Longleaf Pine	14644	805	1487	0.365	–	0.332	–	0.342	0.384	886	1038	172
	Slash Pine	15975	725	1189	0.444	–	0.392	–	0.387	0.447	843	883	157
Forest Prod. Lab. (1979)	Douglas Fir	13400	670	911	0.45	0.02	0.29	0.02	0.29	0.39	1045	858	94
Bucur (2006)[2]	Sitks Spruce	9564	487	1037	0.45	0.49	0.43	–	–	–	1095	1196	91
Goncalves et al. (2011)[3]	Blue Gum	13617	2180	3680	0.78	0.060	0.333	0.038	0.300	0.420	1172	2360	829
	Garapeira	14333	1452	2323	0.250	0.078	0.180	0.040	0.330	0.790	1489	1865	536
Janowiak et al. (2001)[4]	South. Pine LVL	16500	580	-	0.644	–	–	–	–	–	476	354	64
	Douglas-fir LVL	18300	500	-	0.580	–	–	–	–	–	405	331	46
	Yellow-Popl. LVL	15200	450	-	0.604	–	–	–	–	–	247	314	96

1: Values converted from psi to MPa
2: Using acoustic testing methods
3: Average values taken from static testing
4: Poisson's ratios taken from compression test and shear values taken from five-point bending test

3.7 Conclusions

- Experimental testing of Radiata Pine LVL manufactured in New Zealand has resulted in a greater understanding of the material behaviour under compression. Strength and stiffness in three material directions have been evaluated. Testing has been performed based on rail tests as specified by the Australian/New Zealand standard and block tests according to the European standards. The small number of specimens is somewhat limiting for the calculation of characteristic values for use in design, but the main focus of testing was to determine material properties for the development of a constitutive model of LVL.

- A design compressive strength of 44MPa parallel to grain found by experimental testing compares well with the 45MPa specified by manufacturers. The compressive strength perpendicular to grain of 12MPa is only reached under specific loading conditions. A better approach is to use a compressive strength of 8MPa under uniform compression with small deformations and 10MPa when plastic deformation is acceptable. In the radial direction 7MPa and 9MPa can be used for elastic and plastic strengths, respectively. The rail test, as specified by the Australian and New Zealand standard (AS/NZS 4063.1:2010), only gives appropriate strength values if stress spreading can occur. No proper stiffness values can be found as stress spreading influences the results. Therefore recommended strength and stiffness values based on the European test method (EN 14374:2004 and EN 408:2010) are given.

- The plasticity model of van der Put provides a good prediction of strength increase under different loading configurations due to spreading of perpendicular to grain stresses. This method can be used for design at serviceability and ultimate limit states for tangential loads, but care should be taken for radial loading as spreading of stresses cannot be fully relied on. It was also found that cross-banded LVL hardly experiences any spreading of stresses and this should not be allowed for in design.

- Modulus of elasticity values from experimental testing of LVL11 were 12200MPa, 426MPa and 371MPa in longitudinal, tangential and radial

directions, respectively. It has been found that modulus of elasticity in the radial direction is lower than in the tangential direction, which is in contrast with literature values of sawn timber.

- Recommended shear strength values for design are 6MPa for loading as a beam, 3.5MPa for loading as a plank and 1MPa for rolling shear. Shear strength of 6MPa, as specified by the manufacturer for loading as a beam (G_{TL}), corresponds well with experimental testing results. Shear moduli have been determined using digital image correlation on testing according to the European timber testing standard. Values of 856MPa and 901MPa have been found for longitudinal shear moduli and 96MPa for the rolling shear modulus. These results are in line with literature values for sawn timber, but higher than those for LVL manufactured from different species.

- The use of digital cameras and digital image correlation has made it possible to extract Poisson's ratios from compression testing. Recommended values are $\nu_{LT} = 0.59$, $\nu_{LR} = 0.48$ and $\nu_{TR} = 0.22$. These Poisson's ratios compare well with values of other LVL products found in literature, but differ from literature values of sawn timber. The use of DSLR cameras for digital image correlation has proven to give very satisfactory results, although accuracy for two Poisson's ratios was limited due to very small strains along the grain direction whereby variations of up to 70% were found. Variation in results for moduli of elasticity was less than 9% and for shear moduli less than 17%.

- The reported elastic material properties make it possible to generate the constitutive matrix needed for FEM analysis. Diagonal terms follow directly from moduli of elasticity and shear moduli. Non-diagonal terms, calculated using Poisson's ratios and moduli of elasticity, are not all symmetrical but for practical purposes assumptions can be made to keep the benefits of a symmetrical constitutive matrix. Non-linear material data which can be used for FEM modelling was published in Table 3.8.

Chapter IV

Post-tensioned timber beams

4.1 Introduction

Design of long span timber beams is often governed by deflection criteria, resulting in an underutilization of the strength of timber. This can be partly resolved by adding a precamber which can be achieved during fabrication of glulam beams, but is difficult for LVL beams. Similar to concrete applications, the use of post-tensioning induces a precamber to hollow core box beams resulting in decreased deflections. Beams can be manufactured and stressed off-site, similar to precast concrete beams. On the building site beams can be placed between columns onto corbels.

Deflection behaviour of post-tensioned timber beams has been experimentally validated by Lago and Dibenedetto (2009) and it was concluded that the precamber was very useful in terms of reducing deformations in SLS design. The stiffness of the beams did not increase compared to a beam without post-tensioning, except for highly eccentric tendon configurations (external of the box beam). More details can be found in Section 2.4.4.

Application of unbonded post-tensioning also improves the load-carrying capacity since the compressive strength of LVL is considerably higher than the tensile strength. The ultimate limit state load-carrying capacity of post-tensioned timber box beams has not been tested before, and is the objective for this chapter.

Objectives for the experimental testing campaign are to:

1. Determine effects of post-tensioning on the failure strength of timber box beams.
2. Evaluate effects of post-tensioning on precamber and beam shortening.
3. Assess short-term deflection behaviour of post-tensioned timber box beams.

4. Determine global material properties (modulus of elasticity and shear modulus) for timber box beams.

This chapter first describes the design and test procedure of four box beams. Testing results of stiffness testing (without post-tensioning) are evaluated first and material properties are derived from these tests. Next, the results of beam stressing is shown, followed by results of testing until failure. Digital Image Correlation (DIC) techniques have been used to measure displacements and strains. Results of this and comparisons with traditional instrumentation are shown at the end of the results section. The chapter finishes with conclusions which can be drawn from the experimental testing and provides answers to the objectives stated above.

4.2 Beam design

Four box beams were designed. Beam 1 was a benchmark and did not have post-tensioning. Beam 2 had straight tendons running along the top of the bottom flange of the beam. Beams 3 and 4 both had draped tendons, but were designed to have different failure mechanisms. The design of the beams is further described in Appendix A.1.

Section properties of the four box beams are shown in Figure 4.1. Seven tendons (7-wire strands) of 12.7mm diameter were used to apply the post-tensioning force of 910kN. Design of the beams was based on the combined bending and axial load strength, shear strength and short term deflection limit of span over 300. The long-term deflection design check was ignored as this was not part of the objective of experimental testing.

4.3 Test Setup

4.3.1 Overview

Testing was performed as a four point bending test with a 9.15m span (Figure 4.2). One end of the beam was supported by a pin and the other end by a roller support. Two hydraulic actuators were used. One actuator was programmed to follow a displacement based loading protocol and the second actuator was

programmed to match load in the first actuator. This was done as one actuator combined with a spreader bar was not a viable option due to high loads.

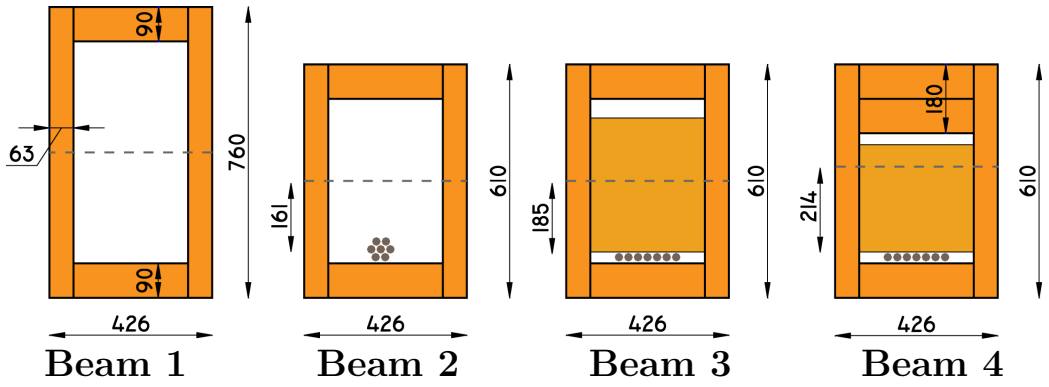

$A = 150 \cdot 10^3 mm^2$	$A = 130 \cdot 10^3 mm^2$	$A = 130 \cdot 10^3 mm^2$	$A = 158 \cdot 10^3 mm^2$
$A_s = 74.4 \cdot 10^3 mm^2$	$A_s = 59.7 \cdot 10^3 mm^2$	$A_s = 59.7 \cdot 10^3 mm^2$	$A_s = 57.2 \cdot 10^3 mm^2$
$Z = 28.2 \cdot 10^6 mm^3$	$Z = 19.9 \cdot 10^6 mm^3$	$Z = 19.9 \cdot 10^6 mm^3$	$Z = 20.2 \cdot 10^6 mm^3$
$I = 10.7 \cdot 10^9 mm^4$	$I = 6.07 \cdot 10^9 mm^4$	$I = 6.07 \cdot 10^9 mm^4$	$I = 6.74 \cdot 10^9 mm^4$

Figure 4.1: Section properties of tested beams

4.3.2 Testing schedule

All four beams were first tested without post-tensioning in order to determine material properties of each beam. This was done by cyclic testing up to 15, 30, 45 and 60mm mid-span deflection. Next the beams were stressed to the full design force, after which the beams were tested up to failure. An overview of the testing schedule is given in Table 4.1.

4.3.3 Instrumentation

Three 1000kN load cells were used, one for each hydraulic actuator and one for the post-tensioning force (Figure 4.3a). Above each support, at the location of the neutral axis of the beam, an inclinometer was placed to measure rotations at the end of the beam (Figure 4.3b). Rotary pots were measuring deflections at mid-span and at both deviators (Figure 4.3c). Another rotary pot was fixed to the beam and measured shortening of the beam (Figure 4.3b). A series of seven strain gauges was glued to the middle of the beam (Figure 4.3c). On each

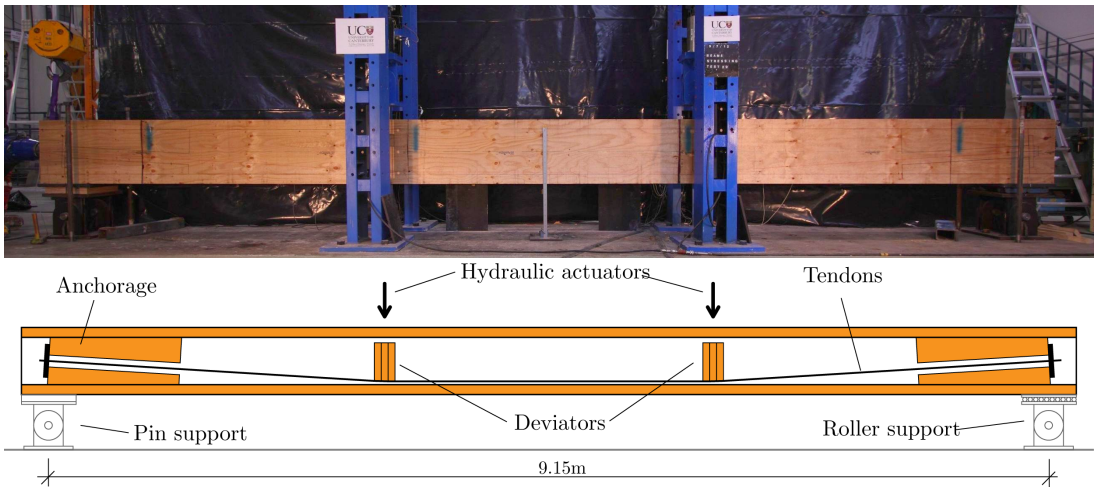

Figure 4.2: Photo and drawing of four-point bending test setup for beam with draped tendons

Table 4.1: Schedule of beam testing

Test	Beam		PT	Type
1.1	1	Benchmark	no	Stiffness
1.2	1	Benchmark	no	Strength
2.1	2	Straight PT	no	Stiffness
2.2	2	Straight PT	yes	Strength
3.1	3	Draped PT	no	Stiffness
3.2	3	Draped PT	yes	Strength
4.1	4	Draped PT (2)	no	Stiffness
4.2	4	Draped PT (2)	yes	Strength

side, half way between the support and the deviator, two potentiometers were placed at a 90 degree angle to measure shear deformation (Figure 4.3d). These potentiometers were removed for failure testing. This method for measurement of shear deformation is taken from EN 408:2010 (CEN, 2010). Drawings of the exact location of instrumentation are given in Appendix G. A list of instrumentation and corresponding data channels is given in Appendix C.1

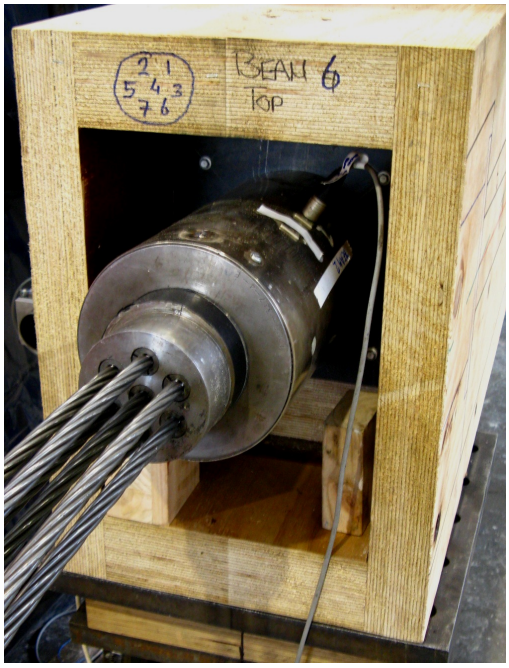

(a) Load cell for PT

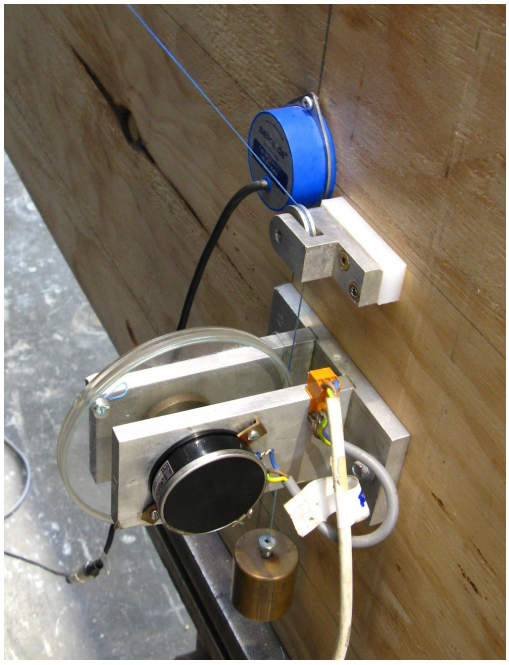

(b) Inclinometer and rotary pot

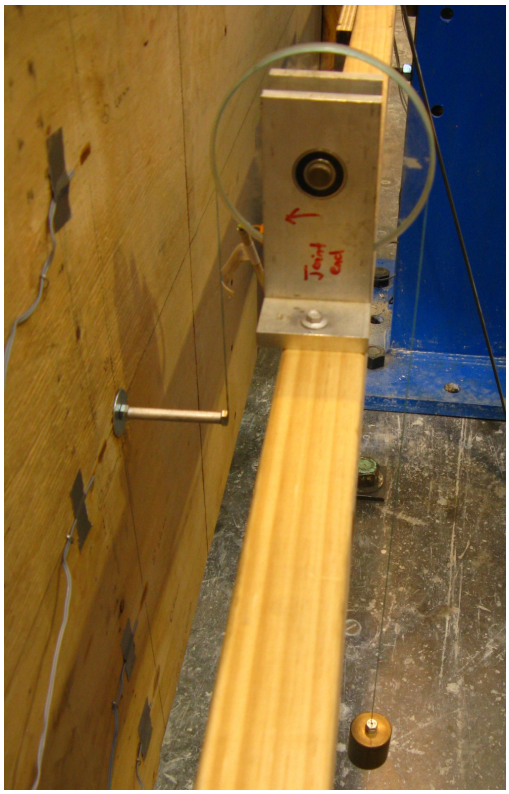

(c) Strain gauges and deflections

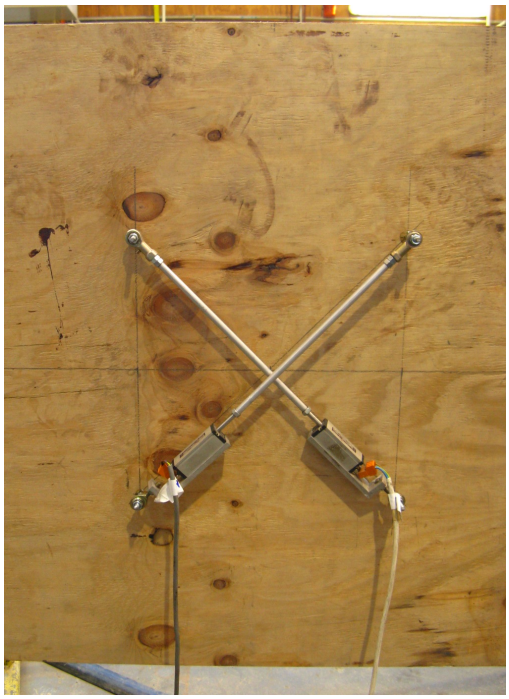

(d) Shear deformation

Figure 4.3: Instrumentation for beam testing

4.4 Test Results

This section describes the test results for all four beams. First the stiffness tests are evaluated in order to determine the actual material properties. Next results of the strength testing are evaluated.

4.4.1 Stiffness testing

From testing without post-tensioning (Figure 4.4a) the material properties, modulus of elasticity and shear modulus, were derived. Shear deformation was measured on both sides of the beam. Two potentiometers were placed diagonally in a square grid of 300 by 300mm (Figure 4.3d). Measurements of both potentiometers (Δs_1 and Δs_2) were used to calculate shear deformation using Equation 4.1.

$$\gamma_{shear} = \frac{(\Delta s_1 - \Delta s_2)\sqrt{a^2 + b^2}}{2ab} \tag{4.1}$$

Where:

- γ_{shear} = Shear deformation (mrad)
- Δs_1 = Measurements from diagonal potentiometer 1 (mm)
- Δs_2 = Measurements from diagonal potentiometer 2 (mm)
- a = Horizontal distance between potentiometers (mm)
- b = Vertical distance between potentiometers (mm)

The shear force distribution is equal on both sides and equals the force (F) of the hydraulic actuator (Figure 4.4b). The shear stress distribution in the cross-section is shown in Figure 4.5. The shear stress at every point can be calculated using structural mechanics equations as shown in Equation 4.2. The average shear stress over the centre 300mm of the beam was calculated as in Equation 4.3. When plotting shear stress versus shear deformation, the shear stiffness can be found as the slope of the graph.

$$\tau_i = \frac{V \cdot Z_i}{2 \cdot t_i \cdot I} \tag{4.2}$$

Where:

- τ_i = Shear stress at location i (MPa)

- V = Shear force (N)
- Z_i = Section modulus for area above location i (mm^3)
- t_i = Section thickness at location i (mm)
- I = Moment of inertia of full section (mm^4)

$$\tau_{average} = \tau_2 + \frac{2}{3}(\tau_1 - \tau_2) \tag{4.3}$$

The bending moment distribution in the whole beam is shown in Figure 4.4c. The mid-section of the beam can be isolated (Figure 4.4d) and has a constant bending moment M_{mid} (Figure 4.4e) without any shear. From this section, the modulus of elasticity of the beam in pure bending can be calculated. Mid-span displacement, relative to the deviator displacement, was calculated using Equation 4.4. The modulus of elasticity was calculated using Equations 4.5 and 4.6.

$$u_{mid,rel} = u_{mid} - \frac{u_{dev,1} + u_{dev,2}}{2} \tag{4.4}$$

$$\Delta u_{mid,rel} = \frac{\Delta M_{mid} \cdot (l/3)^2}{8EI} \tag{4.5}$$

$$E = \frac{\Delta M_{mid} \cdot (l/3)^2}{\Delta u_{mid,rel} \cdot 8I} = \frac{\Delta F \cdot l^3}{\Delta u_{mid,rel} \cdot 216I} \tag{4.6}$$

An example of the above procedure to determine material properties is shown in Figure 4.6. The slope of the trendline of shear stiffness measurements result in a shear stiffness of 654MPa and 713MPa for side 1 and 2, respectively. The slope of the trendline of modulus of elasticity results in a MoE of 10.7GPa. This evaluation has been done for all four beams and the results can be seen in Table 6.2. It can be seen that modulus of elasticity corresponds very well with the specified value of 11GPa. But the shear modulus is 26% higher than the suggested value 550MPa. The ratio of $E/G = 11100/694 = 16$ seems more suitable for this batch of LVL.

An alternative way for determining the modulus of elasticity is based on using strain gauges. These strain gauges were fixed to mid-span of the beam. The average of top and bottom strain gauge was used to determine the bending strain in the beam. The bending moment under a four-point bending test was

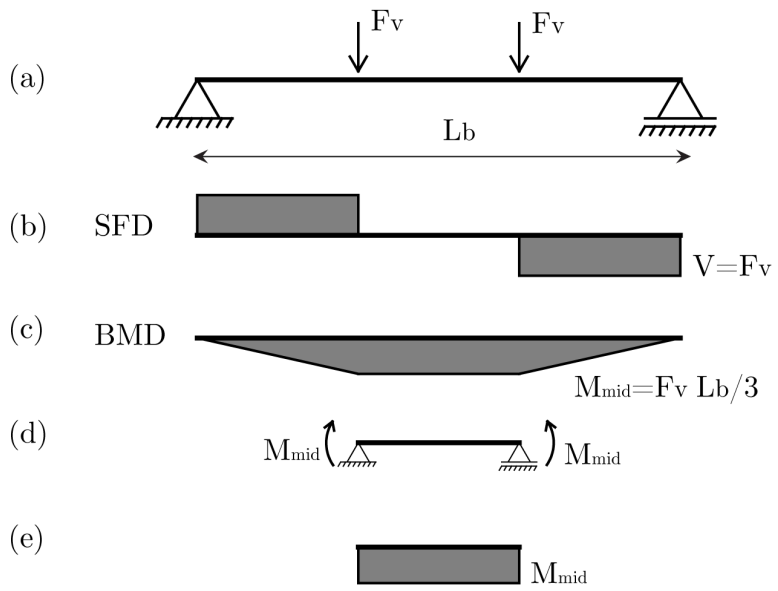

Figure 4.4: (a) Schematics of 4 point bending test; (b) shear force diagram; (c) bending moment diagram, (d) isolation of mid-section and (e) pure bending in mid-section.

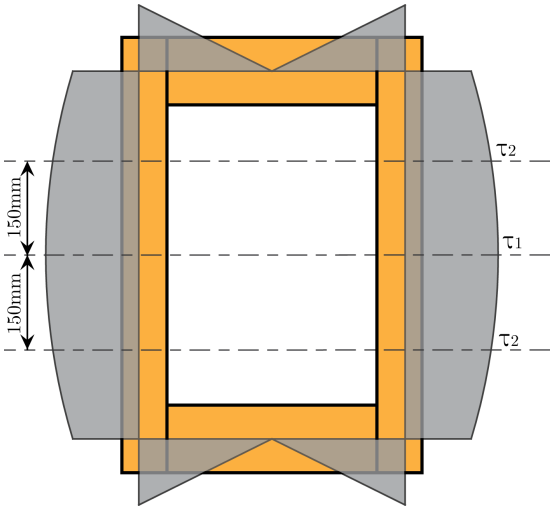

Figure 4.5: Shear stress distribution in box beam

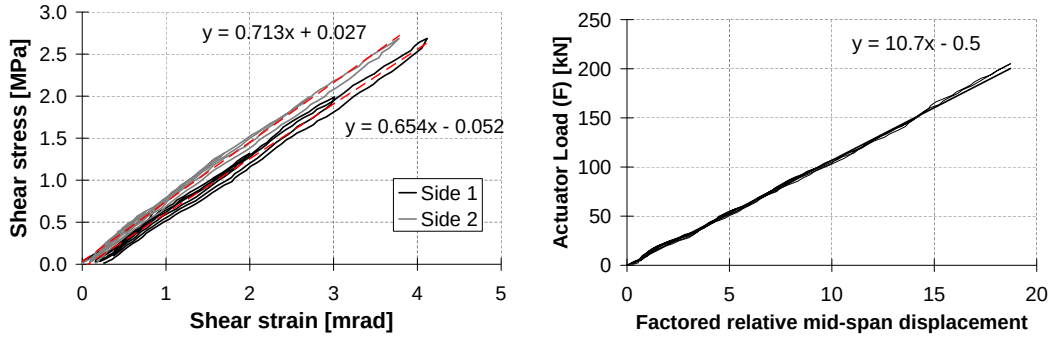

(a) Shear Modulus (b) Modulus of Elasticity

Figure 4.6: Determining shear modulus from slope of shear stress-strain plot and modulus of elasticity from slope of load-displacement plot, for Beam 1

calculated using Equation 4.7. From this bending moment the bending stress could be calculated by dividing bending moment by section modulus. The slope of a stress-strain plot resulted in the modulus of elasticity, as shown in Figure 4.7. This procedure was performed for all stiffness tests (results for Beam 4 were not available) and resulting moduli of elasticity are presented in Table 4.2. It can be seen that the difference between the two methods of determining the modulus of elasticity are small, with a maximum difference of 6%.

$$M_{mid} = F_v \cdot L_b/3 \tag{4.7}$$

Table 4.2: Shear modulus for left and right section of beam, and modulus of elasticity based on displacement and strain gauge measurements for all four beams. Also shown are average values and coefficients of variation (CoV).

Beam	Shear modulus		Modulus of Elasticity	
	Left (MPa)	Right (MPa)	Displacement (GPa)	Strain gauges (GPa)
1	654	713	10.7	10.6
2	593	669	10.9	11.6
3	713	694	11.2	11.8
4	722	791	11.4	-
Average	*694*		*11.1*	*11.3*
CoV	*8.6%*		*2.7%*	*5.7%*

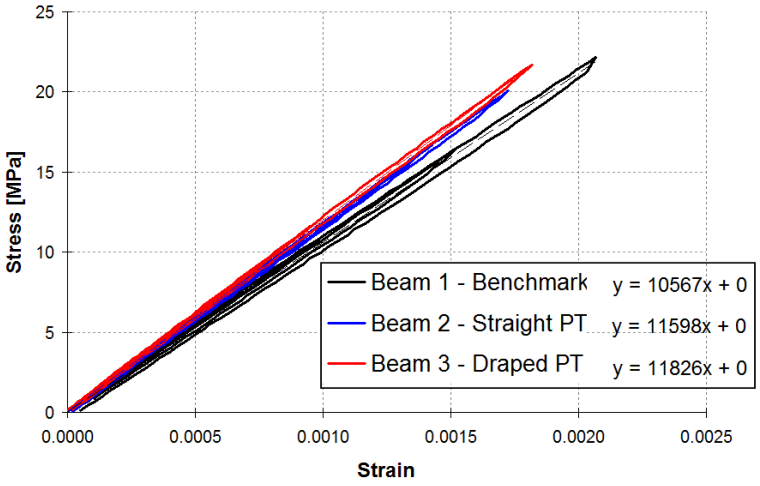

Figure 4.7: Stress-strain plots for determination of modulus of elasticity

4.4.2 Stressing of beams

Stressing of beams introduces stresses and deflections making it an integral part of testing. Instrumentation was zeroed shortly before stressing and data was recorded every second during stressing. The design post-tensioning force was 910kN. Beam 2 was stressed up to 882kN, Beam 3 up to 904kN and Beam 4 up to 878kN, all within 5% of the design value of 910kN. Figure 4.8a shows the post-tensioning force over time during stressing for each beam. It can be seen that all beams were first stressed to a higher level and the force subsequently dropped as pressure in the post-tensioning jack was released and the anchorage wedges gripped the tendons and set into the anchorage disk. The loss of post-tensioning force ranged between 85 and 107kN, which was 9% to 11% of the post-tensioning force before releasing the jack. This showed the amount of overstressing which is needed to achieve the required post-tensioning force.

Figure 4.8b shows shortening of the beam, measured at location of neutral axis, during the stressing operation. Shortening of Beams 2 and 3 was 4.2 and 4.9mm, respectively. For Beam 4 shortening was less, around 2mm, partly due to increased cross-sectional area. Shortening can be calculated using Equation 4.8, for Beams 2 and 3 this resulted in 5.8mm shortening. Similar calculations for Beam 4 resulted in 4.7mm. It can be seen that these values of shortening are higher than values measured in the laboratory. One explanation is that modulus

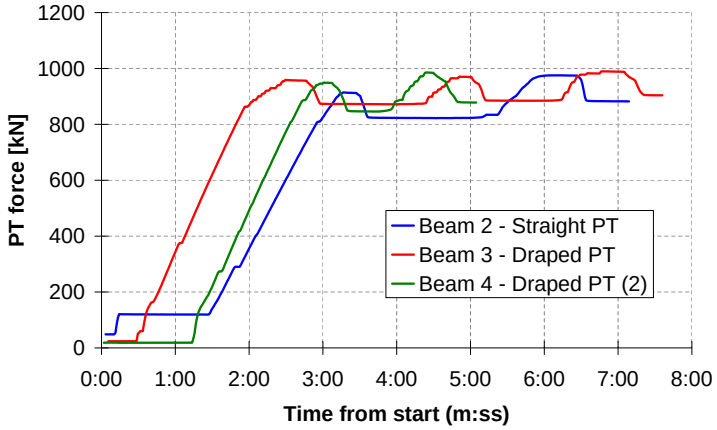

(a) Post-tensioning force over time

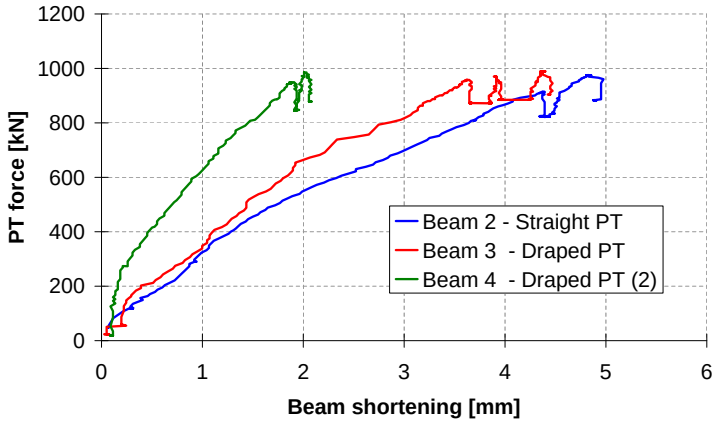

(b) Shortening of beam due to post-tensioning force

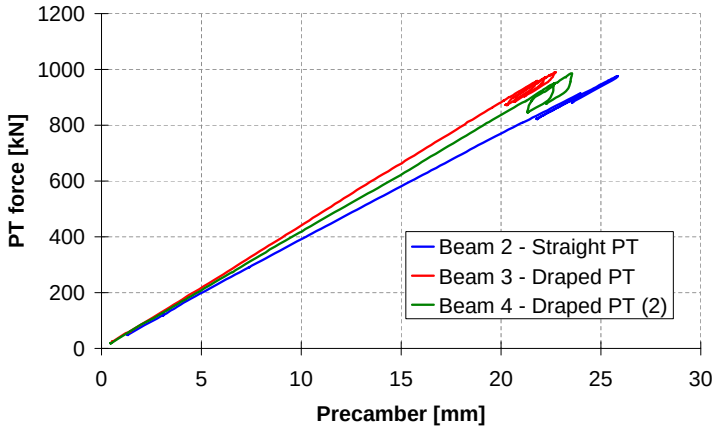

(c) Precamber at mid-span

Figure 4.8: Measurements during stressing operation

of elasticity in pure compression is different from modulus of elasticity in bending. When using a modulus of elasticity of 12100MPa, based on experimental testing data presented in Section 3.3, beam shortening becomes 5.2 and 4.3mm. These values are closer to the measured values. In the design process this shortening should be allowed for, either by designing the beam slightly longer or by having adequate construction tolerances.

$$\Delta l = l \cdot \epsilon = \frac{N \cdot l}{EA} = \frac{900 \cdot 10^3 \times 9144}{11000 \times 130 \cdot 10^3} = 5.8mm \tag{4.8}$$

Where:

- Δl = Change in length (mm)
- N = Compression force (N)
- l = Beam length (mm)
- E = Modulus of Elasticity in compression (MPa)
- A = Cross-sectional area (mm^2)

Mid-span precamber during stressing is shown in Figure 4.8c. The final precamber was 23.5, 21.4 and 22.1mm for beams 2 to 4. All three beams had the same post-tensioning force (within 2%), but precamber was largest for Beam 2. Beam 4 had less precamber due to the higher stiffness of the cross-section. Beam 3 had less precamber as the area of the bending moment diagram was smaller, but the added contribution of shear uplift should have increased the uplift. It is unclear why this did not happen.

During stressing of Beam 2 one of the anchorages failed due to stress spreading which resulted in tensile stresses perpendicular to grain (Appendix B.2). The failure resulted in partial cracking of the web of the beam. An attempt was made to repair the crack by gluing on an extra sheet of LVL. Furthermore after repairing the anchorage block, fully threaded screws were inserted to prevent splitting from happening. Based on experimental testing and numerical modelling of the anchorages (Appendix B.2), the anchorage blocks for Beams 3 and 4 were increased in length and screws were inserted to resist the tensile stresses.

4.4.3 Strength testing

Images taken just after failure of each beam can be seen in Figure 4.9.

(a) Failure of Beam 1 - Benchmark

(b) Failure of Beam 2 - Straight PT

(c) Failure of Beam 3 - Draped PT

(d) Failure of Beam 4 - Draped PT (2)

Figure 4.9: Failure images of all four beams

Beam 1 had a typical bending failure, starting at the bottom of the beam. Some problems with the post-tensioning anchorage resulted in a partly cracked web for Beam 2. Guidance for anchorage design can be found in Appendix B. An attempt was made to fix this by putting epoxy in the crack and glueing on a patch of LVL. Although pressure was applied directly after glueing, this might not have been enough as a shear failure in the web occurred where the glue line between beam and patch failed. The shear failure was followed by bending/tensile failure at the bottom flange. Beam 3 started to fail in compression in the top flange, just next to the loading plate (Figure 4.10). After compression failure, vertical loading could be increased until the bottom flange failed in tension. Beam 4 had a tensile failure in the bottom flange, but post-tensioning and top flange still resisted about 40% of failure load.

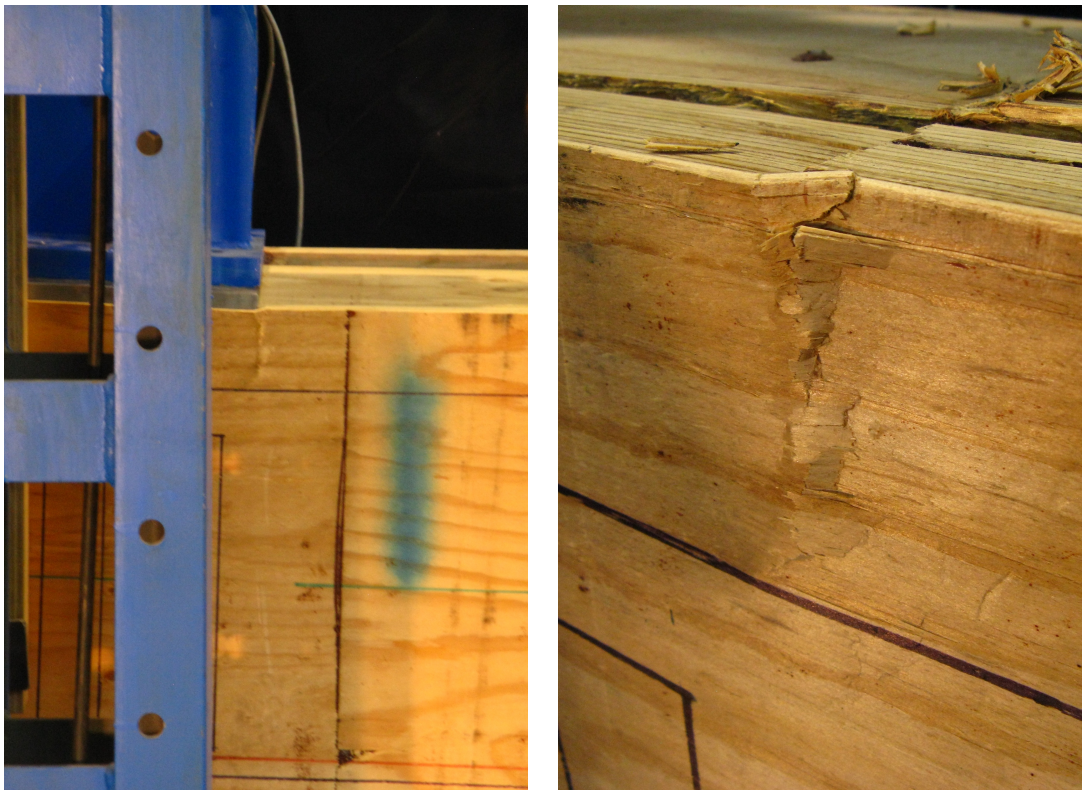

(a) During testing (b) After testing

Figure 4.10: Close-up of compression failure in top flange of Beam 3 - Draped PT

Figure 4.11 shows the load deflection graphs for all four beams. Also shown are the deflection limit of 30mm and the design load of 330kN. Actual load and deflection values at different stages of testing are presented in Table 4.3.

Beam 1, without post-tensioning showed very linear behaviour until sudden brittle failure at bottom of the beam at 695kN loading. The higher stiffness in comparison with the other beams was due to larger section height. Beam 2, with straight PT, started with a precamber of just over 20mm and failed under 536kN load. This was a shear failure in one of the webs due to damage which occurred during initial stressing. Therefore the real section capacity is most likely greater. Beam 3, with draped PT, started with a similar precamber as Beam 2. At 660kN vertical load the top flange recorded the maximum compression strain and compression failure started (Figure 4.10), followed by a load increase until tensile failure at the bottom was reached under a vertical load of 726kN. Beam 4,

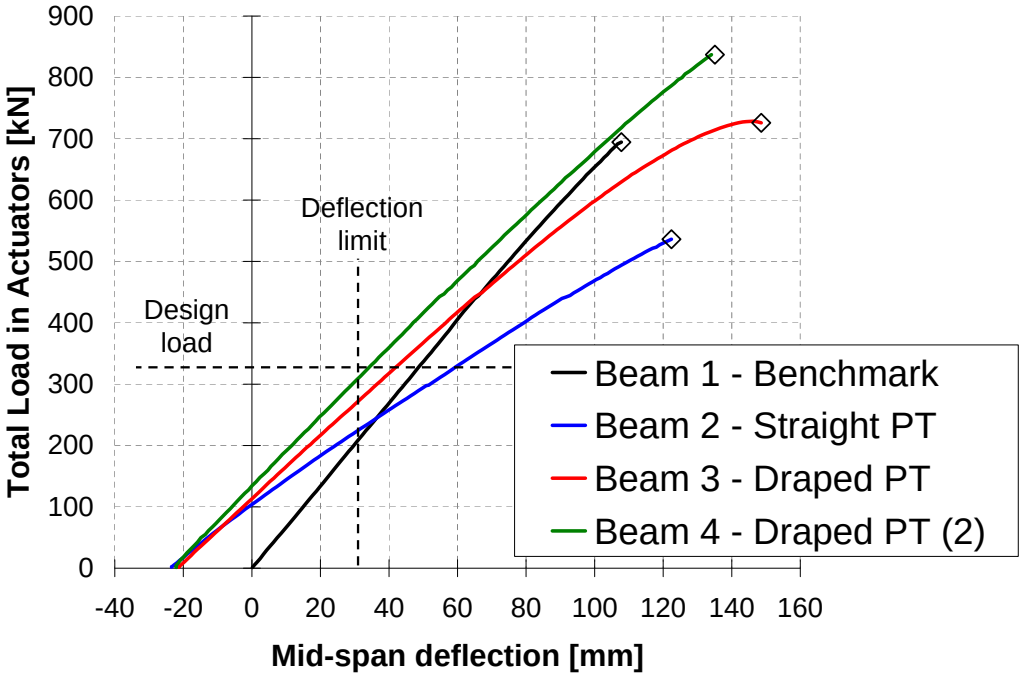

Figure 4.11: Total vertical load versus mid-span deflection curves for all four beams

Table 4.3: Load and deflection values at different stages of experimental testing of post-tensioned beams. For Beam 3 values in brackets correspond to tensile failure.

Beam	Type	Load (kN) / Deflection (mm)			
		After stressing	SLS limit	Design load	Failure
1	Benchmark	0 / 0.0	200 / 30	330 / 49.1	695 / 107.8
2	Straight PT	0 / 23.5	223 / 30	330 / 60.0	536 / 122.4
3	Draped PT	0 / 21.4	267 / 30	330 / 42.5	660 / 116.2 (726 / 148.6)
4	Draped PT (2)	0 / 22.1	307 / 30	330 / 34.9	837 / 135.1

with double top flange, also had just over 20mm precamber and showed a brittle tension failure under 837kN vertical load. The load increase between Beam 3 and 4 is due to the extra timber in the top flange and increased eccentricity of the post-tensioning.

A serviceability limit state design limit of span over 300 results in allowable deflections of 30mm. It can be seen that Beam 1 reaches this at a load of 200kN. For Beams 2 to 4 the loads are 223kN, 267kN and 307kN, respectively (Table 4.3). This is an increase in load carrying capacity at SLS design level of 12%, 34% and 54% despite the reduction in section height. This clearly shows the benefit of the precamber, created by post-tensioning.

The stiffness of the beams was influenced by beam depth and post-tensioning. Stiffness was evaluated from the load-deflection plot (Figure 4.11) on the section between 10% and 40% of maximum load. The resulting stiffness values were 6.76, 3.99, 5.13 and 5.68kN/mm. The reduced stiffness of Beam 2 compared to Beam 3 could have been caused by the damaged web of the beam. Beam 4 has a higher stiffness than Beam 3 due to the thicker top flange. Beam 1 has the highest stiffness as the section height was increased from 610mm to 760mm.

4.4.4 Post-tensioning force

Post-tensioning force increased during testing due to tendon elongation. Elongation happened either due to rotations at the end of the beam, for straight tendons anchored eccentrically, or due to deviator deflection for beams with draped tendons. Tendon elongation during testing can be seen in Figure 4.12. The initial post-tensioning force and maximum post-tensioning force are shown in Table 4.4. It can be seen that beams with draped tendons had more tendon elongation than beams with straight tendons. The yield strength of the tendons was 1064kN ($7 \times 152kN$), for both beams with draped tendon profiles the maximum post-tensioning force was past this level. The post-tensioning force of 1080kN corresponded to 83% of ultimate strength.

4.4.5 Strain profiles

Strain profiles at mid-span were measured using several strain gauges, located at top and bottom of both flanges and at neutral axis height. Figure 4.13 shows the

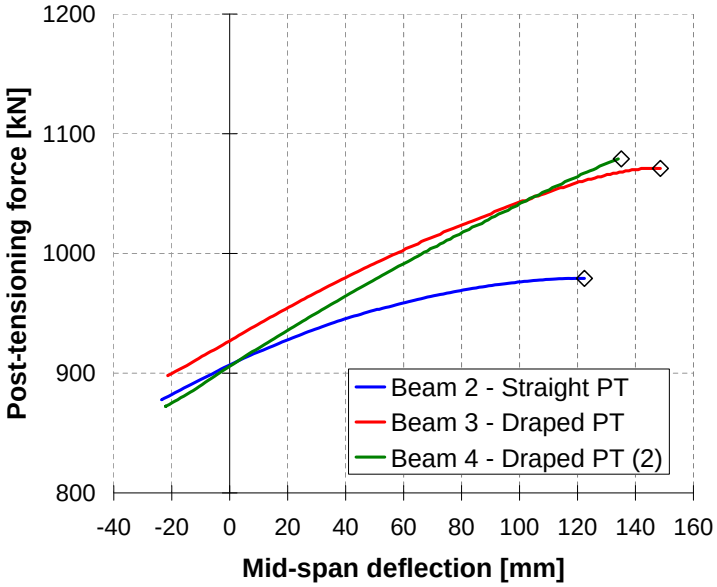

Figure 4.12: Post-tensioning forces during testing

Table 4.4: Initial and maximum post-tensioning force during testing of post-tensioned beams

Beam	Type	$F_{pt,i}$ (kN)	$F_{pt,max}$ (kN)	Increase
1	Benchmark	-	-	-
2	Straight PT	878	979	12%
3	Draped PT	898	1071	19%
4	Draped PT (2)	872	1080	24%

strains at four different points during testing, namely at zero vertical load (PT only), at the SLS deflection limit, at the ULS design limit and at failure.

With zero vertical load (PT only), the post-tensioned timber beams have mainly compression and some tension at the top. Strains are lowest in Beam 4 due to the larger cross-sectional area. The benchmark beam, without post-tensioning, obviously has zero strain.

At SLS deflection limit, strain profiles are almost reversed compared to PT only. The bottom section is in tension, but the beam is mainly in compression. A clear difference with the benchmark beam can be seen, which has half the section

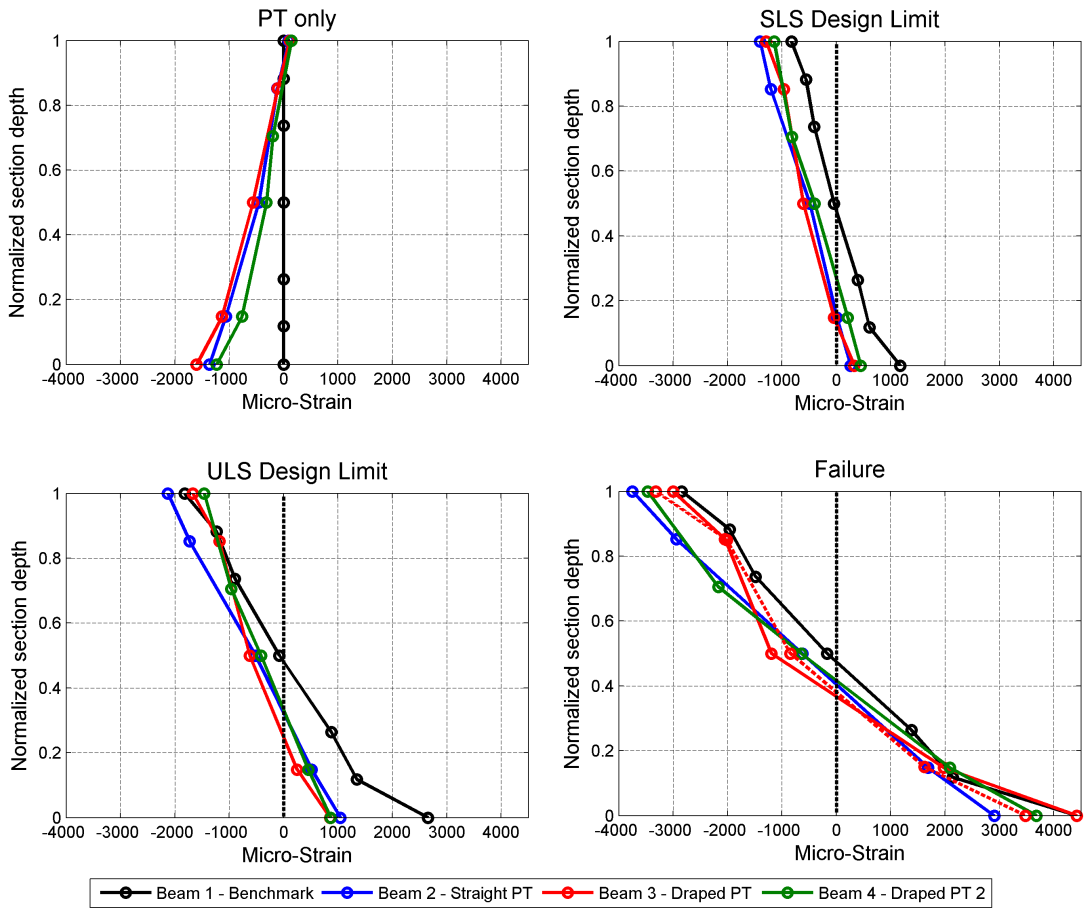

Figure 4.13: Strain profiles at four stages during testing. Vertical axis shows normalized section depth for clearer comparison.

in tension and half in compression. At ULS design limit, the post-tensioned beams still show very linear strain profiles, whereas the benchmark beam shows high tensile strains near the bottom fibres.

At failure, very high tensile strains are shown by Beams 1 and 3. Also Beam 4 shows high tensile strains, whereas Beam 2 (which failed in shear) still showed a very linear strain profile. The neutral axis of Beam 1 is still at the centre of the beam, whereas the neutral axis of the post-tensioned beams are lower. For Beam 3, two failure lines are shown. The dashed line indicates when compression failure started in the top flange and the continuous line is when tensile failure occurred in the bottom flange. It can be seen that between the two failure modes maximum compressive strains at mid-span decreased, the neutral axis moved

down and tensile strains increased.

Figure 4.14 shows the stresses, derived from the strain measurements under final failure load immediately before failure, multiplied with the MoE in bending (Section 4.4.1). The design bending strength (f_b) limit ($k_{24} \times f_b$) is also shown.

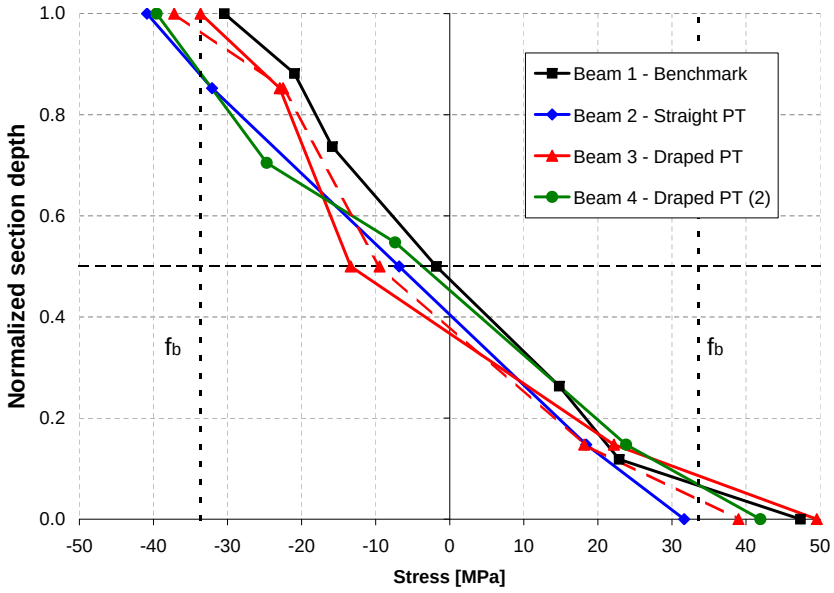

Figure 4.14: Mid-span bending stress profiles immediately before failure. For Beam 3 the dashed line is compression failure, the continuous line is tensile failure. Also shown is the design bending strength limit.

When analysing results at the centroid of the beam it can be seen that Beam 1 was close to zero stress. Beam 2 and Beam 4 had a stress of 6.8 and 7.8MPa, respectively. Beam 3 started to show plastic behaviour at the top flange in compression, resulting in lowering of the neutral axis and thus an increased stress of 13.2MPa at beam mid-height. The maximum tensile stress for all beams, except for Beam 2 which failed prematurely in shear, was between 42 and 50MPa. The maximum compression stresses were between 30 and 41MPa. It can be seen that Beam 1 (benchmark beam) did not reach the compression bending capacity, as tensile failure happened before the maximum bending strength was reached.

4.4.6 Mid-span bending moments

Mid-span bending moments could be directly evaluated from measurements using strain gauges. Bending strains multiplied with the modulus of elasticity, as presented in Table 6.2, resulted in bending stresses. These stresses multiplied with section modulus gave the bending moment at mid-span. The resulting values are plotted against mid-span deflection in Figure 4.15. Maximum bending moments were 1083, 768, 874 and 909kNm for Beams 1 to 4, respectively. A very linear relationship can be seen for all beams. The increased stiffness of Beam 1 is clearly visible as this beam has less mid-span deflection compared to the other beams. It can also be seen that after the compressive failure of Beam 3, further loading resulted in additional deflections with only very minor increase in mid-span bending moment.

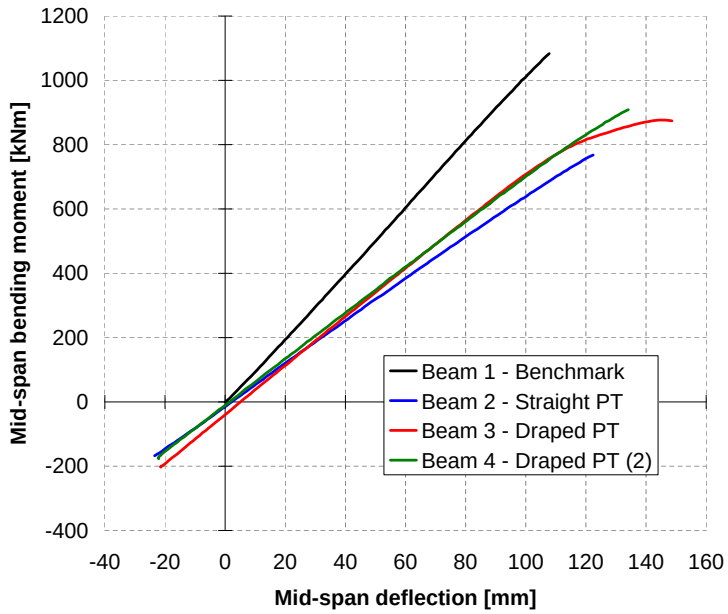

Figure 4.15: Mid-span bending moments versus mid-span deflection

4.4.7 Digital Image Correlation

Two digital SLR cameras were used during testing, Camera 1 was setup to capture the whole beam and Camera 2 was zoomed in on the mid-span. At every step

(a) Full beam

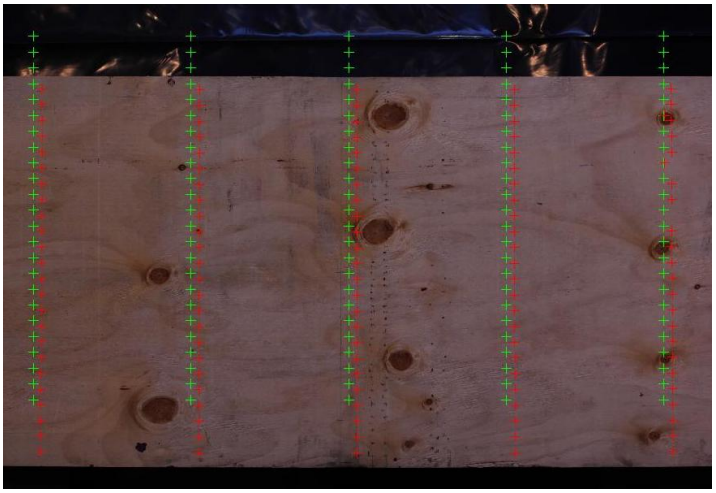

(b) Mid-span of beam

Figure 4.16: Digital Image Correlation tracking of grid, green crosses show initial grid, red crosses show displaced grid.

of the loading protocol a picture was taken. Digital Image Correlation (DIC) software was used to track a grid of pixels through the testing sequence. Figure 4.16 shows an example of the images which were taken with the grid of markers, green crosses show the initial grid and the red crosses show the displaced grid. For every step and for every grid marker the horizontal and vertical position in pixels is calculated. This can be scaled to displacements in millimetres using a scaling factor. The scaling factor is related to resolution of the camera (number of pixels) and size of the object. For Beam 1 this was 2.825mm/pixel and 0.308mm/pixel for Camera 1 and 2, respectively. The software used sub-pixel analysis methods, meaning that it could track displacements smaller than 1 pixel. The first scaling factor gave enough accuracy to track displacements of the beam, whereas the second scaling factor was accurate enough to measure strains.

Displacements found by DIC can be compared with displacements measured using potentiometers. This is done for mid-span displacements in Figure 4.17a.

It can be seen that both measured mid-span displacements are very close. Figure 4.17b shows the difference between mid-span displacements using potentiometer data and DIC measurements. It can be seen that differences between the measurements are always within 3mm, which given the maximum displacements in the order of 140mm is about 2%. This difference is mainly due to calibration factors.

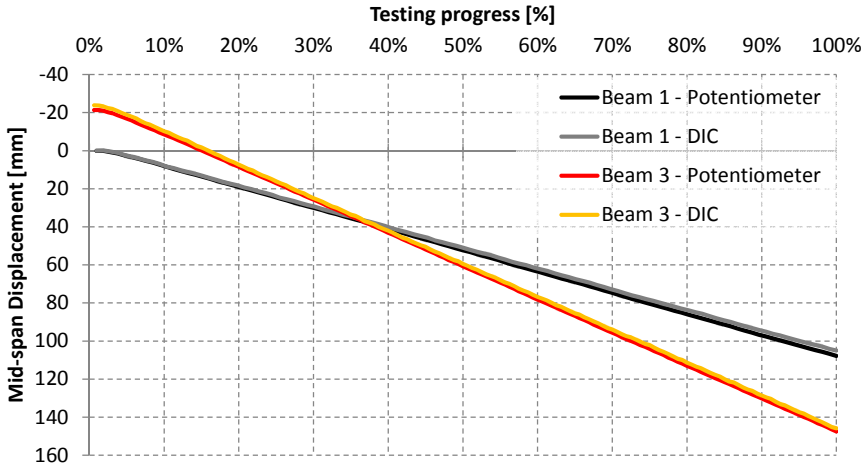

(a) Comparison of mid-span displacements between DIC and potentiometer data for Beams 1 and 3

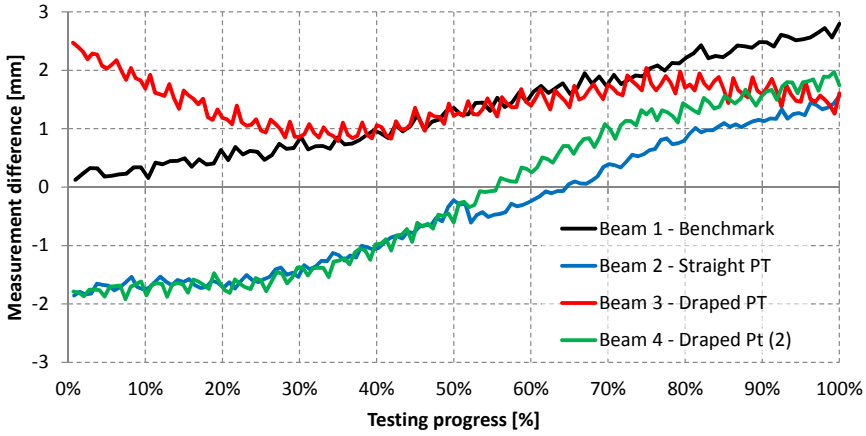

(b) Difference between potentiometer displacements and DIC measurements

Figure 4.17: Comparison of potentiometer and DIC measurements

In Figure 4.18 the full displacement profiles along the length of the beam are shown. There are no markers at 1/3rd and 2/3rd length of the beam due to the

position of the reaction frame. It can also be seen that the ends of the beam, which are situated above the centres of the supports undergo small deflections. This is due to perpendicular to grain compression stresses at the supports.

Strains at mid-span of Beam 1 have been analysed using DIC. The grid used is shown in Figure 4.16b. Several badly tracked markers were removed. Displacements between every row of pixels have been converted to strains and the average strain between the five rows has been calculated. A comparison of strain profiles, measured using Strain Gauges (S.G.) and Digital Image Correlation (DIC), is made in Figure 4.19. It can be seen that the strain profiles found with DIC have a similar profile to the strain gauges, but there is quite a large discrepancy between the strain values. This leads to the conclusion that variations in displacements are too small to measure accurately from the images. Also, markers can not be placed on the edge of the beam which means that the peak in strains at the bottom of beams can not be captured. Therefore it can be concluded that the current camera setup for DIC is not successful in accurately measuring parallel to grain strain profiles in timber beams in bending.

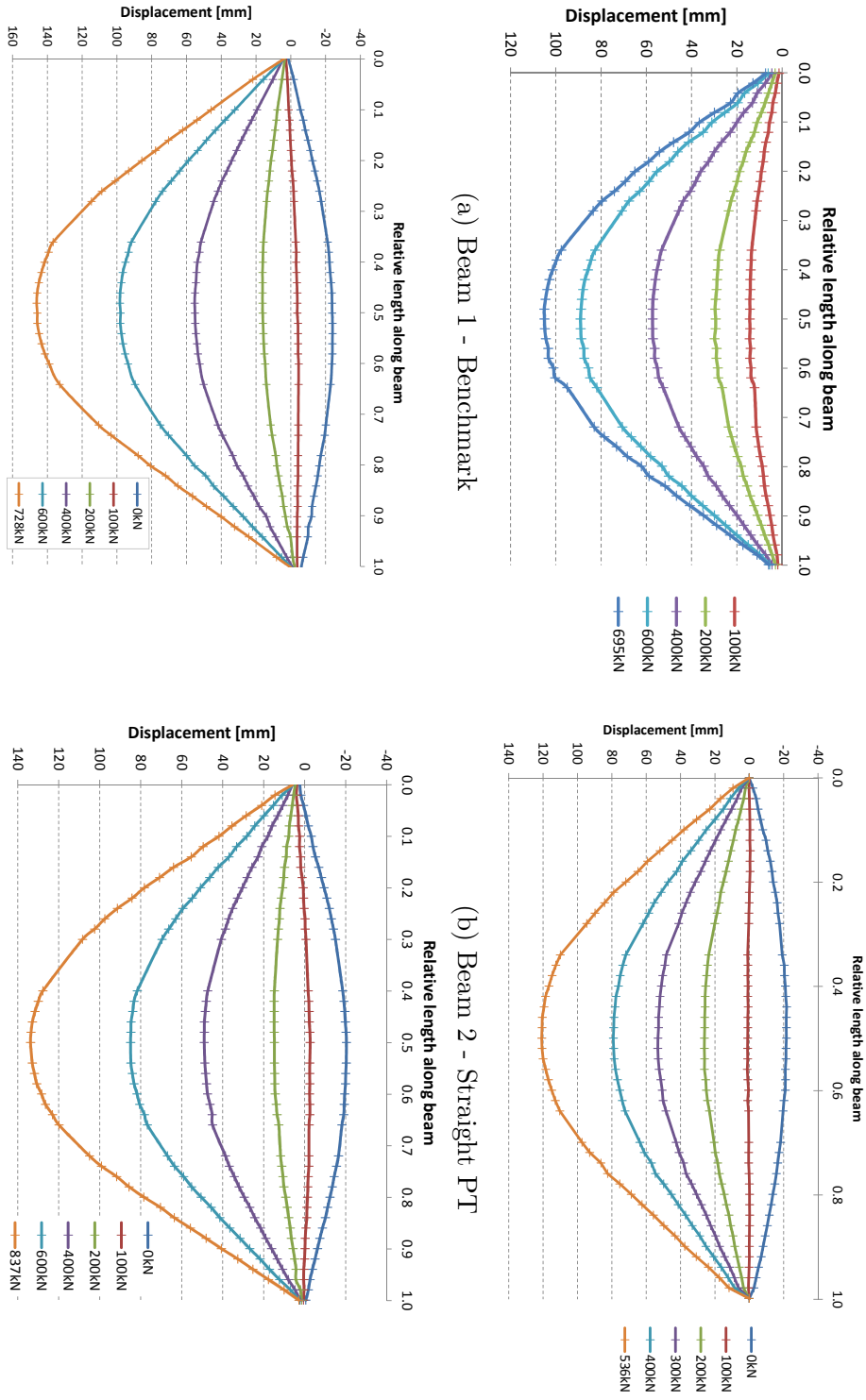

(a) Beam 1 - Benchmark

(b) Beam 2 - Straight PT

(c) Beam 3 - Draped PT

(d) Beam 4 - Draped PT (2)

Figure 4.18: Displacement profiles based on DIC measurements

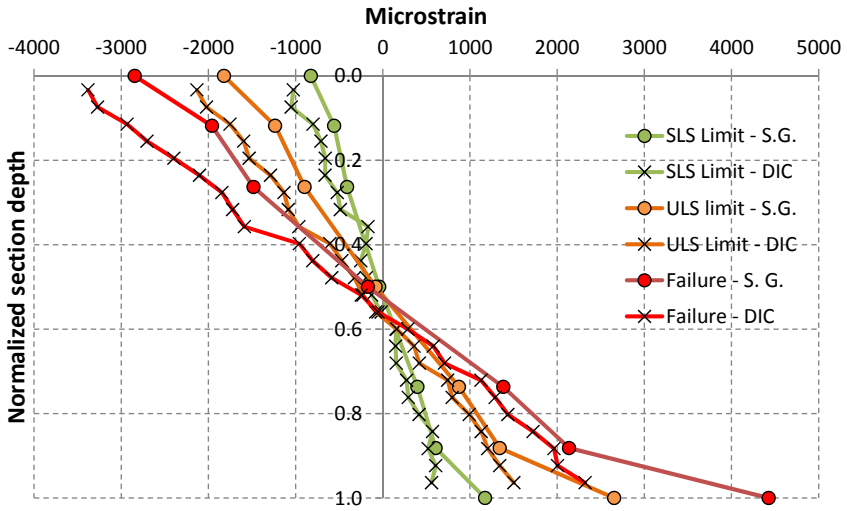

Figure 4.19: Comparison of strain profiles of Beam 1 measured using Strain Gauges (S.G.) and Digital Image Correlation (DIC) technique

4.5 Conclusions

Based on analysis of results from experimental testing of post-tensioned beams the following conclusions can be made.

- A mix of failure mechanisms (tension, compression and shear) were found. Beam 1 without post-tensioning failed due to bending/tension failure at the bottom flange. Beam 2 failed due to a shear failure in the web. Beam 3 (draped PT) showed failure in compression resulting in a lowering of the neutral axis and increase in tensile strains until tensile failure occurred. Beam 4 failed in bending/tension at the bottom flange. Therefore it can be concluded that compression and tensile capacity of top and bottom flanges should be checked in the design as well as the shear strength of the webs. For beams failing in tension, linear load-deflection curves were observed. For Beam 3, with draped PT, which failed first in compression before tensile failure happened, some ductile behaviour was observed.

- A serviceability limit state design limit of span over 300 results in allowable deflections of 30mm. It can be seen that Beam 1 reached this at a load of 200kN. For Beams 2, 3 and 4 the loads were 223kN, 267kN and 307kN,

respectively. This was an increase in load carrying capacity at SLS design level with respect to Beam 1 of 12%, 34% and 54% despite the reduction in section height. This clearly shows the benefit of the precamber, created by post-tensioning.

- The average modulus of elasticity of all four beams of 11.1GPa corresponded very well with the manufacturer specified 11GPa. The shear modulus of 694MPa was 26% higher than the manufacturer specified value of 550MPa.

- Beams needed to be overstressed by about 10% to compensate for anchorage losses. At failure the post-tensioning force increased by 12% to 24%. These aspects should be taken into account for strength design of the beam. Shortening of beams during stressing should be allowed for in the design process, either by designing the beam slightly longer or by having tolerances to allow for beam shortening. Beam shortening can be accurately calculated when modulus of elasticity based on pure compression (which is higher compared to modulus of elasticity in bending) is used.

- Strain profiles during testing remained mainly linear, except for peaks in tensile strains close to failure. The Digital Image Correlation (DIC) technique proved to be very successful in measuring beam deflections, but it was not successful in accurately measuring parallel to grain strain profiles in beams in bending.

Chapter V

Post-tensioned timber beam-column connections

5.1 Introduction

Past research on post-tensioned timber frames has mainly focussed on the seismic behaviour (Newcombe, 2008, 2011). But there is a distinct lack of information for gravity design of post-tensioned timber frames, especially regarding connection behaviour. The major unknown in the design of post-tensioned frames is stiffness of the beam-column connections. This stiffness influences bending moment distribution in the frames and deflections of the beams, therefore it is essential to evaluate this in more detail. The experimental testing program attempted to gather information about the behaviour of these post-tensioned connections, which is used in a later stage for frame design.

In post-tensioned beam-column connections there are large compressive forces acting onto the columns perpendicular to grain. This was reason for concern since compression perpendicular to grain is a weak property of timber. Experimental testing has shown a perpendicular to grain strength of only 8MPa, compared to 44MPa parallel to grain (Section 3.3). The experimental testing program focussed on quantifying this problem and identifying ways to mitigate it. Consultation with industry gave numerous ideas for different connection configurations which reduced perpendicular to grain compression. A selection was made since it was not practical to test all different connection possibilities. Three different column reinforcement options, illustrated in Figure A.12, were selected for testing:

1. Long, fully threaded screws.
2. Rotated timber layers.
3. Cross-banded LVL.

Experimental testing of post-tensioned timber beam-column connections has

the following objectives:

- Test the stiffness of a post-tensioned timber beam-column connections.
- Evaluate the effectiveness of several different column reinforcement methods to reduce plastic deformations.
- Evaluate the effects of plastic deformations on the connection stiffness.
- Evaluate the applicability of proposed design methods for seismic frames.
- Determine the design implications of a semi-rigid connection on the moment distribution in a frame.

This chapter first describes a summary of the design of a prototype building and column reinforcements, a more detailed design can be found in Appendix A.2. Next, in Section 5.3 the experimental test setup is described in more detail, including instrumentation and loading protocol. Test results are presented in Section 5.4, focussing on connection stiffness and joint panel shear deformation. Implications of connection stiffness on the design of post-tensioned timber box beams are presented in Section 5.5.

5.2 Connection Design

This section provides an overview of the main design issues for the post-tensioned beam-column connection. A full design is shown in Section A.2.

A hotel building in Napier was chosen as a prototype building because of its regular layout, this 4 storey concrete building was redesigned as a timber building (Amigo, 2010). A plan view of one of the frames of the building is shown in Figure 5.1.

The timber used for the columns was LVL11 and cross-banded LVL from Nelson Pine Industries Limited (2010). Different configurations of cross-lam layers were possible, based on available thickness of 25mm and 36mm. A mixture of 36mm and 25mm sheets was chosen in order to have a good balance between parallel and perpendicular to grain performance. Section sizes and section properties for beams and columns are shown in Figure 5.2. A post-tensioning force of 440kN was chosen as the vertical uplift forces at the deviators balanced the dead load of the floors. Specimens were tested at the full post-tensioning force and at half the post-tensioning force of 220kN.

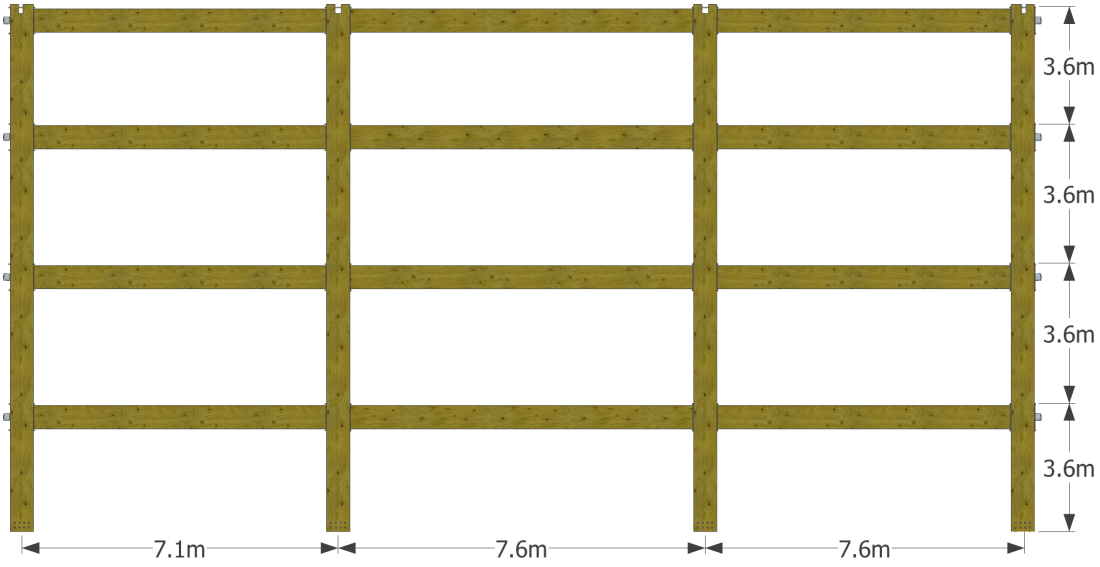

Figure 5.1: Front view of timber frame for prototype building

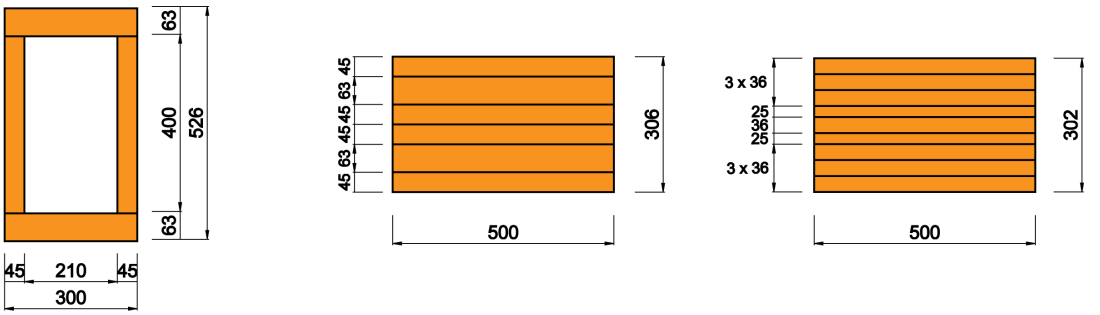

Beam
A = 73800mm^2
A$_s$ = 36700mm^2
Z = 9.58x10^6 mm^3
I = 2.52x10^9 mm^4

Column 1 - LVL11
A = 153000mm^2
A$_s$ = 102000mm^2
Z = 12.7x10^6 mm^3
I = 3.19x10^9 mm^4

Column 2 - CB LVL
A = 151000mm^2
A$_s$ = 100700mm^2
Z = 12.6x10^6 mm^3
I = 3.15x10^9 mm^4

Figure 5.2: Cross-sections of beam and columns

The connection design was based on the design procedure as proposed by Newcombe et al. (2010a). Although this procedure was developed for seismic design, at the time of testing it was the best available tool to predict connection behaviour. The design resulted in the height of compressive zone (c) which was needed to calculate the connection moment. In seismic design connection moment is calculated as the post-tensioning force multiplied by the distance between tendons and the centroid of the stress block in the compression zone. If this is adapted for gravity design, the connection moment is calculated as *Method 1* shown in Figure 5.3. Alternatively the connection moment can be calculated as the post-tensioning force multiplied by the distance between centroid of the beam and centroid of the stress block in the compression zone (*Method 2* in Figure 5.3).

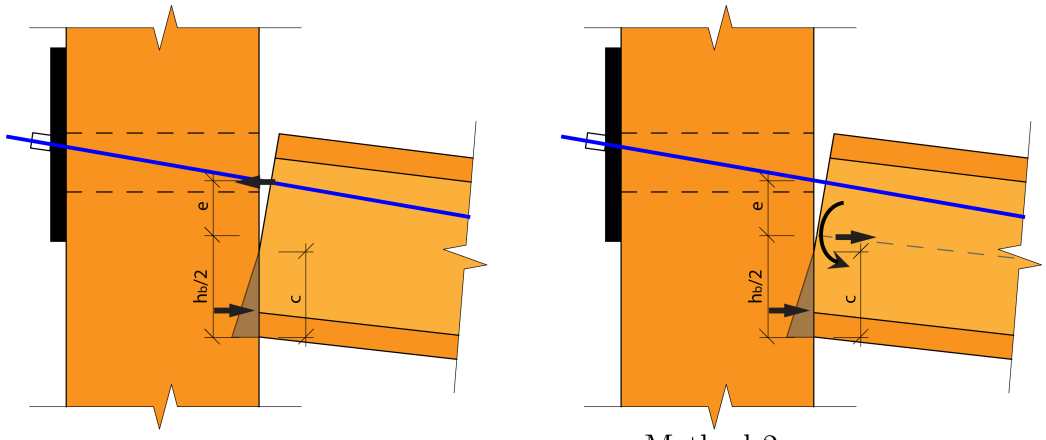

Method 1

$M_{con,1} = F_{pt}\left(e + \frac{h_b}{2} - \frac{c}{3}\right)$

Method 2

$M_{con,2} = F_{pt}\left(\frac{h_b}{2} - \frac{c}{3}\right)$

Figure 5.3: Two methods to calculate connection moment

The compressive strength and stiffness perpendicular to the grain in the column was critical for the connection behaviour, as the post-tensioning force needed to be transferred into the column over a relatively small area. Low strength was limiting the post-tensioning force and low stiffness was resulting in additional connection rotation. In order to increase the connection performance, different methods for timber and steel reinforcing the connection were evaluated. Firstly 3 different column interfaces (on two different columns) were tested. Column 1 was a LVL11 column with two different connection interfaces, one

had all the grains running longitudinally whereas the other interface had the outer 45mm LVL laminates rotated by 90°(Figure 5.4d), which resulted in a combination of compression parallel and perpendicular to grain. Column 2 was made of cross-banded LVL (Figure 5.4c), which had several LVL veneers rotated 90°.

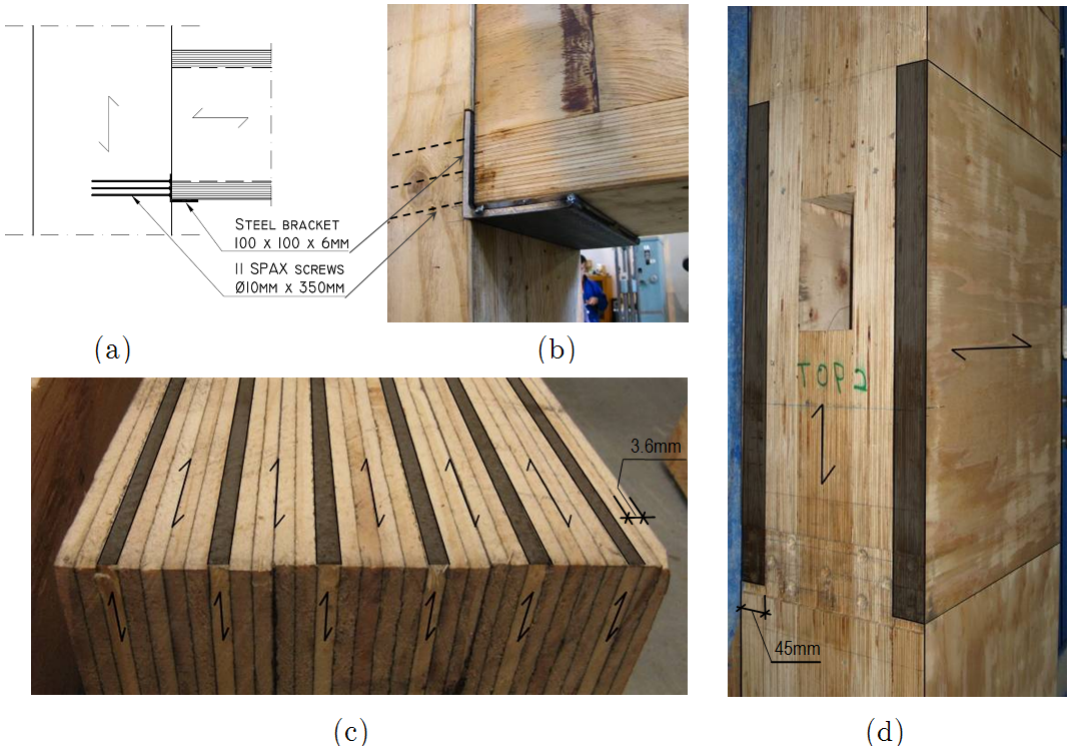

Figure 5.4: Column reinforcement, (a) side view of steel corbel with screw reinforcement, (b) steel corbel, (c) cross-banded LVL with cross layers marked in grey, (d) rotated outer layers of LVL marked in grey

Each of the three column interfaces was tested with and without steel reinforcement. Firstly a timber-to-timber connection without additional steel reinforcement was tested. The second test used steel reinforcement, which consisted of a angle (100 x 100 x 6mm) as corbel and bearing plate, which was supported by eleven 350mm long, ϕ=10mm SPAX (2012a) screws (Figure 5.4a+b). The third test was reinforced with the steel angle but without screws, in order to investigate the effect of the steel angle and screws separately.

5.3 Test Setup

This section describes the experimental test setup. External beam-column connections exhibit column rotation, joint panel shear deformation, interface compression deformation and gap opening. These components are further explained in Chapter 8. Internal beam-column connections exhibit only interface compression deformation and gap opening, therefore an external connection was chosen for experimental testing. The external beam-column connection was extracted from the full frame and the connection in the experimental test was designed to undergo the same bending moment as the connection in the full frame. This section also describes test schedule, instrumentation and loading protocol.

5.3.1 Overview

Figure 5.5a shows the full frame of the prototype building and the section that was chosen for the test setup. Figure 5.5b shows a picture taken of the test setup and an overview of the test setup can be seen in Figure 5.5c. Testing was full-scale, with a column of 3.6m high and the beam 3.6m long. The distance between column and hydraulic ram was prescribed due to fixings on the strong floor. A 150kN hydraulic ram with load cell was used to load the specimen. The column was fixed to the reaction frame using a load cell at a height of 2.82m above the strong floor.

5.3.2 Limitations of test setup

In gravity design, in contrast to seismic design, there is no clear point of contraflexure in the beam due to the distributed loading. The beam length for the test specimen was chosen to be half of full beam length. In a full frame there would be a bending moment in the beam, which was not possible in the test setup. As the goal of the test was to simulate the behaviour of the connection in a real building, the connection moments of the full frame were approximated by the experimental test setup. The post-tensioning force created an initial moment at the connection, which was altered by the force in the hydraulic actuator acting on the beam. The load in the hydraulic actuator was calculated such that the experimental bending

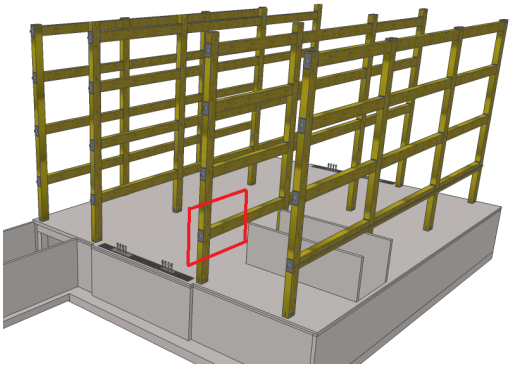

(a) Rendering of timber frame

(b) Picture of test setup

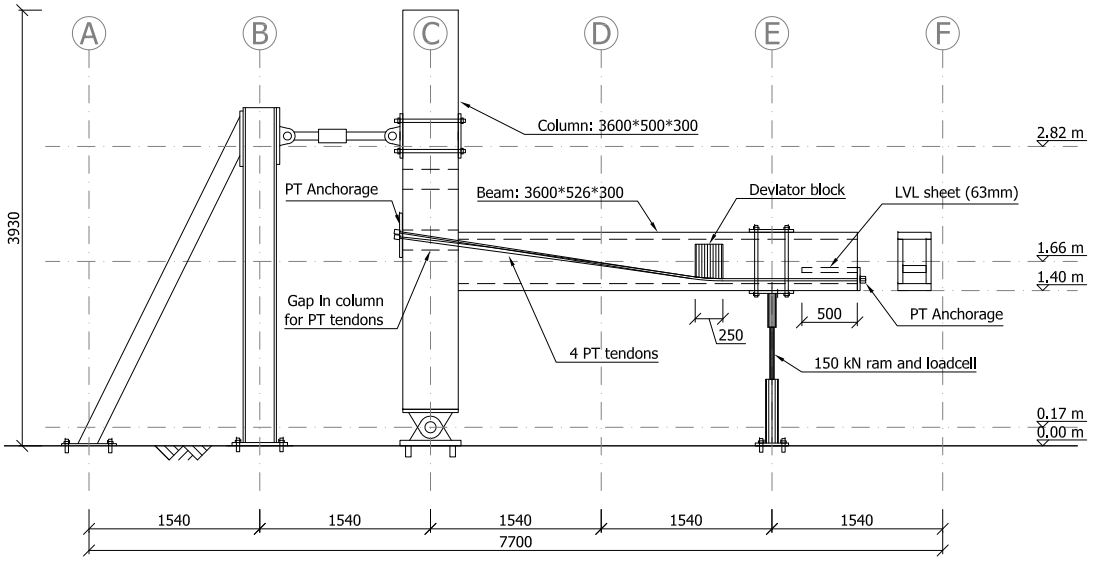

(c) Overview drawing of the test setup

Figure 5.5: Test setup of post-tensioned beam-column connection with draped tendons

moment at the connection was equal to the bending moment at the connection in the frame design.

In this experimental test setup, of the four rotational components (column, joint panel, connection and beam) only joint panel deformation and connection rotation had correspondence with a real structure. Due to laboratory limitations, the column height was too short to represent inter-storey height in a building and the cantilever beam had no representative bending moment distribution for

a beam in a real frame. Therefore of the rotational components, only joint panel shear deformation and connection rotation are analysed in the test results.

5.3.3 Testing schedule

Table 5.1 shows the overview of all tests. Column 1 had an beam-column connection interface of normal LVL and an interface with the outer 45mm layers rotated. Column 2 was made out of cross-banded LVL. The timber reinforcement in Test 10 was an extra LVL sheet glued and screwed to the inside of the bottom flange. Test 11 was a repetition of Test 7, since results of Test 7 needed verification.

Table 5.1: Testing schedule of beam-column connection testing

Test	Col.	Interface	Connection	PT force
1a	1	Normal LVL	timber to timber	220
1b	1	Normal LVL	timber to timber	440
2a	1	Normal LVL	steel corbel + screws	220
2b	1	Normal LVL	steel corbel + screws	440
3a	1	Normal LVL	steel corbel	220
3b	1	Normal LVL	steel corbel	440
4a	1	Rotated outer layers	timber to timber	220
4b	1	Rotated outer layers	timber to timber	440
4c	1	Rotated outer layers	timber to timber (past ULS)	440
5a	1	Rotated outer layers	steel corbel + screws	220
5b	1	Rotated outer layers	steel corbel + screws	440
6a	1	Rotated outer layers	steel corbel	220
6b	1	Rotated outer layers	steel corbel	440
7a	2	Cross-banded	timber to timber	220
7b	2	Cross-banded	timber to timber	440
7c	2	Cross-banded	timber to timber (past ULS)	440
8a	2	Cross-banded	steel corbel + screws	220
8b	2	Cross-banded	steel corbel + screws	440
9a	2	Cross-banded	steel corbel	220
9b	2	Cross-banded	steel corbel	440
10a	2	Cross-banded	timber reinforcement beam	220
10b	2	Cross-banded	timber reinforcement beam	440
11a	2	Cross-banded	timber to timber (re-test of 7a)	220
11b	2	Cross-banded	timber to timber (re-test of 7b)	440

5.3.4 Instrumentation

Several types of instrumentation were installed to monitor the tests. The test was displacement controlled by a hydraulic actuator fixed to the beam. A load cell and a rotary pot were attached to the hydraulic actuator to measure load and displacements. Another load cell and rotary pot were fixed to the top support of the column; the load cell was measuring horizontal reaction force and the rotary pot was measuring reaction frame displacement. Every tendon had an individual load cell to measure the force in it. Two potentiometers were fixed to the column and two more to the beam to measure beam and column rotations. Two potentiometers were placed diagonally over the joint panel region to measure joint panel shear deformation. A further three potentiometers were placed between the beam and column to measure connection stiffness and gap opening (Figure 5.8a). Instrumentation in the joint-panel zone is shown in Figure 5.8b and an overview of all instrumentation can be seen in Appendix G and a list of instrumentation and corresponding data channels is given in Appendix C.1.

The post-tensioning force created compression stresses parallel to grain in beams and perpendicular to grain in columns. This compression perpendicular to grain resulted in local deformations of the column, which caused rotation of the connection. These local deformations can go beyond the elastic range of timber, resulting in permanent deformations. The post-tensioned connection can open up at the top when compressive stresses due to post-tensioning are overcome by tension stresses due to bending moment. This causes a gap to open between beam and column, starting at the top of the connection and with increasing moment opening up further. The compressive force will shift down with the drop in neutral axis position after gap opening starts. The two effects mentioned above, local deformation of the column and gap opening, result in rotation of the beam-column connection. This rotation was measured by two potentiometers which were placed over the connection interface as shown in Figure 5.6a.

The joint panel area was loaded by eccentric compression forces. These forces created an area of high shear stresses and thus shear deformation occurred. Two potentiometers, placed diagonally over the joint panel as shown in Figure 5.6b, were used to measure joint panel deformation (Δs_1 and Δs_2). Equation 5.1 was used to calculate joint panel rotation (θ_{jp}) from the measurements of the two

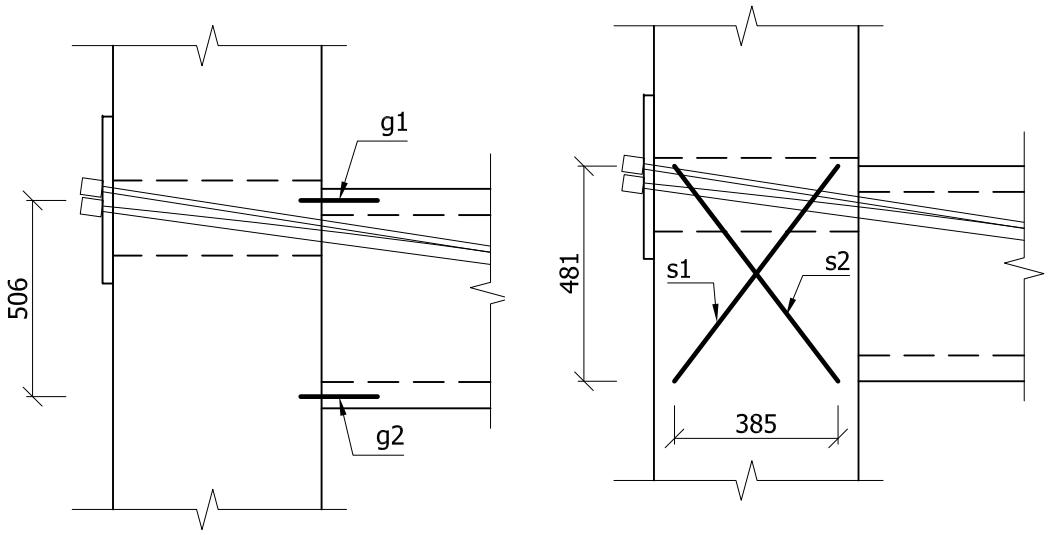

(a) Location of linear potentiometers (g1 and g2) for measuring connection rotation

(b) Measuring of joint panel shear deformation

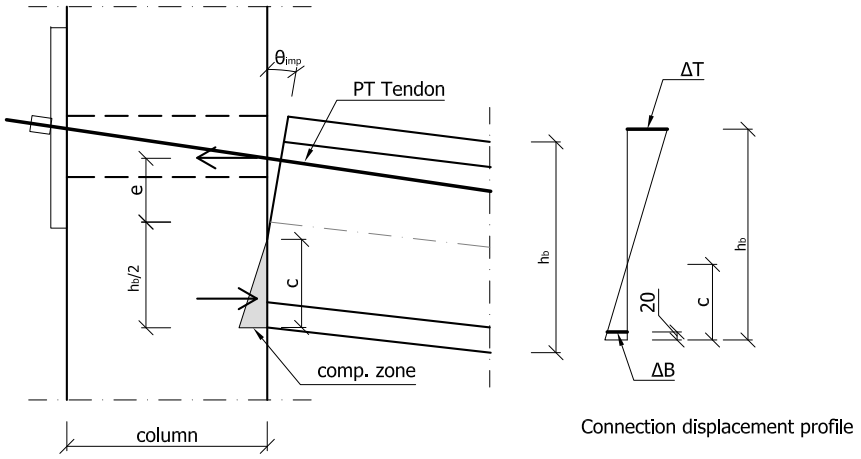

(c) Measurement of neutral axis depth

Figure 5.6: Drawings of instrumentation for gap opening, joint panel shear deformation and neutral axis depth

potentiometers. In this equation a=385mm and b=481mm.

$$\theta_{jp} = \frac{(\Delta s_1 - \Delta s_2)\sqrt{a^2 + b^2}}{2ab} \tag{5.1}$$

The neutral axis depth was calculated using the recording of potentiometers at top (ΔT) and bottom (ΔB) of the connection interface (Figure 5.6c). The top potentiometer was located at the top of the beam and the bottom one 20mm above the bottom of the beam. The angle of the connection interface is given by Equation 5.2. The height of the compressive zone is given by Equation 5.3.

$$\delta = \frac{\Delta T - \Delta B}{506} \tag{5.2}$$

$$c = \frac{\Delta B}{\delta} + 20 \tag{5.3}$$

5.3.5 Loading protocol

Several standard loading protocols were considered, but none was found suitable for this type of test. Timber tests for joints with mechanical fasteners, like EN 26891:1991 (CEN, 1991), would not provided adequate information. Cyclic testing standards, such as EN 12512:2001 (CEN, 2001), seemed more appropriate but were thought to be too rigorous and determination of yield load, yield slip, ductility and energy dissipation where not applicable to this testing program. Therefore the following loading protocol was used (Figure 5.7):

- 2 cycles from the lowest connection moment in a design, which is caused by the post-tensioning load and 0.9 dead load (-35kNm), up to the serviceability limit state (SLS) connection moment (26kNm) to determine the initial stiffness;
- 2 cycles from the lowest connection moment up to the ultimate limit state (ULS) connection moment (101kNm) to determine the decompression moment and the non-linear behaviour;
- 2 cycles similar to the first two to determine if the stiffness decreased after ULS cycles and if permanent rotations due to plastic deformation of the timber occurred (Figure 5.8d).

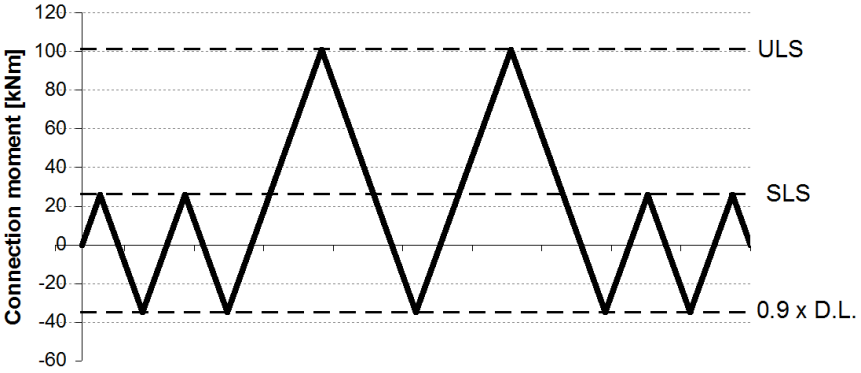

Figure 5.7: Loading protocol for connection testing

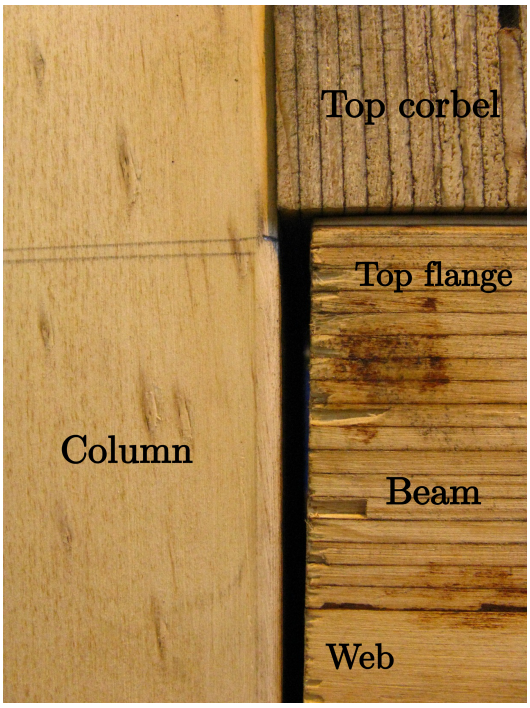

(a) Gap opening under ULS load

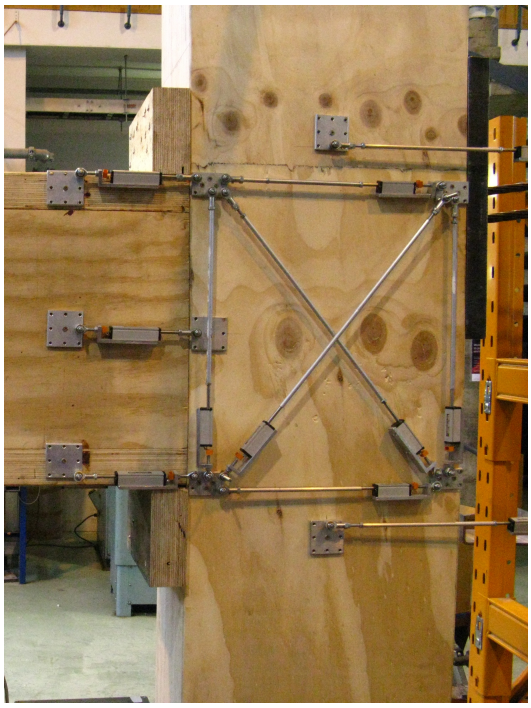

(b) Picture of instrumentation

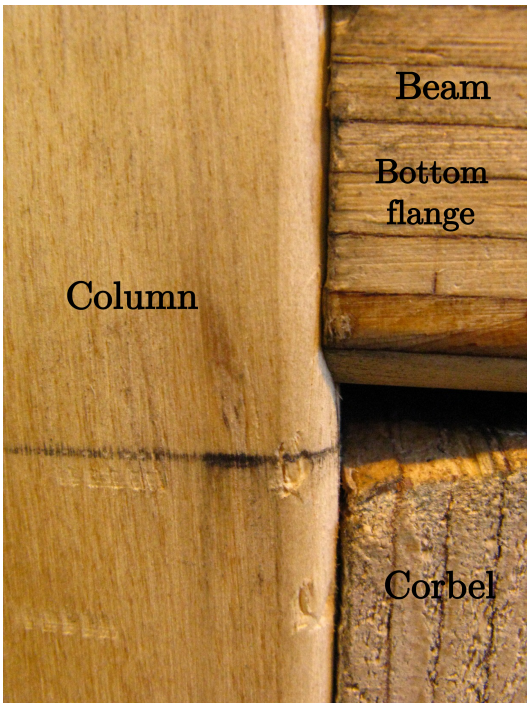

(c) Compression of beam onto column under ULS load

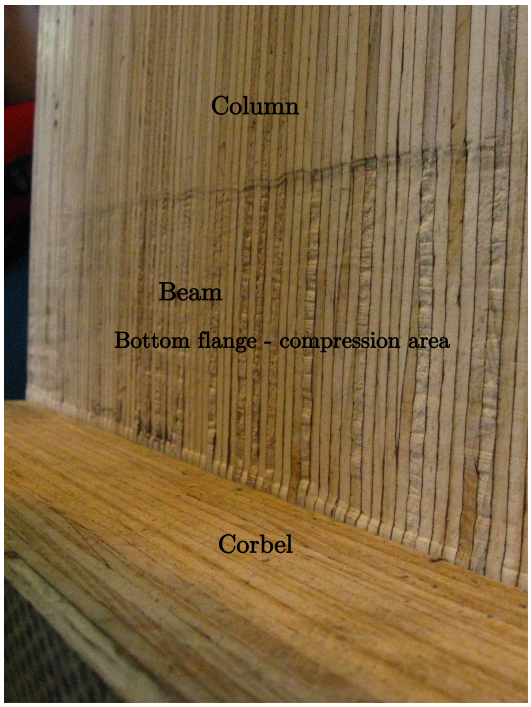

(d) Plastic deformation of cross-banded column

Figure 5.8: Images of experimental testing of beam-column connections

5.4 Test Results

This section explains the analysis of the results and provides a comparison of the different tests. A description of every single test is omitted. The main focus is on the tests with the full post-tensioning force of 440kN, as determined in the building design, though in several parts a comparison with results from tests with a post-tensioning force of 220kN will be made. This section evaluates bending moments, connection stiffness, joint panel shear deformation, tendon elongation and neutral axis depth.

5.4.1 Bending moments

Bending moments in the structure can be calculated based on forces which act on it. Two bending moments are of main interest, the bending moment at the connection (interface between beam and column) and bending moment at the centreline of the column. Both of these moments can be evaluated in two ways; based on forces which act on the beam or based on forces which act on the column. Calculation of column centreline moment, based on forces on the beam, is shown in Equation 5.4. Another way to calculate the centreline moment is based on forces and equilibrium of the column, as shown in Equation 5.5. An overview of the parameters can be seen in Figure 5.9. The two different formulae for calculating the connection moment give nearly identical results as can be seen in Figure 5.10. In this figure the values of centreline moment according to both methods are plotted. A clear linear relationship can be seen, showing that for every step of testing the connection moment calculated by either method is equal.

$$M_{cl,1} = F_{pt} \cdot e - F_{pt,v} \cdot a + F_v \cdot b \tag{5.4}$$

Where:

- F_{pt} = Total post-tensioning force (kN)
- $F_{pt,v}$ = Vertical uplift force at deviator (kN)
- F_v = Vertical force on specimen (kN)
- e = Eccentricity of anchorage (0.167m)
- a = Distance between deviator and connection (2.515m)
- b = Distance between ram and connection (3.08m)

$$M_{cl,2} = -F_{hold} \cdot d - F_h \cdot f + F_{pt,h} \cdot g - F_{pt,v} \cdot h \tag{5.5}$$

Where

- F_{hold} = Reaction force at column support (kN)
- F_h = Horizontal reaction force at column base (=F_{hold}) (kN)
- $F_{pt,h}$ = Horizontal component of the post-tensioning force (kN)
- $F_{pt,v}$ = Vertical component of the post-tensioning force (kN)
- d = Distance between top support and connection (1.386m)
- f = Distance between bottom support and connection (1.266m)
- g = Horizontal eccentricity of anchorage force (0.25m)
- h = Vertical eccentricity of anchorage force (0.236m)

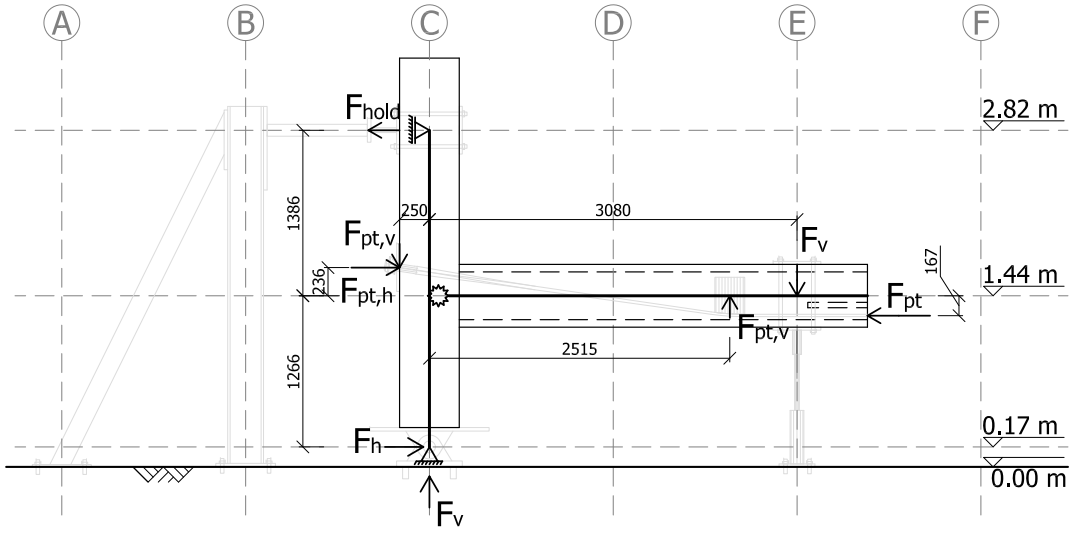

Figure 5.9: Schematization of the test setup

Connection moment can be calculated in a similar manner. The difference between connection moment and centreline moment is shown in Figure 5.11. The progress of the testing protocol can clearly be seen, with the different cycles of SLS and ULS loading. In the figure it can be seen that centreline and connection moment are very similar. The differences between the two moments, shown by the grey line plotted on the right axis, is very small for larger connection

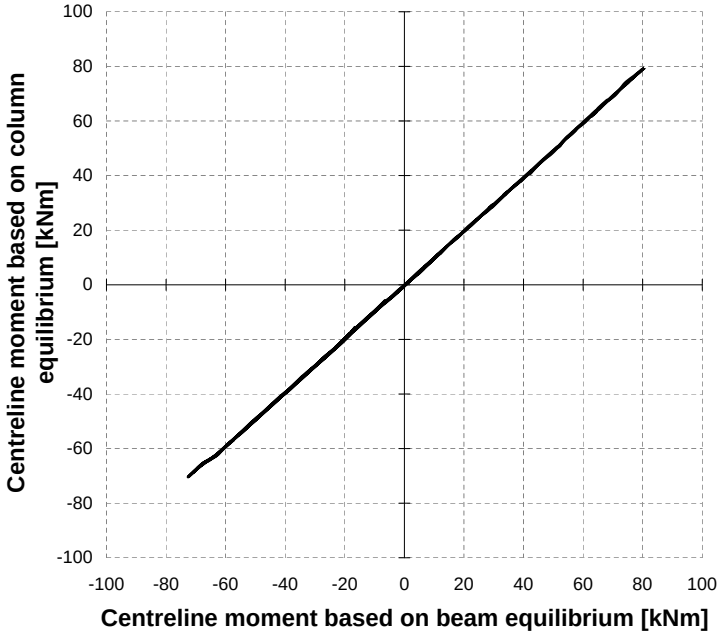

Figure 5.10: Comparison of centreline moment based on beam and column equilibrium

moments. This is because for large connection moments the shear force in the beam is very low, i.e. the uplift force at the deviator and the downwards force of the ram are almost equal. The low shear force results in a constant bending moment and hence no difference between connection and centreline moment. For further analysis the centreline moments have been used.

Decompression moments can be calculated based on post-tensioning force and section properties of the beam. For a post-tensioning force of 220 and 440kN, the compression stress was 3.0 and 6.0MPa, respectively (Equation 5.6). At decompression, the connection moment to overcome this compression was equal to 29 and 57kNm for a post-tensioning force of 220 and 440kN, respectively (Equation 5.7).

$$\sigma_c = \frac{F_{pt}}{A} = \frac{440000}{73800} = 6.0MPa \tag{5.6}$$

$$M_{dec} = Z \cdot \sigma_c = 9.5 \cdot 10^6 \times 6.0 = 57kNm \tag{5.7}$$

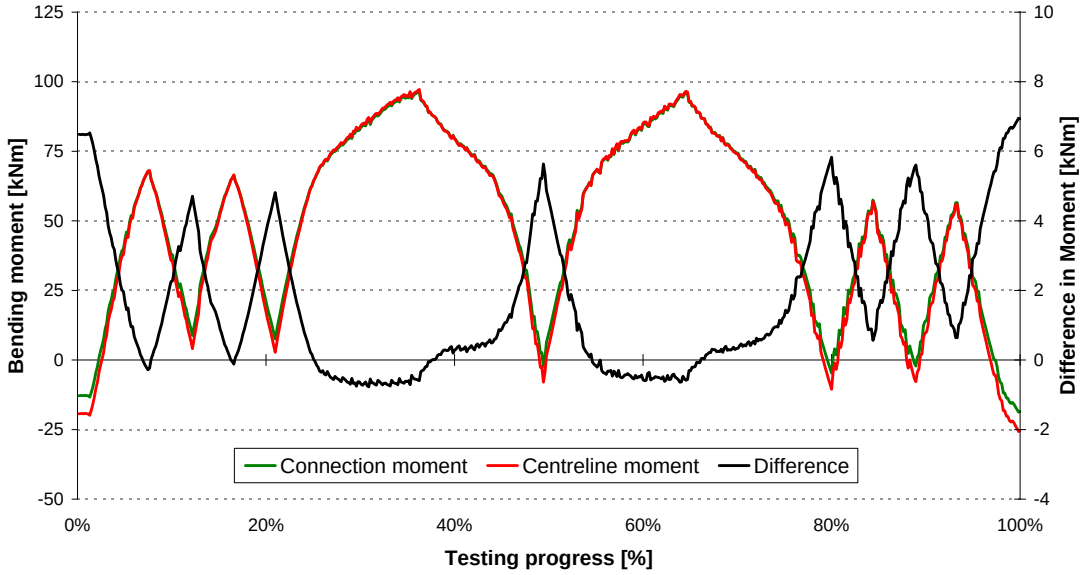

Figure 5.11: Comparison of centreline and connection bending moment

In section A.2.5 the decompression moment has been calculated based on the design procedure, which resulted in $M_{dec,1} = 131kNm$ for the full post-tensioning force when using the distance between centroid of compression zone and tendon location, or $M_{dec,1} = 61kNm$ when using the distance between the centroid of compression zone and centroid of beam. It can be seen that the predicted value of the second method is much closer to the decompression moment based on basic structural mechanics.

The predicted moment-rotation behaviour, based on the two different methods of evaluating the connection moment (Section A.2.5), can be compared with experimental testing results. This is done for the 220kN and 440kN post-tensioning tests without any reinforcement, as shown in Figure 5.12. It can be seen that the second method for calculating connection moment, based on the distance between centroid of compression zone and centroid of beam, gives a much better prediction than the first method which is based on the distance between centroid of compression zone and post-tensioning tendon. For seismic connections, where the distance to tendons is used (Newcombe et al., 2010a), this does not make a difference as tendons run through the centroid of beam, but for connections with eccentric tendons there is a clear difference.

The design method predicted connection behaviour of the 440kN test (Test 1b) well. But for the 220kN test the initial stiffness is overestimated and connection moment over predicted. Although results of Test 1b are well predicted, effects of reinforcement cannot be taken into account by the design procedure, resulting in significant differences between the predicted response and experimental data.

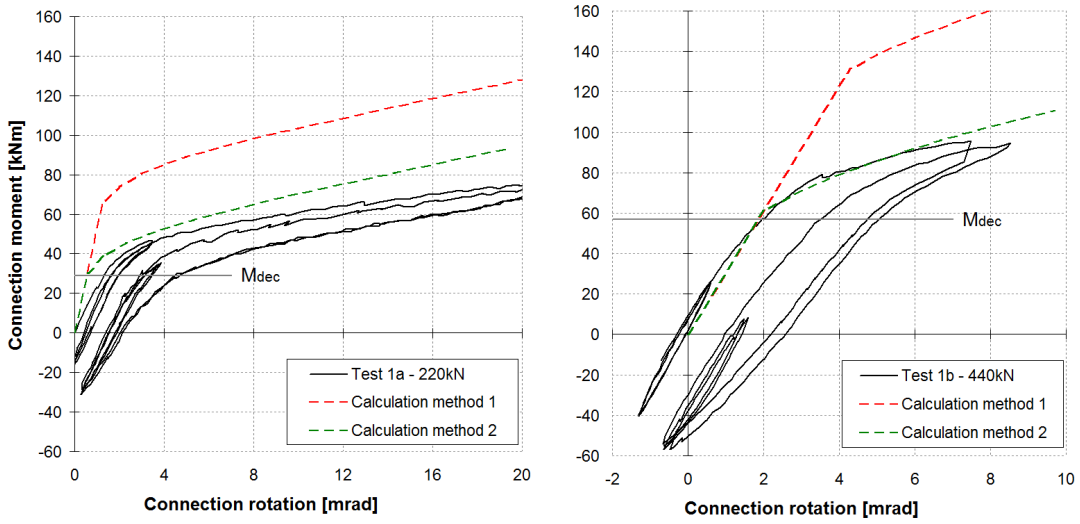

Figure 5.12: Connection moment-rotation behaviour of experimental testing results and predictions for 220kN and 440kN tests without column reinforcement

Tests 4c and 7c, with rotated outer layers and the cross-banded LVL column, were performed past the ULS load limit in order to acquire a better understanding of the connection behaviour. The moment-rotation curves from these tests are shown in Figure 5.13. Symmetric behaviour can be seen, with decompression occurring at approximately the same values for positive and negative rotations. The main difference between positive and negative cycles was an increase in connection moment after gap opening, which was due to tendon elongation effects (see also Figure 5.21). As the tendon was positioned at the top of the connection, elongation was happening when gap opening was at the top but no tendon elongation occurs with gap opening at the bottom.

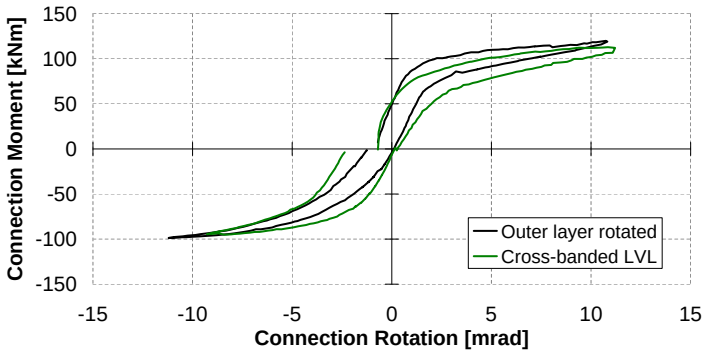

Figure 5.13: Connection moment-rotation behaviour for testing past ULS load limit

5.4.2 Connection stiffness

Connection stiffness, derived from the moment-rotation graphs was one of the key focus points of this test. Figure 5.14 shows connection moment plotted against the connection rotation graph for Test 1. The first two cycles up to SLS provided the initial SLS stiffness (k_1). The next two cycles up to the ULS connection moment showed non-linear behaviour of the connection due to opening of the gap. This opening changes the position of the neutral axis and results in a lower stiffness. The non-linear behaviour was approximated using a bi-linear stiffness function. Stiffness of the non-linear part, k_2, was taken from the last part of the ULS curve. Stiffness during the last two SLS cycles was k_3, this stiffness was compared with the initial stiffness in order to determine if any stiffness degradation had taken place. The intersection of the bi-linear approximation was called the change in stiffness, $M_{\Delta k}$. The rotation at zero moment during the SLS cycles has been compared, and the difference between the first two cycles and the last two cycles gave the permanent rotation, θ_{perm} (shown by the horizontal arrow), due to timber crushing at the connection interface.

Table 5.2 shows test results for all 22 tests. Tests 1, 4 and 7 were timber-to-timber connections without steel reinforcement. Tests 2, 5 and 8 had long fully threaded screws and a steel corbel as reinforcement. Tests 3, 6 and 9 had the steel corbel installed, but no screws. Test 10 was with an extra timber sheet glued into the beam and Test 11 was a repetition of Test 7.

Table 5.2: Test description and stiffness results

Test	Column	Reinforcement	F_{pt} (kN)	k_1 (kNm/mrad)	k_2 (kNm/mrad)	k_3 (kNm/mrad)	$(k_3 - k_1)/k_1$ (kNm/mrad)	$M_{\Delta k}$ (kNm)	θ_{perm} (mrad)
1a	LVL11	None	220	25.6	1.5	22.5	-12%	50	1.4
1b	LVL11	None	440	32.1	4.4	29.9	-7%	74	1.5
2a	LVL11	Screws + Corbel	220	42.0	1.7	39.7	-5%	51	0.6
2b	LVL11	Screws + Corbel	440	51.6	8.3	58.6	14%	87	0.2
3a	LVL11	Corbel only	220	41.0	1.7	26.1	-36%	47	1.0
3b	LVL11	Corbel only	440	35.8	3.9	32.4	-9%	78	1.6
4a	Rotated outer layers	None	220	34.8	2.4	28.7	-18%	48	0.2
4b	Rotated outer layers	None	440	47.3	14.2	46.6	-2%	83	0.2
5a	Rotated outer layers	Screws + Corbel	220	29.2	2.9	26.9	-8%	44	0.4
5b	Rotated outer layers	Screws + Corbel	440	39.5	7.6	36.9	-7%	78	0.1
6a	Rotated outer layers	Corbel only	220	19.6	2.8	18.6	-5%	44	0.2
6b	Rotated outer layers	Corbel only	440	37.7	6.6	33.1	-12%	73	0.1
7a	Cross-banded LVL	None	220	34.3	2.1	32.8	-5%	46	0.3
7b	Cross-banded LVL	None	440	54.5	5.7	82.0	50%	75	0.5
8a	Cross-banded LVL	Screws + Corbel	220	25.3	2.8	27.5	9%	41	0.1
8b	Cross-banded LVL	Screws + Corbel	440	41.4	6.9	39.4	-5%	72	0.2
9a	Cross-banded LVL	Corbel only	220	19.3	2.3	20.1	4%	42	0.5
9b	Cross-banded LVL	Corbel only	440	42.6	5.9	40.3	-6%	72	0.1
10a	Cross-banded LVL	Timber reinf. beam	220	26.6	1.9	23.1	-13%	46	0.3
10b	Cross-banded LVL	Timber reinf. beam	440	48.2	6.0	47.2	-2%	76	0.2
11a	Cross-banded LVL	None	220	28.4	2.5	28.6	1%	45	0.3
11b	Cross-banded LVL	None	440	52.6	5.4	43.8	-17%	78	0.3

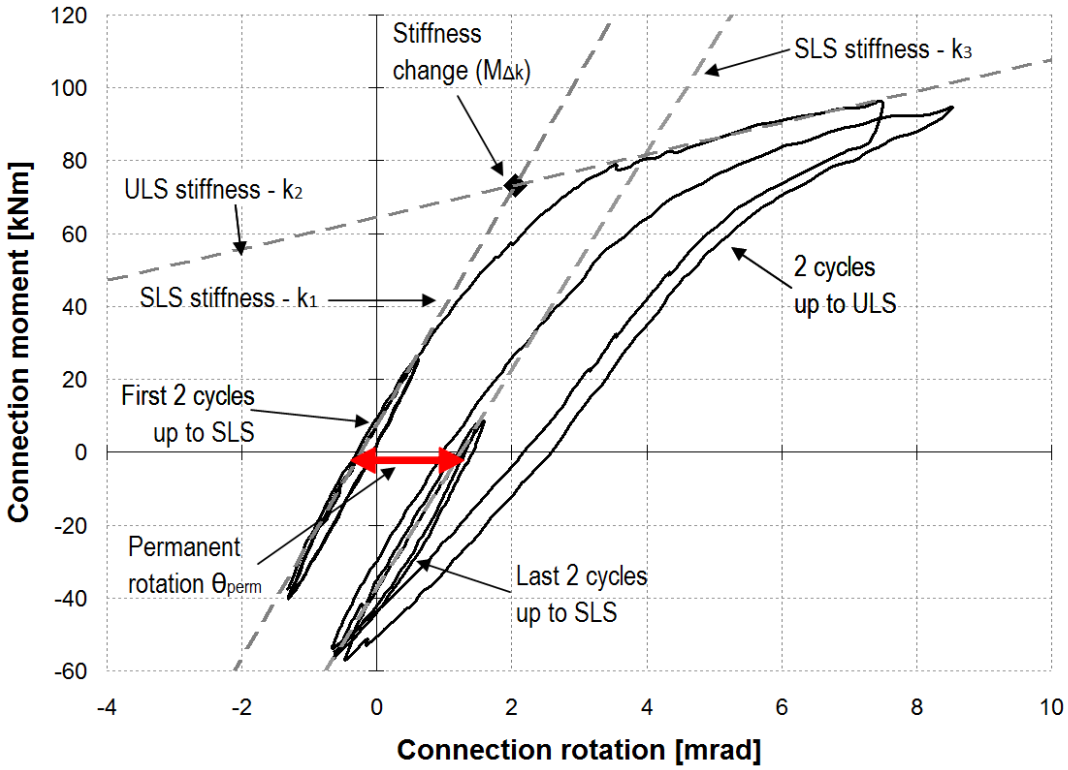

Figure 5.14: Connection moment-rotation graph of Test 1b

The full moment-rotation curves for each of the full post-tensioning tests can be seen in Figures 5.15 and 5.16. The curves have been moved horizontally (with a constant offset in rotation) in order to get a clearer view of the different curves. This was also possible as zero rotation did not have any absolute value, but was only relative to the unstressed specimen. During stressing, when the beam is pressed against the column, small connection rotations occurred due to tolerances in the setup. Therefore no clear point of zero rotation could be defined.

Test 1a, with half post-tensioning force, had an initial stiffness (k_1) of 26kNm/mrad and Test 1b, with full post-tensioning force, of 32kNm/mrad. The full post-tensioning test result of 32kNm/mrad corresponds well with the predicted 30kNm/mrad, but for the half post-tensioning test the value of 26kNm/mrad was only half of the predicted value of 52kNm/mrad. Furthermore it can be seen that column reinforcement had a strong influence on the connection stiffness, which is summarized in Table 5.3.

The column with rotated outer layers (Test 4) increased the initial stiffness

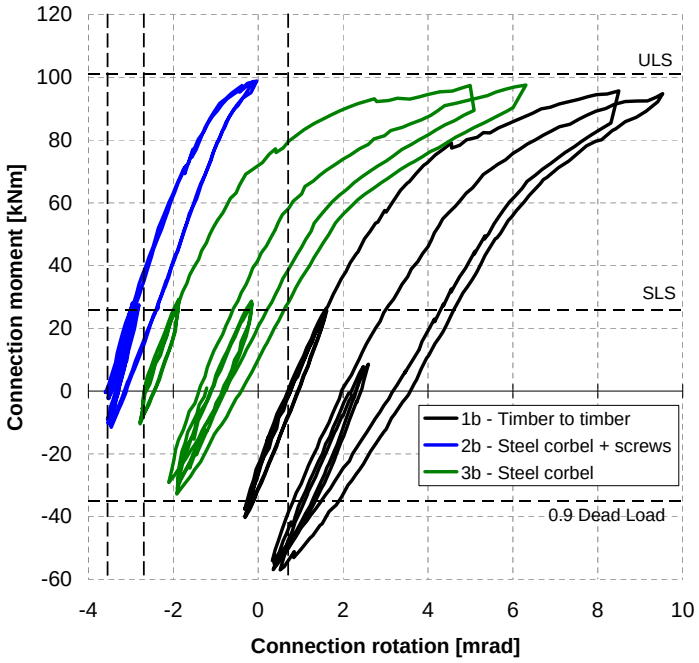

(a) LVL11 column

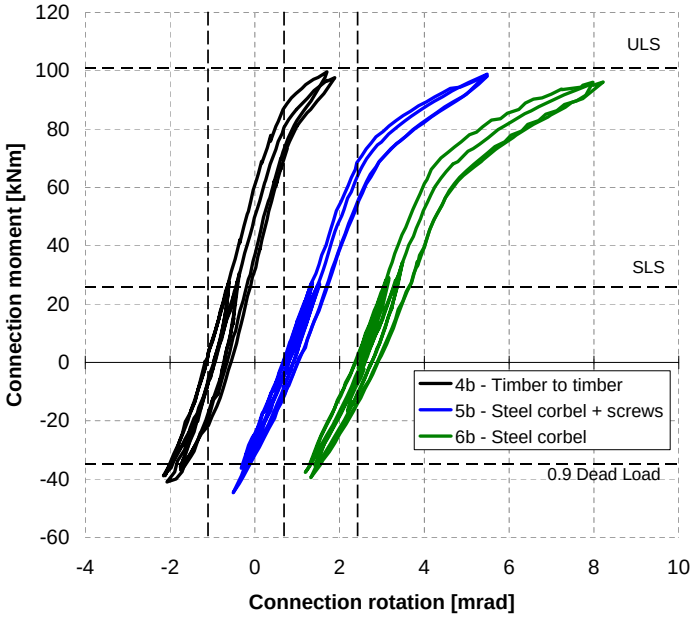

(b) Column with rotated outer layers

Figure 5.15: Moment-rotation graphs for experimental testing of beam-column connection with different types of reinforcement (all curves have been moved horizontally to get a clearer comparison)

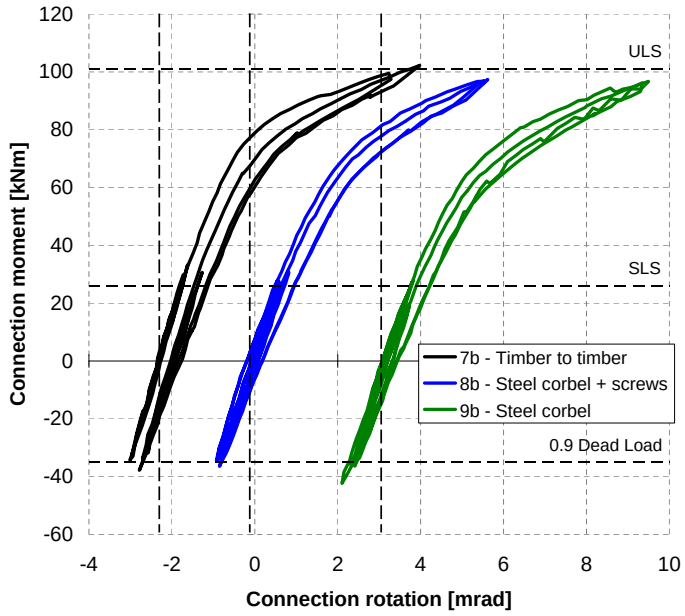

(a) Cross-banded column

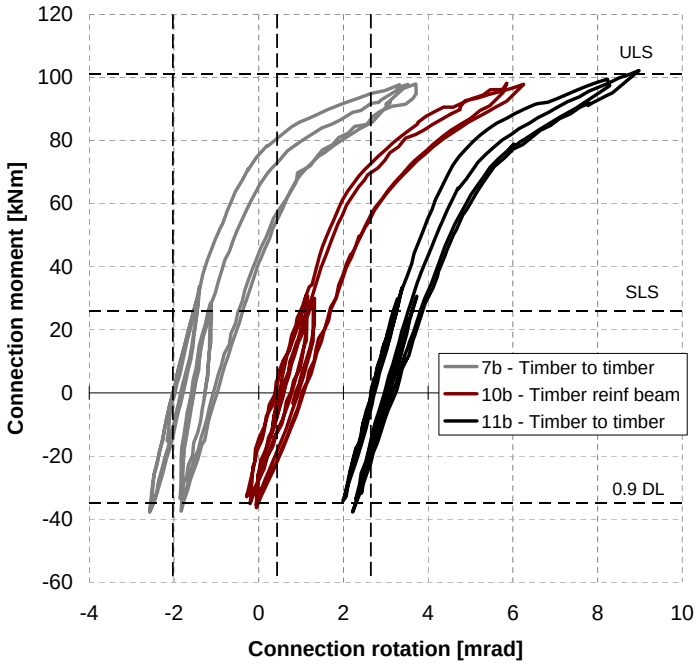

(b) Cross-banded column (2)

Figure 5.16: Moment-rotation graphs for experimental testing of beam-column connection with different types of reinforcement (all curves have been moved horizontally to get a clearer comparison) (continued)

Table 5.3: Overview of effect of column reinforcement on the initial connection stiffness

Reinforcement method	PT force (kN)	Initial connection stiffness (kNm/mrad)		
		Without reinf.	With reinf.	Change
Rotated outer layers	220	25.6	34.8	36%
	440	32.1	47.3	47%
Cross-banded LVL	220	25.6	34.3	34%
	440	32.1	54.5	70%
Screws in LVL11	220	25.6	42.0	64%
	440	32.1	51.6	61%
Screws in LVL with rotated outer layers	220	34.8	29.2	-16%
	440	47.3	39.5	-16%
Screws in cross-banded LVL	220	28.4	25.3	-11%
	440	52.6	41.4	-21%
Timber reinforced beam	220	34.3	26.6	-22%
	440	54.5	48.2	-12%

(k_1) by 36% and 47% for the half and full post-tensioned tests, respectively. Cross-banded LVL (Test 7) increased stiffness by 34% and 70%. Screw reinforcement increased the stiffness for normal LVL11 columns by 64% and 61%, whereas it decreased the stiffness by 16% to 21% for columns with timber reinforcement, both rotated outer layers and cross-banded LVL. Only adding the corbel, without screws, had no improvement in behaviour compared to the timber-to-timber connections, showing the effectiveness of screws but not of the corbel itself without screws. Increasing the contact area between the beam and column, by gluing an extra sheet of timber into the beam (Test 10), did not show any improved performance compared to the other tests with cross-banded LVL.

Stiffness of the two ULS cycles, k_2 was higher for tests with 440kN post-tensioning force, compared to tests with 220kN post-tensioning force. Tests with the full post-tensioning force only showed the start of non-linear behaviour, whereas tests with 220kN post-tensioning force showed a much clearer and longer non-linear curve. Therefore determining stiffness of the bilinear segment for tests with full post-tensioning force was somewhat dubious. This can also be seen for the high stiffness in Test 2b and 4b, which was caused by the short bilinear segment of the test (Figure 5.15) which made it not possible to extract

a more representative stiffness values. The stiffness ratio before and after gap opening, k_2/k_1, varied between 4% and 19%. This ratio was dependent on tendon elongation, which was influenced by frame geometry and tendon length and profile. For the 440kN PT tests the average was around 15% and for the 220kN tests around 8%.

The change in stiffness point ($M_{\Delta k}$) depended on the post-tensioning force. For the 220kN PT tests this point was on average 46kNm, and for the 440kNm tests it was on average 77kNm. The decompression moments of 29 and 57kNm were lower than the point of stiffness change because after decompression was reached, the neutral axis (compression zone) still had to drop down resulting in an increase in connection moment. For larger rotations the neutral axis position was almost constant, but gap opening and the resulting tendon elongation resulted in a further increase of connection moment.

Permanent rotation (θ_{perm}) between the initial two SLS cycles and last two SLS cycles indicated plastic deformation of timber. This effect was significant for Test 1 and Test 3 with permanent rotations ranging between 1.0 and 1.6mrad, whereas for the other tests it was less than 0.6mrad. This indicated that unreinforced columns should not be used for a design. All tested reinforcement methods showed significantly reduced permanent rotations after ULS loading.

Only a minor degradation in stiffness between k_1 and k_3 was seen for all tests. Even in the case of damage to the column (Test 1a and Test 1b) there was only very minor stiffness degradation. The 50% stiffness increase for test 7b was unexpected, therefore the test had been repeated (Test 11b) which resulted in more realistic stiffness values. Furthermore the results of Test 11 and 7 correspond well, showing a repeatability of experimental results.

5.4.3 Joint Panel Shear deformation

Stiffness of the joint panel was evaluated by plotting the joint panel rotation versus connection moment. Figure 5.17 shows these graphs for Tests 1 and 11. The red line shows joint panel deformation during stressing, the thin line is measurements during 220kN PT test and the thick black line during 440kN PT test. Data from Test 11 shows a clear linear relationship between connection moment and joint panel rotation. Test 1 also showed a linear relationship, but exhibited some

hysteretic behaviour. This was due to timber deformation under compression perpendicular to grain stresses at the connection interface. The potentiometers were fixed closely to the connection interface, which meant that some deformation of the column perpendicular to grain was included in the measurements. It can be seen that the level of post-tensioning did not influence the joint panel stiffness as both moment-rotation lines have the same slope. Furthermore, it can be seen that the moment-rotation graphs have an offset from the origin, at zero connection moment there was a certain level of rotation and zero rotation at a negative connection moment. This was due to the post-tensioning anchorage being at the level of the top of the beam, hence there was no shear force in the joint panel when the compression force at the connection was acting on the top of the beam, which was around negative decompression moment.

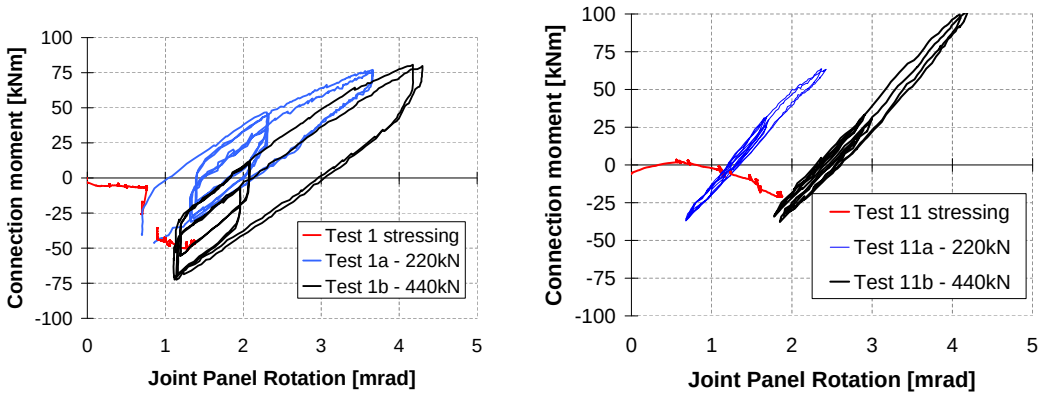

(a) Test 1 - Normal LVL column (b) Test 11 - Crossbanded LVL column

Figure 5.17: Joint panel deformation during stressing and at 220kN and 440kN PT tests

Slopes of the lines in Figure 5.17 gave rotational stiffness of the joint panel. Not all results were as linear as the data of Test 1 and 11. Therefore, the stiffness was evaluated during the first two cycles of SLS testing. This was further justified as the stiffness changed after the decompression point was reached. Results for all tests are shown in Figure 5.18. From the table it can be concluded that stiffness of the joint panel is not influenced by the level of post-tensioning. When analysing stiffness based on the three column types, it can be seen that the column with normal LVL had an average stiffness of 47kNm/mrad, the column

with the rotated outer layers had an average stiffness of 59kNm/mrad and the cross-banded LVL column had an average stiffness of 59kNm/mrad. From this it can be concluded that stiffness is material dependent and that cross layers of LVL (whether in the outer layers or within the product) add to stiffness of the joint panel. Screw reinforcement (Tests 2, 5 and 8) at the column interface did not seem to alter the joint panel shear stiffness.

Test	Column	JP stiffness (kNm/mrad) 220kN	440kN
1	Normal	41	49
2		50	46
3		54	44
4	Rotated	56	53
5		57	62
6		55	63
7	Crossb.	55	54
8		- *	- *
9		54	58
10		69	59
11		66	57

* *No stiffness readings possible*

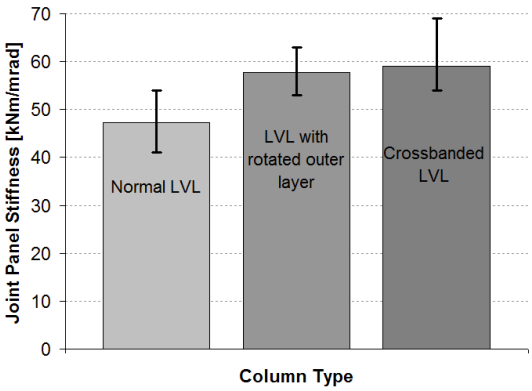

Figure 5.18: Joint panel stiffness per column type

5.4.4 Tendon elongation

Gap opening at the connection and beam deflections cause tendons to elongate. This elongation results in an increase in post-tensioning force. Depending on frame geometry this tendon elongation can have a significant influence on behaviour of the frame (Palermo et al., 2010).

Figure 5.19 shows the tendon force plotted against connection rotation for the first three tests at full post-tensioning force of 440kN. It can be seen that tendon force had an almost linear relationship with connection rotation. Test 2b showed only a small amount of connection rotation and tendon elongation, which was due to the increased connection stiffness as this connection had screw reinforcement in the column. Therefore less gap opening and less tendon elongation was required to reach the ULS connection moment. Figure 5.20 shows the tendon elongation measured during the loading curve of the first ULS cycle for all performed tests, only this part is plotted to get a more clear representation of the data. It can be

seen that there are no significant differences between the tests and the maximum increase in post-tensioning force was 5%. Tendon elongation happened directly from the start of testing and not only after gap opening, as tendon elongation was also caused by beam deflections.

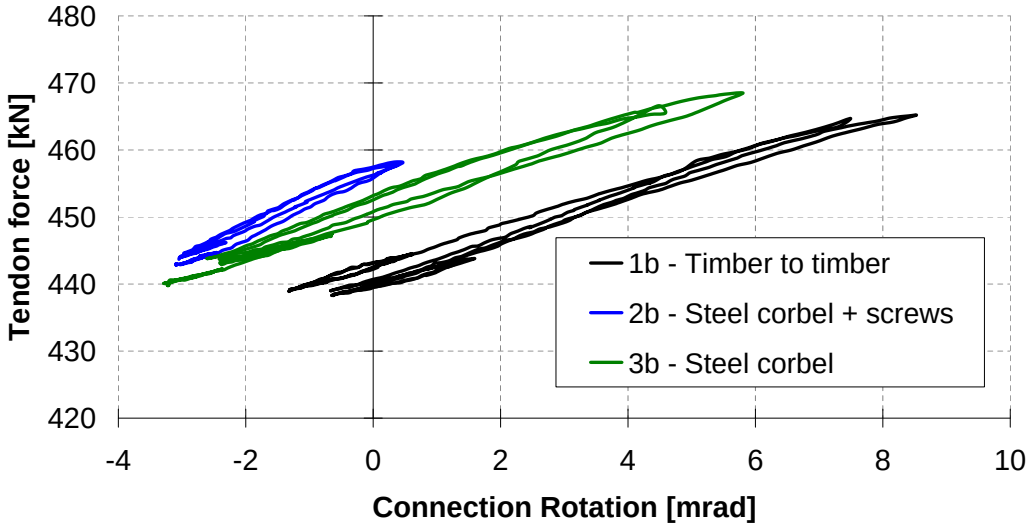

Figure 5.19: Increase in post-tensioning force due to tendon elongation for LVL11 column

Two tests were performed past the ULS design limit, in order to get a better understanding of the connection behaviour. The tendon forces during these tests are shown in Figure 5.21. A clear non-symmetric behaviour can be seen. For positive rotations, the gap opened at the top of the connection and the tendon elongated. For negative rotations, the gap opened at the bottom and there was no tendon elongation. In both tests there was a loss of about 10kN in post-tensioning force after the cycles to a positive and negative connection rotation of 10mrad.

An analytical evaluation of tendon elongation can be performed as outlined in Palermo et al. (2010) (Equation 5.8). A connection rotation of 9mrad (Test 1b) resulted in a gap opening of approximately 2.4mm, taking into account the compression into the column at the bottom and the gap opening at the top. The initial post-tensioning force of 440kN corresponded with a stress of 1111MPa and a strain of 0.56% (short dashed line in Figure 5.22). The tendon had a length of 4.2m, and the increase in length of 2.4mm resulted in an increase in strain of

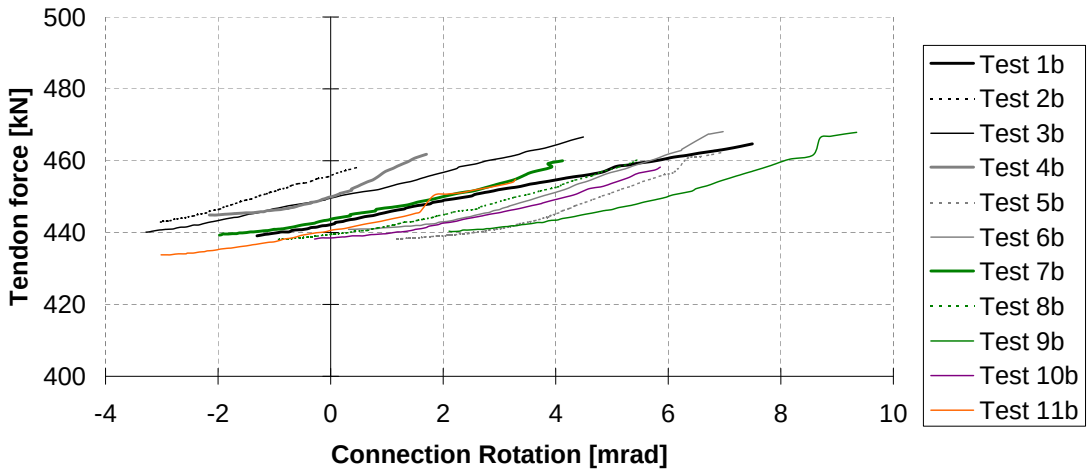

Figure 5.20: Increase of post-tensioning force for all tests under first ULS loading cycle

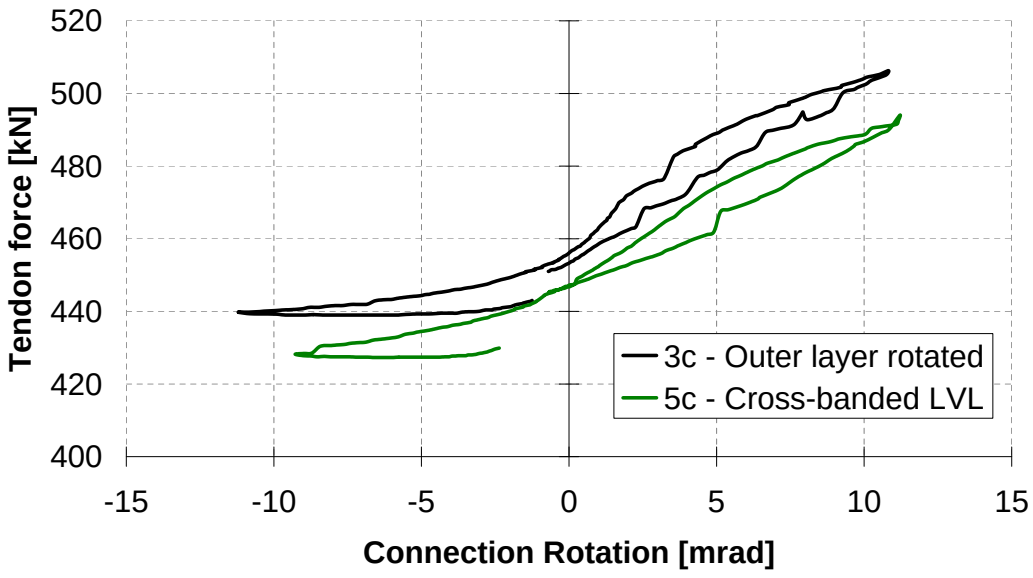

Figure 5.21: Tendon elongation for Test 4c and 7c

0.06%. The new strain became 0.62% which corresponded to a stress of 1225MPa (long dashed line in Figure 5.22) or a post-tensioning force of 485kN, which was well below the yield strength of the post-tensioning steel.

$$
\begin{aligned}
L_{p0} &= 4200mm \\
\Delta L_1 &= 2.4mm \\
\epsilon_0 &= \frac{N_0}{A_p E_{pt}} = \frac{440000}{4 \cdot 99 \cdot 200000} = 0.56\% \\
\epsilon_1 &= \epsilon_0 + \frac{\Delta L_1}{L_{p0}} = 0.56\% + \frac{2.4}{4200} = 0.56\% + 0.06\% = 0.62\% \\
N_1 &= \epsilon_1 \times A_{pt} E_{pt} = 0.62\% \cdot 4 \cdot 99 \cdot 200000 = 485kN
\end{aligned}
\tag{5.8}
$$

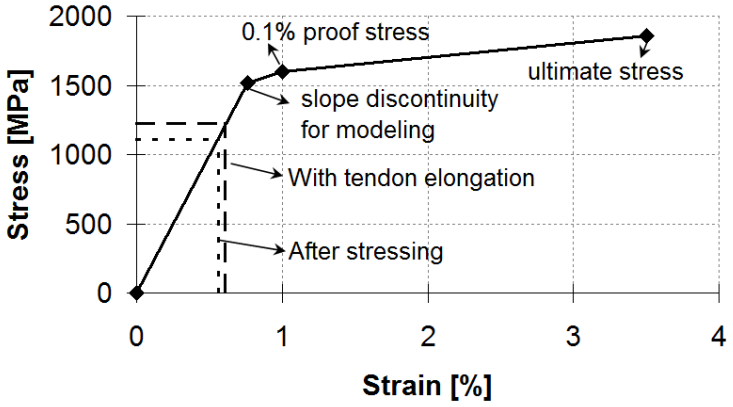

Figure 5.22: Stress-strain relationship for post-tensioning steel showing the stress and strain levels after stressing and including tendon elongation

The analytical calculated post-tensioning force is larger than the post-tensioning force measured during experimental testing. This is due to losses occurring in anchorages, load-cells and elastic shortening of beam and column, resulting in shortening of the tendon which partly offsets the tendon elongation during testing. Part of this effect will also happen in real buildings. Therefore calculating tendon elongation without accounting for frame shortening will overestimate the increase in post-tensioning force.

5.4.5 Neutral axis depth

The design of post-tensioned connections (in either concrete or timber) relies on the use of the Monolitic Beam Analogy (MBA) as a design procedure (Pampanin et al., 2001). This design procedure is based on a neutral axis depth, which defines the height of the compressive zone. The neutral axis depth is strongly dependent on the rotation at the connection. In a seismic design this rotation is mainly prescribed by the inter-storey drift level, but in a gravity design the rotation is due to the deflection of the beam.

The depth of the neutral axis varied for the different connection types which were tested. Figure 5.23 shows the normalized neutral axis depth (c/d, where d = beam height = 526mm) versus the connection rotation. The cycles up to the ULS limit state gave information about the neutral axis depth. The first cycle up to the ULS gave the lowest of the curves on the graph (varying between 0.6 and 0.4). During this loading curve some damage perpendicular to the grain in the column occurred. Therefore the neutral axis shifted up and the unloading curve and the sequential loading curve had a larger neutral axis depth. At small rotations decompression had not yet occurred and neutral axis depth was theoretical above 1.0. The SLS cycles did not reach the decompression point, although during the last SLS cycles there was some permanent rotation which influenced the results. The black line is a trendline curve of the form $y = a \cdot x^b$ which has been made for every test and is used for comparing the different tests.

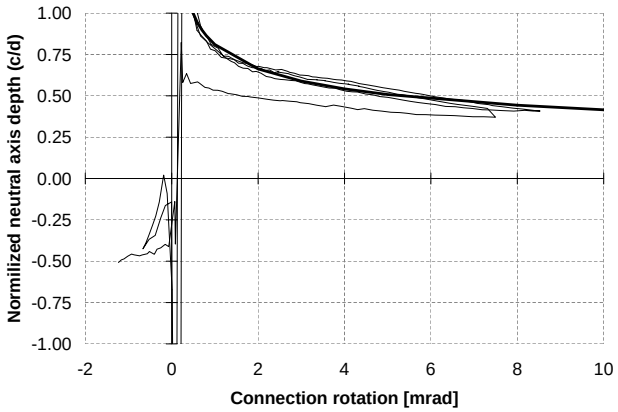

Figure 5.23: Normalized neutral axis depth (c/d) for Test 1b

A complete overview of the neutral axis depths for all tests at 440kN is given in Figure 5.24. Table 5.4 shows the normalized neutral axis depth at 4mrad rotation, where the last column shows the percentage relative to Test 1b (without any reinforcement). Predictions of the seismic design procedure, as explained in Section A.2.5, are shown in Figure 5.24 by the thick black line, it can be seen that this over estimates the neutral axis depth.

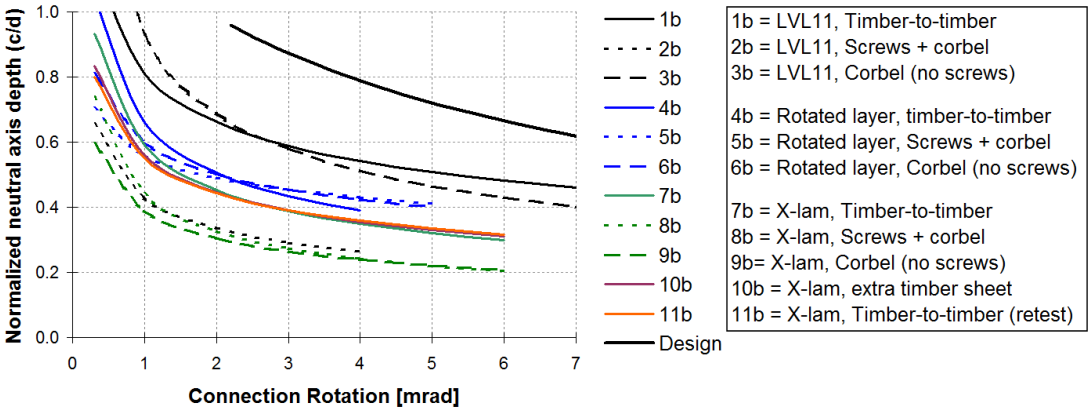

Figure 5.24: Comparison of neutral axis depth versus connection rotation for all tests

Table 5.4: Overview of neutral axis depth at 4mrad connection rotation, with last column showing percentage relative to Test 1b

Test nr	Column interface	Steel reinforcement	Norm. neutral axis depth	
1b	Normal LVL	Timber to timber	0.54	100%
2b	Normal LVL	Steel corbel + screws	0.26	49%
3b	Normal LVL	Steel corbel	0.51	95%
4b	Rotated outer layer	Timber to timber	0.39	72%
5b	Rotated outer layer	Steel corbel + screws	0.43	79%
6b	Rotated outer layer	Steel corbel	0.42	78%
7b	Cross-banded	Timber to timber	0.35	64%
8b	Cross-banded	Steel corbel + screws	0.24	45%
9b	Cross-banded	Steel corbel	0.24	44%
10b	Cross-banded	Timber reinforcement beam	0.35	65%
11b	Cross-banded	Timber to timber (re-test)	0.36	66%

For the first three tests at 440kN with the normal LVL, Test 1b had no

reinforcement, Test 2b had screw reinforcement with the corbel and Test 3b had just the corbel, but no screws. It can be seen that screw reinforcement reduced the neutral axis depth by about 50%. The increased strength and stiffness at the bottom of the connection resulted in higher compressive stresses and due to horizontal force balance (the post-tensioning force must equal the compressive force in the timber) a lower neutral axis depth. It can also be concluded that the corbel itself had no significant influence on the neutral axis depth. Results from Test 2b did not go further than 4mrad as this was the rotation required to achieve the ULS connection moment.

For all tests with the rotated outer layers the neutral axis depth was quite constant, but compared to the normal LVL values between 20 and 30% lower were recorded. The cross-banded LVL showed a reduction of about 35% compared to the unreinforced column. The screws and corbel in cross-banded LVL (Test 8b) did lower the neutral axis depth even more compared to cross-banded LVL without any steel reinforcement (Test 7b). Surprisingly also the cross-banded LVL with just the steel corbel (Test 9b) had similar results compared to the test with the screw reinforcement. Testing with the extra timber sheet inside the beam (Test 10b) and Test 11b (re-test of Test 7b) showed the same neutral axis depth as Test 7b, indicating no improved performance.

5.5 Design implications

This section describes how results from experimental testing can be used in a preliminary design. The same 7.6m span beam as in Section A.2.3 is analysed with a post-tensioning force of 440kN. Testing has shown that, depending on the connection details, initial connection stiffness is between 30 and 59kNm/mrad. The lower bound of 30kNm/mrad is chosen here, although different values will be evaluated later. The experimental testing showed that the connection stiffness can be approximated using a bi-linear curve as shown in Figure 5.25. The post-tensioning force of 440kN gives an initial stiffness of 30kNm/mrad, the change in stiffness moment of 77kNm and second stiffness of 15% of the initial stiffness, which is 4.5kNm/mrad.

The connection rotation has three components (Figure 5.26): rotation due to uplift force at the deviator, rotation due to connection moment and rotation due

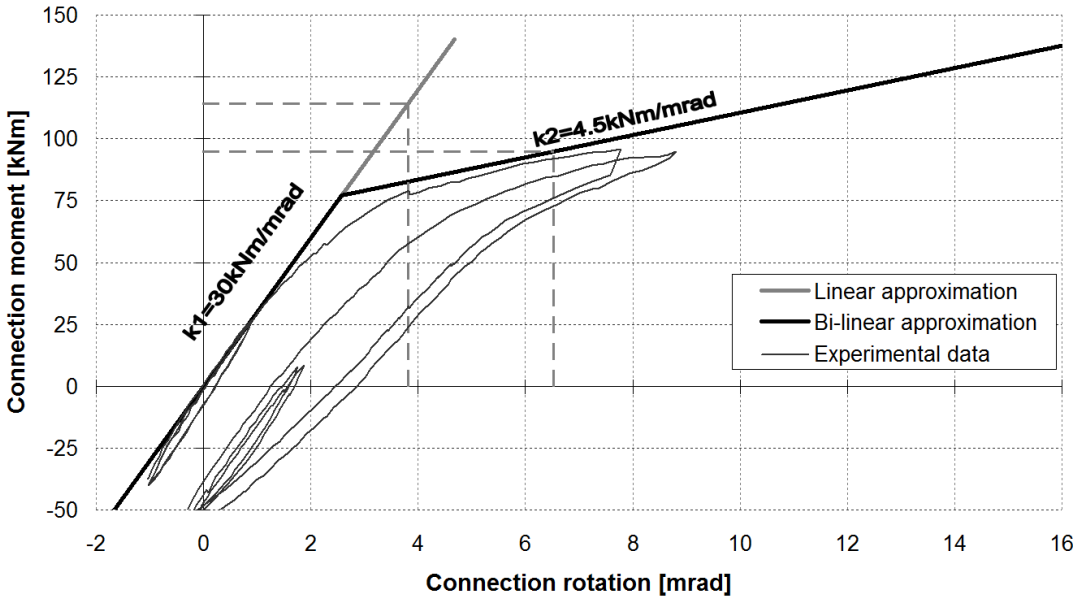

Figure 5.25: Graph of connection rotation versus connection moment

to load on the beam. Analytical expressions for each component can be derived from structural mechanics. The total connection rotation is the sum of these three components (Equation 5.9). This connection rotation relates directly to the connection moment as shown in Figure 5.25 and is described by Equation 5.10. Combining the three analytical expressions in Figure 5.26 with Equation 5.9 and Equation 5.10 makes it possible to solve for the connection moment. The result is shown in Equation 5.11.

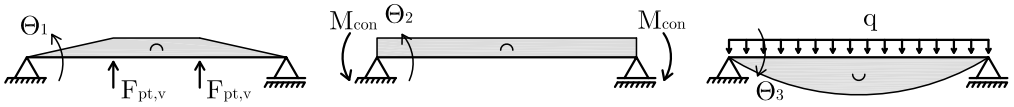

$$\theta_1 = \frac{F_{pt,v} \cdot L_b^2}{9EI} \qquad \theta_2 = \frac{M_{con} \cdot L_b}{2EI} \qquad \theta_3 = \frac{q \cdot L_b^3}{24EI}$$

Figure 5.26: Rotations due to uplift force at deviators, connection moment and distributed load on beam

$$\theta = -\theta_1 - \theta_2 + \theta_3 \tag{5.9}$$

$$M_{con} = \begin{cases} \theta \times k_1 & \text{if } M_{con} < M_{\Delta k} \\ (\theta - \theta_{\Delta k}) \cdot k_2 + M_{\Delta k} & \text{if } M_{con} > M_{\Delta k} \end{cases} \tag{5.10}$$

$$M_{con} = \begin{cases} \left(\dfrac{q \cdot L_b^3}{24EI} - \dfrac{F_{pt,v} \cdot L_b^2}{9EI} \right) / \left(\dfrac{1}{k_1} + \dfrac{L_b}{2EI} \right) & \text{if } M_{con} < M_{\Delta k} \\ \left(\dfrac{q \cdot L_b^3}{24EI} - \dfrac{F_{pt,v} \cdot L_b^2}{9EI} + M_{\Delta k} \cdot \dfrac{k_1 - k_2}{k_1 k_2} \right) / \left(\dfrac{1}{k_1} + \dfrac{L_b}{2EI} \right) & \text{if } M_{con} > M_{\Delta k} \end{cases} \tag{5.11}$$

Equation 5.11 is graphically shown in Figure 5.27 by the black line. This bi-linear approximation, with $q = 50kN/m$ and $F_{pt,v} = 57kN$, gives the ULS connection moment of 95kNm for the initial connection stiffness of 30kNm/mrad.

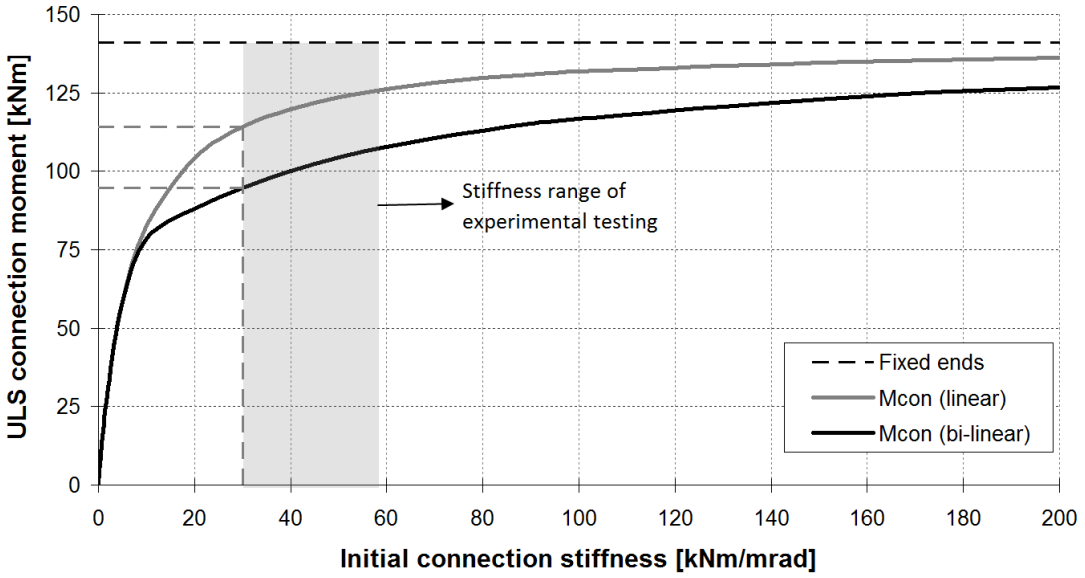

Figure 5.27: Graph of connection moment-rotation for different connection models; bi-linear, linear and fixed

A simplification would be to ignore the bi-linear part and only use the initial stiffness, shown in Figure 5.25 and Figure 5.27 by the solid grey lines. The ULS connection moment will increase to 114kNm which is a conservative design for the connection moment. Care needs to be taken when evaluating the beam mid-span moment since this value will decrease and thus be unconservative. A greater

simplification would be to ignore the connection stiffness completely and assume the connection to be fixed, resulting in a connection moment of 141kNm. This is an even more conservative assumption, as is shown by the black dashed line in Figure 5.27. A quick way to take the connection behaviour into account is by taking the ratio of real connection moment over the fixed connection moment, which is 95/141=0.67. This shows that the real connection moment is about 2/3rd of the connection moment which would occur if the connection was fully fixed. Figure 5.27 also shows that the variation in connection stiffness which was found in the experimental testing, ranging from 30 - 59kNm/mrad, does not have a large influence on the connection moment.

5.6 Conclusions

Conclusions which can be drawn from the experimental testing of beam-column connections under gravity loading with different types of column reinforcement are as follows:

- The connection design method proposed by Newcombe et al. (2010a) predicts the moment-rotation behaviour of timber-to-timber connections well for the test with 440kN post-tensioning, but proved to be less accurate for the test with 220kN post-tensioning force. Furthermore, the design method does not account for effects of column reinforcement. Connection moment is best predicted by multiplying the compressive force (or post-tensioning force) with distance between centroid of compression zone and centroid of beam. For connections with eccentric tendons, the connection moment-rotation behaviour is symmetric, except for the effect of moment increase due to tendon elongation.

- Tested connections, with full post-tensioning force of 440kN, had an initial stiffness ranging between 30 - 60kNm/mrad. Connection stiffness after two cycles to ULS loading was very similar to the stiffness before ULS loading, even for tests without any column reinforcement. Timber reinforcement in the column was an effective way to minimize permanent connection rotations. The reinforcement allowed for higher stresses in the column while the material remained linear elastic. Screw reinforcement in the column

compression zone was also effective in increasing the initial elastic stiffness and minimizing permanent rotations. Combining timber reinforcement with screw reinforcement did not improve the stiffness of the connections.

- Joint panel shear stiffness did not depend on the level of post-tensioning, but it was found to be material dependent and timber cross-layers increase the shear stiffness. Tendon elongation before decompression was caused by beam deflections and after decompression gap opening also contributed to tendon elongation. It was found that calculating tendon elongation without accounting for frame shortening will overestimate the increase in post-tensioning force. Neutral axis depths ranged between 20%-40% of beam height for reinforced connections at maximum connection moment. Unreinforced connections have a large neutral axis depth due to the plastic behaviour of the column.

- Ignoring the initial connection stiffness results in a conservative design of the connection and assuming it fully fixed, but an unconservative design for the mid-span of the beam. As a first approximation the connection moment due to the connection stiffness is about 2/3rd of the moment of a beam with fully fixed ends.

Chapter VI

Post-tensioned timber frames

6.1 Introduction

Traditional timber frame design, with simply supported beams, is often governed by deflections as was shown in the design of beams used for experimental testing in Chapter 4. Moment resisting beam-column connections can help to limit deflections, but making moment resisting connections in timber often involves extensive fabrication (Buchanan and Fairweather, 1993) and design of section sizes is often governed by connection details. When using draped post-tensioning tendons, uplift forces at deviators create a precamber to the beams which helps to satisfy deflection criteria. Furthermore, continuous unbonded post-tensioning tendons, anchored at exterior columns, clamp beams and columns together, creating moment resisting connections. One stressing operation can create several beam-column connections at once, making it an efficient construction system (Buchanan et al., 2009).

The ultimate limit state (ULS) strength of the beams is linked to deflections as post-tensioning tendons extend when beams deflect, resulting in an increase in post-tensioning force. Connection strength is governed by the limited compressive strength perpendicular to grain of the column, although this area can be reinforced using long fully threaded screws. This form of steel reinforcement also helps to reduce post-tensioning losses. Draped tendons have a larger inclination compared to simply supported beams, thus resulting in an increased vertical force at deviators. Therefore post-tensioning forces in frames can be lower than for simply supported beams.

Research objectives for experimental testing were:

- Evaluate connection behaviour of internal and external connections in post-tensioned timber gravity frames.

- Determine effectiveness of screw reinforcement in column interface.
- Gather data for verification of frame models.
- Use Digital Image Correlation (DIC) techniques to verify measurement of deformation components and to acquire full displacement fields.

This chapter describes the experimental testing campaign on one-bay and two-bay post-tensioned timber gravity frames. Design of the frame is presented in Appendix A.3 and summarized in Section 6.2. A description of the test setup, testing schedule, construction and instrumentation is given in Section 6.3. Results of testing without post-tensioning are presented in Section 6.4. Results of one-bay testing are presented in Section 6.5 and for two-bay testing in Section 6.6.

6.2 Frame design

The design of a post-tensioned timber gravity frame which was used for experimental testing was based on a 9m beam length, similar to design of post-tensioned beams in Chapter 4. The frames were designed to be part of a four storey commercial office building with a 6m floor span. A partial contact connection, with only top and bottom flange in contact with the column was used, based on analysis described in Chapter 8. Screw reinforcement at the column interface was chosen as the preferred reinforcement option, based on results of experimental testing on beam-column connections as described in Chapter 5.

For testing a range of post-tensioning forces were considered, namely 0, 100, 200, 300 and 400kN. A framework model of the frame was made and used to perform a parameter study on the beam height. Based on the results a beam height of 500mm was chosen. A detailed description of the design of the post-tensioned timber frame is given in Appendix A.3.

6.3 Test setup

6.3.1 Overview

The beam span was designed for 9m, but due to laboratory restrictions column centre to centre distance was 9144mm and beam length 8644mm for the one-bay frame. The length of the strong floor meant that the two-bay frame needed to be scaled down to 2/3-scale resulting in to two bays of 6096mm and beam lengths

of 5596mm. The inter-storey height was taken as 3.6m. An overview of the main dimensions for both tests can be seen in Figure 6.1 and pictures of both test setup are shown in Figure 6.2.

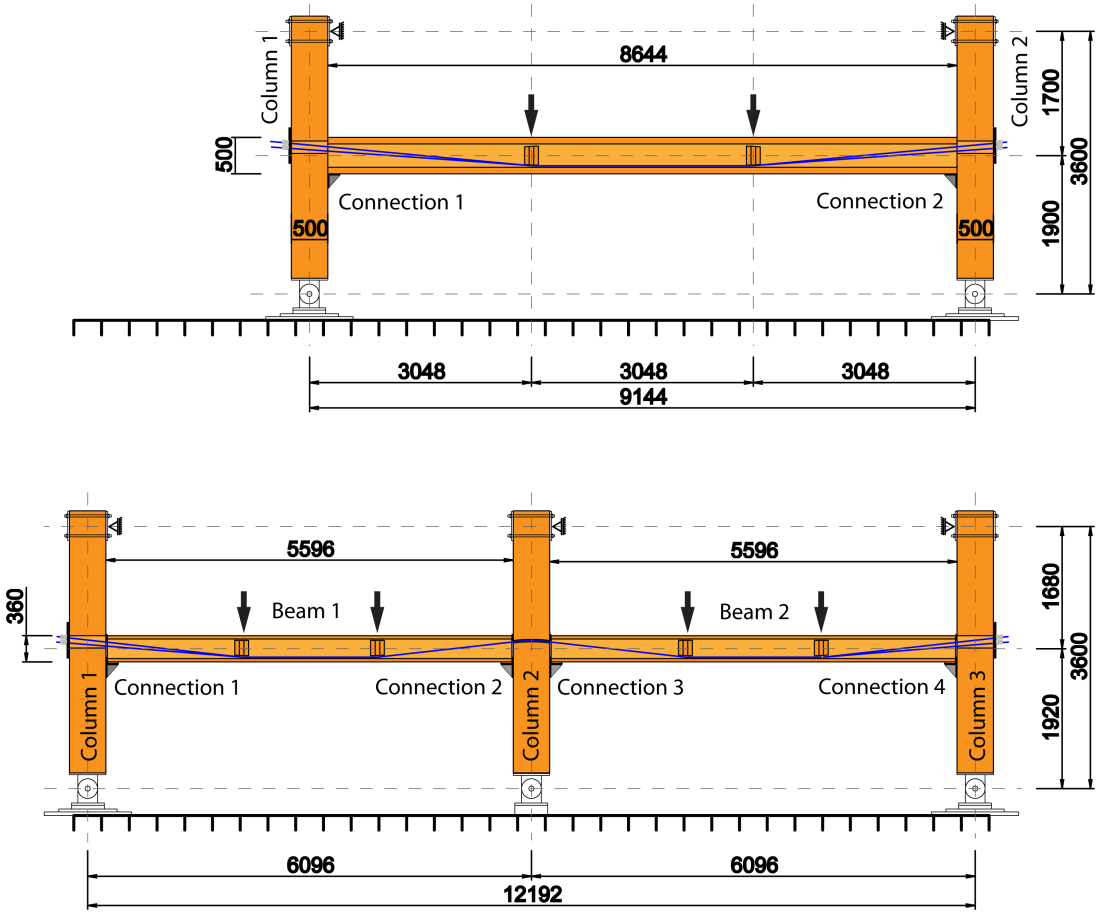

Figure 6.1: Overview of one-bay and two-bay frames for experimental testing

Cross-sections of beams and columns can be seen in Figure 6.3. The webs of all beams were designed with a thickness of 45mm, as draped tendons reduced the shear force in the beams. These thin webs can create issues with fire performance in a building design (Spellman et al., 2012), but this was not considered in the scope of this research. For the one-bay frame the thickness of top and bottom flanges of 90mm was chosen. This was needed to have enough timber area in the connection zone after gap opening. Beams for the two-bay frame had a top and bottom flange thickness of 45mm. As the span was much shorter, compared to the one-bay frame, a more flexible beam was needed in order to achieve sufficient

(a) One-bay frame (full-scale)

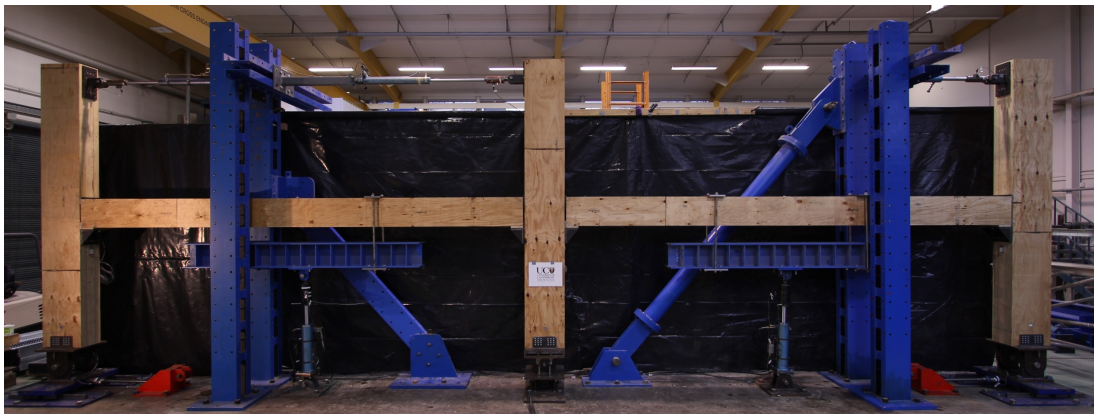

(b) Two-bay frame (2/3-scale beams)

Figure 6.2: Pictures of frame test setups

rotations at the ends of the beams. This meant that the post-tensioning force for the two-bay frame could not be as high as for the one-bay frame. Section width of beams and columns were kept equal. The column was fabricated using two layers of 90mm LVL on the outsides and a 63mm and 45mm layer in between. The middle two layers had openings to allow tendons to pass through. Deviators were glued inside the box beams using Phenol Resorcinol Formaldehyde resin. The top of the deviators were reinforced with screws to prevent splitting, as described in Appendix B.1. Technical drawings of beams and columns can be found in Appendix G.

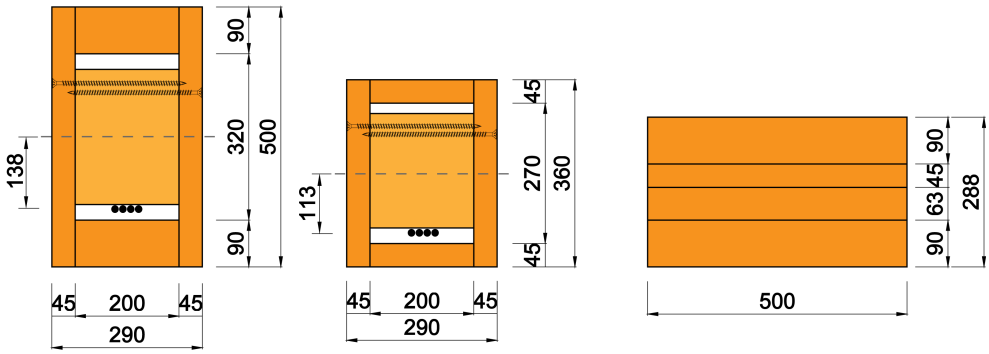

Beam one-bay frame	Beam two-bay frame	Column
$A = 80.6 \cdot 10^3 mm^2$	$A = 50.2 \cdot 10^3 mm^2$	$A = 144 \cdot 10^3 mm^2$
$A_s = 34.2 \cdot 10^3 mm^2$	$A_s = 25.0 \cdot 10^3 mm^2$	$A_s = 96.0 \cdot 10^3 mm^2$
$Z = 9.84 \cdot 10^6 mm^3$	$Z = 4.41 \cdot 10^6 mm^3$	$Z = 12.0 \cdot 10^6 mm^3$
$I = 2.46 \cdot 10^9 mm^4$	$I = 0.79 \cdot 10^9 mm^4$	$I = 3.00 \cdot 10^9 mm^4$

Figure 6.3: Cross-sections and properties of beams and columns for one-bay and two-bay frame tests

6.3.2 Testing schedule

The testing schedule for one-bay and two-bay frame testing is shown in Table 6.1. As stressing introduces deformations and stresses in the structure, this was an integral part of the testing procedure. The one-bay frame tests were performed at four different levels of post-tensioning (up to 400kN) whereas the two-bay frame testing was only performed at three different levels (up to 300kN). After every level of post-tensioning the frame was destressed and all instrumentation was reset to zero before performing the next stressing operation. The maximum displacement of the hydraulic actuators was based on the maximum allowable stresses in top and bottom flanges, which were monitored during testing. This load level was passed the ULS design load.

The one-bay frame testing had two tests where the beam was pulled down and pushed up (push-pull tests, Figure 6.4a), which allowed to record data past both the positive and negative decompression moments. The two-bay frame testing was performed with symmetric loading, whereby both rams applied the same load to the structure, and with asymmetric loading. For the asymmetric loading one actuator applied a force representative to the dead load only, and the other actuator a force equivalent to the maximum design load (Figure 6.4b).

Table 6.1: Testing schedule for frame testing

Frame	Test	PT (kN)	Description
One-bay	1	0	Benchmark
	2S	100	Stressing
	2a	100	Normal test
	2b	100	Push-pull test
	3S	200	Stressing
	3a	200	Normal test
	3b	200	Repeat of test 3a
	3c	200	Push-pull test
	4S	300	Stressing
	4a	300	Normal test
	5S	400	Stressing
	5a	400	Normal test
Two-bay	1a	0	Benchmark, symmetric loading
	1b	0	Benchmark, asymmetric loading
	2S	100	Stressing
	2a	100	Normal test, symmetric loading
	2b	100	Normal test, asymmetric loading
	3S	200	Stressing
	3a	200	Normal test, symmetric loading
	3b	200	Normal test, asymmetric loading
	3c	200	Repeat of test 3a
	3d	200	Repeat of test 3a
	4S	300	Stressing
	4a	300	Normal test, symmetric loading
	4b	300	Normal test, asymmetric loading

6.3.3 Construction

Columns and beams were manufactured by Hunters Laminates Nelson Ltd using Nelson Pine LVL 11. Figure 6.5a shows the timber deviators glued to the inside of the box beams. The beams were fitted with PVC sleeves to allow the post-tensioning tendons to slide through. Installing long fully threaded screws into the LVL columns (Figure 6.5b) posed some difficulties as high torque values are needed to insert long screws. A solution was found by pre-drilling with a long series drill bit with a diameter smaller than the core diameter of the screw. In the

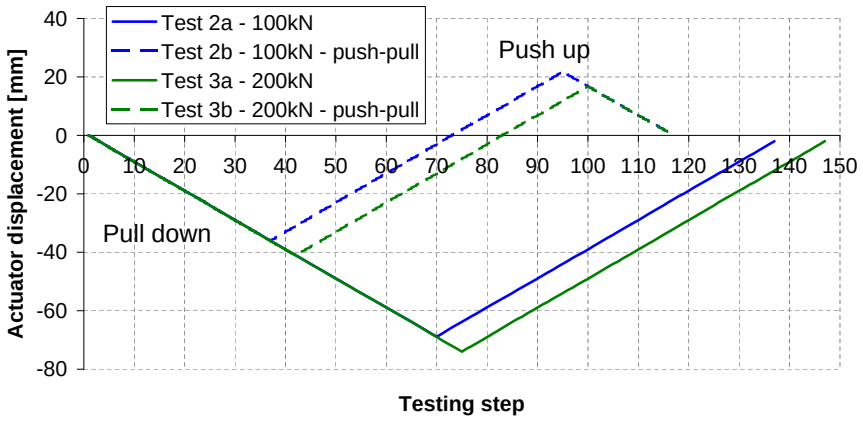

(a) One-bay frame for 100kN and 200kN tests

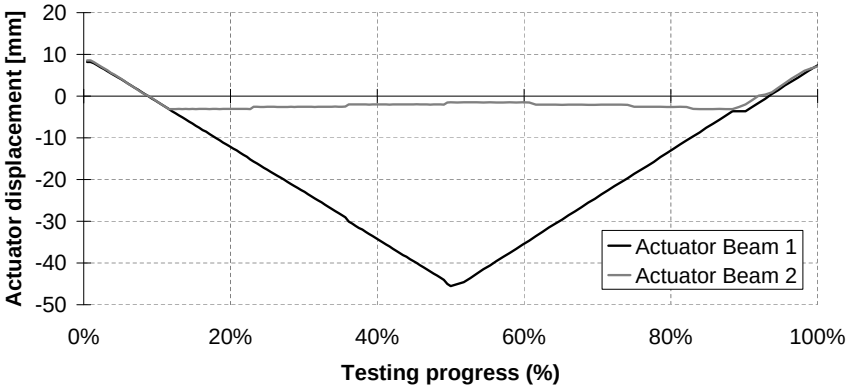

(b) Two-bay frame for 200kN tests with asymmetric loading

Figure 6.4: Examples of loading protocol for frame testing

case of 10mm diameter screws with a core diameter of 6.1mm a 6mm drill was used. Steel corbels and plates for the interface (Figure 6.5c) were manufactured in-house in the structures laboratory of the University of Canterbury. Corbel manufacturing was complicated due to the angled screws which needed to be recessed into the steel plate. This steel fabrication work took a long time and could require significant time and costs when many need to be manufactured for an entire building. Alternatively, some screw manufacturers have steel components which can be used to fix screws under a 45° angle, although availability in New Zealand can be an issue.

(a) Manufacturing of deviator

(b) Screw reinforcement in column

(c) Screwing corbel to column

Figure 6.5: Manufacturing of post-tensioned timber frame

6.3.4 Instrumentation

Several types of instrumentation were used on the test setup, below is an overview of every type. Pictures of the test setup with instrumentation can be seen in Figure 6.6. Drawings of the exact location of instrumentation are given in Appendix G. A list of instrumentation and corresponding data channels is given in Appendix C.1

Load cells Every ram was fixed with a 400kN load cell in order to measure the loads which were put on the structure during testing. The four post-tensioning tendons also had each their own load cell. The exterior columns were placed on sliding base connections, which were held in place with a load cell in order to measure the horizontal reaction force. The top of every column was in the horizontal direction fixed to the reaction frame with a load cell. For the internal connection of the two-bay frame the horizontal reaction force could be calculated based on equilibrium of the test setup. Vertical reaction forces at the column bases could be calculated based on symmetry and vertical equilibrium of the test setup.

Potentiometers Every connection zone was fitted with potentiometers in order to measure three different deformation components; joint panel shear deformation,

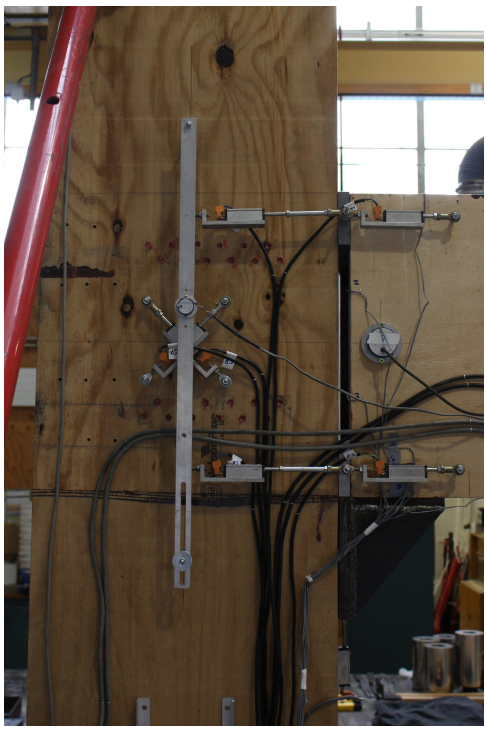

(a) External connection

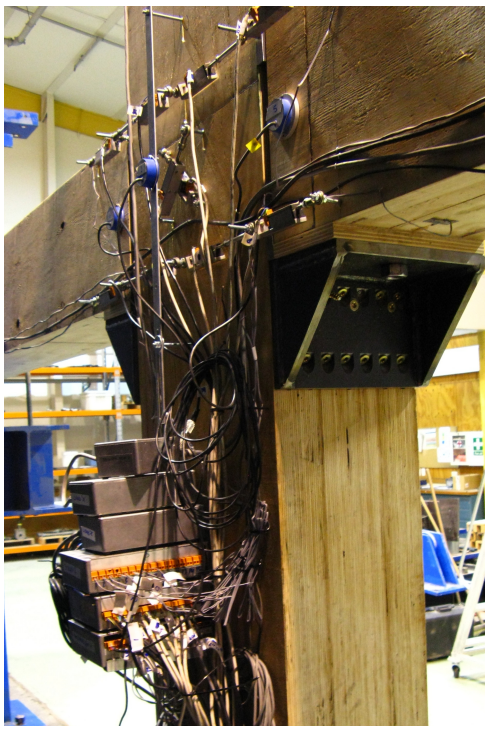

(b) Internal connection

(c) Load cells for post-tensioning

(d) Slider connection with load cell

Figure 6.6: Instrumentation on frame test setup

interface compression and gap opening. Furthermore, two potentiometers were placed diagonally along each beam in order to measure shear deformation. Three rotary potentiometers measured vertical deflections at the deviators and at mid-span. Spring loaded potentiometers were placed below the corbels to measure displacements between the corbel and column.

Inclinometers Inclinometers were placed at both ends of the beams. Also every column was fitted with an inclinometer, which was fixed above and below the joint panel, in order to measure column and reaction frame rotations.

Strain gauges Strain gauges were fitted at beam mid-span on top, centreline and bottom of the beam. They were also placed at the connection at inside and outside of top and bottom flanges. Furthermore, several strain gauges were placed on the bottom flange, in the compression zone, in order to study the stress profile at the connection after gap opening.

Digital Image Correlation Two digital SLR cameras were taking images during testing. One camera used a wide-angle lens in order to take images of the full frame. The second camera was fitted with a zoom lens and took close-up pictures of the connections. An image was taken at every step of the loading protocol, which was at every millimetre of beam deflection. These images were run through a Matlab script which tracks marker points through the series of images.

6.4 Test results without post-tensioning

This section presents the results of the one and two-bay frame testing without post-tensioning. Further results in the next sections are split between the one-bay frame testing and two-bay frame testing.

Before stressing the frames a test was performed without post-tensioning in order to determine material properties of the beams. This was performed in a similar manner as for beam testing as described in Chapter 4, therefore the procedure for measuring and calculating the necessary parameters is not repeated here. The resulting graphs can be seen in Figure 6.7 and material properties are shown in Table 6.2. Not all properties were measured for every beam due to instrumentation limitations. It can be seen that the average Modulus of Elasticity (MoE) of 12.0GPa was higher than the specified 11GPa and the average shear modulus of 663MPa was higher than the specified 550MPa.

Table 6.2: Shear modulus and modulus of elasticity based on experimental testing of frames.

Frame	Shear modulus		Modulus of Elasticity	
	Left side (MPa)	Right side (MPa)	Displacement (GPa)	Strain gauges (GPa)
One-bay	656	720	12.2	13.8
Two-bay (Beam 1)	624	-	11.8	13.1
Two-bay (Beam 2)	652	-	-	14.5

The modulus of elasticity was also determined using data from strain gauges fixed at mid-span. The bending moment was calculated based on Equation 4.6 and used for beam length the distance between centres of the corbels. Due to rotations at ends of the beams the frame wanted to elongate. This elongation was restricted by the columns which resulted in a compression force in the beams. This compression was acting on the bottom flange, resulting in a negative bending moment which was at most of 5% of total bending moment. Even though this effect was small, it was taken into account in calculation of the bending moment. The bending moment divided by section modulus gave the bending stress in the section. Strains were calculated from the strain gauges at top and bottom of the beam. The slope of the stress-strain plot gave the modulus of elasticity,

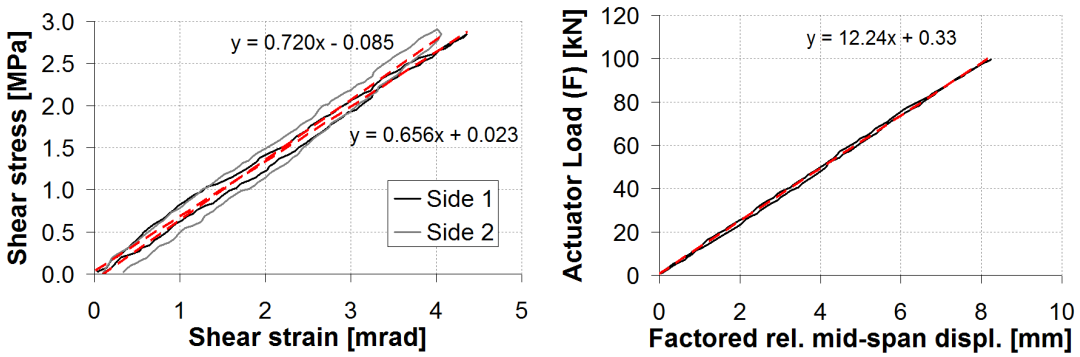

(a) One-bay frame

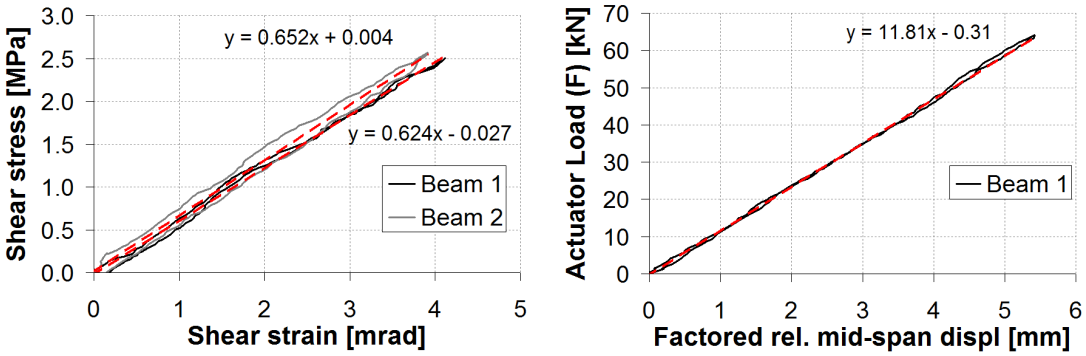

(b) Two-bay frame

Figure 6.7: Determining shear modulus and modulus of elasticity for frame testing, red lines show linear trend-lines

as presented in the last column of Table 6.2. The difference between the two methods for measuring the modulus of elasticity is about 12%, which can be caused by several factors like calibration of instrumentation, non-linearity of strain profile and accuracy of strain gauges.

6.5 Test results of the one-bay frame

This section presents the results of one-bay frame testing (Figure 6.8). Data acquired during stressing is presented followed by evaluation of bending moments and beam deflections. Four deformation components are evaluated, namely column stiffness, joint panel shear stiffness, interface compression stiffness and gap opening. For the connection behaviour after decompression the compression block is evaluated in more detail. Finally results from digital image correlation are presented and compared with measurements of inclinometers and potentiometers. The results which are analysed will be used in later chapters to verify analytical models of the connection behaviour.

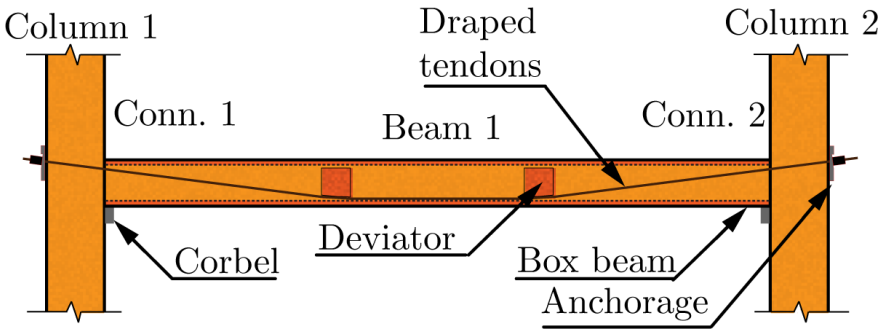

Figure 6.8: Overview and nomenclature of one-bay frame testing

6.5.1 *Stressing of frame*

Testing was performed at four different levels of post-tensioning, namely 100, 200, 300 and 400kN (Section A.3.2). After each level of post-tensioning the frame was fully destressed so that instrumentation could be zeroed again. Testing with 100kN post-tensioning force was done with only two tendons. The other tests were all performed with four tendons. Stressing of tendons was done individually and every tendon was monitored with a load cell.

Figure 6.9 shows the mid-span deflection for the four stressing operations. Deflection values are negative as the beam bends upwards. A very linear load-displacement behaviour can be seen. Also shown in the figure are the ratios of the span length over the precamber.

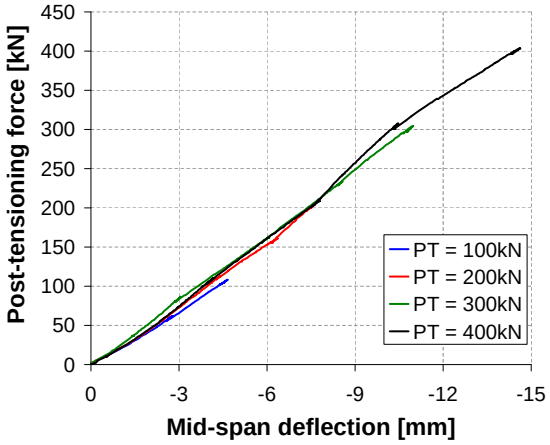

F_{pt} (kN)	precamber (mm)	Span over (-)
100	4.5	1921
200	7.5	1153
300	10.8	800
400	14.4	600

Figure 6.9: Mid-span deflection for different levels of post-tensioning

Due to construction tolerances there were small gaps between the beam and column interface. Therefore during the initial stages of stressing some gap opening, or rather gap closing, was measured. This is shown in Figure 6.10 where connection moment versus gap opening is plotted for both connections. Calculation of connection moment is further explained in Section 6.5.4. It can be seen that most rotation happened for low connection moments, whereas after the connection was fully closed a very stiff moment-rotation behaviour was observed. The final rotation values of around 1 and 2mrad are thus not real rotations, but represent movement in instrumentation due to tolerances. Therefore, further figures with gap opening will have a similar offset.

6.5.2 Beam deflections

Figure 6.11 shows the curves of mid-span displacement of beam versus the total vertical load in the actuator for different levels of post-tensioning. This gives an indication of the stiffness of the frame. It can be seen that the benchmark test (PT = 0kN) has a linear stiffness, whereas the other tests with post-tensioning show a bi-linear stiffness behaviour. This bi-linear behaviour is due to the change in end conditions of the beam, changing from semi-rigid (before decompression) to almost pinned after decompression.

Stiffness values for the different tests are described in Table 6.3, where k_1 is the stiffness before decompression and k_2 is the stiffness after decompression.

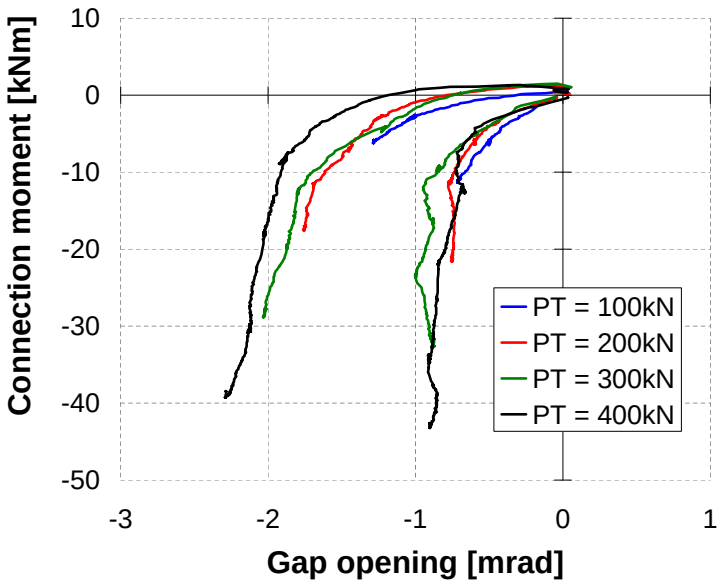

Figure 6.10: Gap opening (closing) during stressing of frame

Although the absolute value of the stiffness is not of much interest, the differences in stiffness are more useful. For tests with post-tensioning the initial stiffness is increased compared to the benchmark test. After decompression, with almost pinned connections, the stiffness of the beam is closer to the stiffness of the simply supported benchmark test. The stiffness of the benchmark beam can be calculated using the analytical expression for a simply supported beam, as given in Equation 6.1. The analytical stiffness of 2.44kN/mm is lower than the 2.74kN/mm found from experimental testing, even though real material properties (from Section 6.4) were used.

Table 6.3: Stiffness values for beam mid-span displacement of one-bay frame

F_{pt} (kN)	k_1 (kN/mm)	k_2 (kN/mm)
0	-	2.74
100	4.17	3.05
200	4.43	3.26
300	4.49	3.19
400	4.61	3.23

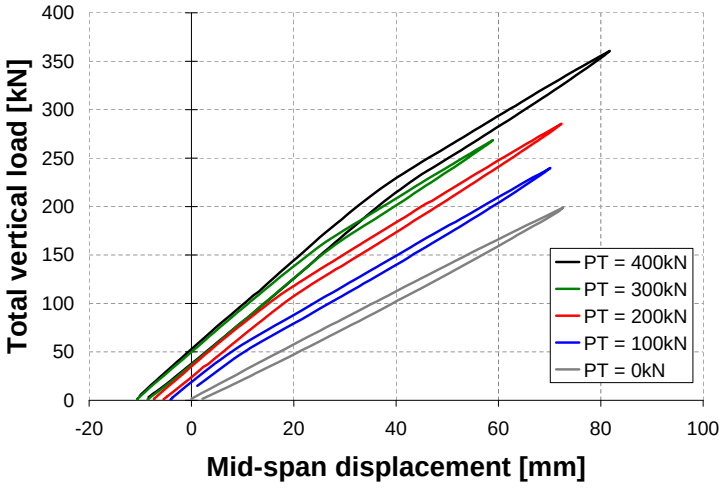

Figure 6.11: Graph of mid-span displacement versus total vertical load

$$k_{beam} = 2 \cdot \left(\frac{23}{648} \frac{L_b^3}{E_t I_x} + \frac{L_b}{3GA_s} \right)^{-1}$$
$$= 2 \cdot \left(\frac{23}{648} \frac{8494^3}{12000 \cdot 2.46 \cdot 10^9} + \frac{8494}{3 \cdot 663 \cdot 34233} \right)^{-1} = 2.44 kN/mm \quad (6.1)$$

Where:

- k_{beam} = Stiffness of beam mid-span $[N/mm]$;
- L_b = Length of beam between centre of supports $[mm]$;
- E_t = Modulus of elasticity of timber $[MPa]$;
- I_x = Major moment of inertia of beam $[mm^4]$;
- G = Shear modulus of timber $[MPa]$;
- A_s = Shear area of beam $[mm^2]$.

6.5.3 Post-tensioning forces

The post-tensioning force increased during testing due to beam deflection and due to gap opening of the connections. A table with post-tensioning forces at different stages, Table 6.4, shows that the initial post-tensioning force was within 2.5% of the design post-tensioning force. At decompression the post-tensioning

force was on average 10% higher compared to the initial post-tensioning force. Furthermore it can be seen that the lower post-tensioning force tests showed a very high percentage of increase in post-tensioning during testing, up to 65%. This was caused due to large amounts of gap opening. For tests with higher post-tenioning forces the maximum tendon elongation was 27%.

Table 6.4: Design, initial (i), decompression (dec) and maximum (max) post-tensioning forces during testing of the one-bay frame. Percentages show increases in post-tensioning force relative to initial post-tensioning force.

$F_{pt,design}$ (kN)	$F_{pt,i}$ (kN)		$F_{pt,dec}$ (kN)		$F_{pt,max}$ (kN)	
100	101	*1.0%*	108	*7%*	167	*65%*
200	199	*-0.5%*	221	*11%*	303	*52%*
300	296	*-1.3%*	325	*10%*	377	*27%*
400	390	*-2.5%*	432	*11%*	497	*27%*

A plot of post-tensioning force versus mid-span deflection for the four different tests is shown in Figure 6.12. It can be seen that from the outset of testing an increase in post-tensioning force was observed due to deviator deflections. After decompression, indicated by orange diamonds, an extra increase in force can be seen due to gap opening.

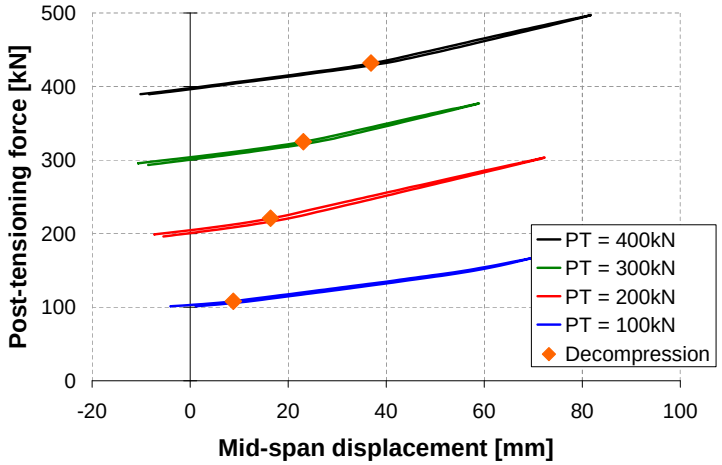

Figure 6.12: Post-tensioning force during experimental testing of one-bay frame

6.5.4 Bending moments

Bending moments in the structure were calculated by evaluating a free-body diagram as shown in Figure 6.13. Two different moments were calculated, bending moments at the centreline of the column (M_{cl}) and bending moments at the connection interface (M_{con}). An overview of the column centreline and connection bending moments during experimental testing for Test 3 is shown in Figure 6.14. Other tests showed very similar curves but obviously up to different bending moment levels.

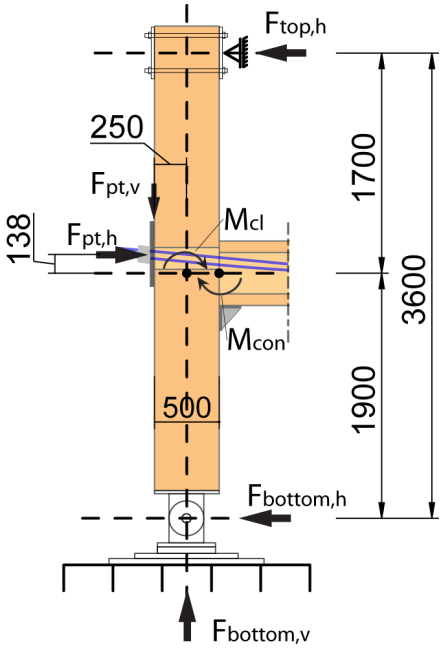

$$M_{cl} = F_{top,h} \cdot 1.7 - F_{bottom,h} \cdot 1.9 + F_{pt,h} \cdot 0.138 - F_{pt,v} \cdot 0.25$$

$$M_{con} = F_{top,h} \cdot 1.7 - F_{bottom,h} \cdot 1.9 + F_{bottom,v} \cdot 0.25 + F_{pt,h} \cdot 0.138 - F_{pt,v} \cdot 0.5$$

Figure 6.13: Free body diagram of column for evaluation of centreline and connection moment

Decompression moment is defined as the bending moment where bending stresses in the outer fibres equal compressive stresses due to post-tensioning, and thus result in zero stresses at the outer fibres. For a beam-column connection only supported at the top and bottom flanges, the so called partial contact connection, the resulting stress profiles are shown in Figure 6.15.

The compressive stresses (σ_c) are calculated by dividing the post-tensioning force at decompression ($F_{pt,dec}$) by the area of the supported flanges. At decompression, bending stresses (σ_{bend}) in the outer fibres equal the compressive stresses

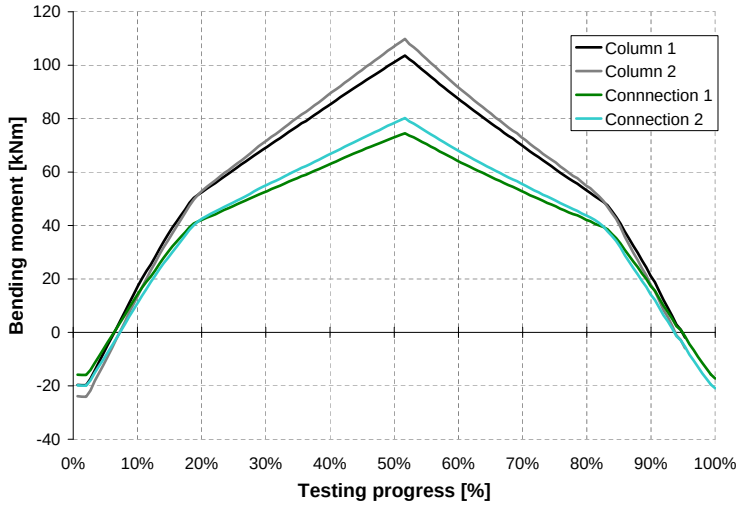

Figure 6.14: Column centreline and connection bending moments during testing of Test 3 (PT = 300kN)

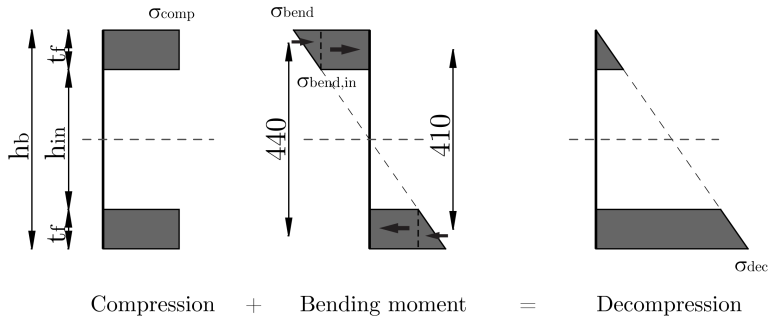

Figure 6.15: Compression and bending stresses at decompression for a partial contact beam-column connection

due to post-tensioning. The bending stresses on the inside of the flanges ($\sigma_{bend,in}$) can be found using geometric equations. The bending moment at decompression can be calculated by integrating the bending stresses over the area they are acting on. Following this procedure results in Equation 6.2 to calculate the decompression moment. Table 6.5 shows the values used for calculation of the decompression moment. The post-tensioning force at decompression is based on experimental test data.

$$M_{dec} = 0.5F_{pt,dec}\left(h_b - 2t_f + \frac{4t_f^2}{3h_b}\right) \tag{6.2}$$

Table 6.5: Calculation of decompression moment

F_{pt} (kN)	$F_{pt,dec}$ (kN)	σ_c (MPa)	M_{dec} (kNm)
100	108	2.1	18.4
200	221	4.3	37.7
300	325	6.3	55.5
400	432	8.3	73.8

6.5.5 Rotation components

Four different rotational components which have an influence on the connection response were identified in Chapter 8. These are, column rotation, joint panel shear deformation, interface compression and gap opening. Each of these four components were measured during experimental testing. An overview of experimental results is presented in the following sections. Tables with experimental values for each of the rotation components are presented in Appendix C.2.

A comparison of rotation components is shown in Figure 6.16a for a beam mid-span deflection of 30mm. This was reached under different load levels, as can be seen from Figure 6.11. The frame had two connections and thus two bars are shown for every level of post-tensioning. The figure shows that total rotation was approximately 10mrad. For the test without post-tensioning almost all rotation was due to gap opening. For increased levels of post-tensioning a lower amount of gap opening was measured and other rotational components increased. Although the frame was symmetric, rotation components were not identical for both connections. For column rotation this could have been due to different supports and for gap opening and interface compression this could have been due to tolerances during construction.

Figure 6.16b shows again the rotational components, but this time for a constant vertical load of 200kN. With higher post-tensioning forces a decrease in connection rotation, and thus a decrease in beam mid-span deflection is shown. For an increase in post-tensioning a decrease in gap opening and an increase in interface, joint panel and column rotations is shown. In the following sections the four rotational components are further analysed.

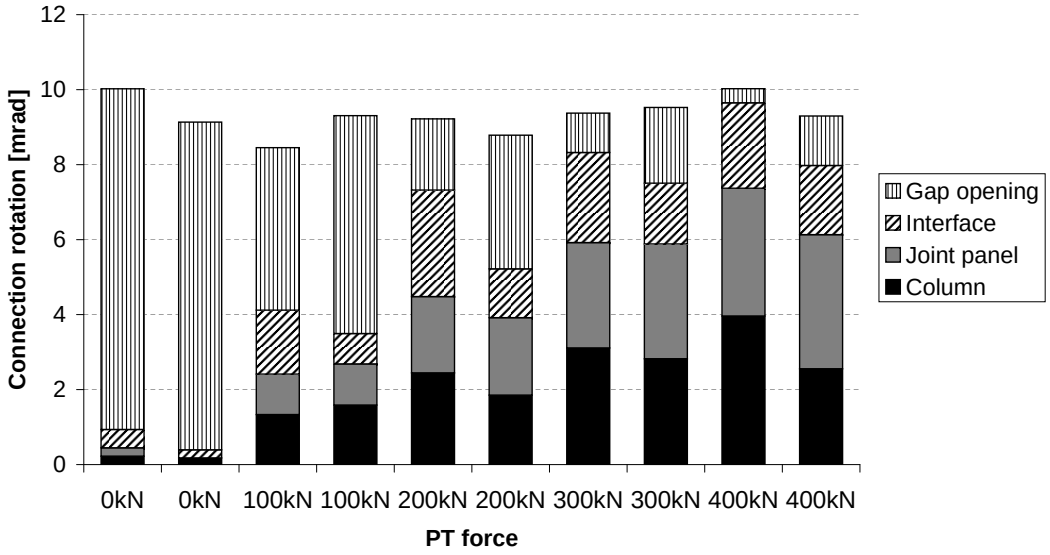

(a) At 30mm mid-span deflection

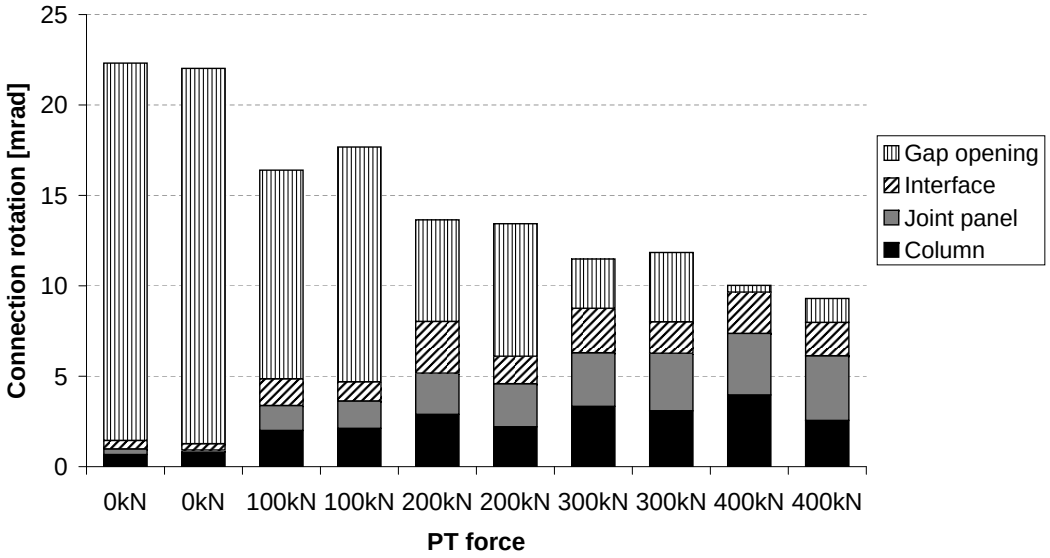

(b) At 200kN vertical load

Figure 6.16: Rotation components of external connections in one-bay frame (left Conn. 1 and right Conn. 2)

6.5.6 Column stiffness

Column rotations were measured using inclinometers fixed to points above and below the joint panel, in order to eliminate joint panel deformation in the measurements. The measurements did include rotations coming from displacements of the reaction frame. A plot of column centreline moment versus column rotation can be seen in Figure 6.17. The slope of the lines gives the rotational stiffness of the column. These stiffness values are presented in Table 6.6. Column 1 has an average stiffness of 35kN/mrad and column 2 of 42kNm/mrad. It should be noted that this stiffness also includes the stiffness of the reaction frame. As the reaction frame movement was not measured it is not possible to separate these contributions. For the test with 400kN post-tensioning it can be seem that there was a sudden jump in rotations at a column moment of about 100kNm. This was most likely caused by some slip in the reaction frame of the column.

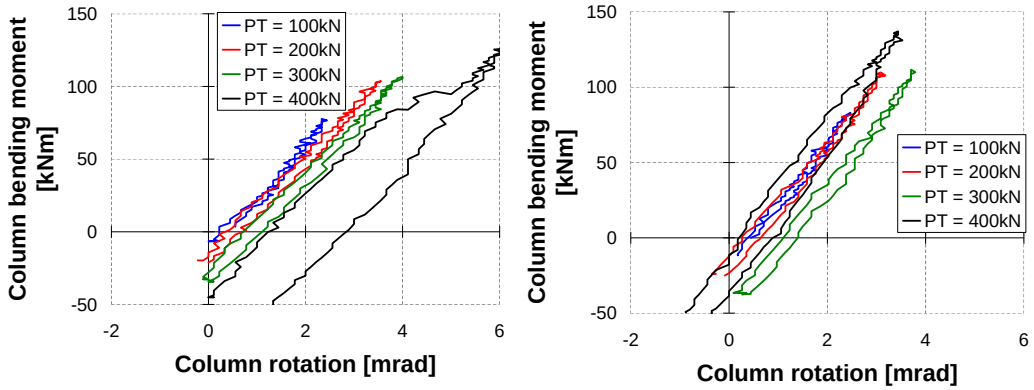

(a) Column 1 (b) Column 2

Figure 6.17: Column stiffness for columns of one-bay frame

An analytical expression for column stiffness is given by Equation 6.3, more information about the derivation of this equation can be found in Chapter 8. It can be seen that the analytical stiffness of 76kNm/mrad is about twice that of the experimental value. This means that rotation due to reaction frame movement was similar to rotation of the column. This equation requires material properties of the column, which have not been measured. Therefore specified values have been used. If the LVL had the same properties as the beams, $E = 12000MPa$ and $G = 663MPa$, column stiffness would have been 85kNm/mrad.

Table 6.6: Experimental measured column rotational stiffness

PT (kN)	$k_{col,1}$ (kNm/mrad)	$k_{col,2}$ (kNm/mrad)
100	37	41
200	34	39
300	35	42
400	35	45

$$k_{col} = \left(\frac{H}{12E_tI_{col}} + \frac{1}{\alpha GA_{col}}\right)^{-1}$$
$$= \left(\frac{3600}{12 \cdot 11000 \cdot 3.0 \cdot 10^9} + \frac{1}{0.86 \cdot 550 \cdot 144000}\right)^{-1} = 76kNm/mrad \quad (6.3)$$

Where:

- k_{col} = Stiffness of column (N/rad);
- H = Height of column (mm);
- E_t = Modulus of elasticity of timber (MPa);
- I_{col} = Major moment of inertia of column (mm^4);
- α = Factor to account for shear area (-);
- G = Shear modulus of timber (MPa);
- A_{col} = Area of column (mm^2).

6.5.7 Joint panel shear stiffness

Joint panel deformation was measured by two potentiometers placed diagonally over the middle of the connection (Figure 6.6a). They were shortened compared to the connection testing, in order to eliminate any interface compression deformation into the measurements. The analysis was done in the same way as for connection testing (Section 5.3.4). Results for both connections for four different levels of post-tensioning are shown in Figure 6.18. It can be seen that an increase in post-tensioning force resulted in a vertical offset (negative moment at zero rotation), but rotational stiffness (slope of lines) did not change. The horizontal lines in the figure indicate decompression moment. It can be seen that after

the decompression was reached the stiffness of the joint panel changed slightly. Therefore stiffness values were evaluated based on data until decompression. An average joint panel shear stiffness of 31kNm/mrad with a coefficient of variation of 11% was found.

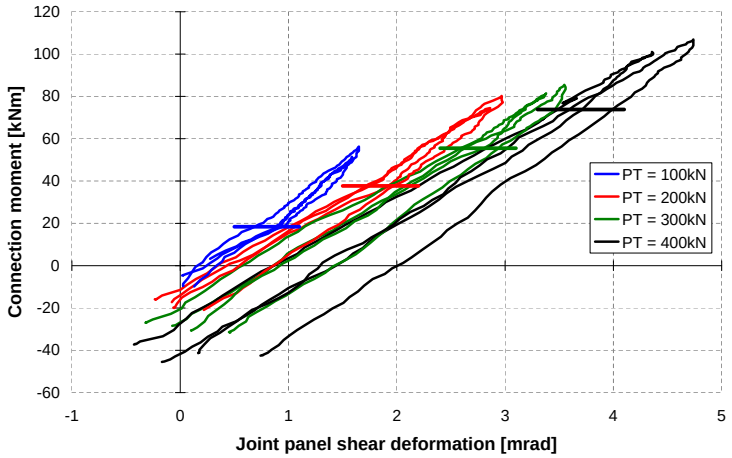

Figure 6.18: Joint panel deformation of one-bay frame, horizontal lines showing decompression moment

6.5.8 Interface compression stiffness

Interface compression was measured by two potentiometers fixed to the steel plate (between beam and column) and centreline of column. A graph of the interface compression versus connection moment can be seen in Figure 6.19. A clear linear behaviour can be seen until decompression. After decompression there was a significant increase in stiffness. The negative stiffness of the interface compression of Column 1 with a post-tensioning force of 100kN is unexplained. All data curve of Column 2 go through the origin of the graph, zero rotation at zero moment. For the data curves of Column 1 an offset is shown which occurs during stressing due to construction tolerances. All tests show very similar initial stiffness, showing that no permanent deformation occurred and that the interface remains linear elastic in behaviour. This shows that the screw reinforcement is working as the timber compressive capacity is exceeded for tests with 300kN and 400kN post-tensioning force.

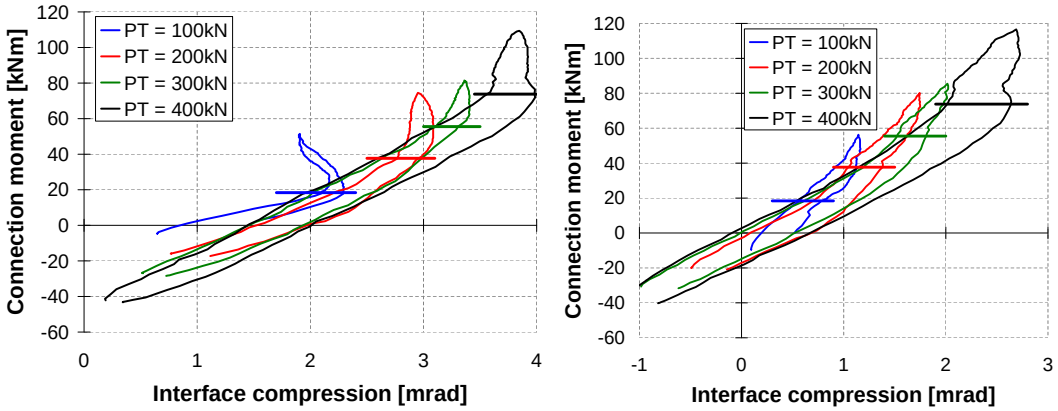

(a) Column 1 (b) Column 2

Figure 6.19: Interface compression stiffness of one-bay frame, horizontal lines showing decompression moment

The interface stiffness before decompression was evaluated for Column 1 ($k_{int,1}$) and Column 2 ($k_{int,2}$), as shown in Table 6.7. The average of the two columns (k_{int}) was also calculated. Except for the test with 100kN PT, the stiffness values were on average 31kNm/mrad with a coefficient of variation of 9%.

Table 6.7: Interface compression stiffness for one-bay frame

PT (kN)	$k_{int,1}$ (kNm/mrad)	$k_{int,2}$ (kNm/mrad)	k_{int} (kNm/mrad)
100	16	57	36
200	26	34	30
300	31	31	31
400	33	32	32

6.5.9 Gap opening

Moment rotation curves for gap opening of the two connections in the one-bay frame are shown in Figure 6.20. These curves show an almost infinite initial stiffness before decompression. The slope is mainly due to bending in the beam, as it was not practical to fix the pots all the way at the end of the beam. The orange

lines show the decompression moments as calculated in Section 6.5.4. It can be seen that the calculated decompression moments align very well with the points where gap opening starts. Around decompression there is a transition stage where the top of the beam starts to open up and the neutral axis at the connection shifts down. After decompression, the connection moment increases due to tendon elongation. The horizontal offset was due to tolerances in manufacturing and assembling, as explained in Section 6.5.1.

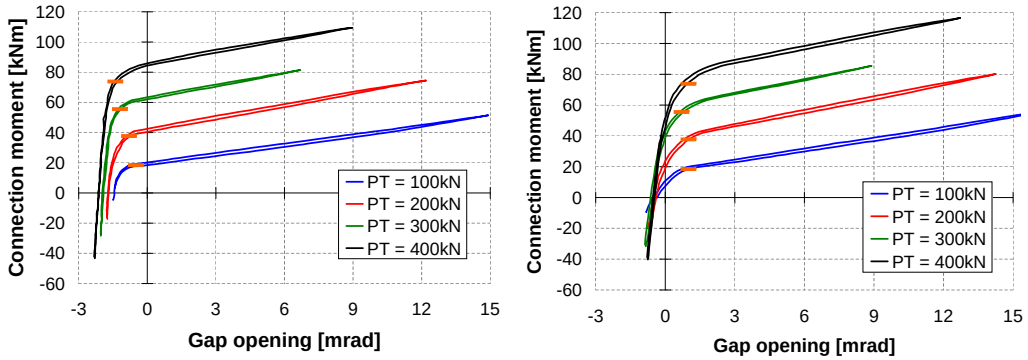

(a) Connection 1 (b) Connection 2

Figure 6.20: Gap opening of connections in one-bay frame, orange lines showing calculated decompression moments

For two tests, 2b and 3c, the beam was not only pulled down but also pushed up. This meant that decompression would be reached for a positive and negative connection moments, resulting in additional information about the connection behaviour. Figure 6.21 shows the gap opening for both connections (side 1 and 2) for the 100kN and 200kN post-tensioning tests. These tests were not performed with higher post-tensioning forces as the connection was not designed to resist large upwards shear forces.

From the figure it can be seen that decompression happened at the same connection moment for positive and negative rotations. The main difference was after decompression, under positive connection moments (gap opening at top) there was tendon elongation due to gap opening and beam deflections which resulted in an increase in connection moment. Whereas for negative connection moments (gap opening at bottom) no tendon elongation happened which resulted in a constant bending moment.

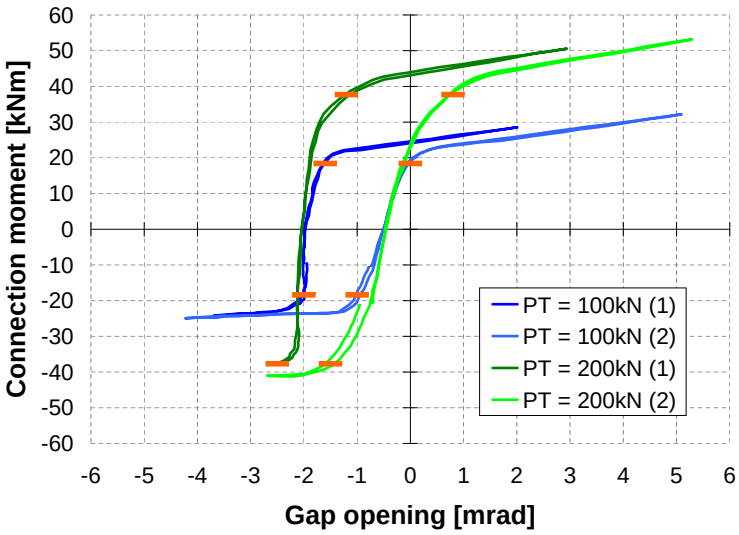

Figure 6.21: Gap opening during push-pull tests of one-bay frame, orange lines showing calculated decompression moments

6.5.10 Compression block

After gap opening connection moment can be calculated by multiplying the ultimate post-tensioning force by the distance from the centroid of the compression block to the centroid of beam. Four strain gauges were placed on both sides of the bottom flange in order to measure the shape of the compression stress block. For every test, strain profiles on the bottom flange were analysed at maximum load. Measuring strains in the compression zone was not very straight forward as it was only a point-wise measurement at the outermost fibres where the strain gauges were fixed. These outermost fibres were not always perfectly aligned with the steel plate and therefore they did not always show an accurate representation of strains in the compression zone. The best results of the strain gauges were for Connection 1 on the front side, which are shown in Figure 6.22. It can be seen that a linear approximation of the strain profile fits well with the testing data. The test with a post-tensioning force of 100kN showed zero strain in the top 30mm of the bottom flange. This meant that the compression block was not over the full depth of the bottom flange, but only over the lower 60mm.

The linear assumption of strains, and thus stresses, in the compression block means that the centroid of the compression block is at 1/3rd the height of

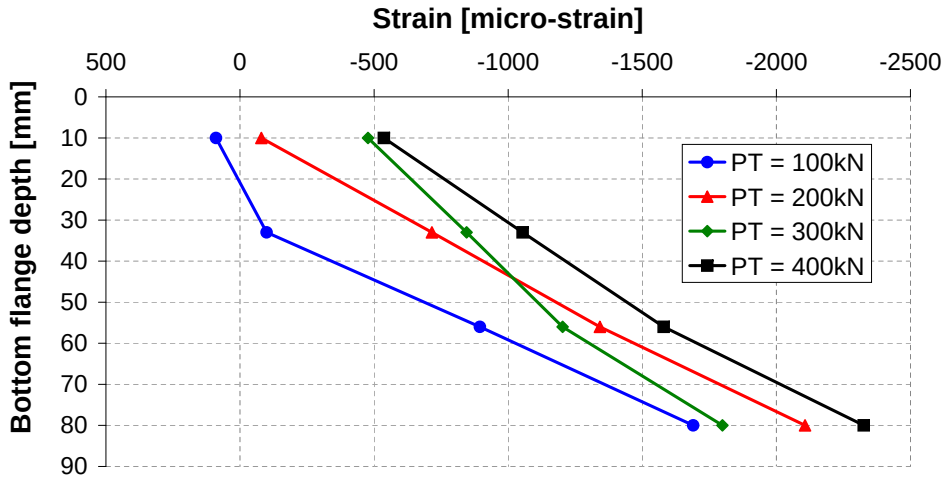

Figure 6.22: Strain profiles in the compression zone under maximum load

the flange (relative to the bottom of the beam). The maximum connection moment after decompression ($M_{con,max}$) can therefore be defined as in Equation 6.4. In Table 6.8 the maximum connection moment measured in experimental testing (M_{max}) is compared with the results of Equation 6.4. The maximum post-tensioning force is based on measured values during experimental testing. In the last column, the difference between the calculated connection moment and the average of both measured connection moments is shown. It can be seen that the predictions match very well with the measured values for higher post-tensioning forces, but are under predicting the connection moment for lower post-tensioning forces. One reason for this could be that the neutral axis depth is smaller than the full height of the bottom flange, resulting in a larger distance between the centroid of the compressive stress and the neutral axis of the beam. Another reason could be that the connection moment is not measured directly. It depends on several load measurements each with a small error. Therefore the relative error in measured connection moment will be larger for tests with a lower post-tensioning force, and hence the difference between predicted value and measured value will be larger for tests with lower post-tensioning.

$$M_{con,max} = F_{pt,max} \cdot \left(\frac{h_b}{2} - \frac{t_f}{3} \right) \tag{6.4}$$

Table 6.8: Comparison of maximum connection moment between experimental data and analytical formula

F_{pt}	$F_{pt,max}$	$M_{con,max}$	M_{max}			Difference
			Conn 1	Conn 2	Average	
(kN)	(kN)	(kNm)	(kNm)	(kNm)	(kNm)	(%)
100	167	37	51	56	54	-31%
200	303	67	75	80	78	-14%
300	377	83	81	85	83	0%
400	497	109	109	116	113	-3%

6.5.11 Digital Image Correlation

Digital Image Correlation (DIC) has been used to track displacements of centrelines of the frame during Test 3 with 200kN post-tensioning force. The grid can be seen in Figure 6.23a. Green crosses show the initial grid and red crosses show the grid under maximum load. Deflections of the beam can clearly be seen, but column rotations are too small to see. Therefore horizontal displacements have been multiplied by a factor of 50 and vertical displacements by a factor 15, as shown in Figure 6.23b. In this figure green diamonds are again the initial grid and red diamonds are the displaced grid under maximum load. Not only beam deflections, but also column bending and column rotation due to reaction frame movement can be seen. Some markers did not track properly and with the magnified displacements these markers show up in incorrect locations. Also under this maginfication is can be seen that the displaced gird is not symmetrical, which is caused by small movements in the reaction frame.

The connection behaviour has been analysed for Test 5, as the higher post-tensioning force results in more column rotation, joint panel shear deformation and interface compression. Accuracy of DIC depends strongly on the area of measurement and the number of pixels in the camera sensor. For analysis of connection behaviour, the images captured an area of about 1m by 0.8m. The camera had an 18 Mega-pixel sensor, with 5148 by 3456 pixels. This gave a scaling factor of approximately 0.2mm per pixel. Detailed measurements resulted in a scaling factor of 0.197mm/pixel. The Matlab software was capable of achieving a sub-pixel accuracy, resulting in an accuracy in the range of 0.02mm to 0.1mm.

(a) Grid on one-bay frame

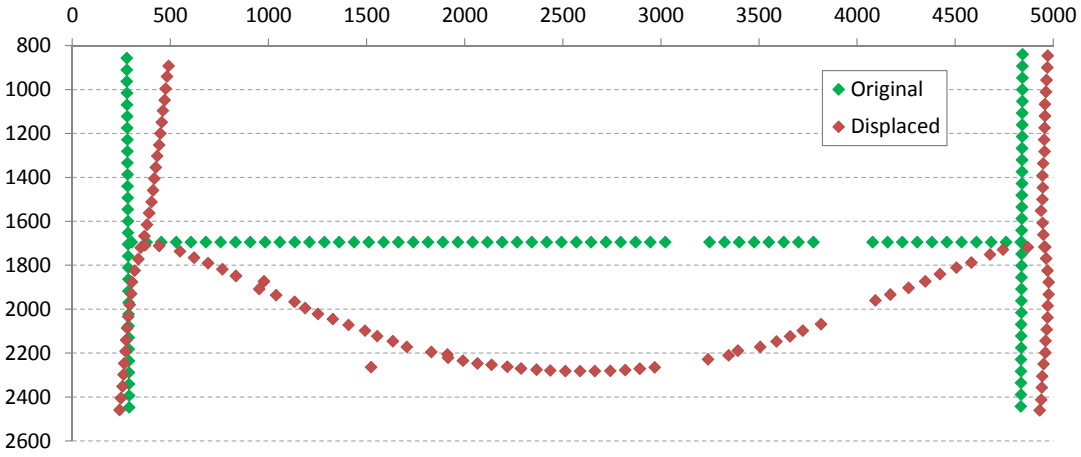

(b) Original and displaced grid of one-bay frame, horizontal displacements magnified by factor 50 and vertical displacements by factor 15

Figure 6.23: DIC measurements of frame displacements. Green is initial grid, red is displaced grid under maximum load

Potentiometers used for testing had an accuracy of 0.02mm. This shows that DIC technique achieved a level of accuracy close to potentiometers and it added the capability to track displacements of many points. Another benefit is not having instruments in contact with a specimen, which can be useful for testing until failure which can damage instrumentation.

Column rotations Column rotations, including rotations due to reaction frame movement, have been measured using a line of markers along the centreline of the column, as shown in Figure 6.24a. The central section of these markers is influenced by joint panel deformation, but the markers at either end of the line can be used to calculate column rotation. The rotation values are plotted in Figure 6.24b where it can be seen that they are very well matching the measured values using the inclinometer. Inclinometer data had an accuracy of 0.11mrad per step, which resulted in a jagged data curve. The data curve from DIC showed a smoother curve indicating a higher accuracy compared to inclinometer data. Also initial negative column rotation due to post-tensioning was picked up by DIC measurements and not by inclinometer data.

Joint panel deformation Joint panel deformation was measured using a grid of 15 by 15 markers over the centre section of the joint panel as shown in Figure 6.24c. From displacements of this grid horizontal and vertical shear was calculated. These two shears were converted to rigid body rotation and joint panel shear in a similar way as described in Section 3.5. The resulting joint panel shear is plotted against the column centreline moment in Figure 6.24d. It can be seen that the measurements differ slightly from measurements using potentiometers. The joint panel stiffness found using potentiometers was 38kNm/mrad and the stiffness from DIC was 42kNm/mrad, resulting in a difference of 10%.

Interface compression Interface compression could be made visible by tracking a line of markers close to the edge of the column. The results are shown in Figure 6.26. On the vertical axis the distance from the centroid of the beam is shown and on the horizontal axis the displacement in mm. Grey marked areas indicate the compression zones where steel plates between beam and column were positioned. Initially there was zero displacement as shown by the blue

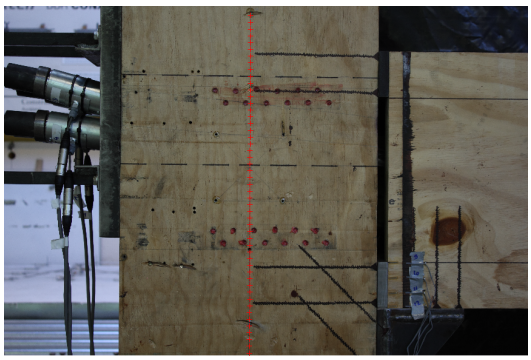

(a) Grid used for measuring of column rotations

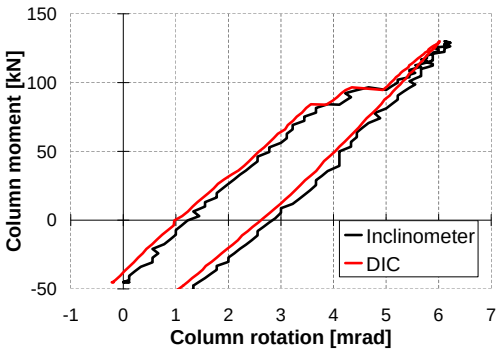

(b) Comparison between column rotations measured using inclinometers and DIC

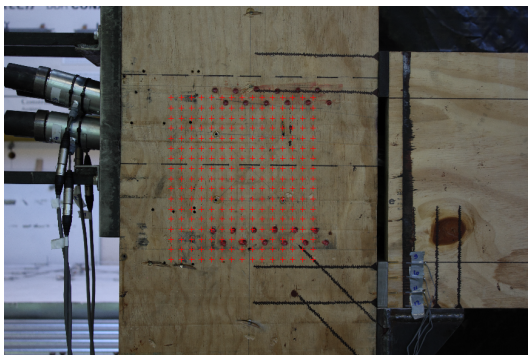

(c) Grid used for measuring of joint panel rotations

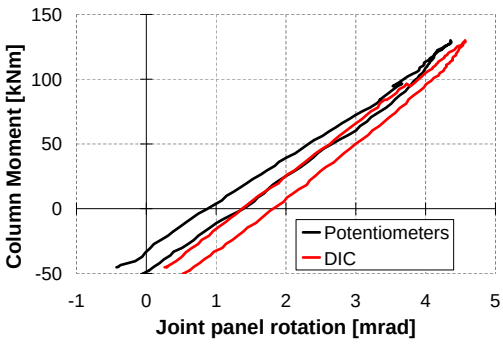

(d) Comparison between joint panel rotations measured using potentiometers and DIC

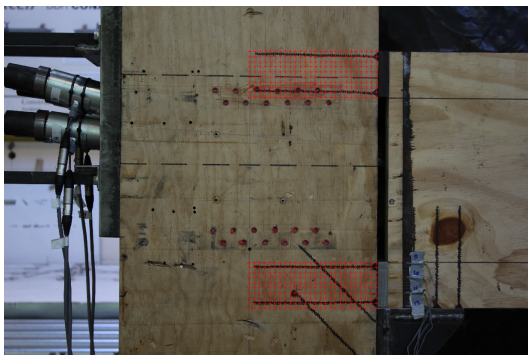

(e) Grid used for measuring of interface rotations

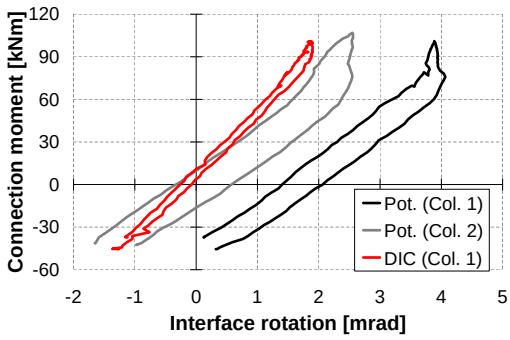

(f) Comparison between interface rotations measured using potentiometers (Pot.) and DIC

Figure 6.24: DIC measurement of connection deformation components

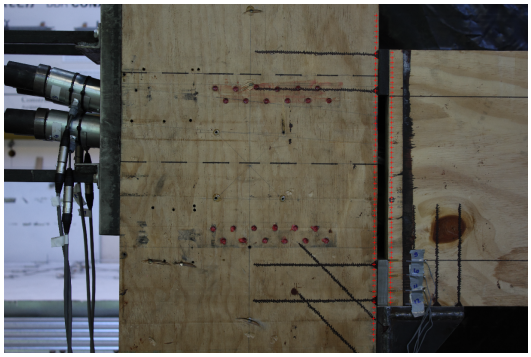

(a) Grid used for measuring of gap opening

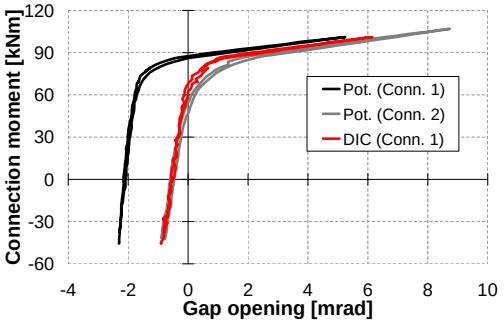

(b) Comparison between gap opening measured using potentiometers and DIC

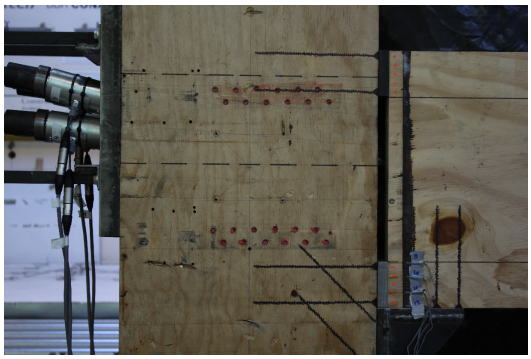

(c) Grid used for measuring of beam rotation

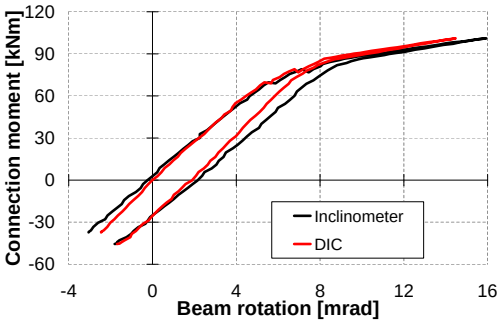

(d) Comparison between beam rotation measured using inclinometers and DIC

Figure 6.25: DIC measurement of connection deformation components (continued)

line. After stressing the whole column moved to the right, due to shortening of the frame, and rotated upwards as can be seen by the slope between the top and bottom marker. As there was a negative moment, interface compression can be seen at the top where most of the post-tensioning force was transferred. At zero connection moment some interface compression can be seen at top and bottom compression zones, and very little rotation in the column is shown. At decompression and under maximum load all interface deformation was located at the bottom compression zone.

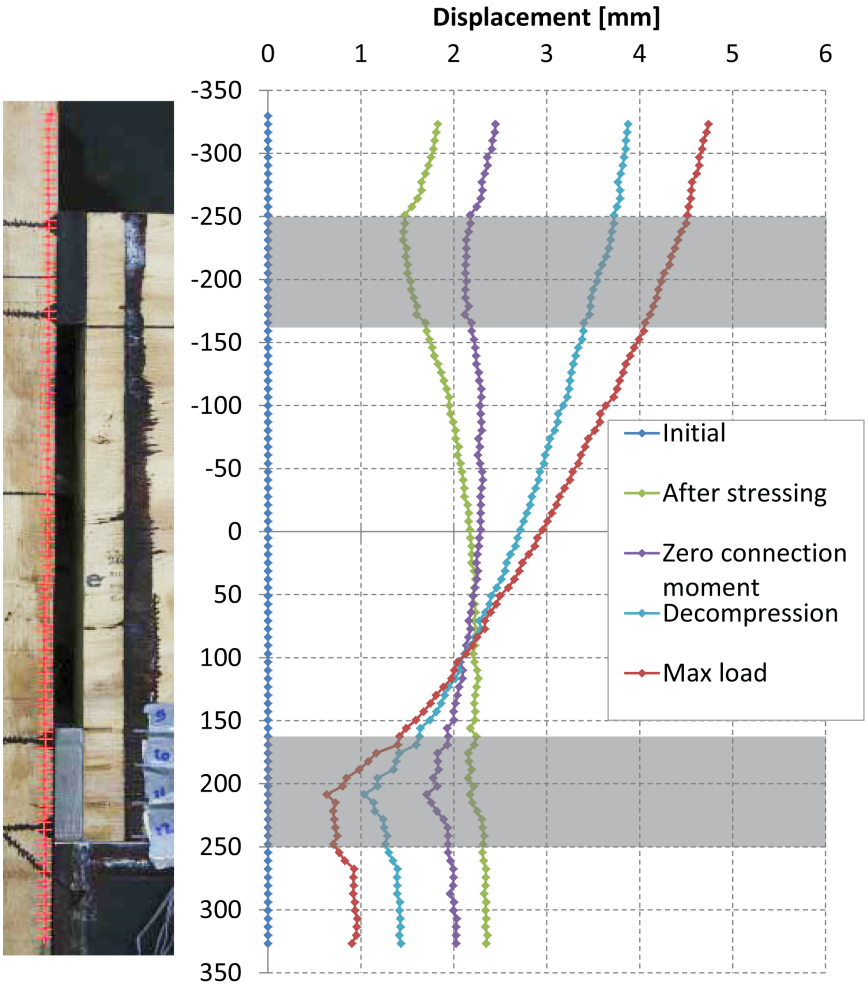

Figure 6.26: Column interface displacement at different stages of testing

Interface compression rotation was analysed using a grid of markers in the two compression zones of the column, as shown in Figure 6.24e. The displacement

of markers along the centreline of the column in the compression zone were averaged and subtracted from the averaged displacement of the markers close to the interface. This was done for top and bottom compression zones. The resulting displacement was divided by the distance between the centres of the compression zones, resulting in interface rotation. The interface rotation is plotted in Figure 6.24f where it is compared with measurements from potentiometers. The measurements using DIC show a 22% higher stiffness, 44kNm/mrad, compared to measurements from potentiometers, 36kNm/mrad. This difference is partly caused by the fact that the outer timber fibres, which deform the most, are not included in the DIC measurements as markers cannot be on the edge in order to track them properly. Furthermore the DIC data passes through the origin of the graph, which would be expected as top and bottom compression zone are equally stressed at zero moment. The potentiometer data for Column 1 has a clear offset which is most likely caused due to tolerances in the test setup which resulted in movement during stressing. Potentiometer data for Column 2 passes through the origin, similar to DIC data for Column 1.

Gap opening The last deformation component, gap opening, was measured using a line of markers close to the edge of beam and edge of column, Figure 6.25a. The difference in displacement of beam and column interface was calculated and rotations due to gap opening were calculated. Gap rotation versus connection moment was plotted in Figure 6.25b. From this it can be seen that the shape of the curve measured using potentiometers matches very closely with the curve measured using DIC. The main difference is an offset of approximately 2mrad in the measurement of potentiometers for Connection 1. This was most likely caused by some initial movement in the instrumentation, as this rotation was not measured using DIC.

A graphical representation from gap opening can be seen in Figure 6.27. Displacements, multiplied by a factor of 3, of column edge and beam edge have been plotted for four different stages of testing. Initially (grey lines) both column and beam interface markers are vertically aligned and spaced about 12mm apart, which is 10mm of steel plate and about 1mm on each side of the edge. After stressing (black lines) there is some frame shortening, resulting in a constant displacement of the beam and column, and the negative connection moment

results in negative rotations of column and beam. Also interface compression of the column at the top level of the beam can be seen. Until decompression (green lines) the rotation (slope of lines) of beam and column interface is equal. Under maximum load (red lines) it can be seen that the beam rotated more than the column interface, which shows occurrence of gap opening. Also visible is a linear displacement profile of the beam, in the bottom compression zone this is closely followed by column rotation. This indicates that the steel plate at the interface rotates with the beam and compresses into the column interface.

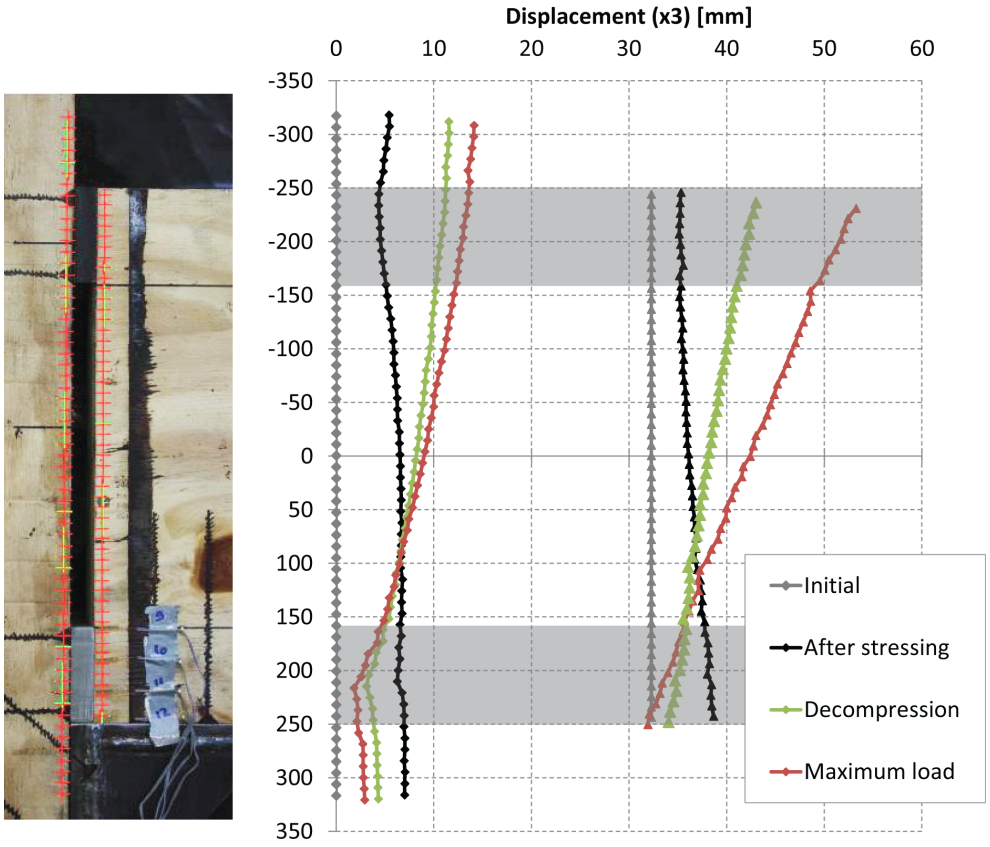

Figure 6.27: DIC measurements of gap opening at different stages of testing, left lines showing the column interface and right lines the end of the beam

Beam rotation Beam rotation was also measured using DIC. A line of markers was placed at top and bottom flanges, as shown in Figure 6.25c. Using the average displacement of top and bottom flanges the rotation was calculated. A

comparison between beam rotation measured using DIC and inclinometers is shown in Figure 6.25d. It can be seen that DIC measurements resulted in less rotation than the inclinometer data.

Total rotations A comparison of the four deformation components using DIC and potentiometers is shown in Figure 6.28. Column rotation is very similar for both measurements, although the curve of DIC is smoother than the curve from inclinometer data. More joint panel shear deformation is measured by DIC, but rotation during stressing shows some discrepancy, positive rotation from DIC measurements and negative rotation from potentiometers. Although they are different, their magnitude is very small. Interface compression and gap opening show significant different rotation from the start onwards. This is most likely caused by movement of the steel plate on the connection interface where the potentiometers were fixed to. This initial movement has been corrected for in the dashed curves.

All four deformation components, column, joint panel, interface and gap opening should add up to the total beam rotation. The beam rotation was measured using inclinometers and also using DIC. The summation of the individual deformation components and directly measured beam rotation is shown in Figure 6.29. The horizontal axis shows three different stages of testing, namely stressing of the frame, loading up to maximum design load and unloading. DIC measurements (red lines) show on average 10-15% less rotation than measurements using potentiometers and inclinometers (black lines), this can be caused by deformation close to the edge of beam and column, where grid markers could not be placed. Furthermore, it can be seen that the sum of deformation components (dashed lines) for both measurement methods is higher than directly measured beam rotation (continuous lines). Under maximum load the sum was 26% more than the direct measurement. This could be caused by deformation components which influence each other, e.g. interface compression influencing joint panel measurements. Further research could focus on evaluating this in more detail using DIC. The grey dashed line shows the original measured potentiometer data, but this was corrected for the initial offset of interface compression and gap opening as shown in Figures 6.24f and 6.25b. Overall a good correspondence is found between DIC measurements and potentiometer data, suggesting that all

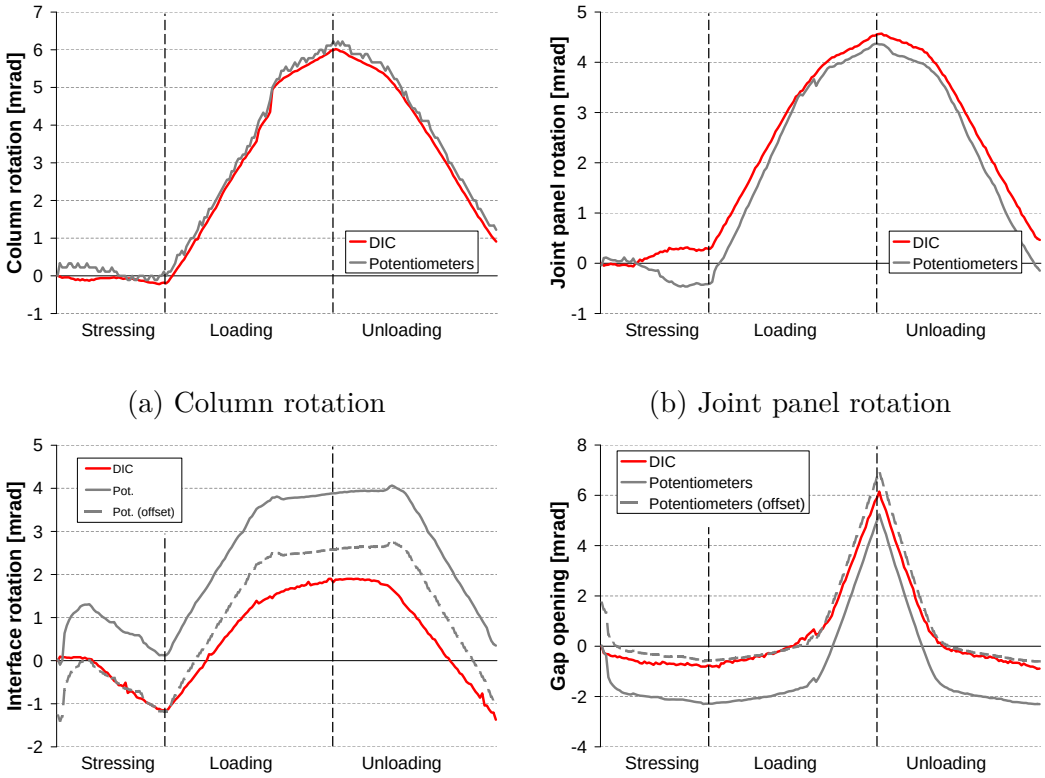

(a) Column rotation

(b) Joint panel rotation

(c) Interface compression rotation

(d) Gap opening rotation

Figure 6.28: Comparison of connection deformation components between DIC and potentiometers

deformation components were measured correctly.

6.5.12 Summary

Experimental testing of a one-bay post-tensioned timber gravity frame with draped tendons has given valuable insight on the behaviour of these types of frames. Testing was performed at four levels of post-tensioning. Deformation components in the connection were evaluated using potentiometers and inclinometers and also using DIC technique. These results will be compared with analytical models in Chapter 8. It has been shown that the decompression and ultimate bending moment capacity of the connections can be accurately predicted using the formulas presented in this section. It has also been shown that the connection behaviour is almost symmetric, even though the tendon is not placed in the centre of

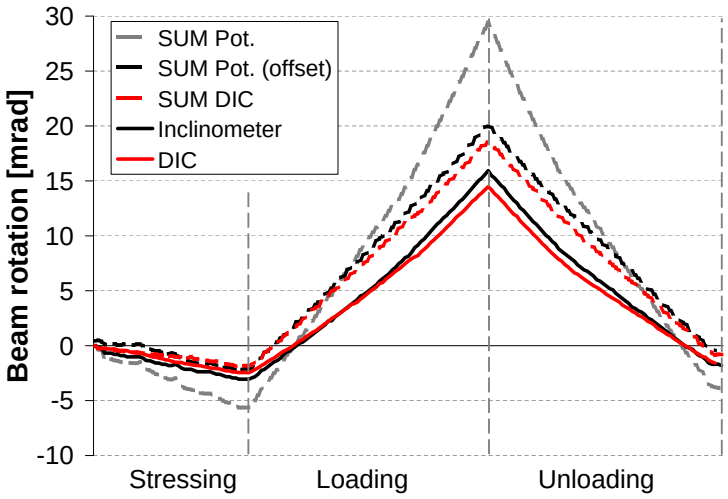

Figure 6.29: Comparison of summation of individual deformation components and directly measured beam rotation using DIC and potentiometer data

the beam. Finally it was shown that the stress block in the compression zone after decompression is linear. Validation of measurements using DIC technique showed that all four deformation components were measured accurately, but that summation of these four components resulted in overestimation of beam rotation when compared with direct measurements.

6.6 Test results of the two-bay frame

In this section the results of experimental testing the two-bay post-tensioned timber frame, Figure 6.30, are presented. Data presented in this section is very similar to results of the one-bay testing, therefore not all procedures are repeated here.

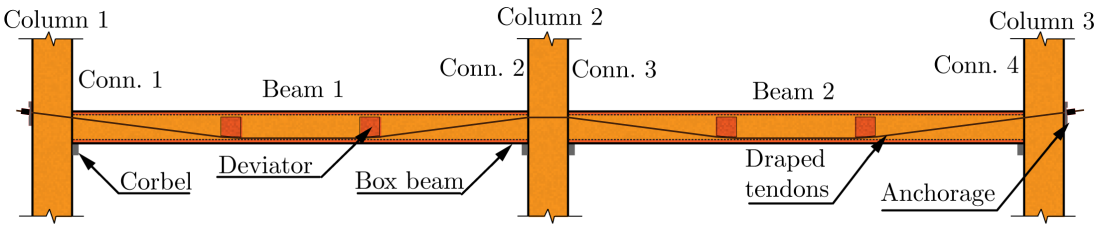

Figure 6.30: Overview and nomenclature of two-bay frame test setup

6.6.1 Stressing of frame

Stressing of the frame induced precambers in both beams, as shown in Figure 6.31. The maximum precamber was 5.7mm, 7.7mm and 10.9mm with 100, 200 and 300kN post-tensioning force, respectively. It can be seen that both beams have a very similar behaviour, although for small forces some differences are seen. The curves are not smooth as measuring was stopped when changing the post-tensioning jack from one tendon to the next. The sudden jump during stressing to 100kN was caused by the hydraulic rams keeping the beam in place and they were released during stressing, causing the beam to lift up. Also shown in the figure by the grey lines is the post-tensioning force during initial stages of testing.

During the initial stages of stressing small gaps between beam and column, due to construction tolerances, were closed. As instrumentation was set to zero before stressing this showed up in the measurements. Examples of this are shown in Figure 6.32 where gap opening and interface compression rotation are shown during stressing up to 300kN. For interface compression rotation of Connections 1, 3 and 4 a clear jump can be seen at the start of stressing. After that a very linear behaviour, towards negative (creating upwards deflections of the beam)

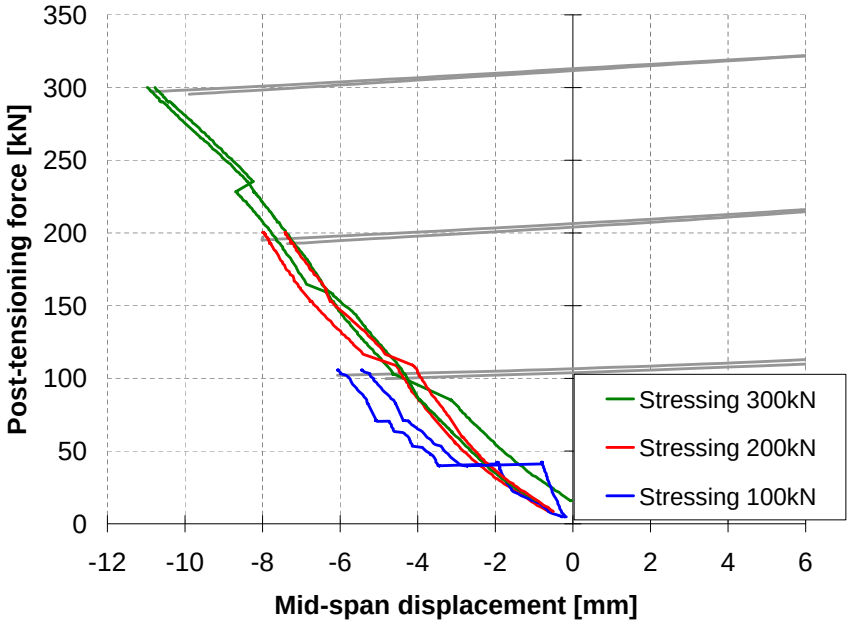

Figure 6.31: Precamber created during stressing of two-bay frame, negative displacements indicating uplift and grey lines show data recorded during testing

rotations, is shown. For gap opening a clear jump can be seen for Connections 3 and 4, after which a small negative rotation was measured.

6.6.2 Beam deflections

Figure 6.33 shows mid-span beam deflections versus the vertical load on the beams. Stiffness values for mid-span deflections are shown in Table 6.9, where k_1 is stiffness before decompression and k_2 is stiffness after decompression. Both beams have a very similar stiffness and increase in stiffness as a result of the changed connection behaviour due to post-tensioning is clearly visible.

6.6.3 Post-tensioning forces

The post-tensioning force during testing is shown in Figure 6.34. Similar to the one-bay frame, a direct increase in post-tensioning force after the start of testing was measured. Also shown are the internal (diamonds) and external (triangles) decompression points, which are further explained in Section 6.6.4.

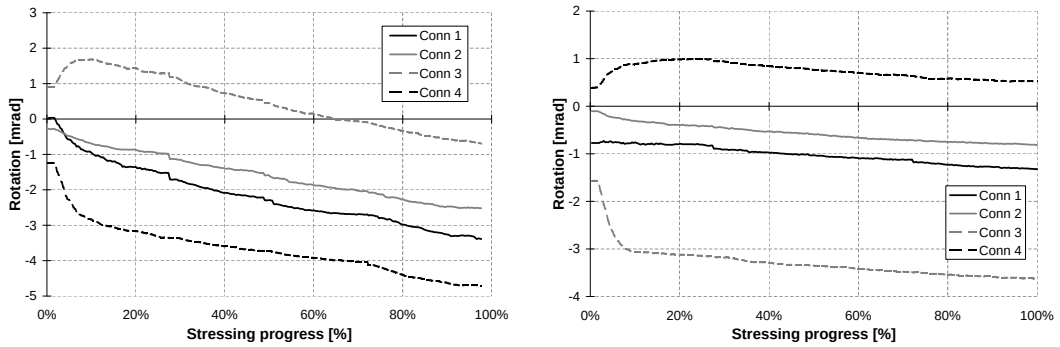

(a) Interface compression rotation (b) Gap opening

Figure 6.32: Rotation components during stressing of two-bay frame up to 300kN post-tensioning force

Table 6.9: Stiffness values for beam mid-span displacement of two-bay frame

F_{pt}	k_1		k_2	
	Beam 1	Beam 2	Beam 1	Beam 2
(kN)	(kN/mm)	(kN/mm)	(kN/mm)	(kN/mm)
0	-	-	3.13	3.15
100	5.30	5.38	3.79	3.76
200	5.72	5.63	4.25	4.22
300	5.80	5.60	4.29	4.36

Table 6.10 shows the post-tensioning force at different stages of testing. The first column shows the design post-tensioning force and the second column shows the initial post-tensioning force which was achieved after stressing. It can be seen that this was within 3% of the design value. The next two columns show the post-tensioning force at decompression of internal and external connections. This is different as no column rotation and joint panel deformation happens at Column 2 resulting in stiffer connections. Tendon force increased on average 11% for decompression of internal connections and 24% for external connections. The last column shows the maximum post-tensioning force achieved during testing. The maximum increase in post-tensioning force was very similar to values reached during testing of the one-bay frame.

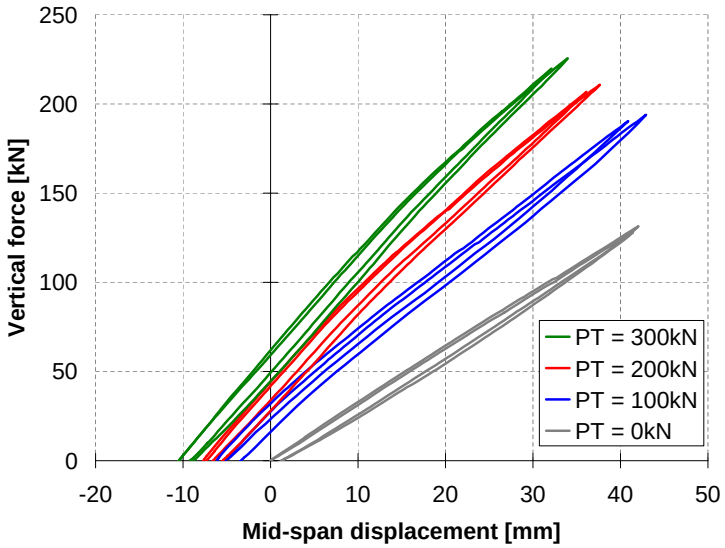

Figure 6.33: Graph of mid-span displacement versus vertical load for two-bay frame

Table 6.10: Design, initial (i), decompression (dec) and maximum (max) post-tensioning forces during testing of two-bay frame. Percentages show increase of post-tensioning force relative to initial post-tensioning force.

$F_{pt,design}$ (kN)	$F_{pt,i}$ (kN)		$F_{pt,dec,int}$ (kN)		$F_{pt,dec,ext}$ (kN)		F_{max} (kN)	
100	102	*2%*	110	*8%*	121	*19%*	168	*65%*
200	195	*-3%*	220	*13%*	254	*30%*	284	*46%*
300	297	*-1%*	336	*13%*	369	*24%*	372	*25%*

6.6.4 Bending moments

Mid-span bending moments were evaluated using measurements from strain gauges. The modulus of elasticity which was calibrated for the strain gauges (Table 6.2) was used. The bending moments were plotted against vertical load on the beam (force in actuator), as shown in Figure 6.35. From this figure it can be seen that post-tensioned beams all start with a negative (upwards) bending moment. For a given bending moment in the beam, e.g. 60kNm, the vertical load on a beam without post-tensioning is 77kN whereas for the post-tensioned beams the vertical load is increased to 127, 160 and 190kN for the 100, 200 and

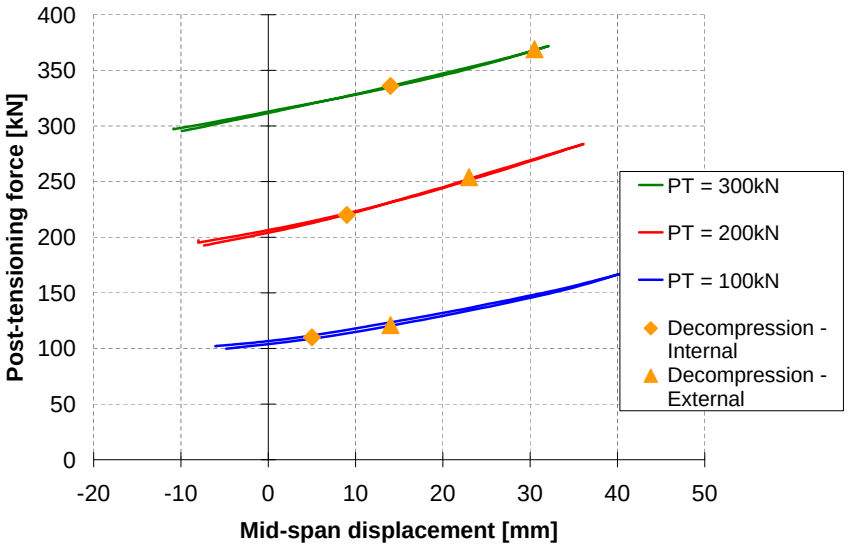

Figure 6.34: Post-tensioning force during testing of two-bay frame. Diamonds indicate decompression of internal connections and triangles indicate decompression of external connections.

300kN post-tensioning, respectively. This illustrates the increase in load-carrying capacity of a post-tensioned timber frame.

Calculation of connection moments for the two-bay frame was complicated. For the one-bay frame, vertical support reactions of the two columns could be assumed similar due to symmetry of the test setup. For the two-bay frame the three vertical support reactions are unknown. Due to differences in connection stiffness, namely internal connections being stiffer than external connections, the centre column (Column 2) resisted a higher percentage of the vertical load compared to the outer columns (Columns 1 and 3). Furthermore, after gap opening the stiffness changed and the vertical force distribution also changed. Three assumptions were tested for vertical force distribution, 50% to external and 50% to internal columns, 45% to external and 55% to internal columns, and 40% to external and 60% to internal columns. The resulting connection moments are shown in Figure 6.36. From this figure it can be seen that the external connection moments (continuous lines) did not change much, whereas the internal connection moments were very sensitive to changes in force distribution. Therefore it was not possible to accurately calculate the internal connection moment. Strain gauges

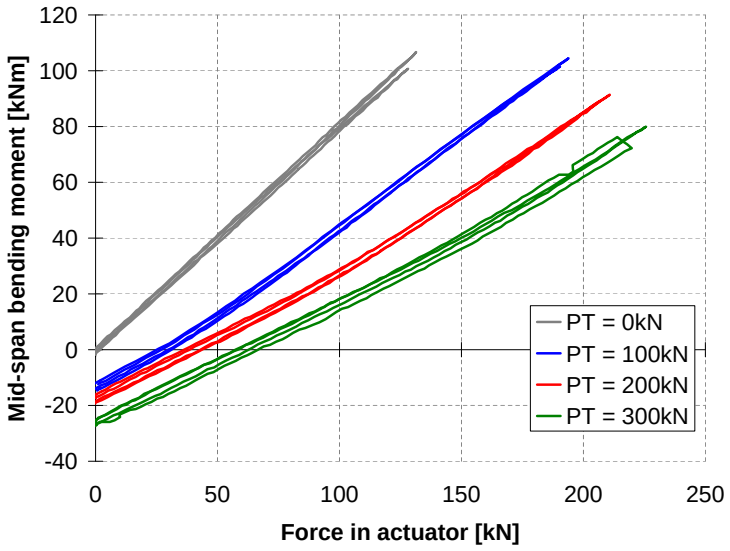

Figure 6.35: Mid-span bending moments versus vertical load applied to the beams of the two-bay frame

were placed close to the connection interface, but strain profiles were not linear after decompression, therefore these measurements could not be used to calculate connection moments.

Decompression moment can be calculated using Equation 6.2, as presented in the one-bay frame testing results, using a beam height of 360mm and a flange thickness of 45mm. The resulting decompression moments are presented in Table 6.11. Decompression for internal and external connections happened at different stages during testing, as can be seen in Figure 6.37 for Test 3 with 200kN post-tensioning. Internal connections (in blue) opened around 20% of the testing sequence and closed again around 80% of testing sequence, whereas external connections (in black) opened around 40% and closed around 60% of testing sequence. This resulted in two different decompression moments, due to different values of post-tensioning, as shown in Figure 6.34.

6.6.5 Rotation components

Four different rotational components which have an influence on the connection response were identified in Chapter 8. These are, column rotation, joint panel shear deformation, interface compression and gap opening. Each of these four

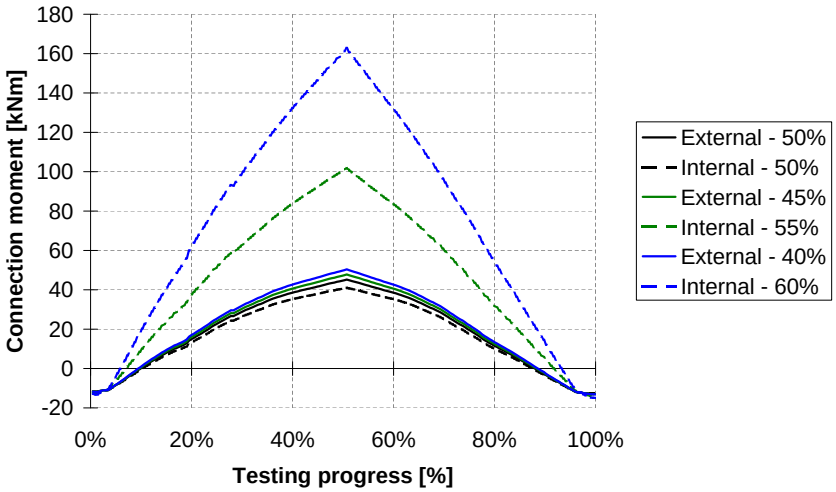

Figure 6.36: Connection moments for different distributions of forces to internal and external columns

Table 6.11: Internal and external decompression moments for different levels of post-tensioning

F_{pt} (kN)	$F_{pt,dec,int}$ (kN)	$M_{dec,int}$ (kNm)	$F_{pt,dec,ext}$ (kN)	$M_{dec,ext}$ (kNm)
100	110	15	121	17
200	220	31	254	35
300	336	47	369	51

components was measured during experimental testing. Numerical values for the rotation components are presented in Appendix C.2. In the following sections the four rotational components are further analysed.

A comparison of rotation components is shown in Figure 6.38a for a beam mid-span deflection of 20mm. This was reached under different load levels, as can be seen from Figure 6.33. The figure is split in external and internal connections for different levels of post-tensioning. The data presented is of Connections 1 and 2, Connections 3 and 4 showed very similar values. Without post-tensioning almost all rotation at the end of the beam was due to gap opening, as was expected for a pinned connection. With an increase in post-tensioning a decrease in gap opening was seen. For external connections no gap opening was measured for tests with 200

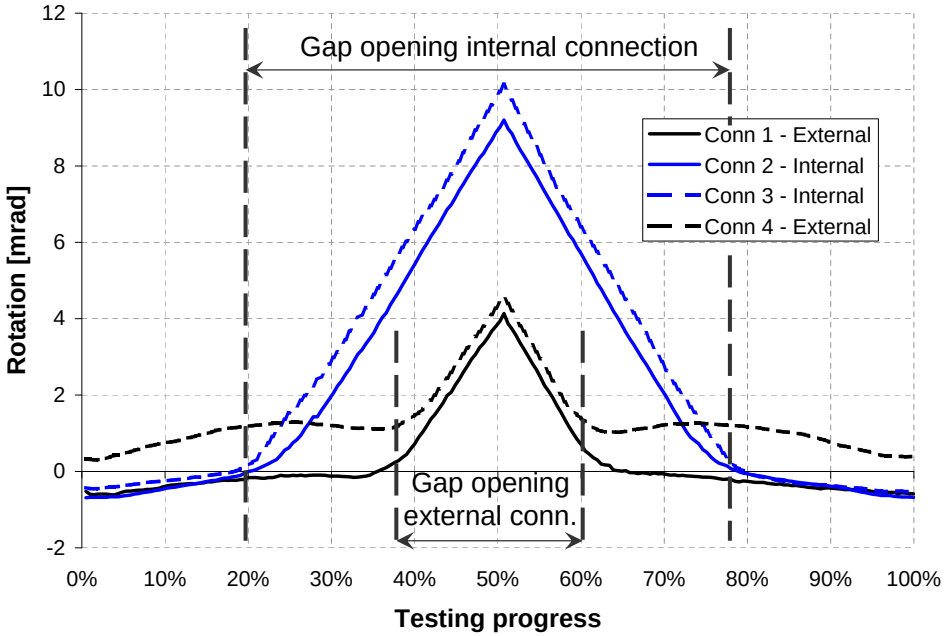

Figure 6.37: Comparison of gap opening for internal and external connections during testing for Test 3, PT = 200kN

and 300kN post-tensioning force, whereas for internal connections there was still gap opening. For internal connections the contribution of column rotation and joint panel deformation was negligible, whereas for external connections a clear contribution of these two components was visible. Internal connections showed lower total rotations compared to external connections. Some negative column rotation was measured for the internal column during testing. Theoretically this column should not show any rotations but due to imperfections in the test setup some rotation occurred.

Another comparison is shown in Figure 6.38b for a vertical load of 130kN applied to the beam. The load was reached at different amounts of beam deflection, as post-tensioning reduced deflections. These reduced deflections resulted in reduced rotations at the end of the beams, which is clearly visible in Figure 6.38b. Testing without post-tensioning force showed almost only gap opening, up to 18mrad. Tests with post-tensioning showed increased column, joint panel and interface rotations.

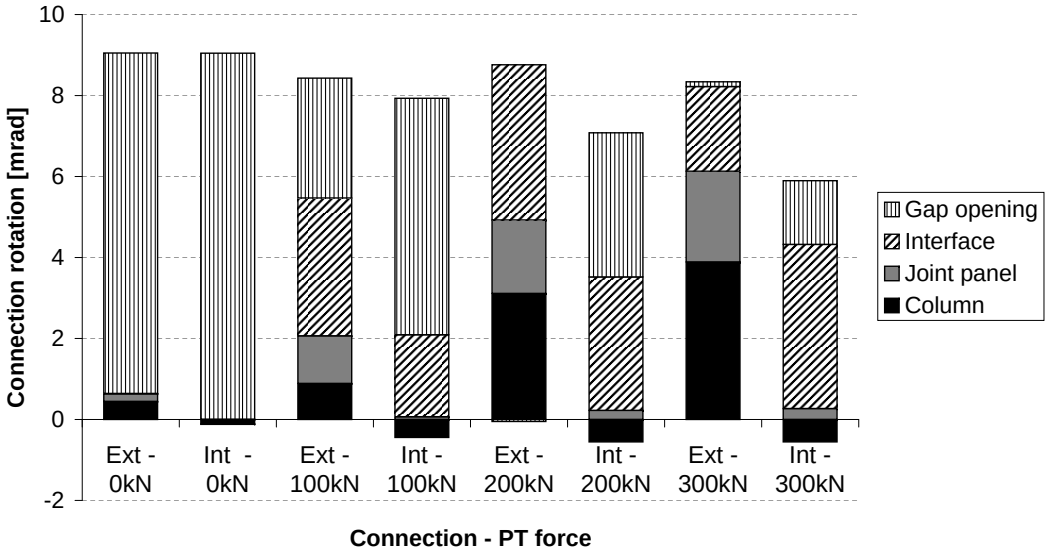

(a) At 20mm mid-span deflection

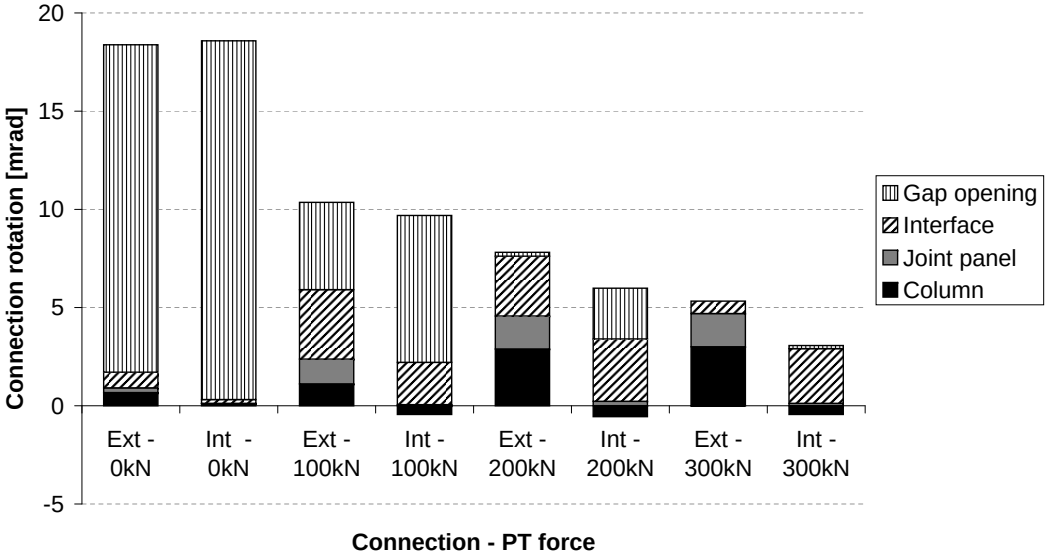

(b) At 130kN vertical load

Figure 6.38: Rotation components of external (Ext, connection 1) and internal (Int, connection 2) connections in two-bay frame

6.6.6 Column stiffness

Column bending moments were calculated based on forces at top and bottom, measured with load-cells and post-tensioning force (for external columns only). This procedure is shown in Figure 6.13. Column and reaction frame rotation was measured directly using inclinometers. Moment-rotation plots for symmetric loading tests and asymmetric loading tests are shown in Figure 6.39. The solid lines are for external Column 1, thin lines are for internal Column 2 and dashed lines are for external Column 3. For symmetric loading clear rotations for the two external columns can be seen, whereas the internal column has almost no rotations. For asymmetric loading external Column 1 has a clear rotation. Column 2 has more rotation compared to symmetric testing and Column 3 has much less rotation. Column stiffness could only be evaluated for the two external columns for testing with symmetric loading. The internal column did not rotate enough to get valid stiffness values. The stiffness values are shown in Table 6.12. It should be noted that this stiffness includes reaction frame rotation and is thus not the stiffness of only the column. Comparing the stiffness values with those found for the one-bay frame testing (35kNm/mrad and 42kNm/mrad), it can be seen that the stiffness values are lower. This is most likely caused by an increase in flexibility of the reaction frame which was used for the two-bay frame.

Table 6.12: Column stiffness for two-bay frame testing under symmetric load, Column 1 and 3 are external, Column 2 is internal

F_{pt} (kN)	$k_{col,1}$ (kNm/mrad)	$k_{col,2}$ (kNm/mrad)	$k_{col,3}$ (kNm/mrad)
100	30	-	26
200	23	-	28
300	21	-	25

6.6.7 Joint panel shear stiffness

Joint panel shear stiffness for external connections were evaluated in a similar way as done for the one-bay frame testing. The results are shown in Figure 6.40. The average joint panel shear stiffness was 26kNm/mrad, which was lower

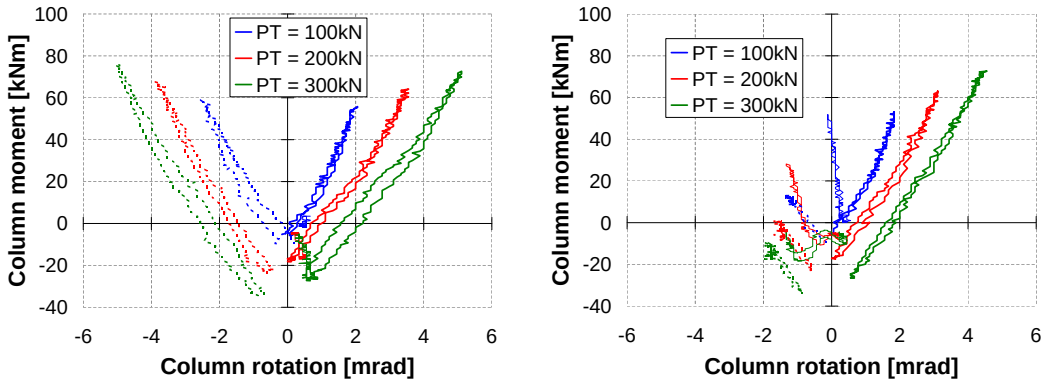

(a) Symmetric testing (b) Asymmetric testing

Figure 6.39: Column stiffness of two-bay frame, continuous line is Column 1, dashed line is Column 3

than the 31kNm/mrad which was found for the one-bay frame test. Internal connections showed almost no joint panel shear deformation during symmetric testing. During asymmetric testing joint panel shear deformation was measured, but no stiffness value could be derived as internal connection moments could not be calculated.

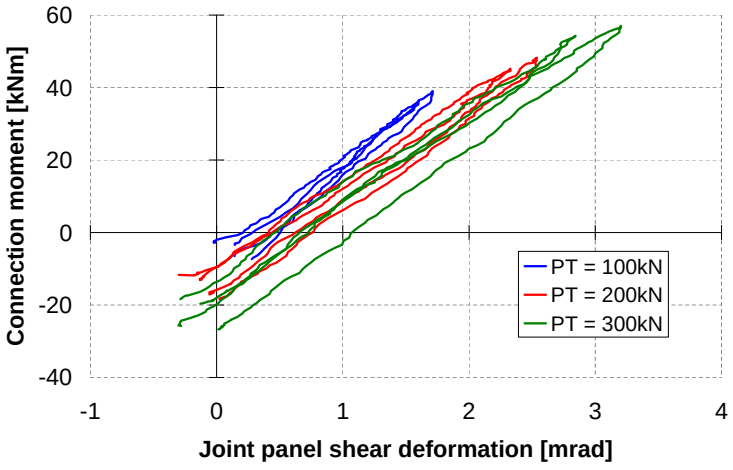

Figure 6.40: Joint panel shear stiffness of two-bay frame

6.6.8 Interface compression stiffness

Interface compression rotation for all connections of Test 3 are shown in Figure 6.41. In this figure it can be seen that internal connections rotation changes significantly at 20% of testing and at 80% of testing. These percentages were exactly when gap opening happened (Figure 6.37). Behaviour of internal connections was clearly bilinear, with a change in stiffness at decompression. External connection behaviour also changed at decompression, but before decompression the behaviour was not as linear as for internal connections.

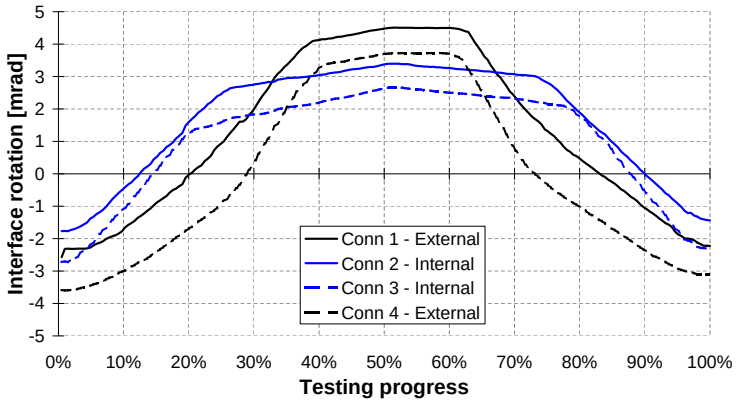

Figure 6.41: Interface compression rotation of external and internal connections in two-bay frame during Test 3 (PT = 200kN)

The interface stiffness of external connections for all post-tensioned tests is shown in Figure 6.42. In this figure, for tests with 100 and 200kN post-tensioning force, a clear spike in stiffness can be seen after decompression. The test with 300kN post-tensioning force did not reach decompression of external connections. Before decompression the stiffness is not linear, the exact reason for this is unknown, but the main change in stiffness occurs when internal connections reach decompression. This might have influenced the bending moment distribution, which was not accurately reflected in the calculation of connection moment. Therefore the initial section of the curves has been used for calculation of interface compression stiffness. For test with 100kN post-tensioning force this initial section was too short to calculate an accurate stiffness value. For testing with 200kN and 300kN post-tensioning force the initial stiffness was approximately 17kNm/mrad.

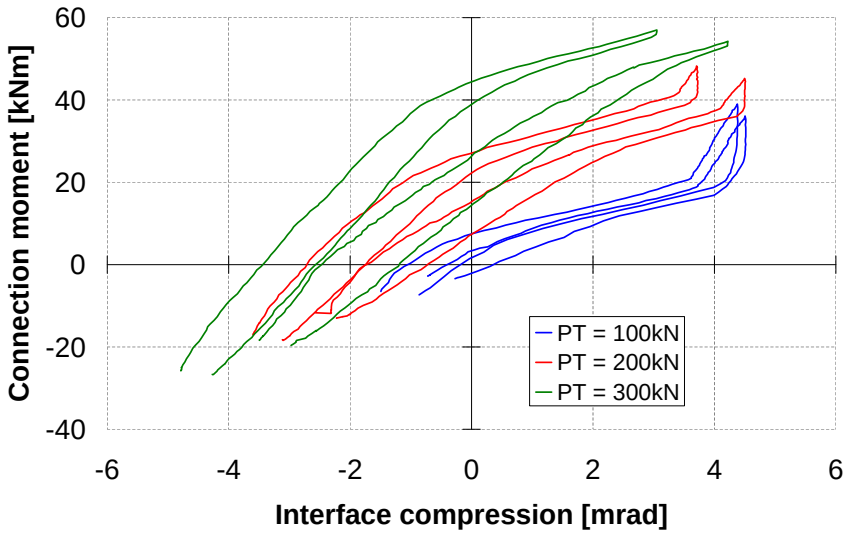

Figure 6.42: Interface compression stiffness of external connections for two-bay frame

6.6.9 Gap opening

Gap opening for external connections is shown in Figure 6.43. Similar to one-bay frame results the initial stiffness is very high. After decompression, indicated by the orange lines, gap opening starts. Testing with low post-tensioning forces exhibited significant gap opening, whereas testing with 300kN post-tensioning force just reached decompression moment for external connections. Gap opening curves for internal connections could not be presented as internal connection moment could not be calculated. But a comparison between internal and external gap opening is shown in Figure 6.37.

6.6.10 Digital Image Correlation

Digital SLR cameras were used to capture images of the test setup during testing. Using Matlab software, markers could be tracked through the sequence of images. Displacement values of the markers were stored for every step of testing. These displacement values could be multiplied with a scaling factor to make displacements more visible. This is done in Figure 6.44, where a grid is placed along centrelines of beams and columns. Images were taken during stressing and during testing. Displacements were multiplied by a factor of 40 and

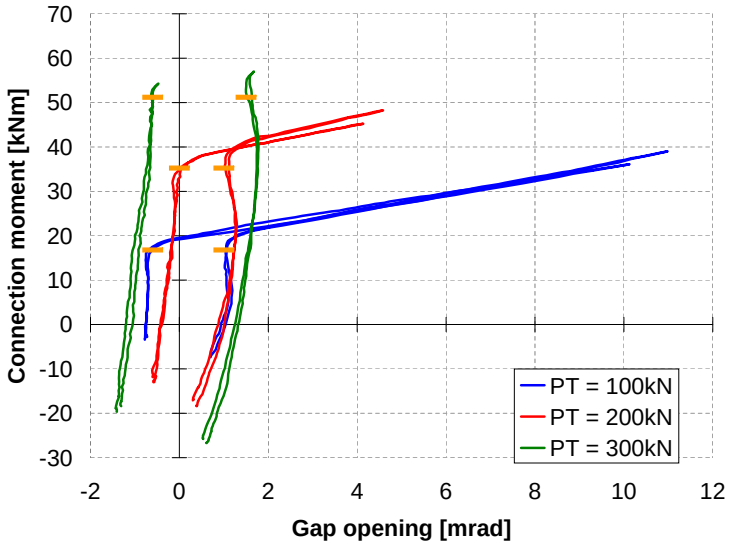

Figure 6.43: Gap opening of external connections in two-bay frame, horizontal offset is caused by construction tolerances

plotted in Figure 6.44b. The grey markers are from the test setup before stressing. Black markers show displacements after stressing, orange under 18mm mid-span displacement (load of 134kN per bay) and red under maximum displacement of 36mm (load of 208kN per bay). Both axes show the location of original markers in pixels relative to top left corner. For sections where the reaction frame blocked the view of the frame it was obviously not possible to track any marker. From the displaced shapes it can be seen that both beams had very similar displaced shapes. Furthermore, it can be seen that external columns showed displacements at both ends whereas the internal column showed minor displacement at top. These displacements were due to flexibility of the support. The displaced shape is not symmetrical due to differences in reaction frame on both sides.

Another sequence of images was taken of the internal connection for Test 3 with 200kN post-tensioning force. A grid was placed over the column and over the ends of both beams, as shown in Figure 6.45a. The resulting deformation is plotted using black diamonds in Figure 6.45b whereby displacements are multiplied with a factor of 15. The original grid is also plotted as grey diamonds. Beam rotations and gap opening can clearly be seen. Also interface compression of the column is visible. When analysing top and bottom grid lines of the column, a small

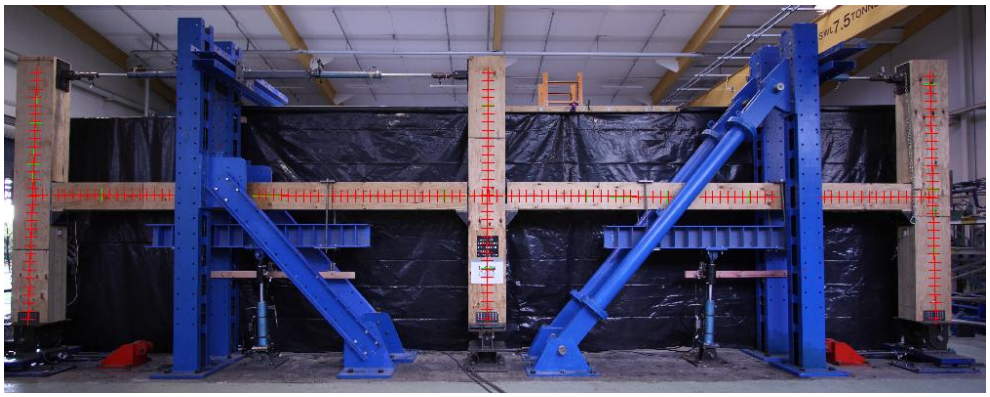

(a) Gird on image

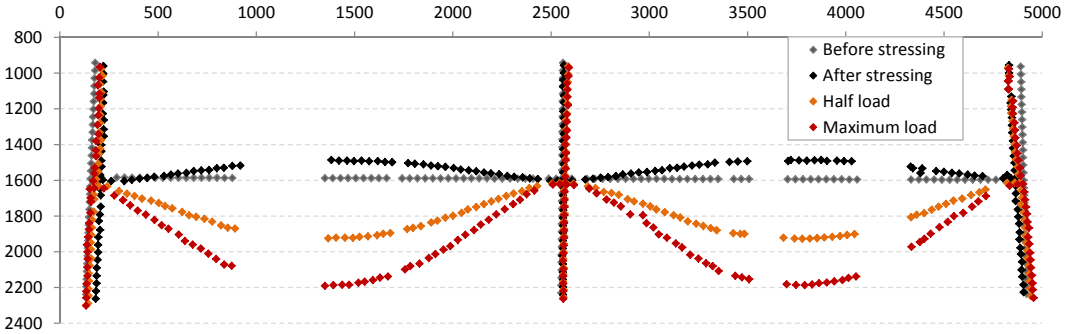

(b) Displaced grid of two-bay frame after image analysis (multiplied with a factor of 40)

Figure 6.44: DIC tracking of displacements of two-bay frame during testing with 200kN post-tensioning force

clockwise rotation is seen. This corresponds with the DIC analysis of the full frame whereby the internal column showed minor movement at the top.

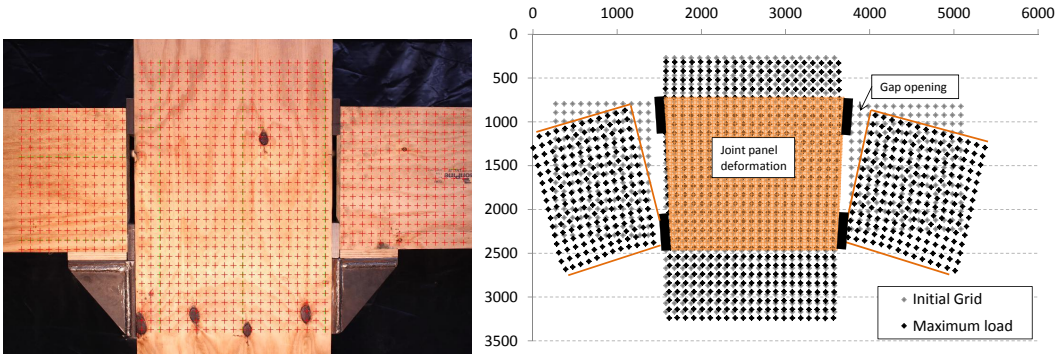

(a) Gird on image

(b) Displaced grid of internal connection (multiplied with a factor of 15)

Figure 6.45: DIC tracking of displacements of internal connection in two-bay frame during testing with 200kN post-tensioning force

A final series of images was taken of the external connection for Test 3 with 200kN post-tensioning force. Again a grid was placed over the column and over the end of the beam, as shown in Figure 6.46a. The deformed grid, multiplied with a factor 15, is shown in Figure 6.46b. In this figure the different deformation components are highlighted. Top and bottom grid lines show column rotation. The central area of the column shows joint panel deformation, although this is hard to see due to the combined effect of column rotation. The interface shows compression at the bottom. Clearly shown is the gap opening between beam and column.

6.6.11 Summary

Experimental testing of a two-bay post-tensioned timber gravity frame with draped tendons has given valuable insight in the behaviour of these types of frames. Testing was performed at different three levels of post-tensioning. Deformation components in the connection were evaluated and will be compared with analytical models in Chapter 8. It turned out not to be possible to accurately calculate the internal connection moment, but clear differences between internal and external connections were shown. Internal connections reached decompression before

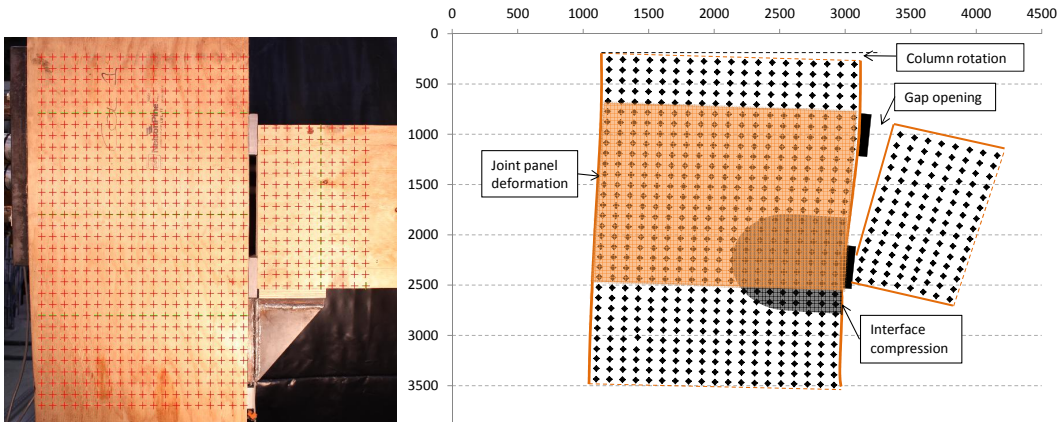

(a) Gird on image (b) Displaced grid of external connection (multiplied with a factor of 15)

Figure 6.46: DIC tracking of displacements of external connection in two-bay frame during testing with 200kN post-tensioning force

external connections did. Internal connections showed very little column rotation or joint panel deformation. Interface compression and gap opening were recorded for both internal and external connections, although for tests with 200 and 300kN post-tensioning force external connections did not reach decompression. Digital Image Correlation was successfully used to track global frame displacements. Additionally, connection deformation components could be made clearly visible from series of images of the connections.

6.7 Conclusions

General conclusions based on one-bay and two-bay frame testing are listed below.

- A parameter study on the beam height (Appendix A.3) showed that a height of 500mm satisfied strength and short term deflection criteria for a 9m post-tensioned timber beam in an office building. But long-term deflections (according to the design specified by the design standard) would govern the design for a real building and increase the beam height to at least 600mm. An anchorage plate of 500mm by 288mm and 40mm thick was needed in order to achieve sufficiently low stress levels in steel and timber for a post-tensioning force of 600kN. A steel corbel with 12 inclined

screws of 10mm diameter and 240mm length was designed to resist a 200kN shear force. Steel plates used to fabricate the corbel needed to be at least 20mm thick. Fabrication of the corbel was complicated and time consuming due to the angular recesses for the inclined screws. As a first indication, the stiffness of inclined screws between corbel and column was close to values specified for axial loaded screws.

- Bending and shear stiffness of beams were 12GPa and 660MPa, respectively. These were higher than the specified properties of LVL11. Different moduli of elasticity were found when using strain gauges to calculate the strain compared to calculations using beam deflections. This was taken into account when calculating bending moments in the beam from strain gauges measurements.

- Construction tolerances resulted in initial rotations during stressing which influenced experimental testing results.

- The post-tensioning force showed a direct increase after the start of testing due to deviator deflections. A further increase was seen after decompression which was due to gap opening.

- Digital Image Correlation was successfully used to track global frame displacements. Also connection deformation components could be made clearly visible from series of images of the connections. Validation of measurements using DIC techniques showed that all four deformation components were measured accurately, but that summation of these four components resulted in overestimation of beam rotation when compared with direct measurements. This could be caused by deformation components which influence each other, e.g. interface compression influencing joint panel measurements.

Conclusions based on one-bay frame testing are listed below.

- At decompression the post-tensioning force was on average 10% higher compared to the initial post-tensioning force. Calculated decompression

moments using Equation 6.2 matched well with experimental testing results. Moment-rotation plots for gap opening showed an almost infinite initial stiffness before decompression. After decompression, the connection moment increased due to tendon elongation. Push-pull tests showed that decompression happened at the same positive and negative connection moments, only after decompression a difference was seen due to the asymmetry of the tendon position.

- For the test without post-tensioning almost all rotation was due to gap opening. For an increase in post-tensioning force a decrease in gap opening and increases in interface, joint panel and column rotations were shown. Column stiffness was evaluated, but this included rotations due to reaction frame movement. An average joint panel shear stiffness of 31kNm/mrad with a coefficient of variation of 11% was found. Interface compression stiffness was on average 31kNm/mrad with a coefficient of variation of 9%.

- A linear approximation of the strain profile in the compression zone of the beam after decompression fits well with testing data. The connection moment after decompression calculated using Equation 6.4 matched very well with experimental testing data.

Conclusions based on two-bay frame testing are listed below.

- Internal connection moments were very sensitive to changes in force distribution, therefore it was not possible to accurately calculate the internal connection moment. As a result not all stiffness components of internal connections could be calculated, but rotation measurements still provided useful insight in the difference between internal and external connection behaviour. Due to stiffness differences internal connections reached decompression earlier than external connections. Tendon force increased on average 11% for decompression of internal connections and 24% for external connections.

- For internal connections the contributions of column rotation and joint panel deformation were negligible, whereas for external connections a clear

contribution of these two components was visible. The average joint panel shear stiffness was 26kNm/mrad, which was lower than the 31kNm/mrad which was found for the one-bay frame test. For testing with 200kN and 300kN post-tensioning force the initial interface compression stiffness was approximately 17kNm/mrad.

Part III

Analysis

Chapter VII

Post-tensioned timber beams

7.1 Introduction

Experimental testing of four LVL box beams was presented in Chapter 4. One beam was used as a benchmark without post-tensioning, one beam had straight post-tensioning tendons and two beams had draped post-tensioning tendons. The precamber, stiffness and ultimate strength of the beams were tested. Models representing the behaviour of post-tensioned timber beams need to be developed, as it is impractical to test a large range of beams required for development of design guidelines. The accuracy of these models is validated with experimental testing results. Although detailed and accurate models are useful for research purposes, quick design steps to estimate section size and post-tensioning force are of interest for practising engineers.

Analysis of post-tensioned timber beams has the following objectives:

- Develop numerical and analytical models to describe behaviour of post-tensioned timber beams.
- Evaluate applicability of current timber design code procedures to predict the failure load of post-tensioned timber beams.
- Perform a parameter study on the design of post-tensioned timber beams to identify critical design parameters.
- Propose a simplified design for post-tensioned timber beams.

This chapter presents an in-depth analysis of post-tensioned timber beams. The four beams (Figure 7.1) tested in Chapter 4 have been modelled in a finite element program (Section 7.2). Two analytical models, one for beams with straight tendons and one for beams with draped tendons, are presented in Section 7.3. The analytical model and finite element model (FEM) results were verified

with experimental testing results in Section 7.4. Comparisons of failure loads with predictions based on the New Zealand timber design standard, NZS 3603:1993 (Standards New Zealand, 1993), and European timber design standard, EN 1995:2004 (CEN, 2004b), are presented in Section 7.5.

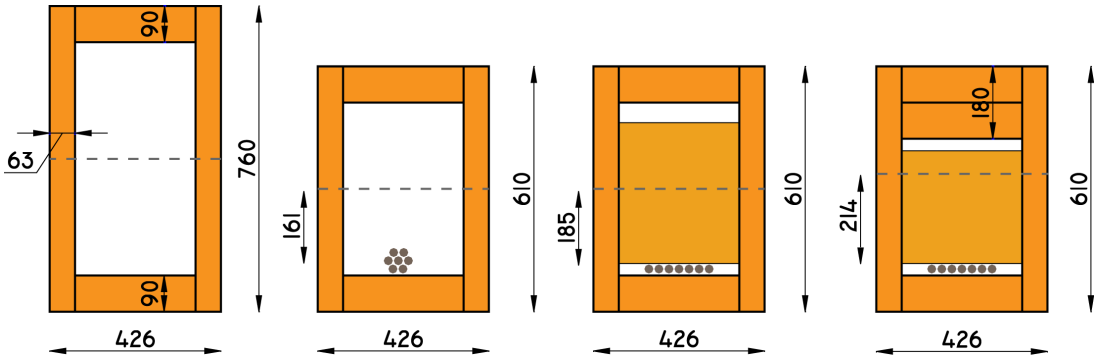

Figure 7.1: Cross-sections of beams used for experimental testing, Beam 1 was benchmark without PT, Beams 2 used straight PT, Beam 3 and 4 used draped PT

The analytical model was then used to perform a parameter study on a range of post-tensioning forces and beam lengths for four different cross-sections (Section 7.6). The main results of the parameter study shows that design is governed by long-term deflections. This was used to develop a quick design procedure (Section 7.7). The quick design procedure balances precamber with long-term deflections and presents an easy four step process to estimate section size and post-tensioning force. Furthermore, some simplifications to the iterative analytical model are presented at the end of this chapter.

7.2 Numerical modelling

This section describes the development of a Finite Element Model (FEM) in Abaqus CAE (Simulia, 2010) of the four timber beams which were used for experimental testing as described in Chapter 4. A 3D model was made in order to evaluate the stresses in the webs, flanges, deviators and anchorages, something which would not be possible with a 2D plane stress model. Technical drawings of the beams with dimensions can be found in Appendix G. This section describes

parts, material properties, boundary conditions, loading, contact and interaction of different parts.

7.2.1 Parts

This section describes the finite element model for the beam with draped tendons (Beam 3). Models of the other beams were made in a similar manner. Only a quarter of the beam was modelled due to symmetry at mid-span of the beam and along the length of the beam.

Timber beam The beam was modelled as a 3D deformable solid. The anchorage block was added into the beam. It was partitioned in several parts in order to apply local material directions. Material directions were defined as 1 = longitudinal (parallel to grain), 2 = tangential (perpendicular to grain but parallel to glue lines) and 3 = radial (perpendicular to grain and perpendicular to glue lines). First order elements with reduced integration brick elements (C3D8R) were used, Figure 7.2a. Although second order elements usually perform better in bending, they require a lot of computational power and give stability issues with the contact analysis. Reduced integration was chosen to avoid shear locking, which would result in a too stiff behaviour in bending. Default hourglass control was used and it was minimized by distributing the loading and supports over multiple nodes.

Deviator Deviator blocks were modelled separately from the beam to allow for easier meshing of the objects. The deviator was made up of linear 3D stress bricks with reduced integration (C3D8R), Figure 7.2b. The bottom of the deviator was given a curvature with a radius of two meters, similar to the tendon. To assure accurate modelling a cross-sectional drawing of the deviator was made in AutoCAD and imported into Abaqus.

Support and loading plate The steel support and loading plates were included in the model in order to create realistic loading and boundary conditions. The plates were modelled as 3D deformable solids, Figures 7.2c and 7.2d. The support plate had dimensions of 500mm by 213mm (half the beam width), the loading plate had dimensions of 300mm by 213mm and the thickness of both

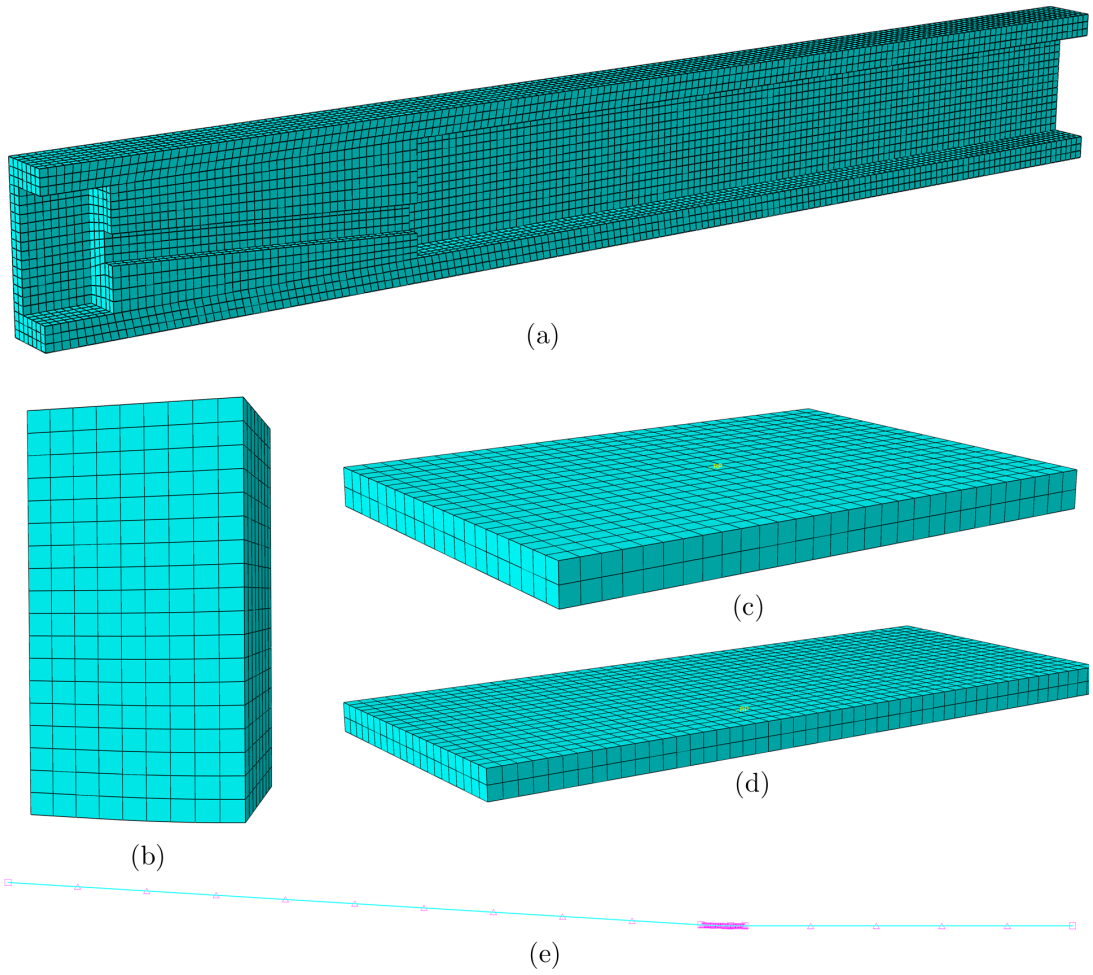

Figure 7.2: Mesh of parts for FEM model; (a) Timber beam, (b) Deviator, (c) Loading plate, (d) Support plate, (e) Tendon

plates was 20mm. A reference point was placed at the centre of both plates and fixed to all nodes on the surface. This was done to spread the load and boundary condition to all nodes.

Post-tensioning tendons The post-tensioning tendons were modelled as 3D deformable wire elements. One wire element represented 3.5 tendons, half of the seven tendons (due to symmetry). The wire had a length of half the beam length and had a draped profile (or straight for beams with straight tendons). The radius of curvature was 2 meters, similar to the deviator. The wire was assigned

a beam type section (a truss type was tried, but gave numerical instability at the start of the post-tensioning phase). The beam was given a circular profile with a radius of 10.55mm, which corresponds with an area of 350mm^2, equivalent to 3.5 (half of 7) 12.7mm diameter post-tensioning tendons. The post-tensioning tendon was meshed with linear beam elements (B31, a 2-node linear beam), Figure 7.2e. Each element had a length of approximately 250mm. A mesh with a length of about 3mm was used for the curved part, where the tendon was in contact with the deviator block.

Anchorage plate The anchorage was modelled as a rectangular solid 3D deformable body with a height of 287mm, depth of 143.5mm (half of 287mm) and a thickness of 40mm. A datum point was added at the location where the tendon was attached to the anchorage plate. The material properties were chosen to be linear elastic. Due to simplifications in modelling, the post-tensioning tendons were connected to the anchorage plate at a single point. This caused very high localized stresses in the model, which were not happening in reality as the post-tensioning force was distributed over a larger area by the anchorage barrels. This simplification was deemed justified as the local anchorage performance was not of interest in this chapter.

7.2.2 Material properties

Steel The steel material model for anchorage, loading and support plates was defined as linear isotropic with $E = 200000N/mm^2$, $\nu = 0.3$ and a density of $7.85 \times 10^{-9} tonne/mm^3$ (equals to $7850kg/m^3$).

Post-tensioning steel Post-tensioning tendons were modelled with non-linear material behaviour, as experimental testing showed that the maximum stress in the tendons exceeded the elastic range (Section 4.4.3). A non-linear model as shown in Figure 7.3 was implemented.

Timber Timber was modelled as an elastic material with engineering constants. The modulus of elasticity in bending and shear modulus of the timber beams were measured during testing of beams without post-tensioning. These values were used for E_1 and G_{12}. The remaining seven material properties were based

Stress (MPa)	Strain (%)	Plastic strain
0	0	0
1520	0.76	0
1600	1.0	0.0024
1860	3.5	0.0274

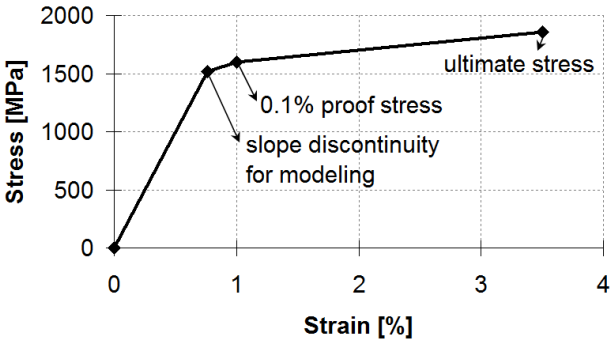

Figure 7.3: Material model for post-tensioning steel

on values derived in Section 3.6. An overview of timber material properties is given in Table 7.1.

Table 7.1: Material properties (MPa) for LVL used in Abaqus

Property	Beam 1	2	3	4
E1	10700	10900	11200	11400
E2		426		
E3		371		
$\nu 12$		0.59		
$\nu 13$		0.48		
$\nu 23$		0.22		
G12	683	631	703	757
G13		901		
G23		96		

Since Beam 3 started to fail in compression before tensile failure in the bottom flange was reached, a non-linear material model for LVL was implemented. This was done using the plasticity option and defining isotropic hardening. Although the material is far from isotropic, the stresses in the tangential and radial were well below the yield stress. Therefore the non-linear stress-strain data was only effective in the parallel to grain direction. The non-linear stress-strain data as presented in Section 3.3 was used.

7.2.3 Assembly

The parts were put together in an assembly, as shown in Figure 7.4. The anchorage plate was positioned at mid-height of the beam. The support plate was placed below the end of the beam and the loading plate at 1/3rd the total length of the beam. The tendon and deviator block were placed inside the box beam. The loading plate and support plate had reference points placed at the centre where load and boundary conditions were introduced.

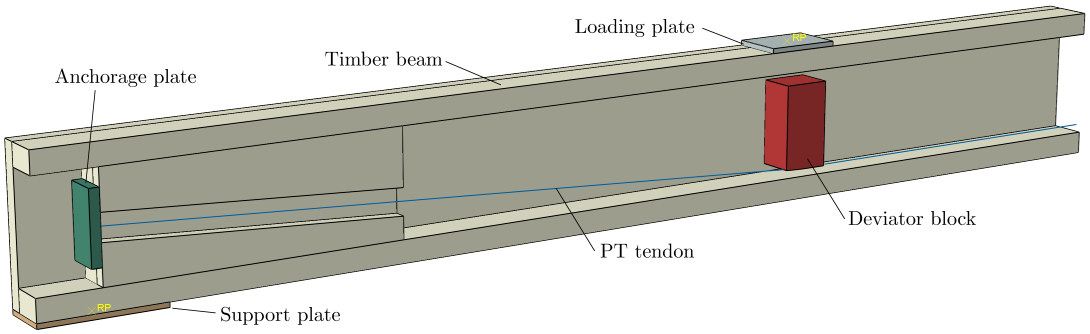

Figure 7.4: Assembly of parts in finite element model

7.2.4 Steps

Three steps were defined. The first step was the initial step, generated automatically by Abaqus. The second step was the stressing step, where the post-tensioning force was applied. The third step was the loading step, where the vertical load was applied to the beam. The option non-linear geometry (Nlgeom) was turned on in Abaqus due to the large-displacement effects. Each step had a time period of 1, although this absolute value had no specific meaning or unit. The initial time step was 0.001 for the post-tensioning step. This was necessary since the initial unstressed cable gave a highly unstable behaviour when the post-tensioning force was introduced and the tendon was touching the deviator. Very small increments were needed in order to converge to a solution.

7.2.5 Interaction

The anchorage plate was connected to the anchorage block inside the beam using tie constraints (Figure 7.5a), which connected nodes of the steel plate and the

timber anchorage block. Although this was not a realistic representation, it simplified the analysis as no contact analysis was needed. In a similar way the loading plate and support plate (Figure 7.5b) were fixed with tie constraints to the beam. And also the post-tensioning tendons were attached to the anchorage plate using a tie constraint (Figure 7.5c). This tie constraint was simulating the post-tensioning anchorage. The surface of the anchorage plate was the master surface and the node at the end of the tendons was the slave region.

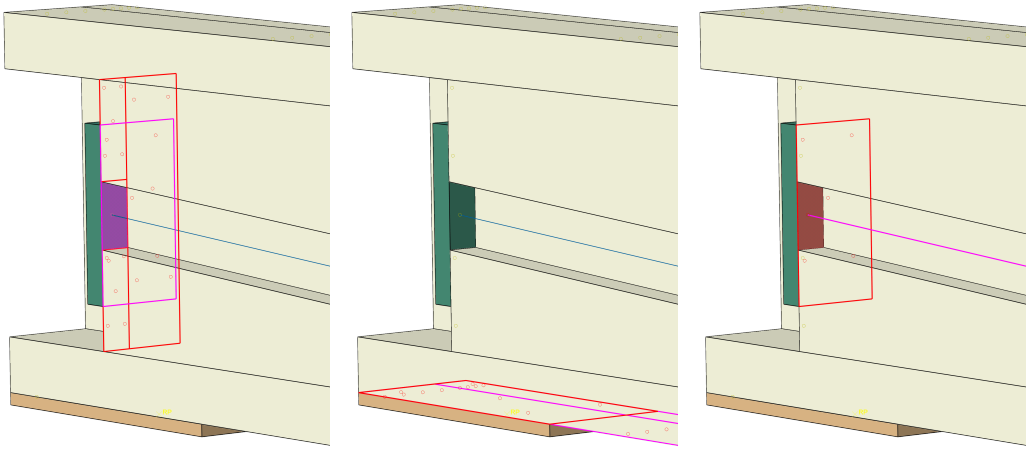

(a) Anchorage plate to anchorage block (b) Support plate to beam (c) Post-tensioning wire to anchorage plate

Figure 7.5: Tie constraints between parts in FEM

Contact between the tendon and the deviator was modelled as a surface-to-surface contact. The master surface was the bottom of the deviator and the slave surface was the circumference of the tendon. The centreline of the tendon (since it was modelled as a wire element) was placed at 0.005mm from the deviator in order to initiate contact as soon as possible in the analysis. The contact interaction property was set to hard contact for normal behaviour and frictionless for tangential behaviour. The tendons within the plastic sleeves were assumed to have a negligible friction.

7.2.6 Boundary conditions

The beam was constrained from moving in the vertical directions over a distance of 500mm at the end of the beam. This was done by placing a steel plate below the

beam which was tied to the beam. The plate had a reference point in the centre and movement of this point in the vertical direction was restrained, horizontal movement was free to allow for shortening of the beam. Rotations around the horizontal axis, perpendicular to the beam were free and the other two rotation components were restrained.

As only a quarter of the beam was modelled, symmetric boundary conditions were added (Figure 7.6). The faces of the beam at mid span and the end node of the tendon were assigned with Z-symmetry boundary conditions, fixing movement in the Z-direction and rotation about X and Y axes. The sides of the beam, anchorage, loading and support plates were assigned with X-symmetry boundary conditions, fixing movement in X-direction and rotation about Y and Z axes.

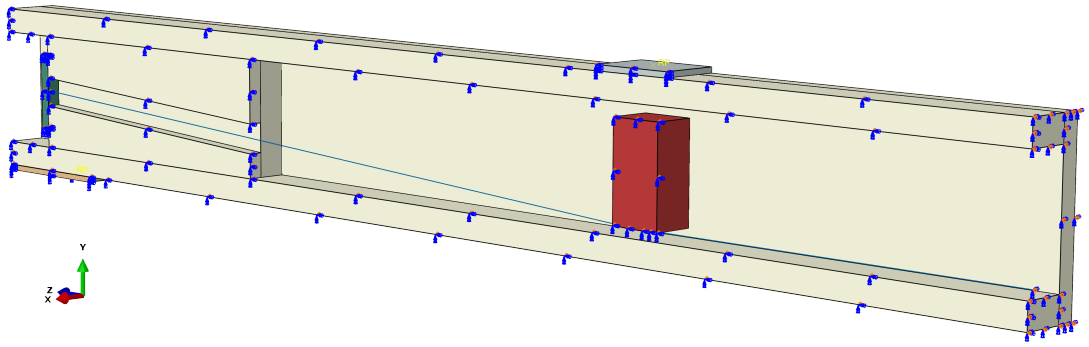

Figure 7.6: Symmetric boundary conditions

7.2.7 Loads

The load on the beam was introduced through the loading plate. A point load was placed on a central reference point on the plate. The point load was a quarter of the maximum experimental load, as only a quarter of the beam was modelled. The failure loads were 694, 536, 726 and 836kN for beams 1,2,3 and 4, respectively. The loads in the model were 173.5, 134, 181.5 and 209kN.

The post-tensioning force was modelled as a bolt load. This is a loading scenario which was developed for pre-tensioned bolts, where the user can specify a tightening force or a length adjustment. This loading scenario can be adapted to simulate post-tensioning force. The wire was stressed (tightened) up to the initial force during the stressing step. Then it was anchored, which in the model

meant that the length was fixed at that point. After fixing the length the force in the tendon could still increase due to tendon elongation.

7.2.8 Results

Results are presented for the model of Beam 3 with the non-linear material properties. Results from other models are similar, and are presented in Appendix D.1. A comprehensive comparison between experimental, numerical and analytical models is made in Section 7.4.

Deflections of the beam under maximum load are shown in Figure 7.7. The black outlines show the position of the beam without any vertical load or post-tensioning force. The maximum displacement at mid-span was 158mm and at the deviator about 140mm. A small uplift, up to 20mm, is seen at the end of the beam. This was due to the support being 250mm inwards from the beam, and rotations around the support created this small uplift.

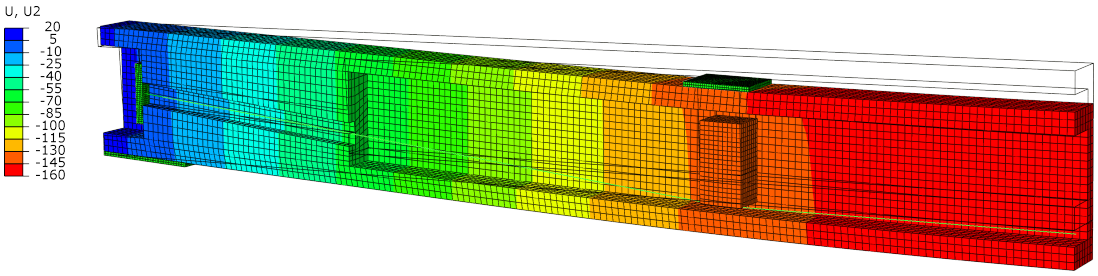

Figure 7.7: Results of FEM for beam deflections of Beam 3, the outline showing the original position

Parallel to grain stresses are shown in Figure 7.8a. At mid-span the maximum compressive stress was 47MPa and tensile stress 37MPa. The stress profile was non-linear, as can be seen from the large red/orange part at the top of the beam. Perpendicular to grain stresses are shown in Figure 7.8b. These show stresses of up to 5MPa above the support and up to 7MPa below the loading plate. Shear stresses in the web are shown in Figure 7.8c. High, localised shear stresses were visible under the ends of the loading plate. The main shear stress in the web was up to 6MPa, which was close to the failure strength. Shear stresses in the web were close to zero in the middle part of the beam and below 3MPa at the location of the anchorage block.

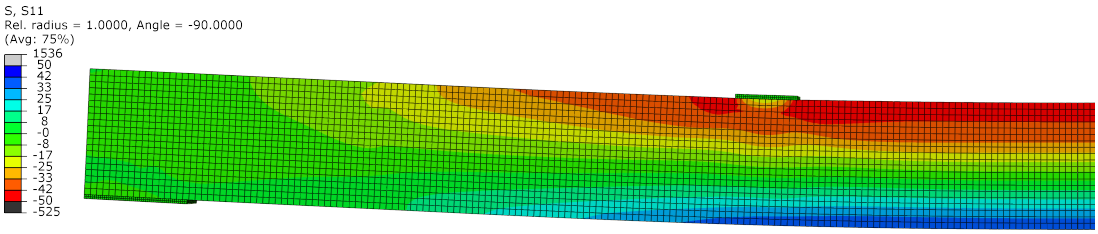

(a) Parallel to grain stresses

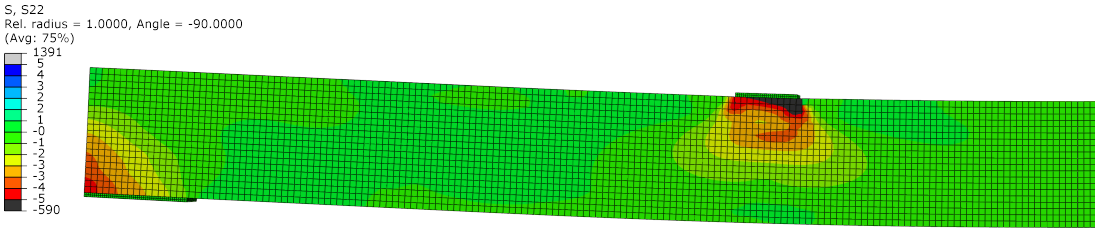

(b) Perpendicular to grain stresses

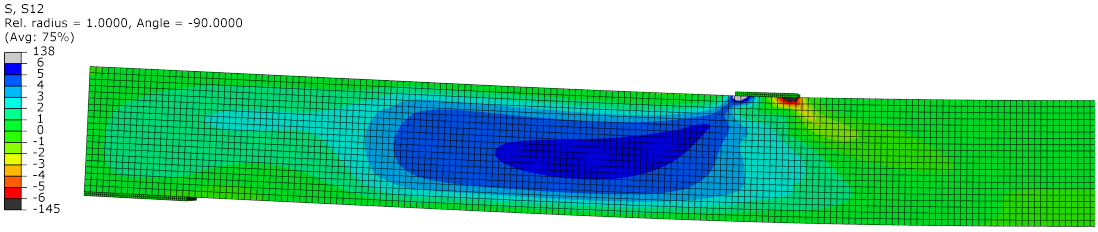

(c) Shear stresses in web

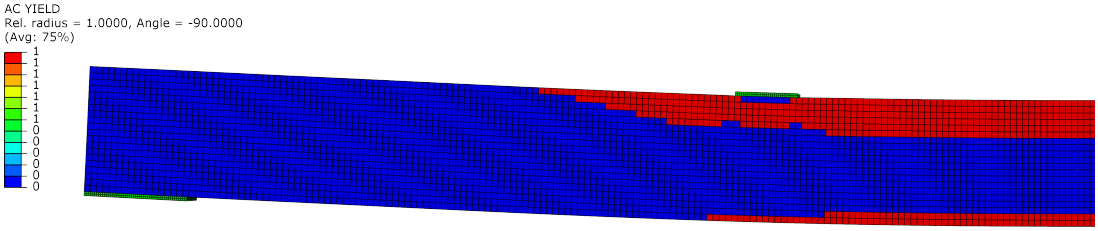

(d) Elements which showed non-linear behaviour parallel to grain(s_{11}>35MPa)

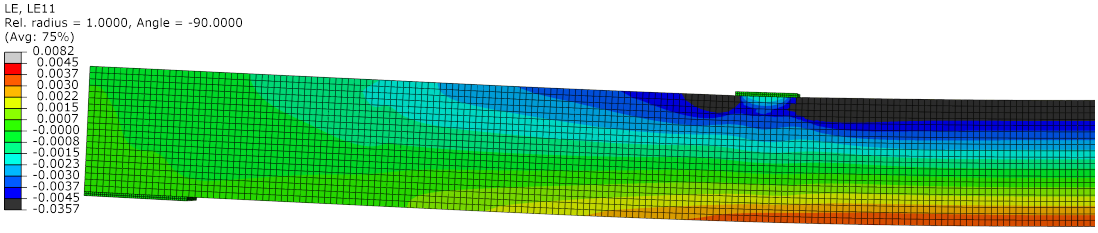

(e) Parallel to grain strains

Figure 7.8: Results of FEM for Beam 3

Figure 7.8d shows in red the elements which have reached non-linear material behaviour. This started at 35MPa, as defined by the input data. It can be seen that a significant part of the top flange reached this limit and also part of the bottom flange. The bottom flange, which was in tension, should not have any non-linear behaviour, but Abaqus uses the yield data for tension and compression. No build-in material model was found which could prevent this behaviour. A work-around would be to make two materials, one linear-elastic model which was assigned to the bottom flange and one non-linear material model which was assigned to the top flange. Although this is possible, it was not performed as the bottom flange did not reach the maximum stress of 47MPa and thus only showed a small amount of non-linear behaviour. This can also be seen from Figure 7.8e, where the parallel to grain strains in the beam are shown. The bottom fibres have a maximum strain of 0.35%, which was part way between the start of non-linearity at 0.28% strain and the maximum strength at 0.45% strain. It can be seen that the top of the beam exceeded the maximum strain of 0.45% in a significant section. Abaqus showed the highest strains at the corner of the loading plate (Figure 7.9a), which also showed the compression failure during experimental testing.

Contact stresses between tendon and deviator are shown in Figure 7.9b. As the tendon is a wire element and only one tendon is modelled for simplicity, the contact stresses are very localized and very large (up to 5000MPa). In reality with multiple tendons in sleeves the contact stresses are much lower.

The beam is supported by a 500mm long support plate. This creates a large contact area between beam and support plate, resulting in low stresses. The stresses in the web are tangential (S22) and in the bottom flange radial (S33). Both of these stress components are visualized in Figures 7.9c and 7.9d. The tangential stresses in the web range from 2 to 4MPa. The radial stresses in the bottom flange range from 0 to 2MPa. Especially at the end of the beam, where there is no anchorage block, the radial stresses in the middle part of the bottom flange are close to 0MPa. This indicates that not the full contact area should be used when analysing contact stresses between beam and support. Larger stresses will occur under the webs and smaller stresses under the flange.

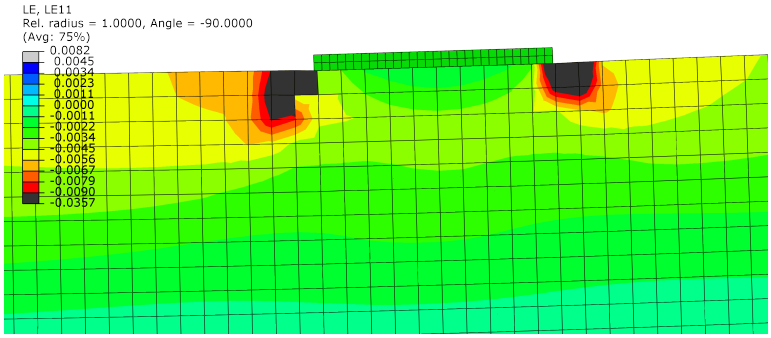

(a) Strain concentrations around loading plate

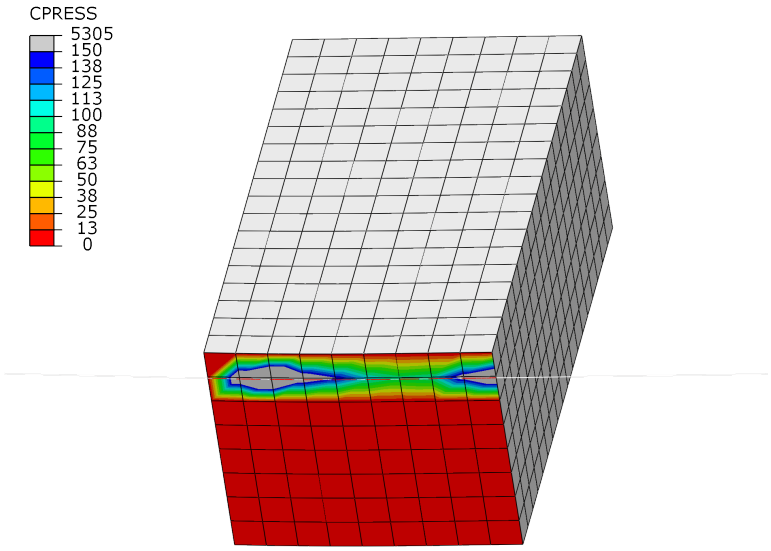

(b) Contact stress between tendon and deviator

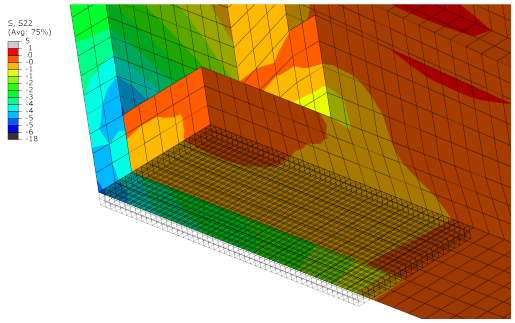

(c) Tangential stresses between beam and support plate

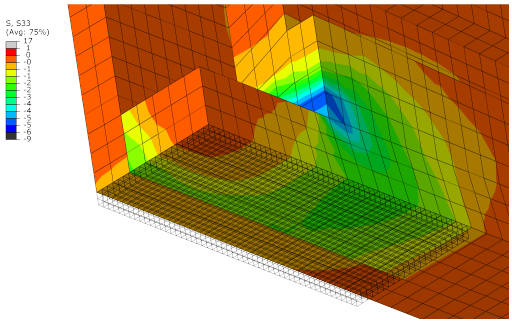

(d) Radial stresses between beam and support plate

Figure 7.9: Results of FEM for Beam 3 (continued)

7.3 Analytical modelling

This section explains the analytical procedure to predict the behaviour of post-tensioned timber beams with straight and draped tendons. These predictions are later compared with experimental testing results.

7.3.1 Straight PT beam

The procedure to predict the behaviour of post-tensioned beams with straight tendons (Figure 7.10a) is split into five parts:

1. Evaluation of forces
2. Evaluation of bending moments
3. Evaluation of deflections
4. Evaluation of rotations
5. Evaluation of tendon elongation

The procedure includes three iterative loops, which are further clarified by the bold arrows in the flowchart in Figure 7.10b:

1. Rotations at the ends of the beam resulting in tendon elongation and thus an increase in post-tensioning force.
2. Deflections of the beam result in a second order bending moments.
3. Elastic beam shortening reduces tendon elongation.

The procedure is further elaborated in the next pages. In order to be able to compare the procedure with experimental results, the assumption is made that the beam is loaded by two vertical point loads (at 1/3 and 2/3 of the beam length). The procedure can be adapted for different loading configurations, like a distributed load. A flowchart with the equations for this scenario is shown in Appendix D.2.

Evaluation of forces The beam is loaded by a vertical force ($F_{vertical}$) which push the beam at two points each 1/3 from the end. The vertical force (F_v) at each point is given by Equation 7.1.

$$F_v = \frac{F_{vertical}}{2} \tag{7.1}$$

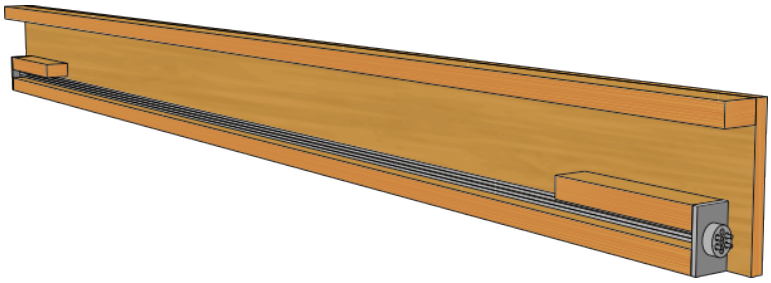

(a) Rendering of post-tensioned timber beam with straight tendons

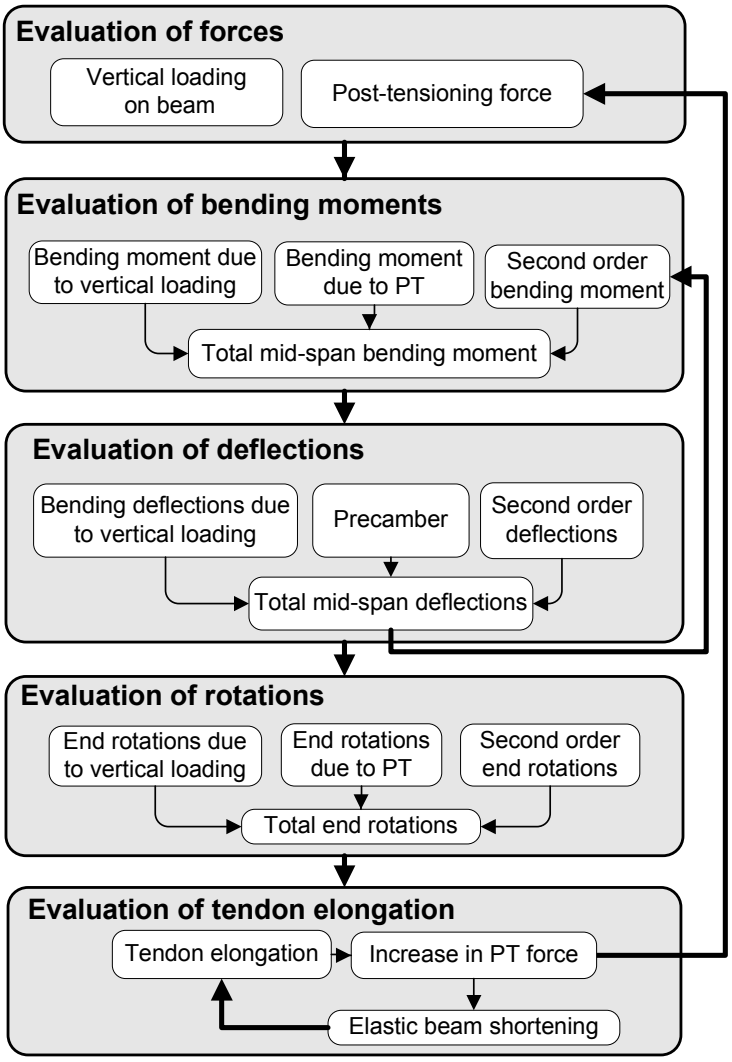

(b) Flowchart for analytical design of PT timber beams with straight tendons

Figure 7.10: Analytical design procedure for PT timber beams with straight tendons

The post-tensioning force (F_{pt}) is the initial post-tensioning force ($F_{pt,i}$) plus increase in force due to tendon elongation (ΔF_{pt}) from Equation 7.17.

$$F_{pt} = F_{pt,i} + \Delta F_{pt} \tag{7.2}$$

Evaluation of bending moments Three different loading contributions result in bending moments in the beam (Figure 7.11); vertical loading, post-tensioning and second order effects.

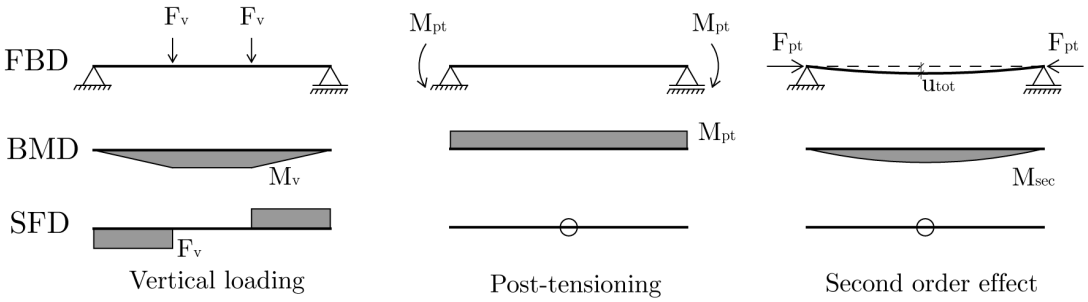

Figure 7.11: Free body diagram (FBD), bending moment diagram (BMD) and shear force diagram (SFD) for post-tensioned timber beam with straight tendons

The vertical loading results in a bending moment (M_v) in the mid section of the beam, as given by Equation 7.3.

$$M_v = F_v \cdot \frac{l}{3} \tag{7.3}$$

The post-tensioning force is eccentric at the end of the beam (e). This results in a constant (negative) bending moment along the full length of the beam (M_{pt}) given by Equation 7.4.

$$M_{pt} = -F_{pt} \cdot e \tag{7.4}$$

The total beam deflections, u_{tot} following from Equation 7.10, result in a second order bending moment (M_{sec}), which is assumed to have a parabolic distribution with a maximum in the middle of the beam, as given by Equation 7.5.

$$M_{sec} = F_{pt} \cdot u_{tot} \tag{7.5}$$

The total mid-span bending moment (M_{mid}) is found by adding Equations 7.3, 7.4 and 7.5, as shown in Equation 7.6.

$$M_{mid} = M_v + M_{pt} + M_{sec} \tag{7.6}$$

Evaluation of deflections Vertical loading results in bending ($u_{v,bend}$) and shear ($u_{v,shear}$) deformation. Mid-span deflections are derived in Equation D.9, which is repeated here as Equation 7.7.

$$u_v = u_{v,bend} + u_{v,shear} = \frac{23}{216}\frac{M_v \cdot l^2}{EI} + \frac{F_v \cdot l}{3 \cdot GA_s} \tag{7.7}$$

The bending moment due to the post-tensioning creates a precamber (u_{pt}) as given by Equation 7.8. This value will be negative, indicating uplift, as M_{pt} is negative.

$$u_{pt} = \frac{M_{pt} \cdot l^2}{8 \cdot EI} \tag{7.8}$$

The second order bending moment results in second order deflections (u_{sec}) as given by Equation 7.9. This formula is derived in Equation D.16.

$$u_{sec} = \frac{5}{48} \cdot \frac{M_{sec} \cdot l^2}{EI} \tag{7.9}$$

Total mid-span deflection is given by adding the previous three deflections; Equations 7.7, 7.8 and 7.9, as shown by Equation 7.10.

$$u_{tot} = u_v + u_{pt} + u_{sec} \tag{7.10}$$

Evaluation of rotations The end of the beam rotates due to vertical loading (F_v), Equation 7.11.

$$\theta_v = \frac{F_v \cdot l^2}{9 \cdot EI} \tag{7.11}$$

The bending moment due to post-tensioning (M_{pt}) results in a rotation at the end of the beam, Equation 7.12.

$$\theta_{pt} = \frac{M_{pt} \cdot l}{2 \cdot EI} \tag{7.12}$$

The second order bending moment (M_{sec}) also results in rotations at the end of the beam, Equation 7.13.

$$\theta_{sec} = \frac{5}{12} \cdot \frac{M_{sec} \cdot l}{EI} \tag{7.13}$$

Total rotation at end of the beam is the sum of the previous three rotations, Equations 7.11, 7.12 and 7.13. This is shown in Equation 7.14.

$$\theta_{end} = \theta_v + \theta_{pt} + \theta_{sec} \tag{7.14}$$

Evaluation of tendon elongation The tendon elongation (Figure 7.12) is given by the rotation at the end of the beam (θ_{end}) multiplied with the eccentricity (e). This needs to be multiplied by a factor of two because elongation is happening at both ends. The elastic shortening of the beam due to the increase in PT force, Equation 7.18, needs to be subtracted. Also initial shortening (Δl_i) of the tendon needs to be subtracted. The resulting formula is shown in Equation 7.15.

$$\Delta l_{pt} = 2 \cdot \theta_{end} \cdot e - \Delta l_{beam} - \Delta l_i \tag{7.15}$$

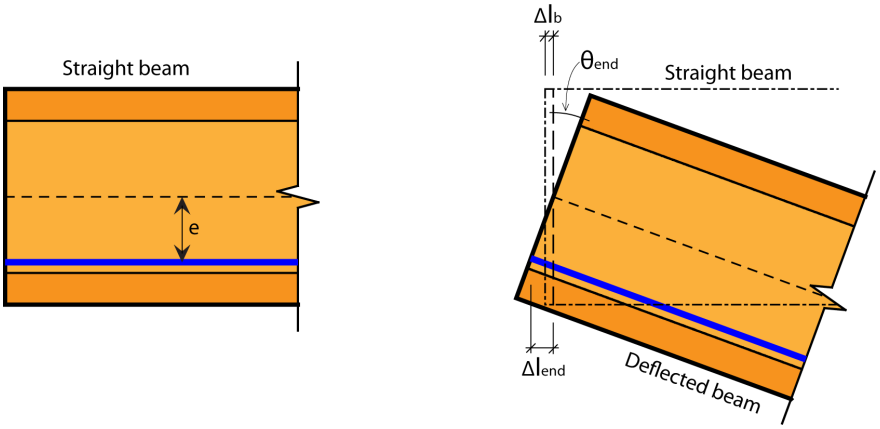

Figure 7.12: Tendon elongation for beam with straight tendons

The initial shortening of the beam is given by Equation 7.16.

$$\Delta l_i = \frac{F_{pt,i} \cdot l}{EA} \tag{7.16}$$

The increase in length results in an increase of post-tensioning force (ΔF_{pt}), shown in Equation 7.17. This increase is used in the Equation 7.2 to calculate the total post-tensioning force.

$$\Delta F_{pt} = \frac{\Delta l_{pt}}{L_{pt}} \cdot E_{pt} \cdot A_{pt} \tag{7.17}$$

The increase in PT force results in an elastic shortening of the beam (Δl_{beam}), Equation 7.18. This shortening is used in Equation 7.15.

$$\Delta l_{beam} = \frac{\Delta F_{pt} \cdot l}{EA} \tag{7.18}$$

7.3.2 Draped PT beam

The procedure to predict the behaviour of post-tensioned beams with draped tendons (Figure 7.13a) is very similar to beams with straight tendons. The procedure is split into the same five parts, only this time not the end rotations are calculated but deviator deflections as these result in tendon elongation. An extra iterative loop is added as beam deflections result in a change in angle of the post-tensioning force. An overview of the procedure is shown in Figure 7.13b.

Similar to beams with straight tendons, the assumption is made that the beam is loaded by two vertical point loads (at 1/3 and 2/3 of the beam length) in order to be able to compare the procedure with experimental results. Also the deviator location is fixed at 1/3 and 2/3 of the beam length. The procedure can be adapted for different loading configurations, like a distributed load. A flowchart with the equations for this scenario is shown in Appendix D.2.

Evaluation of forces The beam is loaded by a vertical force ($F_{vertical}$) which push the beam at two points each 1/3 from the end. The vertical force (F_v) at each point is given by equation 7.19.

$$F_v = \frac{F_{vertical}}{2} \tag{7.19}$$

The post-tensioning force (F_{pt}) is the initial post-tensioning force ($F_{pt,i}$) plus increase in force due to tendon elongation (ΔF_{pt}) from Equation 7.37.

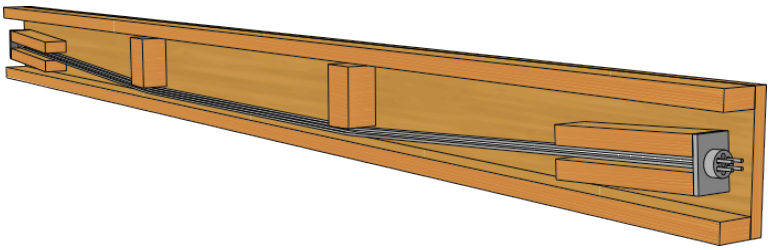

(a) Rendering of post-tensioned timber beam with draped tendons

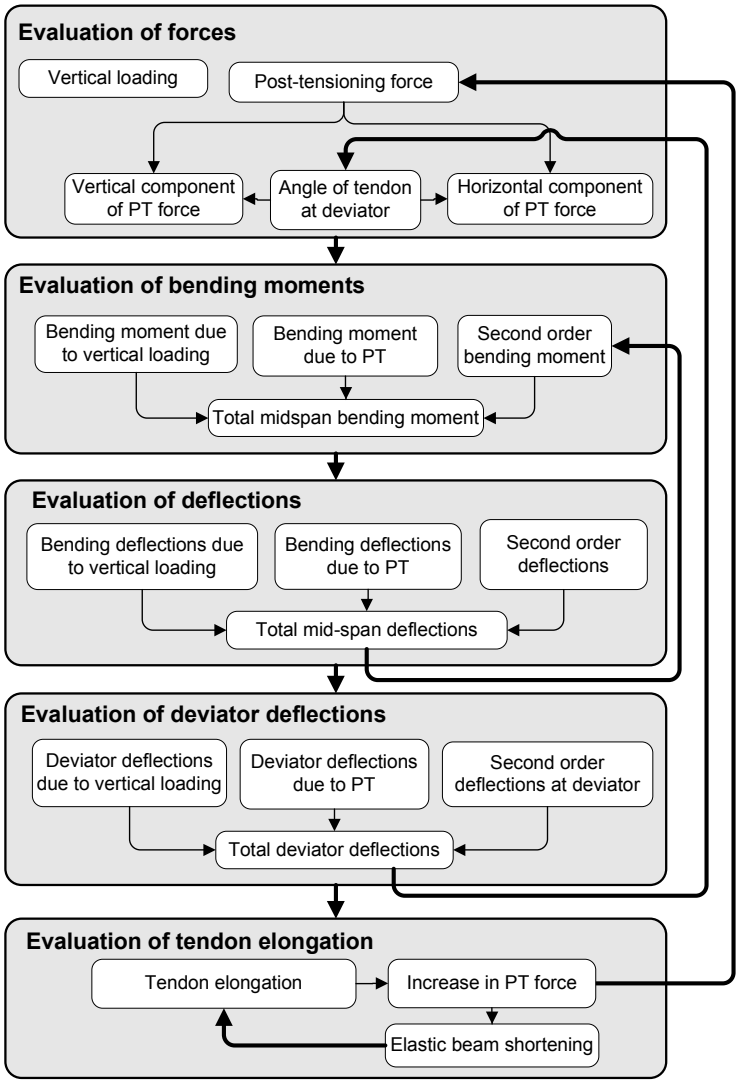

(b) Flowchart for analytical design of PT timber beams with draped tendons

Figure 7.13: Analytical design procedure for PT timber beams with draped tendons

$$F_{pt} = F_{pt,i} + \Delta F_{pt} \tag{7.20}$$

The post-tensioning tendon has got an angle (α) which is given by the distance to the deviator ($l/3$) and the eccentricity of the deviator plus the deflection at the location of the deviator, as shown in Equation 7.21.

$$\alpha = \frac{e + u_{dev,tot}}{l/3} \tag{7.21}$$

This angle gives a horizontal compression force ($F_{pt,h}$) and a (negative) vertical uplift force ($F_{pt,v}$) at deviator locations, as given by Equations 7.22 and 7.23.

$$F_{pt,h} = F_{pt} \cdot \cos\alpha \tag{7.22}$$

$$F_{pt,v} = -F_{pt} \cdot \sin\alpha \tag{7.23}$$

Evaluation of bending moments Three different loading contributions result in bending moments in the beam (Figure 7.14): vertical loading, post-tensioning and second order effects.

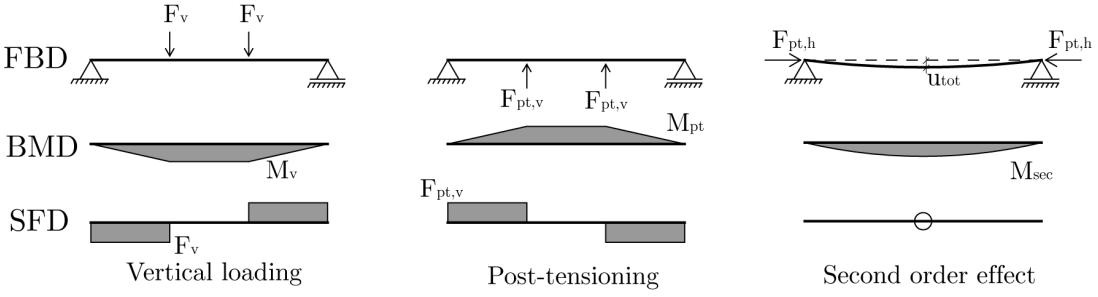

Figure 7.14: Free body diagram (FBD), bending moment diagram (BMD) and shear force diagram (SFD) for post-tensioned timber beam with draped tendons

The vertical loading results in a bending moment (M_v) in the mid section of the beam, as given by Equation 7.24.

$$M_v = F_v \cdot \frac{l}{3} \tag{7.24}$$

The vertical uplift force at the deviator results in a bending moment (M_{pt}) in the mid section of the beam given by Equation 7.25.

$$M_{pt} = F_{pt,v} \cdot \frac{l}{3} \tag{7.25}$$

The beam deflections (u_{tot}) result in a second order bending moment (M_{sec}), which is assumed to have a parabolic distribution with a maximum in the middle of the beam, as given by Equation 7.26.

$$M_{sec} = F_{pt} \cdot u_{tot} \tag{7.26}$$

The total mid-span bending moment (M_{mid}) is found by adding Equations 7.24, 7.25 and 7.26, as shown in Equation 7.27.

$$M_{mid} = M_v + M_{pt} + M_{sec} \tag{7.27}$$

Evaluation of deflections Vertical loading results in bending ($u_{v,bend}$) and shear ($u_{v,shear}$) deformation. Mid-span deflections are derived in Equation D.9, which is repeated here as Equation 7.28.

$$u_v = u_{v,bend} + u_{v,shear} = \frac{23}{216}\frac{M_v \cdot l^2}{EI} + \frac{F_v \cdot l}{3 \cdot GA_s} \tag{7.28}$$

The vertical uplift due to the post-tensioning also results in bending and shear deformation (u_{pt}), as given by Equation 7.29.

$$u_{pt} = \frac{23}{216}\frac{M_{pt} \cdot l^2}{EI} + \frac{F_{pt,v} \cdot l}{3 \cdot GA_s} \tag{7.29}$$

The second order bending moment results in second order deflections (u_{sec}) as given by Equation 7.30.

$$u_{sec} = \frac{5}{48} \cdot \frac{M_{sec} \cdot l^2}{EI} \tag{7.30}$$

Total mid-span deflection is given by adding the previous three deflections;

Equations 7.28, 7.29 and 7.30, as shown by Equation 7.31.

$$u_{tot} = u_v + u_{pt} + u_{sec} \tag{7.31}$$

Evaluation of deviator deflections The deflections at the deviator need to be known in order to accurately calculate the tendon elongation. Shear deformations at the deviator is the same as for mid-span, since there is no shear force between deviator and mid-span. Deviator deflections due to vertical loading ($u_{dev,v}$) are derived in Equation D.11 and repeated here as Equation 7.32.

$$u_{dev,v} = \frac{5}{54} \cdot \frac{M_v \cdot l^2}{EI} + \frac{F_v \cdot l}{3 \cdot GA_s} \tag{7.32}$$

Uplift of the deviator due to vertical forces of the post-tensioning tendons ($u_{dev,pt}$) are shown in Equation 7.33.

$$u_{dev,pt} = \frac{5}{54} \cdot \frac{M_{pt} \cdot l^2}{EI} + \frac{F_v \cdot l}{3 \cdot GA_s} \tag{7.33}$$

Second order bending deformations at the location of the deviator are derived in Equation D.17 and repeated here as Equation 7.34.

$$u_{dev,sec} = \frac{22}{243} \cdot \frac{M_{sec} \cdot l^2}{EI} \tag{7.34}$$

Total deformation at location of deviator is the summation of the above three deformations, Equations 7.32, 7.33 and 7.34, and is shown in Equation 7.35.

$$u_{dev,tot} = u_{dev,v} + u_{dev,v} + u_{dev,sec} \tag{7.35}$$

Evaluation of tendon elongation Tendon elongation (Figure 7.15) is calculated by evaluating the new tendon length using the Pythagorean Theorem and subtracting the original tendon length. This is multiplied by two (both sides of the beam) and the elastic shortening of the beam is subtracted, as shown in Equation 7.36. Also initial shortening of the tendon during stressing (Δl_i) needs to be subtracted from the total tendon elongation.

$$\Delta l_{pt} = 2 \cdot \left(\sqrt{(l/3)^2 + (e + u_{dev,tot})^2} - \sqrt{(l/3)^2 + e^2} \right) - \Delta l_{beam} - \Delta l_i \tag{7.36}$$

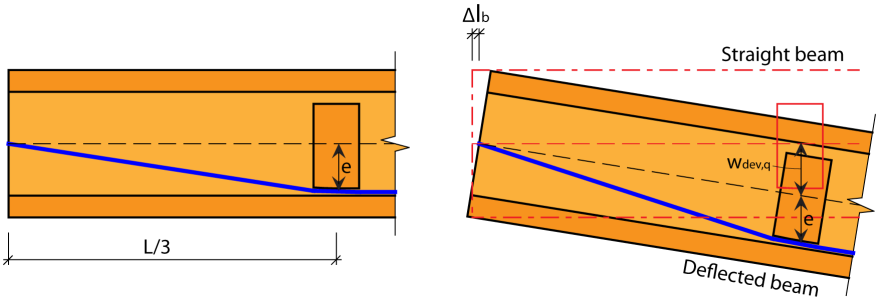

Figure 7.15: Tendon elongation for beam with draped tendons

The increase in length results in an increase of post-tensioning force (ΔF_{pt}), shown in Equation 7.37. This increase is used in the Equation 7.20 to calculate the total post-tensioning force.

$$\Delta F_{pt} = \frac{\Delta l_{pt}}{L_{pt}} \cdot E_{pt} \cdot A_{pt} \tag{7.37}$$

The increase in PT force results in an elastic shortening of the beam (Δl_{beam}), Equation 7.38. This shortening is used in Equation 7.36.

$$\Delta l_{beam} = \frac{\Delta F_{pt} \cdot l}{EA} \tag{7.38}$$

7.3.3 Input parameters

The analytical models presented in the previous two sections have been implemented in Excel for the four beams used for experimental testing. Parameters of each beam used for the implementation are shown in Table 7.2. Iterative calculations had to be turned on in Excel in order to handle the iterative steps. The vertical force on the four beams was varied in steps of 20kN ranging from 0kN up to the failure load of the beam.

7.3.4 Results

Table 7.3 shows the results of the analytical procedure for Beam 1 (benchmark beam without PT) at failure and for Beam 2 (with straight PT) after stressing and at failure. Table 7.4 shows the results after stressing and at failure for Beam 3 (with draped PT) and Beam 4 (with draped PT and double top flange).

Table 7.2: Parameters for implementation of analytical models

Parameter	Sym.	Unit	Beam			
			1	2	3	4
Moment of Inertia	I	mm^4	1.07E+10	6.07E+09	6.07E+09	6.74E+09
Section modulus	Z	mm^3	2.82E+07	1.99E+07	1.99E+07	2.02E+07
Timber area	A	mm^2	149760	1.31E+05	1.31E+05	1.58E+05
Shear area	A_s	mm^2	74354	59752	59752	57198
Modulus of Elasticity	E	MPa	10700	10900	11200	11400
Shear modulus	G	MPa	684	631	703	757
Beam length	l	mm	9144	9144	9144	9144
Tendon length	L_{pt}	mm	-	9144	9155	9162
Initial PT force	$F_{pt,i}$	kN	-	878	898	872
Eccentricity of PT	e	mm	-	161	185	215
Modulus of Elasticity PT	E_{pt}	MPa	-	200000	200000	200000
Area of PT	A_{pt}	mm^2	-	693	693	693
Initial tendon shortening	Δl_i	mm	-	3.56	2.57	3.06

Table 7.3: Analytical model data for Beams 1 and 2 after stressing and at failure

Parameter	Unit	Beam 1	Beam 2	
		At failure	After stressing	At failure
$F_{vertical}$	kN	700	0	540
F_v	kN	350	0	270
F_{pt}	kN	-	878	1076
M_v	kNm	1067	0	823
M_{pt}	kNm	-	-141	-173
M_{sec}	kNm	-	-22	132
M_{mid}	kNm	1067	-164	782
u_{mid}	mm	103.9	0.0	132.6
u_{pt}	mm	-	-22.3	-27.4
u_{sec}	mm	-	-2.9	17.4
u_{tot}	mm	103.9	-25.2	122.6
θ_v	mrad	28.4	0.0	37.9
θ_{pt}	mrad	-	-9.8	-12
θ_{sec}	mrad	-	-1.3	7.6
θ_{end}	mrad	28.4	-11.0	33.5
Δ l_{pt}	mm	-	0.0	13.1
Δ F_{pt}	kN	-	0	198
Δ l_{beam}	mm	-	0.0	1.3

Table 7.4: Analytical model data for Beams 3 and 4 after stressing and at failure

Parameter	Unit	Beam 3		Beam 4	
		After stressing	At failure	After stressing	At failure
$F_{vertical}$	kN	0	720	0	840
F_v	kN	0	360	0	420
F_{pt}	kN	898	1196	872	1230
α	mrad	53	100	63	111
$F_{pt,h}$	kN	897	1190	870	1222
$F_{pt,v}$	kN	-48	-119	-55	-136
M_v	kNm	0	1097	0	1280
M_{pt}	kNm	-146	-363	-167	-416
M_{sec}	kNm	-23	160	-22	171
M_{mid}	kNm	-169	897	-190	1035
u_v	mm	0.0	169.8	0.0	178.0
u_{pt}	mm	-22.6	-56.2	-23.3	-57.8
u_{sec}	mm	-2.9	20.5	-2.5	19.3
u_{tot}	mm	-25.5	134.1	-25.8	139.5
$u_{dev,v}$	mm	0.0	151.1	0.0	158.6
$u_{dev,pt}$	mm	-20.1	-50.0	-20.7	-51.6
$u_{dev,sec}$	mm	-2.5	17.8	-2.2	16.8
$u_{dev,tot}$	mm	-22.6	118.9	-23.0	123.9
$\Delta\ l_{pt}$	mm	0.0	19.7	0.0	23.7
$\Delta\ F_{pt}$	kN	0	298	0	358
$\Delta\ l_{beam}$	mm	0.0	1.9	0.0	1.8

A detailed analysis of mid-span bending moments at failure is shown in Table 7.5 for all four beams. For Beam 1 it is obvious that the bending moment due to vertical loading (M_v) is 100% of the total bending moment. For Beam 2 the contribution of vertical loading is only 5% more than the total bending moment. The bending moment due to post-tensioning and second order effects are almost balancing each other. Whereas for Beam 3 and Beam 4 the moment due to vertical loading is 22% - 24% more than the total bending moment, and the post-tensioning reduces the total bending by 40%. The second order bending moment is constant at 17 to 18%. A similar analysis is made for deflection components, as is shown in Table 7.6. Similar trends as for the bending moments are shown. Straight tendons reduced deflections by 22% and draped tendons with 41 to 42%. This improved performance of beams with draped tendons is due to tendon elongation and an increase in angle of tendons at the deviators,

which almost doubled for Beams 3 and 4. This combination lead to a 2.5 times increase in vertical uplift force at the deviator under ultimate load. Second order deflections were between 14 and 15% of the total mid-span deflections.

Table 7.5: Analysis of bending moment components (in kN) for the four beams

Bending moment contribution	Beam			
	1	2	3	4
M_{mid}	1067	782	897	1035
M_v	1067	823	1097	1280
M_v/M_{mid}	*100%*	*105%*	*122%*	*124%*
M_{pt}	0	-173	-363	-416
M_{pt}/M_{mid}	*0%*	*-22%*	*-40%*	*-40%*
M_{sec}	0	132	160	171
M_{sec}/M_{mid}	*0%*	*17%*	*18%*	*17%*

Table 7.6: Analysis of deflection components (in mm) for the four beams

Deflection contributions	Beam			
	1	2	3	4
u_{tot}	103.9	122.6	134.1	139.5
u_v	103.9	132.6	169.8	178.0
u_v/u_{tot}	*100%*	*108%*	*127%*	*128%*
u_{pt}	0	-27.4	-56.2	-57.8
u_{pt}/u_{tot}	*0%*	*-22%*	*-42%*	*-41%*
u_{sec}	0	17.4	20.5	19.3
u_{sec}/u_{tot}	*0%*	*14%*	*15%*	*14%*

7.4 Comparison of models

This section compares results of experimental testing with results of numerical and analytical models. Experimental testing results were presented in Chapter 4. The numerical modelling using Abaqus is described in Section 7.2 and the analytical model in section 7.3.

Figure 7.16 shows the total vertical load on the beam versus the mid-span displacement for all four beams. The stiffness (slope of the load-displacement graph, in kN/mm) for each of the models is shown in Table 7.7. It can be seen that for Beam 1 the three different models give very similar results, with a maximum difference of 1.3%. For Beam 2 the FEM model predicts a 9.5% higher stiffness and analytical model a 8.5% lower stiffness compared to experimental testing. Numerical and analytical results for Beam 3 have a stiffness of between 10% and 12% lower compared to experimental testing. The two FEM data curves represent the two different timber material models, the FEM curve has a linear elastic material model, whereas the FEM-NL curve has a non-linear material model which captures compression failure. It can be seen that the behaviour close to failure is captured better by the FEM-NL model compared to the linear FEM model, but the vertical load is slightly under-predicted. The stiffness of Beam 4 (with the double top flange) is underpredicted by both models by about 10%.

Table 7.7: Stiffness values (kN/mm) of four beams based on experimental testing, numerical and analytical models. Percentages show the difference between model and experimental data

Model	Beam			
	1	2	3	4
Experimental	6.76	3.99	5.13	5.68
Numerical (FEM)	6.85	4.37	4.6	5.18
	1.3%	*9.5%*	*-10.3%*	*-8.8%*
Analytical	6.74	3.65	4.51	5.08
	-0.3%	*-8.5%*	*-12.1%*	*-10.6%*

A comparison of rotations at the end of the beam different models is shown in Figure 7.17. Only results for Beam 1 and Beam 2 are shown. For Beam 1 both models, analytical and numerical, compare very will with experimental testing

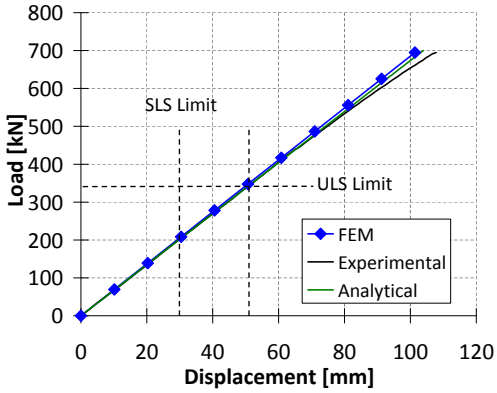

(a) Beam 1 - Benchmark

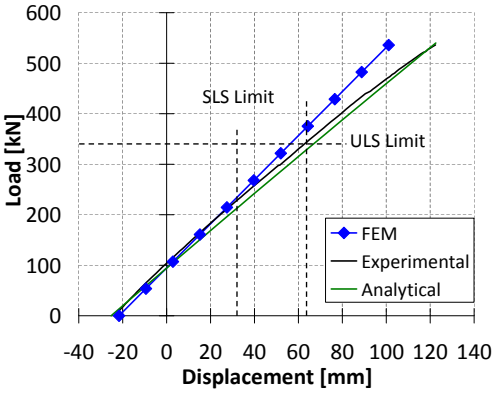

(b) Beam 2 - Straight PT

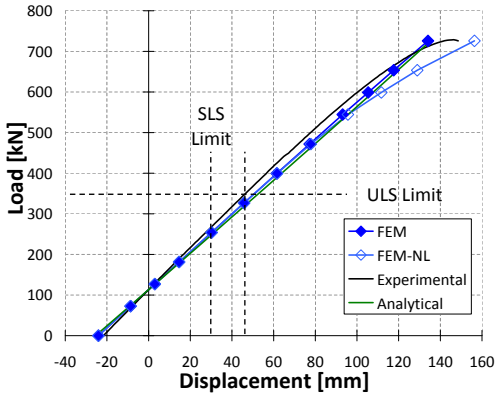

(c) Beam 3 - Draped PT

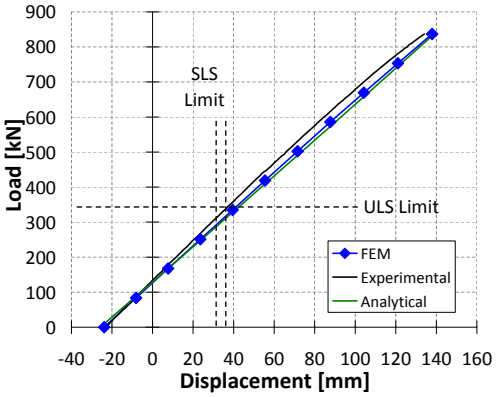

(d) Beam 4 - Draped PT (2)

Figure 7.16: Comparison of experimental, analytical and numerical data for vertical load versus mid-span displacement, FEM-NL is finite element model with non-linear material properties

results. For Beam 2, with straight tendons where rotations influence tendon elongation, the analytical model is over predicting the rotations whereas the FEM model is under predicting the rotations. The difference at failure is 12% for the analytical model and 18% for the FEM model.

Post-tensioning force from the different models is compared in Figure 7.18. The initial post-tensioning force is an input for the analytical and numerical model and is thus an exact match with the experimental data. During the initial loading of the beam the analytical and FEM model follow experimental data very closely. Although under larger displacements both models over predict the post-tensioning force. Beam shortening due to increase in post-tensioning

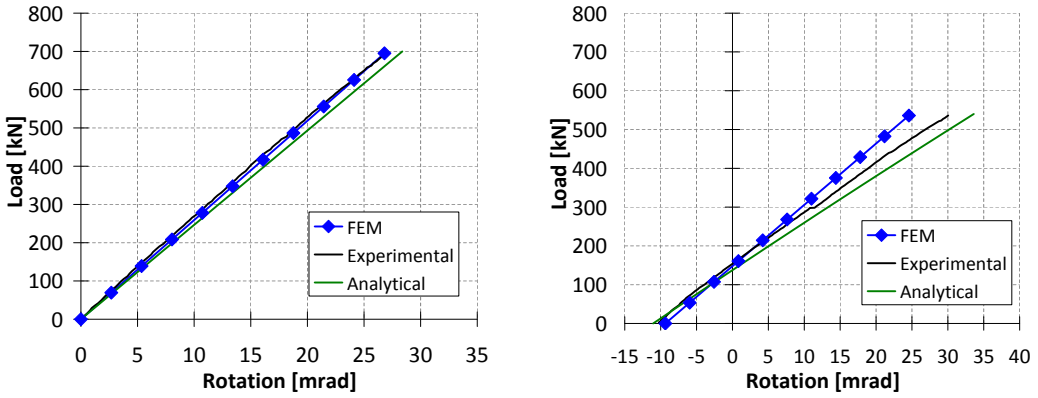

(a) Beam 1 - Benchmark (b) Beam 2 - Straight PT

Figure 7.17: Comparison of experimental, analytical and numerical data for rotations at beam ends

force is taken into account in both models. But other aspects, like settlement of anchorages and local indentation of deviators is not taken into account in the models. On the other hand experimental testing had a load-cell in the system which resulted in an increased tendon length and additional components which might have reduced tendon elongation. For design limits, which at SLS condition is 30mm deflection and at ULS condition is at a vertical load of 340kN, the difference between the models and experimental testing is small. The FEM model comes close to the experimental data as tendons reach yielding. Yielding of the tendons is not included in the analytical model and a very large difference in post-tensioning force is shown. This is not so much an issue as for a design of a building tendons should be prevented from yielding.

Mid-span bending moments for the different models and experimental testing are compared in Figure 7.19. Bending moments from experimental testing are taken based on readings from strain gauges at mid-span. It can be seen that the results for Beam 1 are matching experimental testing data very well. For Beam 2 the analytical model is an almost perfect fit with experimental data whereas the FEM follows experimental data very closely, but it under estimates the both bending moments and displacement under maximum load. For Beam 3 the analytical model and FEM show a small difference with experimental data, and at failure the difference increases. The non-linear finite element model (FEM-

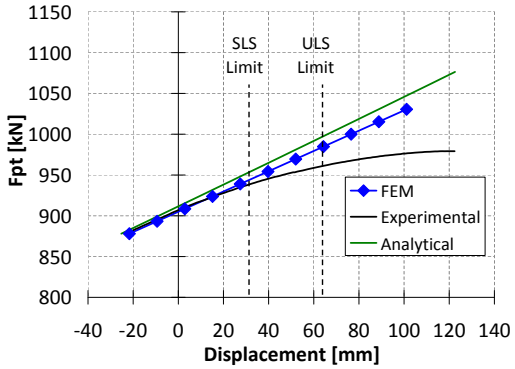

(a) Beam 2 - Straight PT

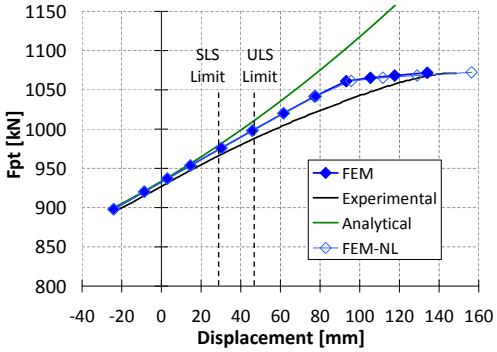

(b) Beam 3 - Draped PT

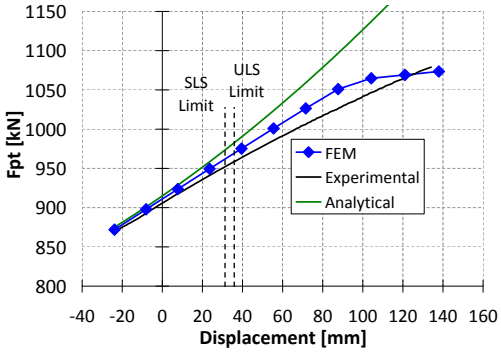

(c) Beam 4 - Draped PT (2)

Figure 7.18: Comparison of experimental, analytical and numerical data for post-tensioning force

NL) captures the increased displacements better, but over predicts the bending moments. This difference is because in experimental testing plastic deformation only occurred close to one of the loading plate and not at mid-span, whereas the FEM model showed plastic behaviour at mid-span. Also the assumed symmetry in the FEM was not valid any more as plasticity occurred only on one side during experimental testing. For Beam 4 (with double to flange) both models slightly over estimate the bending moments at mid-span, which makes for a conservative design.

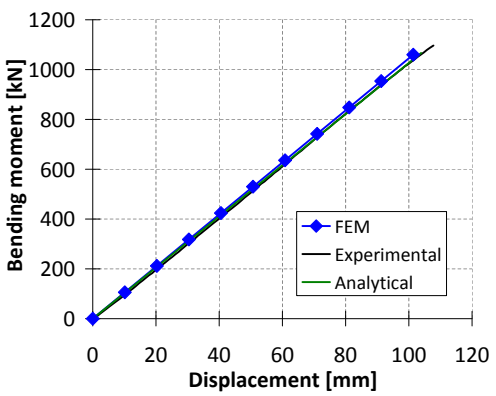

(a) Beam 1 - Benchmark

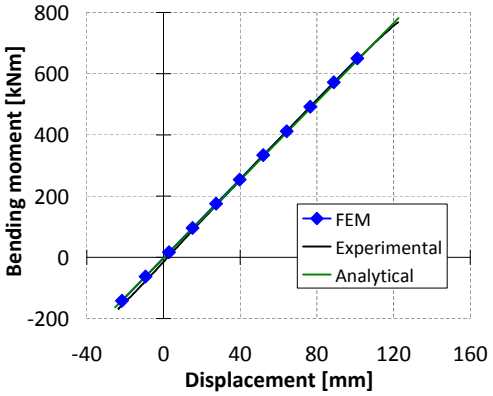

(b) Beam 2 - Straight PT

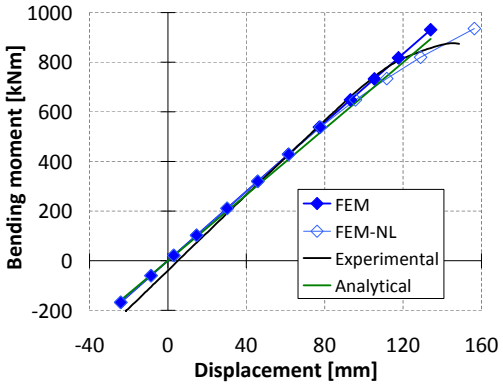

(c) Beam 3 - Draped PT

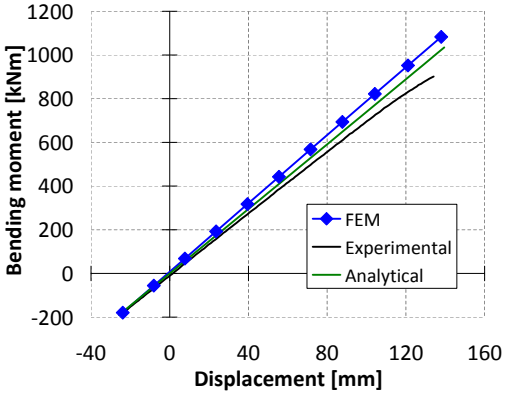

(d) Beam 4 - Draped PT (2)

Figure 7.19: Comparison of experimental, analytical and numerical data for mid-span bending moments

7.5 Failure criteria

This section evaluates two different methods to predict the failure load of post-tensioned timber beams. The first method is based on the combined axial force and bending, as currently in the New Zealand timber design standard, NZS 3603:1993 (Standards New Zealand, 1993). The second method is based on a stress based approach as described in the European timber design standard Eurocode 5 (EC5), 1995-1-1:2004+AC+A1 (CEN, 2004b).

7.5.1 Combined axial force and bending

The first possible design procedure is based on the current New Zealand timber design standard NZS 3603:1993 (Standards New Zealand, 1993), which specifies to check the combination of axial force and bending through Equation 7.39. In this equation the ultimate post-tensioning force in the beam equals design compression force (N^*). Design capacity in compression (ϕN_n) and bending (ϕM_n) are known, based on section size and material properties. Strength reduction factors for load duration and material variability (ϕ) have been taken as 1 in order to get an estimation of the actual failure load. The ratio of design force over design capacity ($N^*/\phi N_n$) can be calculated. Based on Equation 7.40 the design bending moment (M^*_{NZS}) can be calculated. This process for each beam is shown in Table 7.8.

$$\frac{N^*}{\phi N_n} + \frac{M^*_{NZS}}{\phi M_n} \leq 1 \tag{7.39}$$

$$M^*_{NZS} \leq \left(1 - \frac{N^*}{\phi N_n}\right) \cdot \phi M_n \tag{7.40}$$

Table 7.8: Design process according to combined axial force and bending moment

Beam	Type	N^* (kN)	N_n (kN)	$\frac{N^*}{N_n}$ (-)	$\frac{M^*}{M_n}$ (-)	M_n (kNm)	M^*_{NZS} (kNm)
1	Benchmark	0	6739	0.00	1.00	947	947
2	Straight PT	979	5889	0.17	0.83	694	579
3	Draped PT	1071	5889	0.18	0.82	694	568
4	Draped PT 2	1080	7104	0.15	0.85	703	596

The design bending moment in the beam consists of three parts, as shown in Section 7.3: moment due to loading on the beam (M_v), moment due to second order effects (M_{sec}) and moment due to post-tensioning (M_{pt}). The moment due to post-tensioning is negative, as this increases load-carrying capacity of the beam. Using the analytical design procedure as described in Section 7.3, the different moment contributions can be calculated. Then, the moment due to vertical loading can be divided by 1/3rd the length of beam and multiplied by two in order to find the total vertical load ($F_{vertical}$) which can be designed for. The vertical load at failure ($F_{failure}$) can be divided by design vertical load in order to find the factor of safety (F.o.S.) of the beam. This process is shown in Table 7.9.

Table 7.9: Design process according to combined axial force and bending moment (continued)

Beam	M^*_{NZS} (kNm)	M_{sec} (kNm)	M_{pt} (kNm)	M_v (kNm)	$F_{vertical}$ (kN)	$F_{failure}$ (kN)	F.o.S. (-)
1	947	0	0	947	621	695	1.12
2	579	94	-166	651	427	-	-
3	568	93	-283	758	497	571 (726)	1.15 (1.46)
4	596	87	-309	818	537	837	1.56

The design load and displacement can be plotted on the load-displacement graph which was already shown in Section 4.4.3. The resulting plot is shown in Figure 7.20. The design strength of the benchmark beam is close to failure strength (12% difference). Beam 2, with straight post-tensioning, failed prematurely due to shear and conclusions can not be drawn as the ultimate failure strength in bending is not known. But for Beams 3 and 4, with draped tendons, the actual failure strength is 46% to 56% higher than the design strength. This leads to a very conservative design. For the benchmark beam, the factors of safety are much lower, leading to a disadvantage for post-tensioning in the design process. Alternatively it can be concluded that the load carrying capacity of timber box beams without post-tensioning is over predicted by the design standard.

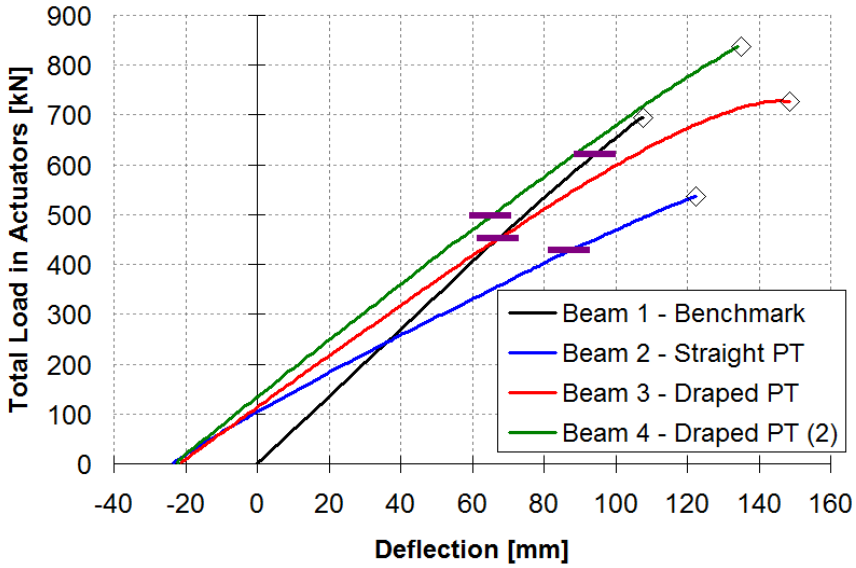

Figure 7.20: Load displacement graph with design strength indicated by horizontal lines

7.5.2 Stress based approach

The Eurocode 5 (EC5), EN 1995:2004 (CEN, 2004b), presents design equations for box beams, which are based on the tensile, compression and bending strength (Figure 7.21). The standard takes into account the possible difference in material between flanges and webs, but for LVL box beams this is not required. The method provides a prediction of the failure mechanism which will occur (tension or compression). The four design checks are:

1. Bending stress at top of beam $\leq$ bending capacity;
   $\sigma_{f,c,max} \leq f_m$
2. Compression stress at centre of top flange $\leq$ compression capacity;
   $\sigma_{f,c} \leq k_c \cdot f_{c,0}$
3. Tensile stress at centre of bottom flange $\leq$ tensile capacity;
   $\sigma_{f,t} \leq f_{t,0}$
4. Bending stress at bottom of beam $\leq$ bending capacity;
   $\sigma_{f,t,max} \leq f_m$

The design compression strength of LVL used in experimental testing was specified as 45MPa, bending strength as 48MPa and tensile strength as 30MPa.

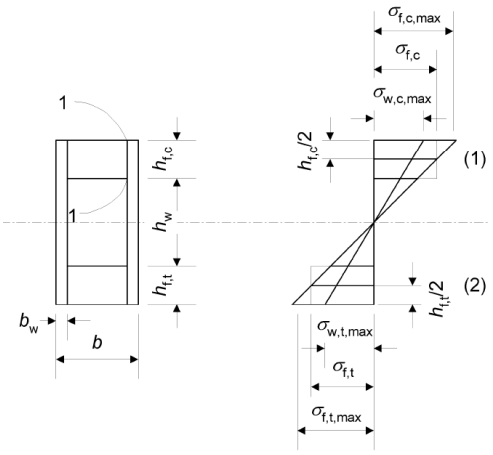

Figure 7.21: Nomenclature of strength check according to EC5 (CEN, 2004b)

Although strength values for bending and tension depend on section size and should be corrected with a size factor. Size factors (k_{24}) are specified by the manufacturer Nelson Pine Industries Limited (2010) as in Equations 7.41 and 7.42 for bending and tension, respectively. In these equations d equals the largest dimension of the section in bending or tension. For the box beams the largest dimension in bending is the height of the section and the largest dimension in tension is width of the section. The resulting design strength values for beams 1 to 4 are shown in Table 7.10.

$$k_{24,bending} = \left(\frac{95}{d}\right)^{0.167} \tag{7.41}$$

$$k_{24,tension} = \left(\frac{150}{d}\right)^{0.167} \tag{7.42}$$

Table 7.10: Characteristic strength values (MPa) for Beams 1 to 4

Beam	f_c	f_b	f_t
1	45.0	33.9	25.2
2	45.0	35.2	25.2
3	45.0	35.2	25.2
4	45.0	35.2	25.2

At failure the post-tensioning force ($F_{pt,failure}$) is known and the compressive stress (σ_c) due to post-tensioning can be calculated. For a chosen design bending moment (M^*_{EC5}, chosen such that one of the unity checks reached a value of 1.0) the maximum bending stress at top and bottom of the beam ($\sigma_{b,max}$) can be calculated. And based on the distance between centroid of the beam and centre of top and bottom flanges (y) the bending stress at the centre of the flanges (σ_b) can also be evaluated. The values resulting from this process are shown in Table 7.11.

Table 7.11: Results of design process according to EC5

Beam	$F_{pt,failure}$	σ_c	M^*_{EC5}	$\sigma_{b,max}$ (MPa)		y (mm)		σ_b (MPa)	
				Top	Bot.	Top	Bot.	Top	Bot.
1	0	0.0	804	-28.5	28.5	335	335	-25.2	25.2
2	979	-7.5	551	-27.7	27.7	260	260	-23.6	23.6
3	1071	-8.2	537	-27.0	27.0	260	260	-23.0	23.0
4	1080	-6.8	693	-28.4	32.0	186	289	-19.1	29.7

The combined stress due to axial load (post-tensioning) and bending moment at the outer fibres and at centre of top and bottom flanges is calculated in Table 7.12. The full stress profiles are shown in Figure 7.22. The four design checks are converted to unity checks, which should be smaller than 1 for a safe design, and are shown in the second part of Table 7.12. The design bending moment (M^*_{EC5}) has been chosen such that one of the unity checks reached a value of 1.0. The resulting bending moment is the design bending moment according to EC5 design checks.

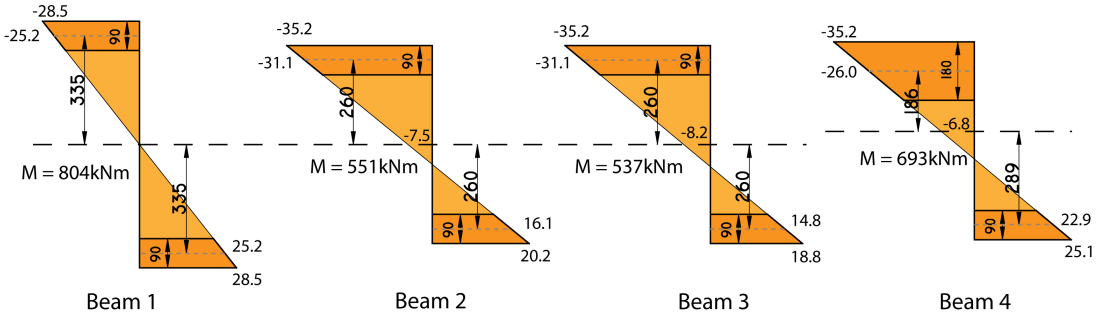

Figure 7.22: Stress profiles based on design according to EC5

Table 7.12: Results of design process according to EC5 (continued), UC = unity check, which is stress divided by strength

Beam	Combined stress in cross-section				UC			
	$\sigma_{f,c,max}$	$\sigma_{f,c}$	$\sigma_{f,t}$	$\sigma_{f,t,max}$	$\frac{\sigma_{f,c,max}}{f_b}$	$\frac{\sigma_{f,c}}{f_c}$	$\frac{\sigma_{f,t}}{f_t}$	$\frac{\sigma_{f,t,max}}{f_b}$
1	-28.5	-25.2	25.2	28.5	0.84	0.56	1.00	0.84
2	-35.2	-31.1	16.1	20.2	1.00	0.69	0.64	0.57
3	-35.2	-31.3	14.8	18.8	1.00	0.69	0.59	0.53
4	-35.2	-26.0	22.9	25.1	1.00	0.58	0.91	0.71

Similar to design according to NZS, the design bending moment can be split in the three different components. Based on the bending moment due to vertical load, the vertical load itself can be calculated. This can be compared with the failure load on the beam in order to determine the factor of safety (F.o.S.). The result of this process is shown in Table 7.13.

Table 7.13: Results of design process according to EC5 (continued 2), showing vertical design and failure load and resulting factor of safety. Values in brackets show bending/tensile failure for beam 3

Beam	M^*_{EC5} (kNm)	M_{sec} (kNm)	M_{pt} (kNm)	M_v (kNm)	$F_{vertical}$ (kN)	$F_{failure}$ (kN)	F.o.S. (-)
1	804	0	0	804	528	695	1.32
2	551	89	-165	627	411	-	-
3	537	87	-276	726	476	571 (726)	1.20 (1.53)
4	693	104	-331	920	604	837	1.39

7.5.3 Comparison

Bending moments at failure from experimental testing can be compared with bending moment design based on the two methods described in the previous sections. This comparison is made in Table 7.14. Beam 1 failed at a bending moment of 1083kNm, the NZS prediction was 947kNm which is 87% of the failure moment and EC5 prediction 804kNm which is 74% of failure load. A clear difference between the two design codes can be seen. For Beam 2 the maximum

bending moment capacity was unknown, as shear failure occured. But it can be seen that NZS and EC5 predictions are close. Beam 3 showed a compression failure at approximately 660kNm bending moment and tension failure at 874kNm. This was 87% and 66% of the design bending moment according to NZS and 81% and 61% according to EC5. For Beam 4 the design values were 66% and 76% of the failure bending moment.

Table 7.15 shows a similar comparison but now based on vertical load carrying capacity. The percentages of design predictions of failure load over the actual failure load are very similar to similar percentages of bending moment comparison.

Table 7.14: Comparison between experimentally determined bending moment (kNm) at failure and predictions based on New Zealand timber design standard (NZS) and Eurocode 5 design standard (EC5)

Beam	$M_{failure}$	M^*_{NZS}		M^*_{EC5}	
1	1083	947	87%	804	74%
2	> 768	579	-	551	-
3 (compr.)	660	575	87%	537	81%
3 (tension)	874	575	66%	537	61%
4	909	604	66%	693	76%

Table 7.15: Comparison between experimentally determined load carrying capacity (kN) at failure and predictions based on New Zealand timber design standard (NZS) and Eurocode 5 design standard (EC5)

Beam	$F_{failure}$	$F_{vertical,NZS}$		$F_{vertical,EC5}$	
1	695	621	89%	528	76%
2	>579	427	-	411	-
3 (compr.)	571	497	87%	476	83%
3 (tension)	726	497	68%	476	66%
4	837	537	64%	604	72%

Predictions of bending moment capacity according to EC5 vary between 74% and 81% of the actual capacity. For predictions according to NZS the variation is between 66% and 87%. The main difference between the two design methods is the bending moment capacity of Beam 1 (without post-tensioning), which is

18% higher according to NZS compared to EC5. This difference is caused by the limited tensile capacity of the bottom flange, which is taken into account in the EC5 design but not in the NZS design. For Beam 2 and Beam 3 the predictions are very similar with variatons between 5% and 7%. For Beam 4 the NZS perdictions are 13% lower than the EC5 predictions. This is caused by the assymetric cross-section, which results in higher bending stresses according to NZS design.

Ignoring the tensile capacity of the bottom flange for no (or low levels of) post-tensioning can lead to an unconservative design. Therefore it is recommended to use the design equations given by EC5. For post-tensioning forces resulting in compression stresses in the range of 6MPa to 8MPa, the difference between NZS and EC5 is small and both design methods can be used.

7.6 Parameter study

This section describes a parameter study on beam performance. The following design checks are considered: bending strength, shear strength and long-term deflections. Short-term deflections checks have been ignored, as they did not govern any of the beam designs.

7.6.1 Parameters

Beam lengths in the range of 6m to 14m were considered. Beams shorter than 6m were deemed not necessary to post-tension and beams longer than 14m were deemed not realistic for commercial/office buildings. Post-tensioning force was varied by changing the compressive stress in the beam, ranging from 0MPa to 10MPa.

The material properties of LVL11 were used, as presented in Table 3.1. Loading on the beam was assumed to be an 8m timber-concrete composite floor with a self weight including services of $G = 3.7kPa$ and a variable loading of $Q = 3.0kPa$. This resulted in an ultimate limit state (ULS) load of $q_{uls} = 8m \cdot (1.2G + 1.5Q) = 8 \cdot (1.2 \cdot 3.7 + 1.5 \cdot 3.0) = 71.5kN/m$, and a long-term serviceability limit state (SLS) load of $q_{sls} = 8m \cdot (G + 0.4Q) = 8 \cdot (3.7 + 0.4 \cdot 3.0) = 39.2kN/m$

Straight and draped tendons were both considered. Although, after an initial comparison (Section 7.6.3) only draped tendons were used for a detailed parameter study. Firstly only symmetric box-sections were considered, with dimensions as shown in Figure 7.23.

7.6.2 Calculation model

Bending strength Bending strength was based on Eurocode 5 approach, which involves checking bending, compression and tensile stresses. This method is described in Section 7.5. The compressive forces due to post-tensioning and bending moments were calculated using the analytical procedure as outlined in Section 7.3. The procedure was slightly modified to change the loading from two point loads to a distributed load. A load duration factor for strength, k_1, of 0.8 was used for medium duration load. A strength reduction factor, ϕ, of 0.9 was used for LVL.

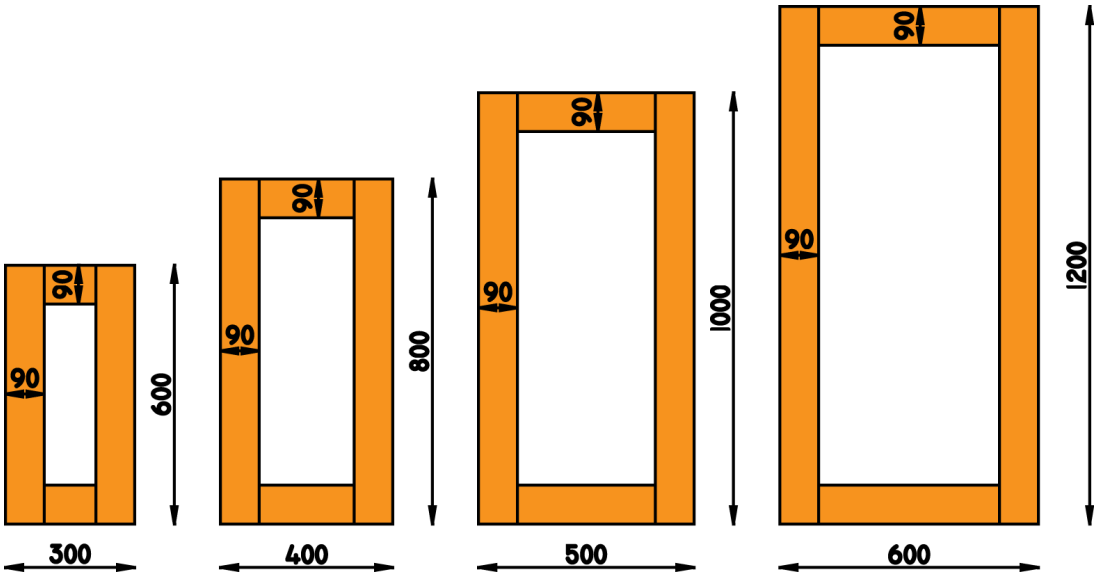

Figure 7.23: Beam sections used for parameter study

Shear strength Shear strength was based on design Equation 7.43.

$$V^* < \phi \cdot V_n = \phi \cdot k_1 \cdot f_s \cdot A_s \tag{7.43}$$

Where:

- V^* = Design shear force
- ϕ = Strength reduction factor (0.9)
- V_n = Shear capacity
- k_1 = Load duration factor for strength (0.8)
- f_s = Shear strength (6MPa)
- A_s = Shear area of cross-section

SLS design Serviceability limit state (SLS) design was performed based on long-term deflections. For this a creep factor of $k_2 = 2.0$ was used. Long-term deflections were calculated using Equation 7.44. A long-term post-tensioning loss of 20% was assumed in calculation of post-tensioning force.

$$u_{long} = k_2 \cdot (-u_{pt} + u_q + u_{sec}) \tag{7.44}$$

Where:

- u_{long} = Long-term mid-span deflections
- k_2 = Creep factor
- u_{pt} = Uplift due to post-tensioning
- u_q = Deflection due to distributed load
- u_{sec} = Second order deflections

The long-term deflections were limited to span over 300, based on recommendations for beam deflections in AS/NZS 1170.0:2002 (Standards New Zealand, 2002a). The unity check was calculated as long-term deflections divided by the deflection limit. If this ratio was smaller than 1, the design check was satisfied.

7.6.3 Results

Firstly one section size was chosen, 800mm high and 400mm wide. The post-tensioning force was fixed at 1100kN (6MPa compressive stress). The length of the beam was varied from 6 to 14 meters. The unity checks (design demand over section capacity) for bending, shear and deflections were calculated. This check needs to be smaller than 1.0 to allow for a safe design. The results for beams with straight tendons and draped tendons are plotted in Figure 7.24.

For beams with straight tendons it can be seen that up to a length of about 7.5m the design is governed by bending. For beams between 7.5 and 9m the design is governed by shear, although bending strength is very close. For beams of 9m or longer the design is clearly governed by deflections, with beam lengths of 9.5m and longer failing the deflection check. Also plotted in the figure is the bending check according to NZS 3603:1993 (NZS) (Standards New Zealand, 1993). It can be seen that this is very close to the Eurocode 5 (EC5) bending check.

For beams with draped tendons the design is governed by bending for a length up to 9m. For shorter lengths, this is for the load case of PT only (without vertical load), as the bending moment due to post-tensioning is larger than the moment due to vertical load. For a beam length over 9m the design is governed by deflection, with the design limit reached close to 10m. Comparing straight and draped tendons it can be seen that the reduction in shear is significant for beams with draped tendons. Bending checks are very similar and deflection checks are about 10% lower for beams with draped tendons.

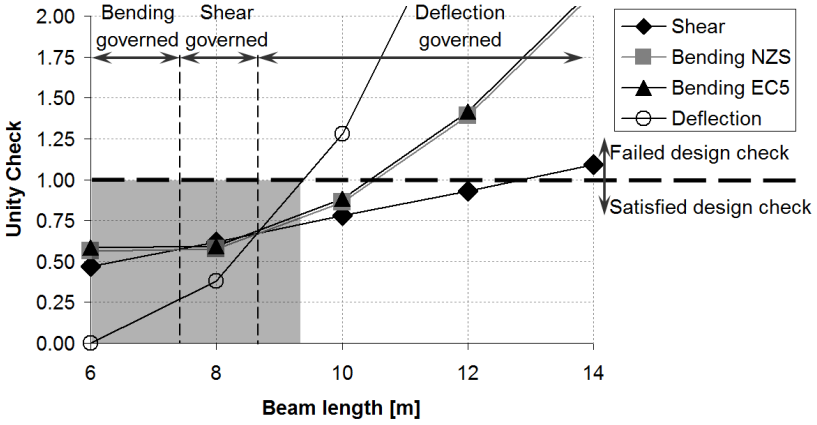

(a) Straight Tendons

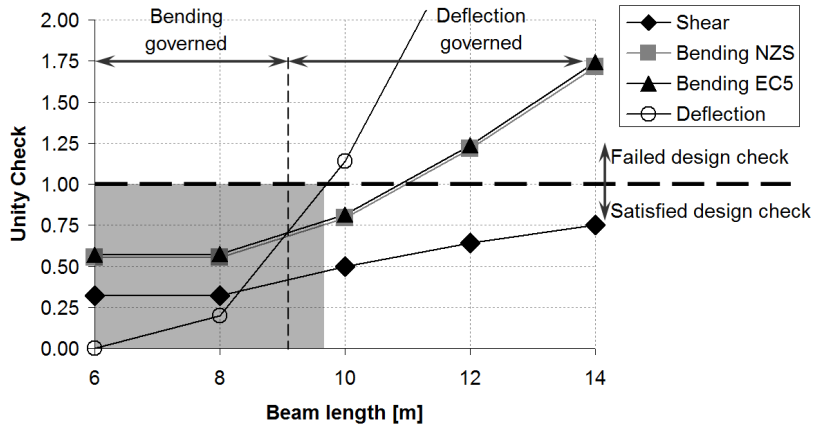

(b) Draped Tendons

Figure 7.24: Results of parameter study on beam length, showing unity checks (UC) for bending, shear and deflection

Secondly the same section was evaluated with a fixed length of 10m and the compressive stress due to post-tensioning force was varied between 0 and 10MPa. Again the unity checks for bending, shear and deflection were calculated. The results for beams with straight and draped tendons are shown in Figure 7.25.

For beams with straight tendons it can be seen that satisfactory beam design is only possible for a post-tensioning stress between 7 and 9MPa. For lower post-tensioning forces the design is strongly governed by deflections, and for higher post-tensioning forces the design is governed by bending. The design check for shear is constant, as straight post-tensioning does not influence shear force in

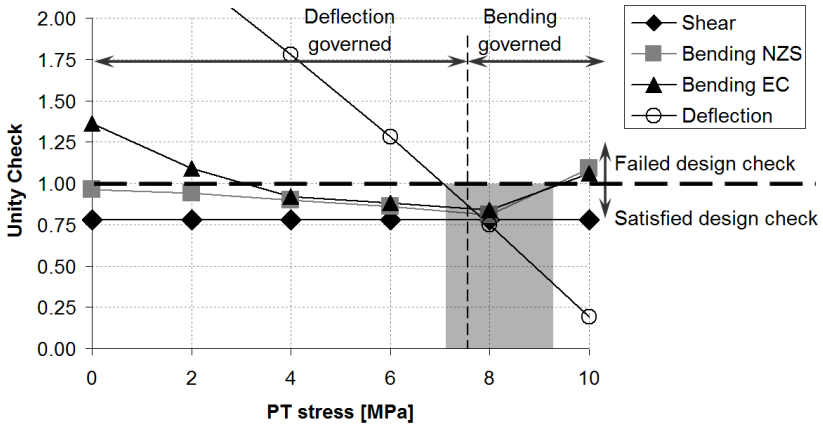

(a) Straight Tendons

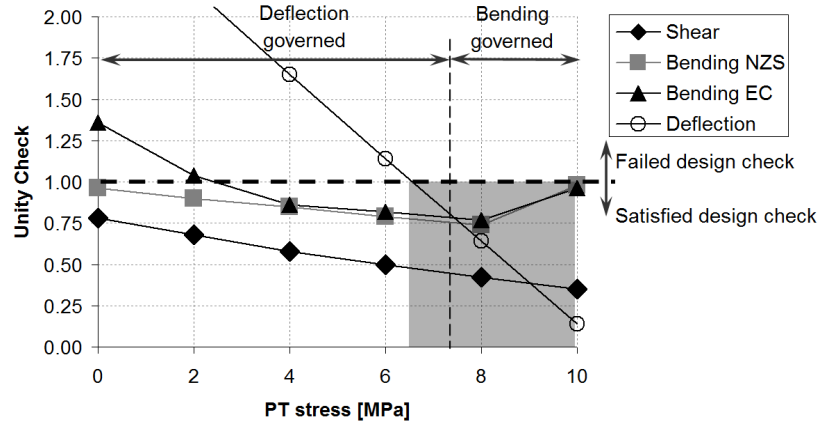

(b) Draped Tendons

Figure 7.25: Results of parameter study on post-tensioning force, showing unity checks (UC) for bending, shear and deflection

the beam. This time a difference between the bending check according to NZS and EC5 check can be seen for low levels of post-tensioning. This is due to the limited tensile capacity of the bottom flange, which is included in the EC5 checks. This is in line with earlier findings in Section 7.5.

For beams with draped tendons a satisfactory design is possible for post-tensioning forces with a stress between 6.5 and 10MPa, giving a larger range than beams with straight tendons. For post-tensioning forces lower than 7.5MPa long-term deflections govern the design for post-tensioning forces lower than 6.5MPa they fail the long-term deflection check. Shear strength check is decreasing as post-tensioning force increases, which is due to the increased uplift force at

the deviators. Based on comparisons between beams with straight and draped tendons it can be concluded that draped tendons are slightly more beneficial, as all design checks are lower. For the next steps in the parameter study only beams with draped tendons are therefore considered. Conclusions based on bending and deflections will be very similar for beams with straight tendons, but shear strength might influence the results.

Thirdly, the variation in length and post-tensioning force was combined and plotted in a three dimensional graph as shown in Figure 7.26. In this figure each unity check is represented by a plane instead of a line. The deflection plane is indicated by long dashed lines, the shear plane by continuous lines and the bending plane by dotted lines. The vertical axis shows the unity check values, which have been limited between 0 and 2, the colours give an extra indication of the unity check value. Also added are two grey planes which represent a constant length of 10m and a constant stress of 6MPa. Intersections of these planes with the unity check planes result in the previously shown Figures 7.24b and 7.25b.

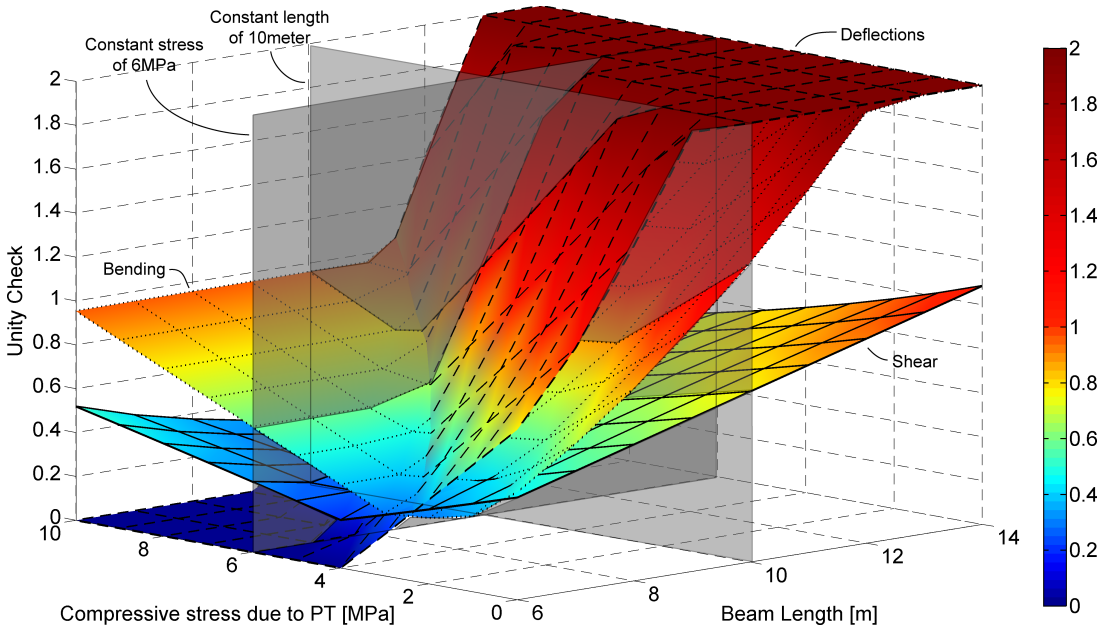

Figure 7.26: Results of parameter study on beam length and post-tensioning stress for 800x400mm section with draped tendons, showing unity checks for bending, shear and deflections

In this figure all combinations between beam length and post-tensioning force can be seen. For zero post-tensioning, which is the right front face, deflections govern the design and the design check fails for lengths longer than 6.5m. This is to be expected as for timber beam design long-term deflections are usually governing. For the maximum post-tensioning force of 10MPa, the design is governed by bending up to 11.5m length. For longer beams both bending and deflection unity checks become larger than 1. For short beam lengths and high post-tensioning forces the design is governed by bending, which is due to the post-tensioning only load case (bending moment due to post-tensioning alone is higher than bending under post-tensioning and ULS loading). For long beam lengths and low post-tensioning force deflections are governing the design. It can be seen that the plane for deflections is steeper compared to the planes for bending and shear, showing that deflections are most sensitive to changes in beam length and post-tensioning force.

Fourthly, the three dimensional view was changed to a plan view of the same graph. This plan view is shown in Figures 7.27 and 7.28 for the four different section sizes, as presented in Figure 7.23. In these figures bending governed regions are shown by dotted lines, deflection governed by dashed lines and shear governed by continuous lines. Furthermore, the area where the maximum unity check is larger than 1 is hatched with diagonal lines.

For a beam of 600x300mm only spans up to 7.5m are possible with post-tensioning ranging between 4 and 10MPa, for longer spans and lower post-tensioning stresses long-term deflections are too large. A beam of 800x400mm is possible for spans up to 11.5m, which has already been discussed earlier in this section. A beam of 1000x500mm is possible without post-tensioning for a length up to 8.5m and with post-tensioning up to 14m. For higher post-tensioning forces bending is the governing design check, and for lower post-tensioning forces deflections govern. Several combinations of short beams with low post-tensioning result in shear governing the design. A beam of 1200x600mm without post-tensioning is possible for a length up to 10.5m and with post-tensioning up to (and even past) 14m. For the higher range of post-tensioning forces, the design is governed by bending. This is caused by the post-tensioning only load-case, where the critical design check is under only post-tensioning load. For the largest section a post-tensioning compressive stress of 10MPa does not longer satisfy the

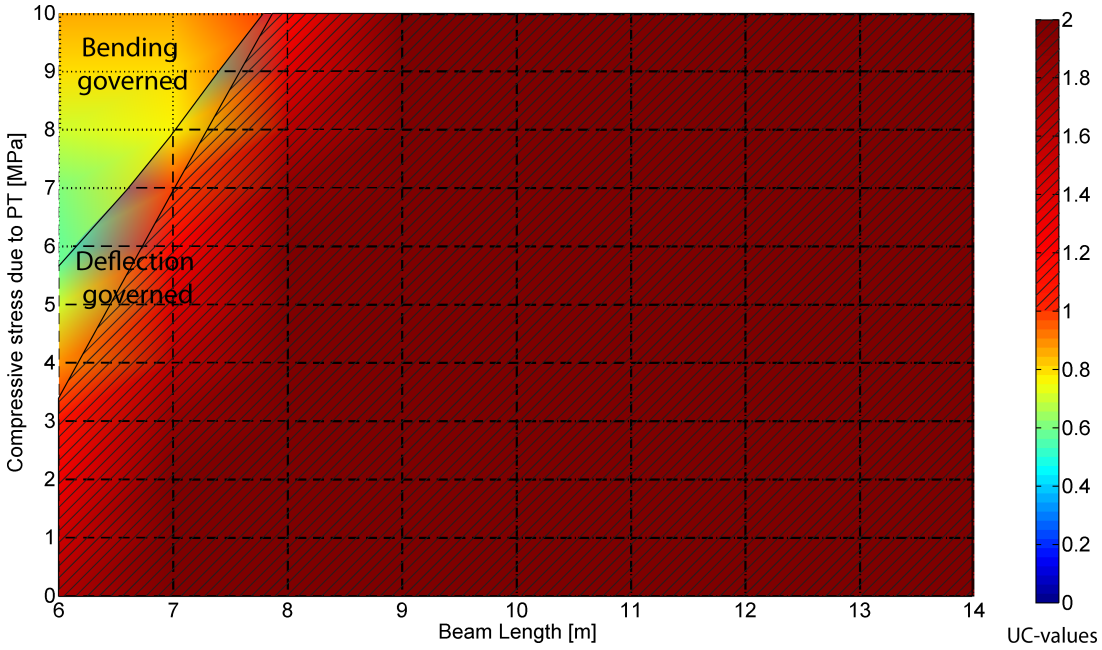

(a) 600 x 300 Beam

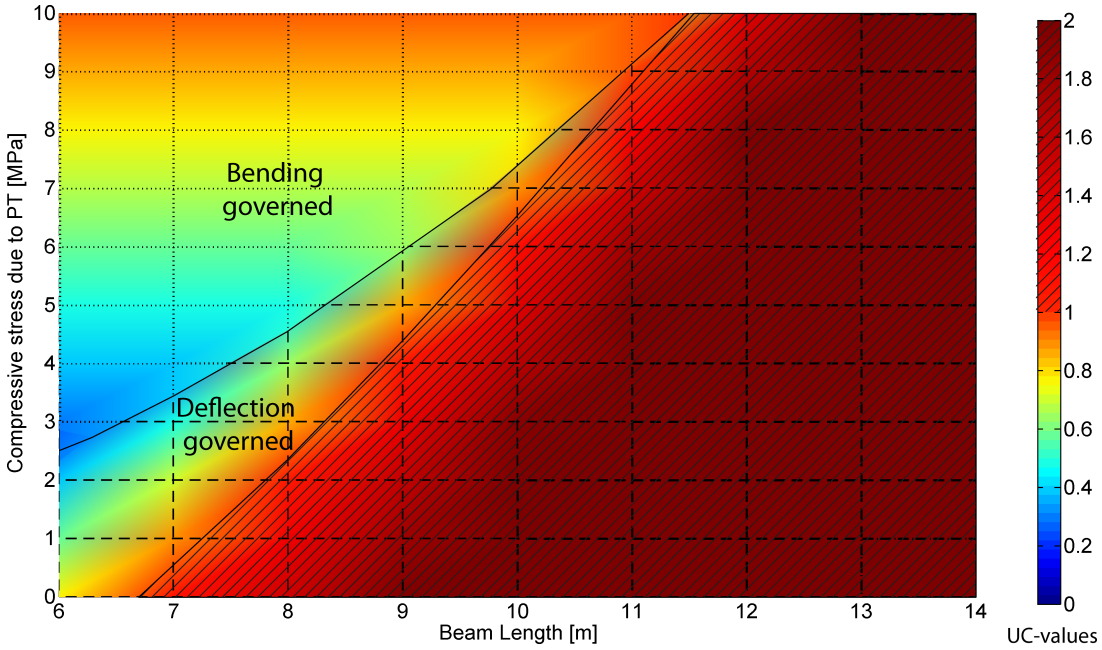

(b) 800 x 400 Beam

Figure 7.27: Results of parameter study on beam length and post-tensioning stress, showing unity checks (UC) for bending, shear and deflections

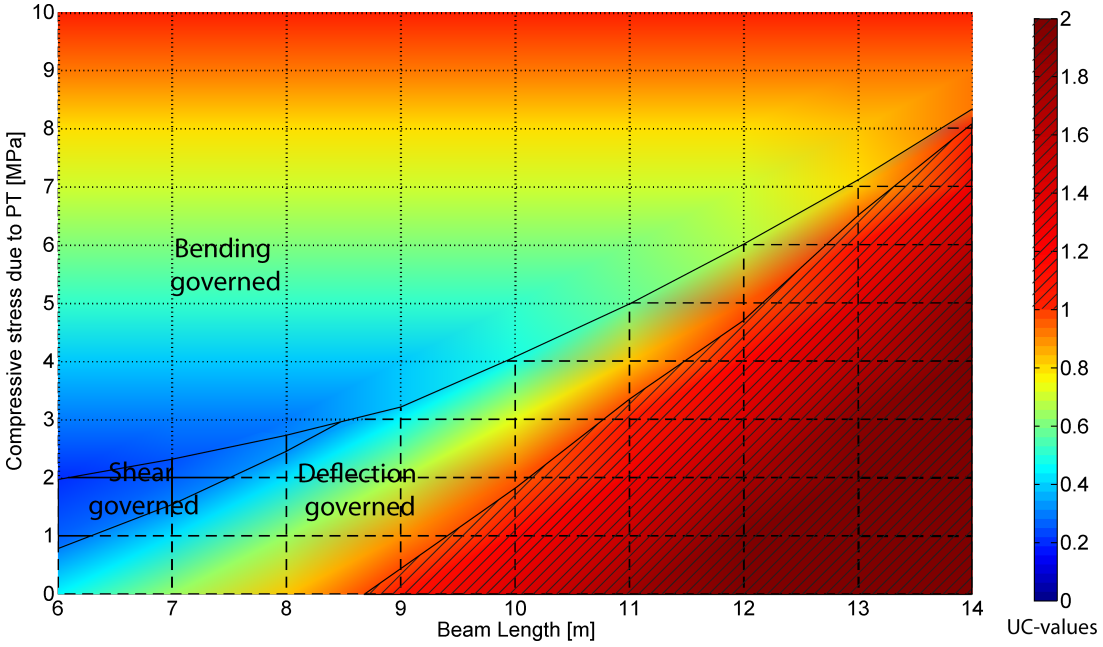

(a) 1000 x 500 Beam

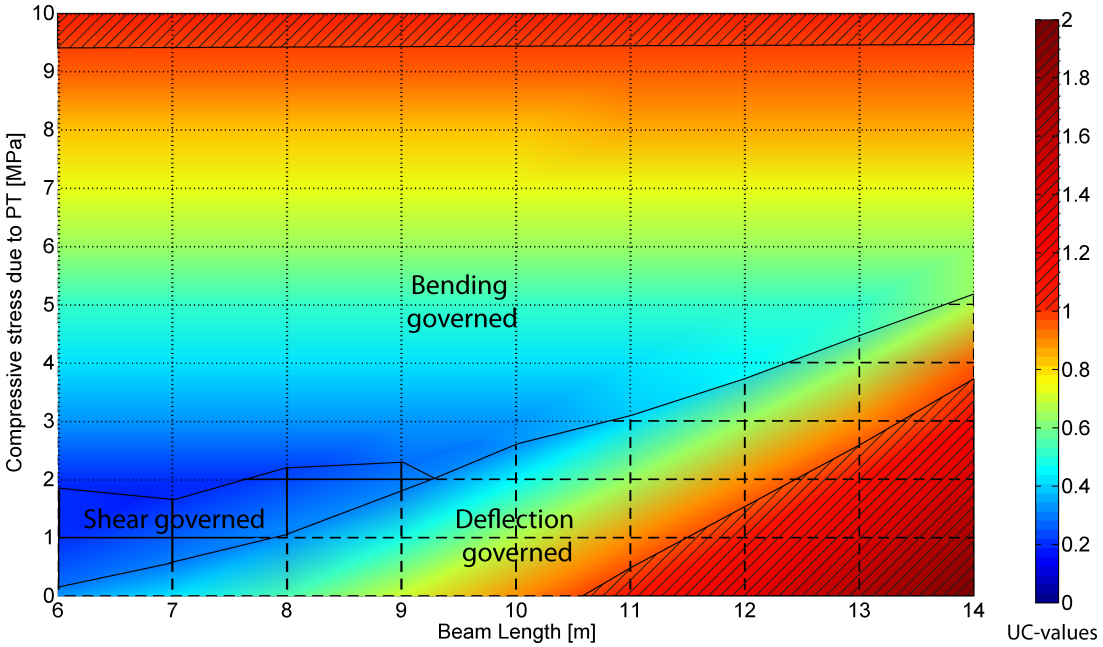

(b) 1200 x 600 Beam

Figure 7.28: Results of parameter study on beam length and post-tensioning stress, showing unity checks (UC) for bending, shear and deflections (continued)

bending design check, showing that too much post-tensioning is added to the section. Again a small part of the design options is governed by shear, but that range has very low unity checks, around 0.2, which make for an over designed section. For beams with straight tendons the range where shear is governing will be larger. Furthermore, in case of fire, where charring will occur to the bottom and both sides of the beam, the thickness of webs will reduce significantly and shear could become governing (Spellman et al., 2012).

7.6.4 Design guidance

An optimal design for a given section would be the largest span with a minimum of post-tensioning. Or for a given span, the smallest section with a minimum required post-tensioning force, e.g. for a 10m span a 800x400 section with 7MPa compressive stress due to post-tensioning, or a 1000x500 section with 2MPa post-tensioning or a 1200x600 section without post-tensioning. For all presented geometries the optimal design is governed by long-term deflections. An indication of suitable section size for a certain length and post-tensioning force is presented in Table 7.16 and Figure 7.29. In this figure the regions of interest for design are coloured in grey. These areas are to the left of the governing long-term deflection limit, as otherwise the design check would not be satisfied. But the area is close to governing design check, in order to have an optimal design and not result in an over-conservative design. The upper boundary for post-tensioning force was limited to about 1200kN, as can be seen in Table 7.16. Higher post-tensioning forces are possible, but would create practical problems with the design of anchorage system (Appendix B). A minimum post-tensioning force between 350kN and 600kN was found. Lower post-tensioning forces are possible, but in that case the section size could be reduced to create a more optimal design.

A comparison of span length and section height is shown in Table 7.17. This table compares the maximum span length without and with post-tensioning. It can be seen that post-tensioning increases the possible span length by about 3m, which ranges between 30% to 67% of the span length without post-tensioning. The ratio of span length over section height (L/h) is on average 8 for box beams without post-tensioning and 12 for box beams with post-tensioning.

Table 7.16: Optimal span length and post-tensioning force for four presented box sections

Section size height x width	Area (mm^2)	Span (m)		PT stress (MPa)		PT force (kN)	
		Min.	Max.	Min.	Max.	Min.	Max.
600x300	129600	6.0	7.5	4.0	9.0	518	1166
800x400	183600	7.5	10.0	2.0	6.5	367	1193
1000x500	237600	10.0	11.5	2.5	5.0	594	1188
1200x600	291600	11.5	13.5	1.5	4.0	437	1166

Table 7.17: Comparison of maximum span length and ratio of span length over section height (L/h) for box beams without and with post-tensioning

Section size height x width	Max. span (m)				Increase in length
	No PT	*L/h*	With PT	*L/h*	
600x300	4.5	*7.5*	7.5	*12.5*	67%
800x400	6.5	*8.1*	10.0	*12.5*	54%
1000x500	8.5	*8.5*	11.5	*11.5*	35%
1200x600	10.5	*8.8*	13.5	*11.3*	29%

7.6.5 Summary

This parameter study has lead to the conclusion that beams with straight and draped tendons show a very similar behaviour for strength and deflection checks, but a clear difference in shear performance is shown. For four different sections a range of span and post-tensioning force has been identified for an optimal design. Furthermore, design of post-tensioned timber beams is in most cases governed by long-term deflections. That is with the assumption of 20% post-tensioning loss and a creep factor of 2.0. Both these parameters are current best estimates and they are part of ongoing research on the long-term behaviour of post-tensioned timber beams. This topic falls outside the scope of this research project. The span length of a section can be increased by about 3m when applying post-tensioning. The span length over section depth without post-tensioning is around 8, whereas with post-tensioning this increases to around 12.

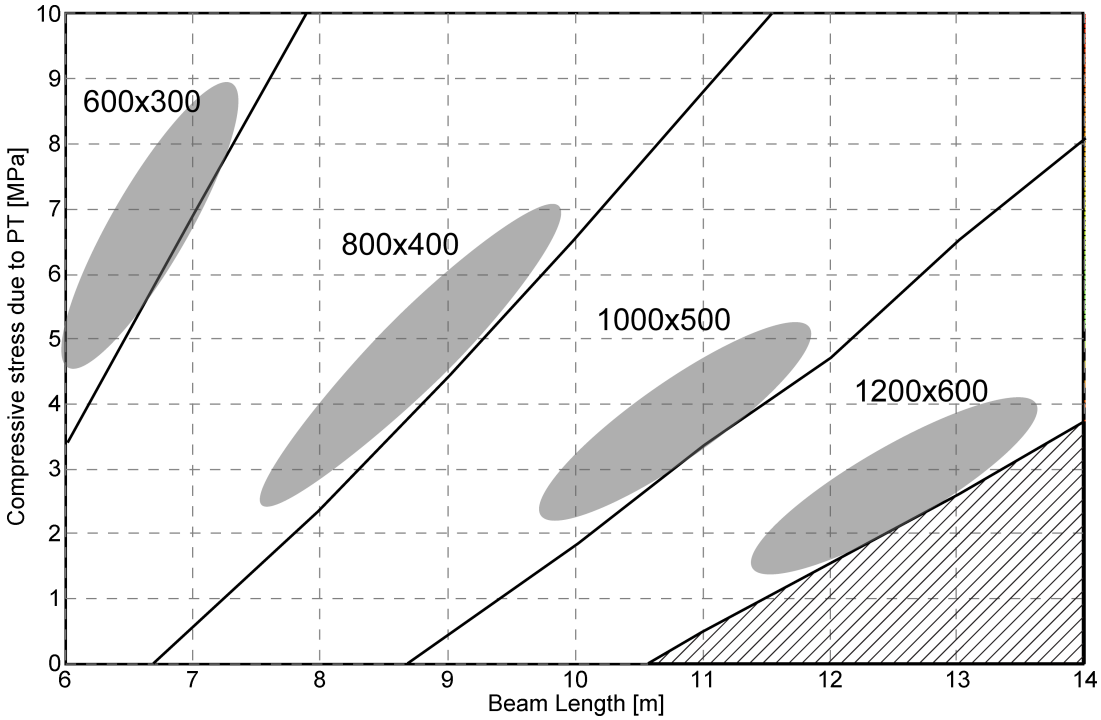

Figure 7.29: Overview of optimal section size and post-tensioning force for given beam length

7.7 Simplified design

7.7.1 Precamber limit

The parameter study in the previous section lead to the conclusion that long-term deflections often govern the design of post-tensioned timber beams. This can be used in design as a first quick design to estimate a required section size. But deflection design is strongly dependent on precamber due to post-tensioning. Therefore an iterative design procedure would be needed, which is not practical for a quick design. If the precamber can be limited, the design would be significantly simplified and an estimation for post-tensioning force would also follow from the design check.

A limit on the precamber can be seen as another design check, therefore similar to the parameter study, and another plane can be plotted on the 3D figure with design checks, as shown in Figure 7.30. This figure shows the results for an 800x400mm beam with draped tendons. The precamber limit was set

to span over 300, similar to the deflection limit. The intersection of the two planes, highlighted by the red line, gives values where unity checks for long-term deflections and precamber are equal. As both unity checks are based on the same design limit, also the long-term deflection and precamber are equal.

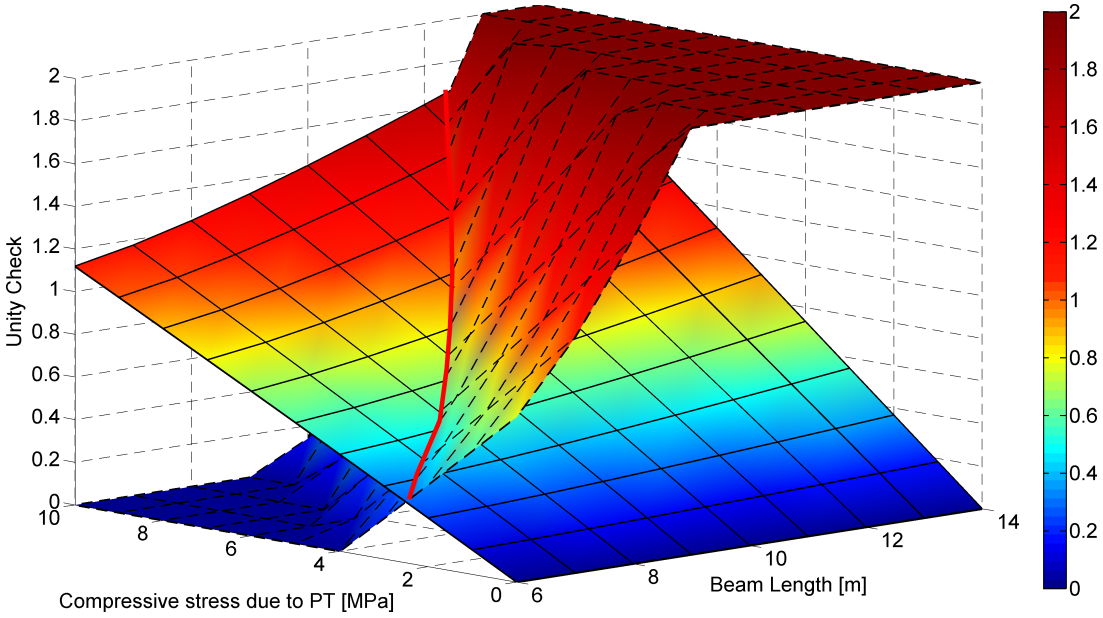

Figure 7.30: Design checks for long-term deflections and precamber

A suitable limit on precamber needs to be found in order to get a good result from the quick design. Three different limits were tried, span over 200, 300 and 400. For each of these limits, and for each of the four beams, the intersection between precamber and deflection unity check was found. In Figure 7.31 these lines have been plotted in red on top of the results of the parameter study (Figure 7.29.

From Figure 7.31 it can be seen that for the 600x300 and 800x400 section sizes, within the design range (grey area), the limit of span over 300 is close to the deflection limit (continuous black lines). Span over 400 would for certain beam lengths lead to an underestimation of section size, as the deflection limit is exceeded. Span over 200 would lead to a conservative design as the section size would have deflections further away from the design limit. For larger section sizes a limit of span over 400 gives better results, but the difference with span over 300 is small. From this it can be concluded that a limit of span over 300 for

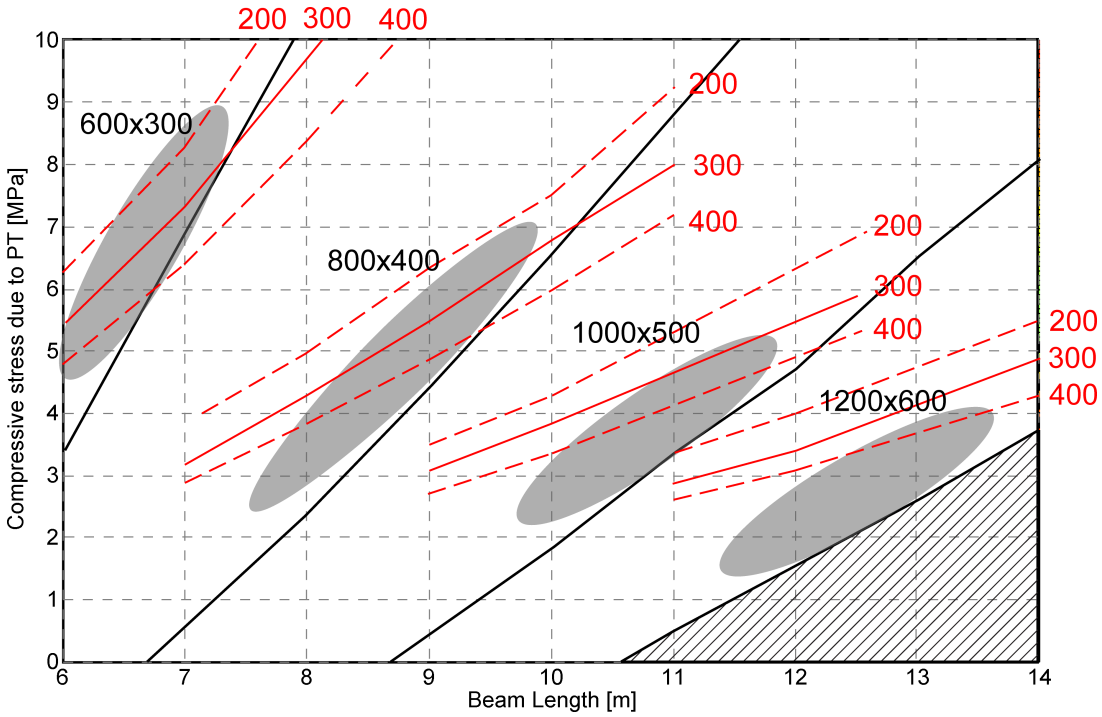

Figure 7.31: Results of parameter study combined with three different precamber limits

the precamber is suitable.

7.7.2 Quick design

For a quick design the long-term deflections are calculated using Equation 7.45. Figure 7.32 shows the nomenclature for different deflection components.

$$u_{long} = k_2(-u_{pt,long} + u_{q,long}) < \frac{L_b}{\eta} \tag{7.45}$$

Where:

- u_{long} = Long-term mid-span deflection (mm)
- k_2 = Duration of load factor (-)
- $u_{pt,long}$ = Long-term precamber due to post-tensioning (mm)
- $u_{q,long}$ = Deflections under long-term distributed load (mm)
- L_b = Beam length (mm)
- η = Deflection limit (300)

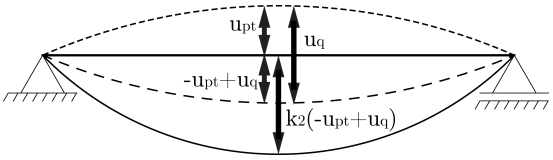

Figure 7.32: Nomenclature for beam deflections

The precamber has also been limited to the same deflection limit, as shown in Equation 7.46. Long-term precamber can be calculated based on the initial precamber, multiplied with long-term post-tensioning losses as in Equation 7.47.

$$u_{pt} < \frac{L_b}{\eta} \tag{7.46}$$

$$u_{pt,long} = \psi_{tl} \cdot u_{pt} \tag{7.47}$$

Where:

- u_{pt} = Precamber due to post-tensioning (mm)
- ψ_{tl} = Factor for long-term post-tensioning losses (-)

Equations 7.45 to 7.47 can be combined to a single equation and solved for the deflection under long-term load, as shown in Equation 7.48.

$$\begin{aligned} k_2(-\psi_{tl} \cdot u_{pt} + u_{q,long}) &< \frac{L_b}{\eta} \\ -\psi_{tl} \cdot \frac{L_b}{\eta} + u_{q,long} &< \frac{L_b}{\eta \cdot k_2} \\ u_{q,long} &< \frac{L_b}{\eta \cdot k_2} + -\psi_{tl} \cdot \frac{L_b}{\eta} \\ u_{q,long} &< \frac{L_b}{\eta} \left(\frac{1}{k_2} + -\psi_{tl} \right) \end{aligned} \tag{7.48}$$

From this derivation it can be seen that the maximum value for long-term deflections can be calculated based only on span length, creep-factor, deflection limit and amount of post-tensioning losses. The deflection under long-term load is given by Equation 7.49.

$$u_{q,long} = \frac{5}{384} \cdot \frac{q_{long} \cdot L_b^4}{E_t I} + \frac{q_{long} \cdot L_b^2}{8 G A_s} \tag{7.49}$$

Where:

- $u_{q,long}$ = Deflections under long-term loading (mm)
- q_{long} = Long-term distributed load (N/mm)
- E_t = Modulus of Elasticity for timber (MPa)
- I = Moment of inertia (mm^4)
- G = Shear modulus of timber (MPa)
- A_s = Shear area (mm^2)

Timber stiffness properties, E and G, beam span and long-term distributed load are known in a design. The only parameters to determine are the moment of inertia and shear area. These two are related, but the relationship is complex as it depends on section geometry. An attempt was made to quantify the ratio of shear deflection over total deflection for a range of cross-sections and beam lengths. These ratios are plotted in Figure 7.33. A list of possible cross-sections is shown in Table 7.18.

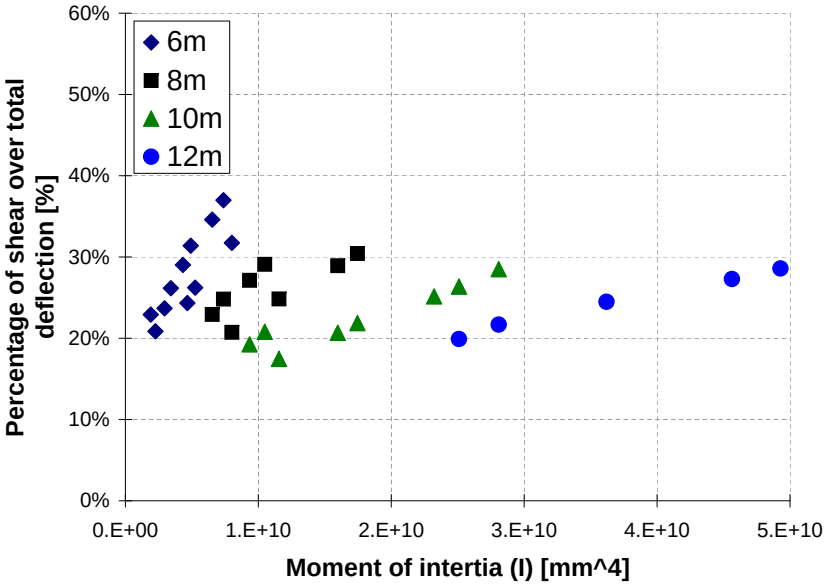

Figure 7.33: Relationship between shear deflection over bending deflection and moment of inertia for a range of beam lengths

It can be seen that there is some spread in contribution of shear deformation, ranging from about 18% to 38%. On average the shear contribution is 25% of total

deflections for box sections, obviously this ratio will be different for solid sections. Therefore Equation 7.49 can be simplified and rewritten to find an expression for the required moment of inertia, as in Equation 7.50. Based on the required moment of inertia a possible cross-sections can be chosen from Table 7.18. In this table a range of section heights and widths are shown with different thickness of flanges and webs. The eccentricity is the distance between the centroid of the section and 30mm above the bottom flange. This 30mm allows for space for anchorage and construction tolerances.

$$\begin{aligned} u_{q,long} &= \frac{5}{384} \cdot \frac{q_{long} \cdot L_b^4}{E_t I} \cdot \frac{4}{3} \\ u_{q,long} &= \frac{5}{288} \cdot \frac{q_{long} \cdot L_b^4}{E_t I} \\ I &= \frac{5}{288} \cdot \frac{q_{long} \cdot L_b^4}{E_t \cdot u_{q,long}} \end{aligned} \tag{7.50}$$

The final step for a quick design is to determine the post-tensioning force. This can be done as the design procedure is based on a balance of long-term deflections and precamber. The required precamber can only be created by a certain post-tensioning force. For a beam with straight tendons the precamber is given by Equation 7.51 and for draped tendons by Equation 7.52.

$$u_{pt} = \frac{F_{pt} \cdot e \cdot L_b^2}{8 E_t I} \tag{7.51}$$

$$u_{pt} = \frac{23}{648} \cdot \frac{F_{pt,v} \cdot L_b^3}{E_t I} + \frac{F_{pt,v} \cdot L_b}{3 G A_s} = F_{pt,v} \left(\frac{23}{648} \cdot \frac{L_b^3}{E_t I} + \frac{L_b}{3 G A_s} \right) \tag{7.52}$$

Using $F_{pt,v} = F_{pt} \cdot 3e/L_b$ for draped tendons (assuming deviators are at 1/3th of beam length), and the precamber limit of L_b/η, the required post-tensioning force can be found. For straight tendons this is given by Equation 7.53 and for draped tendons by Equation 7.54.

$$F_{pt} = \frac{8 E_t I}{\eta \cdot e \cdot L_b} \tag{7.53}$$

Table 7.18: Possible section dimensions for use in quick design procedure

h (mm)	b (mm)	t_w (mm)	t_f (mm)	e (mm)	I ($\cdot 10^9$ mm^4)	A_s ($\cdot 10^3$ mm^2)
400	250	45	63	107	1.1	27
400	250	63	90	80	1.2	36
450	250	45	63	132	1.4	31
450	250	63	90	105	1.7	41
500	250	45	63	157	1.9	34
500	250	63	90	130	2.3	46
550	250	63	90	155	2.9	51
550	300	63	90	155	3.4	52
600	300	63	90	180	4.3	56
600	300	90	90	180	4.7	77
600	350	63	90	180	4.9	57
600	350	90	90	180	5.3	79
700	300	63	90	230	6.5	66
700	350	63	90	230	7.4	67
700	350	90	90	230	8.0	92
800	300	63	90	280	9.3	75
800	350	63	90	280	10.5	77
800	400	90	90	280	12.7	107
900	350	90	90	330	16.0	118
900	400	90	90	330	17.5	120
900	450	90	90	330	18.9	121
1000	400	90	90	380	23.2	133
1000	450	90	90	380	25.1	135
1000	450	90	126	344	28.1	135
1100	450	90	126	394	36.2	149
1200	450	90	126	444	45.6	162
1200	500	90	126	444	49.3	164

Where:

- h = Height of beam (mm)
- b = Breadth of beam (mm)
- t_w = Thickness of web (mm)
- t_f = Thickness of flange (mm)
- e = Eccentricity of post-tensioning (mm)
- I = Moment of inertia (mm^4)
- A_s = Shear area (mm^2)

$$F_{pt} = \frac{L_b^2}{3\eta e}\left(\frac{23}{648}\cdot\frac{L_b^3}{E_t I} + \frac{L_b}{3GA_s}\right)^{-1} \tag{7.54}$$

The presented quick design consists of four steps. Firstly the deflection limit under long-term load needs to be calculated using Equation 7.48. Secondly the required moment of inertia needs to be calculated using Equation 7.50. Next a beam section can be found using Table 7.18. Finally the post-tensioning force can be estimated using Equations 7.53 and 7.54 for straight and draped post-tensioning profiles, respectively.

7.7.3 Detailed design

This section describes several simplifications to the detailed design of post-tensioned timber beams.

Deviator deflections For beams with draped tendons deviator deflections are calculated as they result in tendon elongation. A simplification would be if the deviator deflections could be related to mid-span deflections, as these are already known. A comparison between deviator and mid-span displacement is presented in Figure 7.34. The comparison is made for Beams 3 and 4 based on displacement data from experimental testing and analytical models. This comparison assumes that deviators are placed at 1/3 of the length of the beam.

From the figure it can be seen that the ratio of deviator displacement over mid-span displacement is almost constant during loading of the beam. The peaks in the figure are caused by experimental measurements of mid-span displacement being close to zero. It can be concluded that deviator displacement is approximately 88% of mid-span displacment.

Tendon elongation (straight) In the analytical design procedure calculation of tendon elongation is an iterative process. Appendix D.4 presents a more detailed investigation of tendon elongation for beams with straight tendons and presents a simplified, closed form equation for calculation of tendon elongation, as given by Equation 7.55.

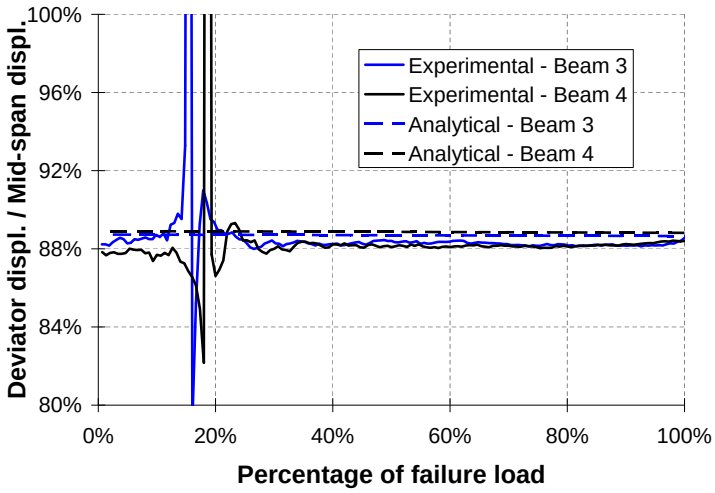

Figure 7.34: Comparison between deviator and mid-span displacement

$$\Delta F_{pt} = \frac{qL^2 + 10F_{pt,i}(u + u_0)}{\dfrac{12EI}{eE_{pt} \cdot A_{pt}} + 12e - 10u + \dfrac{12I}{Ae}} \tag{7.55}$$

Where:

- ΔF_{pt} = Increase in post-tensioning force (N)
- q = Distributed load on beam (N/mm)
- L = Length of beam (mm)
- $F_{pt,i}$ = Initial post-tensioning force (N)
- u = Mid-span deflections of beam (mm)
- u_0 = Precamber of beam under post-tensioning only loading (mm)
- E = Modulus of elasticity of beam (MPa)
- I = Moment of inertia (mm^4)
- e = Eccentricity of post-tensioning (mm)
- E_{pt} = Modulus of elasticity of post-tensioning steel (MPa)
- A_{pt} = Area of post-tensioning tendons (mm^2)
- A = Area of timber beam (mm^2)

This equation originated from several components which resulted in tendon elongation, as shown in Equation 7.56.

$$\Delta l_{pt} = \underbrace{2 \cdot e \cdot (\theta_q + \theta_{sec,pt,i} + \theta_{sec,0})}_{\text{constant part 'C'}} + \underbrace{2 \cdot e \cdot (-\theta_{\Delta pt} + \theta_{sec,\Delta pt}) - \Delta l_{beam}}_{\text{variable part 'V'}} \quad (7.56)$$

Based on the parameters of Beam 2 used for experimental testing, the contribution of each of these components can be evaluated. The total tendon elongation of Beam 2 under maximum vertical load was 13.1mm (Section 7.3.4). The contributions of the different components are presented in Table 7.19.

Table 7.19: Contribution of different components for tendon elongation

Part	Contribution (mm)	Contribution (%)
$2 \cdot e \cdot \theta_q$	12.2	93%
$2 \cdot e \cdot \theta_{sec,pt,i}$	-2.0	15%
$2 \cdot e \cdot \theta_{sec,0}$	0.4	3%
$2 \cdot e \cdot \theta_{\Delta pt}$	-0.7	-5%
$2 \cdot e \cdot \theta_{sec,\Delta pt}$	0.5	3%
Δl_{beam}	-1.3	-10%
Total	13.1	100%

Based on this decomposition of tendon elongation it can be concluded that elongation due to initial second order effects ($\theta_{sec,0}$) is only 3% and can safely be ignored. Also contributions of tendon elongation due to change in post-tensioning force ($\theta_{\Delta pt}$) and second order effects due to change in post-tensioning force ($\theta_{sec,\Delta pt}$) of -5% and 3%, respectively, can be ignored.

The resulting simplified closed form formula for tendon elongation of beams with straight tendons is presented in Equation 7.57.

$$\Delta F_{pt} = \frac{qL^2 + 10F_{pt,i}u}{\frac{12EI}{eE_{pt} \cdot A_{pt}} + \frac{12I}{Ae}} \quad (7.57)$$

Tendon elongation (draped) The calculation of tendon elongation for beams with draped tendons is also an iterative process, similar to beams with straight tendons. The main difference is that the increase of tendon length is based on

deviator deflection. But not only does the post-tensioning force increase, also the angle of the tendon at the location of the deviator increases. For example Beam 3 of the experimental testing campaign had an initial angle of 3.1 degrees, but close to failure this angle had increased to 5.7, almost doubling the vertical uplift force at the deviator. This aspect, and the fact that there is no linear relationship between the deviator deflection and tendon elongation, make it impossible to find a closed form solution for tendon elongation for beams with draped tendons.

7.8 Conclusions

- Three-dimensional finite element models of the four experimentally tested post-tensioned timber box beams were developed. The main difficulty in modelling was the contact of tendons with deviator blocks. Very small step sizes were needed in order to achieve convergence when contact was initiated. Another modelling difficulty was the plastic material behaviour of timber. This only happens in compression and not in tension, but this could not be implemented in Abaqus with available material models. Contact stresses between support plates and the bottoms of the beams were found not to be constant. Larger stresses occurred under the webs and smaller stresses under the flanges. This is of importance when designing supports for the beams.

- The analytical procedure for beams showed that straight tendons only allowed for a 5% increase of mid-span bending moment due to vertical load, whereas draped tendons allowed for a 22% to 24% increase in bending moment due to vertical loading. This improved performance of beams with draped tendons was due to tendon elongation and an increase in angle of tendons at the deviators. This combination led to a 2.5 times increase in vertical uplift force at the deviator under ultimate load. Second order deflections were between 14 and 15% of the total mid-span deflections.

- Numerical models and analytical models matched the stiffness of post-tensioned beams well with a maximum difference of 12%. Mid-span bending moments based on analytical and FEM models matched experimental data very well for Beam 1 (benchmark) and Beam 2 (straight PT). For Beam 3 and 4 (draped tendons) bending moments were slightly over estimated. Post-tensioning forces during loading based on analytical and FEM models followed experimental data very closely. Although under larger displacements both models over predicted the post-tensioning forces.

- Predictions of bending moment capacity according to European timber design standard (EC5) varied between 74% and 81% of the actual capacity. For predictions according to New Zealand timber design standard (NZS3603)

the variation was between 66% and 87%. This difference between predictions based on NZS3603 and EC5 was mainly caused by the limited tensile capacity of the bottom flange, which was taken into account in the EC5 design but not in the NZS3603 design. Ignoring the tensile capacity of the bottom flange for no (or low levels of) post-tensioning could lead to an unconservative design. Therefore it was recommended to use the design equations given by EC5.

- The parameter study showed that deflections were most sensitive to changes in beam length and post-tensioning force, compared to bending and shear. Comparing results of the parameter study for straight and draped tendons, it was shown that the reduction in shear was significant for beams with draped tendons. Bending checks were very similar and deflection checks were about 10% lower for beams with draped tendons. For all considered geometries in the parameter study the optimal design (largest span with a minimum of post-tensioning) was governed by long-term deflections.

- Balancing the long-term deflections with a deflection limit of span over 300 for the precamber was found to give a good estimation for required section size. This was used for a quick design method which consists of four steps. Firstly the deflection limit under long-term load needs to be calculated. Secondly the required moment of inertia needs to be calculated. Next a beam section can be found using a provided table with possible section sizes. Finally the post-tensioning force can be estimated using equations for straight and draped post-tensioning profiles. Shear deformation for post-tensioned timber beams was on average 25% of total deflection, which allowed for the developement of a direct relationship between required moment of inertia of a beam and long-term deflection under distributed load.

- For beams with draped tendons, deviator displacement was approximately 88% of mid-span displacement. And a closed form formula for tendon elongation of beams with straight tendons was found, but this was not possible for beams with draped tendons.

Chapter VIII

Post-tensioned timber beam-column connections

8.1 Introduction

This chapter presents a detailed investigation into the deformation components of post-tensioned timber beam-column connections. The stiffness of these connections is crucial when modelling a post-tensioned timber frame, as it influences deflections (SLS conditions) and moment distributions (ULS conditions) in the frame. Stiff connections can reduce member sizes and increase resistance to lateral loading. Determining this connection stiffness is complex, due to anisotropic timber behaviour and non-uniform contact stresses.

Analysis of post-tensioned timber beam-column connections has the following objectives:

- Analyse the deformation components of post-tensioned timber connections.
- Develop and validate equations to predict the stiffness of post-tensioned timber beam-column connections.
- Adapt the seismic design method using the MMBA to gravity frames.
- Develop design charts for easy estimation of connection stiffness.

The different stiffness contributions are presented in Section 8.2. The following sections analyse each of the rotation components; column rotation, joint panel rotation, interface compression and gap opening. Two different connection types are analysed, a full contact connection (Figure 8.1a) where the full cross-sectional area of the beam is in contact with the column, and a partial contact connection (Figure 8.1b) where only the top and bottom flanges are in contact with the column. This can be achieved with steel plates, as implemented for experimental testing of frames (Chapter 6).

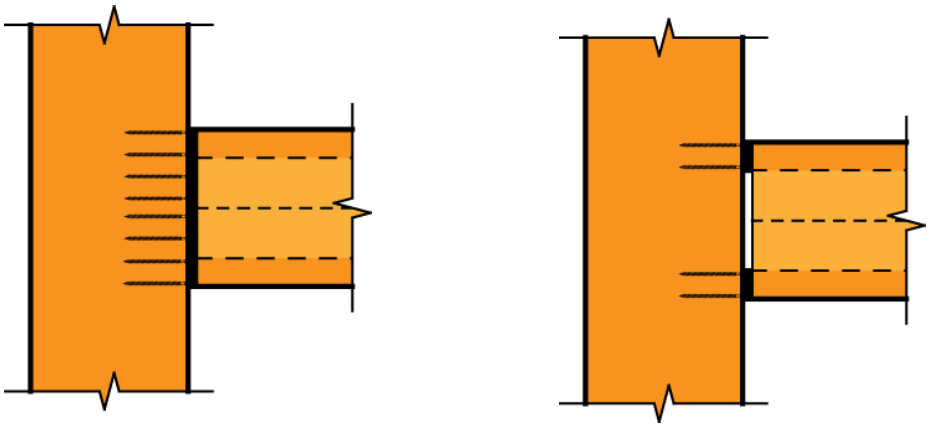

(a) Full contact connection between beam and column

(b) Partial contact connection with only top and bottom flanges in contact

Figure 8.1: Two different beam-column connection models, here shown for external connections with screw reinforcement

Section 8.7 presents design charts for quick estimation of column rotational stiffness, joint panel shear stiffness, interface compression stiffness and gap opening. Finally, a procedure is presented which combines the different deformation components in order to use a single rotational spring.

8.2 Deformation components

The deformation of frames generally consists of three parts, beam deformation (θ_b), joint deformation (θ_{joint}) and column deformation (θ_c) (Buchanan and Fairweather, 1993). In previous publications on post-tensioned timber seismic frames (Newcombe et al., 2010a) the joint deformation was split into joint panel shear deformation (θ_j) and connection deformation (θ_{con}), where connection deformation was evaluated by an empirical relationship as it was suggested that the Modified Monolithic Beam Analogy (MMBA), as presented by Palermo (2004), was inaccurate specifically for timber at small rotations. Evaluation of new experimental test data, as presented in Chapter 5, lead to the conclusion that although the proposed equations worked for some timber-to-timber beam-column connections, the effects of column reinforcement could not be included in the model. Therefore, it was suggested (van Beerschoten et al., 2011b) that the connection deformation should be split into two parts; the gap opening (θ_{gap}),

which can be described by the MMBA, and the interface compression deformation (θ_{int}), as is shown in Figure 8.2.

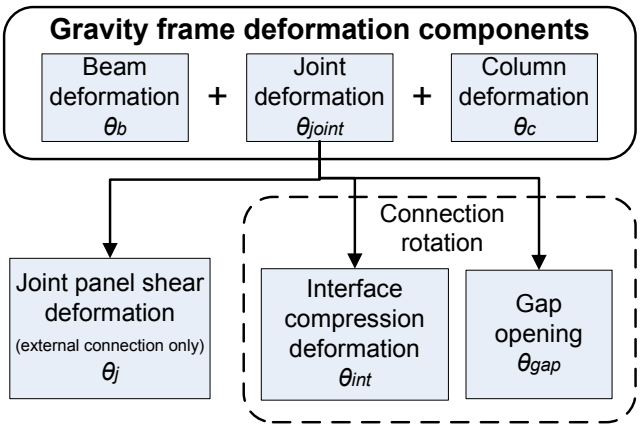

Figure 8.2: Overview of frame deformation components

Modelling a post-tensioned timber frame can be done in two ways, a framework model of the full frame can be made or a simplified model of only a beam can be made, as shown in Figure 8.3. The full frame model consists of column and beam elements. A rigid link can be placed between the centreline of the column and the beam-column connection interface. A rigid link is placed between the centreline of the column and the beam-column interface. At the interface, a rotational spring is placed to model the joint panel deformation (only for external connections), interface compression and gap opening. Post-tensioning loads are represented by forces at the anchorages (under an angle or horizontal and vertical components), at deviators in the beams (uplift force) and at deviators in the columns (double the uplift force). For a beam only model, a rotational spring is placed at each end of the beam. This rotational spring includes all previously mentioned rotational components and also the column rotational stiffness.

The rotational components which need to be taken into account for internal and external connections (Figure 8.4) under different loading scenarios are shown in Table 8.1. For equal bay lengths internal columns are loaded by equal moments on either side, resulting in zero moment in the column. Therefore column rotation does not need to be taken into account for internal connections. Similar for joint panel shear deformation, this only occurs in external connections as shown by experimental testing in Chapter 6. For internal connections the compression

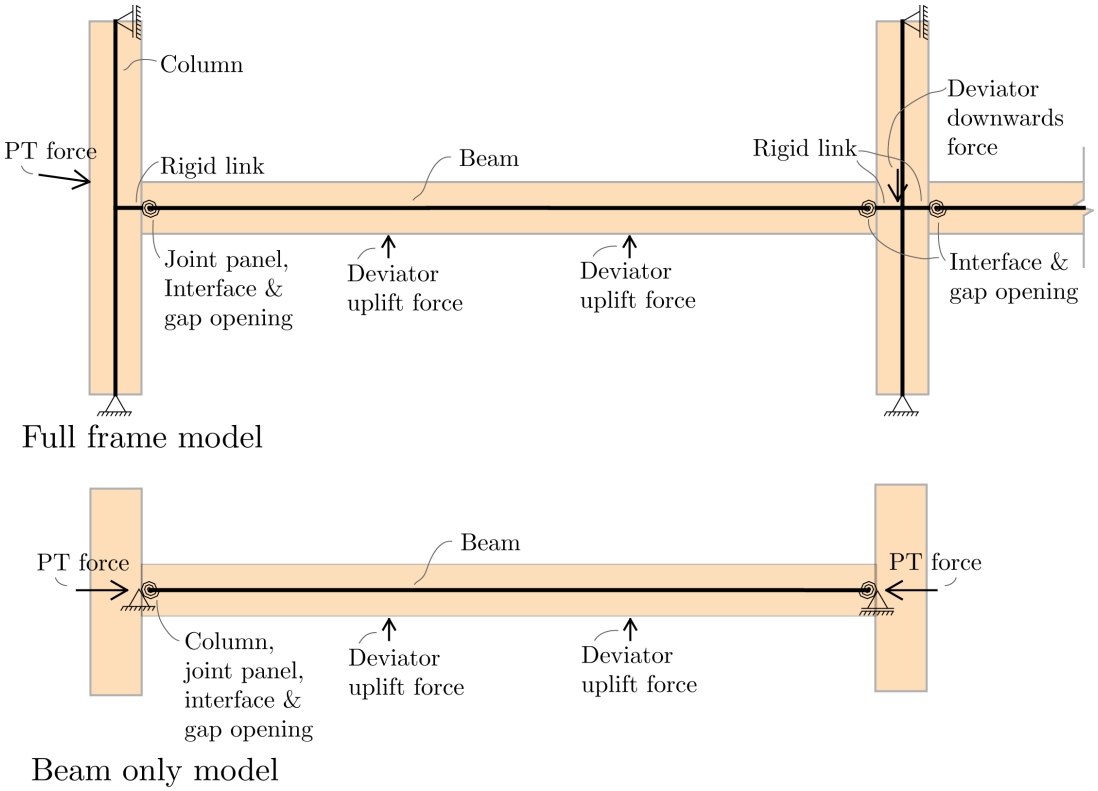

Figure 8.3: Schematics of modelling approach for full frame and beam only models

is located at the bottom for both beams, resulting in zero shear force in the joint panel region. The column interface is loaded by high compressive stresses which are acting perpendicular to grain. This causes deformations on the face of the column, which need to be taken into account for internal and external connections.

Before decompression of the connection, the stiffness is a linear function. This is normally the case for design under Serviceability Limit State (SLS) conditions, when connection moments are small. Under Ultimate Limit State (ULS) loading, once the connection moment exceeds the decompression moment, a gap will open at the beam-column interface. This gap opening results in a non-linear connection stiffness.

Each of the above mentioned deformation components is described in the next sections. Combining the different components is described in Section 8.7.

Table 8.1: Rotation components to take into account for modelling of external and internal connections in SLS and ULS design

Rotation components	Symbol	External		Internal	
		SLS	ULS	SLS	ULS
Column rotation	k_{col}	Yes	Yes	No	No
Joint panel rotation	k_{jp}	Yes	Yes	No	No
Interface compression rotation	k_{int}	Yes	Yes	Yes	Yes
Gap opening	-	No	Yes	No	Yes

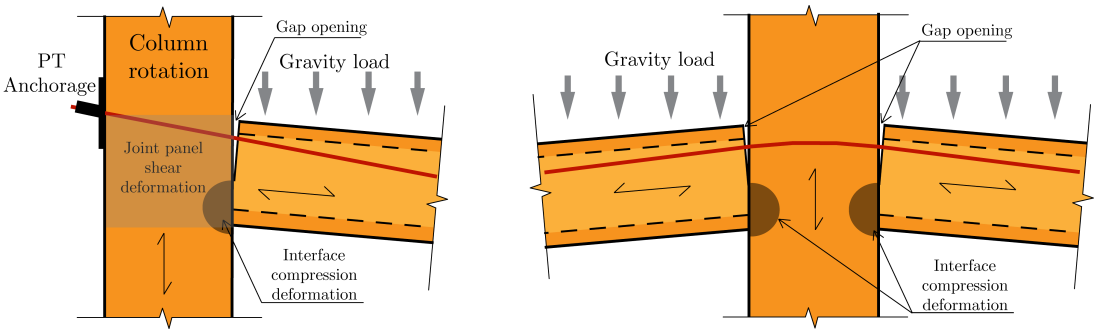

Figure 8.4: Deformation components of external and internal connections

8.3 Column deformation

Column deformation is part of the deformations of any frame. In the full frame model (Figure 8.3) the column is modelled and the framework program should take column rotation into account. But for the beam only model, the column rotational stiffness needs to be determined. This section analyses how to correctly include column deformations. The assumption is made that column stiffness of the storey above and below the level of the frame which is evaluated is equal.

A 3D finite element model (FEM) is made based on the partial contact connection. Two different analytical models are derived and the results from these analytical models are compared with FEM results. Bending and shear deformations and rotations are evaluated separately where possible to show the importance of shear deformations.

8.3.1 FEM model

A 3D linear FEM model of a column, including joint panel region, was made. This model consisted of a column of 3.6m high, 500mm wide and 288mm in depth. The column was pinned at both ends. A pressure load of 8MPa was applied over an area of 90mm in height as shown in Figure 8.5a. This results in a compressive force of 200kN. Quadratic (reduced integration) elements were used for the analysis in order to provide a higher accuracy compared with linear elements. Material properties used in the model followed from experimental testing, as described in section 3. The deformed shape of the column with compression and shear stresses can be seen in Figures 8.5b and 8.5c. A graph of column deformations is shown in Figure 8.5d and column rotations are shown in Figure 8.5e. It can be seen that under this loading the column deflected in an S-shape with a maximum deflection of 0.47mm and maximum rotation of 1.7mrad.

8.3.2 Analytical model

Column deformations of the FEM model can be compared with analytical models. Two analytical models have been made, one with a bending moment acting on the middle of the column and another one with two point loads acting on the model. The first model, called *M*, is representative for a framework analysis program

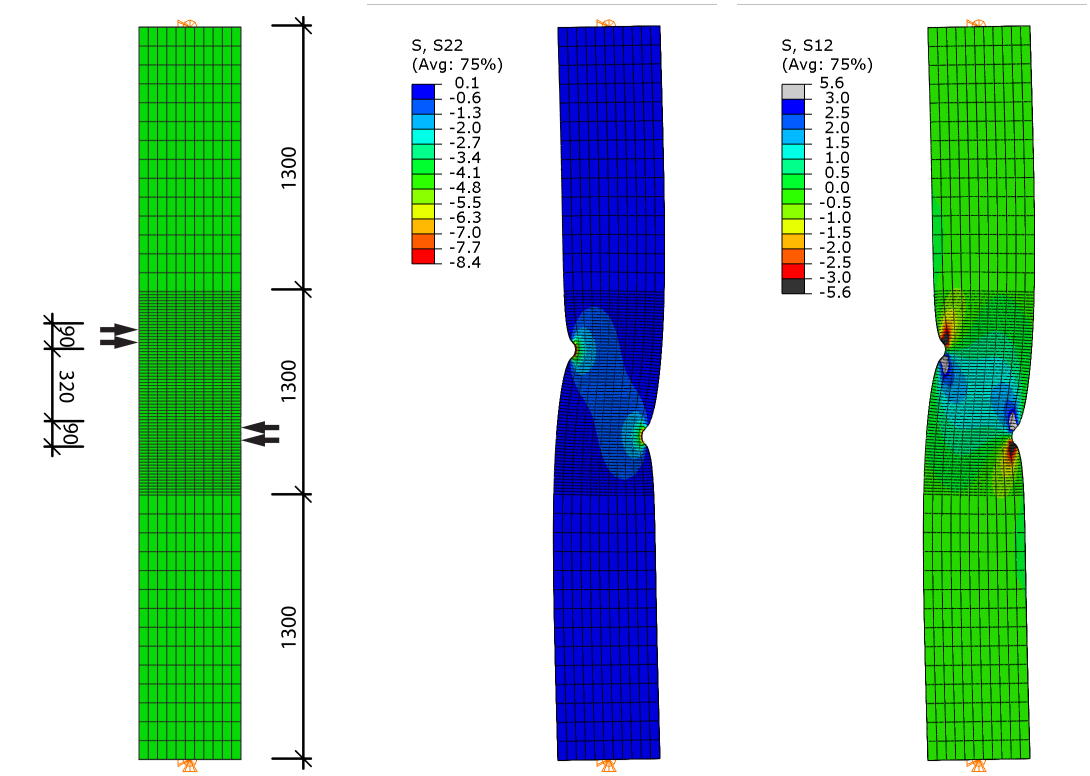

(a) Mesh and loading of column

(b) Perpendicular to grain stresses

(c) Shear stresses

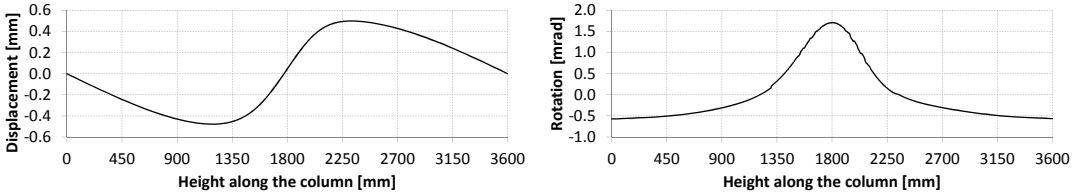

(d) Column deflections at centreline

(e) Column rotations at centreline

Figure 8.5: FEM model of column and resulting stresses, displacement and rotations

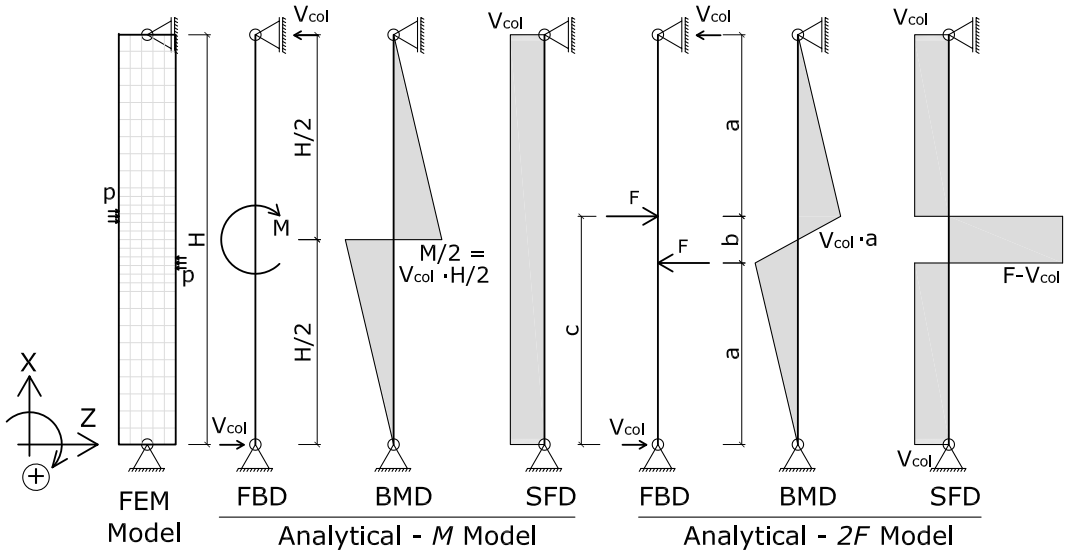

Figure 8.6: Three different column models with free body diagram (FBD), bending moment diagram (BMD) and shear force diagram (SFD)

where the bending moment coming from the beam is acting on the centreline of the column. The second model, called *2F*, is more representative for a real loading scenario, where post-tensioning forces are acting at approximately the height of top and bottom of the beam. The three different models are shown in Figure 8.6. Geometric parameters are: H = 3600mm, a = 1595mm, b = 410mm and c = 2005mm. The column has a width of 500mm and a depth of 288mm, which gives a moment of inertia, I, of $3 \times 10^9 mm^4$. The shear area is dependent on the shear stress distribution within the column and is given by $A_s = \alpha \times A_{col} = \alpha \times 288 \times 500$. The factor α is determined further on in this section, based on comparison with FEM results. The pressure (p) of the FEM model multiplied with the area gives the force, F, of 207kN. The bending moment, M, equals the force F times distance b of 410mm, resulting in M = 85kNm. The horizontal reaction forces at the supports (V_{col}) are the same for the three models, namely M/H = 23.6kN. Material properties for the analytical model are the same as the FEM model; E = 12157MPa and G = 856MPa.

Derivation of the equations for the M model are shown in Appendix E.1. The resulting equation for bending deflection is given in Equation 8.1 and for shear deflection in Equation 8.2.

$$\theta_b(x) = \begin{cases} \frac{V_{col}}{2EI}x^2 - \frac{V_{col}H^2}{24EI} & \text{for } 0 \leq x \leq H/2 \\ \frac{V_{col}}{2EI}x^2 - \frac{V_{col}H}{EI}x + \frac{11V_{col}H^2}{24EI} & \text{for } H/2 \leq x \leq H \end{cases} \tag{8.1}$$

$$\theta_s = \frac{V_{col}}{\alpha GA} \tag{8.2}$$

Derivations for the *2F* model are similar to the *M* model, but it is 3 piecewise. The equations become more complex for this load case and are therefore solved using the software package Maple (Maplesoft, 2009). The full derivation and resulting equations for deformation and rotation can be found in Appendix E.1.

8.3.3 Comparison

The resulting values of rotations and deflections along the height of the column have been plotted in Figure 8.7. The black line shows the results of the FEM model, which is the most accurate representation. The red line is the analytical *M* model and the green line is the analytical *2F* model. The deflections of the *2F* model have been split into bending and shear deflections. It can be seen that the bending deflections of the *M* and *2F* model are almost equal. Thus the simpler equations of the *M* model can be used to calculate the bending deflections. But also shear deflections need to be taken into account. For the chosen geometry, these shear deflections account for almost half of the total deflections. The difference between the FEM and the *2F* model is due to the loading. In the FEM model the applied load is spreading out after it enters at the side of the column, whereas for the *2F* model the load is applied at a single point. This means that the FEM model gives a smooth curve whereas the *2F* model has a discontinuity. If a point load at the centreline was introduced in the FEM model, then the curve would be identical to the *2F* model.

The shear rotation and deformation are based on an average shear stress across the area of the column. Therefore a factor α is introduced to take the stress distribution into account. For a constant shear stress distribution this factor would be 1 and for a parabolic shear stress distribution 0.67. The true stress distribution depends on the Poisson's Ratio, and for a rectangular cross-section the equation is given in Equation 8.3 (Cowper, 1966). The Poisson's Ratio ν_{LT} = 0.59 has been used, based on the results of section 3.4. The influence of the

factor α on rotations is small, but a difference can be seen in terms of deflections, as shown in Figure 8.7b. It can be seen that $\alpha = 0.86$ gives the best comparison with the FEM model.

$$\alpha = \frac{10(1+\nu)}{12+11\nu} = \frac{10(1+0.59)}{12+11\cdot 0.59} = 0.86 \tag{8.3}$$

Rotations of the column are of interest as they influence end rotations, and thus deflections, of the beam. Figure 8.7c shows the rotations of the 3 different models. The 3D FEM model is again a smooth curve. Both analytical models follow rotations of the column well at the ends. The *M* model does not include any joint panel deformation, which results in a significant underestimation of rotations. The *2F* model does include joint panel deformation, but over-estimates the maximum rotations at mid-height of the column. Stresses resulting from the two point loads will spread out into the beam, resulting in a more distributed load on the column instead of a point load. Although analysis of this load case would be interesting from a theoretical perspective, this figure clearly illustrates the need to include joint panel shear deformation into the connection model. This deformation component is further elaborated on in the next section.

Of most interest are rotations at mid-height of the column. Column rotations at mid-height follow from the *M* model and have a magnitude of 0.47mrad. This can be calculated using Equation E.6 and E.8 with x = H/2. The result is shown in Equation 8.4. This can be further rewritten to form the rotational stiffness of the column, as shown in Equation 8.5 and 8.6. In these equations the factor χ is introduced as a conversion factor to convert the column centreline moment (M_{cl}) to the connection moment (M_{con}). This factor is further explained in Section 9.3.

$$\begin{aligned}\theta_{col}(H/2) = \theta_b(H/2) + \theta_s(H/2) &= \frac{V_{col}(H/2)^2}{2EI} - \frac{V_{col}H^2}{24EI} + \frac{V_{col}}{\alpha GA} \\ &= \frac{V_{col}H^2}{12EI} + \frac{V_{col}}{\alpha GA} = \frac{M_{cl}H}{12EI} + \frac{M_{cl}}{\alpha GAH}\end{aligned} \tag{8.4}$$

$$M_{con} = M_{cl}\cdot\chi = k_{col}\cdot\theta_{col}\cdot\chi = \frac{\chi}{\frac{H}{12EI} + \frac{1}{\alpha GAH}}\cdot\theta_{col} \tag{8.5}$$

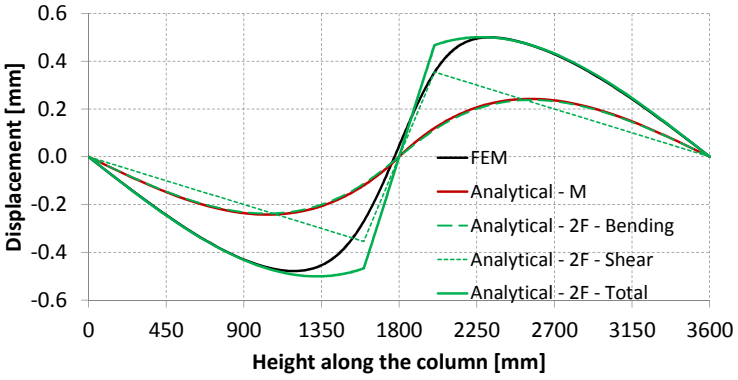

(a) Column Deflections

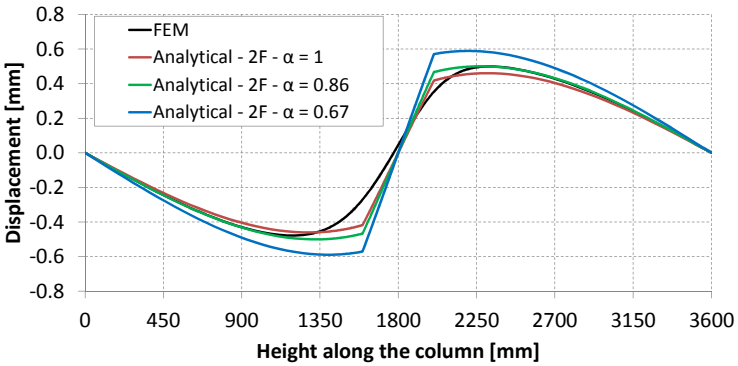

(b) Determination of α-factor

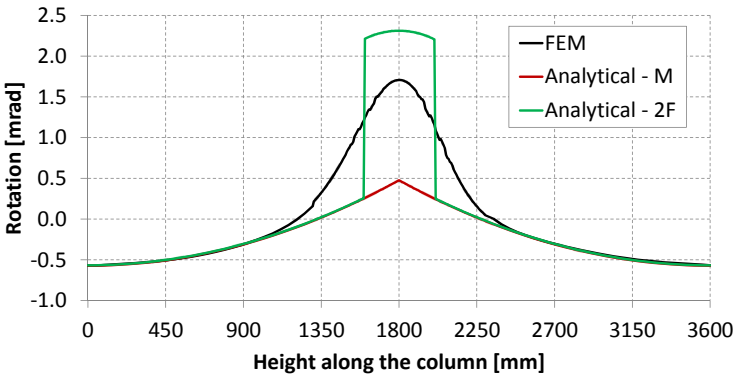

(c) Column Rotations

Figure 8.7: Comparison of deflections and rotations between FEM model and two analytical models of column

$$k_{col} = \frac{\chi}{\frac{H}{12EI} + \frac{1}{\alpha GAH}} \tag{8.6}$$

8.3.4 Model validation

Direct comparison with experimental data was not possible. For the connection testing the column rotation was not measured. For the one-bay and two-bay gravity frame testing, the reaction frame rotation was included in experimental measurements. Although no direct comparison was possible, a lower limit for column stiffness was found. Experimentally determined values for column and reaction frame stiffness ranged between 34kNm/mrad and 45kNm/mrad (Section 6.5.6) for one-bay frame testing and 21kNm/mrad and 30kNm/mrad for two-bay frame testing (Section 6.6.6).

The analytical expression for column stiffness is given by Equation 8.7. In this equation the factor χ is left out as experimental testing used the centreline moment and not the connection moment. It can be seen that the analytical stiffness of 76kNm/mrad is about twice that of the experimental values of the one-bay frame. This means that rotation due to reaction frame movement was similar to rotation of the column.

$$\begin{aligned} k_{col} &= \left(\frac{H}{12E_tI_{col}} + \frac{1}{\alpha GA_{col}}\right)^{-1} \\ &= \left(\frac{3600}{12 \cdot 11000 \cdot 3.0 \cdot 10^9} + \frac{1}{0.86 \cdot 550 \cdot 144000}\right)^{-1} = 76kNm/mrad \end{aligned} \tag{8.7}$$

Where:

- k_{col} = Stiffness of column $[N/rad]$;
- H = Height of column $[mm]$;
- E_t = Modulus of elasticity of timber $[MPa]$;
- I_{col} = Major moment of inertia of column $[mm^4]$;
- α = Factor to account for shear area;
- G = Shear modulus of timber $[MPa]$;
- A_{col} = Area of column $[mm^2]$.

8.3.5 Summary

For the full frame model, as shown in Figure 8.3, column rotation is already taken into account by the framework program. But joint-panel rotations need to be included separately, which is further analysed in the next section. In the case of a beam only model, the rotational spring needs to include a component of column rotation. An equation for column stiffness was derived, but validation with experimental data was not possible as the experimental data included rotations due to reaction frame movement.

In the beam only model the rotational spring is placed at the beam-column interface and thus the connection moment is applied to the rotational spring. The equation for column stiffness is based on centreline moment, therefore a correction factor χ, is introduced. This factor is further analysed in Section 9.3.

8.4 Joint panel shear deformation

This section evaluates joint panel shear deformation in more detail. Joint panel shear deformation is caused by high shear stresses within the joint panel zone and increased rotations in the joint region, as shown in the previous section on column deformation. Equations for the rotational stiffness of this spring will be derived and compared with experimental data.

For seismic frames with post-tensioned only connections, joint flexibility is most significant for small displacements corresponding to the serviceability limit state for typical frame structures. Up to 30% of the total frame drift can be attributed to the flexibility of the joint (Cursiel et al., 2012). Internal gravity connections do not exhibit any joint panel shear deformation, as has been shown by experimental results of Section 6.6. External connections in gravity frames however, do experience joint panel shear deformation. The main contribution for gravity frames is during SLS calculations, where it adds extra rotation to the joint and thus creates more deflections of the beam (Section 6.5.5).

8.4.1 Theoretical derivation

Based on results of experimental testing (Section 5.4.3) it was concluded that the joint panel stiffness did not depend on the post-tensioning force and that a linear relationship between connection moment and shear deformation was found until decompression. In this section this linear relationship is evaluated and therefore this theory is limited to the behaviour of the joint panel before decompression. After decompression the stiffness of the joint panel changes. Although this effect has been identified and shown in experimental testing, the error on the overall performance of the frame by assuming linear behaviour is small.

Figure 8.8 shows the shear forces which are acting on the joint panel region, the column shear force, V_{col}, the shear forces due to connection moment, $V_{jp,con}$, and the resulting joint panel shear force, V_{jp}. The column shear force is already in the framework model, so only the shear force due to connection moment should be modelled using the rotational spring.

At the connection there is a compressive force acting due to post-tensioning (F_{pt}) and a bending moment (M_{con}). The compressive post-tensioning force does not result in any shear stresses. The bending moment results in a tension and

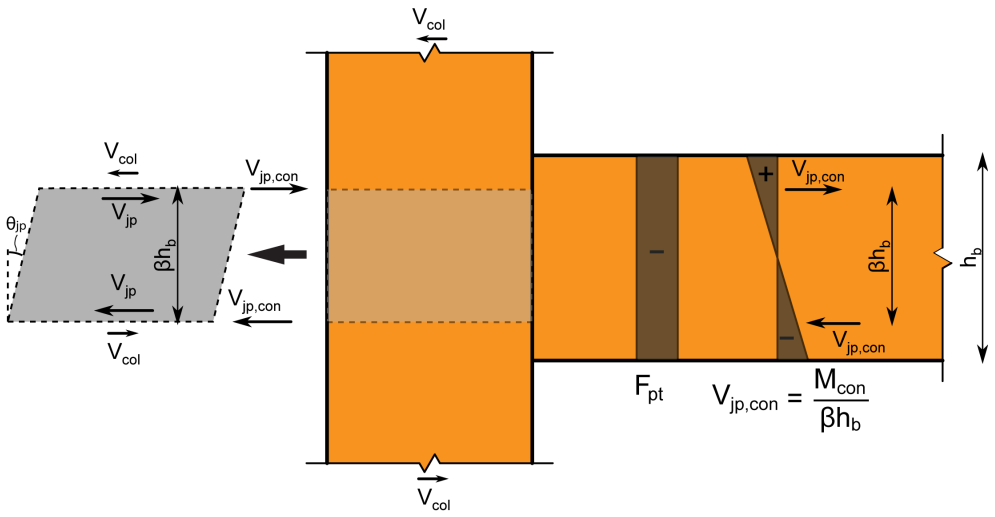

Figure 8.8: Schematics of shear forces in joint panel region

compression area. Although there is no real tension force acting on the column as a result of the initial compressive stresses due to the post-tensioning. The tension is a reduction in initial compression, which will create shear stresses and deformations as if it is a tensile force. The connection moment can be expressed in terms of the tensile (or compressive force) and the distance between these two forces. The tension and compression forces, which are the shear forces in the joint panel due to the connection moment, $V_{jp,con}$, can be calculated using Equation 8.8.

$$V_{jp,con} = \frac{M_{con}}{\beta h_b} \tag{8.8}$$

Where:

- $V_{jp,con}$ = Shear force in joint panel due to connection moment
- M_{con} = Connection moment
- h_b = Beam height
- β = Factor to calculate the effective height of joint panel

The factor βh_b can be seen as height of the joint panel which is acting in shear. For a rectangle this is $2/3h_b$, whereas for a box section this is between 0.75 to 0.9 h_b, depending on geometry of the box section. For partial contact connections the factor is the distance between the two flanges. The mathematical

expression for βh_b is given in Equation 8.9. This is based on the derivation shown in Equation 8.10.

$$\beta h_b = \frac{I}{Z_h} = \frac{\int_A z^2 \, \mathrm{d}A}{\int_{A_h} z \, \mathrm{d}A_h} \tag{8.9}$$

Where:

- I = Second moment of area of the full section
- Z_h = First moment of area of half the section (subscript h stands for 'half')
- z = Distance from point on section to neutral axis
- A = Area of beam
- A_h = Half the area of the beam

$$\begin{aligned}
\sigma_b(z) &= \frac{M_{con} \cdot z}{I} \\
V_{jp,con} &= \int_{A_h} \sigma_b(z) \, \mathrm{d}A_h \\
V_{jp,con} &= \int_{A_h} \frac{M_{con} \cdot z}{I} \, \mathrm{d}A_h \\
V_{jp,con} &= \frac{M_{con}}{I} \cdot \int_{A_h} z \, \mathrm{d}A_h \\
V_{jp,con} &= M_{con} \cdot \frac{Z_h}{I} = \frac{M_{con}}{\beta h_b} \rightarrow \beta h_b = \frac{I}{Z_h}
\end{aligned} \tag{8.10}$$

The shear force in the joint panel has to be converted to shear stress, as shown in Equation 8.11.

$$\tau_{jp,con} = \frac{V_{jp,con}}{\alpha A_{col}} \tag{8.11}$$

Where:

- $\tau_{jp,con}$ = Shear stress in joint panel due to connection moment
- α = Factor to calculate effective shear area of cross-section of column
- A_{col} = Cross-sectional area of column

The shear stress results in a shear rotation of the joint panel area, as in Equation 8.12.

$$\theta_{jp,con} = \frac{\tau_{jp,con}}{G} \tag{8.12}$$

Where:

- $\theta_{jp,con}$ = Shear rotation of joint panel due to connection moment
- G = Shear modulus of timber

Combining the Equations 8.8 to 8.12 one can find the relationship between the connection moment and the joint panel shear rotation, as shown in Equation 8.13.

$$M_{con} = \alpha G A_{col} \cdot \beta h_b \cdot \theta_{jp,con} \tag{8.13}$$

The stiffness to use in the beam or frame model is given in Equation 8.14.

$$k_{jp} = \alpha G A_{col} \cdot \beta h_b \tag{8.14}$$

For gravity frames the force of the post-tensioning anchorage is not acting along the centreline of the beam. Therefore, at zero connection moment, there is shear deformation in the joint panel, as was shown by experimental testing results in Figures 6.18 and 6.40. The shear deformation is approximately zero at negative decompression moment. In the framework model the compressive force of the post-tensioning should be located eccentrically from the centre of the connection. This results in part of the joint panel having a constant shear deformation. This is a way of off-setting the joint panel shear deformation.

8.4.2 Experimental measurements

When measuring joint panel shear in an experimental test setup, the measurement is of the total joint panel shear (V_{jp}) deformation, which includes column shear (V_{col}) and shear due to connection moment ($V_{jp,con}$). Therefore values found from experimental testing should not be used directly in a framework analysis program.

The total shear force in the joint panel zone is given by Equation 8.15.

$$V_{jp} = V_{jp,con} - V_{col} \tag{8.15}$$

Both terms in Equation 8.15 can be expressed in terms of connection moment, as shown in Equations 8.16 and 8.17. In this equation H is the inter-storey height.

$$V_{jp,con} = \frac{M_{con}}{\beta h_b} \tag{8.16}$$

$$V_{col} = \frac{M_{cl}}{H} = \frac{M_{con}}{\chi H} \tag{8.17}$$

Combining Equations 8.15 to 8.17 results in a relationship between the joint panel shear force and connection moment, as shown in Equation 8.18.

$$V_{jp} = \frac{M_{con}}{\beta h_b} - \frac{M_{con}}{\chi H} = M_{con} \cdot \left(\frac{1}{\beta h_b} - \frac{1}{\chi H} \right) \tag{8.18}$$

Similar as in the previous section, the shear force in the joint panel can be converted to a shear deformation. This leads to the Equation 8.19 for the stiffness of the joint panel based on experimental testing measurements.

$$k_{jp} = \frac{\alpha G A_{col}}{\left(\frac{1}{\beta h_b} - \frac{1}{\chi H} \right)} \tag{8.19}$$

It can be seen that the Equation 8.19 differs from Equation 8.14 of the joint panel rotational spring due to the influence of the shear force in the column.

8.4.3 Model validation

In order to validate the analytical model a comparison with experimental testing data is made. The beam column connection, as described in Chapter (5), is used. Only data from the column made of LVL11 with all grains running parallel have been used, the rotated sheet and cross-banded LVL had unknown material properties (E and G) which meant that the analytical model could not be used. Also the post-tensioned beam column connection using glue-laminated (Glulam) timber (Smith et al., 2012) is used for comparison. The comparison for these two tests can be found in Table 8.2. Data from the one-bay and two-bay frame testing, as presented in Chapter 6, are used for comparison and values can be found in Table 8.3.

Table 8.2: Comparison of joint panel stiffness from analytical model and experimental data

Test	Image	Experimental data	Analytical data	Stiffness values
Experimental testing of beam-column connection with draped tendons		Nelson Pine LVL 11 $E = 11\text{GPa}$ $G = 550\text{MPa}$ $A_{col} = 153000\text{mm}^2$ $h_b = 526\text{mm}$ $L_b \approx 8\text{m}$ $h_{col} = 500\text{mm}$ $H = 2.5\text{m}$	$\alpha = 0.86$ $I = 2.52 \cdot 10^9\ \text{mm}^4$ $Z_h = 6.18 \cdot 10^6\ \text{mm}^3$ $\beta = 0.78$ $\chi = 0.81$	Analytical: $k_{jp} = 36\text{kNm/mrad}$ $k_{jp,ext} = 37\text{kNm/mrad}$ Experimental: $k_{jp} = 41\text{-}54\text{kNm/mrad}$
Experimental testing of beam-column connection using Glulam	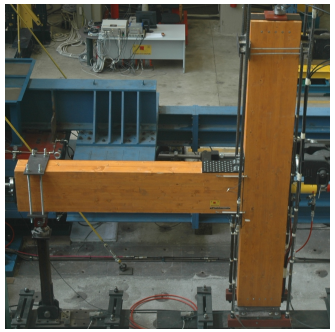	GL32h $E = 13.7\text{GPa}$ $G = 850\text{MPa}$ $A_{col} = 115920\ \text{mm}^2$ $h_b = 483\text{mm}$ $L_b = 4.64\text{m}$ $h_{col} = 483\text{mm}$ $H = 3.3\text{m}$	$\alpha = 0.86$ $I = 2.25 \cdot 10^9\ \text{mm}^4$ $Z_h = 7.00 \cdot 10^6\ \text{mm}^3$ $\beta = 0.67$ $\chi = 0.90$	Analytical: $k_{jp} = 30\text{kNm/mrad}$ $k_{jp,exp} = 31\text{kNm/mrad}$ Experimental: $k_{jp} = 28\text{-}33\text{kNm/mrad}$

Table 8.3: Comparison of joint panel stiffness from analytical model and experimental data (continued)

Test	Image	Experimental data	Analytical data	Stiffness
Experimental testing of one-bay frame with draped tendons		Nelson Pine LVL 11 $E = 11$GPa $G = 550$MPa $A_{col} = 144000$ mm^2 $h_b = 500$mm $L_b = 9.14$m $h_{col} = 500$mm $H = 3.6$m	$\alpha = 0.86$ $I = 2.21 \cdot 10^9$ mm^4 $Z_h = 5.31 \cdot 10^6$ mm^3 $\beta = 0.83$ $\chi = 0.84$	Analytical: $k_{jp} = 34$kNm/mrad $k_{jp,exp} = 33$kNm/mrad Experimental: $k_{jp} = 27$-39kNm/mrad
Experimental testing of two-bay frame frame with draped tendons		Nelson Pine LVL 11 $E = 11$GPa $G = 550$MPa $A_{col} = 1144000$ mm^2 $h_b = 360$mm $L_b = 6.1$m $h_{col} = 500$mm $H = 3.6$m	$\alpha = 0.86$ $I = 0.65 \cdot 10^9$ mm^4 $Z_h = 2.04 \cdot 10^6$ mm^3 $\beta = 0.88$ $\chi = 0.75$	Analytical: $k_{jp} = 29$kNm/mrad $k_{jp,exp} = 25$kNm/mrad Experimental: $k_{jp} = 21$-30kNm/mrad

For the frame testing, the first and second moment of area, Z_h and I, have been calculated based on properties of top and bottom flanges only, as they were in contact with the column through the steel plates placed at the connection interface.

In the table stiffness values are presented based on the analytical model for input in framework analysis programs (k_{jp}) and for comparison of experimental measured joint-panel shear deformation ($k_{jp,exp}$). Also presented is a range of experimental values of joint panel shear. It can be seen that all analytical predicted values are within the range of experimental testing results. Only for the beam-column connection with draped tendons is the stiffness slightly underestimated. From this it can be concluded that the analytical model is accurate in predicting the joint panel stiffness.

Plots of joint panel shear rotation versus connection moment are shown in Figure 8.9. It can again be seen that the results of experimental testing and analytical model for experimental results match very well. The offset between analytical model and experimental testing is due to the eccentric anchorage plate. This offset results in shear stresses in the joint panel at zero beam rotation. This can be included in a framework model by applying the post-tensioning force onto the column with an offset, as is shown in Figure 8.3.

8.4.4 Summary

The joint panel shear deformation has been evaluated in this section. In a framework analysis this deformation component is usually not taken into account and should be added as they form an important deformation component in timber frames. A theoretical derivation of shear stresses in the joint panel zone resulted in an equation for the joint panel shear stiffness. This equation can not be directly used to predict experimental measured joint panel shear stiffness. The column shear force is not taken into account, as this is already included in modelling of the column. A modified equation for the joint panel shear stiffness which does include the column shear force is also presented and validated with experimental testing results. A very good correlation between experimental measured values and theoretical values was shown. From this it can be concluded that the analytical model is accurate in predicting the joint panel stiffness.

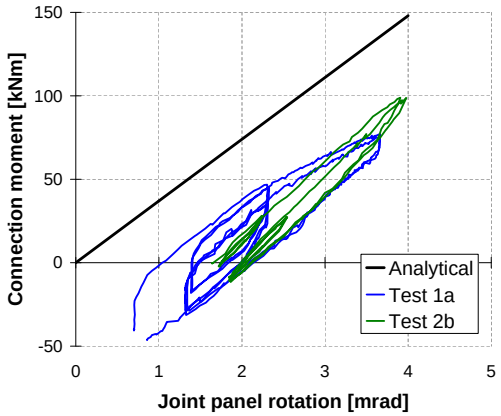

(a) Connection testing

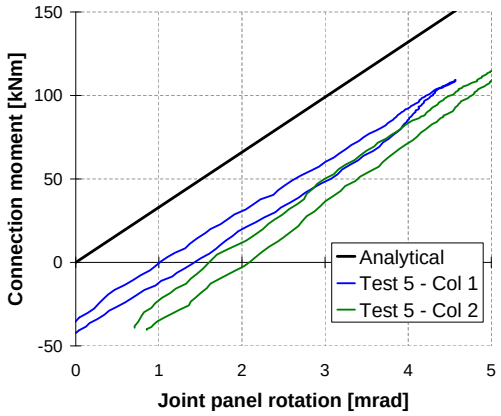

(b) One-bay frame testing

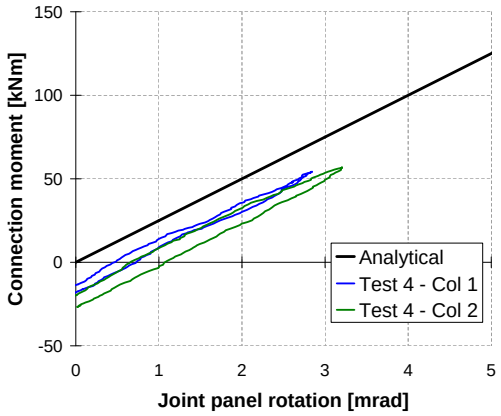

(c) Two-bay frame testing

Figure 8.9: Comparison between experimental results and analytical model for joint panel shear rotation

8.5 Interface compression deformation

Experimental test results of post-tensioned timber beam-column connections, like those described in Chapter 5 show an initial connection stiffness before decompression. This stiffness is not included in the column or joint panel deformation, and it is not captured by the MMBA procedure (Palermo, 2004). This initial stiffness is purely due to deformation of the column interface caused by compression stresses perpendicular to the grain. Therefore this deformation component (θ_{int}) has to be added to the connection design. The separation of the connection rotation into the gap opening (θ_{gap}) and the interface compression deformation (θ_{int}) makes it possible to use existing mechanical models to predict the connection behaviour.

This section derives the interface compression stiffness based on a multi-spring model approach. This approach allows column reinforcement, like screw reinforcement, to be included in the calculation model. Firstly, the partial contact connection is analysed and secondly the full contact connection. Both models are verified with experimental data from connection and frame testing. Similar to the joint panel shear stiffness, the behaviour before decompression is analysed. After decompression the rotational stiffness is no longer linear, but gap opening will dominate the rotations after decompression. Therefore a linear rotational behaviour can be assumed, but further research could be performed to determine a non-linear rotational behaviour.

8.5.1 Partial contact connections

A partial contact connection, with only top and bottom flanges of the beam in contact with the column, as for experimental testing described in Chapter 6, a model consisting of two compression springs can be made, as is shown in Figure 8.10.

For this connection the connection moment can easily be transformed into a tension and a compression force at the interface, F_{int}, as shown in Equation 8.20.

$$F_{int} = \frac{M_{con}}{\beta h_b} \tag{8.20}$$

The tension force is not an actual tension force as the compression due to

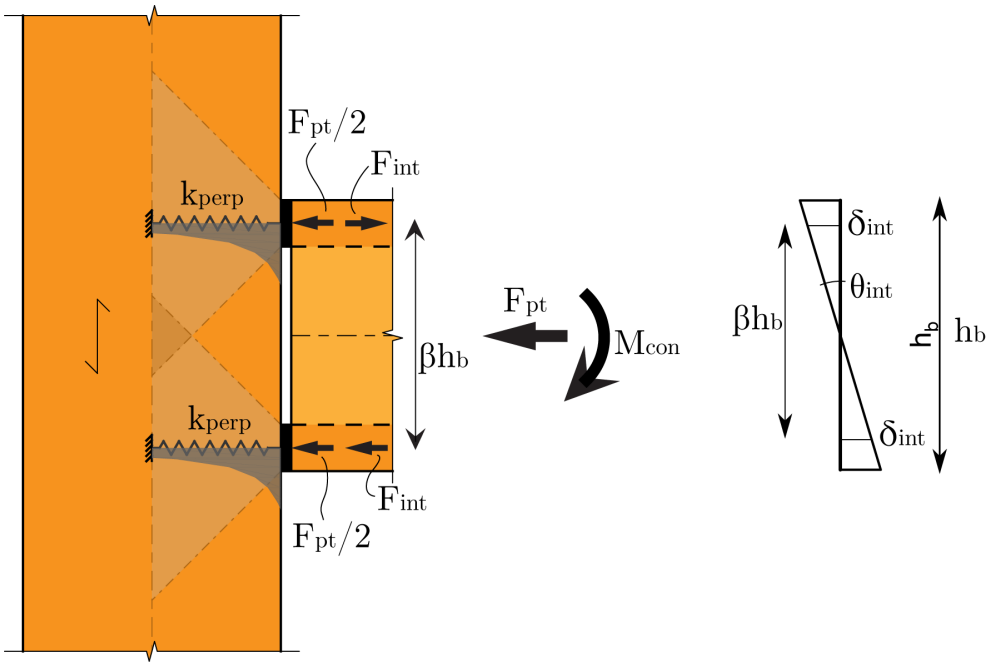

Figure 8.10: Multi-spring model for interface compression based on partial contact connection

post-tensioning (which is uniform and does not cause any rotations) is ignored. Therefore, until decompression, the tension force can be seen as a reduction in compression due to post-tensioning.

This interface force will displace the column interface (Equation 8.21) based on the spring stiffness (k_{perp}) as presented in Equation 8.35.

$$\delta_{int} = \frac{F_{int}}{k_{perp}} \tag{8.21}$$

This displacement results in an interface rotation as shown in Figure 8.10 and Equation 8.22.

$$\theta_{int} = \frac{2\delta_{int}}{\beta h_b} \tag{8.22}$$

Combining Equations 8.20 to 8.22 results in Equation 8.23

$$k_{int} = \frac{M_{con}}{\theta_{int}} = 0.5 k_{perp} (\beta h_b)^2 \tag{8.23}$$

This equation gives the rotational stiffness of the interface, based on the

compressive stiffness of the interface (k_{perp}) and the height between the centre of top and bottom flanges (βh_b). The compressive stiffness of the interface is further evaluated in the next section. It can be seen that the stiffness has a quadratic relationship with the beam height. This is because for larger sections, the decomposition of the moment into a tension and compression force has a larger lever arm, resulting in smaller forces on the column interface (F_{int}), and the resulting deformations give even smaller rotations, as they are spaced further apart.

8.5.2 Full contact connections

For full contact connections a multi-spring model, as presented in Figure 8.11, has been developed which is based on the compression stiffness of the timber column. It is assumed that the deformation of the column interface can be described by a linear function as shown in Equation 8.24. The value of u_0 is the initial compression under post-tensioning load only and no bending moment. The value of θ_{int} is the rotation of the column interface for a given bending moment and y_i is the vertical distance of the top of the beam to the spring.

$$u_i = \theta_{int} \cdot y_i + u_0 \tag{8.24}$$

The spring deformation is linear related to the force in the spring (F_i), as shown in Equation 8.25.

$$F_i = k_{perp} \cdot u_i = \theta_{int} \cdot k_{perp} y_i + u_0 \cdot k_{perp} \tag{8.25}$$

The values of θ_{int} and u_0 can be solved using the two equilibrium equations, one for horizontal force equilibrium (Equation 8.26) and one for bending moment equilibrium (Equation 8.27) taken around the top of the beam.

$$\begin{aligned} F_{pt} &= \sum F_i = \theta_{int} \cdot \sum_{i=1}^{n} k_{perp} y_i + u_0 \cdot \sum_{i=1}^{n} k_{perp} \\ u_0 &= F_{pt} \cdot \frac{1}{\sum_{i=1}^{n} k_{perp}} - \theta_{int} \cdot \frac{\sum_{i=1}^{n} k_{perp} y_i}{\sum_{i=1}^{n} k_{perp}} \end{aligned} \tag{8.26}$$

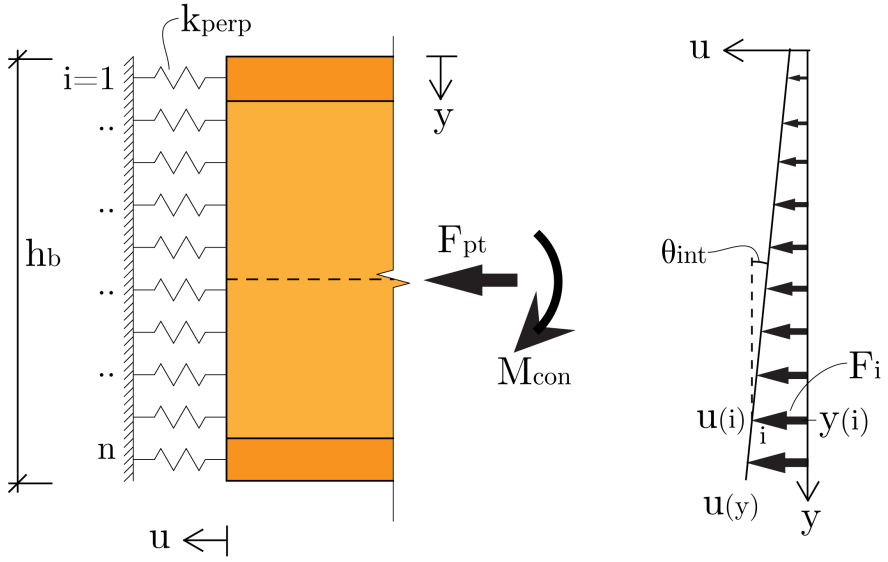

Figure 8.11: Multi-spring model for evaluation of column interface compression

$$M_{con} + F_{pt} \cdot y_{pt} = \sum F_i y_i = \theta_{int} \cdot \sum_{i=1}^{n} k_{perp} y_i^2 + u_0 \cdot \sum_{i=1}^{n} k_{perp} y_i \tag{8.27}$$

The compressive post-tensioning force is acting along the centroid of the cross-section. Therefore y_{pt} (in Equation 8.27) is the distance between the top of the beam and the centroid of the section. This distance can be calculated by dividing the first moment of area of the beam by the total cross-sectional area of the beam. The first moment of area is the area of the cross-section multiplied by the distance to a fixed point, in this case the top of the beam. As the column is assumed homogeneous, the centroid of the springs equals the centroid of the beam. This can also be seen from the point that only a compressive force and no bending moment should result in a constant compression of the springs and no rotation. This derivation is shown in Equation 8.28.

$$y_{pt} = \frac{Z}{A} = \frac{\sum(A_i y_i)}{\sum A_i} = \frac{\sum(k_{perp} y_i)}{\sum k_{perp}} \tag{8.28}$$

Equation 8.27 can be solved for the value of θ_{int}, as shown in Equation 8.29, whereby the result of Equation 8.28 is used. From this derivation it can be seen

that the interface rotation is not dependent on the post-tensioning force and that it is linearly dependent on the connection moment.

$$\begin{aligned}
\theta_{int} \cdot \sum_{i=1}^{n} k_{perp} y_i^2 &= M_{con} + F_{pt} \cdot y_{pt} - u_0 \cdot \sum_{i=1}^{n} k_{perp} y_i \\
\theta_{int} \cdot \sum_{i=1}^{n} k_{perp} y_i^2 &= M_{con} + F_{pt} \cdot \frac{\sum_{i=1}^{n} k_{perp} y_i}{\sum_{i=1}^{n} k_{perp}} - F_{pt} \frac{\sum_{i=1}^{n} k_{perp} y_i}{\sum_{i=1}^{n} k_{perp}} + \dots \\
&\quad \dots \theta_{int} \cdot \frac{\sum_{i=1}^{n} k_{perp} y_i \cdot \sum_{i=1}^{n} k_{perp} y_i}{\sum_{i=1}^{n} k_{perp}} \\
\theta_{int} \cdot \sum_{i=1}^{n} k_{perp} y_i^2 &= M_{con} + \theta_{int} \cdot \frac{\sum_{i=1}^{n} k_i y_i \cdot \sum_{i=1}^{n} k_{perp} y_i}{\sum_{i=1}^{n} k_{perp}} \\
\theta_{int} &= \frac{M_{con}}{\sum_{i=1}^{n} k_{perp} y_i^2 - \frac{\sum_{i=1}^{n} k_{perp} y_i \cdot \sum_{i=1}^{n} k_{perp} y_i}{\sum_{i=1}^{n} k_{perp}}}
\end{aligned} \tag{8.29}$$

From Equation 8.29 it follows that the rotational spring stiffness of the interface is given by the formula as presented in Equation 8.30.

$$k_{int} = \frac{M_{con}}{\theta_{int}} = \sum_{i=1}^{n} k_{perp} y_i^2 - \frac{\left(\sum_{i=1}^{n} k_{perp} y_i\right)^2}{\sum_{i=1}^{n} k_{perp}} \tag{8.30}$$

8.5.3 Compressive stiffness

The partial contact and full contact connections both depend on the compressive stiffness of the column perpendicular to grain. This stiffness is represented by a compression spring with a stiffness k_{perp} as shown in Figure 8.12. The displacement of the spring is given by integrating the strain profile (Equation 8.31) over the depth of the column, as is shown by Equation 8.32.

$$\epsilon(x) = \frac{\sigma(x)}{E_{90}} = \frac{F_i}{E_{90} \cdot A(x)} = \frac{F_i}{E_{90} \cdot w_c \cdot l_c(x)} = \frac{F_i}{E_{90} \cdot w_c} \cdot \frac{1}{l_0 + 2x} \tag{8.31}$$

$$
\begin{aligned}
u_i &= \int_0^{0.5h_c} \epsilon(x)dx = \int_0^{0.5h_c} \frac{F}{E_{90} \cdot w_c} \cdot \frac{1}{l_0 + 2x} dx \\
u_i &= \frac{F_i}{E_{90} \cdot w_c \cdot l_0} \cdot \int_0^{0.5h_c} \frac{1}{1 + 2x/l_0} \\
u_i &= \frac{F_i}{E_{90} \cdot w_c \cdot l_0} \cdot \frac{1}{2/l_0} ln\left(\frac{2}{l_0} 0.5h_c + 1\right) \\
u_i &= \frac{F_i}{2E_{90} \cdot w_c} \cdot ln\left(\frac{h_c}{l_0} + 1\right)
\end{aligned} \tag{8.32}
$$

Where:

- x = Distance from column interface
- $\epsilon(x)$ = Strain in the column at distance x
- $\sigma(x)$ = Stress in the column at distance x
- E_{90} = Modulus of elasticity perpendicular to grain
- F_i = Force in spring i
- $A(x)$ = Area in the column under compression at distance x
- w_c = Width of contact area between beam and column
- $l_c(x)$ = Length of compression area in column at distance x
- l_0 = Length of loading area at column interface (tributary width of spring)
- h_c = Depth of column

The compression stiffness of the spring is given by Equation 8.33. This equation is similar as described by Blass and Görlacher (2004).

$$
k_{perp} = \frac{F_i}{u_i} = \frac{2E_{90} \cdot w_c}{ln\left(\frac{h_c}{l_0} + 1\right)} \tag{8.33}
$$

The spring stiffness can be modified to include compression reinforcement like timber parallel to the grain or screw reinforcement, which are elaborated in the next sections.

Timber reinforcement Timber reinforcement, like cross-banded LVL, can be used to reinforce the compressive stiffness perpendicular to grain. Experimental testing of cross-banded LVL, as described in Section 3.3.4, showed an increase in the compressive stiffness of a block from 500MPa to 2500MPa. But it was

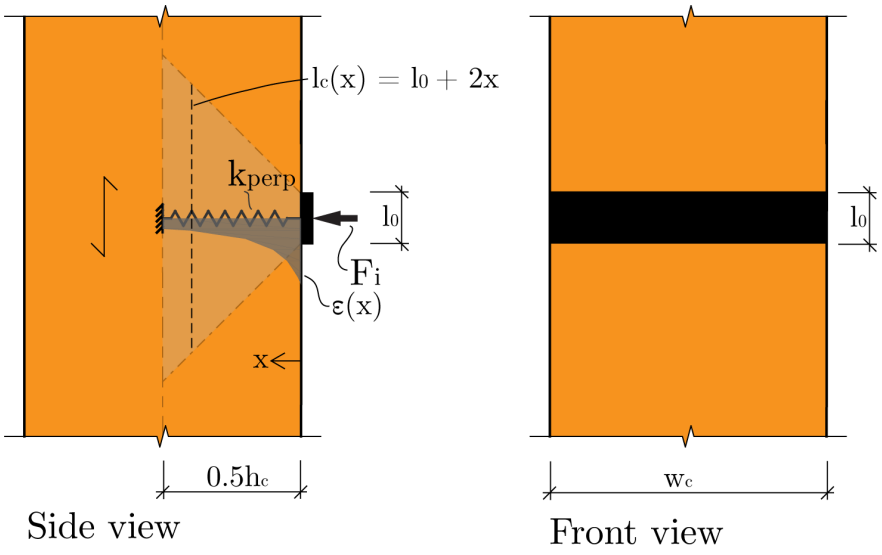

Figure 8.12: Derivation of compression stiffness perpendicular to grain of column interface

also noted that for cross-banded LVL stress-spreading did not occur in the same amount as for normal LVL. The perpendicular to grain stiffness of a block test was 2460MPa, whereas for a rail test (including stress spreading) it was 622MPa. The effect of stress spreading should not be fully taken into account for calculation of compression stiffness if the high modulus of elasticity is used. Alternatively a lower modulus of elasticity of 620MPa should be used, as found from experimental testing or rail specimens. Further research in this area is needed to develop a better understanding of the material behaviour of cross-banded LVL in compression perpendicular to grain.

Screw reinforcement An experimental campaign has been carried out in order to define the elastic stiffness of screw reinforced LVL members in compression perpendicular to the grain. Parameters considered in the investigation include the screw length as a ratio of the LVL depth, the screw reinforcing ratio and the grade of LVL material. Results of this experimental campaign are published in Watson et al. (2013).

The main outcome of this study was a design graph, shown in Figure 8.13, which presents a screw reinforcing stiffness factor, k_{scr}. This is a stiffness modifi-

cation factor and should not be confused with a compression/rotational stiffness. This factor depends on the reinforcement ratio, the area of steel over the area of timber (A_{scr}/A_t), and the screw length over the section depth (l_s/h_c). The empirical equation for the lines is shown in Equation 8.34.

$$k_{scr} = 1 + 54\frac{A_{scr}}{A_t}\left(\frac{l_s}{h_c}\right)^{1.26} \tag{8.34}$$

Where:

- k_{scr} = Screw reinforcing stiffness factor (-)
- A_{scr} = Area of screws (mm^2)
- A_t = Area of timber in compression (mm^2)
- l_s = Length of screw (mm)
- h_c = Depth of column (mm)

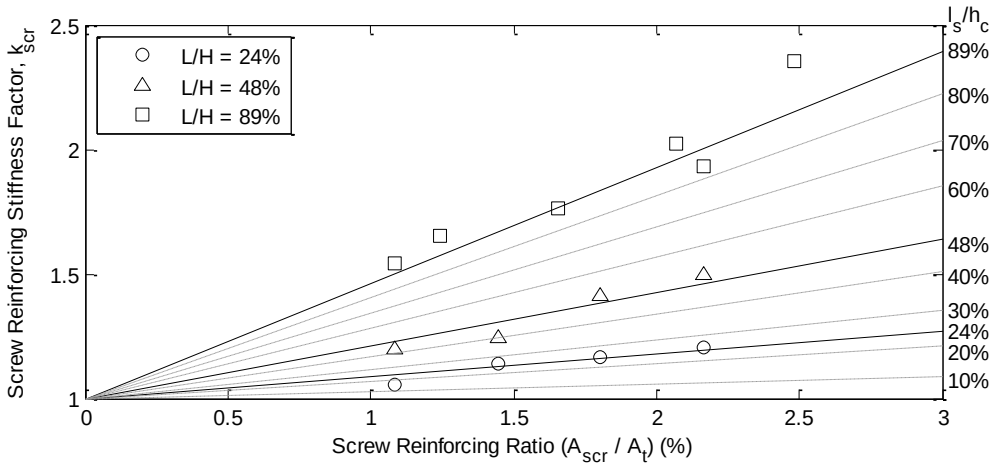

Figure 8.13: Preliminary design chart for screw reinforcing stiffness factor, based on the screw reinforcing ratio and ratio of screw length over section depth

The screw reinforcing stiffness factor, k_{scr}, can be multiplied with the stiffness of timber, k_{perp}, in order to calculate the combined stiffness. The resulting formula for perpendicular to grain compression stiffness of the column is given by Equation 8.35.

$$k_{perp} = k_{scr} \cdot \frac{2E_{90} \cdot w_c}{ln\left(\frac{h_c}{l_0} + 1\right)} \tag{8.35}$$

8.5.4 Model validation

Compressive stiffness of column interface The compressive stiffness of the column interface can be verified using experimental results of partial contact connections for the one-bay and two-bay test setups. After decompression the compressive force on the bottom steel plate attached to the column interface equaled the post-tensioning force, and the potentiometer fixed between the steel plate and the centreline of the column measured the compression displacement. This data was analysed for the one-bay and two-bay frame testing and is plotted in Figure 8.14. The compressive stiffness after decompression is shown in Table 8.4. The external connections of the two-bay frame did not reach decompression for the test with 300kN post-tensioning force, therefore no compression stiffness could be analysed.

Table 8.4: Column compression stiffness values (kN/mm) for one-bay and two-bay frame testing for internal and external connections

PT Force	Internal 2Bay		External 2Bay		External 1Bay	
(kN)	left	right	left	right	left	right
100	199	191	196	214	213	(-345)
200	266	182	220	203	255	(1388)
300	185	160	-	-	250	(708)

The average result of all tests is 210kN/mm with a coefficient of variation of 15%. The behaviour of the right connection of the one-bay frame is unexpected and has been ignored in calculation of the average stiffness value.

Both setups (technical drawings in Appendix G) had a steel plate of 90mm high and 288mm wide and used 14 10mm diameter screws with a length of 200mm for reinforcement in a 500mm deep column. Calculation of the screw stiffness increase factor of k_{scr} is shown in Equation 8.36. The compressive stiffness of the reinforced interface is calculated in Equation 8.37.

$$k_{scr} = 1 + 54\frac{A_{scr}}{A_t}\left(\frac{l_s}{h_c}\right)^{1.26} = 1 + 54\frac{14 \cdot 0.25\pi 10^2}{90 \cdot 288}\left(\frac{200}{500}\right)^{1.26} = 1.72 \qquad (8.36)$$

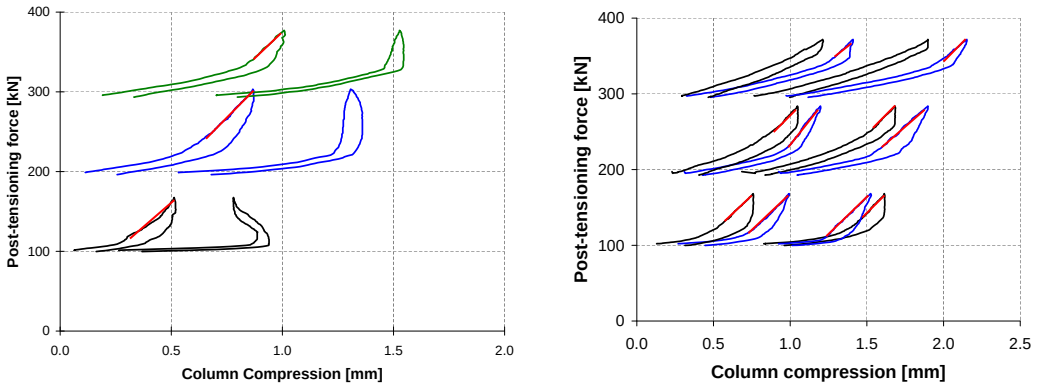

(a) One-bay frame (b) Two-bay frame

Figure 8.14: Analysis of interface compression stiffness for one-bay and two-bay frames

$$k_{perp} = k_{scr} \cdot \frac{2E_{90} \cdot w_c}{ln\left(\frac{h_c}{l_0} + 1\right)} = 1.72 \cdot \frac{2 \cdot 500 \cdot 288}{ln\left(\frac{500}{90} + 1\right)} = 264kN/mm \tag{8.37}$$

It can be seen that the predicted value is higher than the measured values for column compression stiffness, but it is still within the range of experimental testing data. The modulus of elasticity perpendicular to grain was not measured for the columns, but assumed to be the same as the values found in experimental testing of material properties which was described in Section 3.3. If a value of 400MPa was used, a stiffness of 211kN/mm would be found which matches exactly with experimental testing.

Interface rotational stiffness of partial contact connection Experimental testing of the one-bay frame (Section 6.5) resulted in an interface stiffness of 31kNm/mrad. The two-bay frame testing (Section 6.6) showed an interface stiffness of 17kNm/mrad. The rotational stiffness, based on the analytical Equation 8.23, of the interface for the one-bay frame is calculated in Equation 8.38 and for the two-bay frame in Equation 8.39.

$$k_{int} = 0.5k_{perp}(\beta h_b)^2 = 0.5 \cdot 264000 \cdot 410^2 = 22.2kNm/mrad \tag{8.38}$$

$$k_{int} = 0.5 k_{perp} (\beta h_b)^2 = 0.5 \cdot 264000 \cdot 315^2 = 13.1 kNm/mrad \tag{8.39}$$

The resulting rotational stiffness of 22kNm/mrad and 13kNm/mrad are below the measured values of 31kNm/mrad and 19kNm/mrad for the one-bay and two-bay frames, respectively. The comparisons of experimental results with model predictions are shown in Figure 8.15.

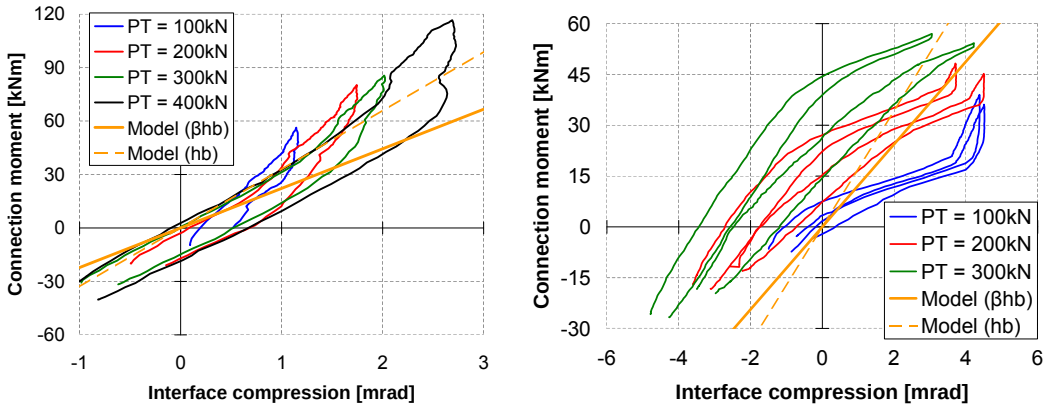

(a) One-bay frame

(b) Two-bay frame

Figure 8.15: Comparing model predictions and experimental results of interface compression stiffness for one-bay and two-bay frames

The difference can be caused by the triangular stress distribution on the steel plate, which is different from the constant stress applied to the specimens on which the screw reinforcement stiffness factor was based. The triangular stress distribution results in a larger distance between tension and compression force at the interface (F_{int}). If the full beam height (h_b)is used, instead of the distance between the centre of top and bottom flanges (βh), than stiffness values of 33kNm/mrad and 17kNm/mrad are found. These values match very well with experimental data until decompression, as can be seen in Figure 8.15. After decompression the interface stiffness changes, but this aspect has been left out of the model. At larger connection moments gap opening is the main contribution to connection rotation, therefore the difference in interface compression has a negligible effect. Also for the two bay frame a good comparison can be seen before

decompression, with the exception of an initial offset, caused by the eccentric post-tensioning anchorage, in experimental data.

Interface rotational stiffness of full contact connection Data from experimental testing of beam-column connection can be used for validation of the multi-spring model for full contact connections. The experimental testing is described in Chapter 5. It was found that an unreinforced timber column resulted in an initial interface stiffness between 22.5 and 32.1 kNm/mrad.

A multi-spring model with 21 springs was made to represent the column interface. Each spring had a tributary height of about 25mm. The springs at the location of top and bottom flanges had a width of 300mm and the springs at the webs had a width of 90mm. The stiffness of timber perpendicular to grain was taken as $E_{90} = 500MPa$, based on experimental testing described in Section 3.3.4 and the column depth was 500mm. The resulting spring stiffness was 97055N/mm for springs at the location of the flanges (Equation 8.40) and 29116N/mm for springs at the webs.

$$k_{perp} = \frac{2E_{90} \cdot w_c}{ln\left(\frac{h_c}{l_0} + 1\right)} = \frac{2 \cdot 500 \cdot 300}{ln\left(\frac{500}{25} + 1\right)} = 97055N/mm \tag{8.40}$$

The rotational stiffness of the interface is given by Equation 8.41. It can be seen that the value of 29.5kNm/mrad is within the range found by experimental testing.

$$\begin{aligned} k_{int} &= \sum_{i=1}^{n} k_{perp} y_i^2 - \frac{\left(\sum_{i=1}^{n} k_{perp} y_i\right)^2}{\sum_{i=1}^{n} k_{perp}} \\ &= 90585200219 - \frac{232280860^2}{883197} = 29.5kNm/mrad \end{aligned} \tag{8.41}$$

For cross-banded LVL, testing results ranged between 28 and 53kNm/mrad. Timber block testing has shown that the modulus of elasticity was 5 times higher compared to normal LVL. But as stress spreading is not happening as much for cross-banded LVL, the interface compression stiffness is based on the reduced modulus of elasticity of 620MPa and full stress spreading was used. The resulting stiffness value is shown in Equation 8.42. It can be seen that the results are again

within range of experimental data.

$$k_{int} = \sum_{i=1}^{n} k_{perp} y_i^2 - \frac{\left(\sum_{i=1}^{n} k_{perp} y_i\right)^2}{\sum_{i=1}^{n} k_{perp}}$$
$$= 112325648271 - \frac{288028267^2}{1095165} = 36.6 kNm/mrad \tag{8.42}$$

8.5.5 Summary

This section presented the derivation of a multi-spring model to account for the compressive stiffness of the column perpendicular to grain for partial contact and full contact connections. It has been shown that the rotational stiffness is independent of the post-tensioning force. The model includes the effects of stress spreading within the column. Also the increase in compressive stiffness due to screw reinforcement can be included. The results from the analytical model match experimental data quite well, but only a limited amount of data is available. Further experimental testing is needed to fully verify the analytical model.

8.6 Gap opening

For seismic design a cantilever is used for the derivation of the MMBA (Palermo, 2004), as presented in Section 2.3.2. This cantilever can represent a bridge pier or half of a beam length in a frame, as shown in Figure 8.16. In gravity design there is no idealized cantilever length due to the distributed load. No fixed point of contra-flexure can be defined and therefore a cantilever beam cannot be used to derive a member analogy. Therefore this section presents an adaptation of the modified monolithic beam analogy (MMBA) which is suitable for gravity frames. The newly derived gravity MMBA has been partly validated with experimental testing results in Section 8.6.5.

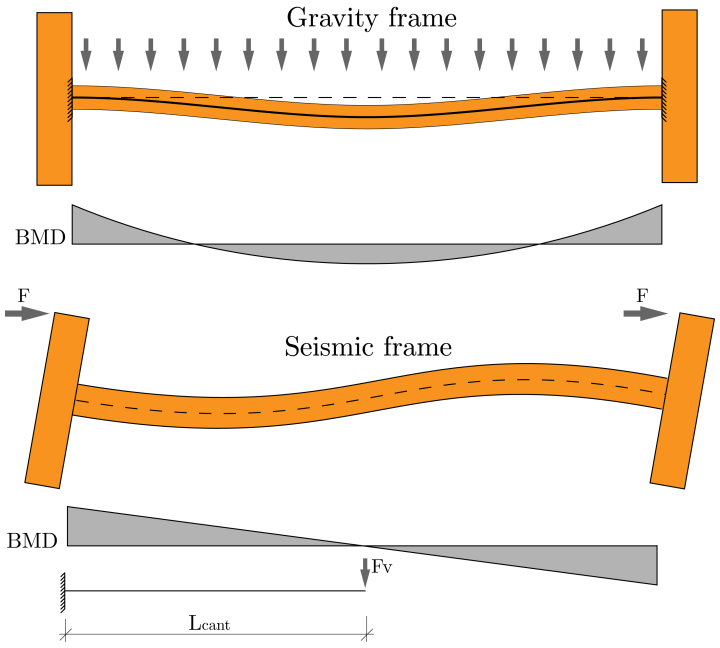

Figure 8.16: Comparison of frame deformation and bending moments (BMD) for gravity and seismic frames

For frame testing, with partial contact connections, a simplified design can be used as the depth of the compression zone (neutral axis depth) is known. This simplified design is presented in Section 8.6.6 and a comparison with experimental testing data is made. A comparison between the connection behaviour of full contact and partial contact connections is shown in Section 8.6.7.

8.6.1 Overview of design procedure

The design procedure to evaluate the gap opening using the MMBA for gravity frames, as shown in Figure 8.17, follows a similar format to the design procedure for seismic frames. First an amount of rotation due to gap opening (θ_{imp}) is chosen. For a full moment-rotation graph of the connection, a range of values needs to be analysed. The procedure is iterative and initially the neutral axis depth (c) needs to be estimated.

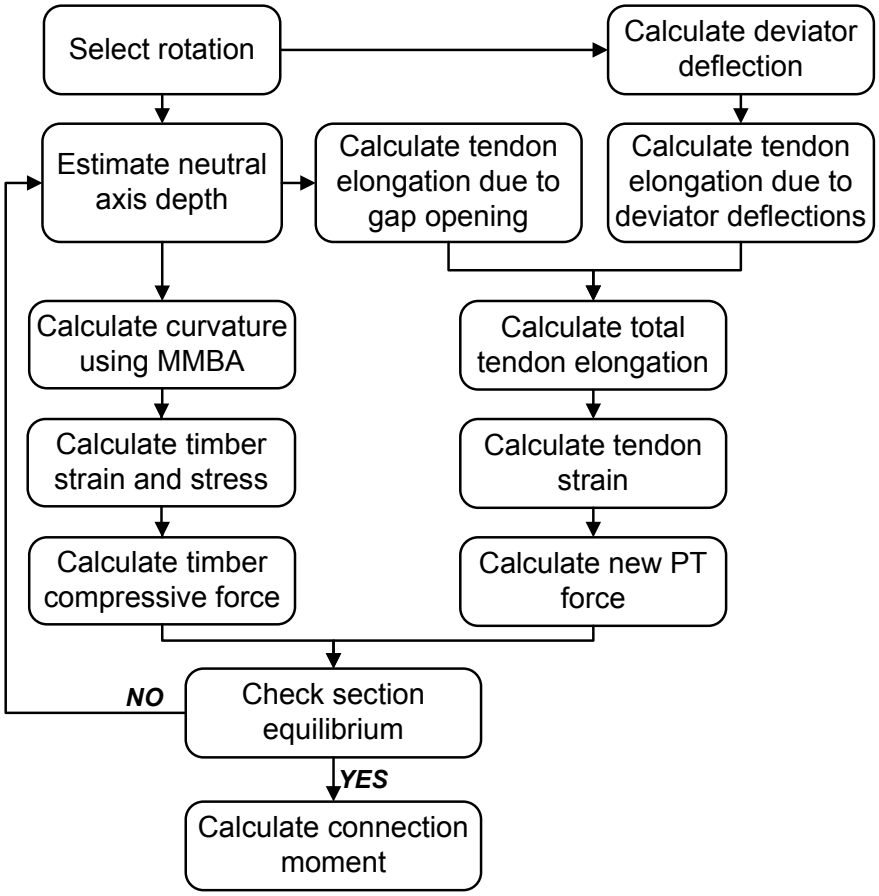

Figure 8.17: Design procedure for connection behaviour of post-tensioned gravity frames using the MMBA method

With this neutral axis depth the curvature at the connection can be calculated using the MMBA procedure. This procedure is explained in Section 8.6.2. The curvature, multiplied with the neutral axis depth results in the maximum timber strain at the connection. This strain can be multiplied by the modulus of elasticity

in order to get the compressive stress in the timber. The timber compressive force can be calculated by integrating the stress profile over the width of the beam. As the section is not solid, the width is a (piece-wise) function of the depth and integration needs to be used for the flange and the webs separately.

Calculation of tendon elongation consists of two parts, due to gap opening and due to deviator deflections as explained in Section 8.6.3. Deviator deflection can be calculated based on the summation of the decompression deflection and the additional deflection due to gap opening. The total deviator deflection can be used to calculate the elongation of the tendon. Using the imposed rotation (or gap opening), the contribution due to gap opening can be calculated by multiplying the rotation by the distance between the tendon and the neutral axis. The total tendon elongation is the sum of elongation due to gap opening and elongation due to deviator deflections. Frame shortening needs to be taken into account as this leads to a reduction in tendon elongation. The resulting tendon elongation divided by the length of the tendon gives the additional strain in the tendon. The additional strain, summed with the initial strain and multiplied by the area of the tendons and by the modulus of elasticity, results in the new post-tensioning force.

After calculating the timber compressive force and the new post-tensioning force, the section equilibrium needs to be verified. If no equilibrium is found, then the neutral axis depth needs to be changed. If equilibrium is found, the connection moment can be calculated based on the timber compressive force multiplied by the distance to the centroid of the beam.

8.6.2 MMBA for gravity systems

A full length beam with a connection on both ends is used for derivation of an MMBA for gravity beams, as shown in Figure 8.16. This beam is loaded with a variable distributed load (q), which is constant along the length of the beam. The assumption is made that the vertical uplift force at the deviators is constant and does not change due to tendon elongation. This assumption means that when displacements of the monolithic case are equal to displacements of a rocking connection, the influence of the constant uplift force cancels out. As this component is not taken into account, deflections calculated by the gravity

MMBA do not represent the total deflections of the beam.

For timber box beams it has been shown in Section 7.7 that shear deflection is about 25% of total beam deflections, therefore this contribution should not be ignored when evaluating displacements. The seismic MMBA does not take shear deformation into account, but an effective modulus of elasticity (E_{con}) was introduced in order to match experimental testing results. Presented below is a derivation of an MMBA for gravity beams whereby shear deformation has been included. In Appendix E.3 a derivation of the MMBA for a seismic cantilever system with the inclusion of shear deflections is presented.

Before decompression Before decompression both ends of the beam are fully fixed, as shown in Figure 8.18. When the beam is being loaded by the distributed load, called q_1, it moves down until the decompression point is reached. Displacement of mid-span of the beam (Δ_{mon}) before decompression is given by the bending and shear displacement of the distributed load, as shown in Equation 8.43. Derivation of this equation can be found in Appendix D.3.

$$\Delta_{mon} = \frac{1}{384}\frac{q_1 L_b^4}{EI} + \frac{q_1 L_b^2}{8GA_s} \tag{8.43}$$

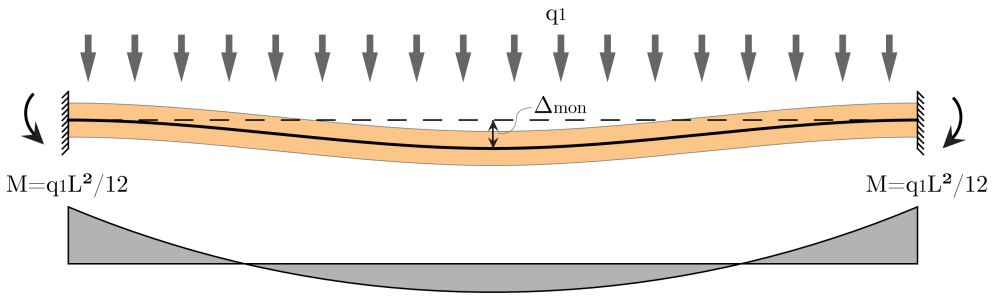

Figure 8.18: Schematics of gravity MMBA before decompression

The connection moment (M_{con}) due to the distributed load (q_1) is given in Equation 8.44.

$$M_{con} = \frac{1}{12} q_1 L_b^2 \tag{8.44}$$

Equation 8.44 can be rewritten to find an expression for the distributed load

(q_1), as shown in Equation 8.45.

$$q_1 = \frac{12M_{con}}{L_b^2} \tag{8.45}$$

The expression for q_1 (Equation 8.45) can be inserted into Equation 8.43.

$$\Delta_{mon} = \frac{1}{384}\frac{L_b^4}{EI} \cdot \frac{12M_{con}}{L_b^2} + \frac{L_b^2}{8GA_s} \cdot \frac{12M_{con}}{L_b^2} \tag{8.46}$$

Equation 8.46 can be simplified and the curvature at the connection ($\phi = M_{con}/EI$) can be inserted, resulting in Equation 8.47.

$$\Delta_{mon} = \phi \cdot \left(\frac{L_b^2}{32} + \frac{3EI}{2GA_s}\right) \tag{8.47}$$

Decompression Gap opening happens after decompression. Decompression is when the compressive stresses due to the post-tensioning equal the bending stresses, as shown in Figure 8.19 and Equation 8.48.

$$\sigma_{comp} = \sigma_{bend} \rightarrow \frac{F_{pt}}{A} = \frac{M_{dec}}{Z} \rightarrow M_{dec} = \frac{F_{pt} \cdot Z}{A} \tag{8.48}$$

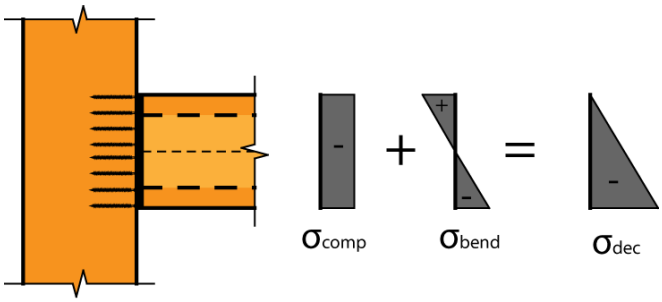

Figure 8.19: Stresses at decompression of beam-column connection

At decompression of the connection ($M_{con} = M_{dec}$) the mid-span displacement is as shown in Equation 8.49.

$$\Delta_{dec} = \phi_{dec} \cdot \left(\frac{L_b^2}{32} + \frac{3EI}{2GA_s}\right) \tag{8.49}$$

The decompression moment is when bending stress due to connection moment equal compressive stress due to the post-tensioning. This gives the equation for the decompression curvature, as shown in Equation 8.50. Due to beam deflections the post-tensioning force increases even before decompression. Therefore, in this equation the initial post-tensioning force is not used, but the increased post-tensioning force at decompression.

$$\phi_{dec} = \frac{F_{pt,dec}}{A}\frac{Z}{EI} \tag{8.50}$$

After decompression After decompression, when the distributed load is increased, a gap opens between beam and column (Figure 8.20). For any given amount of gap opening, the total mid-span deflection is the sum of the decompression displacement (Δ_{dec}) and the displacement as a result of connection rotation (Δ). Gap opening occurs due to the increase in distributed load (q_2), thus mid-span deflections after decompression are a function of the distributed load, as shown in Equation 8.51. Derivation of this equation can be found in Appendix D.3.

$$\Delta = \frac{5}{384}\frac{q_2 L_b^4}{EI} + \frac{q_2 L_b^2}{8GA_s} \tag{8.51}$$

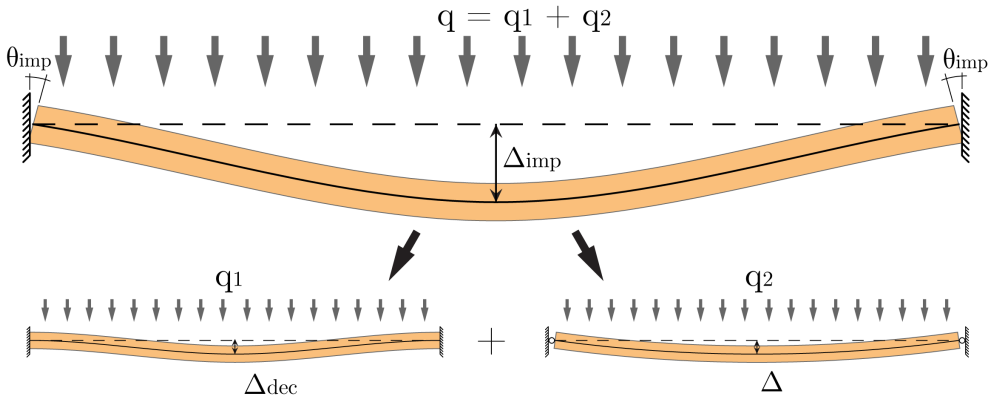

Figure 8.20: Schematics of gravity MMBA after decompression

Imposed rotations at the ends of the beam (θ_{imp}), which is the gap opening, are given by Equation 8.52. This can be re-written to find an expression for the

distributed load, Equation 8.53.

$$\theta_{imp} = \frac{1}{24}\frac{q_2 L_b^3}{EI} \tag{8.52}$$

$$q_2 = \frac{24\theta_{imp} EI}{L_b^3} \tag{8.53}$$

Equation 8.53 can be substituted into Equation 8.51, resulting in Equation 8.54.

$$\begin{aligned}
\Delta &= \frac{5}{384}\frac{L_b^4}{EI} \cdot \frac{24\theta_{imp} EI}{L_b^3} + \frac{L_b^2}{8GA_s} \cdot \frac{24\theta_{imp} EI}{L_b^3} \\
\Delta &= \frac{5}{16}\theta_{imp} \cdot L_b + \theta_{imp}\frac{3EI}{L_b \cdot GA_s} \\
\Delta &= \theta_{imp} \cdot \left(\frac{5L_b}{16} + \frac{3EI}{L_b \cdot GA_s}\right)
\end{aligned} \tag{8.54}$$

Displacement after decompression (Equation 8.54) can be added to displacement at decompression (Equation 8.49), as shown in Equation 8.55.

$$\Delta_{imp} = \Delta + \Delta_{dec} = \theta_{imp} \cdot \left(\frac{5L_b}{16} + \frac{3EI}{L_b \cdot GA_s}\right) + \phi_{dec} \cdot \left(\frac{L_b^2}{32} + \frac{3EI}{2GA_s}\right) \tag{8.55}$$

The monolithic beam analogy equates the displacement of the case with gap opening (Equation 8.55) with the displacement of a monolithic member (Equation 8.47). This can be solved for the curvature (ϕ), as in Equation 8.56. The factor η has been introduced for simplification of the equation, this factor takes into account the effects of bending and shear.

$$\begin{aligned}
\Delta_{mon} &= \Delta_{imp} \\
\phi \cdot \left(\frac{L_b^2}{32} + \frac{3EI}{2GA_s}\right) &= \theta_{imp} \cdot \left(\frac{5L_b}{16} + \frac{3EI}{L_b \cdot GA_s}\right) + \phi_{dec} \cdot \left(\frac{L_b^2}{32} + \frac{3EI}{2GA_s}\right) \\
\phi &= \frac{\dfrac{5L_b}{16} + \dfrac{3EI}{L_b \cdot GA_s}}{\dfrac{L_b^2}{32} + \dfrac{3EI}{2GA_s}} \cdot \theta_{imp} + \phi_{dec} \\
\phi &= \eta \cdot \theta_{imp} + \phi_{dec}
\end{aligned} \tag{8.56}$$

If the shear terms are ignored, then the result of the gravity MMBA is shown as in Equation 8.57.

$$\phi = \frac{10}{L_b} \cdot \theta_{imp} + \phi_{dec} \tag{8.57}$$

This is very similar to the seismic MMBA where the first factor is $3/L_{cant}$. Combining the two equations results in $L_{cant} = 0.3L_b$. This presents an effective cantilever length for gravity frames in order the use the seismic MMBA, assuming that shear deformation does not need to be accounted for.

Plastic deformation In seismic design of concrete structures reinforcement in the monolithic section can yield before ultimate strength is reached, resulting in yield rotation. This is not possible in timber, but the procedure has been further developed for concrete gravity systems. This design procedure is shown in Appendix E.2.

8.6.3 Tendon elongation

Although it is assumed in the derivation of the gravity MMBA that tendon elongation does not influence beam deflections, it does play a role when evaluating section equilibrium, as the timber compressive force should equal the post-tensioning force. Tendon elongation for frames with draped tendons consists of two parts; elongation due to gap opening and elongation due to deviator deflections. The increase in post-tensioning force results in elastic shortening of the frame, which reduces the tendon elongation. Beams and columns shorten and the increase in post-tensioning force results in some additional uplift of the deviators. As tendon elongation results from gap opening and deviator deflections along the full length of the tendon, one can not look at the behaviour of one beam only.

Due to gap opening Tendon elongation due to gap opening can be calculated using Equation 8.58. The factor two is because of the connections on either end of the beam and thus two gaps which open and n is the number of beams in the frame.

$$\Delta l_{pt,gap} = 2n \cdot \theta_{imp}(x_{pt} - c) \tag{8.58}$$

Where:

- $\Delta l_{pt,gap}$ = tendon elongation due to gap opening
- n = number of beams in frame
- θ_{imp} = imposed rotation at the connection (gap opening)
- x_{pt} = location of tendon relative to bottom of beam
- c = neutral axis depth

For frames with multiple bays, there is a difference between gap opening of internal and external connections as shown by experimental testing in Section 6.6. This difference in gap opening is not incorporated in the design procedure, the assumption is made that all connections reach decompression at the same time. To include this difference in the procedure would be very complicated, as the total stiffness of the connection (including all deformation components) influences the bending moment at the connection and thus connection rotation. Therefore only after a full beam/frame analysis has been performed, can it be seen if connections have reached decompression. This means that the connection behaviour needs to be updated after the analysis resulting in a complicated iterative procedure. Analysis for a two-bay frame has shown that approximately 60% of tendon elongation at ULS is due to deviator deflection and only 40% due to gap opening. Therefore, even if this iterative procedure was performed, it would only lead to small differences making it questionable if it is worth the effort.

Due to deviator deflections Tendon elongation due to deviator deflections can be split in two parts, before decompression and after decompression. Before decompression the displacement of the deviators can be evaluated in a similar manner as mid-span displacements for the monolithic case (Δ_{mon}, Equations 8.43 to 8.47). As also the initial precamber results in tendon elongation, this constant term (as F_v is assumed constant) needs to be added to the equation of deviator deflection. The derivation of deviator displacement is shown in Equation 8.59.

Derivation of deviator displacements (Δ_{dev}) can be found in Appendix D.3.

$$\begin{aligned}
\Delta_{dev} &= \frac{1}{486}\frac{q_1 L_b^4}{EI} + \frac{q_1 L_b^2}{9GA_s} + \frac{1}{162}\frac{F_v L_b^3}{EI} + \frac{F_v L_b}{3GA_s} \\
M_{con} &= \frac{1}{12} q_1 L_b^2 \\
q_1 &= \frac{12 M_{con}}{L_b^2} \\
\Delta_{dev} &= \frac{1}{486}\frac{L_b^4}{EI} \cdot \frac{12 M_{con}}{L_b^2} + \frac{L_b^2}{9GA_s} \cdot \frac{12 M_{con}}{L_b^2} + \frac{1}{162}\frac{F_v L_b^3}{EI} + \frac{F_v L_b}{3GA_s} \\
\Delta_{dev} &= \phi \cdot \left(\frac{2}{81} L_b^2 + \frac{4EI}{3GA_s}\right) + \frac{4}{648}\frac{F_v L_b^3}{EI} + \frac{F_v L_b}{3GA_s}
\end{aligned} \tag{8.59}$$

At decompression the deviator deflections are as shown in Equation 8.60.

$$\Delta_{dev,dec} = \phi_{dec} \cdot \left(\frac{2}{81} L_b^2 + \frac{4EI}{3GA_s}\right) + \frac{1}{162}\frac{F_v L_b^3}{EI} + \frac{F_v L_b}{3GA_s} \tag{8.60}$$

After decompression the beam deflections are created by the increased distributed load. Therefore deviator deflection is given by Equation 8.61, where the distributed load is replaced by Equation 8.53. Derivation of this equation can be found in Appendix D.3.

$$\Delta_{dev} = \frac{11}{972}\frac{q_2 L_b^4}{EI} + \frac{q_2 L_b^2}{9GA_s} = \left(\frac{22 L_b}{81} + \frac{8EI}{3GA_s \cdot L_b}\right)\theta_{imp} \tag{8.61}$$

The total deviator deflections are given by the sum of the deflections before decompression (Equation 8.60) and the deflections after decompression (Equation 8.61), as shown in Equation 8.62.

$$\begin{aligned}
\Delta_{imp,dev} &= \Delta_{dev} + \Delta_{dev,dec} \\
\Delta_{imp,dev} &= \left(\frac{22 L_b}{81} + \frac{8EI}{3GA_s \cdot L_b}\right)\theta_{imp} + \left(\frac{2}{81} L_b^2 + \frac{4EI}{3GA_s}\right)\phi_{dec} + \dots \\
&\quad \dots + \frac{1}{162}\frac{F_v L_b^3}{EI} + \frac{F_v L_b}{3GA_s}
\end{aligned} \tag{8.62}$$

Tendon length can be calculated twice using Pythagoras Theorm, once for the initial beam and once for a deflected beam. The difference between the two lengths is the tendon elongation, and is given in Equation 8.63. The factor of two

is due to the two deviators in the beam, elongating the left and the right parts of the tendon, and the factor n has been introduced as the number of beams in the frame.

$$\Delta l_{pt,dev} = 2 \cdot n \left(\sqrt{\left(\frac{L_b}{3}\right)^2 + (\Delta_{imp,dev} + x_{pt})^2} - \sqrt{\left(\frac{L_b}{3}\right)^2 + x_{pt}^2} \right) \tag{8.63}$$

Frame shortening The increase in post-tensioning results in shortening of the frame (beam and column shortening) due to compressive stresses in timber, and extra uplift forces at deviators. All these three components result in a reduction of tendon elongation. These effects need to be taken into account as they reduce the increase of post-tensioning force.

Frame shortening can be represented by a series of springs, as shown in Figure 8.21. Each beam is represented by a spring with a stiffness of $k_{c,beam}$ and each column interface by a spring with a stiffness of $k_{c,col}$. The total number of beams is n and the total number of column interfaces is $2n$. Deformations of the external columns at the anchorage plate are assumed to be negligible as stresses spread out over a large area. Tendon length, L_{pt}, can be approximated as the full length of the frame.

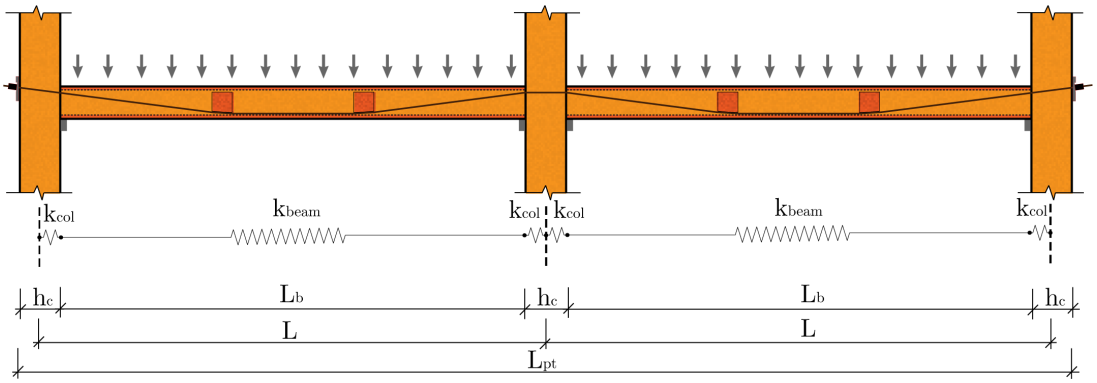

Figure 8.21: Frame shortening modelled using a series of springs

The beam stiffness is given by Equation 8.64. Column stiffness has previously been derived for interface compression and is presented in Equation 8.33, which is repeated here in Equation 8.65 with the inclusion of screw stiffness factor k_{scr}. In this equation the height of the compression zone (l_0) can be taken as the neutral

axis depth. The combined stiffness of the frame, $k_{c,frame}$, is shown in Equation 8.66.

$$k_{c,beam} = \frac{E_t \cdot A_b}{L_b} \tag{8.64}$$

$$k_{c,col} = k_{scr} \cdot \frac{2E_{90} \cdot w_c}{ln\left(\frac{h_c}{l_0} + 1\right)} \tag{8.65}$$

$$k_{c,frame} = \frac{n}{k_{beam}} + \frac{2n}{k_{col}} \tag{8.66}$$

The post-tensioning tendons can also be represented by a spring with a stiffness, k_{pt}, as given by Equation 8.67.

$$k_{pt} = \frac{E_{pt} \cdot A_{pt}}{L_{pt}} \tag{8.67}$$

The increase in post-tensioning force is equal in both the tendon and the frame. Therefore these two components can be seen as two springs in series with an equivalent stiffness, k_{eq}, which can be calculated using Equation 8.68. This can be rewritten using Equation 8.66. The factor ω is introduced as a reduction factor for the spring stiffness of the tendons, k_{pt}, and thus as a reduction factor for the increase in post-tensioning force.

The effect of beam and column shortening is described using analytical equations 8.64 and 8.65. The effect of deviator uplift is not easy to include as there is no linear relationship between deviator deflection and tendon elongation. An iterative procedure can used as described in Section 7.3. This iterative procedure has been performed for several different frame geometries, and a reduction in tendon elongation of about 10% was found. Therefore it is suggested to use $\omega_{dev} = 0.1$

$$\begin{aligned}
\frac{1}{k_{eq}} &= \frac{1}{k_{pt}} + \frac{1}{k_{c,frame}} \\
\frac{k_{pt}}{k_{eq}} &= \frac{k_{pt}}{k_{pt}} + \frac{k_{pt}}{k_{c,frame}} \\
\frac{k_{pt}}{k_{eq}} &= 1 + \frac{n \cdot k_{pt}}{k_{c,beam}} + \frac{2n \cdot k_{pt}}{k_{c,col}} \\
k_{eq} &= \frac{k_{pt}}{1 + \frac{n \cdot k_{pt}}{k_{c,beam}} + \frac{2n \cdot k_{pt}}{k_{c,col}}} \\
k_{eq} &= \frac{k_{pt}}{1 + \omega_{beam} + \omega_{col} + \omega_{dev}}
\end{aligned} \tag{8.68}$$

Where:

- ω_{beam} = Reduction factor for beam shortening
- ω_{col} = Reduction factor for column shortening
- ω_{dev} = Reduction factor for deviator uplift
- k_{beam} = Axial stiffness of beam
- k_{col} = Stiffness of column interface under compression
- k_{frame} = Axial stiffness of post-tensioned frame
- k_{pt} = Stiffness of post-tensioning tendons
- k_{eq} = Equivalent stiffness of tendons and frame
- n = number of beams in the frame
- L_b = length of the beam
- L_{pt} = Length of post-tensioning tendon
- h_c = depth of the column
- w_c = Width of column
- l_0 = Height of compression zone on column face
- E_t = Modulus of elasticity of timber parallel to grain
- E_{90} = Modulus of elasticity of timber perpendicular to grain
- A_b = Cross-sectional area of the beam
- E_{pt} = Modulus of elasticity of the post-tensioning steel
- A_{pt} = Area of post-tensioning steel

Total tendon elongation The total tendon elongation is the sum of elongation due to gap opening and elongation due to deviator deflections, divided by the reduction factors to account for frame shortening. This is shown in Equation 8.69.

$$\Delta l_{pt} = \frac{\Delta l_{pt,dev} + \Delta l_{pt,gap}}{1 + \omega_{beam} + \omega_{col} + \omega_{dev}} \tag{8.69}$$

The tendon elongation divided by the length of the tendon gives the additional strain in the tendon. The additional strain, summed with the initial strain ($\epsilon_{pt,i}$) and multiplied by the area and modulus of elasticity of the tendons, results in the new post-tensioning force, as shown in Equation 8.70.

$$F_{pt} = \left(\epsilon_{pt,i} + \frac{\Delta l_{pt}}{L_{pt}}\right) \cdot E_{pt} A_{pt} \tag{8.70}$$

8.6.4 Summary of design procedure

An summary of the full design procedure to determine the moment-rotation behaviour under gap opening is shown in Figure 8.22.

First an amount of rotation due to gap opening (θ_{imp}) is chosen. For a full moment-rotation graph of the connection, a range of values needs to be analysed. The procedure is iterative and initially the neutral axis depth (c) needs to be estimated. With this neutral axis depth the curvature (ϕ) at the connection can be calculated. This curvature, multiplied with the neutral axis depth results in the maximum timber strain at the connection. This strain can be multiplied by the modulus of elasticity in order to get the compressive stress in the timber. The timber compressive force can be calculated by integrating the stress profile over the width of the beam. As the section is not solid, the width is a (piece-wise) function of the depth and integration needs to be done for the bottom flange and the webs separately.

Calculation of tendon elongation consists of two parts. Using the imposed rotation (or gap opening), the first contribution can be calculated by multiplying the rotation by the distance between the tendon and the neutral axis. This needs to be multiplied by $2n$ as connections at both ends of all beams open up. Deviator deflection can be calculated based on the summation of the decompression deflection and the additional deflection due to gap opening. The total deviator

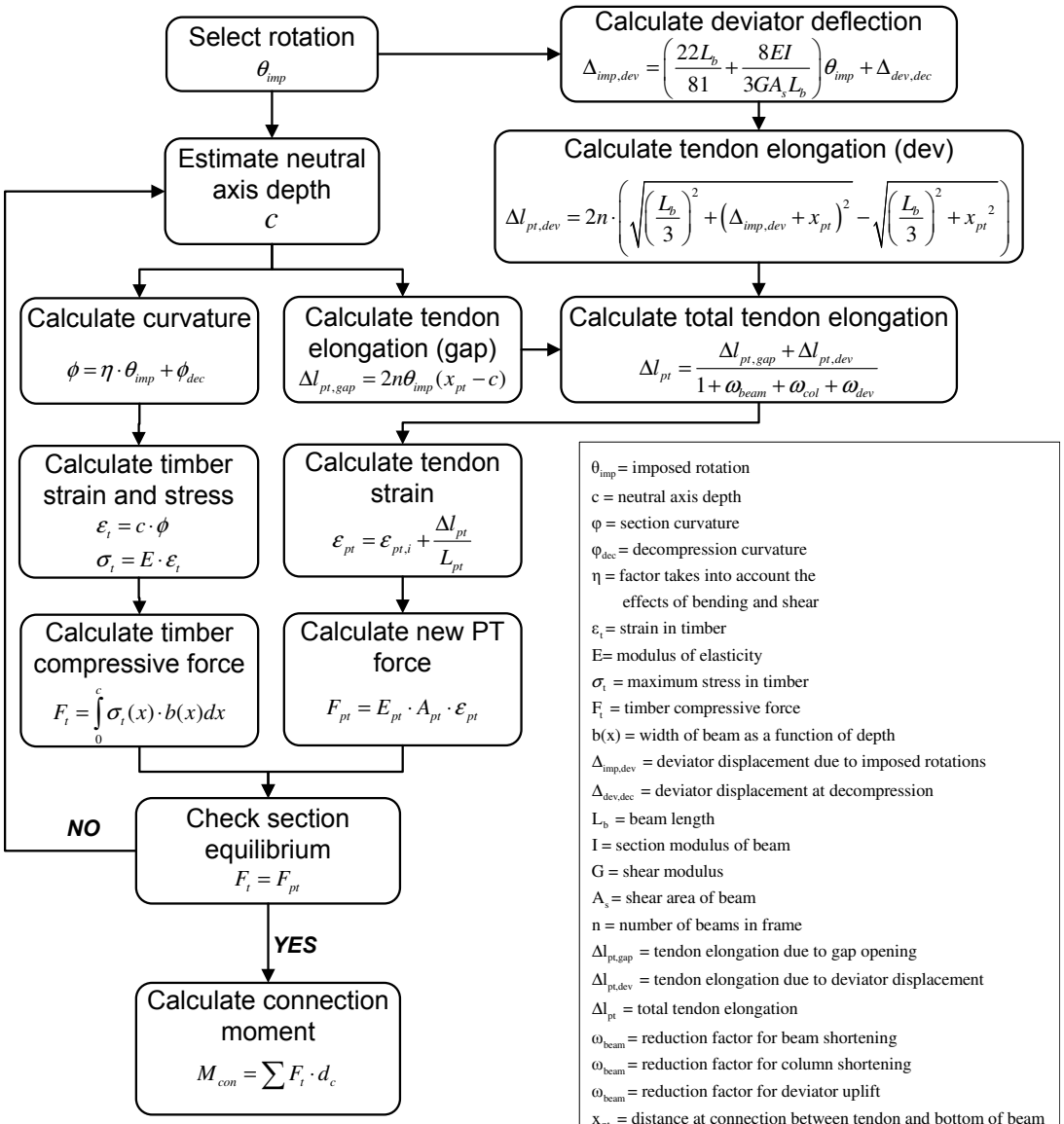

Figure 8.22: Full overview of design procedure for connection behaviour of post-tensioned gravity frames using the MMBA design procedure

deflection can be used to calculate the elongation of the tendon. The total tendon elongation is the sum of elongation due to gap opening and elongation due to deviator deflections and divided by the reduction factors to take frame shortening into account. The resulting tendon elongation divided by the length of the tendon gives the additional strain in the tendon. The additional strain, summed with the initial strain and multiplied by the area of the tendons and by the modulus of elasticity, results in the new post-tensioning force.

After calculating the timber compressive force and the new post-tensioning force, the section equilibrium needs to be verified. If no equilibrium is found, then the neutral axis depth needs to be changed. If equilibrium is found, the connection moment can be calculated based on the timber compressive force multiplied by the distance to the centroid of the beam.

8.6.5 Model validation

Validation of the gravity MMBA based on experimental data is not fully possible as no appropriate experimental data is available. Connection testing gave an insight on connection performance, but the cantilever beam did not accurately represent a post-tensioned timber beam. Therefore tendon elongation cannot be performed accurately. One-bay and two-bay frame testing had supporting plates below top and bottom flanges, which fixed the neutral axis depth. Therefore the iterative procedure of the MMBA is no longer required. A simplified approach, without the iterative procedure, is presented in the next section.

But partial validation was possible with data from connection testing. The MMBA procedure could be followed with the exception of calculation of tendon elongation. Therefore two assumptions had to be made, firstly that only gap opening added to tendon elongation and secondly that the reduction factor on tendon elongation due to frame shortening was 15%.

Experimental testing results of moment-rotation data included the interface compression stiffness. This stiffness of 29kNm/mrad was calculated using the multi-spring equations as presented in the model validation of Section 8.5. For comparison only experimental testing results of the unreinforced column with 220kN and 440kN initial post-tensioning force were used.

Two calculations were made, one using the seismic MMBA procedure with

$L_{cant} = 0.3L_b$ and one using the gravity MMBA procedure as derived above. The difference between the two procedures is that the gravity MMBA procedure includes shear deformation, whereas the seismic MMBA procedure only includes bending deformation. A comparison of connection moment, post-tensioning force and normalized neutral axis depth can be seen in Figure 8.23.

The connection moment-rotation behaviour is captured very well by the seismic MMBA procedure, whereas the gravity MMBA procedure slightly under predicts the connection moment. The initial stiffness until decompression is captured very well by the multi-spring model. The red squares show the decompression point, from which the MMBA curve starts.

From the figures it can be seen that the assumptions for tendon elongation result in a good prediction of the post-tensioning force. The gravity MMBA, which includes shear deformation predicts a higher neutral axis depth and thus a smaller increase in post-tensioning force, resulting in a lower connection moment.

When comparing the neutral axis depth, the first loading cycle (lowest one) of experimental testing data should be used, as timber crushing in the column led to a larger neutral axis depth in subsequent loading and unloading cycles. It can be seen that the experimental testing results of this first cycle are between predictions of the seismic and gravity MMBA. Although for larger rotations the gravity MMBA provides a better match with experimental testing data.

This comparison shows a good agreement between experimental testing results and the gravity MMBA procedure. But further validation, which includes calculation of tendon elongation needs to be performed.

8.6.6 Partial contact connection design

For experimental testing of one-bay and two-bay frames, as presented in Chapter 6, only the top and bottom flanges of the beams were in contact with the column (partial contact connection). After gap opening this resulted in a fixed neutral axis depth of the thickness of the bottom flange. As the neutral axis depth is known, the iterative procedure of the MMBA is no longer necessary. The increase in connection moment after decompression is only caused by the increase in post-tensioning force due to tendon elongation.

In Chapter 6 it was already shown that the decompression moment could be

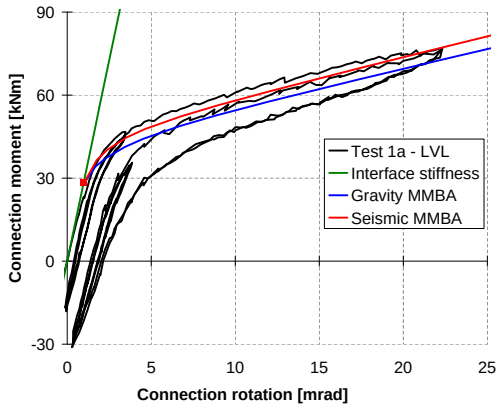

(a) Conn. moment for 220kN PT test

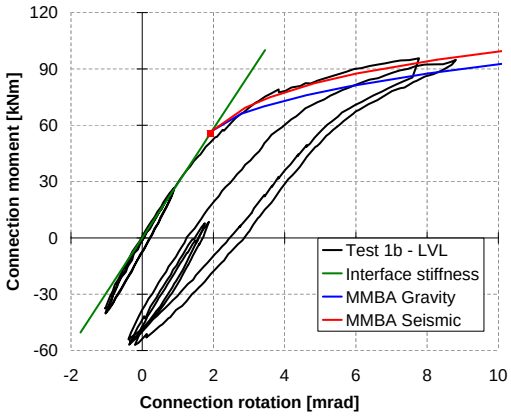

(b) Conn. moment for 440kN PT test

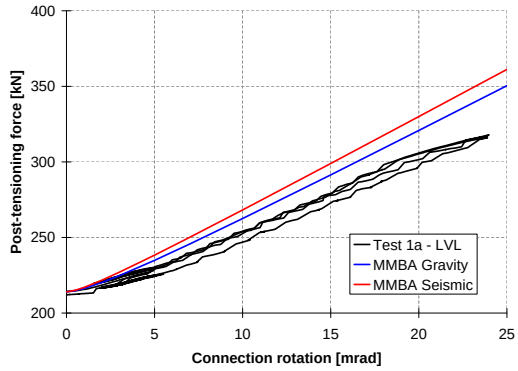

(c) PT force for 220kN PT test

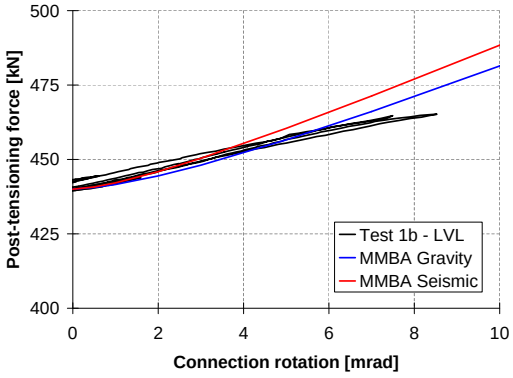

(d) PT force for 440kN PT test

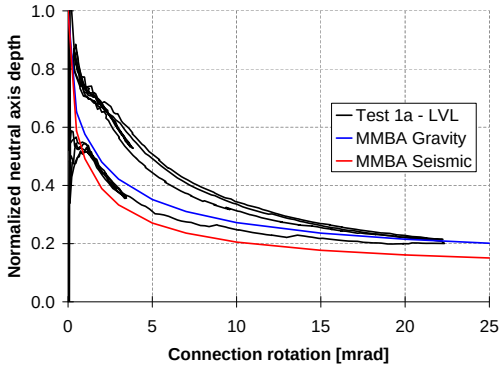

(e) Neutral axis depth for 220kN PT test

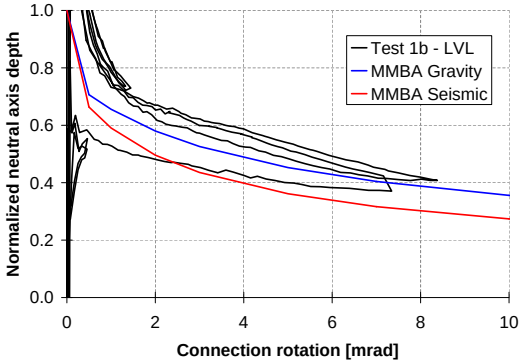

(f) Neutral axis depth for 440kN PT test

Figure 8.23: Comparison of experimental results with seismic and gravity MMBA design procedures

calculated using Equation 8.71.

$$M_{dec} = 0.5F_{pt,dec}\left(h_b - 2t_f + \frac{4t_f^2}{3h_b}\right) \tag{8.71}$$

After decompression there is a transition stage where the compressive force shifts further down until a triangular stress distribution in the bottom flange is achieved (Figure 6.22). The resulting connection moment after this transition stage is given by Equation 8.72.

$$M_{con} = F_{pt}\left(\frac{h_b}{2} - \frac{t_f}{3}\right) \tag{8.72}$$

Tendon elongation, and thus post-tensioning force, is dependent on the amount of gap opening and deviator deflections. Tendon elongation can be calculated in the same way as for the MMBA procedure. The part due to gap opening can be calculated using Equation 8.58, and the part due to deviator deflection can be calculated using Equations 8.62 and 8.63. The new post-tensioning force can be calculated using Equation 8.70.

Model validation In order to validate this simplified procedure for partial contact connections, it has been implemented and compared with results of the one-bay and two-bay frame testing. The values used as input in the design procedure are shown in Table 8.5. The results of the design procedure for the one-bay frame are shown in Table 8.6 and for the two-bay frame in Table 8.7.

A comparison between simplified design procedures and experimental testing results of connection moment versus gap opening for the one-bay frame is presented in Figure 8.24, and a comparison of post-tensioning force is shown in Figure 8.25. It should be noted again that the horizontal offset, especially visible for Column 1, is due to initial imperfections. From these figures, it can be seen that the predicted post-tensioning force matches very well with experimental results, although a small over prediction can be seen. This could be due to anchorage set which has not been taken into account in the model. Another reduction factor on tendon elongation could be added to the model to account for this, but further research in this area is needed to quantify this effect. The increase in moment capacity after decompression is slightly under predicted, even though the predictions of

Table 8.5: Constant values used for simplified procedure for calculating gap opening for one-bay and two-bay frames

Parameter	Symbol	One-bay frame	Two-bay frame
Number of beams	n	1	2
Beam length	L_b	8644mm	5596mm
Beam height	h_b	500mm	360mm
Beam width	b	288mm	288mm
Flange thickness	t_f	90mm	45mm
Web thickness	t_w	45mm	45mm
Timber area	A	80600mm^2	50200mm^2
Shear area	A_s	34200mm^2	25000mm^2
Moment of Inertia	I	2.46×10^9 mm^4	0.79×10^9 mm^4
Modulus of Elasticity	E	11000MPa	11000MPa
Shear modulus	G	660MPa	660MPa
Position of tendon	x_{pt}	380mm	285mm
Tendon length	L_{pt}	10m	13m
MoE of tendons	E_{pt}	200000MPa	200000MPa
Area of tendons	A_{pt}	400mm^2	400mm^2
Screw reinforcing stiffness factor	k_{scr}	2.5	2.5
Stiffness of beam	$k_{c,beam}$	103kN/mm	99kN/mm
Stiffness of column	$k_{c,col}$	383kN/mm	288kN/mm
Stiffness of post-tensioning	k_{pt}	8.0kN/mm	6.2kN/mm
Red. factor for beam shortening	ω_{beam}	7.8%	12.5%
Red. factor for column shortening	ω_{col}	4.2%	8.5%
Red. factor for deviator uplift	ω_{dev}	10%	10%
Equivalent stiffness	k_{eq}	6.56kN/mm	4.70kN/mm

post-tensioning force are matching very well with experimental data. This can lead to the conclusion that the neutral axis depth is smaller than the thickness of the bottom flange, as this is the only other way that the connection moment can increase. There is no easy way to take this effect into account. Experimental testing has shown that gap opening under ULS load is between 0mrad and 8mrad. Therefore it can be concluded that for design purposes the predictions are close to experimental observed behaviour.

The initial decompression point is predicted well, but the behaviour directly after decompression is not correct. After reaching zero stress at the top fibre a transition will happen before all the compressive force is located at the bottom flange and the triangular stress distribution occurs. This transitional phase is not

Table 8.6: Results at decompression, 1mrad and 10mrad rotation, of simplified procedure for calculating gap opening of one-bay frame with initial post-tensioning force of 400kN

Parameter	Symbol	Decompression	1mrad rot.	10mrad rot.
Imposed rotation	θ_{imp}	0 mrad	1mrad	10mrad
Max. timber stress in beam	σ_t	16.1MPa	32.7MPa	38.0MPa
Deviator deflection	Δ_{dev}	20.2mm	22.9mm	47.3mm
Tendon elongation gap	$\Delta l_{pt,gap}$	0.0mm	0.58mm	5.80mm
Tendon elongation deviator	$\Delta l_{pt,dev}$	4.04mm	4.61mm	9.92mm
Total tendon elongation	Δl_{pt}	3.31mm	4.25mm	12.89mm
Tendon strain	ϵ_{pt}	0.49%	0.53%	0.62%
Tendon stress	f_{pt}	1041MPa	1060MPa	1233MPa
Post-tensioning force	F_{pt}	417kN	424kN	493kN
Connection moment	M_{con}	71kNm	93kNm	109kNm

Table 8.7: Results at decompression, 1mrad and 10mrad rotation, of simplified procedure for calculating gap opening of two-bay frame with initial post-tensioning force of 200kN

Parameter	Symbol	Decompression	1mrad rot.	10mrad rot.
Imposed rotation	θ_{imp}	0 mrad	1mrad	10mrad
Max. timber stress in beam	σ_t	17.2MPa	35.7MPa	48.2MPa
Deviator deflection	Δ_{dev}	11.8mm	13.6mm	29.5mm
Tendon elongation gap	$\Delta l_{pt,gap}$	0.0mm	0.48mm	4.8mm
Tendon elongation deviator	$\Delta l_{pt,dev}$	3.0mm	3.4mm	7.7mm
Total tendon elongation	Δl_{pt}	4.5mm	6.0mm	19.1mm
Tendon strain	ϵ_{pt}	0.28%	0.29%	0.39%
Tendon stress	f_{pt}	557MPa	579MPa	781MPa
Post-tensioning force	F_{pt}	223kN	231kN	312kN
Connection moment	M_{con}	30.9kNm	38.2kNm	51.5kNm

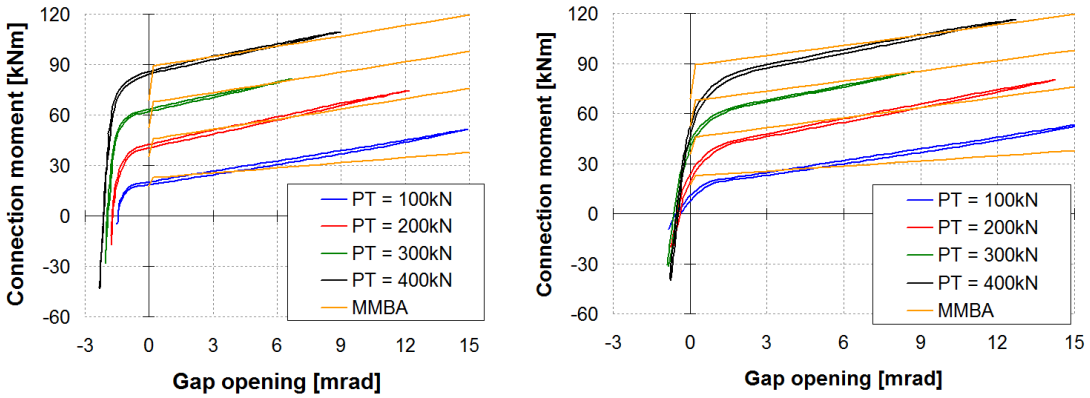

Figure 8.24: Comparison of connection moment-rotation prediction of MMBA design procedure and experimental testing for one-bay frame, left for Column 1 and right for Column 2

included in the model. A simplified method would be to state that this transition phase occurs during the first 2mrad of rotation. A bilinear function could be made between 0 and 2mrad rotation and between 2mrad and the maximum expected rotation.

A comparison between the simplified design procedure and experimental testing results of connection moment versus gap opening for the two-bay frame is presented in Figure 8.26. And a comparison of post-tensioning force is shown in Figure 8.27. From these two figures it can be seen that again the increase in moment capacity is under predicted, but that decompression is very well matched. A bi-linear approximation of the moment-rotation behaviour can be made, with a change in stiffness around 1mrad of rotation.

Gap opening is different for internal and external connections, hence the two different graphs in Figure 8.27. It can be seen that the predictions of post-tensioning force versus internal gap opening (right graph) are well predicted for small rotations, but over estimated for larger rotations. This is due to the fact that the model assumes all connections exhibit the same amount of gap opening, whereas internal connections will exhibit more gap opening than external connections. And as a result, the post-tensioning force versus external gap opening (left graph) is under predicted.

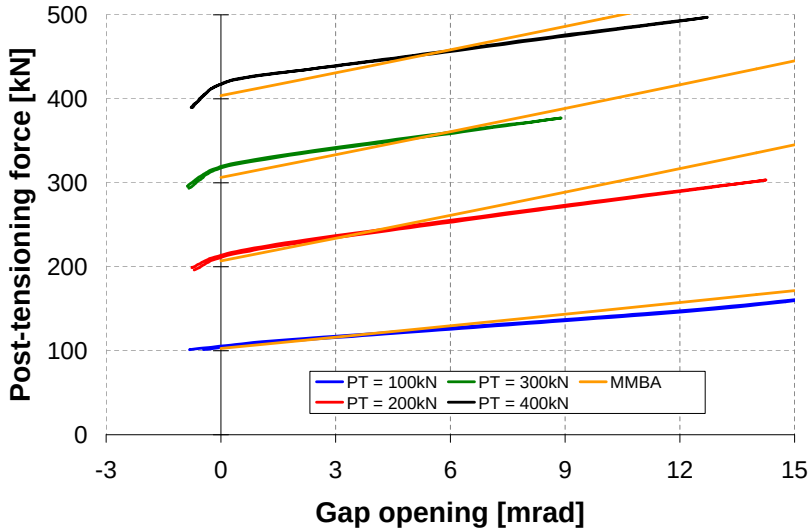

Figure 8.25: Comparison of post-tensioning force prediction of MMBA design procedure and experimental testing for one-bay frame

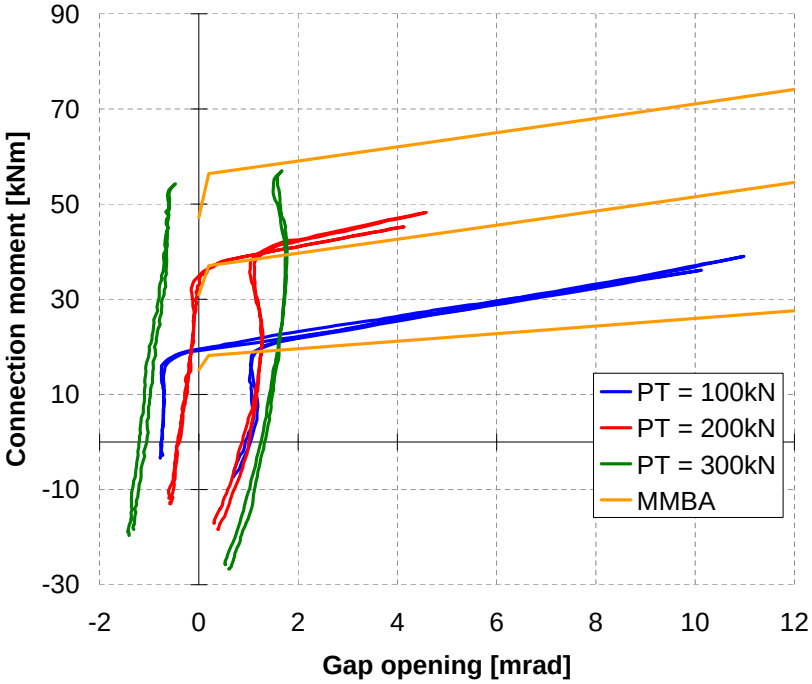

Figure 8.26: Comparison of external connection moment-rotation prediction of MMBA design procedure and experimental testing results of two-bay frame

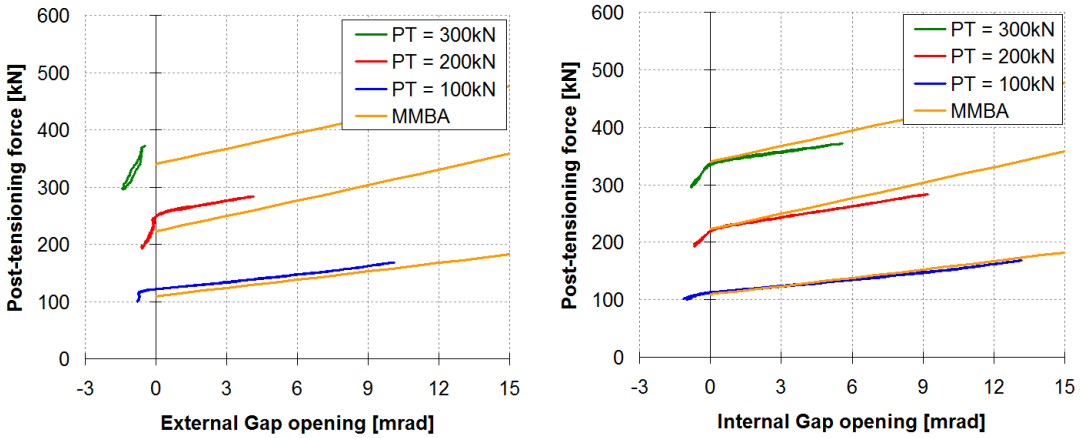

Figure 8.27: Comparison of post-tensioning force prediction of MMBA design procedure and experimental testing for two-bay frame, left plotted against external gap opening and right against internal gap opening

8.6.7 Comparison between connection models

A comparison can be made between beam-column connections with full contact and with partial contact. This is done for the geometry of the one-bay frame test setup. A list of parameters can be seen in Table 8.8.

For the beam-column connection with full contact, the compressive stress is lower than for the connection with partial contact. Therefore also the decompression moment is lower in the case of full contact. Calculated values of post-tensioning force, decompression moment and tendon elongation at decompression are shown in Table 8.9.

The results of the comparison can be seen in Figure 8.28.

From the moment-rotation plot it can be seen that the partial contact connection has a higher decompression moment and that the connection moment exceeds that of the full contact connection for all rotations. It can also be seen that the post-tensioning force is higher for the partial contact connection. As the neutral axis drops directly after decompression, the tendon elongation due to gap opening starts directly. For the full contact connection tendon elongation only starts when the neutral axis depth has reached the position of the tendon, which is located at 76% of the section height. From the plot of the neutral axis it can be seen that this is at about 2mrad. Furthermore, due to the larger decompression

Table 8.8: Overview of constants used for comparison of full contact and partial contact models

Property	Symbol	Value
Beam length	L_b	8644mm
Modulus of Elasticity timber	E	11000MPa
Modulus of Elasticity perp. To grain	E_{90}	500MPa
Shear modulus timber	G	550MPa
Moment of inertia	I	2.46×10^9mm^4
Section modulus	Z	9.84×10^6mm^3
Beam area	A	80600mm^2
Shear area	A_s	34243mm^2
Height of beam	h_b	500mm
Width of beam	b	288mm
Flange thickness	t_f	90mm
Web thickness	t_w	45mm
Initial post-tensioning force	$F_{pt,i}$	390kN
Uplift force at deviator	$F_{pt,v}$	40kN
Post-tensioning length	L_{pt}	10000mm
Area of PT	A_{pt}	400mm^2
Modulus of elasticity PT	E_{pt}	200000MPa
Initial PT strain	$\epsilon_{pt,i}$	0.49%
Stiffness of post-tensioning tendons	k_{pt}	8000N/mm
Axial stiffness of beam	k_{beam}	102568N/mm
Stiffness of column interface under compression	k_{col}	383000N/mm
Axial stiffness of post-tensioned frame	k_{frame}	808899N/mm
Reduction factor for beam shortening	ω_{beam}	7.8%
Reduction factor for column shortening	ω_{col}	4.2%
Reduction factor for deviator uplift	ω_{dev}	10%

Table 8.9: Decompression data for full contact and partial contact models

Property	Symbol	Full contact	Partial contact
PT force at decompression	$F_{pt,dec}$	415kN	419kN
Decompression moment	M_{dec}	50.7kNm	71.6kNm
Deviator deflection at decompression	$\Delta_{dec,dev}$	19.2mm	22.2mm
Tendon elongation at decompression	$\Delta_{pt,dev}$	3.1mm	3.7mm

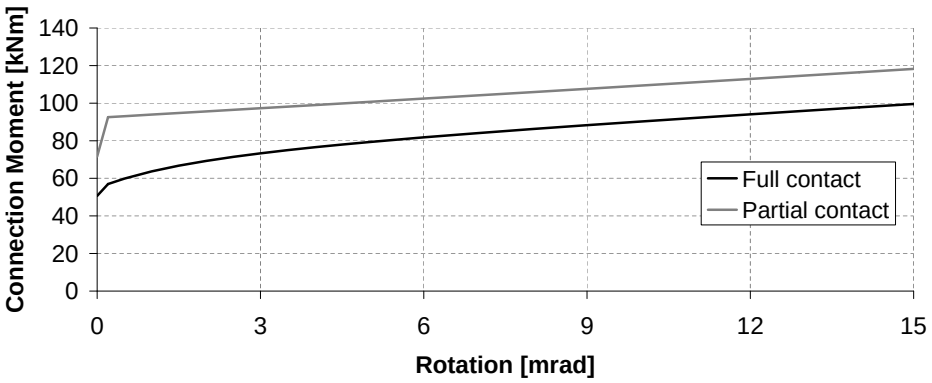

(a) Moment-rotation

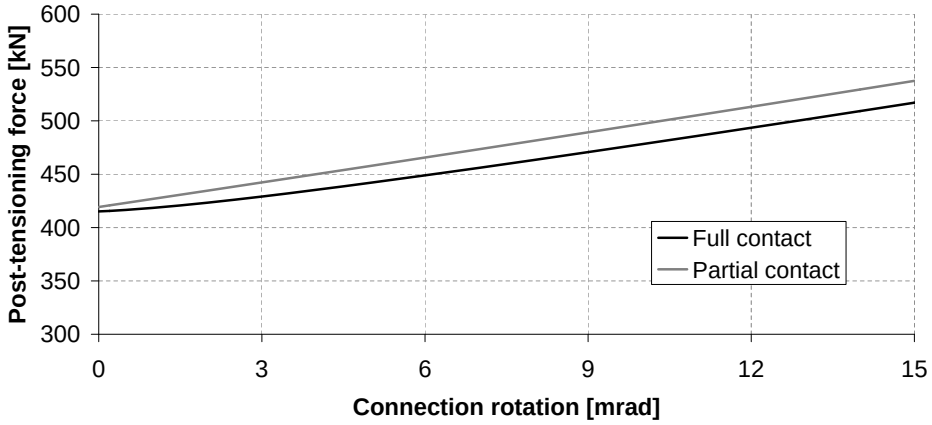

(b) Post-tensioning force vs. rotation

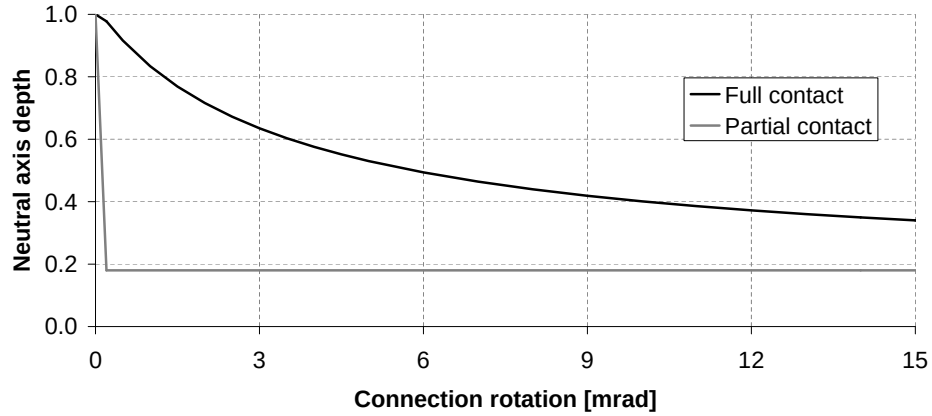

(c) Normalized neutral axis depth

Figure 8.28: Comparison of beam-column connection behaviour between full contact connection and partial contact connection

moment of the partial contact connection, there are larger deflections of the beam (and thus of the deviators) at decompression. This leads to an increased tendon force at decompression. From the plot of the normalized neutral axis depth (neutral axis depth divided by section height) it can be seen that for the full contact connection the neutral axis gradually drops to about 35% of the section depth, where the partial contact connection drops directly after decompression to 18% of the section depth. This smaller neutral axis, combined with the higher post-tensioning force results in a larger connection moment.

From this comparison it can be concluded that it is beneficial to have partial contact connections as this increases the moment capacity of the connection. But the smaller neutral axis depth results in higher timber stresses as the full post-tensioning force needs to be transferred through a smaller area. Therefore care needs to be taken that the maximum compressive strength of the flange of the beam and the strength of the column are not exceeded.

8.6.8 Summary

A newly derived MMBA for gravity frames has been presented. This design procedure includes shear deformation, which is an essential part for timber frames. The procedure has the potential to be also used for concrete frames under gravity loading, whereby the shear terms can be ignored. Furthermore, in Appendix E is the derivation of the MMBA for seismic systems with the inclusion of shear deformation. Evaluation of tendon elongation for gravity frames is complicated as gap opening and deviator deflection lead to gap opening. In addition, frame shortening needs to be taken into account to prevent over prediction of the increase in post-tensioning force.

From the validation it can be concluded that the MMBA procedure provides an excellent tool for predicting the behaviour of post-tensioned timber connections, when the initial column interface stiffness is taken into account separately. Not enough data was available to fully verify the gravity MMBA procedure, but a partial validation shows that the model predictions are close to experimental measurements.

A comparison between full contact beam-column connections and partial contact connections has concluded that the latter is beneficial as this increases the

moment capacity of the connection. But the smaller neutral axis depth results in higher timber stresses as the full post-tensioning force needs to be transferred through a smaller area. Therefore care needs to be taken that the maximum compressive strength of the flange of the beam and the strength of the column are not exceeded.

8.7 Design charts

This section presents design charts for quick estimation of column rotational stiffness, joint panel shear stiffness and interface compression stiffness. These stiffness values can be used for rotational springs in a framework or beam-only model.

8.7.1 Column stiffness

In Section 8.3 the column stiffness was derived as shown in Equation 8.73.

$$k_{col} = \frac{\chi}{\frac{H}{12EI} + \frac{1}{\alpha GAH}} \tag{8.73}$$

A design chart can be constructed when assuming the use of LVL11, a rectangular column and a range of column sizes. This results in the following parameters:

- Modulus of elasticity: E = 11000MPa
- Shear modulus: G = 550MPa
- Inter-storey height: H = 3.6m
- Effective shear area: $\alpha = 0.86$
- Column width: 300 / 400 / 500mm
- Column depth: ranging from 300 to 800mm

The factor χ is calculated for the range of column depths using Equation 8.74, whereby the beam length is taken as 10m. This factor is further explained in Section 9.3.

$$\chi = \frac{L/6 - h_c}{L/6} \tag{8.74}$$

The resulting design chart is shown in Figure 8.29.

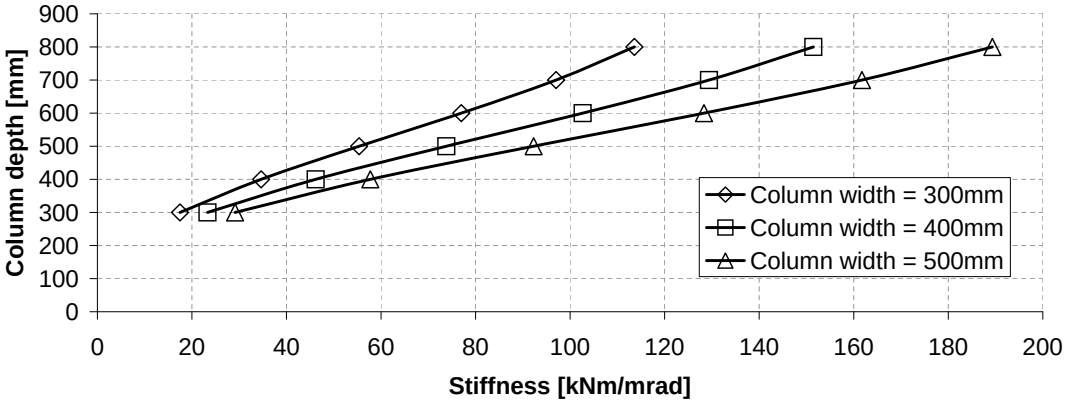

Figure 8.29: Design chart for column rotational stiffness

8.7.2 Joint panel shear stiffness

In Section 8.4 the joint panel shear stiffness was derived, as shown in Equation 8.75.

$$k_{jp} = \alpha G A_{col} \cdot \beta h_b \tag{8.75}$$

A design chart can be constructed when assuming the use of a solid column made of LVL11 with a range of cross-sectional areas. The same range of timber box section with 90mm thick flanges as was used for the parameter study on beams (Figure 7.23) is used for the design charts. The effective beam height depends on the full geometry of the beam. For simplicity the connection detailing having only contact between the top and bottom flanges and the column is used (Figure 8.1b). This results in the following parameters:

- Shear modulus: G = 550MPa
- Effective shear area of column: $\alpha = 0.86$
- Beam height: 600 / 800 / 1000 / 1200mm
- Effective beam height: $\beta = 0.85$ / 0.89 / 0.91 / 0.93
- Column area: ranging from 90000mm^2 (300x300) to 400000mm^2 (800x500)

The resulting design chart is shown in Figure 8.30.

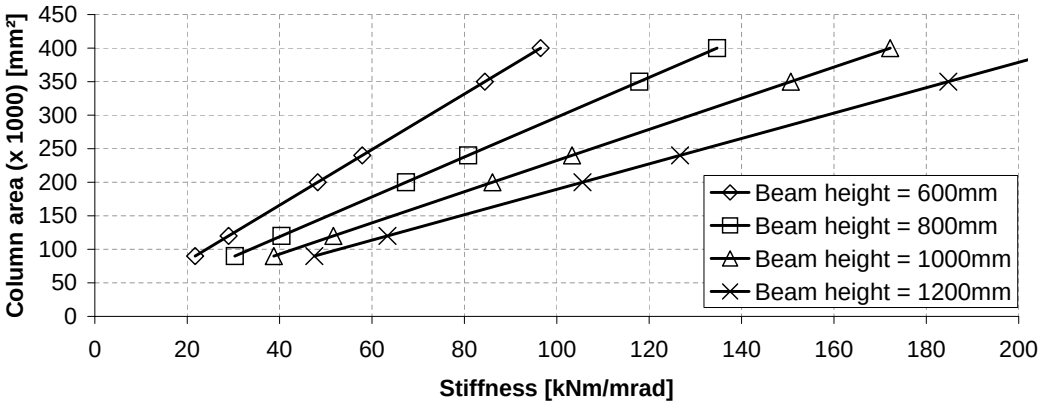

Figure 8.30: Design chart for joint panel shear stiffness

8.7.3 Interface compression stiffness

In Section 8.5 the interface compression stiffness was derived, but this multi-spring model does not allow for an easy design. Therefore the simplified design, as presented in Figure 8.10, using only top and bottom flanges is used for the design chart. The resulting interface compression stiffness is shown in Equation 8.76.

$$k_{int} = 0.5 k_{perp} (\beta h_b)^2 \tag{8.76}$$

In this equation the value of k_{perp} is given by Equation 8.77.

$$k_{perp} = k_{scr} \cdot \frac{2E_{90} \cdot w_c}{ln\left(\frac{h_c}{l_0} + 1\right)} \tag{8.77}$$

A design chart can be constructed when assuming the following parameters:

- Modulus of elasticity perpendicular to grain : E_{90} = 500MPa
- Column width: w_c = 300 / 500mm
- Column depth: h_c = 600 / 700mm
- Contact length: l_0 = 90mm (flange thickness)
- Screw reinforcement: k_{scr} = 1 / 1.4 / 2 / 4
- Beam height: ranging from 600 to 1200mm
- Effective beam height: β = 0.85 / 0.89 / 0.91 / 0.93

The resulting design chart is shown in Figure 8.31.

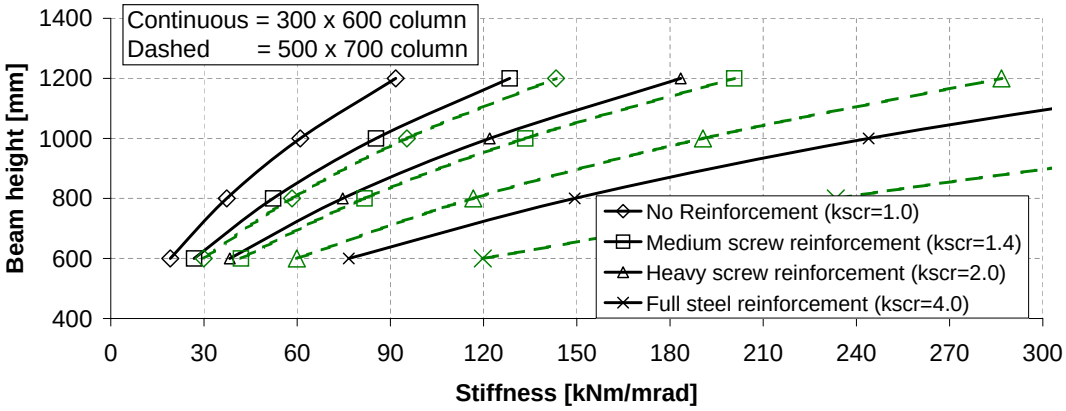

Figure 8.31: Design chart for interface compression stiffness

8.7.4 Gap opening

For a preliminary design the simplification can be made that there is no increase in connection moment after gap opening. This eliminates the calculation procedure for neutral axis depth and tendon elongation. Instead an elasto-plastic moment-rotation behaviour can be assumed, and only the decompression moment needs to be calculated as shown in Equation 8.78. The post-tensioning force at decompression can be calculated as shown in Section 8.6.3, or for a simplified initial design it can be assumed as $1.1 \cdot F_{pt,i}$, based on experimental data is presented in Section 6.5.3.

$$M_{dec} = \frac{F_{pt,dec} \cdot Z}{A} \tag{8.78}$$

As a result the connection moment will be slightly under estimated and the mid-span bending moment will be over estimated. Also beam deflections will be over estimated as larger connection rotations will occur. The over estimations of mid-span bending moment and deflections makes for a conservative initial design. Care should be taken when designing the compression area in beams and columns as these areas will be subjected to higher forces due to tendon elongation, which is not taken into account.

8.7.5 Combining rotation components

The rotational components which need to be taken into account for different connections and loading scenarios are shown in Table 8.10.

Table 8.10: Rotation components to take into account for modelling of external and internal connections in SLS and ULS design

Rotation components	Symbol	External		Internal	
		SLS	ULS	SLS	ULS
Column rotation	k_{col}	Yes	Yes	No	No
Joint panel rotation	k_{jp}	Yes	Yes	No	No
Interface rotation	k_{int}	Yes	Yes	Yes	Yes
Gap opening	-	No	Yes	No	Yes

The internal connection stiffness for SLS design equals the interface compression stiffness, and for external connections the total rotational stiffness for SLS design is a combination of column, joint panel and interface stiffness. This is shown in Equation 8.79.

$$k = \begin{cases} k_{internal} = k_{int} \\ k_{external} = \left(\frac{1}{k_{col}} + \frac{1}{k_{jp}} + \frac{1}{k_{int}}\right)^{-1} \end{cases} \tag{8.79}$$

A graphical representation of the stiffness of internal and external connections is shown in Figure 8.32. It can be seen that the internal connection stiffness only consists of interface rotation, whereas the external connection stiffness consists of column rotation, joint panel rotation and interface rotation. The effects of gap opening result in an elasto-plastic curve with a maximum value of the decompression moment. This moment-rotation behaviour can be implemented in a beam model, which is presented in the next chapter.

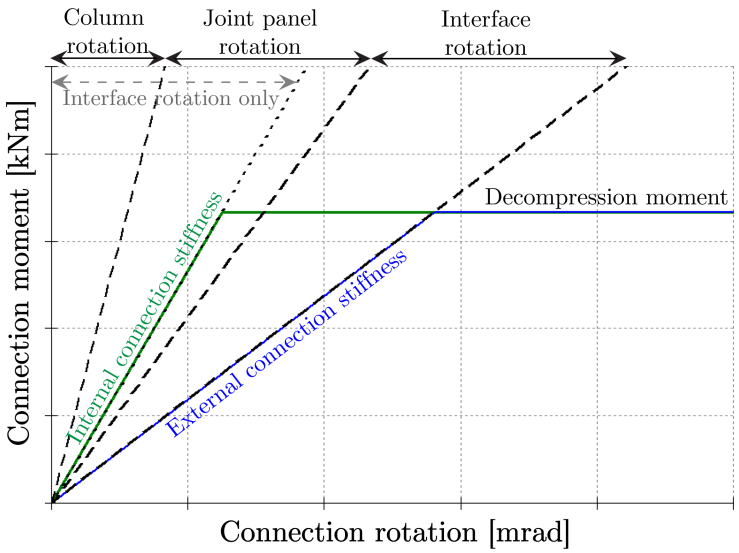

Figure 8.32: Moment rotation graph for internal and external connections

8.8 Conclusions

Conclusions

- Frame deformation components are beam, joint and column deformation. The joint deformation is split into joint panel shear deformation, interface compression deformation and gap opening. Two modelling approaches for a post-tensioned timber gravity frame are presented. One is a framework model of the full frame, the other one a simplified model of only a beam. Rotational springs can be included in the models to account for joint flexibility.

- Finite element modelling and analytical modelling have shown the importance of accounting for shear deformation of the column. They also show the increased shear stresses in the joint region. An analytical expression for column rotational stiffness has been presented, but this could not be validated with experimental results. A theoretical derivation of joint panel shear deformation was presented. This resulted in an equation for the joint panel shear stiffness, which can be used in beam and frame models. A second equation was derived for comparison with experimental testing

results. Validation has shown a very good correspondence between the analytical equation and experimental testing data.

- Interface compression deformation has been analysed using a multi-spring model. This model included the effects of stress spreading and also column reinforcement could be taken into account.

- A design procedure for gap opening in post-tensioned gravity frames was derived. This procedure was based on the MBA, as presented for concrete seismic frames. As shear deformation is significant for timber frames, this was included in the new design procedure. The design procedure has been partly verified with experimental testing results, but further validation is necessary. Analysis of tendon elongation in gravity frames is complex as it is caused by gap opening and beam deflections. Furthermore, frame shortening should be taken into account. Design equations for evaluation of tendon elongation are presented.

- Simplified design equations have been presented for interface compression and gap opening for cases where only top and bottom flanges are in contact with the column. Design charts for quick initial estimation of rotational stiffness of column, joint panel and interface were presented. For a quick design it was suggested to use an elasto-plastic model to take gap opening into account as this eliminates the need of any gap opening calculation. This design assumption will lead to a conservative design for beam deflections and bending moments.

Chapter IX

Post-tensioned timber frames

9.1 Introduction

Beams benefit from post-tensioning due to reduced deflections as shown in Chapters 4 and 7. Experimental testing has shown an increase in load carrying capacity at SLS design level of up to 54%, despite a reduction in section height for post-tensioned beams. Post-tensioned frames (Figure 9.1) have the additional benefit that with one stressing operation several moment-resisting beam-column connections are created. These connections further reduce deflections and bending stresses in the beam. Tendons can be anchored at the exteriour columns above the level of the centroid of the beam, resulting in a higher angle of tendons at the deviators. Therefore the post-tensioning force can be lower than for post-tensioned beams, whilst still resulting in the same uplift force.

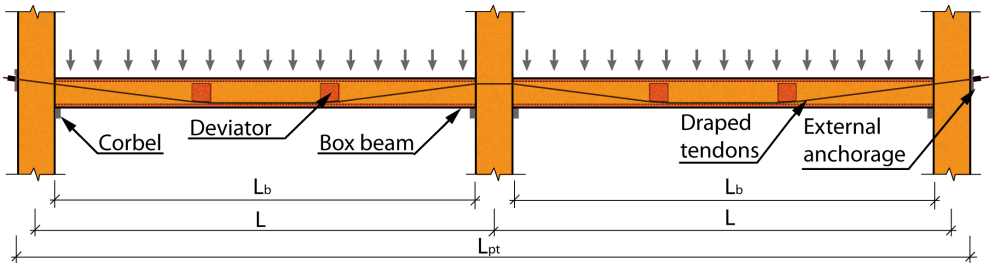

Figure 9.1: Schematics of post-tensioned timber frame

Analysis of post-tensioned timber frames has the following objectives:

- Develop a modelling approach for post-tensioned timber frames.
- Evaluate the effect of tendon elongation on the design of post-tensioned timber frames.

- Develop an analytical model for analysis of bending moments and deflections in post-tensioned timber frames.
- Evaluate the effect of different connection models on bending moments and deflections of post-tensioned timber frames.
- Perform a parameter study on the design of post-tensioned timber beams to identify critical design parameters.
- Compare the performance of simply supported post-tensioned beams with post-tensioned timber frames.

This chapter presents the analysis of PT timber frames. Two different models are used for the analysis, a full frame model and a beam model. The full frame model requires the use of software programs to evaluate deflections, shear forces and bending moments, where the beam model can be evaluated using software programs or using analytical equations when applying a simplified connection behaviour.

The connection behaviour, which has been presented in Chapter 8, is used in this chapter for the frame design. The partial contact solution (only top and bottom flanges are in contact with the column, as presented in Chapter 8) is used as this results in an improved connection behaviour. For the detailed designs non-linear connection behaviour (due to gap opening) is used, whereas for the simplified design an elasto-plastic connection behaviour is assumed. This makes it possible to create an analytical model for calculation of bending moments and deflections. In total four design methods are described:

1. a detailed design using framework analysis software for the full frame model.
2. a detailed design using framework analysis software for the beam model.
3. a simplified design using framework analysis software for the beam model.
4. a simplified design based on analytical equations for the beam model.

The final part of this chapter provides a parameter study on a range of post-tensioning forces and beam lengths. This parameter study follows a very similar format as the parameter study on post-tensioned beams which was presented in Chapter 7. After the parameter study comparisons are made between the performance of post-tensioned beams and frames.

9.2 Framework model

The most detailed analysis model is a framework model of the full frame, as shown in Figure 9.2. The full frame model consists of column and beam elements. A rigid link is placed between the centreline of the column and the beam-column interface. At the interface, a rotational spring is placed to model the joint panel deformation (only for external connections), interface compression and gap opening. Post-tensioning loads are represented by forces at the anchorages (under an angle or horizontal and vertical components), at deviators in the beams (uplift force) and at deviators in the columns (double the uplift force).

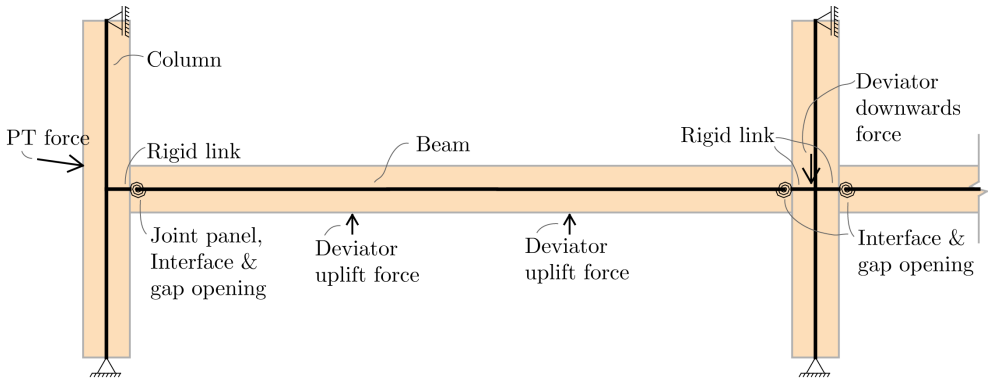

Figure 9.2: Schematics of modelling approach for full frame model

This analysis is performed for a frame with a beam length of 10m and a box section of 800 x 400mm with flange and web thickness of 90mm. The column was estimated to have a solid section size of 600 x 400mm. The design of the frame is presented in Appendix F.2. Five different levels of post-tensioning have been used for the design, ranging from 1MPa to 5MPa compressive stress due to post-tensioning. Furthermore two models without post-tensioning were made, one with pinned beam-column connections and one with fully fixed beam-column connections.

Four different load-cases were used for the analysis. Further information about the load-cases is presented in Appendix F.2.

- PT only: 1.1 PT
- ULS: 1.2G + 1.5Q + ψ_{te}PT

- SLS Short: G + 0.7Q + PT
- SLS Long: G + 0.4Q + 0.75PT

9.2.1 Connection design

For the beam-column connection it was assumed that only top and bottom flanges touch the column. This makes it possible to avoid the iterative part of the MMBA procedure as the neutral axis depth is fixed. This is further explained in Section 8.6.

Joint panel stiffness The joint panel stiffness in the model was based on the calculation in Equation 9.1, as presented in Section 8.4.

$$k_{jp} = \alpha G A_{col} \cdot \beta h_b = 0.86 \cdot 550 \cdot 240000 \cdot 710 = 81 kNm/mrad \tag{9.1}$$

Where:

- α = Factor to calculate effective shear area of cross-section of column
- A_{col} = Cross-sectional area of column (mm^2)
- G = Shear modulus of timber (MPa)
- h_b = Beam height (mm)
- β = Factor to calculate the effective height of joint panel

Interface compression stiffness The interface compression stiffness is based on the perpendicular to grain stiffness of the column, as presented in Section 8.5. It is assumed that medium screw reinforcement of 10 12mm diameter screws with a length of 300mm are placed in the column to increase the strength and stiffness, therefore the factor k_{scr} is as shown in Equation 9.2.

$$k_{scr} = 1 + 54\frac{A_{scr}}{A_t} \cdot \left(\frac{l_s}{h_c}\right)^{1.26} = 1 + 54\frac{1131}{36000} \cdot \left(\frac{300}{600}\right)^{1.26} = 1.7 \tag{9.2}$$

The resulting perpendicular to grain stiffness is given in Equation 9.3 and the interface stiffness in Equation 9.4.

$$k_{perp} = k_{scr}\frac{2E_{90} \cdot w_c}{ln\left(\frac{h_c}{l_0}+1\right)} = 1.7 \cdot \frac{2 \cdot 500 \cdot 400}{ln\left(\frac{600}{90}+1\right)} = 334kN/mm \tag{9.3}$$

$$k_{int} = 0.5k_{perp}(\beta h_b)^2 = 0.5 \cdot 334 \cdot 0.710^2 = 84kNm/mrad \tag{9.4}$$

Gap opening Details of the calculation of gap opening for the connection design can be found in Appendix (F.3). The resulting moment-rotation relationship can be seen in Figure 9.3. The stiffness is infinite until decompression. After decompression there is a transition phase where the compressive forces moves fully to the bottom flange. This is assumed to be the case at 2mrad rotation. After that gap opening will result in rotations but only a limit increase in connection moment. The maximum rotation shown is 15mrad, but the connection will be able to undergo larger rotations.

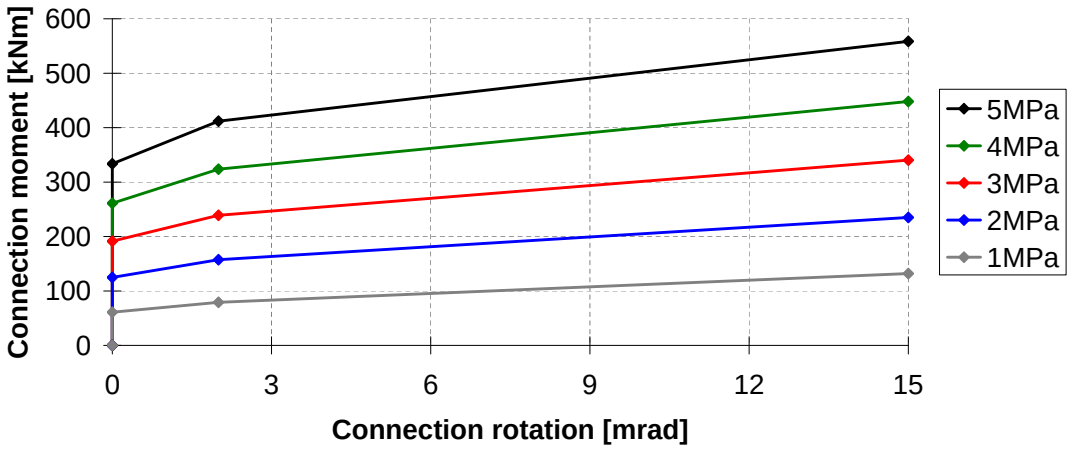

Figure 9.3: Moment-rotation graph of beam-column connection for different levels of post-tensioning stress for the use in framework analysis

Total joint stiffness A classification of joint stiffness is presented in Eurcode 3 (EC3), EN 1993-1-8:2005 (CEN, 2005), for design of joints in steel structures. This classification makes the distinction between pinned, semi-rigid and fully rigid connections. The distinction between the three categories is based on the initial rotational stiffness, $S_{j,ini}$, which is defined as in Equation 9.5. In this

equation the factor for joint stiffness (k_b) equals 0.5 is used as a lower bound and 8 as upper bound for semi-rigid joints.

$$S_{j,ini} = k_b \frac{EI_b}{L_b} \tag{9.5}$$

Where:

- $S_{j,ini}$ = Initial joint rotational stiffness (Nmm/rad)
- k_b = factor for joint stiffness (-)
- E = Modulus of elasticity (MPa)
- I_b = Second moment of area of a beam (mm^4)
- L_b = Length of beam (mm)

The total joint stiffness for external connections, which is the combined effect of joint panel deformation, interface compression and gap opening, is shown in Figure 9.4. In this figure a comparison with the classification of joint stiffness based on EC3 has been included. If similar boundaries to those used for steel structures are applied in timber design, it can be seen that the design falls in the semi-rigid area and the joint stiffness should thus be included in the design. It can be seen that the post-tensioning force does not change the stiffness of the connection, but it does effect the moment capacity (strength). Achieving fully fixed connections (before decompression) is not practically possible with timber columns (unless it reaches the dimensions of a wall and has a significant amount of steel to reinforce the interface), but could be achieved with steel or concrete columns.

9.2.2 Post-tensioning design

The post-tensioning system is modelled by equivalent forces which act on the timber structure. At the anchorage the full post-tensioning force is acting on the column. At the deviators the uplift forces are acting on the beam and at the central columns the downward force from the tendons is acting on the column.

A modelling issue arises as the beams want to shorten due to the compressive post-tensioning force. This compression is restrained by the supports of the columns, resulting in large bending moments in the columns. In a multi-storey building there is no actual support of the columns, except at ground floor, and

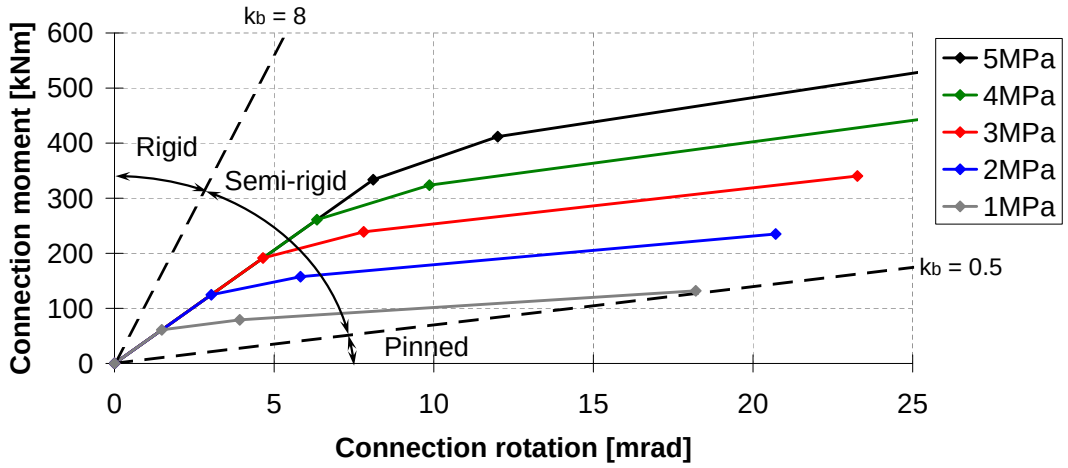

Figure 9.4: Moment-rotation graph of external beam-column joint for different levels of post-tensioning stress and comparison with Eurocode 3 joint stiffness classification (CEN, 2005)

the frame is allowed to shorten. Allowing horizontal movement of the column supports in the model is not possible, as that would result in zero column moments and thus essentially pinned connections.

One option would be to model a full multi-storey frame, including the foundation connections. In that way frame shortening would be allowed for. A work-around in the single-storey model used in this section was to apply the post-tensioning force not only at the anchorages, but also at the external beam-column connection interface. This resulted in the large shear force in the joint panel, but not in the compressive force in the beams meaning that no frame shortening took place. A disadvantage of this work-around is that second order effects are not taken into account in the model. It was shown in Section 7.3 that these second order effects can be 17% of the total bending moment and 15% of the total deflections.

Tendon elongation under ULS loading is not taken into account in the framework analysis program. An iterative procedure has been followed in order to accurately determine the amount of tendon elongation. The procedure as described in Section 8.6 has been implemented, where beam deflections and gap opening follow from the framework analysis program. The amount of tendon elongation is then updated by changing the combination factor for tendon elon-

gation in the load-combination ($\psi_{te} = \Delta F_{pt}/F_{pt,i}$). This iterative procedure has been implemented for all five levels of post-tensioning and the resulting amount of tendon elongation is shown in Table 9.1.

Table 9.1: Calculation of tendon elongation (Δl_{pt}) due to deviator deflections (w_{dev}) and gap opening (θ_{gap}) under ULS loading for different levels of initial post-tensioning stress ($\sigma_{pt,i}$)

$\sigma_{pt,i}$ (MPa)	$F_{pt,i}$ (kN)	w_{dev} (mm)	θ_{gap} (mrad)	$\Delta l_{pt,dev}$ (mm)	$\Delta l_{pt,gap}$ (mm)	Δl_{pt} (mm)	ΔF_{pt} (kN)	ψ_{te} (-)
1	184	47	64	49	36	85	131	1.71
2	368	39	30	40	17	49	122	1.33
3	552	33	7	34	4	32	113	1.20
4	736	32	0.0	32	0	27	117	1.16
5	920	31	0.0	31	0	25	134	1.15

Deviator deflection is the average deflection of the deviators in the three beams and gap opening is the total of all six connections. The change in length of post-tensioning tendons takes elastic shortening of the frame into account, as presented in Table F.6. From Table 9.1 it can be seen that for low post-tensioning forces a large amount of tendon elongation (up to 71%) occurs due to deviator deflections and gap opening. For high post-tensioning forces no gap opening occurs and about 15% tendon elongation occurs due to deviator deflections.

9.2.3 Results

This section gives an overview of the results of the framework model. Detailed results for all load cases are shown in Appendix F.4.

Deflections Beam mid-span deflections for four different load cases are shown in Table 9.2.

The post-tensioning only load case shows the precamber of the beams. This is increasing from about 6mm to 30mm with an increase in post-tensioning force. Deflections of the external bay are larger than the internal bay due to the lower stiffness of the external connection (column and joint panel deformation). SLS deflections under short term loading should be checked against the deflection limit of span over 300, which is 33mm. It can be seen that only the frames

Table 9.2: Mid-span deflections (mm) from framework analysis for external bay (Ext.) and internal bay (Int.) under four different load cases

PT stress	PT only		SLS - short-term		SLS - long-term		ULS	
(MPa)	Ext.	Int.	Ext.	Int.	Ext.	Int.	Ext.	Int.
pinned	-	-	53.4	53.4	45.1	45.1	82.3	82.4
1	6.1	5.5	35.5	35.0	30.0	29.6	55.9	55.3
2	12.2	10.9	22.2	20.7	19.6	17.9	41.6	40.6
3	18.3	16.4	14.8	12.3	14.1	11.9	30.3	27.2
4	24.4	21.9	9.2	7.4	9.9	8.1	23.3	19.5
5	30.4	27.2	3.7	2.5	5.8	4.4	16.6	13.5
fixed	-	-	22.0	18.4	18.6	15.5	34.0	28.3

without post-tensioning and with 1MPa do not satisfy this check. It can also be seen that even a modest amount of post-tensioning (1MPa compressive stress) results in a decrease of deflections of 35% (35mm compared to 53mm). A frame without post-tensioning but with fully fixed connections has larger deflections than a frame with a post-tensioning stress of 4MPa or larger, as the uplift force at the deviators is not acting in this model.

Long-term deflections should be multiplied by the creep factor, or alternatively the deflection limit can be divided by the creep factor. If this factor is taken as 2.0, then the allowable long-term deflections should be lower than 16.6mm. It can be seen that a minimum of 2.5MPa post-tensioning stress is needed in order to reduce long-term deflections within this limit. ULS deflections do not need to be checked according to a deflection limit, but are of interest for evaluation of tendon elongation. Larger post-tensioning forces reduce beam deflections and thus limit the amount of tendon elongation. This effect can also be seen in Table 9.1. For beams with a post-tensioning stress of over 4MPa the precamber (PT only) is larger than the ULS deflections.

Connection rotation Rotations of external connections under different load cases are shown in Figure 9.5.

For the post-tensioning only load case, the main rotation is due to joint panel and interface rotation. A linear increase in rotation can be seen with an increase in post-tensioning force. Pinned and rigid connections are not shown as they do not have a post-tensioning only load case. Under ULS load there is gap opening for 1

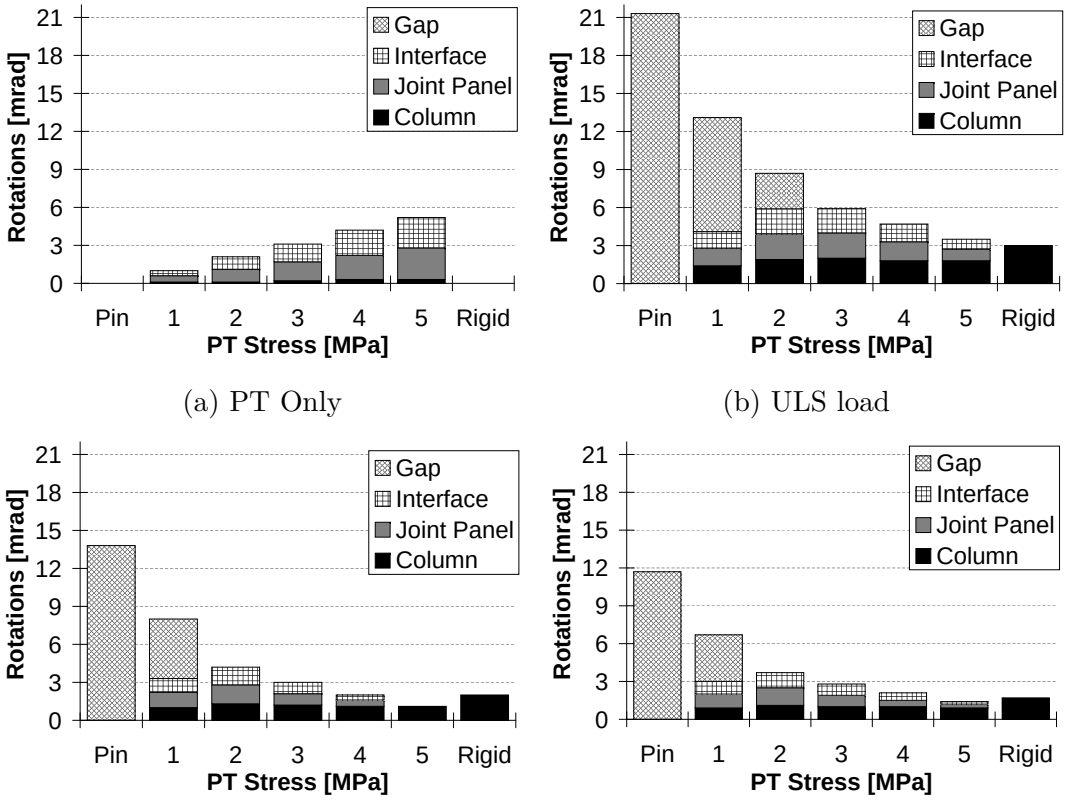

(a) PT Only

(b) ULS load

(c) Short term SLS

(d) Long-term SLS

Figure 9.5: External connection rotation results of framework analysis for different load combinations

and 2MPa post-tensioning stress, but no gap opening under larger post-tensioning forces. The amount of column, joint panel and interface rotation depends on the connection moment. For low post-tensioning forces and for high post-tensioning forces the connection moment is small whereas for 2 and 3MPa post-tensioning stress the bending moments are the highest. The pinned connection only exhibits gap opening and the rigid connection only column rotation.

Under short and long-term SLS loading the connection rotations are very similar. With an increase in post-tensioning force the rotations decrease, resulting in less beam deflection. For post-tensioning stresses of 1MPa there is still gap opening under SLS load but for higher stresses no gap opening occurs.

Bending moments An overview of maximum bending moments at internal connections (Conn.) and along the beam (Field) for different load cases is shown in Table 9.3.

Table 9.3: Maximum bending moments (kNm) at internal connections and along the beam (Field) for different load cases

PT stress	PT only		SLS - short-term		SLS - long-term		ULS	
(MPa)	Field	Conn.	Field	Conn.	Field	Conn.	Field	Conn.
pinned	-	-	580	0	490	0	893	0
1	-67	60	382	-98	323	-93	603	-118
2	-133	121	237	-155	209	-147	447	-180
3	-199	182	159	-151	151	-144	324	-238
4	-265	243	102	-96	108	-102	251	-239
5	-331	303	58	-41	65	-61	181	-172
fixed	-	-	225	-424	190	-358	348	-653

The simply supported beam (no post-tensioning) has a maximum bending moment of 893kNm under ULS load. For beams with post-tensioning this reduces to 181kNm. The connection moment increases with an increase of post-tensioning force. For a post-tensioning stress of 4MPa the connection moment is almost equal to the field moment, indicating an optimal design for bending moments. For 4MPa and over, the bending moments during stressing (PT only) are larger than ULS bending moments. For the frame with fixed connections the connection bending moment is almost double the field moment.

The section capacity of the beam is 931kNm. It can be seen that the ULS bending moment in the pinned frame (893kNm) is very close to this maximum value. The lowest bending moment values are reached when the PT only load case reaches similar values as the ULS load case, which is with a post-tensioning stress of 4MPa. The maximum bending moment is 265kNm, which is a reduction in maximum bending moment of 70%.

Connection behaviour The moment-rotation behaviour of the internal and external connections under different load cases are shown in Figure 9.6. The curves for the different levels of post-tensioning have been limited to 15mrad gap opening (Figure 9.3) and this value is increased by the other rotational components. Although the curves are limited the connection will be able to

undergo larger rotations. But the maximum rotation from the framework analysis with post-tensioning is 13mrad, which is within the range of the moment-rotation curve.

On the horizontal axis is the pinned connection, which has large rotations (21.3mrad under ULS loading) and no bending moments. On the vertical axis is the fully fixed connection which has no rotations and large connection moments (up to 653kNm for internal connections at ULS loading). No gap opening occurs for all results which are along the line of the initial stiffness. Once gap opening occurs the stiffness changes and results will be to the right of the line of the initial stiffness. For external connections it can be seen that there is gap opening under SLS loading with a low post-tensioning stress of 1MPa, but no gap opening for higher post-tensioning stresses. For internal connections gap opening under SLS loading occurs for 1 and 2MPa post-tensioning stress, and for larger post-tensioning stresses the connections stay closed.

Under post-tensioning only load all connections remain closed, only rotation due to interface compression occurs. For ULS loading gap opening of internal and external connections occurs for a post-tensioning stress of 1MPa and 2MPa. For 3MPa only internal connections are opening and for 4MPa and 5MPa both connections do not reach decompression under ULS load.

Shear forces The maximum shear forces in the beam and column are shown in Table 9.4.

Table 9.4: Shear force (kN) in beam and column based on framework analysis

PT stress	PT only		ULS	
(MPa)	Beam	Column	Beam	Column
pinned	-	-	358	30
1	36	183	305	208
2	72	366	277	342
3	108	549	254	491
4	144	732	230	648
5	190	850	180	914
fixed	-	-	378	152

With an increase in post-tensioning force, a decrease in shear force can be seen for beams under ULS load. For beams with a post-tensioning stress of 5MPa

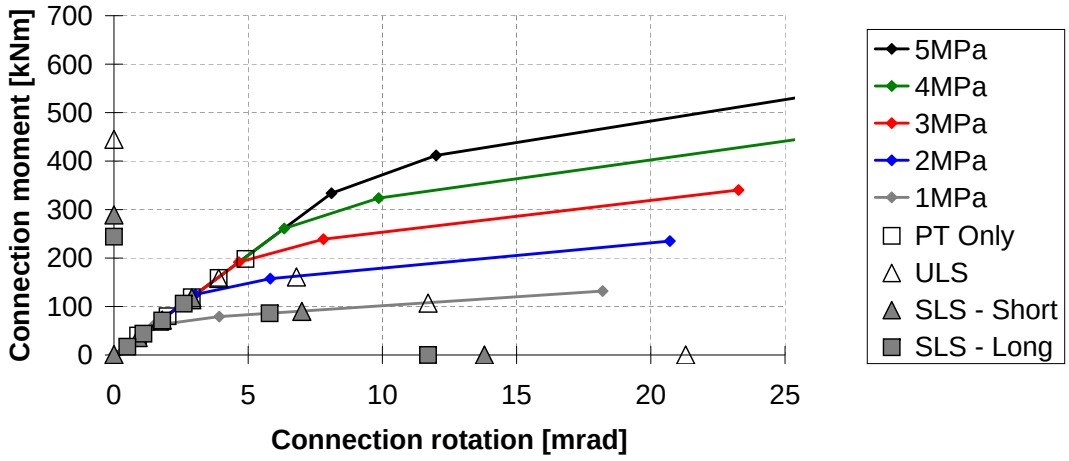

(a) External connection

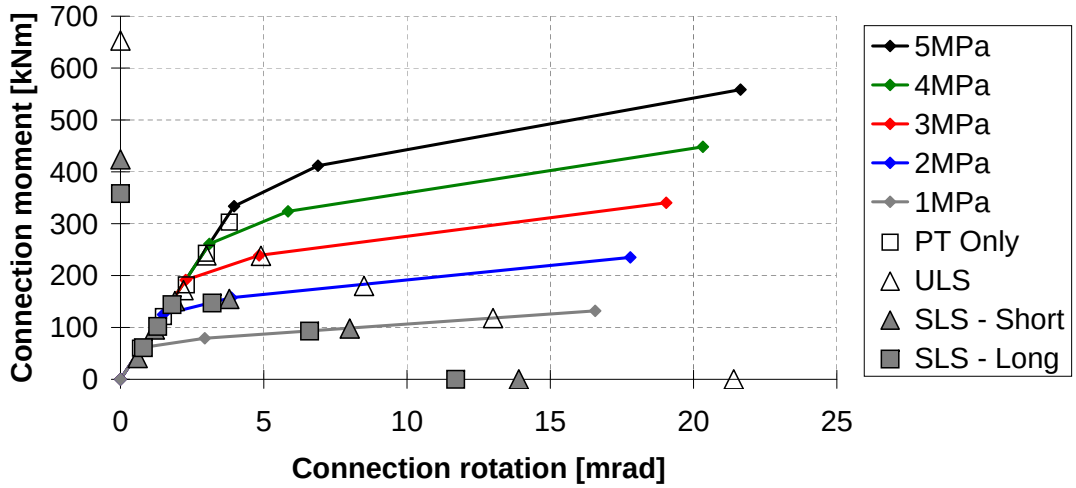

(b) Internal connection

Figure 9.6: Connection moment-rotation results of framework analysis under different load combinations and for a range of post-tensioning stresses. Horizontal axis shows pinned connection results and vertical axis shows fully fixed connection results

the shear force due to post-tensioning only is larger than under ULS loading, indicating that possibly too much post-tensioning was applied to the frame. The maximum shear in the beam is for a frame with fixed connections, which is slightly larger than for the simply supported beam. This is caused by the difference in connection stiffness in an external frame, resulting in a larger shear force on the side of the internal connection.

The maximum shear capacity of the beam with 90mm webs is 461kN, and it can be seen that this is sufficient for all beam designs. If the web thickness is reduced to 63mm the shear strength is 336kN, which is sufficient for all beam designs with post-tensioning but not for the beams without post-tensioning. A beam with 45mm web thickness has a shear strength of 248kN, which is only sufficient for beams with 4MPa post-tensioning stress or higher. It can be seen that for beams with a post-tensioning stress of 5MPa the shear demand is about half of the shear demand of a simply supported beam.

The column is loaded by high shear forces in the joint panel zone. The maximum shear strength of a 600mm by 400mm column is 691kN. This limits the maximum allowable post-tensioning stress in the beam to about 3.8MPa.

9.2.4 Summary

A detailed framework model of a post-tensioned timber frame with various levels of post-tensioning has resulted in data about deflections, rotations, bending moments and shear forces. The data can be used as a base-line for comparison with simplified models. It was shown that deflections, bending moments and shear forces can be significantly reduced by post-tensioning. Even a small amount of post-tensioning can lead to significant benefits in the design. For large post-tensioning forces the bending moments and shear forces due to post-tensioning only were larger than under ULS loading, indicating that possibly too much post-tensioning was applied to the frame. The optimal level of post-tensioning is further evaluated in Section 9.6.

9.3 Beam model

This section presents a simplified calculation model which is based on the beam only model.

9.3.1 Model description

The beam only model is shown in Figure 9.7. The beam length is the length between the supports. On both ends a rotational spring is placed to model the connection behaviour. The stiffness of the rotational springs is discussed in the next section. The same loads and load combinations as for the frame model were used.

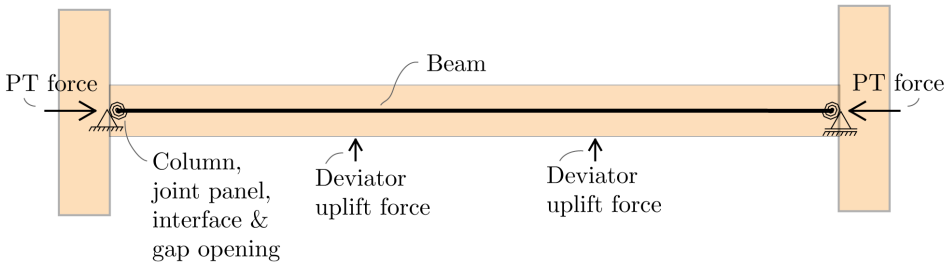

Figure 9.7: Schematics of beam only model

The post-tensioning forces are represented by equivalent forces. The post-tensioning force is acting directly onto the beam and shortening of the beam is allowed to happen. Therefore, contrary to the full frame model, second order effects are taken into account in the beam only model.

Detailed evaluation of tendon elongation for the frame model showed that this varied between 16% and 71% (Section 9.2). For this simplified model the iterative procedure to evaluate tendon elongation was skipped and the contribution was estimated to be 20% which is based on the average tendon elongation of the designs with post-tensioning stresses ranging from 2MPa to 5MPa.

9.3.2 Connection behaviour

In Section 9.2 the stiffness of the joint panel, interface and gap opening was already presented. The column rotational stiffness needs to be taken into account

for the beam only model. The column rotational stiffness was derived in Section 8.3 and the formula is repeated here in Equation 9.6.

$$k_{col} = \frac{\chi}{\frac{H}{12EI} + \frac{1}{\alpha GAH}} \tag{9.6}$$

Where:

- k_{col} = Stiffness of column (Nmm/rad)
- χ = Factor to convert connection moment into centreline moment
- H = Height of column (mm)
- E_t = Modulus of elasticity of timber (MPa)
- I_{col} = Major moment of inertia of column (mm^4)
- α = Factor to account for shear area
- G = Shear modulus of timber (MPa)
- A_{col} = Area of column (mm^2)

The factor χ to convert connection moment into centreline moment is needed as the rotational spring which models the column is placed at the end of the beam, and thus the beam bending moment is applied. This moment is smaller than the centreline moment, and thus smaller rotations would result if the real column stiffness is used. In order to get the same rotation, a lower stiffness is needed. The relationship between the connection moment and centreline moment is dependent on the shear force at the connection, as shown in Equation 9.7.

$$M_{cl} = M_{con} + F_{v,con} \cdot 0.5h_c \tag{9.7}$$

The shear force is dependent on the post-tensioning force and the external loading on the beam. This means that the conversion factor is different for every load-case and level of post-tensioning, making it not practical for the use in a design. An average value for χ can be found based on the framework model, as described in Section 9.2. The values of connection moment over centreline moment are shown in Table 9.5. From this table it can indeed be seen that the value of χ varies with different levels of post-tensioning and different load cases. The average value for all load cases is 0.64.

Table 9.5: Values of χ for different load-cases and post-tensioning forces

PT stress (MPa)	Load case			
	PT only	ULS	SLS short	SLS long
1	0.82	0.54	0.60	0.63
2	0.81	0.66	0.70	0.71
3	0.80	0.69	0.65	0.66
4	0.81	0.65	0.55	0.60
5	0.80	0.58	0.05	0.43
Average	0.81	0.62	0.51	0.61

This approximation is obviously dependent on the length of the beam and the depth of the column. The bending moment can reasonably be assumed linear between the centreline of the column and about 1/12th of the bay length as shown in Figure 9.8. For this area a geometric equation can be used to convert connection moment into centreline moment. The factor for this conversion is χ, as presented in Equation 9.8.

$$\frac{M_{con}}{L/12 - h_c/2} = \frac{M_{cl}}{L/12} \rightarrow M_{con} = M_{cl} \cdot \frac{L/6 - h_c}{L/6} = M_{cl} \cdot \chi \tag{9.8}$$

Where:

- L = Length of bay
- h_c = Width of column
- χ = Factor to convert connection moment into centreline moment

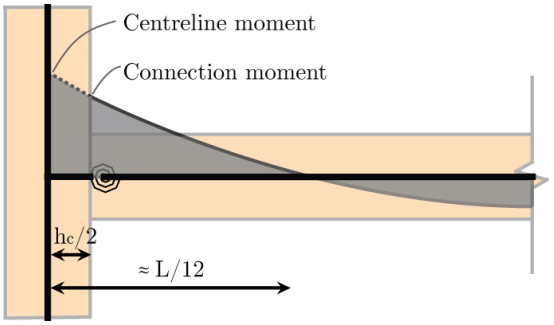

Figure 9.8: Definition of connection and centreline moments and derivation of conversion factor, χ

For the frame design the bay length was 10.6m and the column depth 0.6m. This results in a factor of $\chi = 0.66$ which is close to the result of the framework program. The resulting column rotational stiffness is shown in Equation 9.9.

$$\begin{aligned} k_{col} &= \frac{\chi}{\frac{H}{12EI} + \frac{1}{\alpha GAH}} \\ &= \frac{0.66}{\frac{3600}{12 \cdot 11000 \cdot 7.2 \cdot 10^9} + \frac{1}{0.86 \cdot 550 \cdot 240000 \cdot 3600}} \\ &= 0.66 \cdot 160 = 106 kNm/mrad \end{aligned} \tag{9.9}$$

The total rotational stiffness for internal and external connections is shown in Figure 9.9.

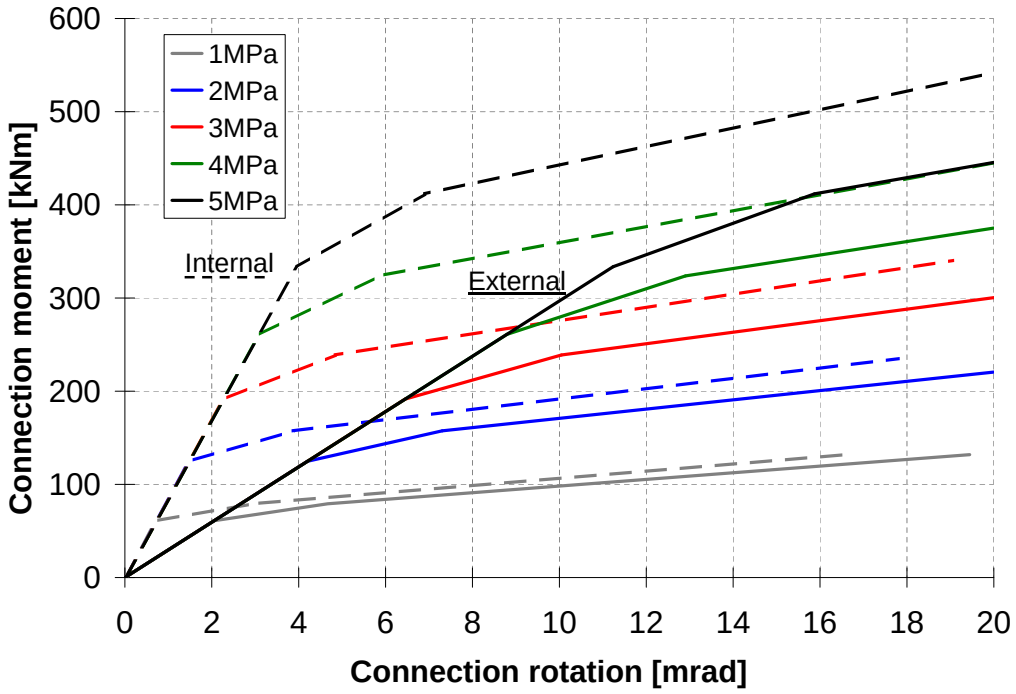

Figure 9.9: Connection moment-rotation behaviour for internal and external connections

9.3.3 Results

Deflections following from the beam only model for different load combinations are shown in Table 9.6. Also shown in this table are the comparisons with values from the frame model.

Table 9.6: Mid-span deflections of beam only model for different load combinations and comparison with full frame model

PT stress (MPa)	PT only (mm)		SLS - Short-term (mm)		SLS - Long-term (mm)		ULS (mm)	
pinned	-	-	53.2	0%	44.9	0%	81.9	0%
1	6.4	5%	35.5	0%	30.0	0%	60.9	9%
2	12.8	5%	21.9	-1%	19.3	-2%	44.5	7%
3	19.3	5%	14.2	-4%	13.6	-4%	30.2	0%
4	26	7%	8.4	-9%	9.3	-6%	21.2	-9%
5	32.8	8%	2.6	-30%	4.9	-16%	14.2	-14%
fixed	-	-	18.6	-15%	15.7	-16%	28.6	-16%

From the table it can be seen that most results are within 10% of the full frame model. The difference between the two models is larger for beams with a higher post-tensioning force, which is partly due to the smaller absolute deflections, resulting in a larger percentage difference. This is especially noticeable for the short term SLS deflections of the beam with 5MPa post-tensioning stress, where the absolute difference is only 1.1mm, but the percentage difference is 30%. For the ULS load case the difference is also partly caused by the constant tendon elongation in the beam model which underestimates tendon elongation for lower levels of post-tensioning resulting in larger deflections, and vice versa for higher post-tensioning forces. The model with fixed ends has a 15% difference as column rotation is not included in the beam only model, whereas it is included in external connections in the full frame model.

Bending moments for the post-tensioning only and ULS load case are shown in Table 9.7. Also shown in this table are the comparisons with values from the frame model.

A similar result as for deflections can be seen. Most bending moments are within 10% of the full frame model. The higher bending moments for tests with lower post-tensioning forces are caused by second order effects. These are not

Table 9.7: Bending moments along the beam (Field) and at the connection for two different load combinations and comparisons with full frame model

PT stress (MPa)	PT only - Field (kNm)		PT only - Conn. (kNm)		ULS - Field (kNm)		ULS - Conn. (kNm)	
pinned	-	-	-	-	894	0%	-	-
1	-71	6%	62	3%	663	10%	-123	4%
2	-142	7%	126	4%	485	9%	-187	4%
3	-214	8%	193	6%	331	2%	-240	1%
4	-288	9%	262	8%	235	-6%	-231	-3%
5	-362	9%	332	10%	163	-10%	-160	-7%
fixed	-	-	-	-	298	-14%	-596	-9%

included in the frame model, but are included in the beam-only model. For lower post-tensioning forces the deflections are larger and thus the second order effects more significant. For higher post-tensioning stresses the bending moments are under PT only load are slightly over predicted and under ULS load slightly under predicted. This is because the tendon elongation is fixed at 20%, whereas in the frame model it was shown to be 15-16%. The extra tendon elongation results in aditional uplift forces at the deviators and thus higher bending moments under PT only load and lower bending moments under ULS loading.

It can be concluded that the results of the beam only model match the full framework model very well. Therefore simplification steps of the beam-only model can be used for further frame design.

9.4 Simplified beam model

A further simplification to the beam model would be to model the connection stiffness as linear elastic up to decompression and assume a fully plastic behaviour after decompression, i.e. no increase in moment capacity. In that case, the calculation of gap opening and corresponding tendon elongation do not need to be performed. The resulting moment rotation curves are shown in Figure 9.10.

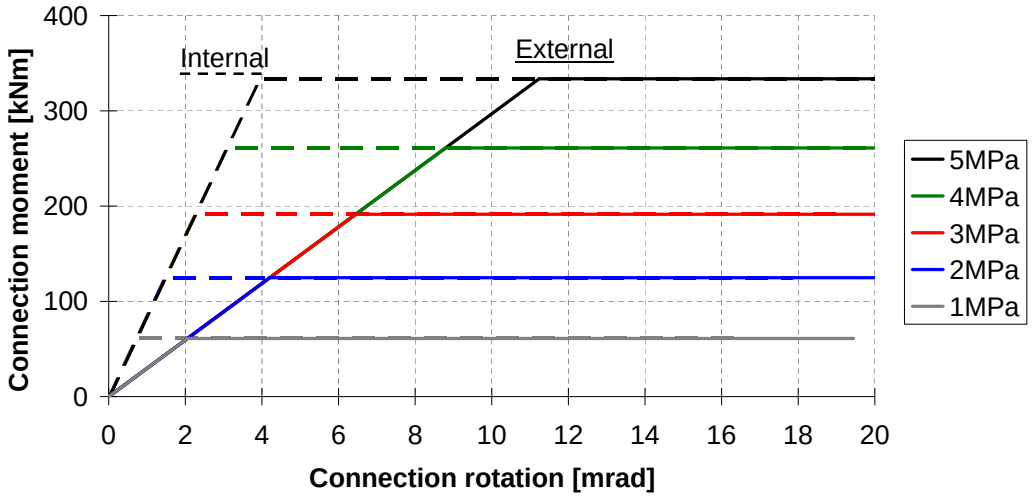

Figure 9.10: Moment rotation behaviour of elasto-plastic connection model

The same analysis as for the beam only model presented in the previous section was run. The resulting beam deflections are shown in Table 9.8.

Deflections according to the simplified model are the same for beams with large post-tensioning forces as gap opening is not reached. For beams with low post-tensioning forces the deflections of the beam are larger by up to 11%. Larger deflections make for a more conservative design and can therefore be used safely.

The bending moments from the simplified model are shown in Table 9.9. This table also shows the comparisons of bending moments with the beam only model with non-linear connection behaviour.

It can again be seen that bending moments between the two models are the same for higher post-tensioning forces where gap opening does not occur. The field moment under ULS loading is up to 11% higher, again making for a conservative

Table 9.8: Mid-span deflections of beam only model with elasto-plastic connections for different load combinations and comparisons with the beam model having non-linear connections

PT stress (MPa)	PT only (mm)		SLS - Short-term (mm)		SLS - Long-term (mm)		ULS (mm)	
pinned	-	-	53.2	0%	44.9	0%	81.9	0%
1	6.4	0%	38.7	9%	32.6	9%	66.2	9%
2	12.8	0%	23.4	7%	20.1	4%	49.5	11%
3	19.4	1%	14.2	0%	13.6	0%	32.1	6%
4	26.0	0%	8.4	0%	9.3	0%	21.2	0%
5	32.8	0%	2.6	0%	4.9	0%	14.2	0%
fixed	-	-	18.6	0%	15.7	0%	28.6	0%

Table 9.9: Bending moments along the beam and at the connection based on elasto-plastic connection behaviour for two different load combinations and comparisons with the beam only model

PT stress (MPa)	PT only - Field (kNm)		PT only - Conn. (kNm)		ULS - Field (kNm)		ULS - Conn. (kNm)	
pinned	-	-	-	-	894	0%	-	-
1	-71	0%	61	-2%	722	9%	-61	-50%
2	-142	0%	125	-1%	540	11%	-125	-33%
3	-215	0%	191	-1%	352	6%	-191	-20%
4	-288	0%	261	0%	235	0%	-231	0%
5	-362	0%	332	0%	163	0%	-160	0%
fixed	-	-	-	-	298	0%	-596	0%

design. The connection moment at ULS is up to 50% lower, which makes for an unconservative connection design. Therefore, when applying an elasto-plastic connection behaviour for frames with low post-tensioning forces, the connection moment in the design should be increased.

It can be concluded that the elasto-plastic assumption for connection behaviour gives results which match the beam only and full frame model for larger post-tensioning forces where gap opening does not occur. For frames with lower post-tensioning forces it results in a conservative design, except for the connection moment which is underestimated.

9.5 Analytical beam model

The analytical beam model, as shown in Figure 9.11, uses the elasto-plastic connection behaviour as shown in the previous section. In this section a beam located in an external bay of a post-tensioned frame is analysed, with an external connection and an internal connection. Although the equations are also valid when using the same connection stiffness for both sides. The principle of superposition can be used to evaluate the bending moment and deflection contribution from four components: vertical distributed load (q), post-tensioning uplift force at the deviators ($F_{pt,v}$), internal connection moment ($M_{con,int}$) and external connection moment ($M_{con,ext}$). Second order effects are ignored as in Section 7.3 it was shown that at failure the second order effect on bending moments was about 17% and for deflections about 14%. In a ULS design with all safety factors, the second order effects are expected to be about half of that at failure and therefore deemed small enough to be ignored in this analytical model.

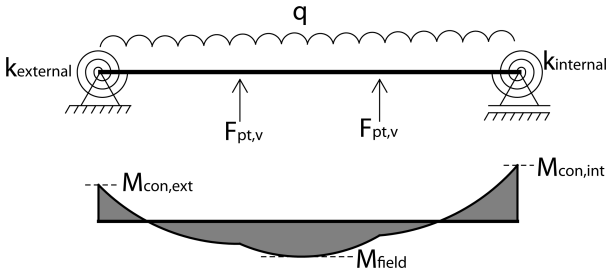

Figure 9.11: Beam only model with bending moment distribution

9.5.1 Bending moment distribution

Closed form analytical equations, based on standard beam theory, can be used to calculate the bending moment distribution in a post-tensioned timber frame. These are shown below for 3 different cases:

1. Internal and external connections moment before decompression
2. Internal connection reached decompression and has a constant bending moment, external connection still before decompression
3. Internal and external connections have reached decompression and have constant bending moments

Derivation of the analytical solutions is presented in Appendix F.1. This derivation is based on the vertical distributed load, the uplift force at the deviators and the connection moments.

Case 1 Before decompression internal and external rotational spring stiffness ($k_{internal}$ and $k_{external}$) need to be accounted for and bending moments at internal and external ($M_{con,int}$ and $M_{con,ext}$) and maximum mid-span moment (M_{mid}) can be calculated as in Equation 9.10. In these equations the factors a and b are given by Equation 9.11.

$$\begin{aligned} M_{con,ext} &= \frac{a(1 + b \cdot k_{internal})k_{external}}{1 + 2b \cdot k_{external} + 2b \cdot k_{internal} + 3b^2 \cdot k_{external} \cdot k_{internal}} \\ M_{con,int} &= \frac{a - b \cdot M_{con,ext}}{1/k_{internal} + 2b} \\ M_{mid} &= 0.5(M_{con,ext} + M_{con,int}) - \frac{1}{8}qL_b^2 + \frac{1}{3}F_{pt,v} \cdot L_b \end{aligned} \tag{9.10}$$

$$\begin{aligned} a &= \frac{q \cdot L_b^3}{24EI} - \frac{F_{pt,v} \cdot L_b^2}{9EI} \\ b &= \frac{L_b}{6EI} \end{aligned} \tag{9.11}$$

Where:

- $k_{internal}$ = Internal connection stiffness (Nmm/mrad)
- $k_{external}$ = External connection stiffness (Nmm/mrad)
- $M_{con,int}$ = Internal connection moment (Nmm)
- $M_{con,ext}$ = External connection moment (Nmm)
- M_{mid} = Maximum mid-span bending moment in the beam (Nmm)
- q = Distributed load on beam (N/mm)
- $F_{pt,v}$ = Vertical post-tensioning force at deviator (N)
- L_b = Length of beam (mm)
- E = Modulus of elasticity of timber (MPa)
- I = Moment of inertia around strong axis of beam (mm^4)

Case 2 In the case of different connection stiffness, the stiffest connection will reach decompression moment first; i.e. only one gap will open. If assuming that the connection moment does not increase after decompression (M_{dec}) then Equation 9.12 can be used to calculate the bending moment distribution.

$$\begin{aligned} M_{con,int} &= M_{dec} \\ M_{con,ext} &= \frac{a - b \cdot M_{dec}}{1/k_{external} + 2b} \\ M_{mid} &= 0.5(M_{con,ext} + M_{dec}) - \frac{1}{8}qL_b^2 + \frac{1}{3}F_{pt,v} \cdot L_b \end{aligned} \tag{9.12}$$

Case 3 In case that both connections reach the decompression moment, Equation 9.13 can be used to calculate the moment distribution.

$$\begin{aligned} M_{con,int} &= M_{dec} \\ M_{con,ext} &= M_{dec} \\ M_{mid} &= M_{dec} - \frac{1}{8}qL_b^2 + \frac{1}{3}F_{pt,v} \cdot L_b \end{aligned} \tag{9.13}$$

9.5.2 Beam deflections

Beam deflections can be calculated once the bending moment distribution is known. Beam deflection in a post-tensioned timber frame consists of 4 components. Each of these components, listed in Table 9.10, can be analysed separately and added together to find the total beam deflection.

9.5.3 Comparisons

The results of the analytical model can be compared with results of the full framework model. Mid-span deflections of the analytical model are presented in Table 9.11 and bending moments at the connection and beam mid-span in Table 9.12.

It can be seen that results of both deflections and bending moments for the beam with pinned connections match exactly. For post-tensioned frames the deflections based on the analytical model for the PT only load case match very

Table 9.10: Equations to calculate deflection components for a beam in a post-tensioned timber frame

Deflection component	Schematics	Equation
Distributed load	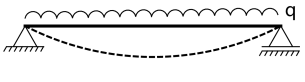	$u_q = \frac{5qL_b^2}{384EI} + \frac{qL_b^2}{8GA_s}$
Post-tensioning	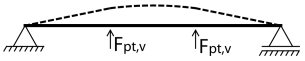	$u_{pt} = \frac{23F_{pt,v}L_b^3}{648EI} + \frac{F_{pt,v}L_b}{3GA_s}$
Int. conn. moment	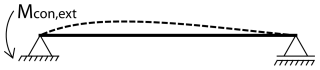	$u_{con,int} = \frac{M_{con,int}L_b^2}{16EI}$
Ext. conn. moment	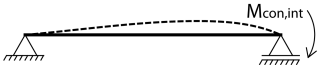	$u_{con,ext} = \frac{M_{con,ext}L_b^2}{16EI}$

Table 9.11: Mid-span deflections of analytical beam model for different load combinations and comparisons with the full framework model

PT stress (MPa)	PT only (mm)		SLS - Short-term (mm)		SLS - Long-term (mm)		ULS (mm)	
pinned	-	-	53.1	-1%	44.9	0%	81.9	0%
1	6.1	0%	37.8	6%	31.9	6%	64.6	16%
2	12.3	1%	23.2	5%	20.3	4%	47.3	14%
3	18.4	1%	13.9	-6%	13.4	-5%	31.8	5%
4	24.6	1%	8.4	-9%	9.2	-7%	20.5	-12%
5	30.7	1%	2.8	-24%	5.0	-14%	13.8	-17%

well with the results of the full framework model. For the other load cases the results are within 17%, except for short term SLS deflections with 5MPa post-tensioning stress. In that case the absolute difference is only 0.9mm, but the percentage difference is 24% due to very small deflections.

The main difference in bending moments for the PT only load case is because the maximum bending moment in the beam is not in the middle but at the deviator. The analytical model only calculates the mid-span bending moment and therefore underestimates the bending moments by about 4%. For the ULS load case the simplified connection model underestimates the connection moments and overestimates the field moments for low post-tensioning stress levels. For high post-tensioning levels both field and connection moments are under predicted as less tendon elongation occurs than is estimated in the analytical model. To

Table 9.12: Bending moments of analytical beam model for different load combinations and comparisons with the full framework model

PT stress (MPa)	PT only - Field (kNm)		PT only - Conn. (kNm)		ULS - Field (kNm)		ULS - Conn. (kNm)	
pinned	-	-	-	-	894	0%	-	-
1	-64	-4%	64	7%	706	17%	-66	-44%
2	-128	-4%	128	6%	518	16%	-130	-28%
3	-192	-4%	192	5%	350	8%	-196	-18%
4	-255	-4%	256	5%	228	-9%	-229	-4%
5	-319	-4%	320	6%	159	-12%	-159	-8%

compensate for the underestimation of the connection moment a design check (see Appendix F.2) has been added to check the compressive strength of the bottom flange of the beam. For low post-tensioning levels gap opening will occur under ULS loading and all the compressive force has to go through the bottom flange. The ULS post-tensioning force, including tendon elongation, is used in this design check.

9.5.4 Summary

An analytical model to calculate the bending moment distribution and deflections in post-tensioned timber frames has been developed. This model assumes elasto-plastic connection behaviour. Based on the comparisons with the full framework model it can be concluded that the analytical model results are accurate, except for the connection moment under ULS loading. To compensate for the underestimation of the connection moment a design check has been added to check the compressive strength of the bottom flange of the beam. Therefore the analytical model can be used for design purposes.

9.6 Parameter study

A parameter study for post-tensioned timber frames has been performed in a very similar manner to the parameter study on post-tensioned timber beams as described in Section 7.6.

9.6.1 Model description

The analytical model as presented in section has been implemented using a spreadsheet following the code based design, as presented in Appendix F.2.

In the parameter study the bending strength, shear strength, long-term deflections and the compressive strength of the bottom flange at the connection are taken into account. Short-term deflections have been ignored, as they did not govern any of the beam designs. Post-tensioning stresses ranging from 0MPa to 5MPa have been considered, and beam lengths between 6m and 14m. The same beam sections (Figure 9.12) as for the beam designs have been used for the analysis. Column dimensions have been taken equal to the width of the beam and an estimate of column depth was made.

The connection stiffness depends on beam and column sizes and an overview of values used in the designs is shown in Table 9.13.

Table 9.13: Overview of beam and column dimensions for parameter study on frames and the resulting connection stiffness

Dimensions (h x b)		Stiffness (kNm/mrad)				
Beam	Column	Column	Joint panel	Interface	External	Internal
600x300	500x300	56	36	35	13	35
800x400	600x400	106	81	84	30	84
1000x500	700x500	170	151	162	54	162
1200x600	800x600	245	252	274	85	274

9.6.2 Results

In the first stage of the parameter study one beam section, 800x400mm, was chosen. For this section a range of post-tensioning stresses was used for a fixed

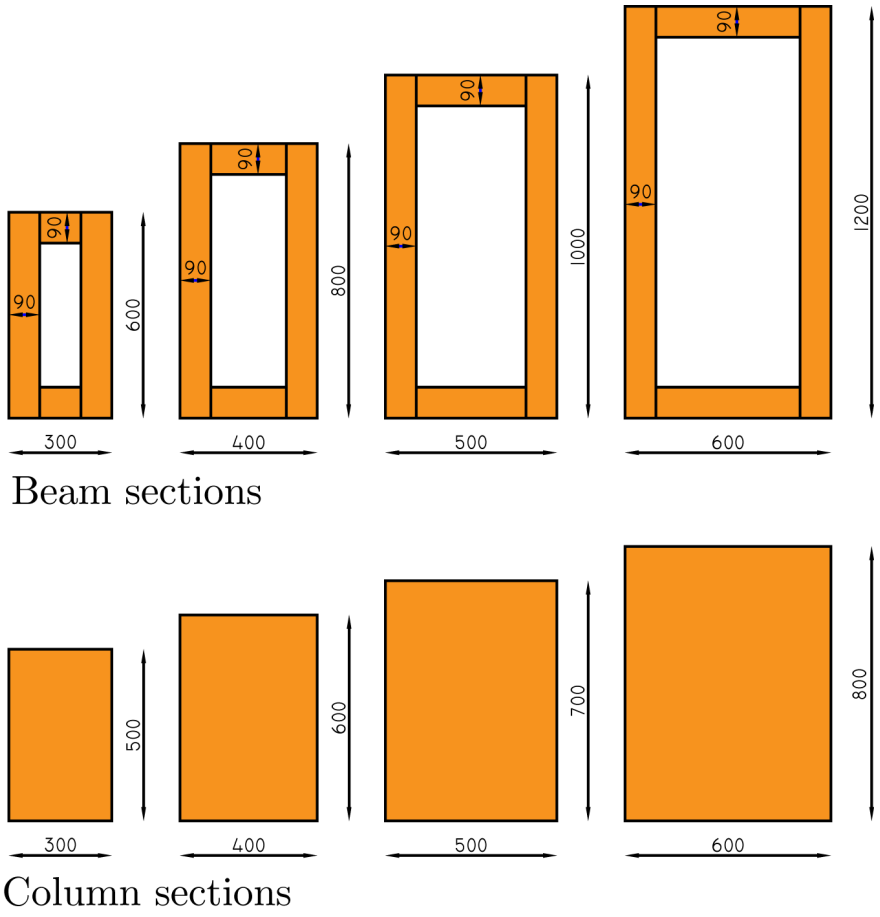

Figure 9.12: Overview of beam and column sections for use in frame parameter study

beam length of 10m. Next a range of beam lengths was used for a fixed post-tensioning stress of 2.5MPa. The results are shown in Figure 9.13 and Figure 9.14.

From these figures it can be seen that only a maximum length of 10m is possible for this cross-section. Larger beam lengths are no longer satisfying the long-term deflection criteria. It can also be seen that for spans smaller than 10m the compression strength of the bottom flange is governing the design.

The variation in post-tensioning stress for a 10m long beam shows that only a small range of post-tensioning stresses around 2.5MPa allows for all unity checks to be below 1. For lower stresses the long-term deflection limit is exceeded and for higher stresses the compression strength of the bottom flange exceeded. It

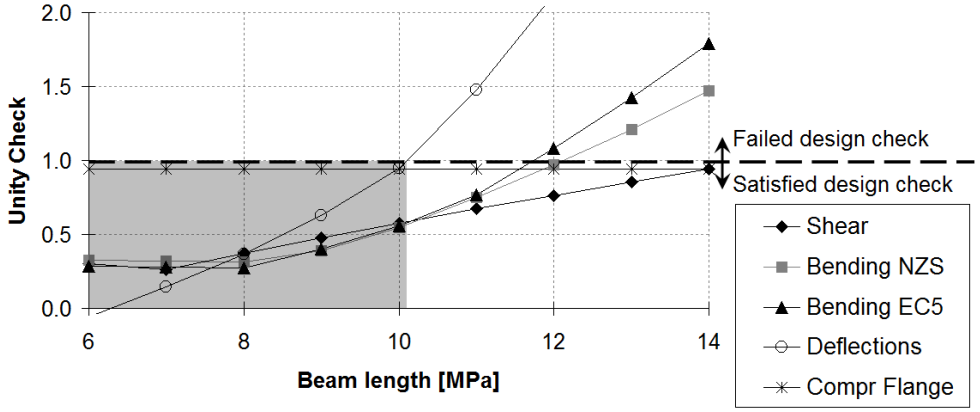

Figure 9.13: Results of frame parameter study on beam length for a constant PT stress of 2.5MPa

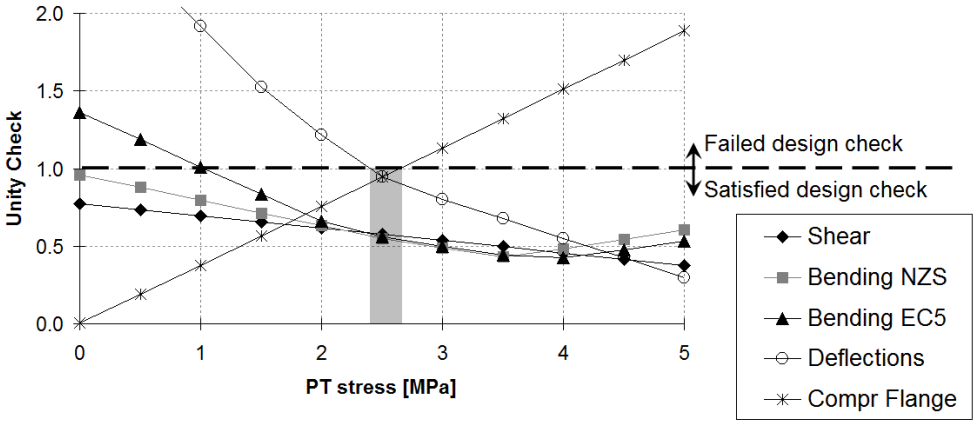

Figure 9.14: Results of frame parameter study on post-tensioning force for a constant length of 10m

can be seen that for post-tensioning stressed under 2.5MPa long-term deflections are always governing the design over bending and shear.

Similar to the parameter study on beams, the two graphs above can be combined in a 3D plot for a range of beam lengths and post-tensioning stresses. This is shown in Figure 9.15.

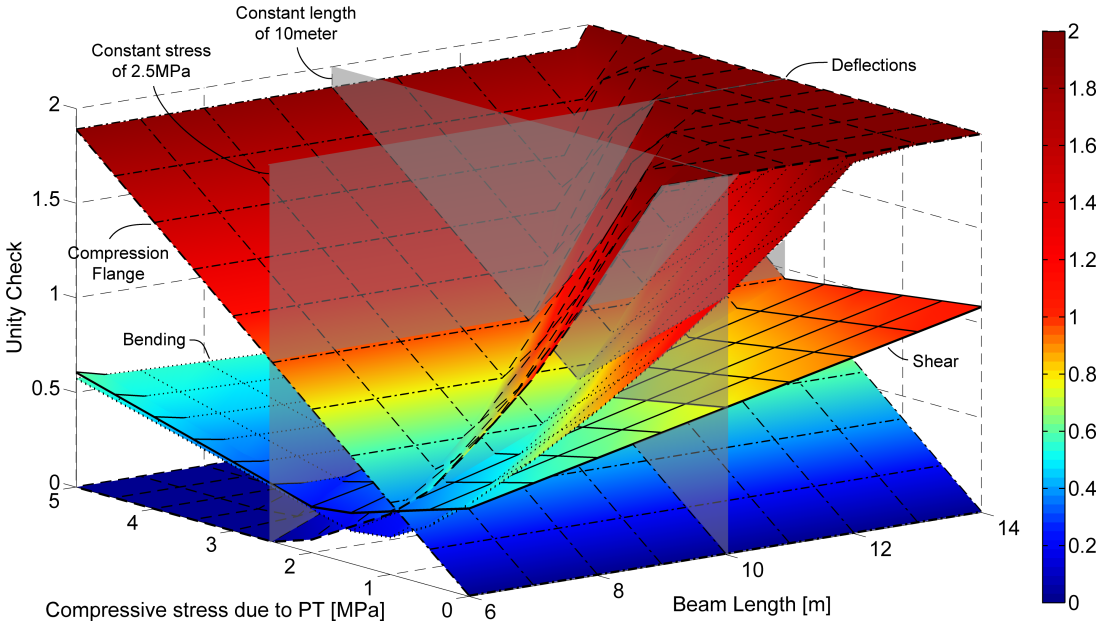

Figure 9.15: Results of frame parameter study on beam length and post-tensioning stress for 800x400mm section

From this 3D plot it can be seen that the plane for compression strength of the bottom flange at the connection is constant for different beam lengths. Obviously this check is zero for no post-tensioning and increases with an increase in post-tensioning force. It can be seen that this check is limiting the amount of post-tensioning which can be applied to the frame. Furthermore, it can be seen that the long-term deflections plane is governing over the bending and shear planes. Similar conclusions can be drawn for the other three cross-sections.

A top view of the 3D plot for all four cross-sections is shown in Figures 9.16 and 9.17.

For all sections it can be seen that the maximum post-tensioning stress is between 2.5 and 3MPa and is limited by the compression strength of the bottom flange after gap opening. If the thickness of the bottom flange is increased, this

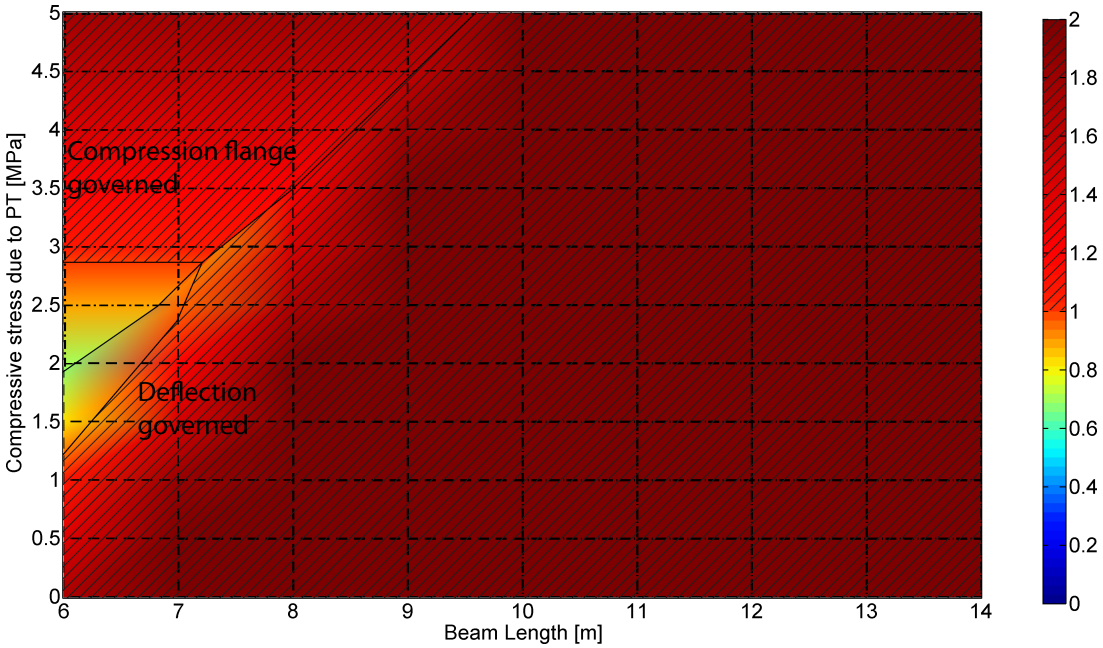

(a) 600 x 300 Beam

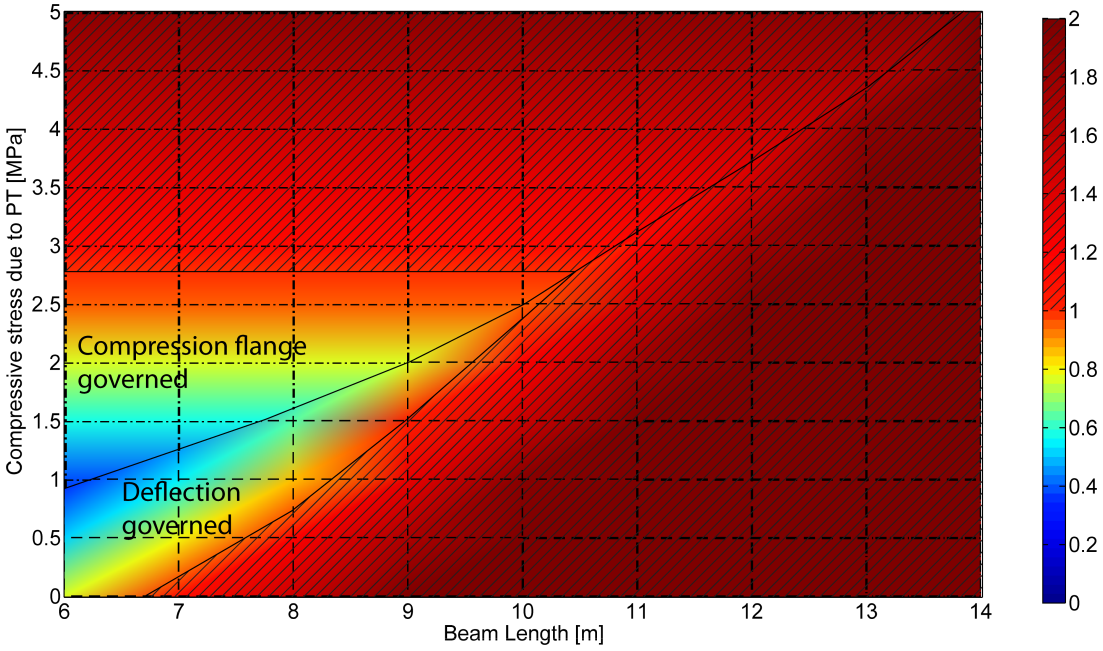

(b) 800 x 400 Beam

Figure 9.16: Results of frame parameter study on beam length and post-tensioning stress, showing unity checks (UC) for bending, shear, flange compression strength and deflections

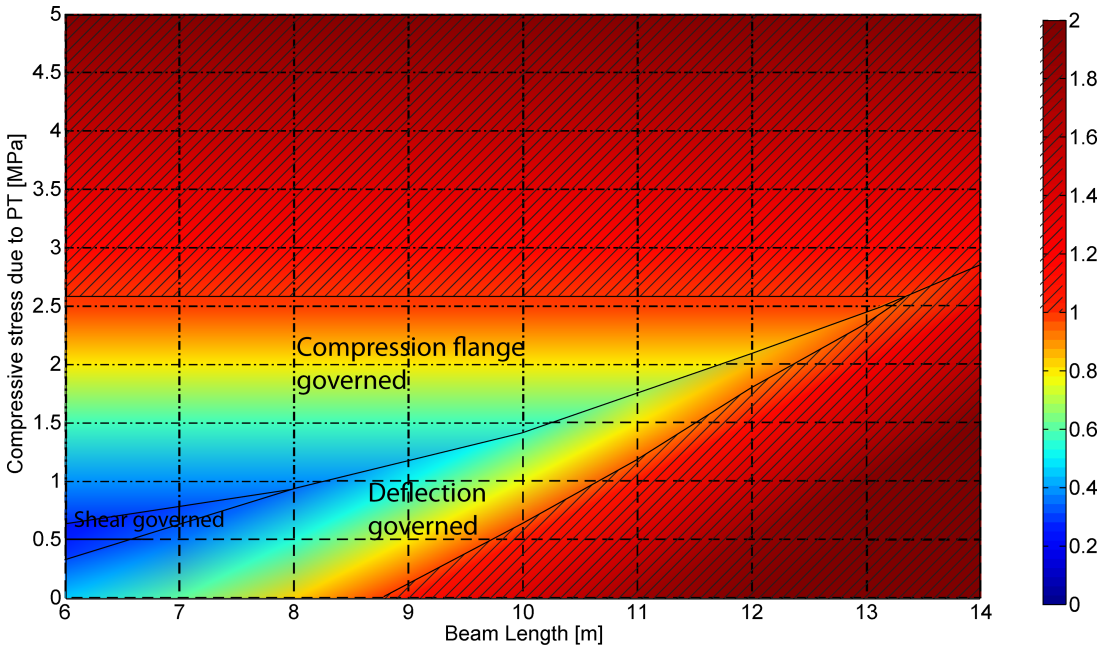

(a) 1000 x 500 Beam

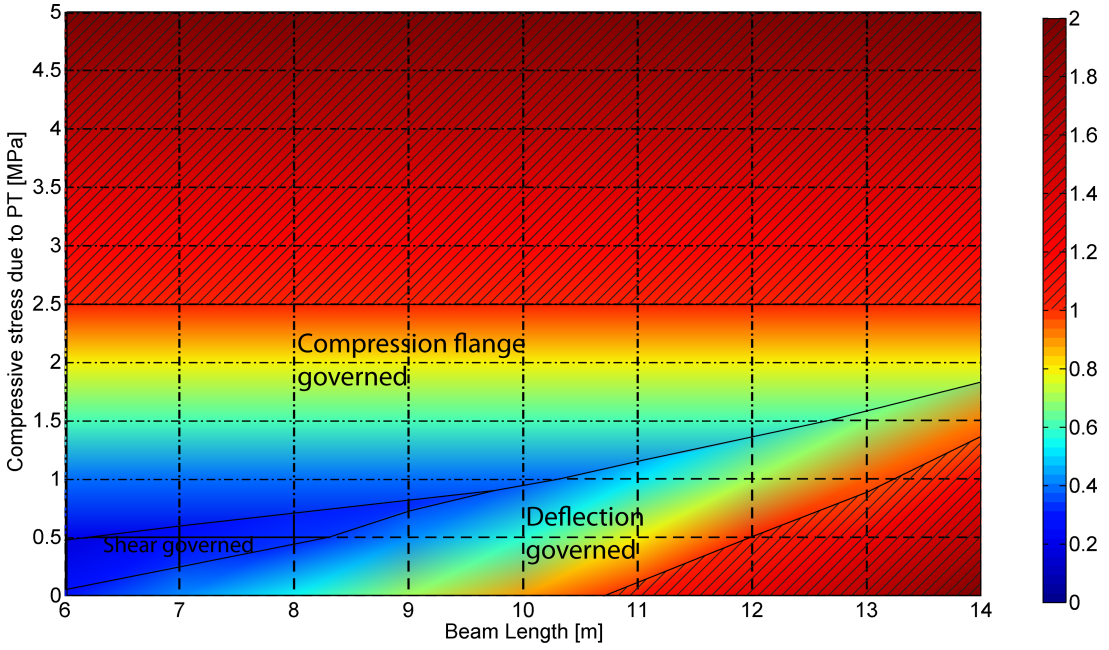

(b) 1200 x 600 Beam

Figure 9.17: Results of frame parameter study on beam length and post-tensioning stress, showing unity checks (UC) for bending, shear, flange compression strength and deflections (continued)

limit will change. But increasing the bottom flange thickness will result in a lower neutral axis and the distance between the neutral axis and the top of the bottom flange (eccentricity of the tendons) and also be significantly reduced. For further research, the section could be optimized by increasing the thickness of the bottom flange only at the connection and not along the full length of the beam.

The beam length is always governed by the long-term deflection limit. For the two largest section sizes combined with short spans, the shear strength can govern the design but this range is not normally expected for designs. For the 600x300mm beam section it can be seen that spans up to 7m are possible. For the 800x400 beam section spans of up to 10m are possible, for 1000x500 beam section up to 13m and for the 1200x600 beam section spans over 14m are possible.

9.7 Comparison between frames and beams

The results of the parameter study on beams and frames can be compared. The results of the 800x400 beam section for simply supported beams and for frames are repeated in Figure 9.18. It should be noted that the scale on the vertical axis, the post-tensioning stress, is different for the two figures.

The 800x400 section without post-tensioning (on the horizontal axis) can achieve a span of about 6.5m, obviously this is the same for both parameter studies. When adding 1MPa of post-tensioning stress the span for beams is increased to 7m and for the frame to 8m. With 2.5MPa post-tensioning stress the maximum beam span becomes 8m for beams and 10m for frames, showing a clear benefit for frames due to the connection behaviour and increased angle at the deviators. Beams have the advantage that larger post-tensioning forces can be applied, therefore a similar span as for frames can be reached. For the 800x400 section the maximum span of a simply supported beam is about 11m with a post-tensioning stress of 9MPa, which is an 70% increase in span length compared to beams without post-tensioning. For a post-tensioned frame the maximum span is about 10m with a post-tensioning stress of 2.5MPa, resulting in a 50% increase in span length. The higher post-tensioning force in frames is problematic due to the limited compressive strength of the bottom flange after gap opening. Also the compressive strength of the column is limited, which causes design problems at the beam-column interface and for the column anchorage (Appendix B.3).

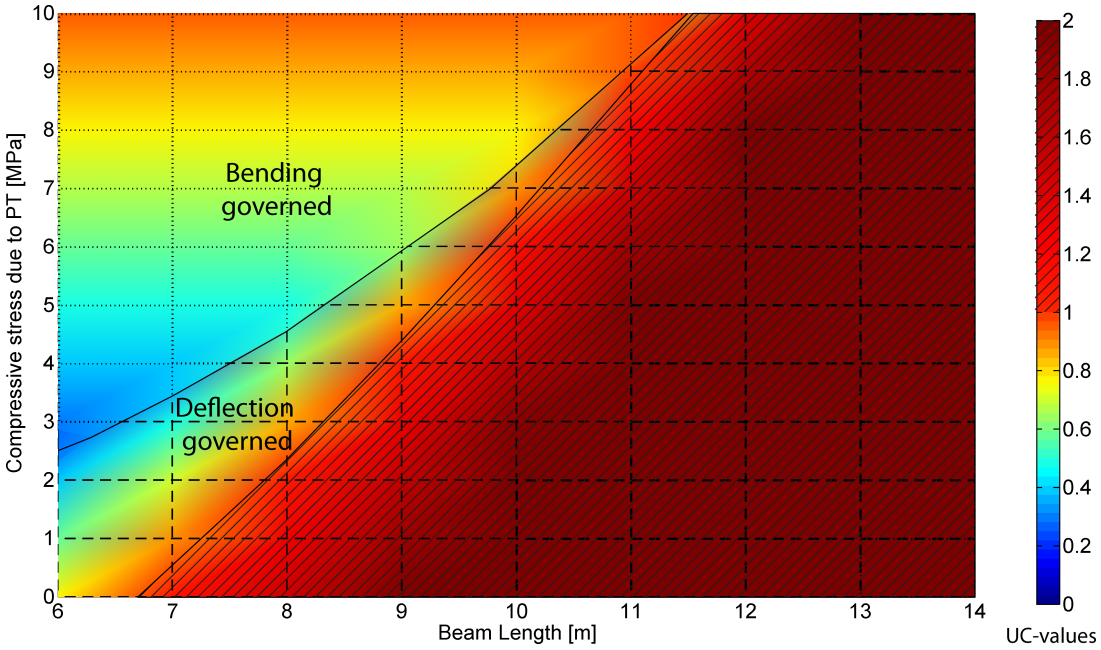

(a) 800 x 400 Beam, simply supported

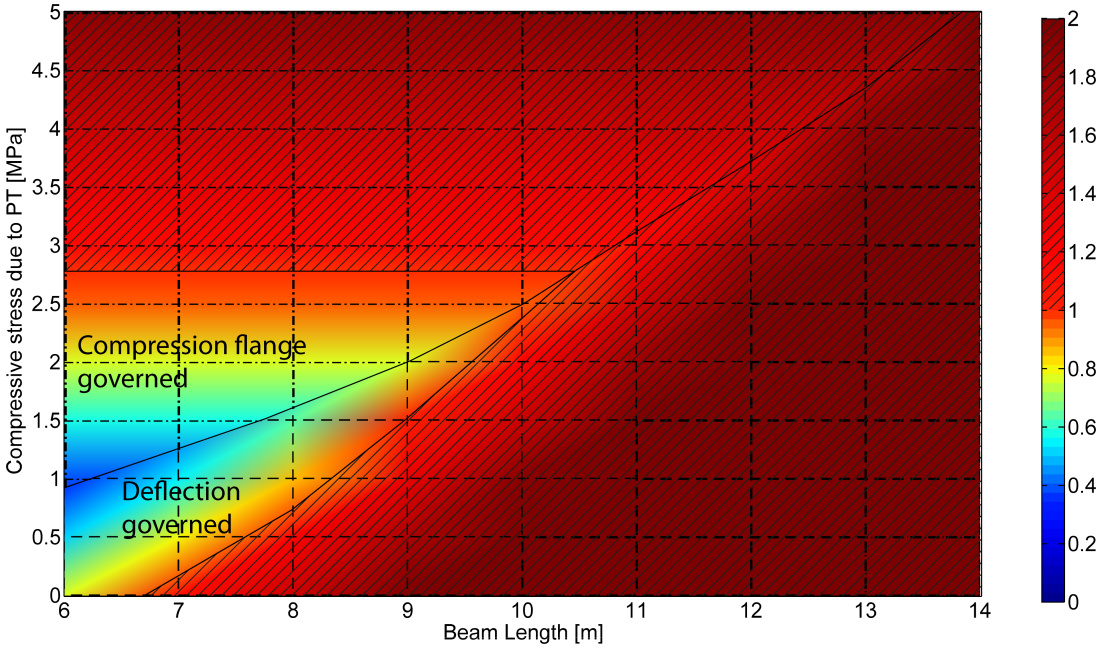

(b) 800 x 400 Beam in PT frame

Figure 9.18: Comparison of parameter study on beam length and post-tensioning stress for beams and frames, showing unity checks (UC) for bending, shear, flange compression strength and deflections

An overview of different span lengths possible for beams and frames under different levels of post-tensioning is shown in Table 9.14. When comparing the maximum possible span length of a section for beams and frames, it can be seen that they are very similar.

Table 9.14: Possible span length (m) for post-tensioned beams and frames with different levels of post-tensioning stress

Dimensions	Type	PT stress (MPa)				
		0.0	1.0	2.5	5.0	8.0
600x300	Beams	<6	<6	<6	6.5	7.0
	Frames	<6	<6	7.0	-	-
800x400	Beams	6.5	7.0	8.0	9.0	10.5
	Frames	6.5	8.0	10.0	-	-
1000x500	Beams	8.5	9.0	10.5	12.0	13.5
	Frames	8.5	10.5	13.0	-	-
1200x600	Beams	10.5	11.5	12.5	>14	>14
	Frames	10.5	13.0	>14	-	-

An optimal design for a given section would be the largest span with a minimum of post-tensioning, or for a given span the smallest section with a minimum required post-tensioning force. This was already analysed for post-tensioned beams in Section 7.6 and the results of the parameter study on frames can be added to this figure. The result is shown in Figure 9.19.

In this figure the design range of beams is shown by black lines and dark grey areas and for frames by the grey lines and light grey areas. A clear downwards shift can be seen, indicating that frames need less post-tensioning stress to achieve the same performance as simply supported beams. But no horizontal shift can be seen, indicating that the same section size is required for a given beam length. Therefore it can be concluded that the section size of post-tensioned beams and frames will be very similar, the only difference is the amount of post-tensioning force that needs to be applied. For the considered geometries the post-tensioning stress in the frame is limited to about 2.5MPa, for different geometries (especially thicker bottom flange) this limit will be different.

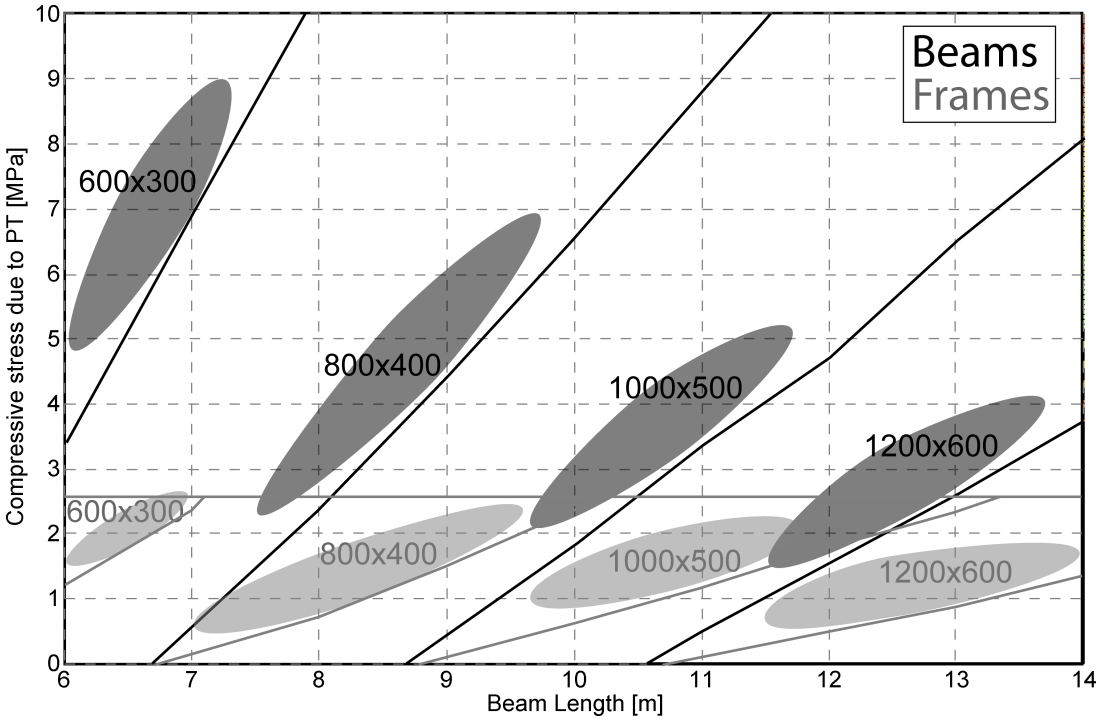

Figure 9.19: Comparison of design range for post-tensioned beams and frames

9.8 Conclusions

- The most detailed analysis model is a framework model of the full frame. Post-tensioning loads are represented by forces at the anchorages and deviators. Joint panel, interface and gap opening are represented by rotational springs at the beam-column interface. Shortening of the frame due to post-tensioning should be allowed for, which makes it complicated to analyse only one storey of a building. A simplification can be to only model vertical components of the post-tensioning, but this means that second order effects are not taken into account. Tendon elongation is not taken into account by the analysis model. It has been shown that this effect varies between 15% and 33% for a range of post-tensioning forces and an average value of 20% is suggested for analysis.

- Comparisons with joint stiffness classifications according to Eurocode 3 (EN 1993-1-8:2005) has shown that the combined stiffness of the joint panel, interface and gap opening falls in the semi-rigid category and should

therefore be included in the analysis model. Achieving fully fixed connections (before decompression) is not practically possible with timber columns, but could be achieved with steel or concrete columns.

- The analysis model has shown that deflections of the external bays are larger than the internal bays due to the lower stiffness of the external connection. It was also shown that even a modest amount of post-tensioning (1MPa compressive stress) can result in a decrease of deflections of 35%. Under short and long-term SLS loading the connection rotations and beam deflections are very similar. Therefore due to creep, long-term deflections will always govern over short-term deflections. For the design which is analysed, the maximum bending moment in the beam is reduced by 70% compared to a simply supported beam. It was shown that for beams with a post-tensioning stress of 5MPa the shear demand is about half of the shear demand of a simply supported beam.

- Inclusion of column rotation in a beam-only model was complicated by the difference in connection moment and column centreline moment. A conversion factor, χ, has been introduced, but this factor was different for every load combination and post-tensioning force making it not practical for the use in design. An average value of 0.64 was found for the geometry of the frame which was analysed, and an equation which can be used for different frame geometries was presented.

- The beam-only model assumed a constant tendon elongation of 20% which led to some differences with the full frame model under ULS loading. It can be concluded that the results of the beam-only model match the full framework model very well with most values being within 10% of the full frame model. A further simplification to ignore the increase in connection moment after decompression, i.e. assume the connection behaviour to be elasto-plastic, resulting in a conservative design with deflections and bending moments in the beam being up to 11% higher than the detailed connection model. Only the connection moment was underestimated.

- An analytical model using closed form equations was presented and made it possible to calculate the bending moment distributions at the connections and at mid-span. The model assumes elasto-plastic connection behaviour. Based on a comparison with the full framework model, it can be concluded that the analytical model results are accurate, except for the connection moment under ULS loading.

- The analytical model was used for a parameter study on beam length and post-tensioning force. In the parameter study the bending strength, shear strength, long-term deflections and the compressive strength of the bottom flange at the connection were taken into account. It was shown that the beam length was always governed by the long-term deflection limit and that for all sections the maximum allowable post-tensioning stress was between 2.5 and 3MPa and was limited by the compression strength of the bottom flange after gap opening. Comparisons with the parameter study for beams have shown that the maximum span for a given section is very similar for beams and frames, but frames need less post-tensioning stress to achieve the same performance as simply supported beams. Comparisons with beams without post-tensioning showed that for the 800x400 section the maximum span is about 11m with a post-tensioning stress of 9MPa for simply supported beams and 10m for frames with a post-tensioning stress of 2.5MPa. This is a 70% increase in span length for beams and a 50% increase for frames compared to beams without post-tensioning.

Part IV

Closure

Chapter X

Conclusions and recommendations

10.1 Conclusions

In this thesis the performance of post-tensioned timber beams and frames under gravity loading was examined using experimental testing, analytical and numerical modelling. The main objective of this work was to develop design procedures for post-tensioned timber buildings under gravity loading. Research was performed in the following four areas: material properties, beams, connections and frames. Conclusions drawn for each of these topics are summarized in the following sections.

10.1.1 Material properties

1. The first objective of experimental testing of LVL material properties was to determine the strength and stiffness of LVL under compression in different orientations, and give guidance on characteristic strength and stiffness values that can be used for timber design. Experimental testing of Radiata Pine LVL (LVL11) has resulted in a greater understanding of the material behaviour under compression. A design compressive strength of 44MPa parallel to grain found by experimental testing compares well with the 45MPa specified by manufacturers. The compressive strength perpendicular to grain of 12MPa is only reached under specific loading conditions. A better approach is to use a compressive strength of 8MPa under uniform compression with small deformations (elastic behaviour) and 10MPa when plastic deformation is acceptable. In the radial direction 7MPa and 9MPa can be used for elastic and plastic strengths, respectively. The plasticity model of van der Put (2008) provides a good prediction of strength increase under different loading configurations due to spreading of perpendicular to

grain stresses. This method can be used for design at serviceability and ultimate limit states for tangential loads, but care should be taken for radial loading as spreading of stresses cannot be fully relied on. Cross-banded LVL hardly experiences any spreading of stresses perpendicular to grain and this should not be allowed for in design. Modulus of elasticity values from experimental testing of LVL11 were 12200MPa, 426MPa and 371MPa in longitudinal, tangential and radial directions, respectively.

2. The second objective was to determine the strength and stiffness of LVL in shear. Experimental testing has resulted in recommended shear strength values for design of 6MPa for loading as a beam, 3.5MPa for loading as a plank and 1MPa for rolling shear. Shear strength of 6MPa, as specified by the manufacturer for loading as a beam (G_{TL}), corresponds well with experimental testing results. Shear moduli have been determined using digital image correlation, values of 856MPa and 901MPa have been found for longitudinal shear moduli and 96MPa for the rolling shear modulus.

3. The third objective was to develop a three-dimensional material model for LVL for the use in FEM and to develop non-linear stress-strain curves for LVL in compression. Modulus of elasticity values from experimental testing of LVL11 were 12200MPa, 426MPa and 371MPa in longitudinal, tangential and radial directions, respectively. The use of digital cameras and digital image correlation has made it possible to extract Poisson's ratios from compression testing. Recommended values are $\nu_{LT} = 0.59$, $\nu_{LR} = 0.48$ and $\nu_{TR} = 0.22$. The use of digital cameras for digital image correlation has proven to give very satisfactory results, although accuracy for two Poisson's ratios was limited due to very small strains along the grain direction whereby variations of up to 70% were found. Values of 856MPa and 901MPa have been found for longitudinal shear moduli and 96MPa for the rolling shear modulus. Non-linear stress-strain curves which can be used for FEM modelling were provided in Table 3.8.

10.1.2 Post-tensioned beams

1. The first objective was to determine effect of post-tensioning on the deflections and failure strength of timber box beams. This was done by full-scale testing four box beams until failure occurred. A mix of failure mechanisms (tension, compression and shear) was designed for and occurred during testing. Beam 1 without post-tensioning failed due to bending/tension failure at the bottom flange. Beam 2 failed due to a shear failure in the web. Beam 3 (draped PT) showed failure in compression resulting in a lowering of the neutral axis and increase in tensile strains until tensile failure occurred. Beam 4 failed in bending/tension at the bottom flange. Therefore it can be concluded that compression and tensile capacity of top and bottom flanges should be checked in the design as well as the shear strength of the webs.

2. The second objective was to assess the short-term deflection behaviour of post-tensioned timber box beams. At the serviceability limit state design limit of span over 300, Beam 1 reached a load of 200kN. For Beams 2, 3 and 4 the loads were 223kN, 267kN and 307kN, respectively. This was an increase in load carrying capacity at SLS design level of 12%, 34% and 54% despite the reduction in section height with respect to Beam 1. This clearly shows the benefit of the precamber, created by post-tensioning.

3. The third objective was to develop numerical and analytical models to describe behaviour of post-tensioned timber beams. Three-dimensional finite element models of the four experimental tested beams were made. The main difficulty in modelling was the contact of tendons with deviator blocks. Also an analytical model for beams was made. This model showed that straight tendons only allow for a 5% increase of mid-span bending moment due to vertical load, whereas draped tendons allow for 22% or 24% increase in bending moment due to vertical load. Second order deflections for straight and draped tendon geometries were about 15% of the total mid-span deflections. Numerical models and analytical models matched the stiffness of post-tensioned beams well with a maximum difference of 12%. Mid-span bending moments based on analytical and FEM models match experimental data very well for Beam 1 (benchmark) and Beam 2 (straight

PT). For Beams 3 and 4 (draped tendons) bending moments were slightly over estimated. Post-tensioning force during loading based on analytical and FEM models follow experimental data very closely. Although under larger displacements both models over predicted the post-tensioning force.

4. The fourth objective was to evaluate the applicability of current timber design code procedures to predict the failure load of post-tensioned timber beams. Predictions of bending moment capacity according to European timber design standard EN 1995:2004 (EC5) (CEN, 2004b) vary between 74% and 81% of the actual capacity. For predictions according to New Zealand timber design standard NZS 3603:1993 (Standards New Zealand, 1993) the variation is between 66% and 87%. This difference between predictions based on NZS3603 and EC5 is mainly caused by the limited tensile capacity of the bottom flange, which is taken into account in the EC5 design but not in the NZS3603 design. Ignoring the tensile capacity of the bottom flange for no (or low levels of) post-tensioning can lead to an unconservative design. Therefore it is recommended to use the design equations given by EC5.

5. The fifth objective was to perform a parameter study on the design of post-tensioned timber beams to identify critical design parameters. The parameter study showed that deflections are most sensitive to changes in beam length and post-tensioning force, compared to bending and shear. Comparing results of the parameter study for straight and draped tendons, it can be seen that the reduction in shear is significant for beams with draped tendons. Bending checks are very similar and deflection checks are about 10% lower for beams with draped tendons. For all considered geometries in the parameter study the optimal design (largest span with a minimum of post-tensioning) is governed by long-term deflections. It was shown that post-tensioning increases the possible span length by about 3m, which ranges between 30% to 67% of the span length without post-tensioning. The ratio of span length over section height (L/h) is on average 8 for box beams without post-tensioning and 12 for box beams with post-tensioning.

6. The final objective was to propose a simplified design for post-tensioned timber beams. It was found that balancing the long-term deflections with a deflection limit of span over 300 for the precamber was found to give a good estimation for required section size. This was used for a quick design method which consists of four steps. Firstly the deflection limit under long-term load needs to be calculated. Secondly the required moment of inertia needs to be calculated. Then a beam section can be found using a design table with possible section sizes. Finally the post-tensioning force can be estimated using equations for straight and draped post-tensioning profiles.

10.1.3 Post-tensioned beam-column connections

1. The first objective was to test the stiffness of post-tensioned timber beam-column connections. Tested connections, with full post-tensioning force of 440kN, had an initial stiffness ranging between 30 - 60kNm/mrad. Connection stiffness after two cycles to ULS loading was very similar to the stiffness before ULS loading, even for tests without any column reinforcement.

2. The second objective was to evaluate the effectiveness of several different column reinforcement methods to reduce plastic deformations and the effect of plastic deformations on the connection stiffness. Experimental testing showed that timber reinforcement in the column (cross-banded LVL or rotated layers) was an effective way to minimize permanent connection rotations. The reinforcement allowed for higher stresses in the column while the material remained linear elastic. Screw reinforcement (long fully-threaded screws at close spacing) in the column compression zone was also effective in increasing the initial elastic stiffness and minimizing permanent rotations. Combining timber reinforcement with screw reinforcement did not improve the stiffness of the connections.

3. The third objective was to determine the design implications of a semi-rigid connection on the moment distribution in a frame. It was found that ignoring the initial connection stiffness and assuming it fully fixed resulted in a conservative design of the connection, but it leads to an unconservative

design for the mid-span bending moment and deflections of the beam. As a first approximation the connection moment due to the connection stiffness is about 2/3rd of the moment of a beam with fully fixed ends.

4. The fourth objective was to analyse the deformation components of post-tensioned timber connections and develop and validate equations to predict the stiffness of post-tensioned timber beam-column connections. Frame deformation components are beam, joint and column deformation. An analytical expression for column rotational stiffness based on structural mechanics has been presented, but this could not be validated with experimental results. The joint deformation is split into joint panel shear deformation, interface compression deformation and gap opening. A theoretical derivation of joint panel shear deformation was presented. Interface compression deformation has been analysed using a multi-spring model. This model included the effects of stress spreading and also column reinforcement could be taken into account. A design procedure for gap opening in post-tensioned gravity frames was derived. This procedure was based on the MBA (Pampanin et al., 2001), as presented for concrete seismic frames. As shear deformation is significant for timber frames, this was included in the new design procedure. The design procedure has been partly verified with experimental testing results, but further validation is necessary.

5. The final objective was to develop design charts for easy estimation of connection stiffness. Design charts for quick initial estimation of rotational stiffness of column, joint panel and interface were presented. For a quick design it was suggested to use an elasto-plastic model (ignoring tendon elongation effects) to take gap opening into account as this eliminates the need of any gap opening calculation. This design assumption will lead to a conservative design for beam deflections and bending moments.

10.1.4 Post-tensioned frames

1. The first objective was to evaluate connection behaviour of internal and external connections in post-tensioned timber gravity frames. It was found that for internal connections the contributions of column rotation and joint panel deformation were negligible, whereas for external connections a clear contribution of these two components was visible. Due to stiffness differences internal connections reached decompression earlier than external connections. Tendon force increased on average 11% for decompression of internal connections and 24% for external connections. The average joint panel shear stiffness was 26kNm/mrad, which was lower than the 31kNm/mrad which was found for the one-bay frame test. For testing with 200kN and 300kN post-tensioning forces the initial interface compression stiffness was approximately 17kNm/mrad for two-bay frame testing and 31kNm/mrad for one-bay frame testing.

2. The second objective was to use Digital Image Correlation (DIC) techniques to verify measurement of deformation components and to acquire full displacement fields. DIC was successfully used to track global frame displacements. Also connection deformation components could be made clearly visible from series of images of the connections. Validation of measurements using DIC techniques showed that all four deformation components were measured accurately.

3. The third objective was to develop a modelling approach for post-tensioned timber frames. The most detailed analysis model is a framework model of the full frame. Post-tensioning loads are represented by forces at the anchorages and deviators. Joint panel, interface and gap opening are represented by rotational springs at the beam-column interface. Shortening of the frame due to post-tensioning should be allowed for, which makes it difficult to realistically analyse only one storey of a building. A simplified beam-only model was developed but inclusion of column rotation in this model needs to take into account the difference in connection moment and column centreline moment.

4. The fourth objective was to evaluate the effect of tendon elongation on the design of post-tensioned timber frames. Using the detailed frame model it has been shown that this effect varies between 15% and 33% for a range of post-tensioning forces and an average value of 20% is suggested for analysis.

5. The fifth objective was to evaluate the effect of different connection models on bending moments and deflections of post-tensioned timber frames. The beam-only model matched the full framework model very well with most values being within 10% of the full frame model. A further simplification was to ignore the increase in connection moment after decompression, i.e. assume the connection behaviour to be elasto-plastic, resulted in a conservative design with deflections and bending moments in the beam being up to 11% higher than the detailed connection model. Only the connection moment was underestimated.

6. The sixth objective was to develop an analytical model for analysis of bending moments and deflections in post-tensioned timber frames and use this to perform a parameter study on the design of post-tensioned timber beams to identify critical design parameters. An analytical model using closed form equations was presented and made it possible to calculate the bending moment distribution at the connections and mid-span. The model assumes elasto-plastic connection behaviour. Based on a comparison with the full framework model it can be concluded that the analytical model results are accurate, except for the connection moment under ULS loading. In the parameter study the bending strength, shear strength, long-term deflections and the compressive strength of the bottom flange at the connection were taken into account. It was shown that the beam length was always governed by the long-term deflection limit and that for the chosen sections the maximum allowable post-tensioning stress was between 2.5 and 3MPa. This was limited by the compression strength of the bottom flange (of 90mm thickness) after gap opening. A thicker bottom flange will allow for higher post-tensioning forces, but reduces the eccentricity of the tendons.

7. The final objective was to compare the performance of simply supported post-tensioned beams with post-tensioned timber frames. The comparison has shown that the maximum span for a given section is very similar for beams and frames, but frames need less post-tensioning stress to achieve the same performance as simply supported beams. Comparison with beams without post-tensioning showed that for the 800x400 section the maximum span is about 11m with a post-tensioning stress of 9MPa for simply supported beams and 10m for frames with a post-tensioning stress of 2.5MPa. This is a 70% increase in span length for beams and an 50% increase for frames compared to beams without post-tensioning.

10.2 Recommendations for further research

Recommendations for further research are listed below. A differentiation has been made between materials, connections and beams and frames.

Materials

- Experimental testing on the compressive strength and stiffness of LVL has been performed, but that work was limited to one batch of LVL from one manufacturer. Timber manufacturers should perform similar testing on larger sample sizes in order to supply design characteristic values. The ratio of modulus of elasticity over shear modulus (E/G) is often taken as 20. For LVL a value of 16 seems more suitable, but further research on these material properties is needed. Better measurements are needed to calculate the Poisson's ratios in LVL with higher accuracy. One option would be to use higher resolution cameras.
- The effects of stress spreading on the strength of timber (and LVL) in compression perpendicular to grain is relatively well understood. Also the effect of screw reinforcement on the increase in strength is known and published by screw manufacturers. But little is known about the perpendicular to grain stiffness of timber, timber with screw reinforcement and cross-banded LVL. An initial testing campaign (Watson et al., 2013) has resulted in an empirical design equation and design chart, but further research is needed in this area. Furthermore, only a couple of methods to increase column strength and stiffness perpendicular to grain were tested and different methods should be explored and tested.
- All work presented in this thesis is based on LVL11. Other timber produces, like glulam could also be used. This is currently being used for post-tensioned seismic frames (Smith et al., 2012), but extension to gravity frames is also possible. Also hybrid constructions, with concrete or steel columns, can be a good method to improve the beam-column connection performance and reduce long-term post-tensioning losses.

Connections

- The interaction of beam-column connection rotation components should be investigated further as the summation of the individual rotation components over predicted the total rotations by about 26%. Analytical equations for joint panel shear deformation can be further developed to better match experimental data and more experimental data is required to further validate the analytical models. Analysis of joint panel shear deformation and interface compression rotation was limited up to the decompression point. Further analysis for the non-linear behaviour after decompression can be performed. This further development can include the effect of stress spreading into the column for column and joint panel deformation.
- A MMBA for gravity frames has been derived, but further experimental testing should be performed to validate this design procedure. This experimental testing could be performed using a timber beam and concrete columns to minimize other rotational components. Previous experimental testing of post-tensioned timber connections under seismic load should be compared with predictions based on the newly derived MMBA which includes shear deformation.

Beams and frames

- The design of post-tensioned timber box beams is governed by long-term deflections. Therefore further research into the creep behaviour and post-tensioning losses is needed to accurately predict long-term deflections. And although not reported in this thesis, vibration testing of post-tensioned timber beams has shown a significant reduction in the maximum amplitude of vibrations. This could be an additional benefit of post-tensioning in floor beams which is worth exploring for long-span floors.
- Post-tensioning force is over-predicted by analytical design methods, even though frame shortening is taken into account. This could be caused by anchorage set. Another reduction factor on tendon elongation could be added to the models to account for this, but further research in this area is needed.

- Further numerical modelling of post-tensioned beams should be performed. These models can focus on different cross-sections and can include the developed non-linear material behaviour. The models can further be expanded with failure models for timber in order to predict failure loads.
- Analysis of internal stress distribution during stressing of post-tensioned frames of multiple levels should be performed. This could give insight into frame shortening effects and effectiveness of post-tensioning a full frame.
- In the parameter study of frames it was shown that the strength of the bottom flange governs the maximum post-tensioning force which can be applied to the frame. For further research, the section of the beam could be optimized by increasing the thickness of the bottom flange only at the connection and not along the full length of the beam. This would allow an increase of post-tensioning force without reducing the eccentricity of the tendons.

10.3 Closure

Post-tensioning of timber frames has the potential to open up new markets for timber construction. For seismic resisting frames there has already been an uptake of the system by the engineering and construction industries. It is hoped that this research will contribute towards an increase in the use of multi-storey timber buildings with large open floor plans suitable for office and commercial applications. The performance of long-span post-tensioned timber frames under gravity loading has been proven in the laboratory and design guidelines have been published to assist engineers in the design of these systems. It is now up to the construction industry to utilize the design information available and explore the new possibilities in timber engineering.

References

Amigo, J. M. M. (2010). ''Feasibility of Multi-storey Pres-Lam Timber Buildings: Design, Construction and Cost.'' Master thesis, Napier University, Napier, New Zealand.

Ardalany, M., Deam, B., Fragiacomo, M., and Crews, K. (2010). ''Tension Perpendicular to Grain Strength of Wood, Laminated Veneer Lumber (LVL), and Cross-Banded LVL (LVL-C).'' *21st Australian Conference on the Mechanics of Structures and Materials*, Melbourne, Australia.

Arnold, D. (2004). ''Development and experimental testing of a seismic damage avoidance designed beam to column connection utilising draped unbonded post-tensioning.'' Master thesis, University of Canterbury, Christchurch, New Zealand.

ASTM (2009). ''D143-09 Standard Test Methods for Small Clear Specimens of Timber.'' ASTM International, West Conshohocken, PA, USA.

ASTM (2010). ''E132-04 Standard Test Method for Poisson's Ratio at Room Temperature.'' ASTM International, West Conshohocken, PA, USA.

Ayd n, I., Çolak, S., Çolako lu, G., and Salih, E. (2004). ''A comparative study on some physical and mechanical properties of Laminated Veneer Lumber (LVL) produced from Beech (Fagus orientalis Lipsky) and Eucalyptus (Eucalyptus camaldulensis Dehn.) veneers.'' *European Journal of Wood and Wood Products*, 62(3), 218--220.

Banks, W. (1999). ''Multi-storey timber construction - A feasibility study.'' *New Zealand Timber Design Journal*, 8(2), 10.

BBR VT International Ltd (2010). ''BBR VT CONA CMX - Strand Post-tensioning Systems.'' *Report no.*, BBR VT International Ltd, Schwerzenbach, Switzerland.

Bejtka, I. and Blass, H. J. (2002). ''Joints with inclined screws.'' *CIB-W18*, number 35-7-4, Kyoto, Japan.

Bejtka, I. and Blass, H. J. (2006). ''Self-tapping screws as reinforcement in beam supports.'' *CIB-W18*, number 39-7-2, Florence, Italy.

Blass, H. J. and Görlacher, R. (2004). ''Compression perpendicular to the grain.'' *World Conference on Timber Engineering*, Lahti, Finland.

Bodig, J. and Goodman, J. R. (1973). ''Prediction of elastic parameters for wood.'' *Wood Science*, 5(4), 249--264.

Bodig, J. and Jayne, B. (1982). *Mechanics of Wood and Wood Composits*. Van Nostrand Reinhold Company, New York, USA.

Bouma, A. (2000). *Mechanica van constructies - Elasto-statica van slanke structuren*. Delft University Press, Delft, the Netherlands, third edition.

Brandner, R., Freytag, B., and Schickhofer, G. (2008). ''Determination of shear modulus by means of standardized four-point bending tests.'' *CIB-W18*, number 41-21-1, St. Andrews, Canada.

BRANZ (2007). ''Potential wood use in nz commercial buildings.'' *Report no.*, BRANZ.

Buchanan, A. (2007a). ''Energy and CO_2 Advantages of Wood for Sustainable Buildings.'' *Institute of Professional Engineers Convention*, Auckland, New Zealand.

Buchanan, A. (2007b). *Timber Design Guide*. New Zealand Timber Industry Federation, Wellington, New Zealand, 3rd edition.

Buchanan, A. and Fairweather, R. (1993). ''Seismic design of glulam structures.'' *Bulletin of the New Zealand National Society for Earthquake Engineering*, 26(4), 415--436.

Buchanan, A., John, S., and Love, S. (2012). ''LCA and Carbon Footprint of Multi-storey Timber Buildings Compared with Steel and Concrete Buildings.'' *World Conference on Timber Engineering*, Auckland, New Zealand.

Buchanan, A., Palermo, A., Carradine, D., and Pampanin, S. (2011). ''Post-tensioned timber frame buildings.'' *The Structural Engineer*, 89(17).

Buchanan, A. H., Pampanin, S., Newcombe, M. P., and Palermo, A. (2009). ''Non-conventional multi-storey timber buildings using post-tensioning.'' *11th International Conference on Non-conventional Materials and Technologies*, Bath, UK.

Bucur, V. (2006). *Acoustics of Wood*. Springer Series in Wood Science. Springer Berlin Heidelberg, 2nd edition.

Burdurlu, E., Kilic, M., Ilce, A. C., and Uzunkavak, O. (2007). ''The effects of ply organization and loading direction on bending strength and modulus of elasticity in laminated veneer lumber (LVL) obtained from beech (Fagus orientalis L.) and lombardy poplar (Populus nigra L.).'' *Construction and Building Materials*, 21(8), 1720--1725.

Carradine, D., Newcombe, M., and Buchanan, A. (2010). ''Screwed corbel connections in laminated veneer lumber.'' *World Conference on Timber Engineering*, Riva del Garda, Italy.

Carradine, D. M., Newcombe, M. P., and Buchanan, A. H. (2009). ''Using screws for structural applications in laminated veneer lumber.'' *CIB-W18*, number 42-7-7, Dubendorf, Switerland.

Carter Holt Harvey (2008). ''Engineering Bulletin No. 1 - Strength Limit States Design Capacity Tables for CHH LVL sections.'' *Report no.*, CHH Woodproducts, Auckland, New Zealand.

Cattanach, A. and Davies, M. (2013). ''College of Creative Arts Building, Massey University, Wellington.'' *New Zealand Timber Design Journal*, 21(1), 13--21.

Cattanach, A. and Pampanin, S. (2008). ''21st century precast: the detailing and manufacture of NZ's first multi-storey PRESSS-Building.'' *New Zealand Concrete Industry Conference*, Rotorua, New Zealand.

CEN (1991). ''EN 26891:1991 Timber structures - Joints made with mechanical fasteners.'' CEN, Brussels, Belgium.

CEN (2001). ''EN 12512:2001 Timber structures - Test methods - Cyclic testing of joints made with mechanical fasteners.'' CEN, Brussels, Belgium.

CEN (2004a). ''EN 14374:2004 Timber structures - Structural laminated veneer lumber - Requirements.'' CEN, Brussels, Belgium.

CEN (2004b). ''EN 1995-1-1:2004 Eurocode 5: Design of timber structures - Part 1-1: General - Common rules and rules for buildings +AC (2006) +A1 (2008).'' CEN, Brussels, Belgium.

CEN (2005). ''EN 1993-1-8:2005 Eurocode 3: Design of steel structures - Part 1-8: Design of joints.'' CEN, Brussels, Belgium.

CEN (2006). ''EN 14358:2006 Timber structures - Calculation of characteristic 5-percentile values and acceptance criteria for a sample.'' CEN, Brussels, Belgium.

CEN (2010). ''EN 408:2010 Timber structures - Structural timber and glue laminated timber - Determination of characteristic values of mechanical properties and density.'' CEN, Brussels, Belgium.

Christopoulos, C., Filiatrault, A., Uang, C.-M., and Folz, B. (2002). ''Posttensioned Energy Dissipating Connections for Moment-Resisting Steel Frames.'' *Journal of Structural Engineering*, 128(9), 10.

Cowper, G. (1966). ''The Shear Coefficient in Timoshenko's Beam Theory.'' *Journal of Applied Mechanics*, 33, 335--340.

Crews, K. (2001). ''Development and Application of Stress Laminated Timber Bridge Decks in Australia.'' *New Zealand Timber Design Journal*, 10(2), 10.

Crocetti, R. and Kliger, R. (2010). ''Anchorage systems to reduce the loss of pre-stress in stress-laminated timber bridges.'' *International Conference on Timber Bridges*, Lillehammer, Norway.

Cursiel, M., Newcombe, M., Pampanin, S., Buchanan, A., and Palermo, A. (2012). ''The Effect of Joint Flexibility on the Seismic Response of Post-tensioned LVL Frames.'' *European Conference on Earthquake Engineering*, Ohrid, Macedonia.

Curtain, B., Dekker, D., Chung, S., and Palermo, A. (2012). ''Design of carterton event centre: An example of innovative collaboration between architecture and timber engineering.'' *World Conference on Timber Engineering*, Auckland, New Zealand.

Davies, M. and Fragiacomo, M. (2007). ''Long Term Behaviour of Laminated Veneer Lumber Members Prestressed with Unbonded Tendons.'' *New Zealand Timber Design Journal*, 16(3), 8.

Deam, B., M., F., and Gross, L. (2008). ''Experimental Behavior of Prestressed LVL-Concrete Composite Beams.'' *Journal of Structural Engineering*, 134(5), 801--809.

Denzler, J. and Glos, P. (2007). ''Determination of shear strength values according to EN 408.'' *Materials and Structures*, 40, 79--86.

Deutsches Instutut fur Bautechnik (2011). ''Allgemeine bauaufsichtliche zulassung (technical approval).'' *Report No. Z-9.1-519*, SPAX International GmbH & Co. KG, Ennepetal, Germany.

Devereux, C., Holden, T., Buchanan, A., and Pampanin, S. (2011). ''NMIT Arts & Media Building-Damage Mitigation Using Post-tensioned Timber Walls.'' *Ninth Pacific Conference on Earthquake Engineering*, Auckland, New Zealand.

Divos, F., Tanaka, T., Nagao, H., and Kato, H. (1998). ''Determination of shear modulus on construction size timber.'' *Wood Science and Technology*, 32, 393--402.

Dunbar, A., van Beerschoten, W., and Carradine, D. (2011). ''Shear Strength and Modulus Testing of New Zealand Laminated Veneer Lumber.'' Final year project, University of Canterbury, Christchurch, New Zealand.

DYWIDAG (2009). ''Dywidag post-tensioning system using strands.'' *Report No. ETA-09/0068*, Setra, Bagneux Cedex, France.

Englekirk, R. (2002). ''Design-Construction of The Paramount - A 39-Story Precast Prestressed Concrete Apartment building.'' *PCI Journal*, 47(4), 56--71.

FIB (2005a). ''Durability of post-tensioning tendons.'' *Report No. 33*, Federation internationale du beton, Lausanne, Switzerland.

FIB (2005b). ''Post-tensioning in buildings: technical report.'' *Report No. 31*, Federation internationale du beton, Lausanne, Switzerland.

Foliente, G. (1998). ''Design of timber structures subjected to extreme loads.'' *Progress in Structural Engineering and Materials*, 1(3), 236--244.

Forest Products Laboratory, Forest Service, U. (1979). *Wood: Its Structure and Properties*. Pennsylvania State University.

Frangi, A. and Fontana, M. (2010). ''Fire safety of multistorey timber buildings.'' *Structures and Buildings*, 163(4), 213--226.

Franke, S., Franke, B., and Rautenstrauch, K. (2007). ''Strain analysis of wood components by close range photogrammetry.'' *Materials and structures*, 40(1), 37--46.

Franke, S. and Quenneville, P. (2010a). ''Compression strength perpendicular to the grain of New Zealand Radiata Pine lumber.'' *Australian Journal of Structural Engineering*, 12(1), 12.

Franke, S. and Quenneville, P. (2010b). ''The material behaviour of radiata pine under compression.'' *World Conference on Timber Engineering*, Riva del Garda, Italy.

FWPA (2009). ''New Applications of Timber in Non-traditional Market Segments: High Rise Residential and Non-residential (commercial) Buildings.'' *Report No. PNA013-0708*, Forest & Wood Products Australia, Melbourna, Australia.

Galloway, T., Fogstad, C., Dolan, C., and Puckett, J. (1996). ''Initial tests of kevlar prestressed timber beams.'' *Proceeding of the National Conference on Wood Transportation Structures*, Madison, Wisconsin, USA.

Garab, J., Keunecke, D., Hering, S., Szalai, J., and Niemz, P. (2010). ''Measurement of standard and off-axis elastic moduli and Poisson's ratios of spruce and yew wood in the transverse plane.'' *Wood Science Technology*, 44(3), 451--464.

Gaul, A., Jager, S., Omenzetter, P., and Morr (2012). ''Dynamic performance assessment of a multi-storey timber building via long-term seismic monitoring and model updating.'' *New Zealand Society of Earthquake Engineering*, Christchurch, New Zealand.

Gehri, E. (1997). ''Timber in compression perpendicular to the grain.'' *International Conference of IUFRO S 5.02 Timber Engineering*, Copenhagen, Denmark.

Giorgini, S. (2010). ''Service load analysis and design of long span unbonded post-tensioned timber beams.'' Master thesis, Politecnico Di Milano, Milan, Italy.

Goncalves, R., Trinca, A., and Cerri, D. (2011). ''Comparison of Elastic Constants of Wood Determined by Ultrasonic Wave Propagation and Static Compression Testing.'' *Wood and Fiber Science*, 43(1), 64--75.

Görlacher, R. and Kürth, J. (1994). ''Determination of shear modulus.'' *CIB-W18*, number 27-10-1, Sydney, Australia.

Green, M. (2012). ''Tall wood - the case for tall wood buildings.'' *Report no.*, mgb Architetcture + Design, Equilibrium Consulting, LMDG Ltd, BTY Group.

Gunnerson, R., Goodman, J., and Bodig, J. (1973). ''Plate test for determination of elastic parameters of wood.'' *Wood Science*, 5(4), 241--248.

Harris, M. (2012). ''Wood goes high-rise.'' *Engineering & Technology*, 7(9), 43--45.

Hassel, B., Berard, P., Modén, C., and Berglund, L. (2009). ''The single cube apparatus for shear testing – Full-field strain data and finite element analysis of wood in transverse shear.'' *Composites Science and Technology*, 69(7), 877--822.

Hearmon, R. (1948). *Elasticity of Wood and Plywood*. London: His Majesty's Stationery Office, forest products research special report number seven edition.

Hoffmeyer, P., Damkilde, L., and Pedersen, T. N. (2000). ''Structural timber and glulam in compression perpendicular to grain.'' *European Journal of Wood and Wood Products*, 58(1), 73--80.

Holmes, M., Crews, K., and Ding, G. (2011). ''The influence building codes and fire regulations have on multi-storey timber construction in Australia.'' *World Sustainable Building Conference*, Helsinki, Finland.

Holmes, M., Crews, K., and Ding, G. (2012). ''Supply chain management strategies for multistorey timber construction in Australia and New Zealand.'' *World Conference on Timber Engineering*, Auckland, New Zealand.

Iqbal, A. (2010). ''Seismic response and design of subassemblies for multi-storey prestressed timber buildings.'' PhD Thesis, University of Canterbury, Christchurch, New Zealand.

Iqbal, A., Pampanin, S., and Buchanan, A. (2010a). ''Seismic response of full-scale prestressed timber beam-column joint.'' *World Conference on Timber Engineering*, Riva del Garda, Italy.

Iqbal, A., Pampanin, S., and Buchanan, A. H. (2010b). ''Seismic performance of prestressed timber beam-column sub-assemblies.'' *New Zealand Society for Eearthquake Engineering Conference*, Wellington, New Zealand.

Janowiak, J., Hindman, D., and Manbeck, H. (2001). ''Orthotropic Behavior of Lumber Composite Materials.'' *Wood and Fiber Science*, 33(4), 580--594.

John, S. and Buchanan, A. (2012). ''Cost and Construction Time for a 3-storey Post-tensioned Timber Building Compared with Concrete and Steel Buildings.'' *World Conference on Earthquake Engineering*, Lisbon, Portugal.

John, S., Mulligan, K., Perez, N., Love, S., and Page, I. (2011). ''Cost, time and environmental impacts of the construction of the new nmit arts and media building.'' *Research report 2011-01*, University of Canterbury, Christchurch, New Zealand.

Kam, W. and Pampanin, S. (2011). ''The seismic performance of RC buildings in the 22 February 2011 Christchurch earthquake.'' *Structural Concrete*, 12(4), 223--233.

Kolb, J. (2008). *Systems in timber engineering: loadbearing structures and component layers*. Birkhauser, Basel.

Korin, U. (1990). ''Timber in compression perpendicular to grain.'' *CIB-W18*, number 23-6-1, Lisbon, Portugal.

Lago, B. A. D. and Dibenedetto, C. (2009). ''Use of longitudinal unbonded post-tensioning in multi-storey timber buildings.'' Master thesis, Technical University of Milan (Politechnico di Milano), Milan, Italy.

Latham, D., Reay, A., and Pampanin, S. (2013). ''Kilmore Street Medical Centre: Application of an Advanced Flag-Shape Steel Rocking System.'' *New Zealand Society of Earthquake Engineering Conference*, Wellington, New Zealand.

Lehmann, S. (2012). ''Sustainable construction for urban infill development using engineered massive wood panel systems.'' *Sustainability*, 4(10), 2707--2741.

Leijten, A. J. M. and Jorissen, A. J. M. (2010). ''Global test standards and code design rules for compressive strength perpendicular to grain.'' *World Conference on Timber Engineering*, Riva del Garda, Italy.

Leijten, A. J. M., Jorissen, A. J. M., and Leijer, B. (2012). ''The local bearing capacity perpendicular to grain of structural timber elements.'' *Construction and Building Materials*, 27(1), 54--59.

Leijten, A. J. M., Larsen, H. J., and Van der Put, T. (2010). ''Structural design for compression strength perpendicular to the grain of timber beams.'' *Construction and Building Materials*, 24(3), 252--257.

Leslie, B. (2012). ''The development and validation of a non-tearing floor precast concrete structural system for seismic regios.'' Master thesis, University of Canterbury, Christchurch, New Zealand.

Ling, H., Samarasinghe, S., and Kulasiri, G. (2009). ''Modelling variability in full-field displacement profiles and poisson ratio of wood in compression using stochastic neural networks.'' *Silva Fennica*, 43(5), 871--887.

Luggin, W. and Bergmeister, K. (2001). ''Vorspannung mit karbonfaserverstärkten kunststoffen im konstruktiven holzbau.'' *Bautechnik*, 78(8), 556--570.

Mahapatra, K. and Gustavsson, L. (2008). ''Multi-storey timber buildings: breaking industry path dependency.'' *Building Research & Information*, 36(6), 11.

Mahapatra, K. and Gustavsson, L. (2012). ''Multi-storey wood-frame buildings in Germany, Sweden and the UK.'' *Construction Innovation: Information, Process, Management*, 12(1), 62--85.

Maplesoft (2009). *Maple 13.0*. Waterloo, Ontario, Canada.

Marriott, D., Pampanin, S., Bull, D., and Palermo, A. (2009). ''A Probabilistic Seismic Loss Assessment of Advanced Post-Tensioned Precast Bridge Systems.'' *New Zealand Society for Earthquake Engineering Conference*, Christchurch, New Zealand.

Mesa, A. (2012). ''Development of Advanced Solutions for Seismis Resisting Precast Concrete Frames.'' PhD Thesis, University of Canterbury, Christchurch, New Zealand.

MetsäWood (2009). ''VTT Certificate.'' *Report No. 184/03*, Metsä, Finland.

Moroder, D., Buchanan, A., and Pampanin, S. (2013). ''Preventing seismic damage to floors in post-tensioned timber frame buildings.'' *New Zealand Society of Earthquake Engineering*, Wellington, New Zealand.

Morris, H., Zhu, M., and Wang, M. (2012). ''The long term instrumentation of the NMIT arts building - Expan shear walls.'' *New Zealand Timber Design Journal*, 20(1), 12.

Muir, C., Pampanin, S., and Bull, D. (2012). ''Preliminary observations from biaxial testing of a two-storey, two-by-one bay, reinforced concrete slotted beam superassembly.'' *New Zealand Society of Earthquake Engineering*, Christchurch, New Zealand.

Nelson Pine Industries Limited (2010). ''Nelson Pine LVL11 - NZ.'' *Report No. NPIL/LVL 04*, Nelson Pine Industries Limited, Richmond, Nelson, New Zealand (November).

Nemetschek (2011). *SCIA Engineer*. Munich, Germany. Structural engineering software.

Newcombe, M. (2011). ''Lateral force design of post-tensioned timber frame and wall buildings.'' PhD Thesis, University of Canterbury, Christchurch, New Zealand.

Newcombe, M., Cursiel, M., Pampanin, S., Palermo, A., and Buchanan, A. (2010a). ''Simplified design of post-tensioned timber frames.'' *CIB-W18*, number 43-7-8, Nelson, New Zealand.

Newcombe, M., Pampanin, S., and Buchanan, A. (2010b). ''Design, fabrication and assembly of a two-storey post-tensioned timber building.'' *World Conference on Timber Engineering*, Riva del Garda, Italy, 9.

Newcombe, M. P. (2008). ''Seismic design of multistorey post-tensioned timber buildings.'' Master thesis, University of Pavia, Pavia, Italy.

Newcombe, M. P., Pampanin, S., Buchanan, A., and Palermo, A. (2008). ''Section Analysis and Cyclic Behavior of Post-Tensioned Jointed Ductile Connections for Multi-Storey Timber Buildings.'' *Journal of Earthquake Engineering*, 12(S1), 83--110.

Newcombe, M. P., Pampanin, S., and Buchanan, A. H. (2010c). ''Global Response of a Two Storey Pres-Lam Timber Building.'' *New Zealand Society of Earthquake Engineering Conference*, Wellington, New Zealand, 8.

Niemz, P. and Caduff, D. (2008). ''Untersuchungen zur bestimmung der poissonschen konstanten an fichtenholz.'' *Holz als Roh-und Werkstoff*, 66(1), 1--4.

O'Neill, J., Abu, A., Carradine, D., Moss, P., and Buchan (2012). ''Modelling prefabricated timber floors in fire.'' *World Conference on Timber Engineering*, Auckland, New Zealand.

Palermo, A. (2004). ''Use of controlled rocking in the seismic design of bridges.'' PhD Thesis, Technical Institute of Milan, Milan, Italy.

Palermo, A., Giorgini, S., Pampanin, S., and Buchanan, A. (2011). ''Potential of Longitudinal Post-Tensioning for Short-to-Medium Span Timber Bridges.'' *Structural Engineering International*, 21(3), 349--355.

Palermo, A., Pampanin, S., and Buchanan, A. (2006). ''Experimental investigations on LVL seismic resistant wall and frame subassemblies.'' *First European Conference in Seismic Engineering and Seismology*, Geneva, Switzerland, 10.

Palermo, A., Pampanin, S., Buchanan, A. H., and Newcombe, M. P. (2005). ''Seismic design of multi-storey buildings using Laminated Veneer Lumber (LVL).'' *New Zealand Society for Earthquake Engineering Conference*, Taupo, New Zealand.

Palermo, A., Pampanin, S., Carradine, D., Buchanan, A., Lago, B., Dibenedetto, C., Giorgini, S., and Ronca, P. (2010). ''Enhanced performance of longitudinally post-tensioned long-span LVL beams.'' *World Conference on Timber Engineering*, Riva del Garda, Italy.

Pampanin, S., Kam, W., Haverland, G., and Gardiner, S. (2011). ''Seismic Performance of a Post-Tensioned Precast Concrete Building (PRESSS Technology) during the 22nd Feb 2011 Christchurch Earthquake: Reality Check meets Community Expectations.'' *New Zealand Concrete Industry Conference*, Rotorua, New Zealand.

Pampanin, S., Pagani, C., and Zambelli, S. (2004). ''Cable-stayed and suspended post-tensioned solutions for precast concrete frames: the Brooklyn system.'' *New Zealand Concrete Society Conference*, Queenstown, New Zealand.

Pampanin, S., Priestley, M., and Sritharan, S. (2001). ''Analytical Modelling of the Seismic Behaviour of Precast Concrete Frames Designed with Ductile Connections.'' *Journal of Earthquake Engineering*, 5(03), 329--367.

Pan, B., Qian, K., Xie, H., and Asundi, A. (2009). ''Two-dimensional digital image correlation for in-plane displacement and strain measurement: a review.'' *Measurement science and technology*, 20(6), 17.

Pasternak, P. (1954). ''On a new method of analysis of an elastic foundation by means of two foundation constants.'' *Gosudarstvennoe Izdatel'stvo Litearturi po Stroitel'stvu i Arkhitekture, Moscow, USSR (in Russian).*

Perez, N. (2012). ''Thermal performance of buildings with post-tensioned timber structure compared with concrete and steel alternatives.'' PhD Thesis, University of Canterbury, Christchurch, New Zealand.

Perez, N., Baird, G., and Buchanan, A. (2008). ''The influence of construction materials on the life cycle energy use and carbon dioxide emission of medium sized commercial buildings.'' *World Sustainable Buildings Conference*, Melbourne, Australia.

Priestley, M. J. N., Sritharan, S., Conley, J. R., and Pampanin, S. (1999). ''Preliminary Results and Conclusions from the PRESSS Five-story Precast Concrete Test-Building.'' *PCI journal*, 44(6), 42--67.

Priestley, M. J. N. and Tao, J. R. (1993). ''Seismic response of precast prestressed concrete frames with partially debonded tendons.'' *PCI Journal*, 38(1), 58--69.

Professner, H. and Mathis, C. (2012). ''Lifecycle tower—high-rise buildings in timber.'' *ASCE Structures Congress*, Chicaco, Illinois, United States.

Riedlbauer, A. (1978). ''Vorgespannte holzkonstruktionen.'' PhD Thesis, TU Graz, Graz, Austria.

Ritter, M., Wacker, J., and Duwadi, S. (1995). ''Field performance of stress-laminated timber bridges on low-volume roads.'' *6th international conference on low-volume roads*, Minneapolis, MN, USA, 25--29.

Sakamoto, I., Kawai, N., Okada, H., Yanaguchi, N., Isoda, H., and Yusa, S. (2004). ''A Final Report of a Research and Development project on Timber-based Hybrid Building Structures.'' *World Conference on Timber Engineering*, Lahti, Finland.

Sarti, F. (2011). ''Simplified design methods for post-tensioned timber buildings.'' Master thesis, Technical University of Milan, Milan, Italy.

Sarti, F., Palermo, A., and Pampanin, S. (2012). ''Design charts and simplified procedures for post-tensioned seismic resistant timber walls.'' *World Conference on Timber Engineering*, Auckland, New Zealand.

Shukla, S. R. and Kamdem, D. P. (2008). ''Properties of laminated veneer lumber (LVL) made with low density hardwood species: effect of the pressure duration.'' *European Journal of Wood and Wood Products*, 66(2), 119--127.

Simulia (2010). *Abaqus FEA*. Dassault Systemes Simulia Corp., Velizy-Villacoublay, France.

Sliker, A. (1972). ‘‘Measuring Poisson’s Ratios in Wood.’’ *Experimental Mechanics*, 12(5), 239--242.

Smith, I. and Frangi, A. (2008). ‘‘Overview of Design Issues for Tall Timber Buildings.’’ *Structural Engineering International*, 18(2), 141--147.

Smith, K. (2012). ‘‘Rise of the plyscrapers?.’’ *Construction Research and Innovation*, 3(4), 28--29.

Smith, T. (2008). ‘‘Feasibility of Multi Storey Post Tensioned Timber Buildings: Detailing, Cost and Construction.’’ Master thesis, University of Canterbury, Christchurch, New Zealand.

Smith, T., Ponzo., F., Cesare, A., Auletta, G., Pampanin, S., Carradine, D., Palermo, A., and Nigro, D. (2012). ‘‘Seismic performance of a post-tensioned glue laminated beam to column joint: Experimental and numerical results.’’ *World Conference on Timber Engineering*, Auckland, New Zealand.

SPAX (2012a). ‘‘Design guide - Notes on the design of load-bearing SPAX connections. Ennepetal, Germany.

SPAX (2012b). ‘‘European technical approval eta-12/0114.’’ *Report No. ETA-12/0114*, ETA-Danmark A/S, Denmark.

Spellman, P., Carradine, D., Abu, A., Moss, P., and Buchanan, A. (2012). ‘‘Full-scale fire tests of post-tensioned timber beams.’’ *World Conference on Timber Engineering*, Auckland, New Zealand.

Sretenovic, A., Müller, U., Gindl, W., and Teischinger, A. (2004). ‘‘New shear assay for the simultaneous determination of shear strength and shear modulus in solid wood finite element modeling and experimental results.’’ *Wood and Fiber Science*, 36(3), 302--310.

Standards Australia (2010). ‘‘AS 1720.1-2012 - Timber structures Part 1: Design methods.’’ Standards Australia, Sydney, Australia.

Standards New Zealand (1993). ‘‘NZS 3063:1993 - Timber structures standard.’’ Standards New Zealand, Wellington, New Zealand.

Standards New Zealand (2002a). ‘‘AS/NZS 1170.0:2002 - Structural design actions - Part 0: General Principles.’’ Standards New Zealand, Wellington, New Zealand.

Standards New Zealand (2002b). ‘‘AS/NZS 1170.1:2002 - Structural design actions - Part 1: Permanent, imposed and other actions.’’ Standards New Zealand, Wellington, New Zealand.

Standards New Zealand (2006a). ‘‘AS/NZS 4357.2:2006 Structural laminated veneer lumber (LVL) - Part 2: Determination of structural properties - Test methods.’’ Standards New Zealand, Wellington, New Zealand.

Standards New Zealand (2006b). ‘‘AS/NZS 4357.3:2006 Structural laminated veneer lumber (LVL) - Part 3: Determination of structural properties - Evaluation methods.’’ Standards New Zealand, Wellington, New Zealand.

Standards New Zealand (2006c). ‘‘NZS3101 - Concrete structures standard.’’ Standards New Zealand, Wellington, New Zealand.

Standards New Zealand (2010a). ‘‘AS/NZS 4063.1:2010 Characterization of structural timber - Part 1: Test methods.’’ Standards New Zealand, Wellington, New Zealand.

Standards New Zealand (2010b). ‘‘AS/NZS 4063.2:2010 Characterization of structural timber - Part 2: Determination of characteristic values.’’ Standards New Zealand, Wellington, New Zealand.

Thelandersson, S. and Mårtensson, A. (1997). ‘‘Design principles for timber in compression perpendicular to grain.’’ *CIB-W18*, number 30-20-1, Vancouver, Canada.

Triantafillou, T. and Deskovic, N. (1991). ‘‘Innovative prestressing with frp sheets: Mechanics of short-term behaviour.’’ *Journal of Engineering Mechanics*, 117(7), 1652--1672.

Ukyo, S., Ido, H., Nagao, H., and Kato, H. (2010). ''Simultaneous determination of shear strength and shear modulus in glued-laminated timber using a full-scale shear block specimen.'' *Journal of wood science*, 56(3), 262--266.

U.S. Department of Agriculture Forest Products Laboratory (1955). *Wood Handbook*. U.S. Government Printing Office.

Uysal, B. (2005). ''Bonding strength and dimentional stability of laminated veneer lumbers manufactured by using different adhesives after the steam test.'' *International Journal of adhesion and adhesives*, 25(5), 395--403.

van Beerschoten, W., Carradine, D., and Carr, A. (2013a). ''Development of Constitutive Model for Laminated Veneer Lumber using Digital Image Correlation Technique.'' *Wood Science and Technology*, 14 (in publication).

van Beerschoten, W., Carradine, D., and Palermo, A. (2013b). ''Compressive strength and stiffness of Radiata Pine Laminated Veneer Lumber.'' *European Journal of Wood and Wood Products*, 71(6), 795--804.

van Beerschoten, W., Palermo, A., Carradine, D., and Pampanin, S. (2012). ''Design procedure for long-span post-tensioned timber frames under gravity loading.'' *World Conference on Timber Engineering*, Auckland, New Zealand.

van Beerschoten, W., Palermo, A., Carradine, D., Sarti, F., and Buchanan, A. (2011a). ''Experimental Investigation on the Stiffness of Beam-Column Connections in Post-Tensioned Timber Frames.'' *Structural Engineering World Conference*, Como, Italy, 12.

van Beerschoten, W., Smith, T., Palermo, A., Pampanin, S., and Ponzo, F. (2011b). ''The stiffness of beam to column connections in post-tensioned timber frames.'' *CIB-W18*, number 44-7-7, Alghero, Italy.

van de Kuilen, J., Ceccotti, A., Xia, Z., and He, M. (2011). ''Very tall wooden buildings with cross laminated timber.'' *The Twelfth East Asia-Pacific Conference on Structural Engineering and Construction*, Hong Kong.

van der Put, T. A. C. M. (2008). ''Derivation of the bearing strength perpendicular to the grain of locally loaded timber blocks.'' *European Journal of Wood and Wood Products*, 66(6), 409--417.

Volkersen, O. (1938). ''Die nietkraftverteilung in zugbeanspruchten mit konstanten laschenquerschritten.'' *Luftfahrtforschung*, 15, 41--47.

Wangaard, F. (1950). *The Mechanical Properties of Wood*. John Wiley & Sons, Inc., New York.

Wanninger, F. and Frangi, A. (2013). ''Experimental analysis of a post-tensioned timber connection.'' *RILEM International Symposium on Materials and Joints in Timber Structures - Recent advancement of technology*, Stuttgart, Germany.

Watson, C., van Beerschoten, W., Smith, T., Pampanin, S., and Buchanan, A. (2013). ''Stiffness of Screw-Reinforced LVL in Compression Perpendicular to the Grain.'' *CIB-W18*, number 46-12-4, Vancouver, Canada.

Waugh, A., Wells, M., and Lindegar, M. (2010). ''Tall timber buildings - application of solid timber construction in multi-storey buildings.'' *Proceedings of the International Convention of Society of Wood Science and Technology and United Nations Economic Commission for Europe – Timber Committee*, Geneva, Switzerland.

Wells (2011). ''Stadthaus, london: raising the bar for timber buildings.'' *Proceedings of ICE - Civil Engineering*, 164(3), 122--128.

Wesbeam (2005). ''e-beam - engineered LVL beams.'' *Report no.*, Wesbeam, Perth, Australia.

Wong, R. (2010). ''Construction time and cost of multi-storey post-tensioned timber structures.'' Master thesis, University of Canterbury, Christchurch, New Zealand.

Zink, A., Hanna, R., and Stelmokas, J. (1997). ''Measurement of Poisson's ratios for yellow-poplar.'' *Forest Products Journal*, 47(3), 78--80.

Part V

Appendices

Appendix A

Experimental test design

This Appendix provides more detailed information about the design of the experimental testing specimens. It is split in three parts, namely for beam testing, connection testing and frame testing. The presented designs might not be similar to the design procedures described in the analytical chapters, as experimental testing was performed before the full design procedures were developed.

A.1 Beam design

Four box beams were designed. Beam 1 was a benchmark and did not have post-tensioning. Beam 2 had straight tendons running along the top of the bottom flange of the beam. Beams 3 and 4 both had draped tendons, but were designed to have different failure mechanisms. All beams were made of LVL 11, with characteristic properties as shown in Table A.1. The shear modulus was not specified, but is commonly taken as $E/20$ which gives $G = 550MPa$. The beams were designed to carry a timber-concrete composite (TCC) floor and services resulting in a total dead load of 3kPa. A live load for office buildings of 3kPa was used in the design. The floor span was taken as 6 meters, resulting in an ultimate limit state (ULS) design load of 48.6kN/m and a serviceability limit state (SLS) design load of 30.6 and 25.2kN/m for short-term and long-term loading, respectively. The ULS design load of 48.6kN/m resulted in a mid-span bending moment of 508kNm. This bending moment level was also reached for a four-point bending test with a total vertical load of 330kN.

Section properties of the four box beams are shown in Table A.2 and Figure A.1. Longitudinal sections can be found in Appendix G. Initial post-tensioning (PT) forces and tendon profiles are also shown. Seven tendons (7-wire strands) of 12.7mm diameter were used to apply the post-tensioning force of 910kN. Each

Table A.1: Characteristic values of LVL 11 supplied by manufacturer Nelson Pine Industries Limited (2010)

Property	Symbol	Value	Unit
Modulus of Elasticity	E	11	GPa
Bending strength	f_b	48	MPa
Tension strength	f_t	30	MPa
Compression strength parallel to grain	$f_{c,par}$	45	MPa
Compression strength perpendicular to grain	$f_{c,perp}$	12	MPa
Shear strength	f_s	6	MPa

tendon was stressed up to 130kN (1300MPa), which was 70% of ultimate strength or 85% of yield strength. Properties for the tendons are found in Table A.3. Deviators were placed at 1/3 or the beam length, as is elaborated on in Appendix B.1. Furthermore, design compression and bending capacities, based on NZS3603 (Standards New Zealand, 1993), are given. These values are based on Equations A.1 and A.2, where the strength reduction factor $\phi = 0.9$, load duration factor $k_1 = 0.8$ and size factor $k_{24} = 0.7$ (for $h = 760mm$) or 0.73 (for $h = 610mm$).

$$\phi N_n = \phi \cdot k_1 \cdot A \cdot f_c \tag{A.1}$$

$$\phi M_n = \phi \cdot k_1 \cdot k_{24} \cdot Z \cdot f_b \tag{A.2}$$

Table A.2: Specimen details of tested beams

Beam No.	Height (mm)	Width (mm)	t_{flange} top/bottom (mm)	t_{web} (mm)	Tendon profile	Initial PT force (kN)	ϕN_n (kN)	ϕM_n (kNm)
1	760	426	90 / 90	63	-	-	4852	682
2	610	426	90 / 90	63	straight	910	4240	500
3	610	426	90 / 90	63	draped	910	4240	500
4	610	426	180 / 90	63	draped	910	5115	506

Design of the beams was based on the combined bending and axial load strength (Equation A.3), shear strength (Equation A.4) and short term deflection limit of span over 300. The long-term deflection design check was ignored as

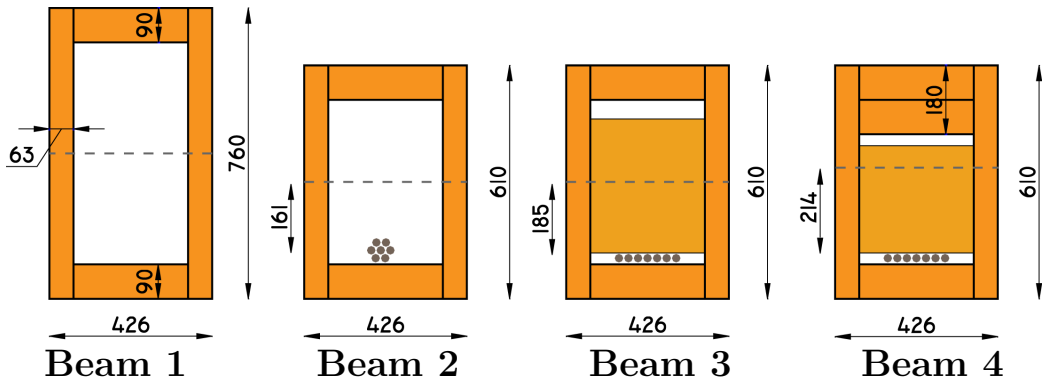

$A = 150 \cdot 10^3 mm^2$	$A = 130 \cdot 10^3 mm^2$	$A = 130 \cdot 10^3 mm^2$	$A = 158 \cdot 10^3 mm^2$
$A_s = 74.4 \cdot 10^3 mm^2$	$A_s = 59.7 \cdot 10^3 mm^2$	$A_s = 59.7 \cdot 10^3 mm^2$	$A_s = 57.2 \cdot 10^3 mm^2$
$Z = 28.2 \cdot 10^6 mm^3$	$Z = 19.9 \cdot 10^6 mm^3$	$Z = 19.9 \cdot 10^6 mm^3$	$Z = 20.2 \cdot 10^6 mm^3$
$I = 10.7 \cdot 10^9 mm^4$	$I = 6.07 \cdot 10^9 mm^4$	$I = 6.07 \cdot 10^9 mm^4$	$I = 6.74 \cdot 10^9 mm^4$

Figure A.1: Section properties of tested beams

Table A.3: Properties of post-tensioning tendons

Property	Symbol	Value	Unit
Diameter	ϕ	12.7	mm
Modulus of elasticity	E_{pt}	200	MPa
Area	A_{pt}	100	mm^2
Yield stress	f_{py}	1520	MPa
Yield strength	$T_{pt,y}$	152	kN
Ultimate stress	f_{pu}	1860	MPa
Ultimate strength	$T_{pt,u}$	186	kN

this was not part of the objective of experimental testing. An overview of design checks is shown in Table A.4. Design checks are the design load divided by design capacity, this value should be smaller than one in order to satisfy SLS and ULS design limits.

$$\frac{N^*}{\phi N_n} + \frac{M^*}{\phi M_n} < 1 \tag{A.3}$$

$$V^* < \phi V_n \tag{A.4}$$

Table A.4: Design checks for all beams

Beam	Type	Design check			
		Bending	Shear	Short-term	Long-term
1	Benchmark	0.75	0.69	0.99	1.63
2	Straight PT	0.99	0.87	0.82	1.31
3	Draped PT	0.99	0.66	0.68	1.06
4	Draped PT (2)	0.88	0.65	0.46	0.70

Design of the deviators for beams with draped tendons is shown in Appendix B.1 and design of the post-tensioning anchorages in Appendix B.2.

A.2 Beam-column connection design

This section describes the prototype building on which testing was based, different possible connection types and the materials used. Also presented are the designs of beams and columns, post-tensioning systems and connection reinforcement.

A.2.1 Prototype building

A hotel building in Napier, Figure A.2, was chosen as a prototype building because of its regular layout. The layout was governed by the parking garage, as is shown in the floor plan in Figure A.3. This 4 storey concrete building was redesigned as a timber building and a feasibility study was performed (Amigo, 2010).

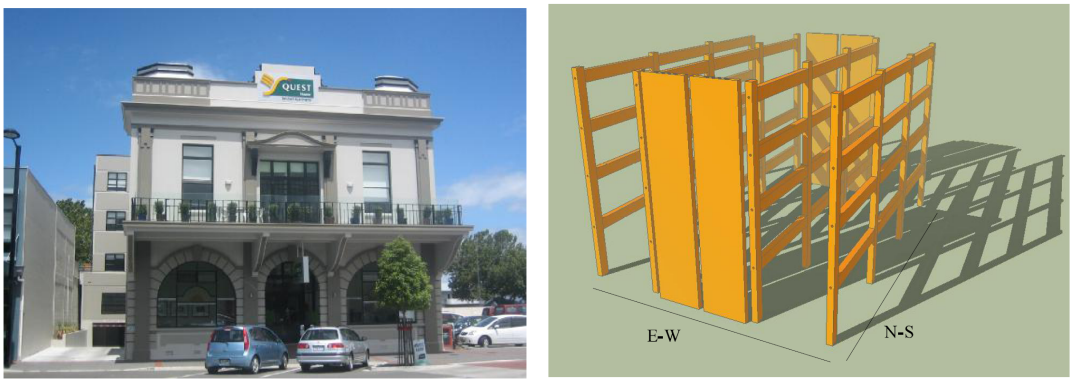

(a) Quest Hotel in Napier (b) Timber redesign of building

Figure A.2: Prototype building (Amigo, 2010) for experimental connection testing

The proposed redesigned floor system was a timber-concrete composite (TCC) floor with 360 x 90mm LVL joists spaced at 750mm centres, a 21mm plywood layer and a 65mm concrete topping. This floor, combined with a 1kPa load for services, gave a dead load of 3kPa. The live load for a typical office building is 3kPa (Standards New Zealand, 2002b). The tributary width of the main beams was 6.1m. Three different load combinations were considered, each with a distributed load of:

1. ULS Design: 1.2G + 1.5Q = 50kN/m.
2. SLS Design (short-term): G + 0.7Q = 31kN/m.
3. SLS Design (long-term): G + 0.4Q = 26kN/m.

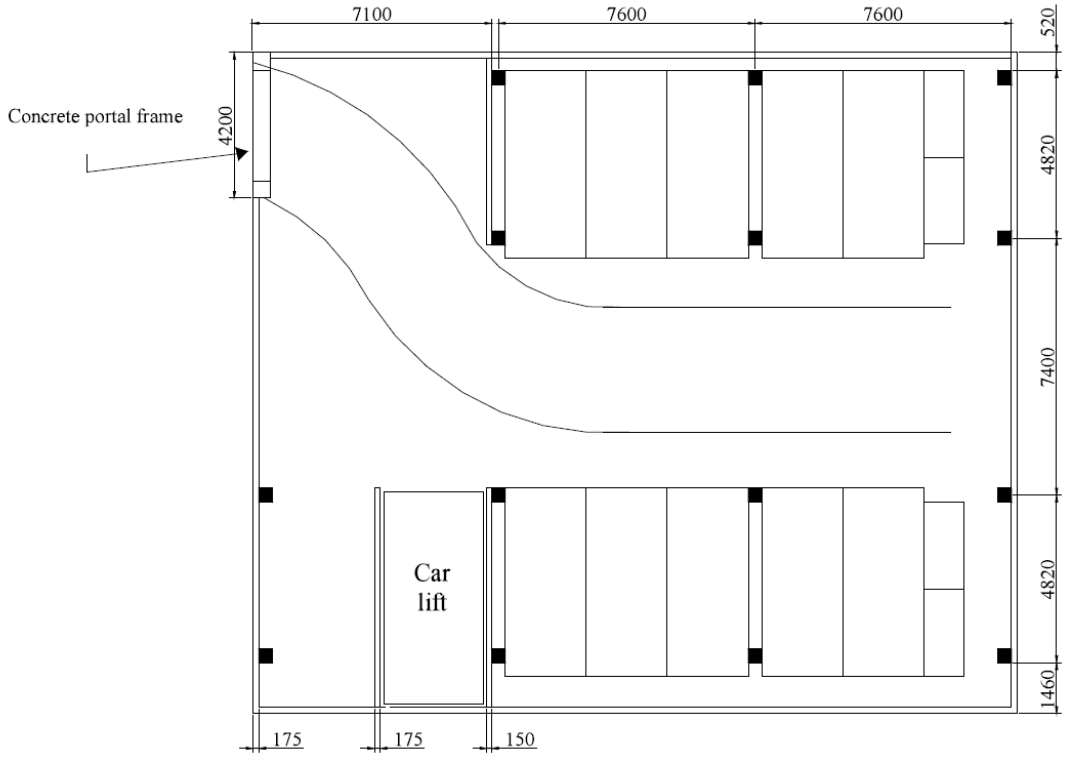

Figure A.3: Floor plan of parking garage beneath Quest hotel building (Amigo, 2010)

A.2.2 Materials

The timber used was LVL11 and cross-banded LVL from Nelson Pine Industries Limited (2010). The characteristic values, supplied by the manufacturer are shown in Table A.5. Two different types of cross-banded LVL were available, 25mm thick sheets with 4 longitudinal and 3 cross-bands and 36mm thick sheets with 8 longitudinal and 2 cross-bands. Each was made up from 3.6mm thick veneers, which had a compressive strength parallel to grain of 28MPa and perpendicular to grain of 6MPa. It should be noted that the 12MPa for compression perpendicular to grain of LVL11 is only reached with significant plastic deformation, the elastic strength is around 8MPa, as was shown in Section 3.3. For cross-banded LVL, although perpendicular to grain strength was increased, bending strength and modulus of elasticity were lower than LVL11.

Table A.5: Characteristic values of LVL 11 and cross-banded LVL supplied by manufacturer Nelson Pine Industries Limited (2010)

Property	Unit	LVL 11	Crossbanded LVL 25mm thick	Crossbanded LVL 36mm thick
E	GPa	11	9	9
f_b	MPa	48	35	35
f_t	MPa	30	22	22
$f_{c,par}$	MPa	45	18.6	23.6
$f_{c,perp}$	MPa	12.0	15.4	10.4
f_s	MPa	6	n/a	n/a

The post-tensioning (PT) tendons were supplied by BBR Contech (BBR VT International Ltd, 2010) and had a 12.7mm diameter, which gave a cross-sectional area of 100mm^2. The ultimate tensile stress of the tendons was 1860MPa, which resulted in an ultimate tensile force of 186kN. The yield strength was 137kN and recommended post-tensioning level was 70% of yield strength, or 106kN per tendon.

A.2.3 Section sizes

Section sizes and section properties for beams and columns are shown in Figure A.4.

Beams The beams were designed as a box section which could easily be manufactured from standard LVL sizes. The preliminary design was based on design tables from Sarti (2011). One bay of the frame (7.6m) was modelled in a framework analysis program. The beam was modelled with rotational springs with a linear stiffness at each end. PT forces were modelled as point loads and did not include tendon elongation effects (van Beerschoten et al., 2012). Eccentricity of the anchorage was neglected as it would mainly influence the column and not the beam. The resulting bending moment diagrams for 4 different load cases, ULS load, SLS load, Dead load only and PT only, are shown in Figure A.5.

From these results it can be seen that the connection moment for the load case of only post-tensioning was almost as large as the ULS connection moment. Therefore, not only the bottom of the connection needed column reinforcement

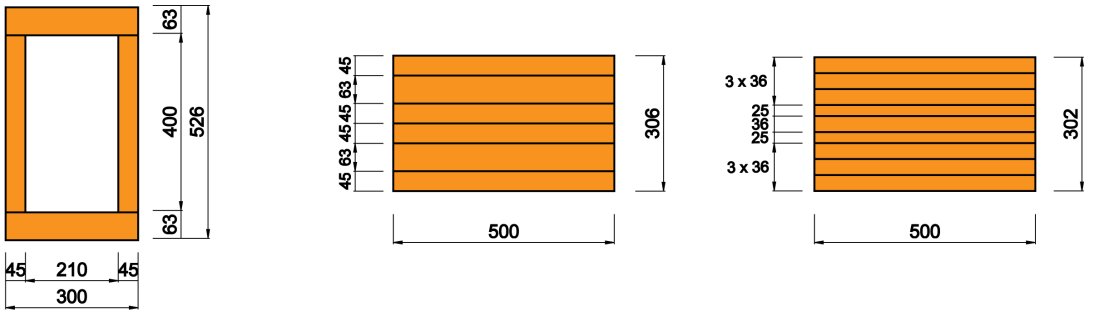

Beam
A = 73800mm^2
A$_s$ = 36700mm^2
Z = 9.58x10^6 mm^3
I = 2.52x10^9 mm^4

Column 1 - LVL11
A = 153000mm^2
A$_s$ = 102000mm^2
Z = 12.7x10^6 mm^3
I = 3.19x10^9 mm^4

Column 2 - CB LVL
A = 151000mm^2
A$_s$ = 100700mm^2
Z = 12.6x10^6 mm^3
I = 3.15x10^9 mm^4

Figure A.4: Cross-sections of beam and columns

against perpendicular to grain stresses, but also the top of the connection needed to be reinforced. Alternatively a dead load could be applied to the beam before stressing, or stressing could happen in stages with application of dead load in between stressing operations. For the experimental testing it was decided to apply some load to the beam to reduce the connection moment under post-tensioning only load.

Columns Two different columns were used for testing, one made from LVL11 and the other from a combination of 25 and 36mm thick cross-banded (CB) LVL. The first column was designed with two different connection interfaces, one with all the grains parallel with the axis of the column and the other with the outer layers (63mm thick) rotated 90 degrees, in order to achieve compression partly parallel to grain. Figure A.4 shows cross-sections of the two columns.

A full frame of the prototype building was modelled in a framework analysis program. The connections were modelled with linear stiffness springs. Different load-combinations were evaluated, and resulting maximum bending moments and normal forces are shown in Figure A.6. The PT forces were not modelled as they would not influence forces in the columns, therefore bending moments in the beams were higher than those seen in Figure A.5.

The compressive axial force was calculated with full dead and live load on

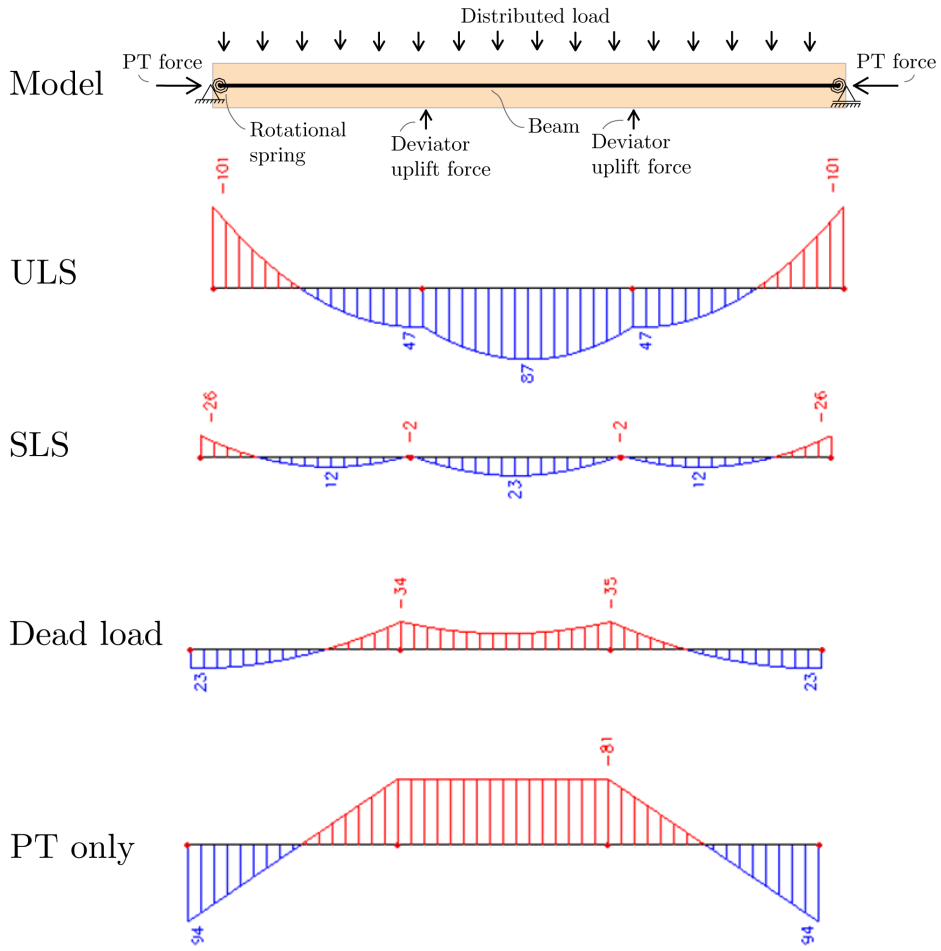

Figure A.5: Bending moments in beam with rotational springs at both ends for different loading scenarios

each floor. No reduction factor ψ (Standards New Zealand, 2002b) was taken into account. The exterior columns had to be designed for a bending moment of $M^* = 84kNm$ and an axial compressive force of $N^* = 676kN$. The interior columns had to be designed for a bending moment of $M^* = 44kNm$ and a compressive force of $N^* = 1366kN$, though that is not presented here as the focus is on exterior beam-column connections. The design equation, based on NZS 3063:1993 (Standards New Zealand, 1993), for the LVL11 column with the outer 45mm layers rotated 90 degrees is shown in Equation A.5. The governing cross-section was at the connection, where bending stresses were highest and the

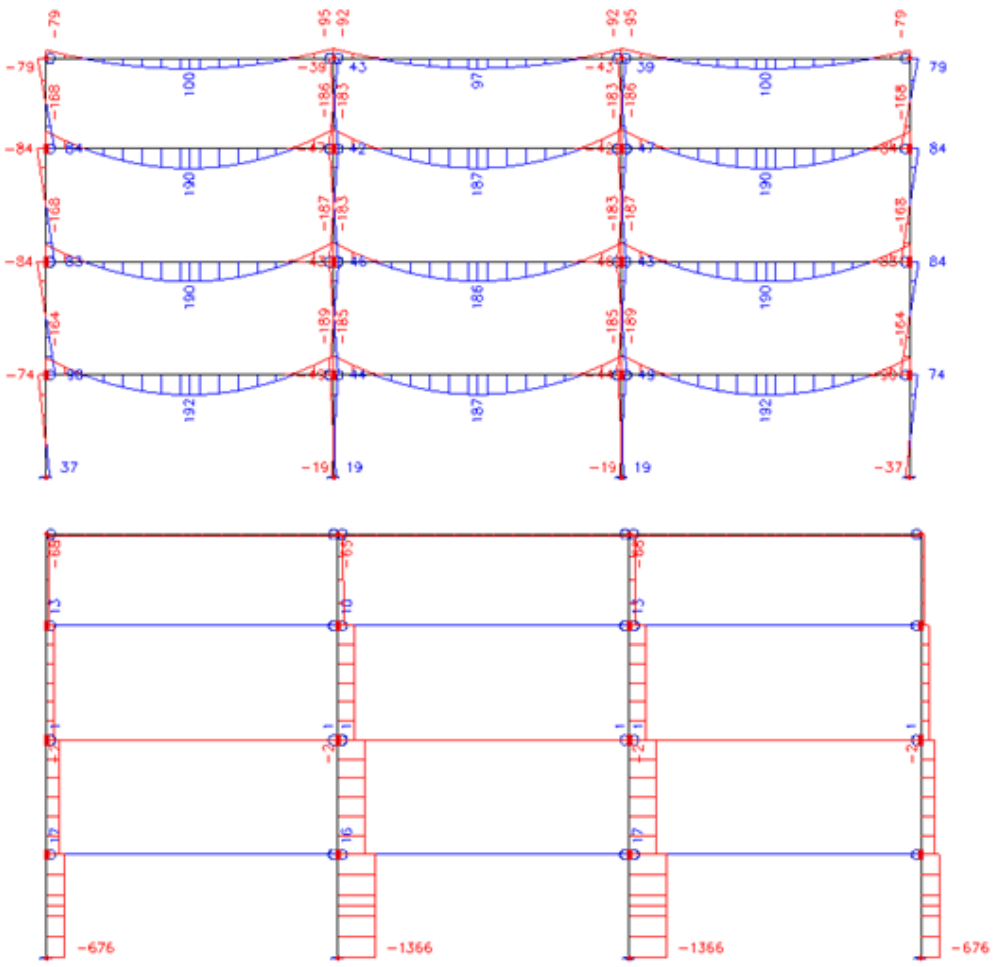

Figure A.6: Results of framework analysis on prototype building, top: bending moments in columns, bottom: compressive forces in columns

hole for post-tensioning cables was located. Furthermore, it was assumed that the rotated outer layers could not transfer any forces.

$$\frac{N^*}{\phi N_n} + \frac{M^*}{\phi M_n} < 1 \rightarrow \frac{676}{0.9 \times 2268} + \frac{84}{0.9 \times 200} = 0.33 + 0.46 = 0.79 < 1 \quad \text{(A.5)}$$

Different configurations of cross-lam layers were possible, based on available thickness of 25mm and 36mm. The best perpendicular to grain performance would be with all 25mm sheets (the highest number of cross veneers), though this would

reduce the parallel to grain strength considerably. A mixture of 36mm and 25mm sheets was therefore chosen, shown in Figure A.4. The design strength check for the critical section of the column (at the connection) is shown in Equation A.6.

$$\frac{N^*}{\phi N_n} + \frac{M^*}{\phi M_n} < 1 \rightarrow \frac{676}{0.9 \times 2039} + \frac{84}{0.9 \times 160} = 0.33 + 0.46 = 0.79 < 1 \quad \text{(A.6)}$$

A.2.4 Post-tensioning

Load-span tables supplied by Sarti (2011) suggested that seven post-tensioning strands with a post-tensioning force of 580kN gave an optimal design for a 7.5m beam with a dead load of 18kN/m. But the table was only valid for simply supported beams; positive influence of the connection was not taken into account, therefore the post-tensioning force was reduced. Geometric limitations resulted in an eccentricity of tendons at the deviator of 165mm; the resulting angle in the post-tensioning tendons at deviators was 8°, as can be seen in Figure A.7. A post-tensioning force of 440kN was chosen as the vertical component of 2 × 69kN balanced the dead load of the floors. This resulted in 4 tendons (ϕ=12.7mm) each stressed to 110kN (70% of yield strength) and gave a compressive stress of 6MPa in the timber. Specimens were tested at full post-tensioning force and at half post-tensioning force of 220kN.

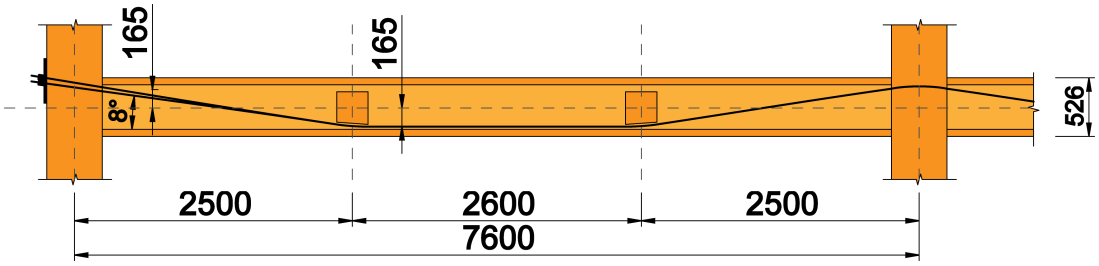

Figure A.7: Geometry of frame with draped post-tensioning tendons

Two deviators were designed, each placed at approximately 1/3 the length of the beam. Deviators were timber blocks which were glued to the inside of the webs of the box beam. Dimensions of the deviators are shown in Figure A.8. The bottom of the deviator had a radius of curvature of 2m as this was the minimum

curvature required for post-tensioning tendons. Design of the deviators is further elaborated on in Appendix B.1.

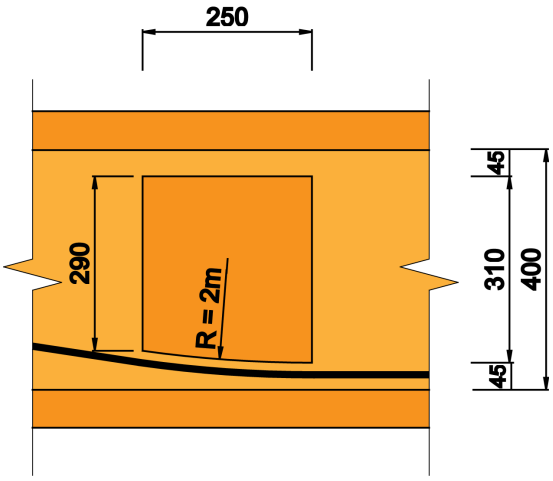

Figure A.8: Dimensions of deviator blocks

The anchorage plate was designed based on 3D FEM modelling, as is further described in Appendix B.3. A 500x300mm plate with a thickness of 40mm was used. Angular recesses were cut out to allow the tendons to be anchored under an 8°angle.

A.2.5 Connection design

The connection design was based on the design procedure proposed by Newcombe et al. (2010a), see Figure A.9. Although this procedure was developed for seismic design, at the time of testing it was the best available tool to predict connection behaviour. The initial post-tensioning force was $F_{pt} = 440kN$, which resulted in an initial compressive stress in the beam of $f_i = 6.0MPa$. The empirically derived equation (A.7), as provided by Newcombe et al. (2010a), resulted in the height of compressive zone (c) and formed the basis for the design procedure.

$$c = \alpha\beta h_b \left(\frac{0.054}{\sqrt{\theta_{imp}}} - 0.12 \right) \tag{A.7}$$

Where:

- $\alpha = \frac{390}{E_{perp}} + 0.42 = \frac{390}{600} + 0.42 = 1.07$

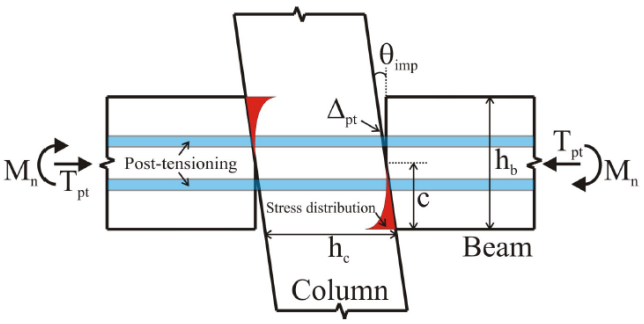

Figure A.9: Gap opening mechanism in internal seismic connection Newcombe et al. (2010a)

- $\beta = \frac{f_i}{4.5} = \frac{6.0}{4.5} = 1.33$
- $h_b = 526mm$
- θ_{imp} = imposed connection rotation

In seismic design connection moment is calculated as the post-tensioning force multiplied by the distance between tendons and the centroid of the stress block in the compression zone. If this is adapted for gravity design, the connection moment is calculated as *Method 1* shown in Figure A.10. The compression stress distribution at the interface is assumed to remain linear. The compressive stress at location of the web is not over the full width of the column, which has been taken into account in the calculation of the connection moment. Eccentricity of post-tensioning tendons at the connection interface, relative to the centroid of the beam, is $e = 160mm$.

Alternatively the connection moment can be calculated as the post-tensioning force multiplied by the distance between centroid of the beam and centroid of the stress block in the compression zone (*Method 2* in Figure A.10). This method can be visualized by taking a free-body diagram of the beam only. In this case the end of the beam is loaded by an eccentric compressive force. The eccentricity of the compressive force is calculated by taking the distance between the centroid of the compression zone and the neutral axis of the beam. The bending moment at the end of the beam is the compressive force, which equals the post-tensioning force, multiplied by the eccentricity of this force.

These two design methods lead to moment-rotation curves as shown in Figure A.11, which shows curves for a post-tensioning force of 220kN and 440kN. The

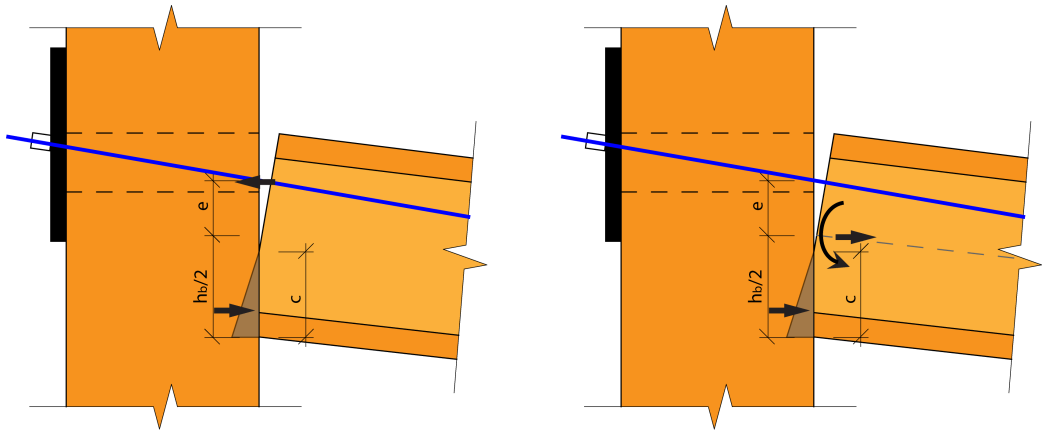

Method 1

$$M_{con,1} = F_{pt}\left(e + \frac{h_b}{2} - \frac{c}{3}\right)$$

Method 2

$$M_{con,2} = F_{pt}\left(\frac{h_b}{2} - \frac{c}{3}\right)$$

Figure A.10: Two methods to calculate connection moment

shape of the two different methods is exactly the same, but connection moment differs by a factor of $F_{pt} \times e$. Stiffness of the connection before decompression was 30kNm/mrad for the 440kN post-tensioning force and 52kNm/mrad for the 220kN post-tensioning force. These values were used in a framework analysis program for design of the frame. It has to be noted that based on this design procedure stiffness before decompression decreased when post-tensioning force increased, something that required verification with experimental data.

Also plotted as dashed lines are the ratios of neutral axis depth over section height (c/d). For the fully stressed specimen (440kN) decompression was predicted to occur at a connection moment of 131kNm and at a rotation of 4.3mrad. The increase in moment capacity after decompression is partly due to tendon elongation and partly due to the shift in neutral axis position, resulting in a larger lever arm between tension and compression forces. At 10mrad rotation, with a connection moment of 181kN, the neutral axis was 0.6 times the beam depth. At this point the strain at the bottom of beam was 3.4%, and a corresponding stress of 20MPa was reached, assuming the timber remained linear elastic. This stress level was no problem for the beam, but for the column loaded perpendicular to grain, these stresses were beyond failure. The post decompression behaviour was therefore more likely to predict the behaviour of a reinforced connection, where timber would stay elastic under high compressive stresses in the column.

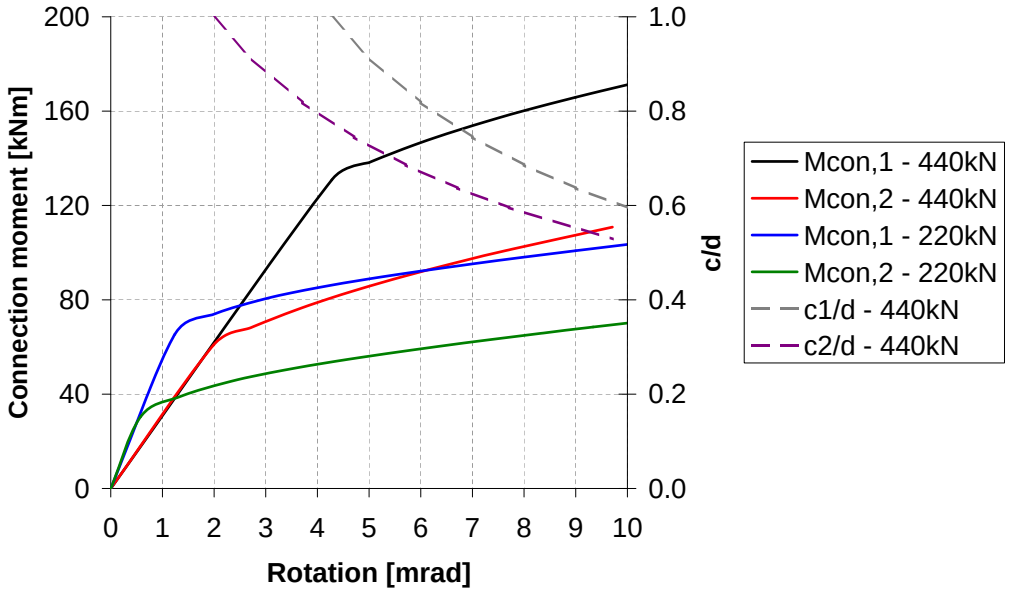

Figure A.11: Moment-rotation predictions according to the proposed design procedure

A.2.6 Connection reinforcement

The compressive strength and stiffness perpendicular to the grain in the column was critical for the connection behaviour, as the post-tensioning force needed to be transferred into the column over a relatively small area. Low strength was limiting the post-tensioning force and low stiffness was resulting in additional connection rotation. In order to increase the connection performance, different methods for timber and steel reinforcing the connection were evaluated.

Firstly 3 different column interfaces (on two different columns) were tested. Column 1 was a LVL11 column with two different connection interfaces, one had all the grains running longitudinally whereas the other interface had the outer 45mm LVL laminates rotated by 90°(Figure A.12d), which resulted in a combination of compression parallel and perpendicular to grain. Column 2 was made of cross-banded LVL (Figure A.12c), which had several LVL veneers rotated 90°.

Each of the three column interfaces was tested with and without steel reinforcement. Firstly a timber-to-timber connection without additional steel reinforcement was tested. The second test used steel reinforcement, which consisted of a angle

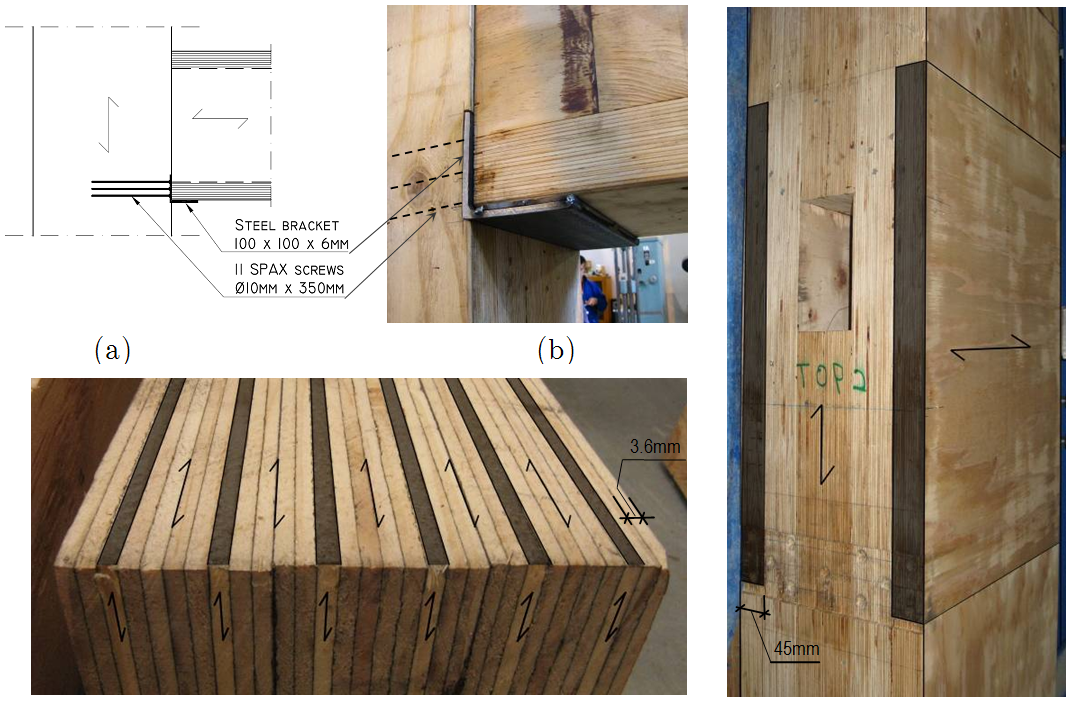

Figure A.12: Column reinforcement, (a) side view of steel corbel with screw reinforcement, (b) steel corbel, (c) cross-banded LVL with cross layers marked in grey, (d) rotated outer layers of LVL marked in grey

(100 x 100 x 6mm) as corbel and bearing plate, which was supported by eleven 350mm long, ϕ=10mm SPAX (2012a) screws (Figure A.12a+b). The number of screws was based on the maximum number of screws that could be placed while still satisfying minimum spacing requirements. It was assumed that all screws were equally sharing the load, which was ensured through the use of the steel corbel and by placing the screw heads flush with the surface of the timber. The third test was reinforced with the steel angle but without screws, in order to investigate the effect of the steel angle and screws separately.

For one test (Test 10) an extra sheet of LVL was glued onto the beam. This was done in order to test if increasing the contact area between beam and column would improve the performance.

The total compressive force in the connection was to be the same as the post-tensioning force, 440kN, because of horizontal force equilibrium. In this

design the timber contact area was 300 × 100mm. The maximum compression stress perpendicular to grain was 12MPa, and thus timber capacity equals 360kN. This was not sufficient to resist the compressive force from the post-tensioning. Furthermore significant plastic deformations would occur in LVL at 12MPa compressive stress. Screw reinforcement was designed according to Bejtka and Blass (2006). The load carrying capacity of the zone with screw reinforcement was determined by the minimum value of three different failure modes, which depended on geometry of the beam and screws.

The first failure mode was most likely with short screws when they are pushed into the timber and the timber contact area reaches its maximum bearing capacity. The compressive force required to push the screws into the timber was considered equal to the withdrawal capacity. The maximum withdrawal capacity of a 350mm long, ϕ=10mm screw was 68kN, based on Equations A.8 and A.9 given in the European Technical Approval (ETA) of screw manufacturer SPAX (Deutsches Instutut fur Bautechnik, 2011). Combined with timber bearing strength this gave a total load carrying capacity of 360 + 11 × 68 = 1108kN. In reality this failure mode would not occur with this length of screws, as they would buckle long before their compressive strength was reached.

$$R_{ax,k} = k_{ax} f_{1,k} l_{ef} d_1 = 1.0 \times 19.5 \times 350 \times 10 = 68kN \tag{A.8}$$

$$f_{1,k} = 60 \cdot 10^{-6} \rho_k^2 = 60 \cdot 10^{-6} \times 570^2 = 19.5N/mm \tag{A.9}$$

The second failure mode was most likely with slender screws when they buckle within timber and timber bearing capacity was reached. The timber bearing capacity was again equal to 360kN. The buckling load of the long screws was given in the ETA of screw manufacturer SPAX (Deutsches Instutut fur Bautechnik, 2011). For a ϕ = 10mm screw, installed at an angle of α = 90°to the grain, in timber with a density of ρ = 450kg/m^3, the buckling load was $R_{ki,d}$ = 16.9kN. Together with the timber bearing capacity this results in a failure load of 360 + 11 × 16.9 = 546kN.

The third failure mode was observed in beams with short screws, when the plain formed by the screw tips reaches its maximum compressive strength. With the long screws in the large column this failure mode would not occur.

From the calculations above it can be concluded that the strength of the screw reinforced column will be sufficient. More interesting would be the increase in stiffness, as that would influence the connection response. The ETA from SPAX did not supply equations to determine the stiffness of screw-reinforced timber. But formulas were given by Bejtka and Blass (2006), based on the Volkersen Theory (Volkersen, 1938). The main formula is shown in Equation A.10, the reader is referred to the paper for explanation of the parameters. The theory applied only to directly loaded beam supports. The compression force from the beam was balanced by compression force from post-tensioning anchorage. Therefore the stress distribution in the column would be similar to directly loaded beams. The formulas resulted in about a five times increased stiffness, from 500N/mm^2 to 2670N/mm^2.

$$E_{tot} = \frac{E_{90} \cdot f_{LD} \cdot n \cdot l_s \left(\frac{\psi}{n} + 1\right) \omega \sinh(\omega \cdot l_s)}{\phi - \psi + n \left(\frac{\psi}{n} + 1\right) \cosh(\omega \cdot l_s) + 0.7 \cdot f_{LD} \cdot l_s \cdot \phi \cdot \omega \sinh(\omega \cdot l_s)} \quad \text{(A.10)}$$

Where:

- $E_{90} = 500MPa$
- $f_{LD} = 2.79$
- $n = 11$
- $l_s = 350mm$
- $\psi = 16.0$
- $\omega = 0.0056$
- $\phi = 0.91$

A.3 Frame design

This section describes the design of a post-tensioned timber gravity frame which was used for experimental testing as described in Chapter 6. This design was based on a 9m beam length, similar to beams designed for experimental testing as described in Appendix A.1. An overview of the frame can be seen in Figure A.13.

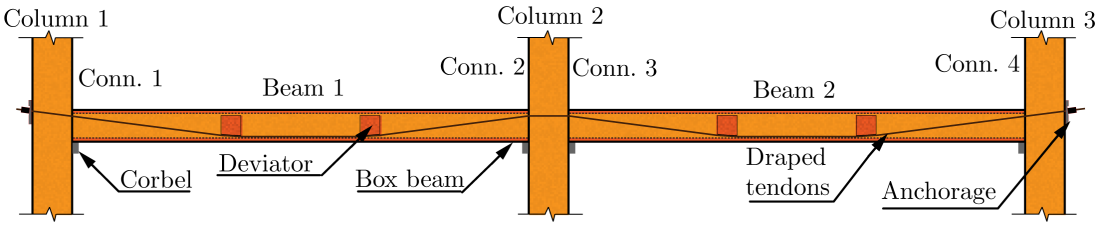

Figure A.13: Rendering of two-bay frame

A.3.1 Loading

The frames were designed to be part of a four storey commercial office building with a 6m floor span. The floor consisted of a TCC-floor with a weight (including partitions) of 3kPa. The live load for an office building was taken as 3kPa. The resulting load on the beam was a dead load of 18kN/m and a live load of also 18kN/m.

A.3.2 Post-tensioning force

The optimal post-tensioning is strongly dependent on the geometry of the frame and beam height. A too high post-tensioning force results in design problems for the connection. A too low post-tensioning force does not create enough precamber to allow reduction in section height and the connection stiffness will be low, reducing the efficiency of the system. For testing, a range of post-tensioning forces were considered (Table A.6), namely 0, 100, 200, 300 and 400kN. Testing with 0kN post-tensioning force resulted in pinned connections. The design of the frame was performed with a post-tensioning force of 400kN.

Table A.6: Range of post-tensioning force used for experimental testing

PT force (kN)	No. tendons (-)	Area tendons (mm^2)	Stress (f_i) (MPa)	f_i/f_y (%)
100	2	200	500	33%
200	4	400	500	33%
300	4	400	750	49%
400	4	400	1000	66%

A.3.3 Framework model

A framework model to predict internal actions in the frame was made as shown in Figure A.14. The model included a rotational spring for joint panel rotation with a stiffness of 40kNm/mrad, based on the results of experimental beam-column connection testing. Another rotational spring was placed at the connection interface, modelling the interface compression and gap opening. This spring had a non-linear rotational stiffness, based on experimental testing data of connection testing (Section 5.4) with screw reinforcement and a post-tensioning force of 440kN. The initial stiffness was 37kNm and decompression moment was at 85kNm.

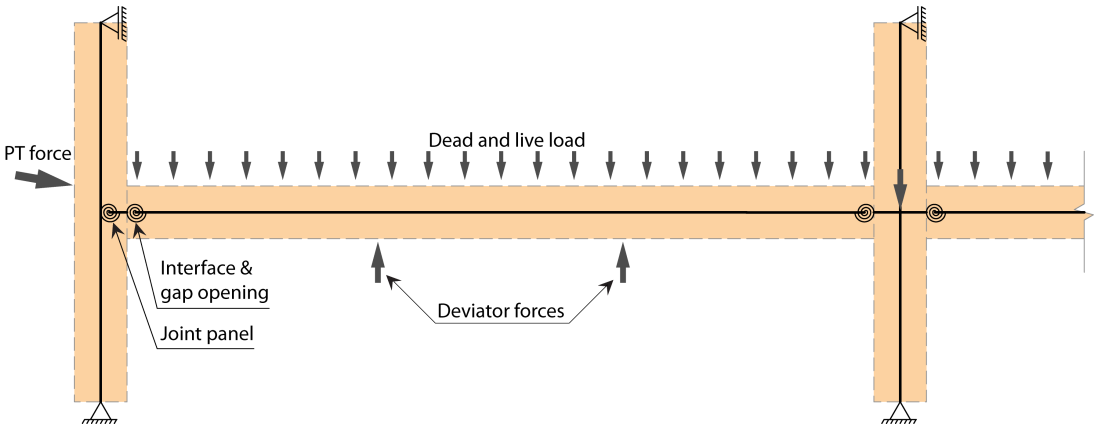

Figure A.14: Framework model of two-bay frame

A parameter study on the beam height was performed using the framework model. Beam height values ranging from 425mm to 600mm were used. The beam height influenced other parameters like cross-sectional properties, angle of tendons at deviator and bending strength (k_{24}-factor). Design checks according

to the New Zealand timber design standard (NZS 3603:1993) were performed. The results can be seen in Figure A.15. The unity check is the design action over the design capacity. This value should be smaller than 1.0 for a safe design. Based on these results a beam height of 500mm was chosen. A web thickness of 45mm was sufficient to resist the design shear force. Top and bottom flanges were 90mm thick. Long-term deflections, calculated with a creep factor (k_2) of 2, were not part of the research objectives and were therefore not taken into account when determining beam height.

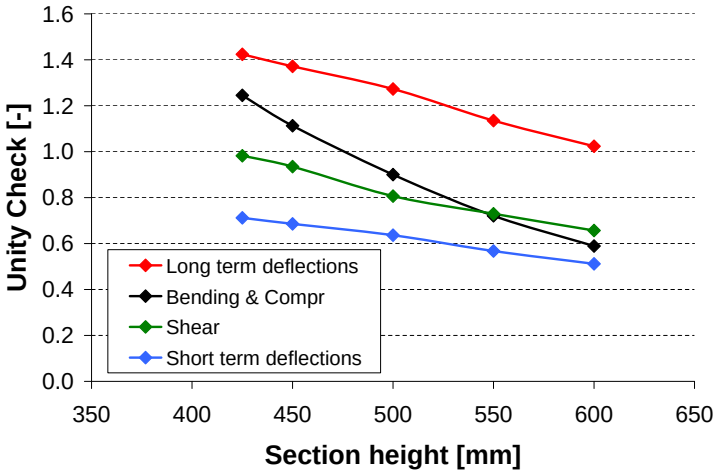

Figure A.15: Results of parameter study on beam height

A.3.4 Column design

From the framework model it followed that the maximum bending moment in an external column was 129kNm. The column is loaded by four stories with each 27m^2 loaded with a maximum design load of 6.3kPa, which included a reduction factor $\psi_a = 0.59$. The resulting design compressive force in the column was $N^* = 680kN$. The critical section of the column was where the opening for the post-tensioning tendons was located. The middle two layers were taken out, leaving two layers of 90mm. The reduced section modulus was $7.5 \cdot 10^6 mm^3$. The bending strength is given by Equation A.11 and the compression strength in Equation A.12. The design check is shown in Equation A.13. It can be seen

that the column is just strong enough to resist the combination of bending and compression.

$$M_n = k_1 \cdot k_{24} \cdot f_b \cdot Z = 0.8 \cdot 0.7 \cdot 48 \cdot 7.5 \cdot 10^6 = 202kNm \tag{A.11}$$

$$N_n = k_1 \cdot f_c \cdot A = 0.8 \cdot 45 \cdot (2 \cdot 90 \cdot 500) = 3240kN \tag{A.12}$$

$$\frac{N^*}{\phi N_n} + \frac{M^*}{\phi M_n} = \frac{680}{0.9 \cdot 3240} + \frac{129}{0.9 \cdot 202} = 0.23 + 0.71 = 0.94 \tag{A.13}$$

A.3.5 Anchorage plate

Design of the anchorage plate was done using a 3D Finite Element Model (FEM), as this was the most detailed method and leads to the most conservative stresses as was shown in Appendix B.3. The model was a 3D linear-elastic model with material properties as described in Section 3.6. The column was modelled along the full length and displacements were fixed on the opposite side from the loading plate. An opening in the column for post-tensioning tendons was included in the model. A steel plate was placed onto the column. The plate was loaded by four pressure loads of 45MPa over a circular area with a diameter of 65mm, which represented the maximum contact force of 150kN from the anchorage barrels.

Results of the FEM under the maximum load of 600kN are shown in Figure A.16. It was found that a plate with a height of 500mm and a thickness of 40mm resulted in steel bending stresses of 250MPa (Figure A.16a), which was lower than the yield strength of 300MPa. Resulting perpendicular to grain stresses in the timber were 6MPa (Figure A.16b) and shear stresses 3MPa (Figure A.16c). These stress levels were well within the design compression strength of 12MPa and shear strength of 6MPa.

A.3.6 Corbel design

The maximum ULS vertical load on the beam was 440kN. The maximum post-tensioning force was estimated at 480kN, which was 400kN initial post-tensioning force and tendon elongation of 20%. This force gave an uplift at the deviators

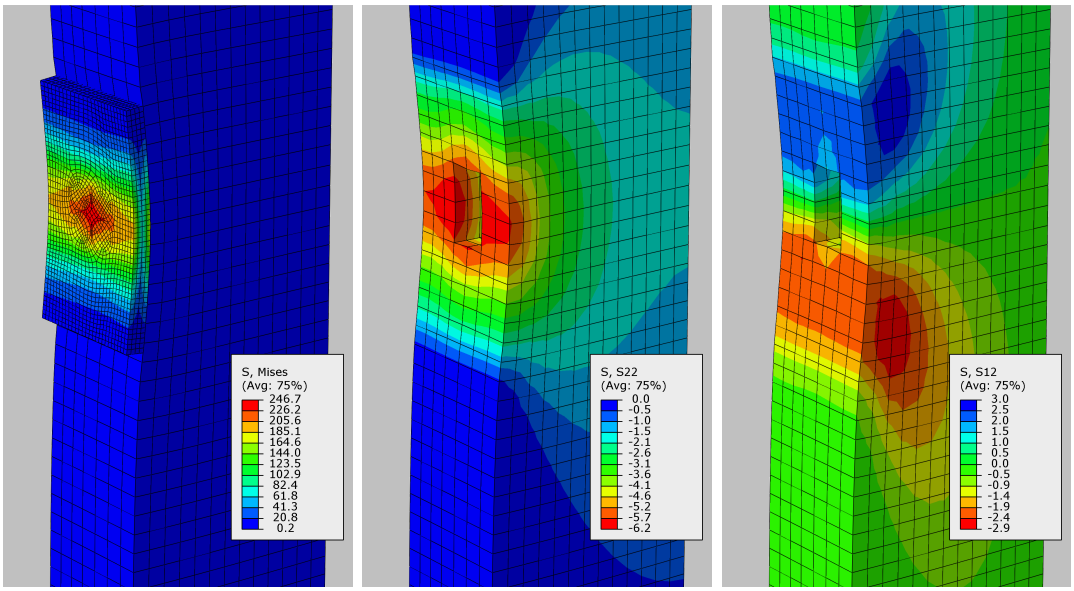

(a) Steel von Mises stresses (b) Perpendicular to grain stresses in column (c) Shear stresses in column

Figure A.16: Results of FEM model of post-tensioning anchorage under a maximum possible load of 600kN

of 40kN, and a maximum shear force in the corbel of 180kN. As testing was also performed with lower post-tensioning forces, the design was performed with 200kN shear force. This design is further described in Section B.4.1.

A.3.7 Column interface design

The column interface was designed for a maximum post-tensioning force of 500kN, which allowed for increase in post-tensioning force due to tendon elongation. After gap opening this force would be transferred into the column through the bottom flange only. The timber area of the column in compression was therefore $90 \times 288 = 26000mm^2$. A compressive strength of the column of 10MPa perpendicular to grain was taken based on experimental testing described in Section 3.3. The resulting timber strength perpendicular to grain was 260kN, the remaining 240kN was resisted by screws. Screws with a diameter of 10mm had a maximum strength of 17kN, governed by buckling of the screws in the timber (SPAX, 2012a), which resulted in a total of 14 screws required to resist the compressive force due to post-tensioning.

Appendix B

Design details

This chapter covers design details which have been evaluated as they were required for experimental testing. Some experimental testing and numerical modelling has taken place on the design of deviators, post-tensioning anchorages and corbels. Several of the findings are presented in this section, but no detailed investigations have taken place on these topics.

B.1 Deviators

This section describes the design of deviators for beams with draped tendon profiles, as presented in Appendix A.1. Experimental testing has been performed to determine the maximum strength and failure mechanisms. It was found that splitting of the deviators was a significant issue and that screw reinforcement should be installed to prevent splitting.

B.1.1 Introduction

Deviators can be manufactured from LVL sheets (Figure B.1a) with grain running vertically, as deviators need high strength in that direction due to the tendon forces. Several sheets can be glued together to create the required geometry. No steel reinforcement at the interface between the tendons and deviators is needed as the compression strength of LVL is sufficient to resist the upward force from tendons. Alternatively, steel deviators have been designed by practising engineers (Figure B.1b).

Post-tensioning tendons require a minimum curvature of 2.0m (BBR VT International Ltd, 2010), which can be achieved by providing curvature to the bottom of deviators. The glue-line between the deviators and the webs is critical. Several beams with draped tendons and timber deviators have been tested (short-

(a) Timber deviator (c/o Hunters Laminates)

(b) Steel deviators designed by Dunning Thornton consultants

Figure B.1: Different types of deviators

term) in the laboratory, and no problems were found with the strength of the glue line.

However, care needs to be taken with splitting of timber deviator blocks (Figure B.2). As the deviator is loaded in the middle and the upwards force is resisted at both ends. A strut-and-tie model can be used to calculate the tensile force in the deviator.

Timber manufacturers do not specify any tensile strength of LVL perpendicular to grain. Experimental testing resulted in a 5^{th}-percentile tensile strength of 1.4MPa (Ardalany et al., 2010). Until manufacturers supply design values it is recommended to use long, fully threaded screws to transfer the total tensile force in the top of the deviator. Using cross-banded LVL (with a higher tensile strength) for the deviators will not make a difference as the crack can still form in the web of the beam, just next to the glue line of the deviator block.

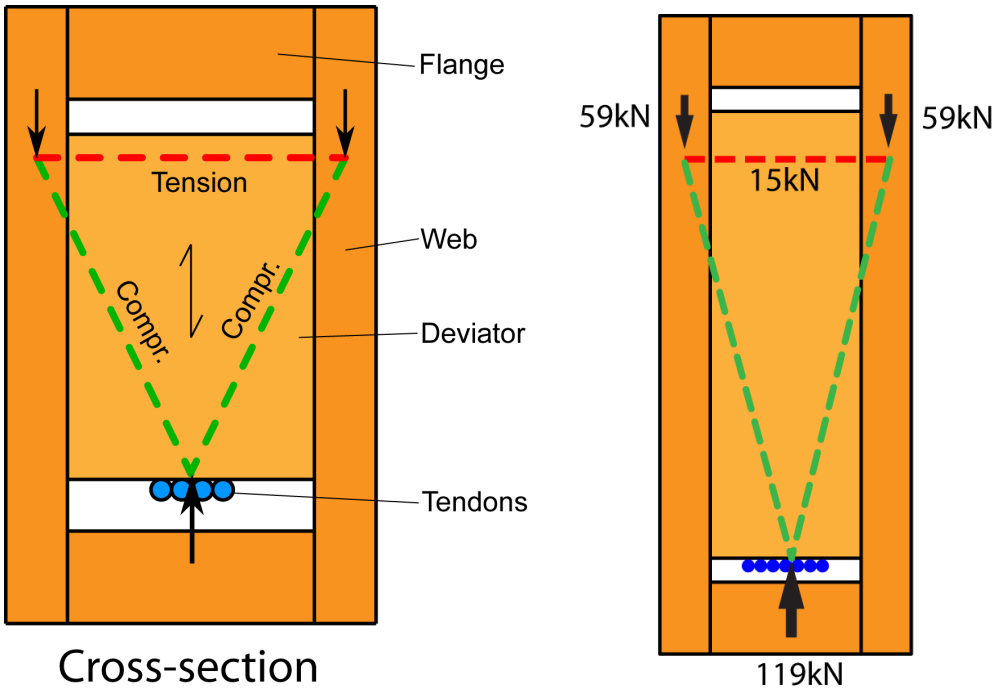

(a) Strut-and-tie model

(b) Example for 800x315mm beam with 119kN uplift force

Figure B.2: Tensile force in deviator due to stress spreading

B.1.2 Deviator location

The location of the deviator can be varied. If the deviator is placed close to the end of the beam there is a large uplift force (as the tendons have a large angle), but only a short distance between the end of the beam and the deviator. Theoretical the best placement for the deviator is as close to the end of the beam as possible, as the resulting moment-area, and thus the precamber, is the largest. If the deviator is placed close to the end of the beam, problems arise due to geometric requirements of a minimum tendon radius of 2m. The deviator size becomes impractical and the large uplift force creates problems with the design of the deviator.

The deviator location relative to the beam length is called X, as shown in Figure B.3. The resulting precamber for a range of deviators positions is shown in Figure B.4. The values are based on a 610mm high box beam with a length of 8.6m and a post-tensioning force of 1000kN. Deflection values are based on

standard beam theory. The precamber due to shear is constant at 6.7mm and the precamber due to bending is decreasing with an increase of X. The dashed line is the precamber for the same beam with straight tendons, resulting in only bending uplift.

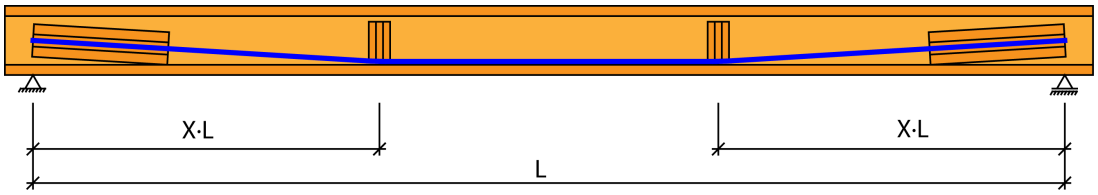

Figure B.3: Definition of deviator location

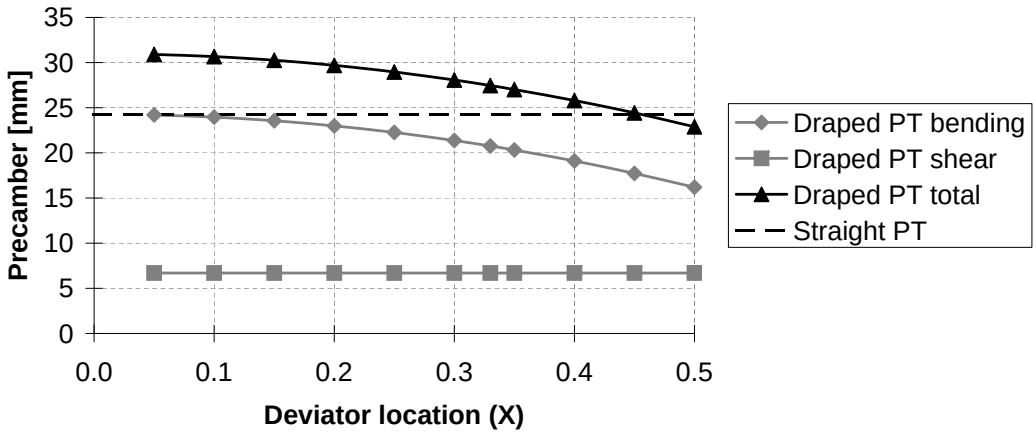

Figure B.4: Precamber of different deviator locations

Placing the deviator at 1/3 of the length of the beam reduces the maximum possible precamber by 11%, but makes the design much more practical. Placing one deviator at the centre of the beam reduces the precamber by 26%. In this thesis the location of the deviators has been chosen as 1/3 of the length of the beam. This location has also been used in all experimental testing on post-tensioned timber gravity beams.

B.1.3 Experimental testing

Experimental testing was performed on two deviators which were reused after experimental testing of beams (Chapter 4). One deviator was unreinforced and

one had screw reinforcement at the top of the deviator. The screw reinforcement consisted of 5 SPAX screws with 8mm diameter and a length of 400mm. The screws were placed 40mm below the top of the deviator and spaced at 30mm apart. Testing was performed in an Avery test frame with a capacity of 1000kN. The load was applied to the bottom of the deviator and an in-line load-cell measured the force. As the deviator was placed inside the box beam no deflections could be measured.

The resulting load data is shown in Figure B.5. It can be seen that the unreinforced deviator reached a load of 234kN before it split (Figure B.6a). After splitting the deviator could resist more loading, but this resulted in formation of a large crack in the deviator (Figure B.6b) and eventual a failure of the box beam itself. The screw-reinforced deviator resisted a maximum load of 342kN after which it a shear failure occurred on one side between the web and the deviator.

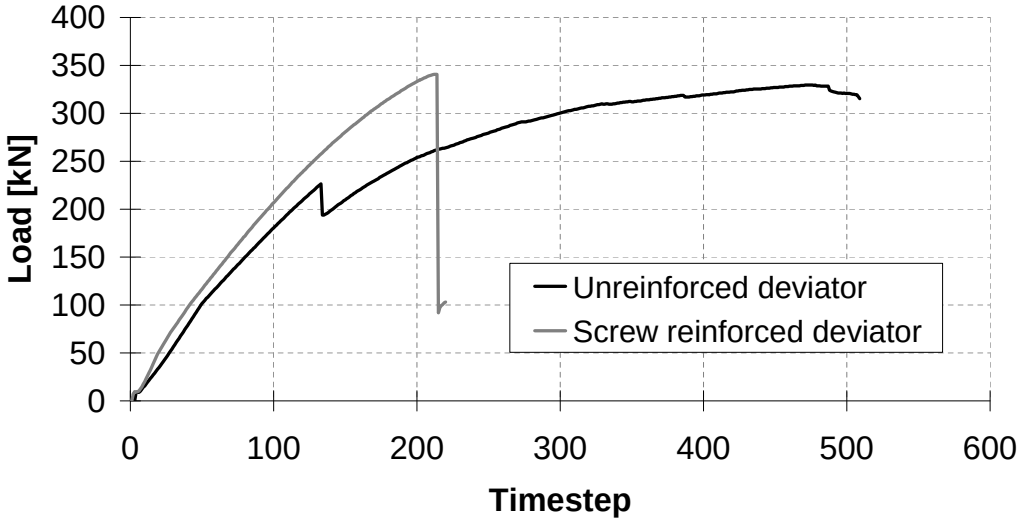

Figure B.5: Load data for deviator testing

The design load of the deviator was 94kN (for Beam 4 of experimental testing) and the ultimate load reached during testing was 124kN. This below the splitting load of the unreinforced deviator, but when taking into account the material strength reduction factor ($\phi = 0.9$) and load duration factor ($k_2 = 0.6$) the maximum design strength becomes 126kN, which is close to the design load. Furthermore the LVL manufacturers do not specify a tensile strength for LVL

(a) At 234kN (b) Under maximum load

Figure B.6: Splitting of timber deviator during experimental testing

perpendicular to grain, therefore screw reinforcement needs to be used for timber deviators.

The deviator had a cross-sectional area of 132000mm^2. The failure load of 342kN resulted in a rolling shear stress (σ_{RT}) between the deviator and the webs of 2.6MPa. This is much higher than the average value of 1.68MPa which was found by experimental testing of small scale specimens (Section 3.5). This difference can be caused by the compressive stress and the screw reinforcement which increases the shear strength. But for a conservative design it is recommended to use the characteristic rolling shear strength of 1MPa.

B.1.4 Design recommendations

Splitting of the deviator can be calculated based on a strut-and-tie model. Assuming no tensile strength perpendicular to grain of the timber, the splitting force needs to be resisted by the screws. The screw strength is based on the lowest withdrawal strength, which is found when there is a tensile failure between the deviator and the webs. The embedment length in that case is only the thickness of the web. The pull-out strength of the screws in the web is given in design guidelines of screw manufacturers.

The shear strength of the interface between the deviator and the webs needs to be checked. The shear strength of the deviator and the glue line is higher than the rolling shear strength of the web. Experimental testing (Section 3.5) has resulted in a characteristic rolling shear strength of 1MPa.

The design equation for shear strength is given in Equation B.1.

$$F_{pt,v} < \phi k_1 f_s \cdot A_s \tag{B.1}$$

Where:

- $F_{pt,v}$ = Uplift force at deviator due to post-tensioning (N)
- ϕ = Strength reduction factor for material (0.9 for LVL)
- k_1 = Load duration factor
- f_s = Rolling shear strength (MPa)
- A_s = Shear area between deviator and webs (mm^2)

The shear strength of the interface between the deviator and the webs needs to be checked for two different loading conditions. Once for the long-term duration uplift force (with $k_1 = 0.6$) and once for the maximum ULS uplift force (with $k_1 = 0.8$).

B.2 Anchorages on beams

This section describes experimental testing and numerical modelling of anchorages for post-tensioned timber beams. This work was performed as part of the design of the beams. The design of these beams is described in Section A.1.

B.2.1 Introduction

Anchorages for post-tensioned timber beams have the advantage that the compressive stresses are parallel to grain, which has a much higher strength than perpendicular to grain anchorages on columns. Two types of post-tensioning anchorage systems can be used, single strand anchorages or anchorage disks for multiple strands. The advantage of single strand anchorages is that a small jack can be used, but all the strands need to be stressed (and re-stressed) one at the time. The advantage of an anchorage disk is that all strands can be stressed (and re-stressed) at once, but a larger jack is required.

Anchorages can be external to the cross section or internal (hidden inside the cross section, as shown in Figure B.7).

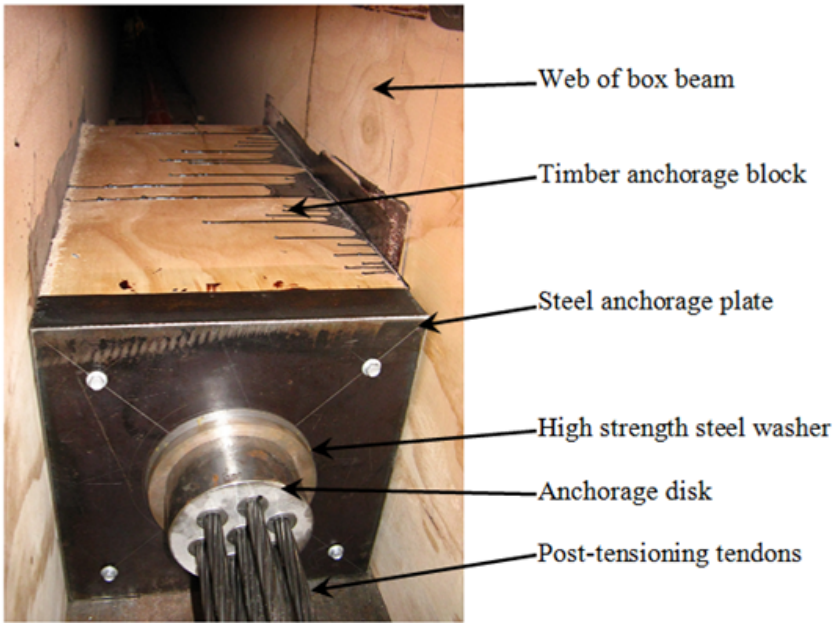

Figure B.7: Example of internal post-tensioning anchorage for beams

External anchorages are easier for manufacturing but internal anchorages allow the beams to be placed between columns. For beams with straight tendons the bottom flange can be used as part of the anchorage. A steel anchorage plate of sufficient thickness is needed to spread the post-tensioning force and limit the compressive stresses in the timber anchorage block. As the stresses between the anchorage disk and the steel anchorage plate can be close to (or larger than) the yield strength of the steel, a high-strength steel washer can be placed in between these two components in order to spread the stresses.

The strength of the glueline between the timber anchorage block and the webs of the beam is of critical importance as this transfers the full post-tensioning force. Experimental testing has been performed to determine the performance of the connection between the timber anchorage block and the webs of the beam for connections which are glued, screwed and a combination of these two. The resulting strength of 1100kN was not enough for experimental testing and therefore numerical modelling of anchorage blocks has been performed to investigate alternative arrangements for steel anchorage plates and timber anchorage blocks in order to increase the capacity of the anchorage system.

Similar to deviators, also anchorages experience stress spreading which leads to tension stresses perpendicular to grain, as shown in Figure B.8. As the post-tensioning force is larger than the deviator uplift force, the tension stresses in the anchorage block can also be higher. Screw reinforcement will be required to resist the tensile force.

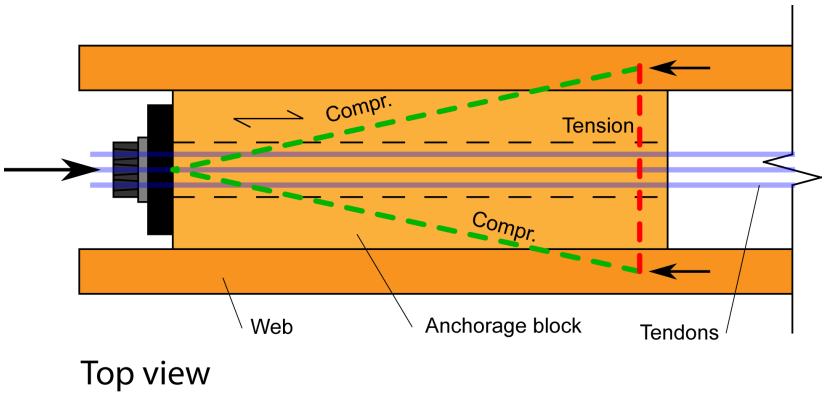

Figure B.8: Stress spreading in anchorage resulting in a tension force in the anchorage block

B.2.2 Experimental testing

Experimental testing was performed on three different connections between the anchorage block and the webs of the beam. One was only glued, one was only screwed and one was glued and screwed. All specimens had four 400mm screws placed on both sides at the end of the anchorage block to prevent splitting. Testing was performed in a DARTEC universal testing machine whereby the loading rate was set to 1mm per minute. Images of the test setup can be seen in Figure B.9.

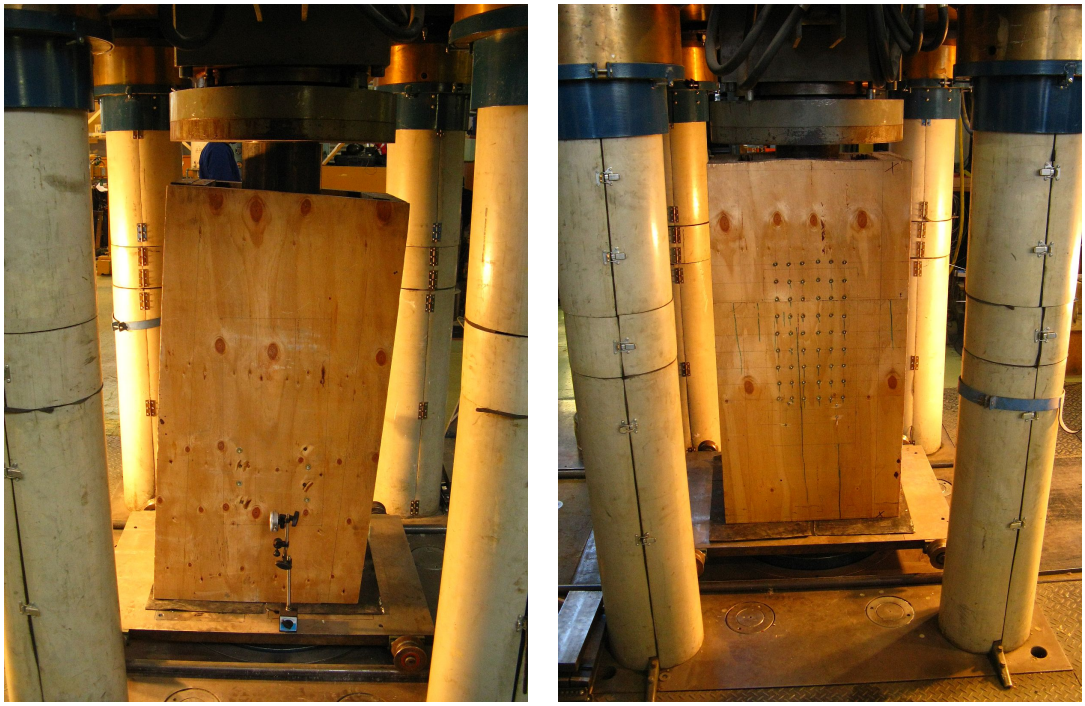

(a) Testing glue only connection (b) Testing screws connection

Figure B.9: Test setup of anchorage block testing

The anchorage block had a length of 600mm and a width of 288mm, resulting in a glue area of 345600mm^2. Experimental testing of small specimens found an average shear strength of 5.5MPa and a characteristic shear strength of 3.5MPa (Section 3.5), resulting in a maximum strength of 1900kN. Using a material reduction factor ($\phi = 0.9$) and a load duration factor ($k_2 = 0.6$) the design strength was 653kN.

The screwed connection consisted 54 fully threaded SPAX screws per side, with a 8mm diameter and a length of 220mm installed at a 45° angle to the grain following the minimum spacing requirements. The calculated maximum strength of the screws was 890kN and the design strength of the screw connection was 410kN. This was based on an effective number of fasteners (n_{ef}) per side of 45, a failure governed by thread extraction in the web (effective length $l_{ef} = 89mm$) and head pull through. The calculation includes a material factor based on the European design standard of $\gamma_{mod} = 1.3$ for screw connections and a load duration factor $k_{mod} = 0.6$.

For the test with glue only a shear failure occurred partly in the deviator block and partly in the web of the beam, as shown in Figure B.10a. For the test with screws only the failure occurred due to splitting of the webs of the beam as the screws got pulled through (Figure B.10b). Failure of the test with glue and screw connections was a combination of shear failure and splitting of the webs.

The load-displacement plot for the three tests can be seen in Figure B.11. It can be seen that the glue only connection reached a strength of 1100kN before failing in a brittle manner. The shear stress between the deviator and the webs of the beam at failure was 3.2MPa, which is lower than the average shear strength of 5.5MPa found by experimental testing (Section 3.5). This difference can due to stress concentrations in the timber close to the loading edge. These stress concentrations are further elaborated on in the next section.

The screw only connection reached a similar strength as the glue only test but failed in a more ductile manner due to timber splitting. The ultimate strength was about 2.7 times higher than the design strength of 410kN, but this was only under instantaneous loading. If material safety factors and load duration factors were ignored the design strength was 890kN, only 24% below the failure load.

The screw and glue connection reached a strength of 1500kN and failed in a very ductile manner. The load-carrying capacity of screws and glue combined is less than the load-carrying capacity of screws only connection added to the load-carrying capacity of the glued only connection. Therefore it can be concluded that the benefit of adding screws to a glued connection is limited. Furthermore, the cost of the screws and installation of numerous fully threaded screws (108 in the case of experimental testing for a design load of 410kN) is most likely significant more than increasing the size of the anchorage block and adding some

(a) Glueline failure between anchorage block and web of beam

(b) Splitting of web due to pull-through of screw heads

Figure B.10: Failure mechanisms of anchorage block testing

extra glue area.

The stiffness of the glue only connection, evaluated between 20% and 60% of maximum load was 350kN/mm, for the screw only connection 223kN/mm and for the screw and glue connection 353kN/mm. The stiffness of the screw and glue connection was very similar to the stiffness of the glue only connection, whereas the screw connection had a 35% lower stiffness. This indicates that the screws do not contribute to the initial stiffness of the connection.

Based on these experimental testing results it was concluded that a glued anchorage block is recommended and that screwed anchorage blocks are possible, but not practical in design. Combining glue and screw increases the strength, but it is questioned if this is cost efficient. Also the long-term stiffness is of importance, as additional displacements will lead to post-tensioning losses, and it

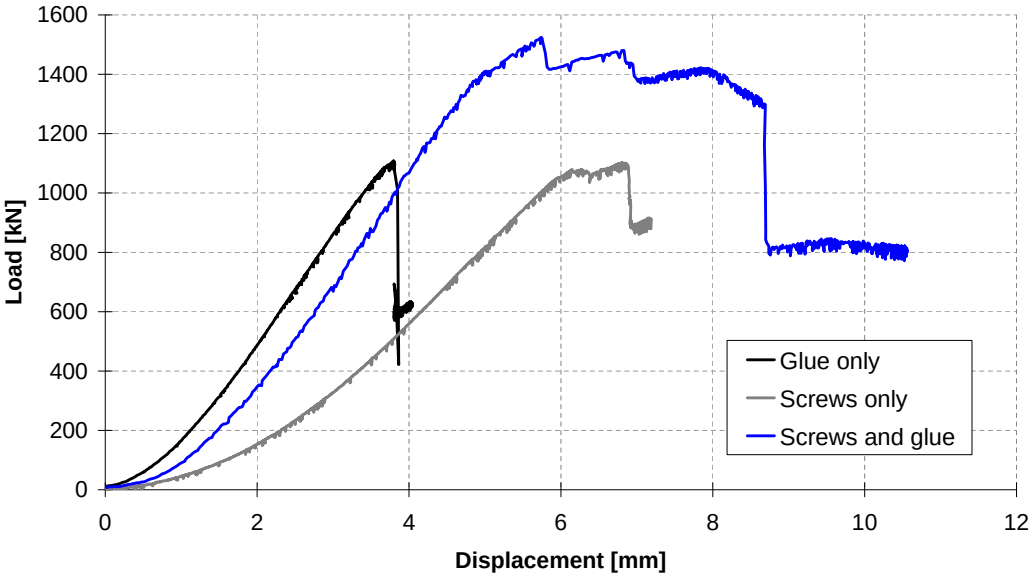

Figure B.11: Load-displacement results for experimental testing of anchorage blocks

is expected that glued connections due to their higher initial stiffness will perform better than screwed connections. As experimental testing of beams requires an initial post-tensioning force of 910kN, and with tendon elongation effects this will increase to about 1100kN, numerical modelling has been performed to analyse methods to improve the performance of glued anchorage systems.

B.2.3 Numerical modelling

The steel anchorage plate, loaded by the post-tensioning force and seated on the timber anchorage block, has a complex 3D stress field. Also the timber anchorage block and webs of the box beam are subjected to tension, compression and shear stresses. In order to evaluate the stresses a model of the box beam with an anchorage block inside, similar to the one used for experimental testing (Figure B.12), was made in Abaqus CAE (Simulia, 2010). The timber beam was modelled as described in Section 7.2. A 54mm thick steel plate was modelled with a 80mm diameter opening for the tendons. A force of 910kN was placed on the steel anchorage plate over the area where the high-strength steel washer was located (outer diameter of 140mm). The steel plate, timber anchorage block and

box beam were connected using tie constraints.

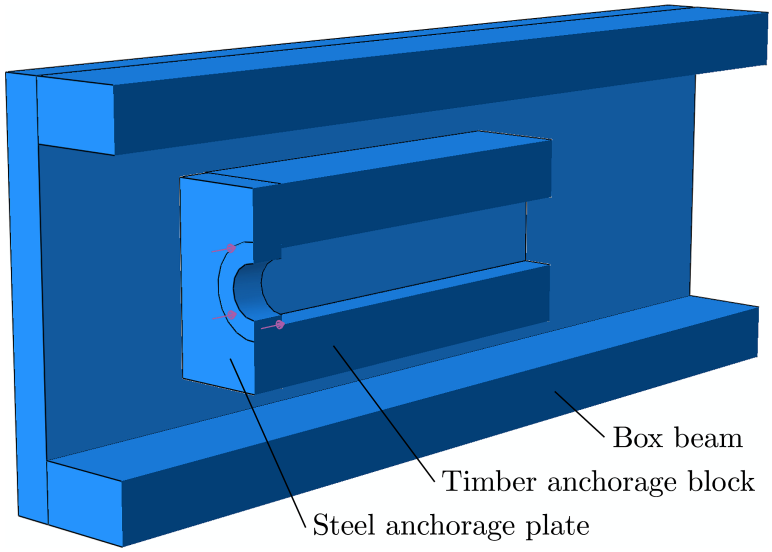

Figure B.12: Rendering of FEM model of box beam with anchorage block and plate

Timber stresses Results of the FEM model are shown in Figure B.13. Figure B.13a shows parallel to grain stresses in the timber anchorage block and webs. It can be seen that the compressive stress in the anchorage block is 22MPa, which is well below the 45MPa compressive strength of LVL parallel to grain. Stress concentrations around the opening in the anchorage block are clearly visible. Also an increase in stresses in the anchorage block close to the glueline is visible. This is despite a 10mm gap which was kept between the side of the steel plate and the web of the beam.

Figure B.13b shows the perpendicular to grain stresses in the timber anchorage block. It can be seen that the maximum stress at the end of the block is about 3.0MPa. This is much larger than the tensile strength perpendicular to grain. These tensile stresses cause the anchorage block to split and should be resisted by screw reinforcement.

Figure B.13c shows the parallel to grain stresses in the web of the beam. It can be seen that there is not only a compressive stress of 19MPa behind the anchorage block, but also a tensile stress of about 8MPa at the front of the block.

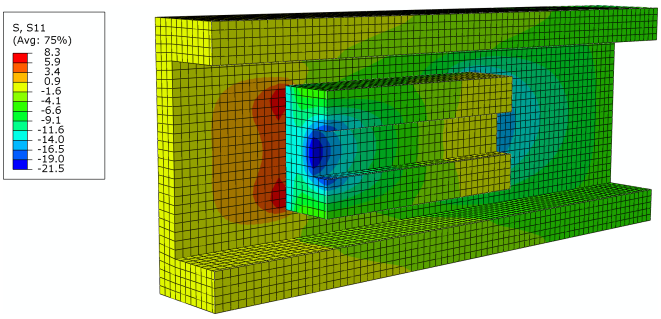

(a) Parallel to grain stresses

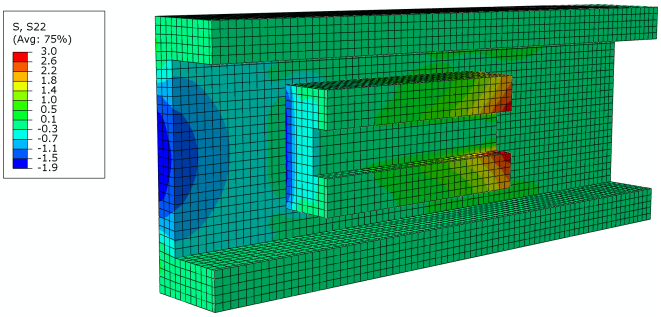

(b) Perpendicular to grain stresses

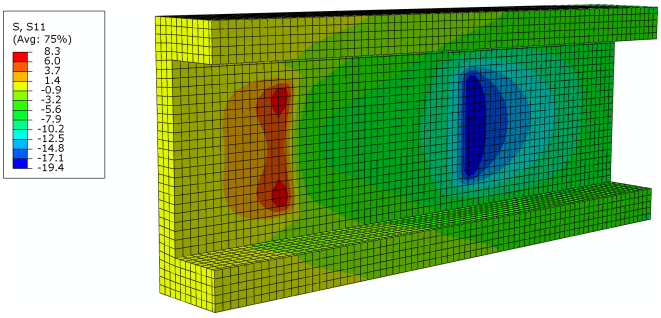

(c) Parallel to grain stresses

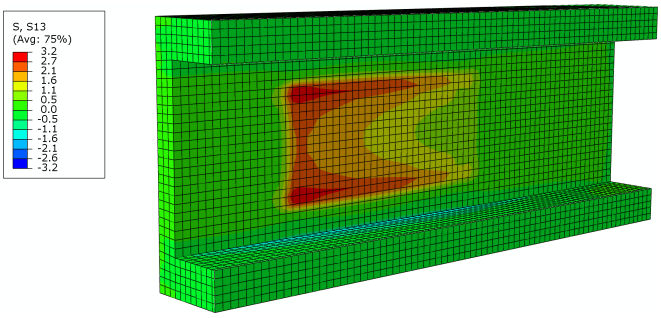

(d) Shear stresses

Figure B.13: FEM results for stresses in timber anchorage block and web of box beam

This shows that the post-tensioning force is resisted not only by compression of the webs but also partly by tension. The shear stresses between the block and the web are shown in Figure B.13d. It can be seen that the stresses are not uniformly distributed with higher values, up to 3.2MPa at the front of the anchorage block and close to 0MPa at the end of the block. This explains why the glued anchorage block failed at an average stress of 3.2MPa which was lower than the average strength of 5.5MPa found by small scale test specimens.

Steel stresses Stresses in the steel plate are shown in Figure B.14

Figure B.14a shows the Mises stresses in the steel. It can be seen that these stresses are highest around the opening for the tendons. The maximum stress is just over 250MPa. The steel was modelled as elastic-plastic with a yield strength of 250MPa. Therefore Figure B.14b shows that a small area around the opening has reached the yield strength. This shows that even a 54mm steel plate reaches yielding under a 910kN post-tensioning force. Although the area which reaches yielding is small and the stress drops quickly when moving away from the opening, therefore it is questionable if this yielding is a source of concern.

Figure B.14c shows the contact stress between the steel plate and the timber. It can be seen that this stress is about 26MPa (green colour) around the opening and gradually drops down when moving further away from the centre. But at the edges there is a peak in contact stress up to 46MPa. As the timber anchorage block is stiffened by the webs of the beam it attracts more load, which results in these stress concentrations.

Alternative solutions Three alternative solutions have been modelled in order to reduce stresses in the timber and in the glue line. The first one is an anchorage block which was twice as long, the second one a steel plate which was also supported on the webs and the third a steel plate (with stiffeners) which was also supported at the top and bottom flanges.

Figure B.15 shows the model with an anchorage block with a length of 1200mm instead of 600mm. The shear stresses in the glue line are reduced to 2.0MPa, compared to the 3.2MPa for the shorter block. Again tension (6MPa) and compression (14MPa) stresses can be seen in the web, but of smaller magnitude compared to the shorter anchorage block. Shear stresses in the web itself are

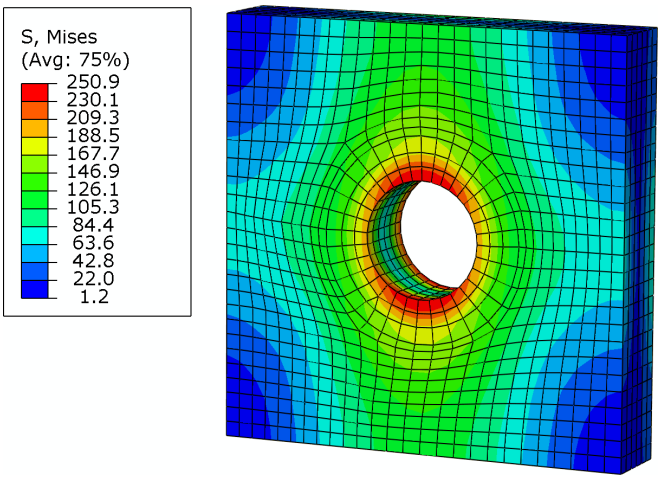

(a) Mises stresses

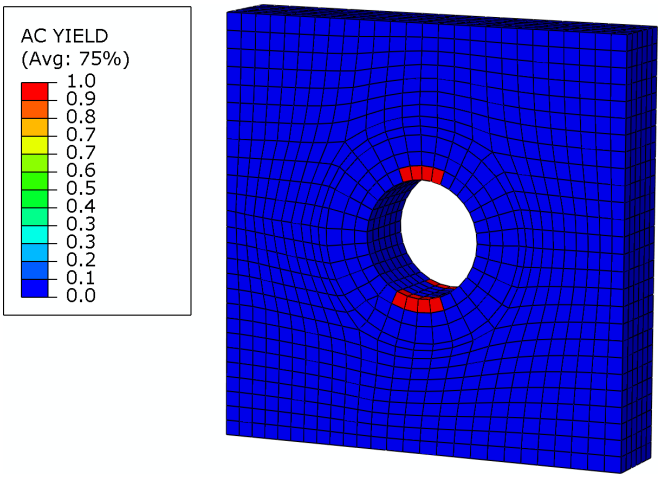

(b) Yield area

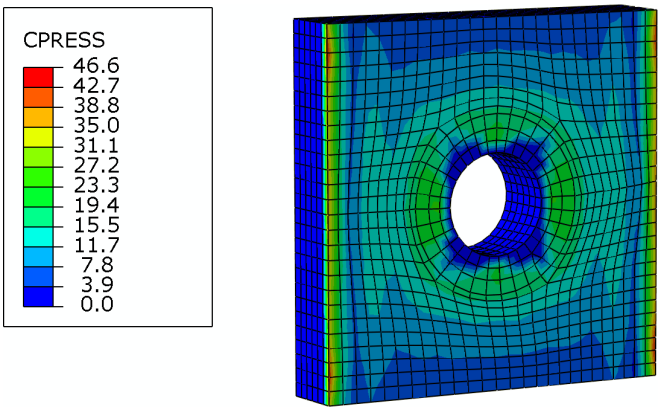

(c) Contact stresses

Figure B.14: FEM results for stresses in steel anchorage plate

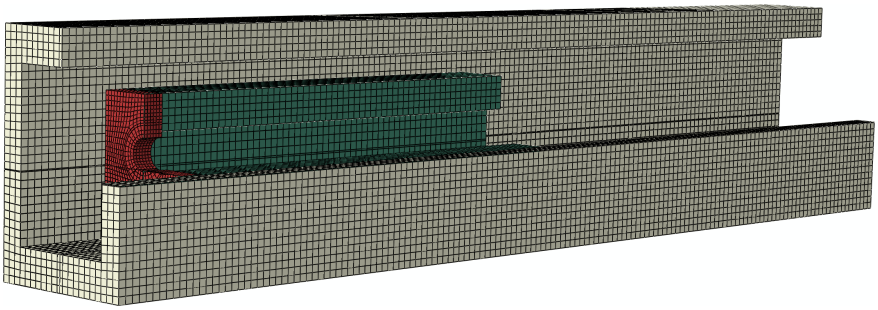

(a) Model

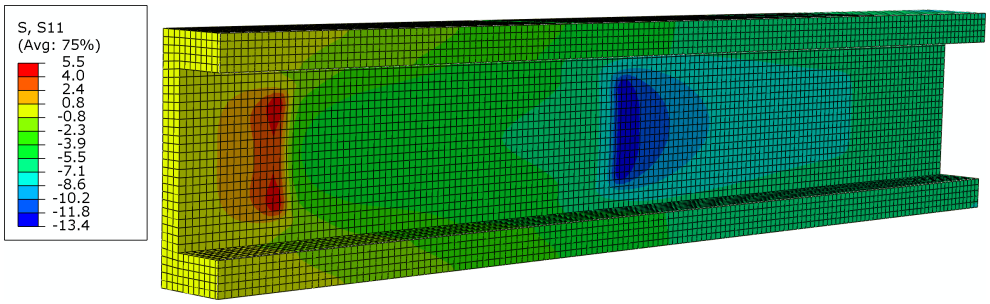

(b) Parallel to grain stresses

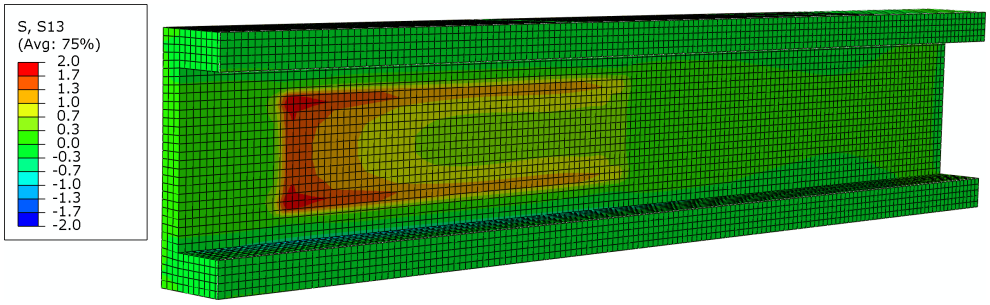

(c) Shear stresses in glueline

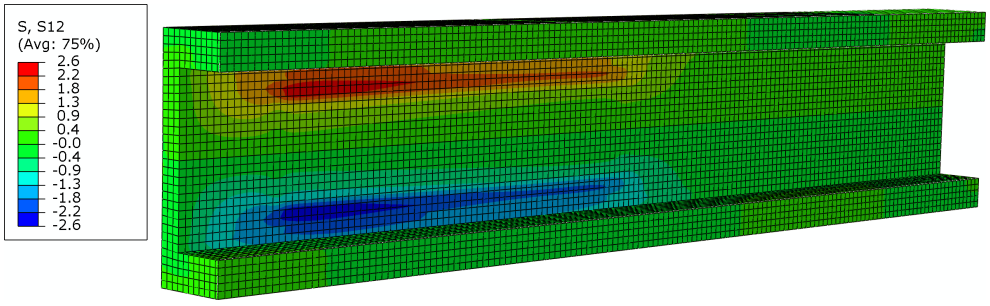

(d) Shear stresses in web

Figure B.15: Double length anchorage block

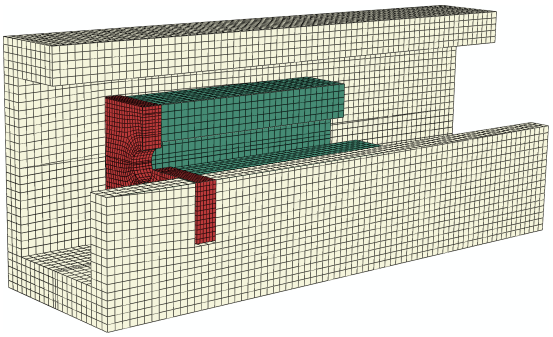

(a) Model

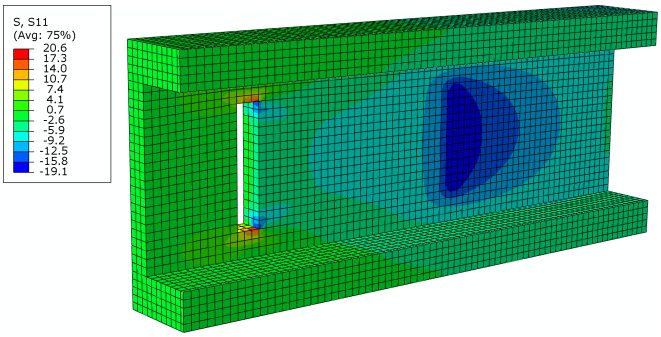

(b) Parallel to grain stresses

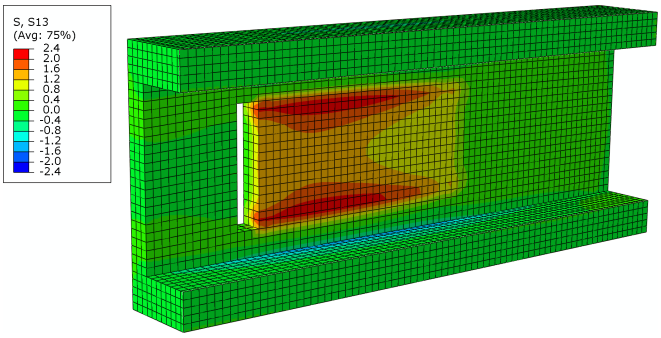

(c) Shear stresses in glueline

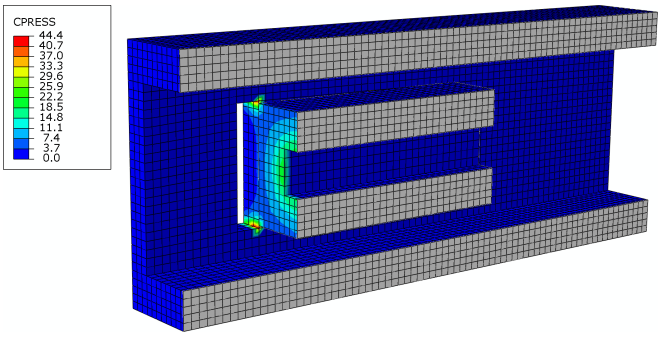

(d) Contact stresses

Figure B.16: Wider anchorage plate

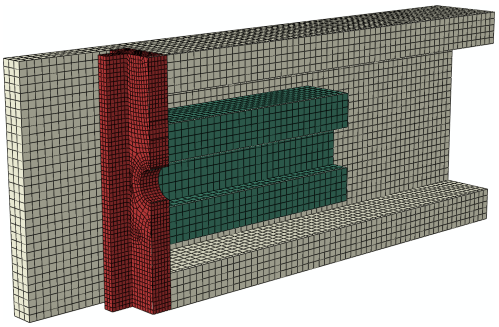

(a) Model

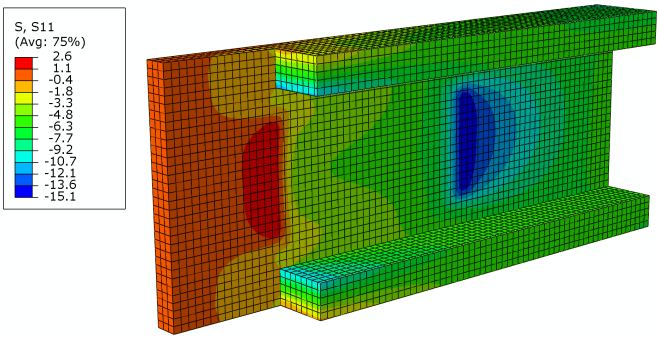

(b) Parallel to grain stresses

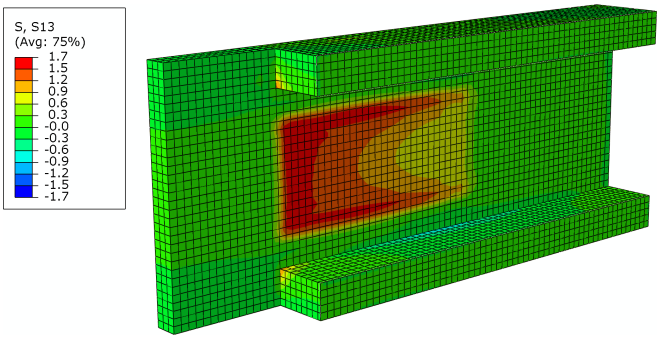

(c) Shear stresses in glueline

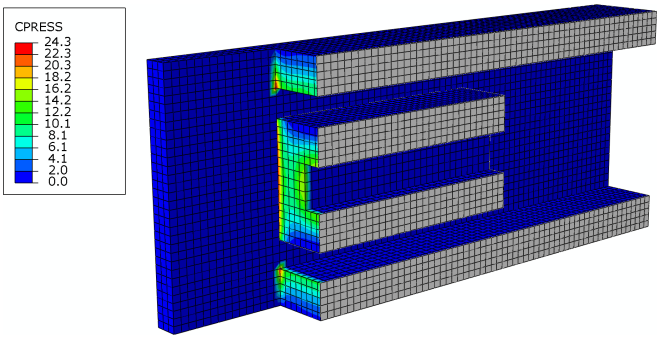

(d) Contact stresses

Figure B.17: Higher anchorage plate

2.6MPa, compared to 3.8MPa for the shorter block. It is not shown in the figure, but also the tension perpendicular to grain stresses in the anchorage block are reduced to 1.6MPa This shows that all stresses are reduced compared to the shorter block and the strength of this anchorage block will be significantly larger.

Figure B.16 shows the model with an wider anchorage plate which is also bearing directly on the webs of the beam. It can be seen that this results in stress concentrations in the corners of the anchorage plate and that there are very low contact stresses over most of the area of the web. The shear stresses in the glueline are reduced to 2.4MPa, but large localized shear stresses of 5.1MPa occur in the web.

Figure B.17 shows the model with an higher anchorage plate which is also bearing on the top and bottom flanges of the beam. In order to achieve any stresses into the flanges the plate needed to be stiffened by two 60x20mm stiffeners. With those stiffeners there is up to 15MPa contact stress in the flanges. Shear stresses in the glueline are reduced to 1.7MPa. The efficiency of this anchorage system can be further improved by increasing the height of the timber anchorage block or even making it solid and glueing it to the top and bottom flange as well.

An overview of stresses is given in Table B.1. From this table it can be seen that the higher anchorage plate reduces the shear stresses in the glueline the most, followed by the longer anchorage block. The wider anchorage plate reduces shear stresses in the glueline, but creates stress concentrations and increases shear stresses in the web. The longer anchorage block almost halves the perpendicular to grain stresses in the anchorage block, resulting in a smaller amount of screws which are needed to prevent splitting. Both the longer anchorage block and the higher anchorage plate are efficient designs and a choice between these two will be mainly based on cost efficiency and ease of manufacturing.

Table B.1: Overview of stresses (MPa) for different anchorage models

Model	Length (mm)	In web				In anchorage block	
		Shear glueline	Shear web	Par. to grain	Perp. to grain	Contact	Perp. to grain
Benchmark	600	3.2	3.8	8.3	19.4	38.2	3.0
Longer block	1200	2.0	2.6	5.5	13.4	28.1	1.6
Wider plate	600	2.4	5.1	20.6	19.1	44.4	2.8
Higher plate	600	1.7	2.1	2.6	15.1	24.3	2.1

Stress concentrations In order to avoid stress concentrations at the edges of the anchorage block, as shown by numerical modelling in Figure B.13a and B.14c, a gap should be allowed for between the side of the steel plate and the side of the web (Figure B.18). This is due to the fact that the side of the timber anchorage block is supported by the webs. Therefore the stiffness of these sides is very high. When the steel anchorage plate is tightly fit between the webs (as in Figure B.7, which is not a good example), high stress concentrations occur at the edges of the steel plate. The size of the gap depends on size of anchorage plate and stiffness differences between timber anchorage block and web.

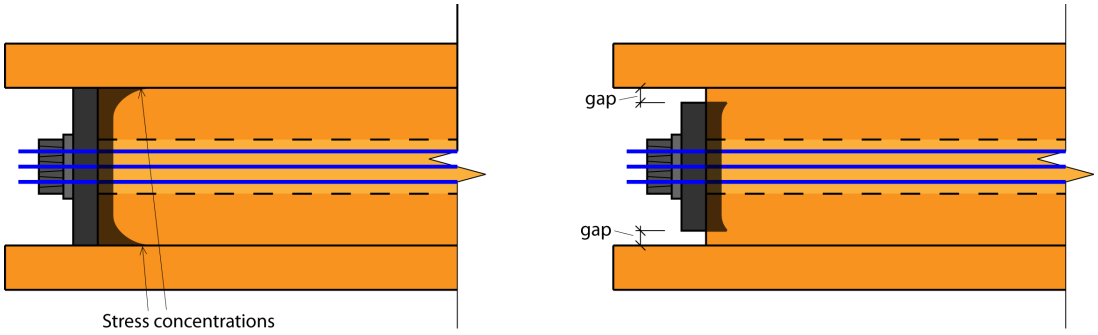

Figure B.18: Top view of anchorage showing allowance for gap between anchorage plate and side of the webs in order to minimize stress concentrations

B.2.4 Summary

Experimental testing of anchorage blocks has shown that the connection between a timber anchorage block and the webs of a box beam is best to be a glued connection. Screwed connections are possible, but not practical due to the large number of screws. It was found that a 600mm long anchorage block resisted 1100kN, which was close to the expected load during experimental testing. Therefore numerical models were made of solutions which could potentially increase the strength of the anchorage system. These models showed that increasing the length of the anchorage block was very effective in reducing stresses in the timber. Alternatively also increasing the height of the anchorage block and adding stiffeners to the steel plate was found to be an acceptable alternative. Increasing the width of the anchorage block led to stress concentrations and was not recommended.

B.3 Anchorages on columns

A short study has been performed in the design of anchorages on columns for beam-column connection testing (Section A.2) and frame testing (Section A.3). The study is based on a post-tensioning force of 450kN which is excreted on a steel anchorage plate with a width of 300mm. This force needs to be transferred into the timber column perpendicular to grain. This section evaluates four different designs in order to calculate the height and the thickness of the anchorage plate, which is required to spread the out the force such that the maximum steel stress and the maximum compressive stress perpendicular to the grain in the timber are not exceeded.

1. Analytical model with an triangular stress distribution
2. Analytical model of an infinite beam on elastic foundation
3. 2D FEM model
4. 3D FEM model

If a maximum allowable bearing stress of 6MPa is considered (which includes a load duration factor of 0.6), then an area of at least 75000mm^2 is needed. This would result in a plate height of about 300mm, taking into account the gap of 180 x 90mm in the column for the PT cables to pass through. Since there is not a constant stress distribution, the plate needs to be larger. A first approximation for the height of the plate of 400mm and a thickness of 35mm is made.

Simplified 2D analytical model

The first model is to assume a 2D model of the plate with a (assumed) trapezoidal stress distribution in the column, as shown in Figure B.19. As the anchorage plate is symmetrical, the centre of the plate has been fixed and half hte plate height is modelled as a cantilever. The centre of the plate is loaded by the post-tensioning force, F_{pt} = 450kN, and this stress is resisted by the trapezoidal stress distribution, resulting in a maximum compressive stress in the timber of 5.6MPa, which below the limit of 6MPa. This stress distribution results in a bending moment of 17kNm in the steel plate. In the 35mm thick plate this results in bending stresses of 278MPa.

These values also follow from a framework analysis program, as can be seen in Figure B.19. It also shows a deformation of 0.5mm of the steel plate.

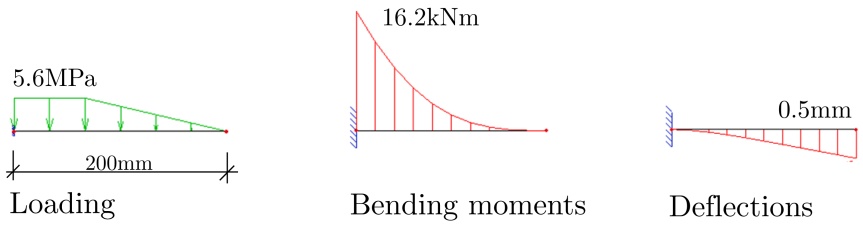

Figure B.19: Framework analysis verification of moment and deflection of anchorage plate

2D Elastic supported beam

A more realistic way of stress distribution is found by approximating the plate as an infinite beam on an elastic support (Bouma, 2000), as shown in Figure B.20. The displacement w is given in Equation B.2. This can be solved using boundary conditions and results in the analytical expressions as given in Equations B.3 (Bouma, 2000). The equations for the displacement and moment distribution result in the graphs as shown in Figure B.20. It must be noted that a length of at least 590mm (on either side, so total length of 1180mm) is needed for the theory of the infinite beam to be valid. This is much more then the dimensions of the plate, but the method is still used for comparison as it is a relatively simple method to use.

$$w = e^{-\beta x} x(C_1 cos\beta x + C_2 sin\beta x) \tag{B.2}$$

$$\begin{aligned} w &= \frac{P\beta\sqrt{2}}{k} e^{-\beta x} sin(\beta x + \frac{\pi}{4}) \\ \phi &= \frac{dw}{dx} = -\frac{2P\beta^2}{k} e^{-\beta x} sin\beta x \\ M &= -\frac{P}{\beta\sqrt{2}} e^{-\beta x} sin(\beta x - \frac{\pi}{4}) \\ V &= P e^{-\beta x} sin(\beta x - \frac{\pi}{2}) \end{aligned} \tag{B.3}$$

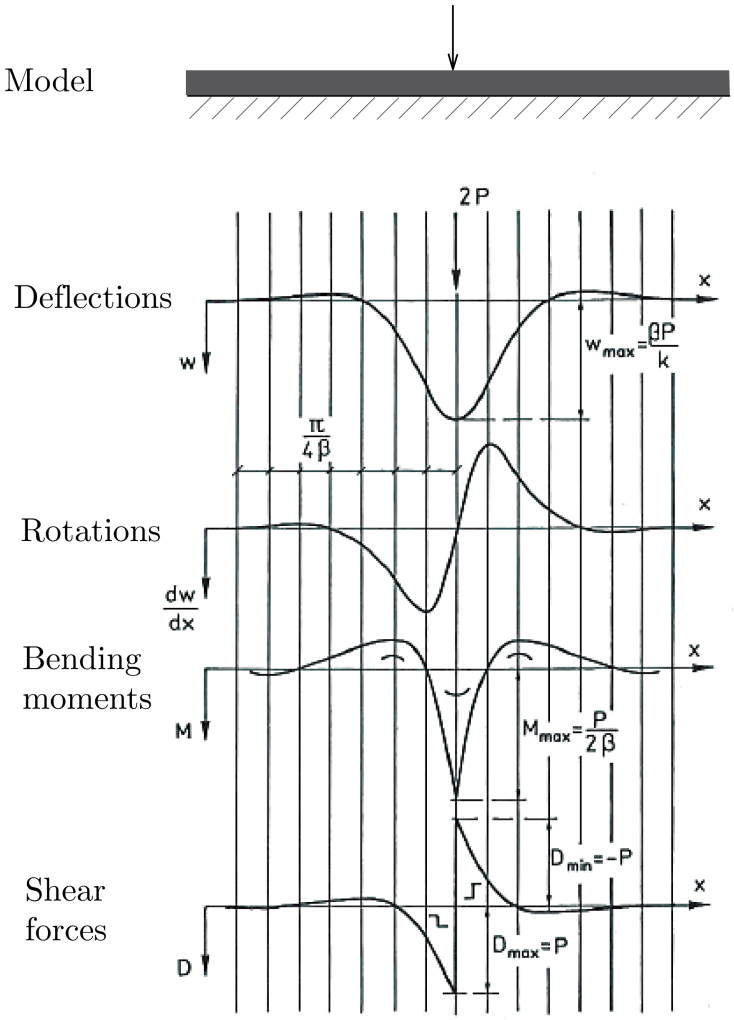

Figure B.20: Beam on elastic support loaded by point load (Bouma, 2000)

The following parameters are used in Equations B.3:

- $4\beta^4 = \frac{k}{E_{steel}I}$
- $k = \frac{bE_{perp}}{h}$
- $E_{perp} = 500\text{MPa}$
- $E_{steel} = 210000\text{MPa}$
- $b = 300\text{mm}$
- $t = 35\text{mm}$
- $I = \frac{1}{12}bt^3 = \frac{1}{12} \cdot 300 \cdot 35^3 = 1072000\text{mm}^4$

Only the depth of the column h has to be determined. It is unlikely that the

whole column depth will feel the influence of the loading. Studies into the bearing strength of timber (Leijten et al., 2010, 2012) suggested an effective height and effective length, where $h_e = 0.35h < 140$mm, which in the case of a 500mm deep column is 140mm. It must be noted that these formulas were derived for significantly smaller specimens and with a significant indentation.

Using $h = 140mm$ one can find:

- $k = 300 \cdot 500/140 = 1070$
- $\beta = 0.00587$

At x = 0 this gives the following values:

- w = 1.23mm
- ϕ = 0rad
- M = 19kNm
- V = 225kN

The maximum moment of 19kNm results in a steel stress of 313N/mm^2, which is past the yield strength of steel. But the approximation of the point load is very conservative. In reality this force will be distributed over an area as shown in Figure B.21. For that loading scenario the maximum moment is 14kNm and the steel stress 230N/mm^2, which is acceptable. The corresponding deflections are 1.2mm.

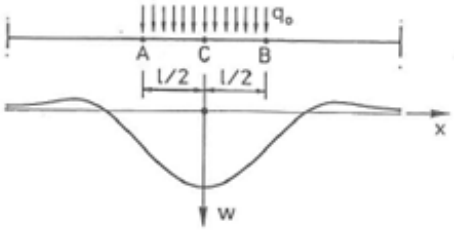

Figure B.21: Beam on elastic support with distributed load (Bouma, 2000)

2D Finite element model

A 2D FEM analysis is made in Abaqus CAE (Simulia, 2010) of a longitudinal slice of the column and anchorage plate (400 x 35mm). The beam was modelled with

a thickness of 1mm and was meshed with CPS4R plane stress elements. Contact between the steel plate and the timber column was modelled using general contact with rough friction behaviour. A 15MPa pressure load was modelled as over the middle 100mm of the anchorage plate. This represented the total post-tensioning force spread out over the full width of the plate. In reality the stress will be higher in the middle of the plate and non-existing towards the sides, but this could not be modelled in the 2D model.

Results of the model can be seen in Figure B.22. It can be seen that the timber perpendicular to grain stresses have a maximum of 4.6MPa. The maximum deflection of the anchorage plate is 2mm and the maximum steel stress is 145MPa.

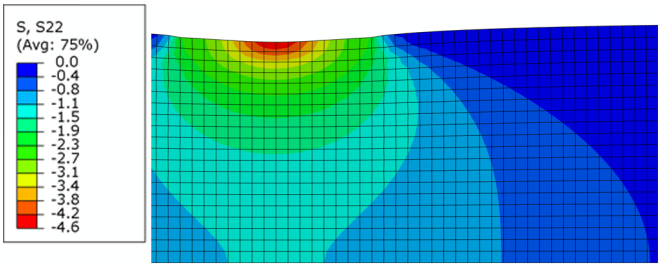

(a) Perpendicular to grain stresses

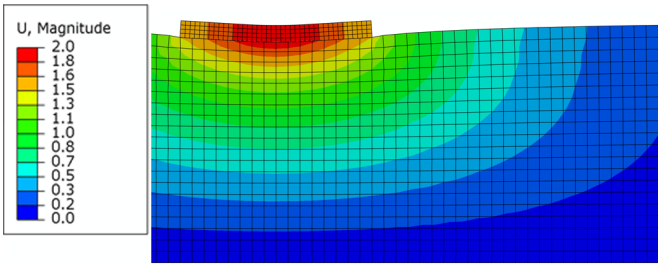

(b) Deflections

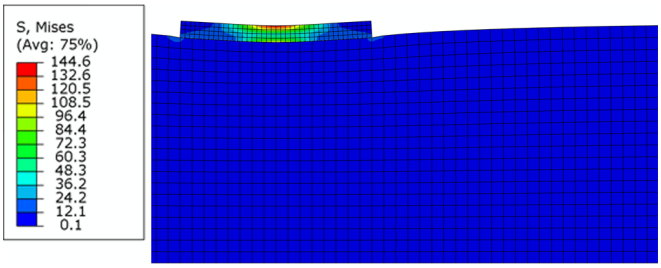

(c) Mises stresses

Figure B.22: Results of 2D FEM of anchorage plate

3D Finite element model

The most detailed model is a 3D finite element model made in Abaqus CAE (Simulia, 2010). The column is modelled along the full height of 3m (see Figure B.23), including the opening of 180x90mm for the post-tensioning tendons. The plate is modelled as a 3D member with a height of 400mm and a thickness of 35mm. A distributed load of 45MPa is applied over the centre section (100x100mm) of the plate, resulting in a total load of 450kN.

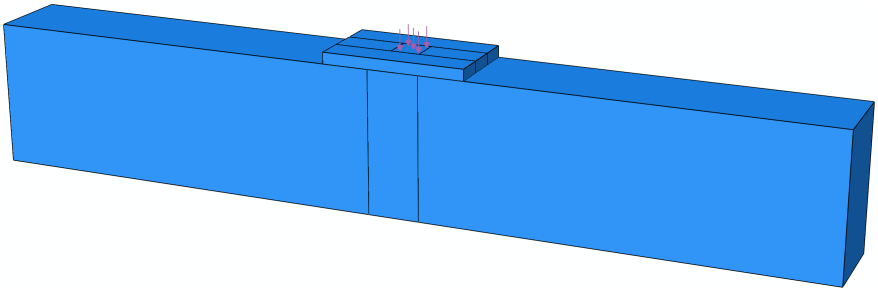

Figure B.23: 3D FEM model of column with anchorage plate

The column is supported on both ends and also over the area where the column would be in contact with the beam (which is not modelled). General contact is applied to let the plate and the column touch each other. The LVL has been modelled with engineering constants and $E_2 = E_{perp} = 500N/mm^2$ is used.

Figure B.24 shows the results of the 3D FEM model. The perpendicular to grain stress in the column are up to 7.1MPa around the opening for the tendons. The deflections are 1.6mm and the steel stresses 250MPa.

B.3.1 Comparison

Results of the four models are compared in Table B.2. It can be seen that the timber stresses are the highest in the 3D FEM model. The steel stresses are highest in the first analytical model, closely followed by the 3D FEM model. It can be seen that the steel and timber stresses are under predicted by the 2D FEM model. The second analytical model (beam on elastic foundation) does not result in stresses in the timber. From the table it can be concluded that the 3D FEM model is best to be used and that simplifications of the complex 3D stress field are under predicting the stresses in the timber.

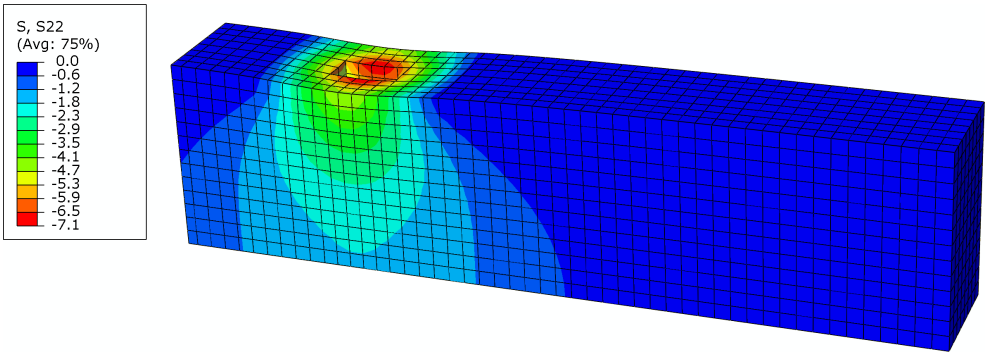

(a) Perpendicular to grain stresses

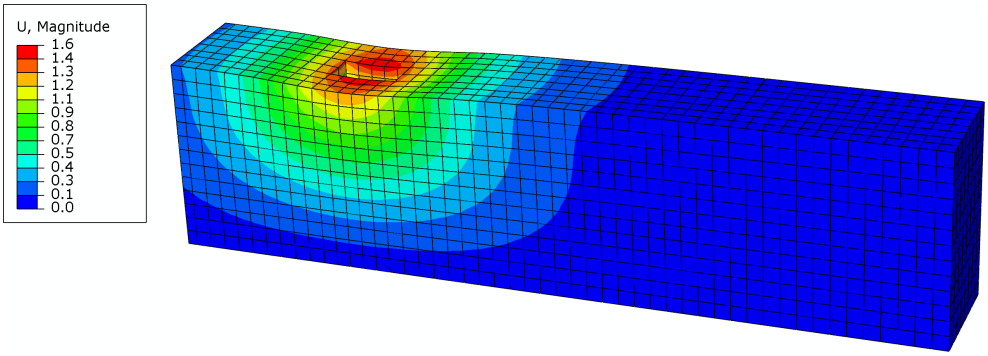

(b) Deflections

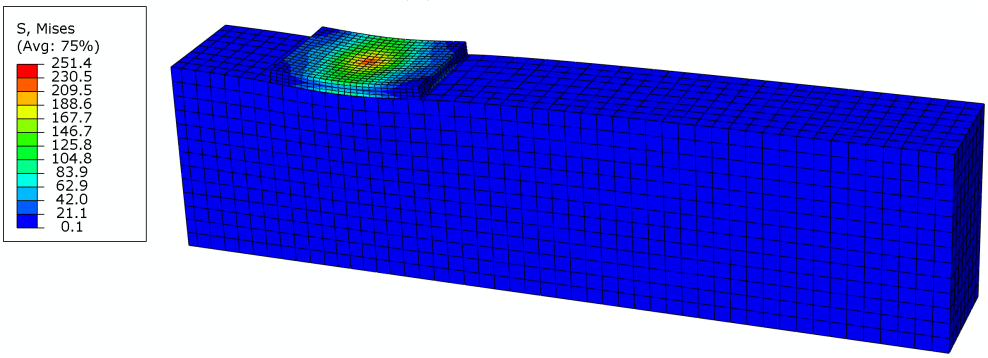

(c) Mises stresses

Figure B.24: Results of 3D FEM of anchorage plate

Table B.2: Comparison of different models to calculate stresses in column anchorages

Model	Method	Max. timber stress (MPa)	Max. deflection (mm)	Max. steel stress (MPa)
1	Analytical	5.6	0.5	278
2	Analytical	-	1.2	230
3	FEM 2D	4.6	2.0	145
4	FEM 3D	7.1	1.6	251

A final 3D FEM model was made of a 500mm long anchorage plate with a thickness of 40mm. This model resulted in timber stresses of 6.5MPa and maximum steel stresses of 170MPa. These levels were deemed appropriate for experimental testing.

B.4 Corbels

The vertical shear force at the beam-column connection needs to be transferred from the beam into the column. The post-tensioning generates a compression force at the connection which results in friction. Depending on the level of post-tensioning, this friction can resist the shear force. The New Zealand concrete design standard (Standards New Zealand, 2006c) does not allow the use of friction for shear transfer in post-tensioned connections. It can therefore be assumed that this is also not allowed for timber structures.

Testing of a two-storey post-tensioned timber building under seismic loading (Newcombe et al., 2010c) has led to an investigation of timber corbels fixed to the column using screws (Carradine et al., 2010). Testing showed a maximum load per connection between 47kN and 88kN. This was enough for the short spans and seismic loading, but in long-span beams under ultimate limit state vertical loading, different solutions are needed.

Inclined screws, installed at a 45 degree angle to the grain, has shown a significant increase in load-carrying capacity compared to screws placed under a 90 degree angle to the grain (Bejtka and Blass, 2002). This can possibly be used for an increased strength needed for gravity frames. Alternatively, the corbel can be glued to the column or a recess in the column can be created to place the beam onto. Another option is to use steel corbels, which can be screwed onto the column. The design of a steel corbel for experimental testing of the one-bay and two-bay frames (Chapter 6) is presented in the next section.

B.4.1 Corbel design for testing of frames

The maximum ULS vertical load on the beam was 440kN. The maximum post-tensioning force was estimated at 480kN, which was 400kN initial post-tensioning force and tendon elongation of 20%. This force gave an uplift at the deviators of 40kN, and a maximum shear force in the corbel of 180kN. As testing was also performed with lower post-tensioning forces, the design was performed with 200kN shear force.

The shear force needed to be transferred in compression perpendicular to grain at end of the beam. The conservative assumption was made that this force needed to be transferred through the webs only, due to stiffness differences

between flanges and webs. A corbel length of 150mm resulted in a compressive strength of the timber, $F_{c,t}$, as shown in Equation B.4.

$$F_{c,t} = l_{corbel} \cdot t_{flange} \cdot f_{c,perp} = 150 \cdot 90 \cdot 10 = 135kN \tag{B.4}$$

Placing screws in the webs helped to increase the load carrying capacity. It was possible to insert 6 screws with a diameter of 8mm given the spacing requirements. The design strength for each screw was 10kN, resulting in an increased capacity of 60kN. The combined strength of timber and screws was close to the conservative design force of 200kN.

A graphical representation of the forces acting on the corbel is shown in Figure B.25b. The vertical force of 200kN could be resisted by 2 rows of 6 10mm diameter screws with a length of 240mm placed under a 45° angle to the grain, as shown in Figure B.25a. These screws had a design tensile strength of 22kN each (SPAX, 2012a), resulting in a vertical component close to 200kN. As the screws were angled, also a horizontal component of 200kN was acting on the corbel. Furthermore, the eccentricity of the vertical shear force resulted in a moment of 19kNm. This moment was resisted by screws in tension close to the top of the corbel and timber and screws in compression at the bottom of the corbel. The horizontal forces due to the moment were 140kN. The screws in tension did not have to resist the full 140kN tensile force as the inclined screws also had a horizontal component of 100kN acting on the corbel. Therefore the screws in tension had to resist 40kN. This was easily achieved by 3 10mm diameter screws with a length of 240mm. The bottom of the corbel had two compression forces acting on it, 100kN from the inclined screws and 140kN from the moment. This compression force was split between two rows of screws and the timber.

Because the corbel was loaded by many forces a FEM was made as shown in Figure B.26. This model was used to determine the required thickness of steel. Steel was modelled as an elasto-plastic material with a yield strength of 300MPa. The model was loaded by a shear force of 200kN which was introduced as a pressure of 11MPa where flanges of the beam touched the corbel (150kN) and 4MPa where part of the web touched the corbel (50kN). This was done as most of the shear force will be introduced through the flanges and only a small part through the web. Holes for screws were modelled and these were given fully

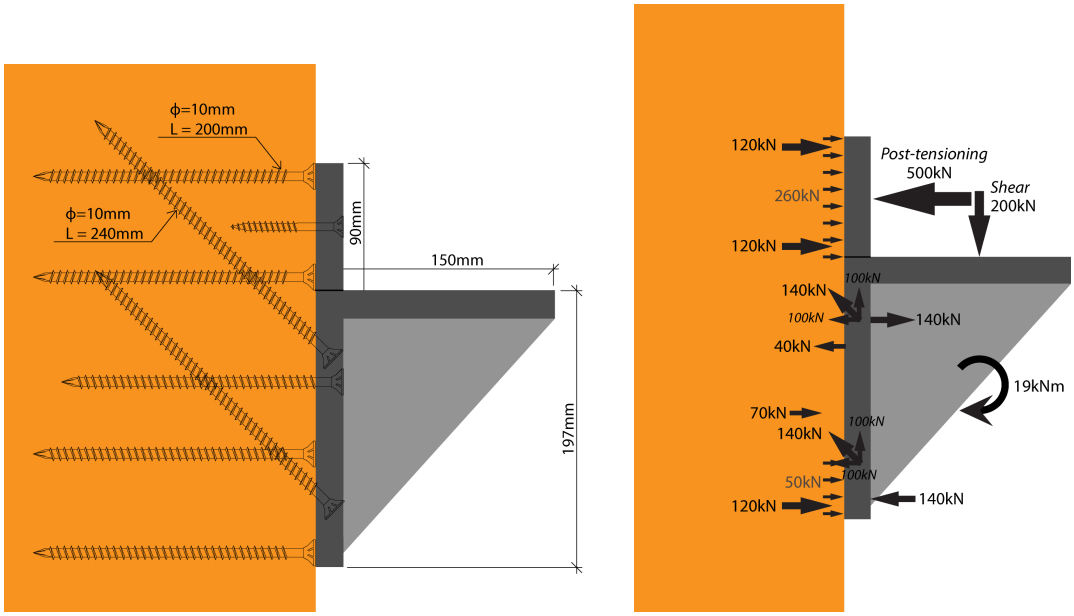

(a) Side view of corbel with screws (b) Forces acting on corbel

Figure B.25: Design of corbel and interface with screw reinforcement

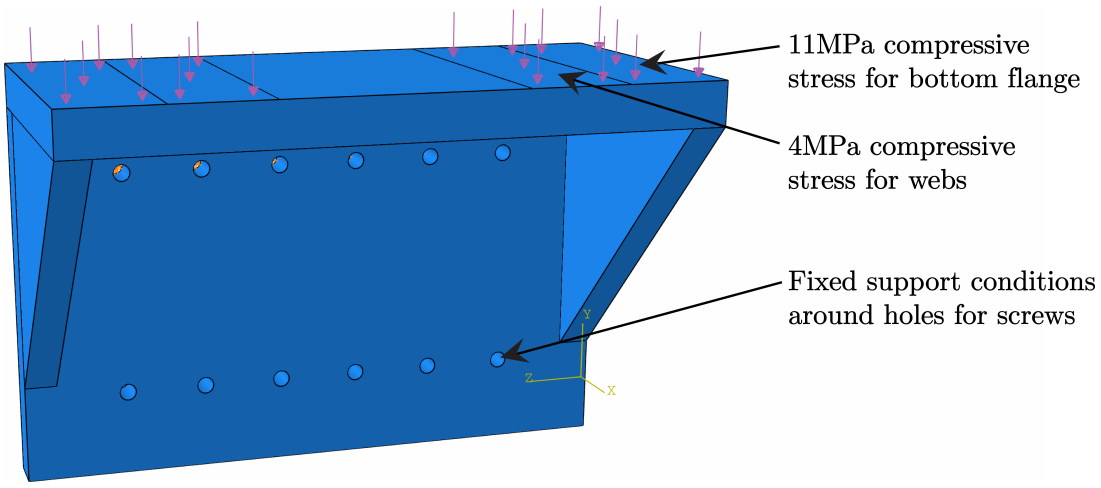

Figure B.26: Loading and boundary conditions of FEM of corbel

fixed boundary conditions. In reality the screws have some stiffness and the connection will not be fully fixed, this was not included in order to simplify the model. As a result stress concentrations around the holes were found, as can be seen in Figure B.27. The model showed that a steel thickness of 20mm was needed. This resulted in stresses close to or over 200MPa in large parts of the corbel. For thinner steel plates, the stiffener plates were very likely to buckle. Also, the recess in the back plate for countersinking the inclined screws with a diameter of 10mm needed to be at least 18mm.

B.4.2 Corbel stiffness

During testing without post-tensioning the stiffness of the connection with inclined screws between the steel corbel and the column was measured. Although not directly of interest when designing a timber frame under gravity loading, this information is of interest for seismic design where stiff connections are needed to connect steel dissipaters to timber members.

A total of twelve 10mm diameter screws with a length of 240mm were placed under a 45°angle to connect the corbel to the column, as shown in Figure 6.5c. The vertical shear force in the connection, which was resisted by the corbel, was directly related to the force in the hydraulic actuators. Displacements were measured using spring potentiometers placed at the bottom of the corbel. The load-displacement plots for the one-bay and two-bay frame can be seen in Figure B.28. The stiffness for the four instrumented corbels was 130, 111, 120 and 100kN/mm. This gave an average value of 115kN/mm, which was 9.6kN/mm per screw. The figure shows that unloading followed a different curve compared to loading and that a residual displacement of about 0.15mm to 0.20mm was present.

The stiffness of screw connections can be calculated with design equations given in Eurocode 5, EN 1995:2010 (CEN, 2004b), but only for dowel type fasteners. No guidance is given for inclined fasteners. In the European Technical Approval (ETA) of the screw manufacturer SPAX (SPAX, 2012b), a design equations for axial slip modulus for screws in softwood is given. The design equations are given in Equation B.5 for EC5 and Equation B.6 for SPAX ETA. The EC5 stiffness of 5.9kN/mm per screw in dowel action is 38% lower compared

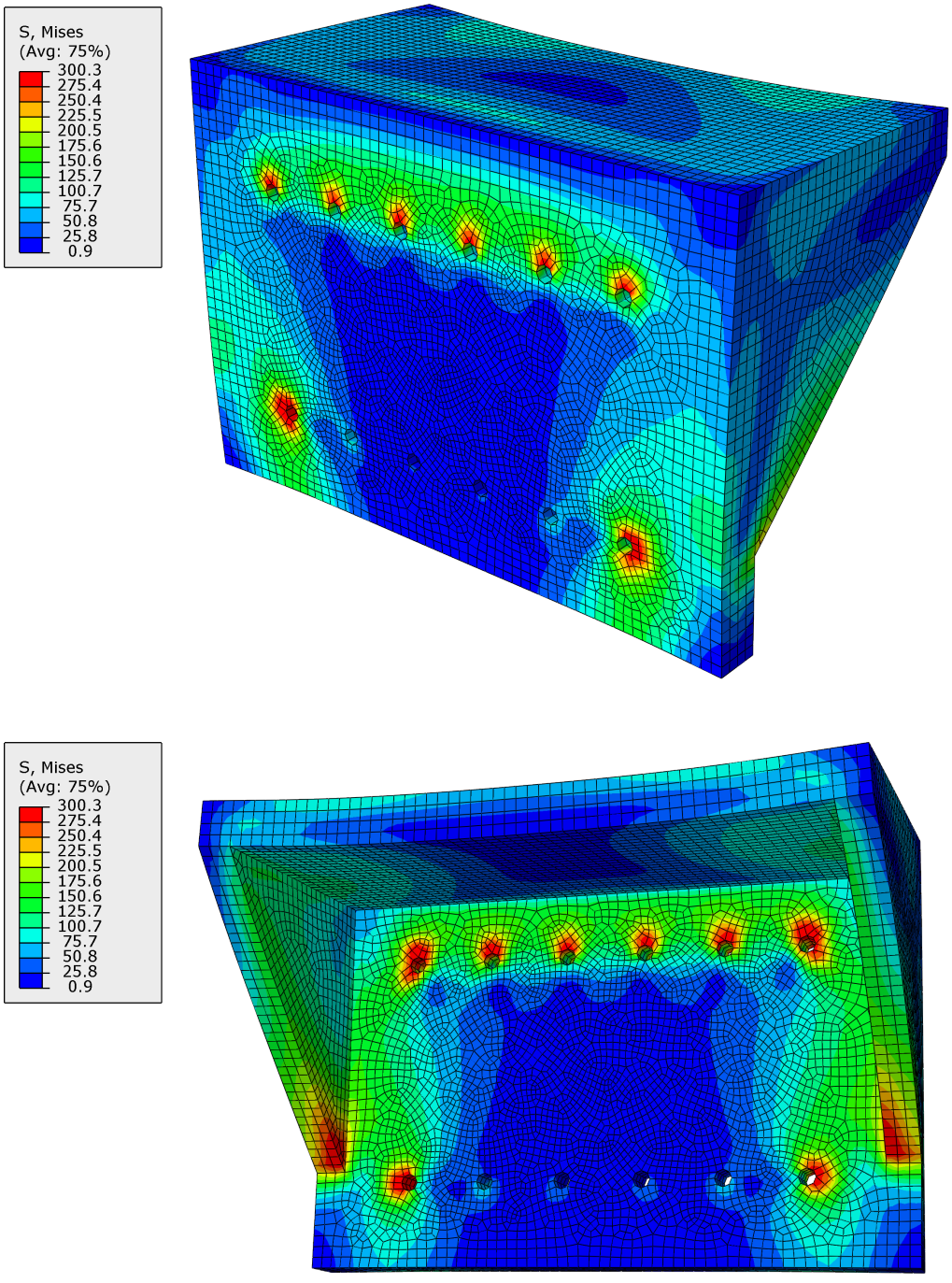

Figure B.27: Steel stresses in corbel under maximum design load

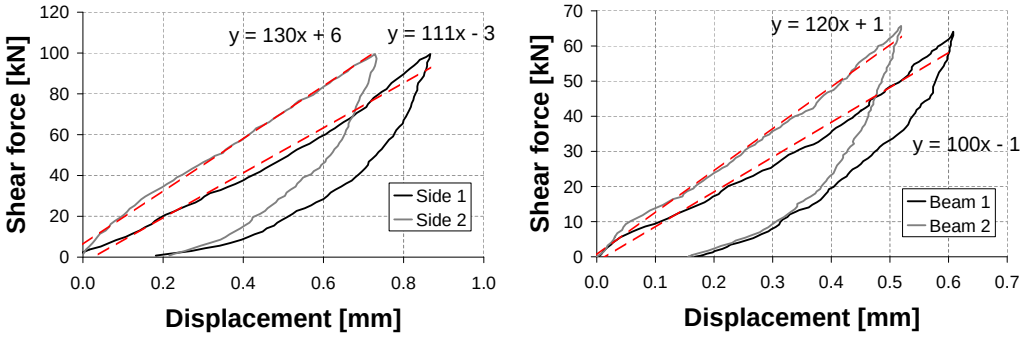

(a) One-bay frame (b) Two-bay frame

Figure B.28: Stiffness of inclined screw connection between corbel and column, red lines showing linear trend-lines during loading stage

to experimental results, whereas the stiffness of 10.5kN/mm for axial slip modulus as found using SPAX ETA is only 9% higher. Therefore it can be concluded that equations for stiffness of axial slip modulus predicts the stiffness of inclined screws in LVL better than equations of EC5 for stiffness of screws under dowel action.

$$K_{ser} = \rho^{1.5} d/23 = 570^{1.5} \cdot 10/23 = 5.9 kN/mm \tag{B.5}$$

$$K_{ser} = 780 d^{0.2} l_{ef}^{0.4} = 780 \cdot 10^{0.2} \cdot (240 - 30)^{0.4} = 10.5 kN/mm \tag{B.6}$$

Where:

- K_{ser} = Stiffness of screw (kN/mm)
- ρ = Density of timber, taken as $570 kg/m^3$
- d = Screw diameter (mm)
- l_{eff} = Effective length of screw (part in timber) (mm).

Appendix C

Experimental testing

This Appendix contains further data corresponding to Chapters 4 to 6.

It contains a list with data channels which were used in the data-logging software UDL. Technical drawings with the location of the instrumentation can be found in Appendix G. In the second part tables are presented with rotation data for experimental testing of the one-bay and two-bay frames.

C.1 Data channel lists

Beam testing

Table C.1: Data channel list beam testing

UDL	Box + CH	Instrument	Measuring
1	a1	Linear Pot	Beam shear 1 (left)
2	a2	Linear Pot	Beam shear 2 (left)
3	a3	Linear Pot	Beam shear 1 (right)
4	a4	Linear Pot	Beam shear 2 (right)
5	a5	Linear Pot	Spare
6	a6	Linear Pot	Spare
12	a12	Rotary Pot	Hydraulic Actuator B displ
13	a13	Rotary Pot	Deviator displacement (left)
14	a14	Rotary Pot	Mid-span displacement
15	a15	Rotary Pot	Deviator displacement (lright)
16	a16	Rotary Pot	Hydraulic Actuator A displ
17	r1	Inclinometer	Beam 2 rotations (right)
18	r2	Inclinometer	Beam 2 rotations (left)
19	r3	Inclinometer	Beam 3 rotations (right)
20	r4	Inclinometer	Beam 3 rotations (left)
21	r5	Inclinometer	Beam 4 rotations (right)
22	r6	Inclinometer	Beam 4 rotations (left)
33	L1	Strain gauge	Top of beam
34	L2	Strain gauge	Bottom of top flange
35	L3	Strain gauge	Centreline
36	L4	Strain gauge	Top of bottom flange
37	L5	Strain gauge	Bottom of beam
38	L6	Strain gauge	Spare
39	L7	Strain gauge	Spare
49	y1	Load cell	Hydraulic Actuator A
50	y2	Load cell	Hydraulic Actuator B
51	w1	Load cell	PT Beam 2
52	z1	Load cell	PT Beam 3
53	x1	Load cell	PT Beam 4
54	J	Trigger	
55	b2	Rotary Pot	Beam shortening

Beam-column connection testing

Table C.2: Data channel list connection testing

UDL	Box + CH	Instrument	Measuring
1	b1	Linear pot 183	Base plate
2	b2	Linear pot 184	Column rotation 1
3	b3	Linear pot 185	Column rotation 2
5	b5	Linear pot 187	Diagonal col 1
6	b6	Linear pot 188	Diagonal col 2
7	b7	Linear pot 205	Gap opening 1
8	b8	Linear pot 206	Gap opening 2
9	b9	Linear pot 207	Gap opening 3
10	b10	Linear pot 208	Beam rotation 1
11	b11	Linear pot 209	Beam rotation 1
13	b13	Spring pot 14	Indentation col. Top
14	b14	Spring pot 19a	Indentation col. Bottom
16	b16	Spring pot 18a	Diff. Col-Base
17	e1	Rotary pot	Top of column
18	e2	Rotary pot	Hydraulic actuator
19	e3	Linear pot 176	Horiz. Col. 1
20	e4	Linear pot 177	Horiz. Col. 2
21	e5	Linear pot 178	Vert. Col. 1
22	e6	Linear pot 179	Vert. Col. 2
33	v1	Load cell	Tendon 1
34	v2	Load cell	Tendon 2
35	u1	Load cell	Tendon 3
36	u2	Load cell	Tendon 4
37	x1	Load cell	PT Jack
41	w1	Load cell	Hydraulic actuator
44	z2	Load cell	Hold column

One-bay frame testing

Table C.3: Data channel list one-bay frame testing

UDL	Box + CH	Instrument	Measuring
1	a1	Linear pot	Gap opening Conn. 1 top
2	a2	Linear pot	Gap opening Conn. 1 bottom
3	a3	Linear pot	Interface Conn. 1 top (140mm)
4	a4	Linear pot	Interface Conn. 1 bottom (140mm)
5	a5	Linear pot	Interface Conn. 1 top (250mm)
6	a6	Linear pot	Interface Conn. 1 bottom (250mm)
7	a7	Linear pot	Joint panel shear 1 Column 1
8	a8	Linear pot	Joint panel shear 2 Column 1
9	a9	Linear pot	Beam shear 1
10	a10	Linear pot	Beam shear 2
11	a11	Spring pot	Corbel deflection Conn. 1
12	a12	Linear pot	-
13	a13	Linear pot	-
14	a14	Linear pot	-
15	a15	Linear pot	-
16	a16	Linear pot	-
17	b1	Linear pot	Beam mid-span Defl.
18	b2	Linear pot	-
19	b3	Linear pot	Beam deviator Defl. (Side Conn. 1)
20	b4	Linear pot	Beam deviator Defl. (Side Conn. 2)
21	b5	Linear pot	-
22	b6	Linear pot	-
23	b7	Linear pot	-
24	b8	Linear pot	-
25	b9	Linear pot	-
26	b10	Linear pot	-
27	b11	Rotary pot	Ram A displacement
28	b12	Rotary pot	Ram B displacement
29	b13	Linear pot	-
30	b14	Linear pot	-
31	b15	Linear pot	-
32	b16	Linear pot	-
33	c1	Linear pot	Gap opening Conn. 2 top
34	c2	Linear pot	Gap opening Conn. 2 bottom
35	c3	Linear pot	Interface Conn. 2 top (140mm)
36	c4	Linear pot	Interface Conn. 2 bottom (140mm)

Data channel list one-bay frame testing (continued)

UDL	Box + CH	Instrument	Measuring
37	c5	Linear pot	Interface Conn. 2 top (250mm)
38	c6	Linear pot	Interface Conn. 2 bottom (250mm)
39	c7	Linear pot	Joint panel shear 1 Column 2
40	c8	Linear pot	Joint panel shear 2 Column 2
41	c9	Linear pot	Beam shear 1
42	c10	Linear pot	Beam shear 2
43	c11	Spring pot	Corbel deflection Conn. 2
44	c12		-
45	c13		-
46	c14		-
47	c15		-
48	c16		-
49	r1	Inclinometer	Column 1
50	r2	Inclinometer	-
51	r3	Inclinometer	Column 3
52	r4	Inclinometer	Beam Conn. 1
53	r5	Inclinometer	-
54	r6	Inclinometer	-
55	r7	Inclinometer	Beam Conn. 2
56	R1	Strain gauge	Conn. 1 Top beam
57	R2	Strain gauge	Conn. 1 Bottom top flange (inside)
58	R3	Strain gauge	Conn. 1 Top bottom flange (inside)
59	R4	Strain gauge	Conn. 1 Bottom beam
60	R5	Strain gauge	Conn. 1 Bottom flange back 10mm
61	R6	Strain gauge	Conn. 1 Bottom flange back 33mm
62	R7	Strain gauge	Conn. 1 Bottom flange back 66mm
63	R8	Strain gauge	Conn. 1 Bottom flange back 80mm
64	M1	Strain gauge	Beam mid-span Top
65	M2	Strain gauge	Beam mid-span Centreline
66	M3	Strain gauge	Beam mid-span Bottom
67	Q1	Strain gauge	Conn. 2 Top beam
68	Q2	Strain gauge	Conn. 2 Bottom top flange (inside)
69	Q3	Strain gauge	Conn. 2 Top bottom flange (inside)
70	Q4	Strain gauge	Conn. 2 Bottom beam
71	Q5	Strain gauge	Conn. 2 Bottom flange back 10mm
72	Q6	Strain gauge	Conn. 2 Bottom flange back 33mm
73	Q7	Strain gauge	Conn. 2 Bottom flange back 66mm
74	Q8	Strain gauge	Conn. 2 Bottom flange back 80mm

Data channel list one-bay frame testing (continued)

UDL	Box + CH	Instrument	Measuring
75	L1	Strain gauge	-
76	L2	Strain gauge	-
77	L3	Strain gauge	-
78	L4	Strain gauge	-
79	L5	Strain gauge	-
80	u1	Load cell	Tendon 1
81	u2	Load cell	Tendon 2
82	v1	Load cell	Tendon 3
83	v2	Load cell	Tendon 4
84	w1	Load cell	Col. 1 Top
85	w2	Load cell	Col. 1 Bottom
86	x1	Load cell	-
87	x2	Load cell	-
88	y1	Load cell	Col. 3 Top
89	y2	Load cell	Col. 3 Bottom
90	z1	Load cell	Ram A
91	z2	Load cell	Ram B
92	J1	Trigger	
93	R9	Strain gauge	Conn. 1 Bottom flange front 0mm
94	R10	Strain gauge	Conn. 1 Bottom flange front 30mm
95	R11	Strain gauge	Conn. 1 Bottom flange front 60mm
96	R12	Strain gauge	Conn. 1 Bottom flange front 90mm
97	Q9	Strain gauge	Conn. 2 Bottom flange front 0mm
98	Q10	Strain gauge	Conn. 2 Bottom flange front 30mm
99	Q11	Strain gauge	Conn. 2 Bottom flange front 60mm
100	Q12	Strain gauge	Conn. 2 Bottom flange front 90mm

Two-bay frame testing

Table C.4: Data channel list two-bay frame testing

UDL	Box + CH	Instrument	Measuring
1	a1	Linear pot	Gap opening Conn. 1 top
2	a2	Linear pot	Gap opening Conn. 1 bottom
3	a3	Linear pot	Interface Conn. 1 top (140mm)
4	a4	Linear pot	Interface Conn. 1 bottom (140mm)
5	a5	Linear pot	Interface Conn. 1 top (250mm)
6	a6	Linear pot	Interface Conn. 1 bottom (250mm)
7	a7	Linear pot	Joint panel shear 1 Column 1
8	a8	Linear pot	Joint panel shear 2 Column 1
9	a9	Linear pot	Beam 1 Shear 1
10	a10	Linear pot	Beam 1 Shear 2
11	a11	Spring pot	Corbel deflection Conn. 1
12	a12	Linear pot	Beam 1 deviator Defl. (Side Conn. 1)
13	a13	Linear pot	Beam 1 mid-span Defl.
14	a14	Linear pot	Beam 1 deviator Defl. (Side Conn. 2)
15	a15	Linear pot	Beam 1 centerline compression Conn. 1
16	a16	Linear pot	-
17	b1	Linear pot	Gap opening Conn. 3 top
18	b2	Linear pot	Gap opening Conn. 3 bottom
19	b3	Linear pot	Interface Conn. 3 top (250mm)
20	b4	Linear pot	Interface Conn. 3 bottom (250mm)
21	b5	Linear pot	Interface Conn. 2 top (250mm)
22	b6	Linear pot	Interface Conn. 2 bottom (250mm)
23	b7	Linear pot	Gap opening Conn. 2 top
24	b8	Linear pot	Gap opening Conn. 2 bottom
25	b9	Linear pot	Joint panel shear 1 Column 2
26	b10	Linear pot	Joint panel shear 2 Column 2
27	b11	Rotary pot	Ram A displacement
28	b12	Rotary pot	Ram B displacement
29	b13	Linear pot	Beam 1 centerline compression Conn. 2
30	b14	Linear pot	-
31	b15	Linear pot	-
32	b16	Linear pot	-
33	c1	Linear pot	Gap opening Conn. 4 top
34	c2	Linear pot	Gap opening Conn. 4 bottom
35	c3	Linear pot	Interface Conn. 4 top (140mm)
36	c4	Linear pot	Interface Conn. 4 bottom (140mm)

Data channel list two-bay frame testing (continued)

UDL	Box + CH	Instrument	Measuring
37	c5	Linear pot	Interface Conn. 4 top (250mm)
38	c6	Linear pot	Interface Conn. 4 bottom (250mm)
39	c7	Linear pot	Joint panel shear 1 Column 3
40	c8	Linear pot	Joint panel shear 2 Column 3
41	c9	Linear pot	Beam 2 Shear 1
42	c10	Linear pot	Beam 2 Shear 2
43	c11	Spring pot	Corbel deflection Conn. 4
44	c12	Rotary pot	Beam 2 mid-span Defl.
45	c13		-
46	c14		-
47	c15		-
48	c16		-
49	r1	Inclinometer	Column 1
50	r2	Inclinometer	Column 2
51	r3	Inclinometer	Column 3
52	r4	Inclinometer	Beam Conn. 1
53	r5	Inclinometer	Beam Conn. 2
54	r6	Inclinometer	Beam Conn. 3
55	r7	Inclinometer	Beam Conn. 4
56	R1	Strain gauge	Conn. 1 Top beam
57	R2	Strain gauge	Conn. 1 Top bottom flange (inside)
58	R3	Strain gauge	Conn. 1 Bottom beam
59	R4	Strain gauge	Column 1 base back side
60	R5	Strain gauge	Column 1 base front side
61	M1	Strain gauge	Beam 1 mid-span Top
62	M2	Strain gauge	Beam 1 mid-span Centreline
63	M3	Strain gauge	Beam 1 mid-span Bottom
64	P1	Strain gauge	Conn. 2 Top beam
65	P2	Strain gauge	Conn. 2 Top bottom flange (inside)
66	P3	Strain gauge	Conn. 2 Bottom beam
67	P4	Strain gauge	Column 2 base back side
68	P5	Strain gauge	Column 2 base front side
69	P6	Strain gauge	Conn. 3 Top beam
70	P7	Strain gauge	Conn. 3 Top bottom flange (inside)
71	P8	Strain gauge	Conn. 3 Bottom beam
72	L1	Strain gauge	Beam 2 mid-span Top
73	L2	Strain gauge	Beam 2 mid-span Centreline
74	L3	Strain gauge	Beam 2 mid-span Bottom

Data channel list two-bay frame testing (continued)

UDL	Box + CH	Instrument	Measuring
75	Q1	Strain gauge	Conn. 4 Top beam
76	Q2	Strain gauge	Conn. 4 Top bottom flange (inside)
77	Q3	Strain gauge	Conn. 4 Bottom beam
78	Q4	Strain gauge	Column 3 base back side
79	Q5	Strain gauge	Column 3 base front side
80	u1	Load cell	Tendon 1
81	u2	Load cell	Tendon 2
82	v1	Load cell	Tendon 3
83	v2	Load cell	Tendon 4
84	w1	Load cell	Col. 1 Top
85	w2	Load cell	Col. 1 Bottom
86	x1	Load cell	Col. 2 Top
87	x2	Load cell	-
88	y1	Load cell	Col. 3 Top
89	y2	Load cell	Col. 3 Bottom
90	z1	Load cell	Ram A
91	z2	Load cell	Ram B
92	J1	Trigger	Trigger

C.2 Rotation data frames

Tables C.5 to C.9 show rotations for the one-bay frame for testing with 0, 100, 200, 300 and 400kN post-tensioning forces, respectively. Rotations for every test are taken at 30mm mid-span deflection and at a vertical load of 200kN acting on the beam. Both external connections are listed. Shown are column rotation, joint panel shear deformation, interface compression and gap opening. These four are summed together and compared with the measured beam rotation. The difference between the sum and the measured beam rotation is shown in the last two rows. It can be seen that there is a good agreement for measured beam rotations and the sum of the four rotational components for Tests 1 and 2. For the other tests the four rotational components together are between 25% and 35% more than the measured beam rotations. It is unclear where this difference comes from.

Table C.5: Rotations (mrad) measured on one-bay frame in Test 1: PT = 0kN

	30mm mid-span deflection		200kN vertical load	
	Conn 1	Conn 2	Conn 1	Conn 2
Column	0.22	0.18	0.67	0.79
Joint panel	0.22	-0.02	0.31	0.13
Interface	0.49	0.22	0.47	0.35
Gap	9.09	8.74	20.87	20.75
SUM	10.02	9.11	22.31	22.02
Beam	8.93	9.19	21.02	21.48
Difference	-1.10	0.08	-1.29	-0.54
	-11%	1%	-6%	-2%

Table C.6: Rotations (mrad) measured on one-bay frame in Test 2: PT = 100kN

	30mm mid-span deflection		200kN vertical load	
	Conn 1	Conn 2	Conn 1	Conn 2
Column	1.33	1.59	2.00	2.12
Joint panel	1.08	1.10	1.38	1.51
Interface	1.71	0.81	1.48	1.06
Gap	4.34	5.81	11.54	12.98
SUM	8.45	9.31	16.40	17.67
Beam	8.02	8.19	15.71	16.05
Difference	-0.43	-1.11	-0.69	-1.62
	-5%	-12%	-4%	-9%

Table C.7: Rotations (mrad) measured on one-bay frame in Test 3: PT = 200kN

	30mm mid-span deflection		200kN vertical load	
	Conn 1	Conn 2	Conn 1	Conn 2
Column	2.44	1.85	2.89	2.20
Joint panel	2.04	2.07	2.28	2.38
Interface	2.84	1.30	2.86	1.52
Gap	1.90	3.57	5.62	7.33
SUM	9.22	8.79	13.65	13.43
Beam	6.78	7.31	11.07	11.40
Difference	-2.44 -26%	-1.48 -17%	-2.58 -19%	-2.03 -15%

Table C.8: Rotations (mrad) measured on one-bay frame in Test 4: PT = 300kN

	30mm mid-span deflection		200kN vertical load	
	Conn 1	Conn 2	Conn 1	Conn 2
Column	3.11	2.82	3.33	3.09
Joint panel	2.81	3.06	2.97	3.18
Interface	2.40	1.62	2.46	1.74
Gap	1.05	2.02	2.73	3.83
SUM	9.37	9.52	11.48	11.84
Beam	6.44	6.75	8.70	8.86
Difference	-2.93 -31%	-2.77 -29%	-2.78 -24%	-2.99 -25%

Table C.9: Rotations (mrad) measured on one-bay frame in Test 5: PT = 400kN

	30mm mid-span deflection		200kN vertical load	
	Conn 1	Conn 2	Conn 1	Conn 2
Column	3.96	2.55	3.96	2.55
Joint panel	3.41	3.58	3.41	3.58
Interface	2.28	1.84	2.28	1.84
Gap	0.38	1.32	0.38	1.32
SUM	10.03	9.30	10.03	9.30
Beam	6.40	6.62	6.40	6.62
Difference	-3.62 -36%	-2.68 -29%	-3.62 -36%	-2.68 -29%

Tables C.10 to C.13 show rotations for the two-bay frame for testing with 0, 100, 200 and 300kN post-tensioning forces, respectively. Rotations for every test are taken at 20mm mid-span deflection and at a vertical load of 130kN acting on the beam. All four connections, external Connections 1 and 4 and internal Connections 2 and 3, are listed. Shown are column rotation, joint panel shear deformation, interface compression and gap opening. These four are summed together and compared with the measured beam rotation. The difference between the sum and the measured beam rotation is shown in the last two rows. It can be seen that differences are generally small, below 1.6mrad. This shows that all rotation components were accurately measured and together added to total beam rotation.

Table C.10: Rotations (mrad) measured on two-bay frame in Test 1a: PT = 0kN

	SLS: 20mm mid-span deflection				ULS: 130kN vertical load			
	External Conn 1	Internal Conn 2	Internal Conn 3	External Conn 4	External Conn 1	Internal Conn 2	Internal Conn 3	External Conn 4
Column	0.44	-0.11	0.11	-1.32	0.67	-0.11	0.11	2.91
Joint panel	0.19	-0.01	-0.01	0.06	0.25	0.01	-0.01	-0.06
Interface	0.01	0.01	-0.03	0.02	0.80	0.19	-0.11	0.03
Gap	8.41	9.04	8.86	10.57	16.67	18.27	19.09	22.40
SUM	9.05	8.92	8.92	9.33	18.38	18.58	19.11	25.28
Beam	9.04	9.18	9.29	9.30	18.08	18.47	18.87	19.37
Difference	-0.01	0.26	0.36	-0.03	-0.30	-0.11	-0.24	-5.91
	0%	3%	4%	0%	-2%	-1%	-1%	-23%

Table C.11: Rotations (mrad) measured on two-bay frame in Test 2a: PT = 100kN

	SLS: 20mm mid-span deflection				ULS: 130kN vertical load			
	External Conn 1	Internal Conn 2	Internal Conn 3	External Conn 4	External Conn 1	Internal Conn 2	Internal Conn 3	External Conn 4
Column	0.89	-0.44	0.44	1.50	1.11	-0.44	0.44	1.50
Joint panel	1.17	0.07	-0.07	1.30	1.26	0.06	-0.06	1.37
Interface	3.40	2.02	1.43	3.25	3.53	2.15	1.53	3.37
Gap	2.96	5.84	7.09	3.58	4.45	7.48	8.74	5.06
SUM	8.43	7.49	8.90	9.63	10.36	9.24	10.66	11.30
Beam	7.68	8.04	9.09	8.30	9.38	9.86	10.97	10.18
Difference	-0.75	0.56	0.19	-1.33	-0.98	0.61	0.31	-1.12
	-9%	7%	2%	-14%	-9%	7%	3%	-10%

Table C.12: Rotations (mrad) measured on two-bay frame in Test 3a: PT = 200kN

	SLS: 20mm mid-span deflection				ULS: 130kN vertical load			
	External Conn 1	Internal Conn 2	Internal Conn 3	External Conn 4	External Conn 1	Internal Conn 2	Internal Conn 3	External Conn 4
Column	3.11	-0.56	0.56	2.56	2.89	-0.56	0.56	2.38
Joint panel	1.81	0.22	-0.22	1.93	1.68	0.22	-0.22	1.82
Interface	3.83	3.30	3.21	3.63	3.04	3.17	3.05	2.72
Gap	-0.05	3.56	4.08	0.76	0.20	2.59	3.11	0.81
SUM	8.71	6.52	7.63	8.88	7.81	5.43	6.49	7.73
Beam	7.23	7.36	8.10	7.64	6.22	6.23	6.92	6.75
Difference	-1.47 -17%	0.84 13%	0.47 6%	-1.24 -14%	-1.60 -20%	0.80 15%	0.43 7%	-0.98 -13%

Table C.13: Rotations (mrad) measured on two-bay frame in Test 4a: PT = 300kN

	SLS: 20mm mid-span deflection				ULS: 130kN vertical load			
	External Conn 1	Internal Conn 2	Internal Conn 3	External Conn 4	External Conn 1	Internal Conn 2	Internal Conn 3	External Conn 4
Column	3.89	-0.56	0.56	3.53	3.00	-0.44	0.44	2.82
Joint panel	2.24	0.27	-0.27	2.33	1.69	0.12	-0.12	1.60
Interface	2.09	4.05	4.11	1.87	0.64	2.78	3.40	0.63
Gap	0.12	1.57	2.31	0.96	-0.01	0.16	0.08	0.83
SUM	8.34	5.34	6.71	8.69	5.32	2.63	3.81	5.89
Beam	7.01	6.12	7.31	7.42	4.52	3.29	4.05	4.87
Difference	-1.33 -16%	0.78 15%	0.60 9%	-1.27 -15%	-0.80 -15%	0.66 25%	0.25 6%	-1.02 -17%

Appendix D

Analysis of beams

This Appendix presents the results of the finite element models created for all the four beams used for experimental testing. Next, two detailed flowcharts for analytical design of beams with straight and draped tendons is presented. Several of the analytical equations used in the flowcharts are derived in the following section. The final section looks in more detail into tendon elongation for beams with straight tendons and simplifies calculation of tendon elongation.

D.1 FEM results all beams

This section presents results of the finite element models created for all four beams which were used for experimental testing as described in Chapter 4. The creation of the FEM is described in Section 7.2. The results shown here are under maximum vertical load which was reached during experimental testing.

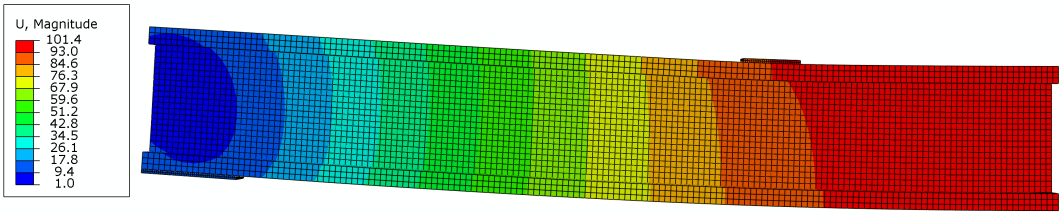

(a) Deflections (mm)

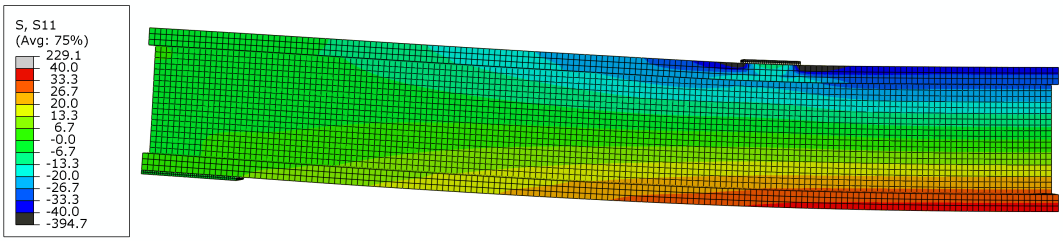

(b) Parallel to grain stresses (MPa)

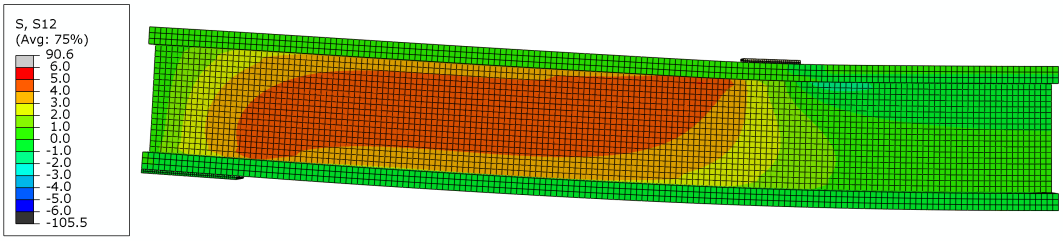

(c) Shear stresses (MPa)

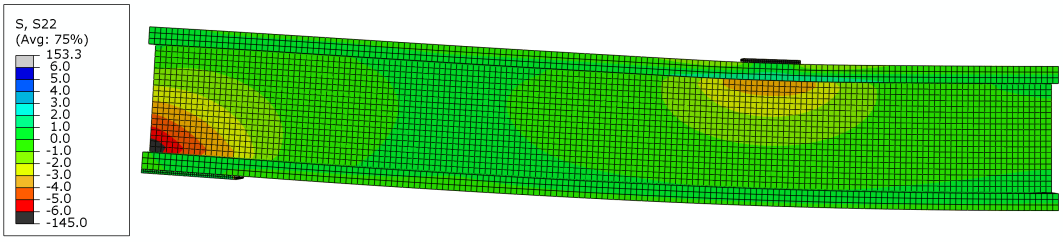

(d) Perpendicular to grain stresses (MPa)

Figure D.1: FEM results of Beam 1 - Benchmark

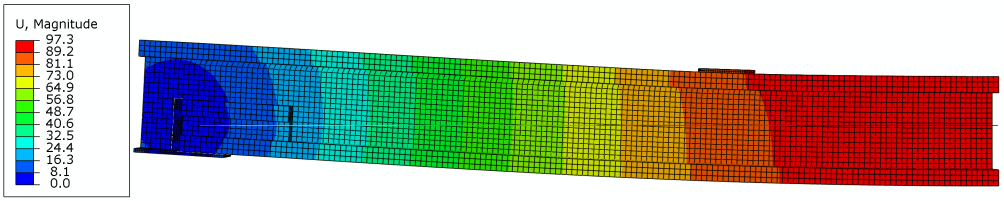

(a) Deflections (mm)

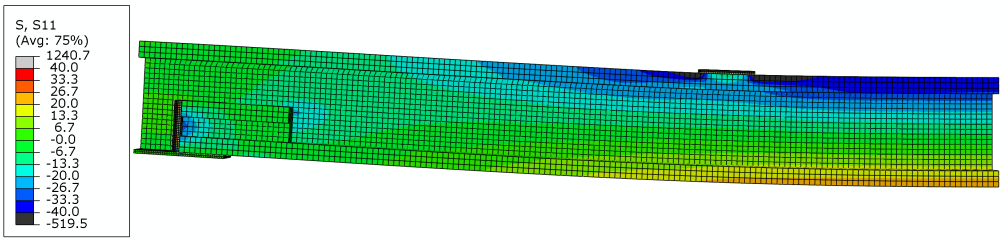

(b) Parallel to grain stresses (MPa)

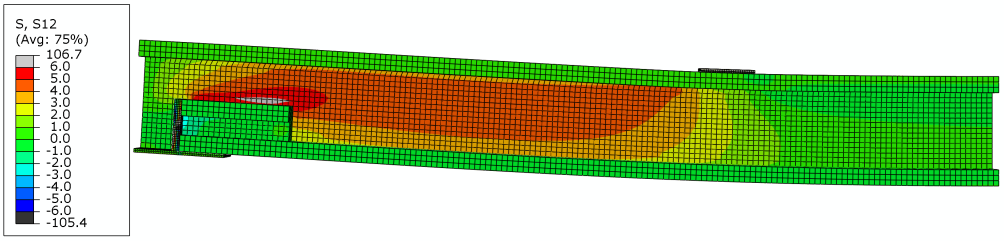

(c) Shear stresses (MPa)

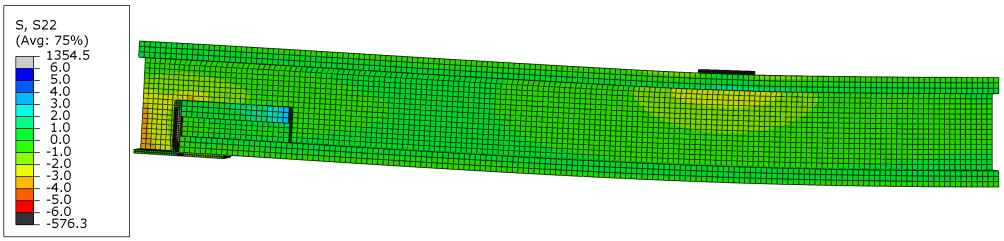

(d) Perpendicular to grain stresses (MPa)

Figure D.2: FEM results of Beam 2 - Straight post-tensioning

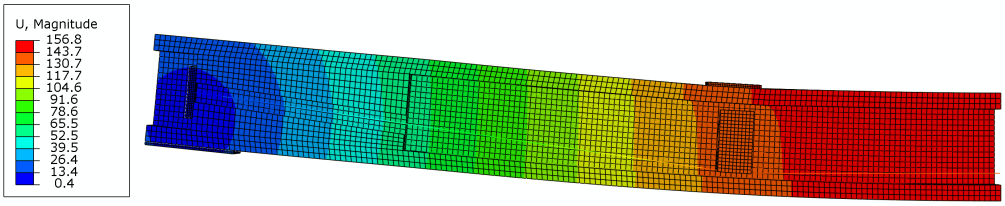

(a) Deflections (mm)

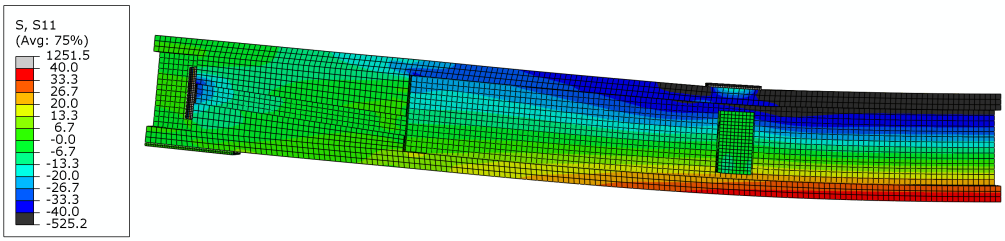

(b) Parallel to grain stresses (MPa)

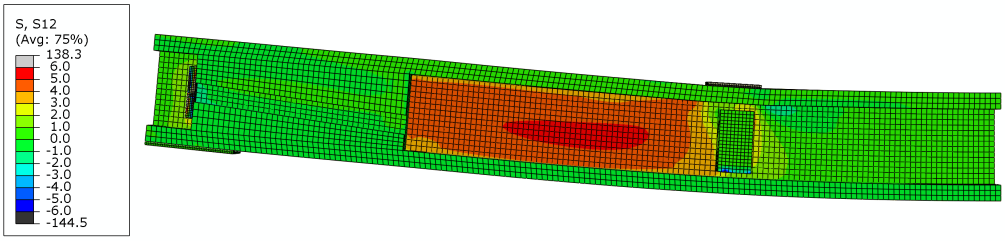

(c) Shear stresses (MPa)

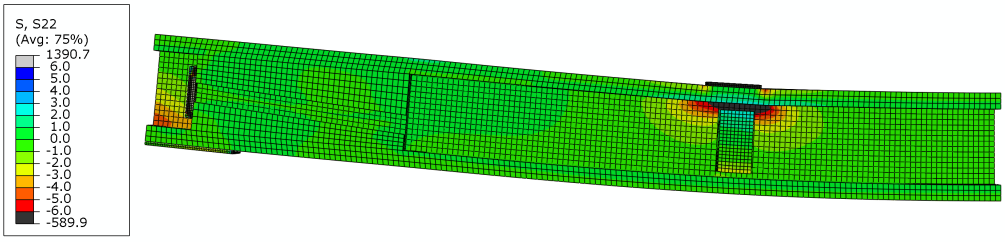

(d) Perpendicular to grain stresses (MPa)

Figure D.3: FEM results of Beam 3 - Draped post-tensioning

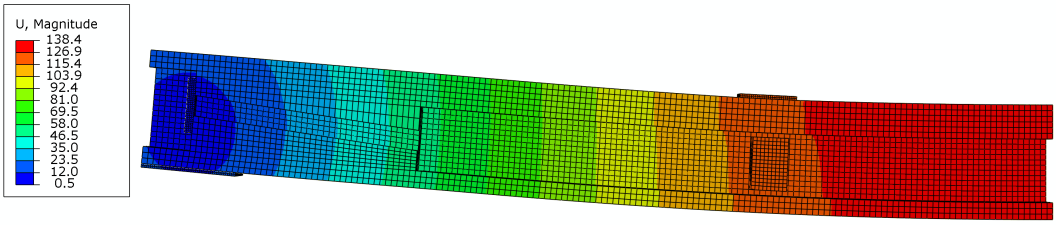

(a) Deflections (mm)

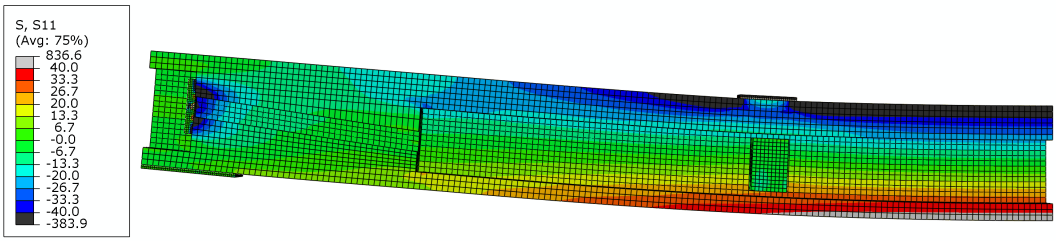

(b) Parallel to grain stresses (MPa)

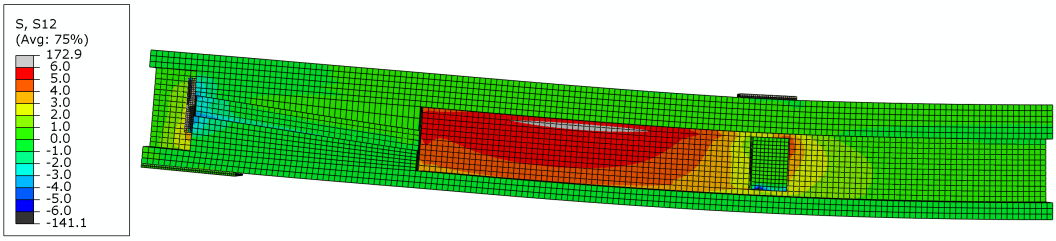

(c) Shear stresses (MPa)

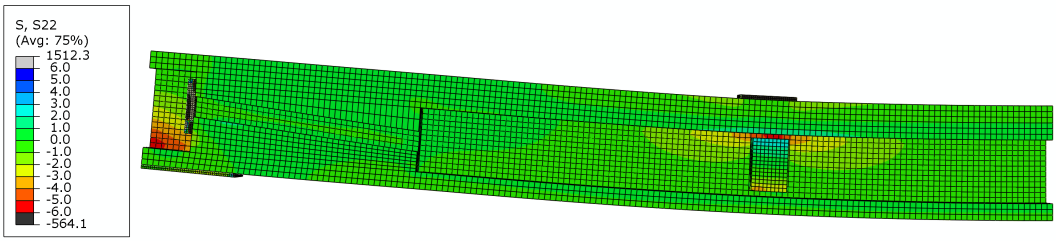

(d) Perpendicular to grain stresses (MPa)

Figure D.4: FEM results of Beam 4 - Draped post-tensioning, double top flange

D.2 Flowcharts

Straight tendons The full analytical design process for post-tensioned beams with straight tendons, as explained in Section 7.3.1, is shown in the flowchart in Figure D.5. The flowchart is split in five steps and the three iterative steps are shown by thick arrows.

Draped tendons , as explained in Section 7.3.2, is shown in the flowchart in Figure D.6. The flowchart is split in the same five steps. The four iterative steps are shown by thick arrows.

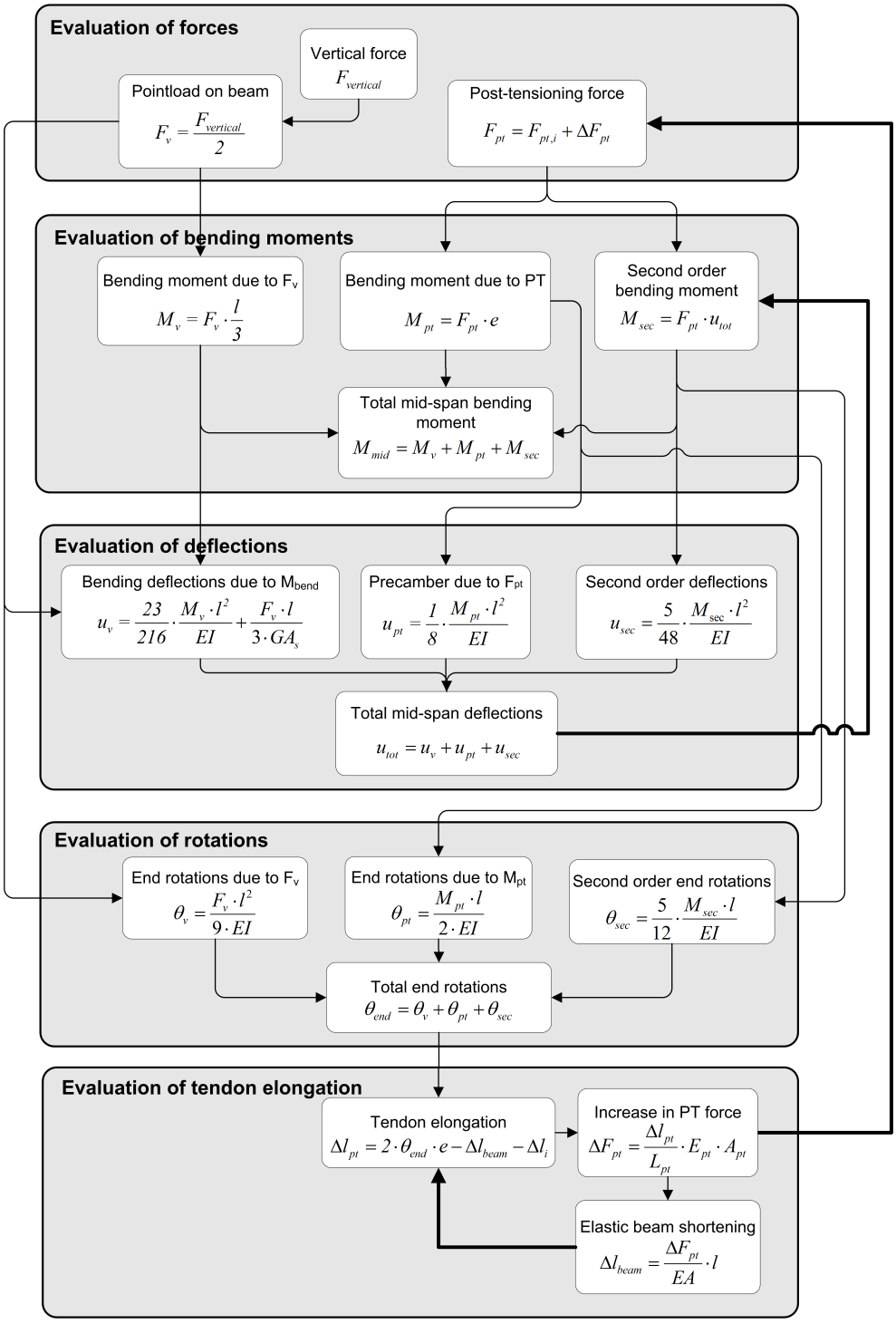

Figure D.5: Flowchart for predicting behaviour of straight post-tensioned beams under four-point bending test, divided in five parts. Thick arrows indicate iterative steps

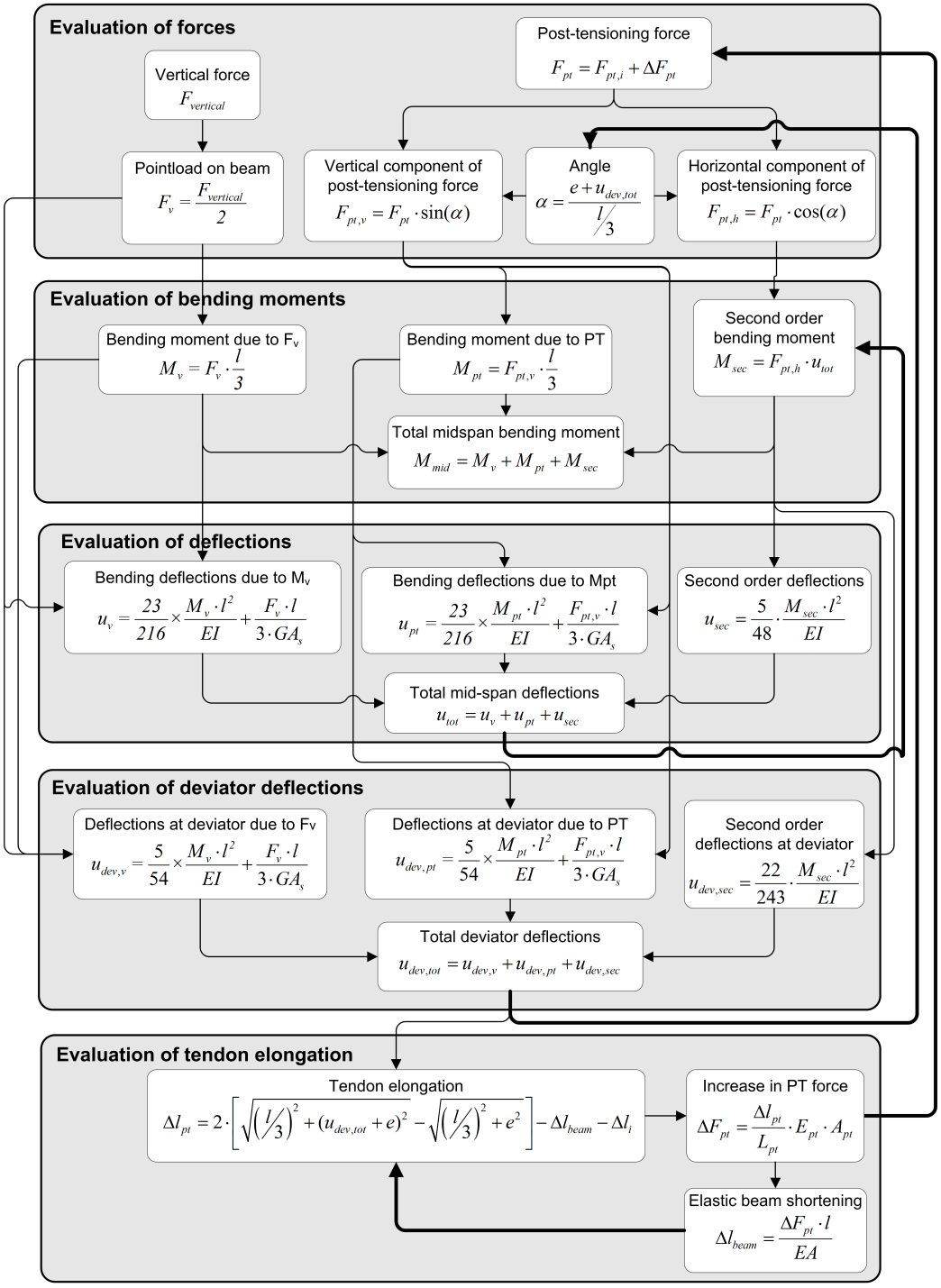

Figure D.6: Flowchart for predicting behaviour of draped post-tensioned beams under four-point bending test, divided in five parts. Thick arrows indicate iterative steps

D.3 Derivation of equations for beam deflections

This section presents the derivation of midspan ($L/2$) and deviator ($L/3$) deflections under several loading conditions. The derivation is based on moment-area theorem.

Pinned - Distributed load - Mid-span Mid-span deflections under distributed load (Figure D.7), consist of bending and shear deflections.

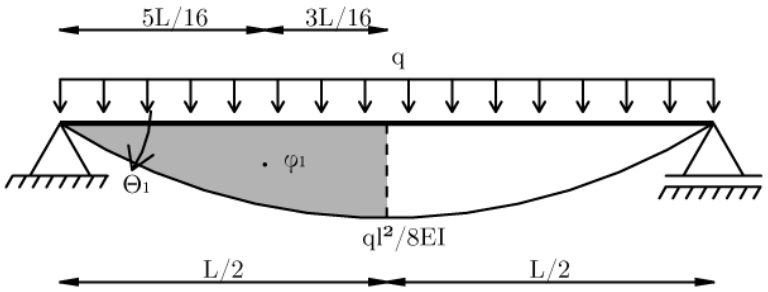

Figure D.7: Mid-span deflections under distributed load

Bending deflections are given by Equation D.1.

$$\begin{aligned}
\varphi_1 &= 2/3 \cdot L/2 \cdot \frac{qL^2}{8EI} = \frac{qL^3}{24EI} \\
\theta_1 &= \frac{qL^3}{24EI} \\
w_{mid,bend} &= \theta_1 \cdot L/2 - \varphi_1 3L/16 \\
w_{mid,bend} &= \frac{qL^4}{48EI} - \frac{qL^4}{128EI} \\
w_{mid,bend} &= \frac{5qL^4}{384EI}
\end{aligned} \tag{D.1}$$

Shear deflections are given by Equation D.2.

$$w_{mid,shear} = \frac{FL}{8GA_s} \tag{D.2}$$

Total midspan deflections are given by Equation D.3.

$$w_{mid} = w_{mid,bend} + w_{mid,shear} = \frac{5qL^4}{384EI} + \frac{qL}{8GA_s} \tag{D.3}$$

Pinned - Distributed load - Deviator Deviator deflections are calculated in a similar way as mid-span deflections (Figure D.8).

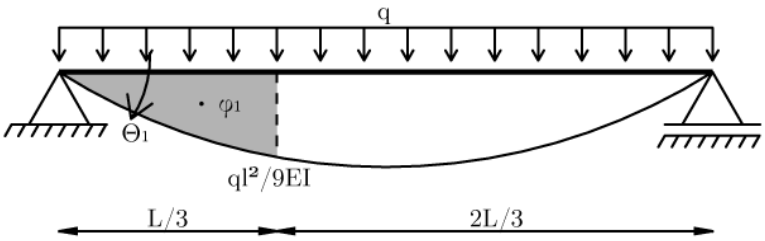

Figure D.8: Deviator deflections under distributed load

Bending deflections are given by Equation D.4.

$$\begin{aligned} \varphi_1 &= 2/3 \cdot L/3 \cdot \frac{qL^2}{9EI} = \frac{2qL^3}{81EI} \\ \theta_1 &= \frac{qL^3}{24EI} \\ w_{dev,bend} &= \theta_1 \cdot L/3 - \varphi_1 3L/24 \\ w_{dev,bend} &= \frac{qL^4}{72EI} - \frac{qL^4}{324EI} \\ w_{dev,bend} &= \frac{11qL^4}{972EI} \end{aligned} \tag{D.4}$$

Shear deflections are given by Equation D.5.

$$w_{dev,shear} = \frac{FL}{9GA_s} \tag{D.5}$$

Total deviator deflections are given by Equation D.6.

$$w_{dev} = w_{dev,bend} + w_{dev,shear} = \frac{11qL^4}{972EI} + \frac{qL}{9GA_s} \tag{D.6}$$

Pinned - Two point loads - Mid-span Mid-span deflections under two point loads, at $L/3$ and $2L/3$ (Figure D.9), consist of bending and shear deflections.

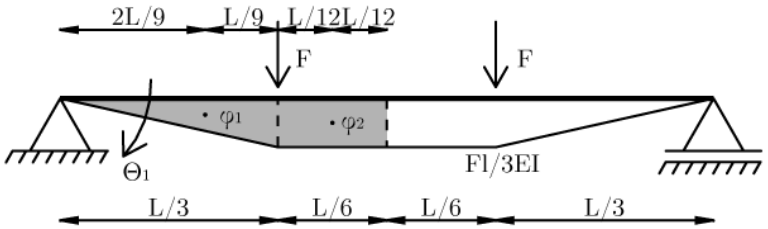

Figure D.9: Mid-span deflections under two point loads

The bending contribution is given by Equation D.7.

$$\begin{aligned}
\varphi_1 &= 0.5 \cdot L/3 \cdot \frac{FL}{3EI} = \frac{FL^2}{18EI} \\
\varphi_2 &= L/6 \cdot \frac{FL}{3EI} = \frac{FL^2}{18EI} \\
\theta_1 &= \frac{FL^2}{9EI} \\
w_{mid,bend} &= \theta_1 \cdot L/2 - \varphi_1(L/9 + L/6) - \varphi_2 L/12 \\
w_{mid,bend} &= \frac{FL^3}{18EI} - \frac{5FL^3}{324EI} - \frac{FL^3}{216EI} \\
w_{mid,bend} &= \frac{23FL^3}{648EI}
\end{aligned} \tag{D.7}$$

The shear contribution is given by Equation D.8.

$$w_{mid,shear} = \frac{FL}{3GA_s} \tag{D.8}$$

Total mid-span deflections are given by Equation D.9.

$$w_{mid} = w_{mid,bend} + w_{mid,shear} = \frac{23FL^3}{648EI} + \frac{FL}{3GA_s} \tag{D.9}$$

Pinned - Two point loads - Deviator The bending contribution is calculated in a similar way as mid-span deflection, and is given by Equation D.10.

$$\begin{aligned} w_{dev,bend} &= \theta_1 \cdot L/3 - \varphi_1 L/9 \\ w_{dev,bend} &= \frac{FL^3}{27EI} - \frac{FL^3}{162EI} \\ w_{dev,bend} &= \frac{5FL^3}{162EI} \end{aligned} \tag{D.10}$$

Shear deflection is the same for deviator as for mid-span. Total deviator deflections are given by Equation D.11.

$$w_{dev} = w_{dev,bend} + w_{mid,shear} = \frac{5FL^3}{162EI} + \frac{FL}{3GA_s} \tag{D.11}$$

Pinned - Second order - Mid-span For calculation of second order deflection ($w_{sec}(x)$) the assumption was made that the deflected shape (u) could be described by a parabolic function with a maximum at mid-span of u_{mid} (Figure D.10). This function is given in Equation D.12.

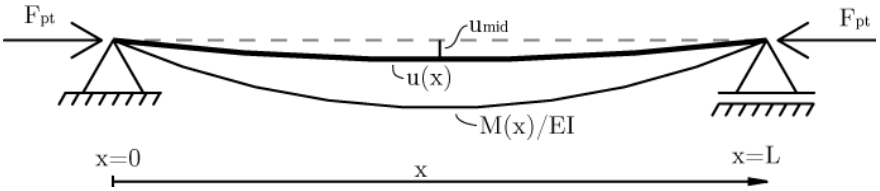

Figure D.10: Second order deflections

$$u(x) = -4\frac{u_{mid}}{L^2}x^2 + \frac{u_{mid}}{L}x = u_{mid}\left(\frac{-4}{L^2}x^2 + \frac{4}{L}x\right) \tag{D.12}$$

The second order bending moments due to the deflections are given by Equation D.13.

$$M_{sec}(x) = F_{pt} \cdot u(x) = F_{pt} \cdot u_{mid}\left(\frac{-4}{L^2}x^2 + \frac{4}{L}x\right) \tag{D.13}$$

Constitutive equations give the relationship between bending moment and deflections. This can be solved to find a function for the deflection, as shown in

Equation D.14.

$$
\begin{aligned}
w_{sec}(x)'' &= -\frac{M_{sec}(x)}{EI} \\
w_{sec}(x)'' &= -\frac{F_{pt} \cdot u_{mid}}{EI} \cdot \left(\frac{-4}{L^2}x^2 + \frac{4}{L}x\right) \\
w_{sec}(x)' &= \int w_{sec}(x)'' = -\frac{F_{pt} \cdot u_{mid}}{EI} \cdot \left(\frac{-4}{3L^2}x^3 + \frac{4}{2L}x^2 + C_1\right) \\
w_{sec}(x) &= \int w_{sec}(x)' = -\frac{F_{pt} \cdot u_{mid}}{EI} \cdot \left(\frac{-4}{12L^2}x^4 + \frac{4}{6L}x^3 + C_1 x + C_2\right)
\end{aligned} \tag{D.14}
$$

This equation can be solved using two boundary conditions, namely $w_{sec}(0) = 0$ and $w_{sec}(L) = 0$. The first equation leads to $C_2 = 0$ and the second equation to $C_1 = -L/3$. The total equation for second order deflections is shown in Equation D.15.

$$
w_{sec}(x) = -\frac{F_{pt} \cdot u_{mid}}{EI} \cdot \left(\frac{-1}{3L^2}x^4 + \frac{2}{3L}x^3 - \frac{L}{3}x\right) \tag{D.15}
$$

This can be evaluated at mid-span of the beam, $x = L/2$, resulting in Equation D.16. In this equation, the term $F_{pt} \cdot u_{mid} = M_{sec}$.

$$
\begin{aligned}
w_{sec}(L/2) &= -\frac{M_{sec}}{EI} \cdot \left(\frac{-1}{3L^2}(L/2)^4 + \frac{2}{3L}(L/2)^3 - \frac{L}{3}(L/2)\right) \\
w_{sec}(L/2) &= -\frac{M_{sec}}{EI} \cdot \left(-\frac{1}{48}L^2 + \frac{4}{48}L^2 - \frac{8}{48}L^2\right) \\
w_{sec}(L/2) &= \frac{5}{48}\frac{M_{sec} \cdot L^2}{EI}
\end{aligned} \tag{D.16}
$$

Pinned - Second order - Deviator Deviator deflections due to second order effects can be calculated by solving Equation D.15 for $x = L/3$. This is shown in Equation D.17.

$$
\begin{aligned}
w_{sec}(L/3) &= -\frac{M_{sec}}{EI} \cdot \left(\frac{-1}{3L^2}(L/3)^4 + \frac{2}{3L}(L/3)^3 - \frac{L}{3}(L/3)\right) \\
w_{sec}(L/3) &= -\frac{M_{sec}}{EI} \cdot \left(-\frac{1}{243}L^2 + \frac{2}{81}L^2 - \frac{1}{9}L^2\right) \\
w_{sec}(L/3) &= \frac{22}{243}\frac{M_{sec} \cdot L^2}{EI}
\end{aligned} \tag{D.17}
$$

Fixed - Distributed load - Midspan For beams with fixed end conditions, like assumed in the derivation of the MBA before decompression, the bending moment distribution (Figure D.11) can be described by Equation D.18.

$$M(x) = -\frac{1}{2}qx^2 + \frac{1}{2}qLx - \frac{1}{12}qL^2 \tag{D.18}$$

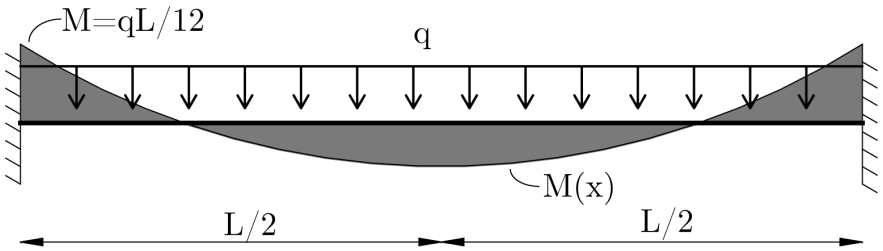

Figure D.11: Bending moment distribution for beam with fixed ends loaded by distributed load

The relationship between the bending moment distribution and bending deflections is given by Equation D.19. This can be solved for the deflections as is shown in Equation D.20.

$$EI\frac{d^2w_b}{dx^2} = -M(x) \tag{D.19}$$

$$w_b(x) = \frac{1}{24}\frac{qx^4}{EI} - \frac{1}{12}\frac{qx^3L}{EI} + \frac{1}{24}\frac{qL^2x^2}{EI} + C_1x + C_2 \tag{D.20}$$

Solving Equation D.20 for the boundary conditions of $w_b(0) = 0$ and $w_b(L) = 0$ results in $C_1 = 0$ and $C_2 = 0$.

The mid-span ($x = 0.5L$) deflections are given by Equation D.21.

$$\begin{aligned} w_b(x = 0.5L) &= \frac{q}{EI}\left(\frac{1}{24}(0.5L)^4 - \frac{1}{12}L\cdot(0.5L)^3 + \frac{1}{24}L^2\cdot(0.5L)^2\right) \\ &= \frac{q}{EI}\left(\frac{L^4}{384} - \frac{L^4}{96} + \frac{L^4}{96}\right) \\ &= \frac{qL^4}{384EI} \end{aligned} \tag{D.21}$$

Shear deflections are the same as for a simply supported beam, as given by Equation D.2. The total mid-span deflections are presented in Equation D.22.

$$w_{mid} = w_b + w_s = \frac{qL^4}{384EI} + \frac{FL}{8GA_s} \tag{D.22}$$

Fixed - Distributed load - Deviator Deviator deflections can be evaluated in a similar manner as the mid-span deflections. Evaluating Equation D.20 for $x = L/3$ results in deviator deflections due to bending as given by Equation D.23.

$$\begin{aligned} w_b(x = L/3) &= \frac{q}{EI}\left(\frac{1}{24}(L/3)^4 - \frac{1}{12}L \cdot (L/3)^3 + \frac{1}{24}L^2 \cdot (L/3)^2\right) \\ &= \frac{q}{EI}\left(\frac{L^4}{1944} - \frac{L^4}{324} + \frac{L^4}{216}\right) \\ &= \frac{qL^4}{486EI} \end{aligned} \tag{D.23}$$

Deviator deflections due to shear are similar as for the beam with pinned connections and are given by Equation D.5. The total deviator deflections are presented in Equation D.24.

$$w_{dev} = w_b + w_s = \frac{qL^4}{486EI} + \frac{FL}{9GA_s} \tag{D.24}$$

Fixed - Two point loads - Deviator For a beam with fixed ends and loaded by two point loads, as shown in Figure D.12, deviator displacements due to bending are given by Equation D.25.

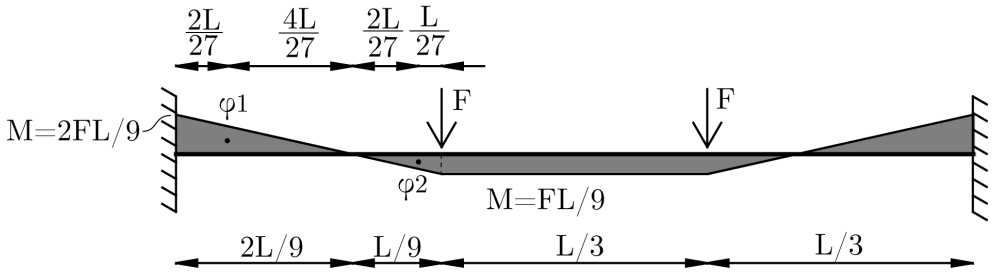

Figure D.12: Bending moment distribution for beam with fixed ends loaded by two point loads

$$\begin{aligned}
\varphi_1 &= \frac{1}{2} \cdot \frac{2L}{9} \cdot \frac{2FL}{9EI} = \frac{2FL^2}{81EI} \\
\varphi_2 &= \frac{1}{2} \cdot \frac{L}{9} \cdot \frac{FL}{9EI} = \frac{FL^2}{162EI} \\
w_{b,dev} &= \varphi_1 \cdot \left(\frac{4}{27}L + \frac{1}{9}L \right) - \varphi_2 \cdot \frac{1}{27}L \\
w_{b,dev} &= \frac{2FL^2}{81EI} \cdot \frac{7}{27}L - \frac{FL^2}{162EI} \cdot \frac{1}{27}L \\
w_{b,dev} &= \frac{FL^3}{162EI}
\end{aligned} \tag{D.25}$$

Deviator deflections due to shear are similar as for the beam with pinned connections and are given by Equation D.8. The total deviator deflections are presented in Equation D.26.

$$w_{dev} = w_b + w_s = \frac{FL^3}{162EI} + \frac{FL}{3GA_s} \tag{D.26}$$

D.4 Tendon elongation for beams with straight PT

In the analytical design procedure calculation of tendon elongation is an iterative process. This section looks more in detail into tendon elongation and simplifies calculation of tendon elongation.

After stressing there is an initial end rotation (θ_0) which is caused by the initial post-tensioning force ($\theta_{pt,i}$) and second order effects due to the initial precamber ($\theta_{sec,0}$). This initial end rotation can be calculated using Equation D.27.

$$\theta_0 = -\theta_{pt,i} - \theta_{sec,0} \tag{D.27}$$

Under maximum load (q) the end rotation (θ_{max}) is caused by the distributed load (θ_q), the initial post-tensioning force ($\theta_{pt,i}$), the increase in post-tensioning force due to tendon elongation ($\theta_{\Delta pt}$), second order effects due to the initial post-tensioning force ($\theta_{sec,pt,i}$) and second order effects due to the increase in post-tensioning force($\theta_{sec,\Delta pt}$).

$$\theta_{max} = \theta_q - \theta_{pt,i} - \theta_{\Delta pt} + \theta_{sec,pt,i} + \theta_{sec,\Delta pt} \tag{D.28}$$

The total end rotation (θ_{end}), starting from the initial position to the new position results in tendon elongation.

$$\theta_{end} = \theta_{max} - \theta_0 = \theta_q - \theta_{pt,i} - \theta_{\Delta pt} + \theta_{sec,pt,i} + \theta_{sec,\Delta pt} - (-\theta_{pt,i} - \theta_{sec,0}) \tag{D.29}$$

It can be seen that in this equation the rotations due to initial post-tensioning force ($\theta_{pt,i}$), being constant, cancel out. The tendon elongation (Δl_{pt}) due to end rotations can be calculated using Equation D.30.

$$\Delta l_{pt} = 2 \cdot \theta_{end} \cdot e - \Delta l_{beam} \tag{D.30}$$

The increase in tendon length results in an increase of post-tensioning force (ΔF_{pt}), shown in Equation D.31.

$$\Delta F_{pt} = \frac{\Delta l_{pt}}{L_{pt}} \cdot E_{pt} \cdot A_{pt} \tag{D.31}$$

This can be rewritten as in Equation D.32.

$$\Delta l_{pt} = \frac{\Delta F_{pt} L_{pt}}{E_{pt} \cdot A_{pt}} \tag{D.32}$$

The increase in PT force results in an elastic shortening of the beam (Δl_{beam}), Equation D.33. This shortening is used in Equation D.30.

$$\Delta l_{beam} = \frac{\Delta F_{pt} \cdot L}{EA} \tag{D.33}$$

Equations D.29 and D.30 can be combined, resulting in Equation D.34.

$$\Delta l_{pt} = 2 \cdot e \cdot (\theta_q - \theta_{\Delta pt} + \theta_{sec,pt,i} + \theta_{sec,\Delta pt} + \theta_{sec,0}) - \Delta l_{beam} \tag{D.34}$$

This can be split in a part which is constant part (C) which is independent of the change in post-tensioning force and a variable part (V) which is dependent on the change in post-tensioning force, as shown in Equation D.35.

$$\Delta l_{pt} = \underbrace{2 \cdot e \cdot (\theta_q + \theta_{sec,pt,i} + \theta_{sec,0})}_{\text{constant part 'C'}} + \underbrace{2 \cdot e \cdot (-\theta_{\Delta pt} + \theta_{sec,\Delta pt}) - \Delta l_{beam}}_{\text{variable part 'V'}} \tag{D.35}$$

These two parts can be further evaluated, as shown in Equations D.36 and D.37.

$$\begin{aligned} C &= 2 \cdot e \cdot (\theta_q + \theta_{sec,pt,i} + \theta_{sec,0}) \\ C &= 2 \cdot e \cdot (\frac{qL^3}{24EI} + \frac{5F_{pt,i} u L_b}{12EI} + \frac{5F_{pt,i} u_0 L}{12EI}) \\ C &= \frac{eqL^3}{12EI} + \frac{10F_{pt,i} u e L_b}{12EI} + \frac{10F_{pt,i} e u_0 L}{12EI} \end{aligned} \tag{D.36}$$

$$
\begin{aligned}
V &= 2 \cdot e \cdot (-\theta_{\Delta pt} + \theta_{sec,\Delta pt}) - \Delta l_{beam} \\
V &= 2 \cdot e \cdot (-\frac{\Delta F_{pt} e L_b}{2EI} + \frac{5 \Delta F_{pt} u L_b}{12EI}) - \frac{\Delta F_{pt} \cdot l}{EA} \\
V &= \Delta F_{pt} \left(-\frac{e^2 L_b}{EI} + \frac{10 e u L_b}{12EI} - \frac{L_b}{EA} \right)
\end{aligned} \tag{D.37}
$$

Equation D.34 can now be rewritten, using Equation D.32, in the form of Equation D.38.

$$
\Delta F_{pt} \frac{L_{pt}}{E_{pt} \cdot A_{pt}} = C + \Delta F_{pt} \left(\cdots \right) \tag{D.38}
$$

This can be solved for ΔF_{pt}, and simplified by multiplying with $12EI/L$, as shown in Equation D.39.

$$
\begin{aligned}
\Delta F_{pt} &= \frac{\frac{eqL^3}{12EI} + \frac{10 F_{pt,i} u e L_b}{12EI} + \frac{10 F_{pt,i} e u_0 L}{12EI}}{\frac{L_{pt}}{E_{pt} \cdot A_{pt}} + \frac{e^2 L_b}{EI} - \frac{10 e u L_b}{12EI} + \frac{L_b}{EA}} \\
\Delta F_{pt} &= \frac{qL^2 + 10 F_{pt,i} u + 10 F_{pt,i} u_0}{\frac{12EI}{eE_{pt} \cdot A_{pt}} + 12e - 10u + \frac{12I}{Ae}} \\
\Delta F_{pt} &= \frac{qL^2 + 10 F_{pt,i} (u + u_0)}{\frac{12EI}{eE_{pt} \cdot A_{pt}} + 12e - 10u + \frac{12I}{Ae}}
\end{aligned} \tag{D.39}
$$

This results in a closed form equation for the increase in post-tensioning force for beams with straight tendons.

Appendix E

Analysis of connections

E.1 Column rotations

M Model For the M model the bending moment distribution can be described by the piecewise function in Equation E.1.

$$M(x) = \begin{cases} -Rx & \text{for } 0 \leq x \leq H/2 \\ -Rx + RH & \text{for } H/2 \leq x \leq H \end{cases} \tag{E.1}$$

The bending rotations and bending deflections can be found by dividing M by -EI and integrating the equation once and twice, respectively. The results are shown in Equations E.2 and E.3.

$$\theta_b(x) = \begin{cases} \frac{R}{2EI}x^2 + C_1 & \text{for } 0 \leq x \leq H/2 \\ \frac{R}{2EI}x^2 - \frac{RH}{EI}x + C_3 & \text{for } H/2 \leq x \leq H \end{cases} \tag{E.2}$$

$$w_b(x) = \begin{cases} \frac{R}{6EI}x^3 + C_1x + C_2 & \text{for } 0 \leq x \leq H/2 \\ \frac{R}{6EI}x^3 - \frac{RH}{2EI}x^2 + C_3x + C_4 & \text{for } H/2 \leq x \leq H \end{cases} \tag{E.3}$$

The four integration constants, C_1 to C_4, can be solved using four boundary conditions, shown in Equation E.4.

$$w_b(0) = 0, w_{b1}(H/2) = w_{b2}(H/2), \theta_{b1}(H/2) = \theta_{b2}(H/2), w_b(H) = 0 \tag{E.4}$$

The resulting integration constants are shown in Equation E.5.

$$C_1 = -\frac{RH^2}{24EI}, C_2 = 0, C_3 = \frac{11RH^2}{24EI}, C_4 = -\frac{RH^3}{8EI} \tag{E.5}$$

The resulting bending rotations and bending deflection are shown in Equations E.6 and E.7.

$$\theta_b(x) = \begin{cases} \frac{R}{2EI}x^2 - \frac{RH^2}{24EI} & \text{for } 0 \leq x \leq H/2 \\ \frac{R}{2EI}x^2 - \frac{RH}{EI}x + \frac{11RH^2}{24EI} & \text{for } H/2 \leq x \leq H \end{cases} \tag{E.6}$$

$$w_b(x) = \begin{cases} \frac{R}{6EI}x^3 - \frac{RH^2}{24EI}x & \text{for } 0 \leq x \leq H/2 \\ \frac{R}{6EI}x^3 - \frac{RH}{2EI}x^2 + \frac{11RH^2}{24EI}x - \frac{RH^3}{8EI} & \text{for } H/2 \leq x \leq H \end{cases} \tag{E.7}$$

Shear rotations and deformations follow from the shear force distribution. As there is no distributed load acting on the column, the shear rotations are constant along the height of the column, as shown in Equation E.8.

$$\theta_s = \frac{R}{\alpha GA} \tag{E.8}$$

The constant shear rotation leads to a linear shear deflection. Though as both ends of the column are restrained from moving, this linear deflection equals zero along the height of the column. Only shear rotations occur due to this shear distribution.

2F Model Derivations for the *2F* model are similar to the *M* model, but it is 3 piecewise. The equations become more complex for this load case and are therefore solved using the software package Maple (Maplesoft, 2009). The full derivation and resulting equations for deformation and rotation can be found in Figures E.1 to E.10.

restart;

First define the Shear equations along the height of the column:

$V1 := -R$:

$V2 := R \cdot \left(\frac{H}{b} - 1 \right)$:

$V3 := -R$:

$V := piecewise(0 < x < a, V1, a < x < c, V2, c < x < H, V3)$;

$$\begin{cases} -R & 0 < x \text{ and } x < a \\ R\left(\frac{H}{b} - 1 \right) & a < x \text{ and } x < c \\ -R & c < x \text{ and } x < H \end{cases} \quad \textbf{(1)}$$

Next define the Moment equations along the height of the column:

$M1 := -R \cdot x$:

$M2 := \frac{2 \cdot R \cdot a}{b} x - \frac{R \cdot H \cdot a}{b}$:

$M3 := -R \cdot x + R \cdot H$:

$M := piecewise(0 < x < a, M1, a < x < c, M2, c < x < H, M3)$;

$$\begin{cases} -R\,x & 0 < x \text{ and } x < a \\ \frac{2\,R\,a\,x}{b} - \frac{R\,H\,a}{b} & a < x \text{ and } x < c \\ -R\,x + R\,H & c < x \text{ and } x < H \end{cases} \quad \textbf{(2)}$$

Now define the variables a, b, c and R, in order to plot M and V:

$a := 1595$;

$b := 410$;

$c := a + b$;

$H := 2 \cdot a + b$;

$R := 23600$;

$$\begin{gathered} 1595 \\ 410 \\ 2005 \\ 3600 \\ 23600 \end{gathered} \quad \textbf{(3)}$$

$plot\left(\frac{M}{1000000}, x = 0..3600 \right)$;

$plot\left(\frac{V}{1000}, x = 0..3600 \right)$;

Figure E.1: Maple worksheet page 1

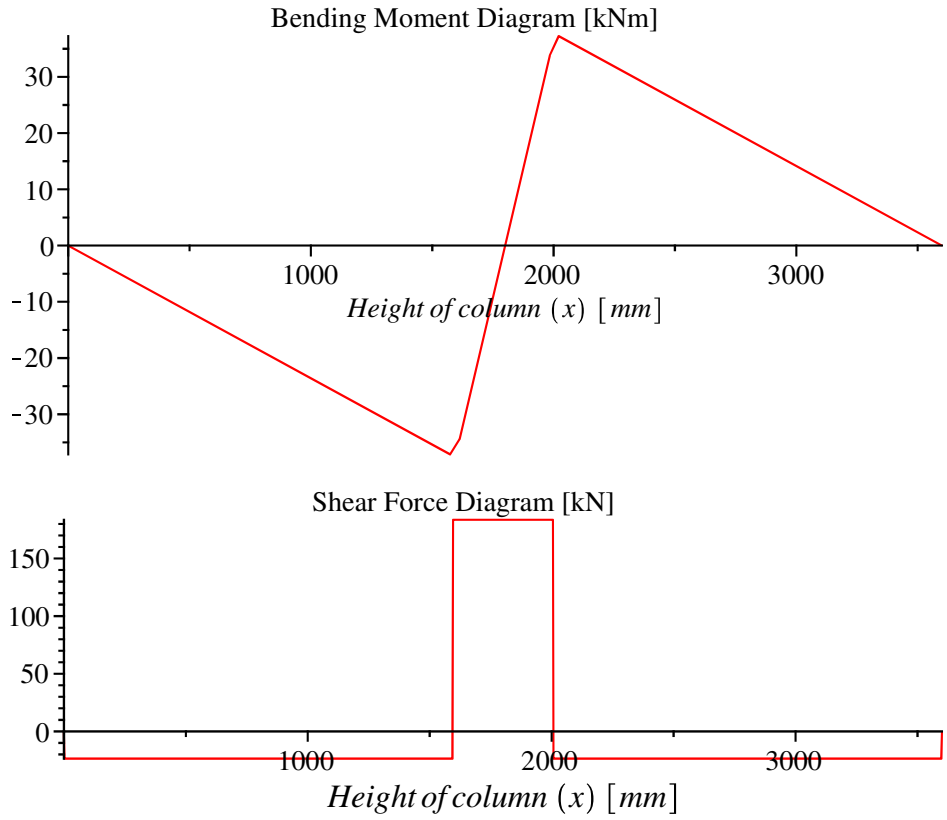

The defined variables need to be unassigned for the analytical solver.

$unassign('a')$:
$unassign('b')$:
$unassign('c')$:
$unassign('H')$:
$unassign('R')$:

The integral of -M/EI gives rotations (t):

$$t1 := -int\left(\frac{M1}{EI}, x\right) + C1 :$$

$$t2 := expand\left(-int\left(\frac{M2}{EI}, x\right) + C3\right) :$$

$$t3 := expand\left(-int\left(\frac{M3}{EI}, x\right) + C5\right) :$$

$$t := piecewise(0 < x < a, t1, a < x < c, t2, c < x < H, t3);$$

$$\begin{cases} \frac{1}{2}\,\frac{R\,x^2}{EI} + C1 & 0 < x \text{ and } x < a \\ -\frac{R\,a\,x^2}{EI\,b} + \frac{R\,H\,a\,x}{EI\,b} + C3 & a < x \text{ and } x < c \\ \frac{1}{2}\,\frac{R\,x^2}{EI} - \frac{R\,H\,x}{EI} + C5 & c < x \text{ and } x < H \end{cases} \quad \textbf{(4)}$$

Figure E.2: Maple worksheet page 2

A second round of integration gives bending deflections (wb):

$wb1 := int(t1, x) + C2$:
$wb2 := int(t2, x) + C4$:
$wb3 := int(t3, x) + C6$:
$wb := piecewise(0 < x < a, wb1, a < x < c, wb2, c < x < H, wb3)$;

$$\begin{cases} \frac{1}{6}\,\frac{R\,x^3}{EI} + C1\,x + C2 & 0 < x \text{ and } x < a \\ -\frac{1}{3}\,\frac{R\,a\,x^3}{EI\,b} + \frac{1}{2}\,\frac{R\,H\,a\,x^2}{EI\,b} + C3\,x + C4 & a < x \text{ and } x < c \\ \frac{1}{6}\,\frac{R\,x^3}{EI} - \frac{1}{2}\,\frac{R\,H\,x^2}{EI} + C5\,x + C6 & c < x \text{ and } x < H \end{cases} \quad \textbf{(5)}$$

There are 6 unknown integration constants, which need solving using 6 equations:

1) wb1(0) = 0
2) wb1(a) = wb2(a)
3) t1(a) = t2(a)
4) wb2(c) = w3(c)
5) t2(c) = t3(c)
6) wb3(H) = 0

Equation 1 gives:

$x := 0$:
$wb1 = 0$;

$$C2 = 0 \quad \textbf{(6)}$$

Equations 2 and 3 give:

$x := a$:
$wb1 = wb2$;
$t1 = t2$;

$$\frac{1}{6}\,\frac{R\,a^3}{EI} + C1\,a + C2 = -\frac{1}{3}\,\frac{R\,a^4}{EI\,b} + \frac{1}{2}\,\frac{R\,H\,a^3}{EI\,b} + C3\,a + C4$$

$$\frac{1}{2}\,\frac{R\,a^2}{EI} + C1 = -\frac{R\,a^3}{EI\,b} + \frac{R\,H\,a^2}{EI\,b} + C3 \quad \textbf{(7)}$$

Equations 4 and 5 give:

$x := c$:
$wb2 = wb3$;
$t2 = t3$;

$$-\frac{1}{3}\,\frac{R\,a\,c^3}{EI\,b} + \frac{1}{2}\,\frac{R\,H\,a\,c^2}{EI\,b} + C3\,c + C4 = \frac{1}{6}\,\frac{R\,c^3}{EI} - \frac{1}{2}\,\frac{R\,H\,c^2}{EI} + C5\,c + C6$$

$$-\frac{R\,a\,c^2}{EI\,b} + \frac{R\,H\,a\,c}{EI\,b} + C3 = \frac{1}{2}\,\frac{R\,c^2}{EI} - \frac{R\,H\,c}{EI} + C5 \quad \textbf{(8)}$$

Equation 6 gives:

$x := H$:
$wb3 = 0$;

$$-\frac{1}{3}\,\frac{R\,H^3}{EI} + C5\,H + C6 = 0 \quad \textbf{(9)}$$

Figure E.3: Maple worksheet page 3

These six equations can be rewritten and formed into a matrix for solving (the term R/EI has been taken out of the right hand equations for simplification):

$$Mat := \left\langle \langle 0, a, 1, 0, 0, 0\rangle \middle| \langle 1, 0, 0, 0, 0, 0\rangle \middle| \langle 0, -a, -1, c, 1, 0\rangle \middle| \langle 0, -1, 0, 1, 0, 0\rangle \middle| \langle 0, 0, 0, -c, -1, H\rangle \middle| \langle 0, 0, 0, -1, 0, 1\rangle \middle| \left\langle 0, -\frac{a^4}{3\cdot b} + \frac{H\cdot a^3}{2\cdot b} - \frac{a^3}{6}, -\frac{a^3}{b} + \frac{H\cdot a^2}{b} - \frac{a^2}{2}, \frac{c^3}{6} - \frac{H\cdot c^2}{2} + \frac{a\cdot c^3}{3\cdot b} - \frac{H\cdot a\cdot c^2}{2\cdot b}, \frac{c^2}{2} - H\cdot c + \frac{a\cdot c^2}{b} - \frac{H\cdot a\cdot c}{b}, -\frac{H^3}{6} + \frac{H^3}{2} \right\rangle \right\rangle;$$

$$\begin{bmatrix} 0 & 1 & 0 & 0 & 0 & 0 & 0 \\ a & 0 & -a & -1 & 0 & 0 & -\frac{1}{3}\,\frac{a^4}{b} + \frac{1}{2}\,\frac{H a^3}{b} - \frac{1}{6}\,a^3 \\ 1 & 0 & -1 & 0 & 0 & 0 & -\frac{a^3}{b} + \frac{H a^2}{b} - \frac{1}{2}\,a^2 \\ 0 & 0 & c & 1 & -c & -1 & \frac{1}{6}\,c^3 - \frac{1}{2}\,H c^2 + \frac{1}{3}\,\frac{a\,c^3}{b} - \frac{1}{2}\,\frac{H a\,c^2}{b} \\ 0 & 0 & 1 & 0 & -1 & 0 & \frac{1}{2}\,c^2 - H c + \frac{a\,c^2}{b} - \frac{H a\,c}{b} \\ 0 & 0 & 0 & 0 & H & 1 & \frac{1}{3}\,H^3 \end{bmatrix} \quad \textbf{(10)}$$

The variables c and H are defined again, to simplify further expressions:

$c := a + b$:

$H := 2\cdot a + b$:

Solving the matrix to reduced row echelon form:

$S := LinearAlgebra:\text{-}ReducedRowEchelonForm(\ Mat\ );$

$$\begin{bmatrix} 1 & 0 & 0 & 0 & 0 & 0 & -\frac{1}{6}\,a\,(a+b) \\ 0 & 1 & 0 & 0 & 0 & 0 & 0 \\ 0 & 0 & 1 & 0 & 0 & 0 & -\frac{1}{6}\,\frac{\left(6\,a^2 + 4\,b\,a + b^2\right) a}{b} \\ 0 & 0 & 0 & 1 & 0 & 0 & \frac{1}{6}\,\frac{(2\,a+b)\,a^3}{b} \\ 0 & 0 & 0 & 0 & 1 & 0 & \frac{11}{6}\,a^2 + \frac{11}{6}\,b\,a + \frac{1}{2}\,b^2 \\ 0 & 0 & 0 & 0 & 0 & 1 & -a^3 - \frac{3}{2}\,a^2 b - \frac{5}{6}\,b^2 a - \frac{1}{6}\,b^3 \end{bmatrix} \quad \textbf{(11)}$$

The six integration constants are now defined in terms of a and b:

$C1 := expand\left(\frac{R}{EI}\cdot S(1,7)\right);$

$C2 := \frac{R}{EI}\cdot S(2,7);$

Figure E.4: Maple worksheet page 4

$C3 := expand\left(\frac{R}{EI}\cdot S(3,7)\right);$
$C4 := expand\left(\frac{R}{EI}\cdot S(4,7)\right);$
$C5 := expand\left(\frac{R}{EI}\cdot S(5,7)\right);$
$C6 := expand\left(\frac{R}{EI}\cdot S(6,7)\right);$

$$-\frac{1}{6}\,\frac{R\,a^2}{EI}-\frac{1}{6}\,\frac{R\,a\,b}{EI}$$

$$0$$

$$-\frac{R\,a^3}{EI\,b}-\frac{2}{3}\,\frac{R\,a^2}{EI}-\frac{1}{6}\,\frac{R\,a\,b}{EI}$$

$$\frac{1}{3}\,\frac{R\,a^4}{EI\,b}+\frac{1}{6}\,\frac{R\,a^3}{EI}$$

$$\frac{11}{6}\,\frac{R\,a^2}{EI}+\frac{11}{6}\,\frac{R\,a\,b}{EI}+\frac{1}{2}\,\frac{R\,b^2}{EI}$$

$$-\frac{R\,a^3}{EI}-\frac{3}{2}\,\frac{R\,a^2\,b}{EI}-\frac{5}{6}\,\frac{R\,b^2\,a}{EI}-\frac{1}{6}\,\frac{R\,b^3}{EI} \qquad \textbf{(12)}$$

The rotations (t) and deformations (w) can be re-evaluated:

```
unassign('c') :
unassign('x') :
unassign('H') :
t;
 wb;
```

$$\begin{cases} \frac{1}{2}\,\frac{R\,x^2}{EI}-\frac{1}{6}\,\frac{R\,a^2}{EI}-\frac{1}{6}\,\frac{R\,a\,b}{EI} & 0<x \text{ and } x<a \\ -\frac{R\,a\,x^2}{EI\,b}+\frac{R\,H\,a\,x}{EI\,b}-\frac{R\,a^3}{EI\,b}-\frac{2}{3}\,\frac{R\,a^2}{EI}-\frac{1}{6}\,\frac{R\,a\,b}{EI} & a<x \text{ and } x<c \\ \frac{1}{2}\,\frac{R\,x^2}{EI}-\frac{R\,H\,x}{EI}+\frac{11}{6}\,\frac{R\,a^2}{EI}+\frac{11}{6}\,\frac{R\,a\,b}{EI}+\frac{1}{2}\,\frac{R\,b^2}{EI} & c<x \text{ and } x<H \end{cases}$$

$$\begin{cases} \frac{1}{6}\,\frac{R\,x^3}{EI}+\left(-\frac{1}{6}\,\frac{R\,a^2}{EI}-\frac{1}{6}\,\frac{R\,a\,b}{EI}\right)x \\ -\frac{1}{3}\,\frac{R\,a\,x^3}{EI\,b}+\frac{1}{2}\,\frac{R\,H\,a\,x^2}{EI\,b}+\left(-\frac{R\,a^3}{EI\,b}-\frac{2}{3}\,\frac{R\,a^2}{EI}-\frac{1}{6}\,\frac{R\,a\,b}{EI}\right)x+\frac{1}{3}\,\frac{R\,a^4}{EI\,b}+\frac{1}{6}\,\frac{R\,a^3}{EI} \\ \frac{1}{6}\,\frac{R\,x^3}{EI}-\frac{1}{2}\,\frac{R\,H\,x^2}{EI}+\left(\frac{11}{6}\,\frac{R\,a^2}{EI}+\frac{11}{6}\,\frac{R\,a\,b}{EI}+\frac{1}{2}\,\frac{R\,b^2}{EI}\right)x-\frac{R\,a^3}{EI}-\frac{3}{2}\,\frac{R\,a^2\,b}{EI}-\frac{5}{6}\,\frac{R\,b^2\,a}{EI}- \end{cases}$$

When defining all variables again, this gets simplified to:

```
a := 1595 :
 b := 410 :
 c := a + b :
```

Figure E.5: Maple worksheet page 5

$H := 2 \cdot a + b$:
$R := 23600$:
$EI := 36471000000000$:
t;
wb;

$$\begin{cases} \frac{59}{182355000000} x^2 - \frac{7547221}{21882600000} & 0 < x \text{ and } x < 1595 \\ -\frac{18821}{7476555000000} x^2 + \frac{56463}{6230462500} x - \frac{6793646981}{897186600000} & 1595 < x \text{ and } x < 2005 \\ \frac{59}{182355000000} x^2 - \frac{177}{75981250} x + \frac{84209579}{21882600000} & 2005 < x \text{ and } x < 3600 \end{cases}$$

$$\begin{cases} \frac{59}{547065000000} x^3 - \frac{7547221}{21882600000} x & 0 < x \text{ and } x < 159 \\ -\frac{18821}{22429665000000} x^3 + \frac{56463}{12460925000} x^2 - \frac{6793646981}{897186600000} x + \frac{1915243781}{498437000} & 1595 < x \text{ and } x < 2(\\ \frac{59}{547065000000} x^3 - \frac{177}{151962500} x^2 + \frac{84209579}{21882600000} x - \frac{23038379}{6078500} & 2005 < x \text{ and } x < 3(\end{cases}$$

These equations can be plotted to show rotations and deflections along the height of the column:

$plot(t \cdot 1000, x = 0..3600)$;
$plot(wb, x = 0..3600)$;

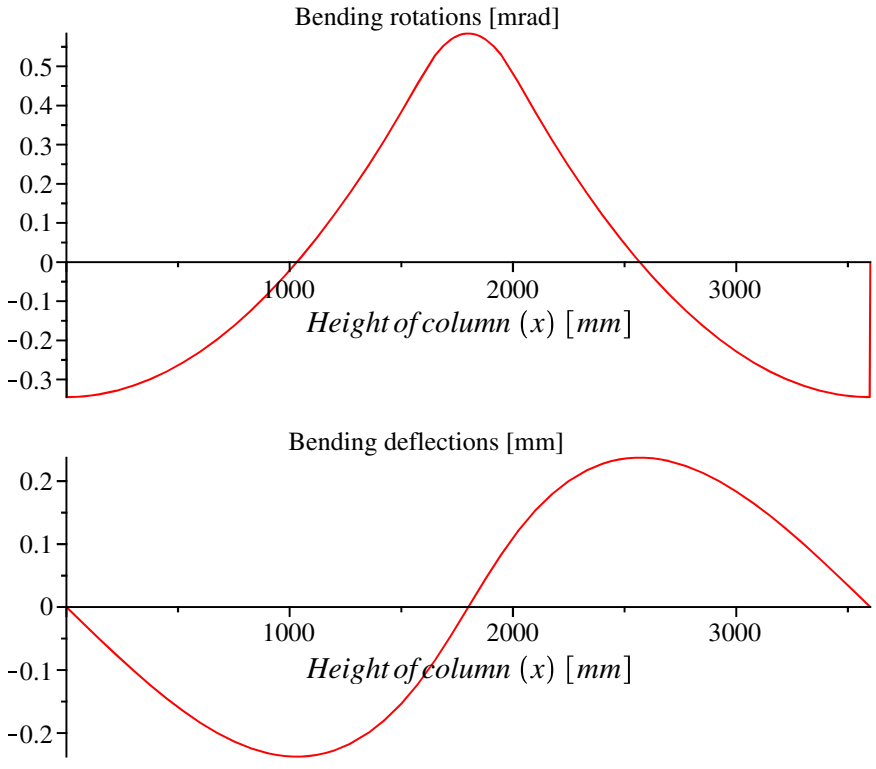

Figure E.6: Maple worksheet page 6

So far only bending deformation has been taken into account. Next the shear deformation is evaluated:

$unassign('a')$:
$unassign('b')$:
$unassign('c')$:
$unassign('H')$:
$unassign('R')$:

Shear rotations are given by gamma = V/GA

$g1 := \frac{V1}{GA}$:

$g2 := \frac{V2}{GA}$:

$g3 := \frac{V3}{GA}$:

$g := piecewise(0 < x < a, g1, a < x < c, g2, c < x < H, g3)$;

$$\begin{cases} -\frac{R}{GA} & 0 < x \text{ and } x < a \\ \frac{R\left(\frac{H}{b} - 1\right)}{GA} & a < x \text{ and } x < c \\ -\frac{R}{GA} & c < x \text{ and } x < H \end{cases} \tag{15}$$

Integration of shear rotations gives the shear deformation (ws):

$ws1 := int(g1, x) + D1$:
$ws2 := int(g2, x) + D2$:
$ws3 := int(g3, x) + D3$:
$ws := piecewise(0 < x < a, ws1, a < x < c, ws2, c < x < H, ws3)$;

$$\begin{cases} -\frac{R\,x}{GA} + D1 & 0 < x \text{ and } x < a \\ \frac{R\left(\frac{H}{b} - 1\right)x}{GA} + D2 & a < x \text{ and } x < c \\ -\frac{R\,x}{GA} + D3 & c < x \text{ and } x < H \end{cases} \tag{16}$$

The three integration constants can be solved using three boundary conditions:
1) ws1(0) = 0
2) ws1(a) = ws2(a)
2) ws3(H) = 0

Equation 1 gives:

$x := 0$:
$ws1 = 0$;

$$D1 = 0 \tag{17}$$

Equation 3 gives:

$x := H$:
$ws3 = 0$;
$D3 = solve(\ ws3 = 0, D3)$;

Figure E.7: Maple worksheet page 7

$$-\frac{R\,H}{GA}+D3=0$$

$$D3=\frac{R\,H}{GA} \tag{18}$$

Equation 2 gives:

$x := a$:

$ws1 = ws2$;

$$-\frac{R\,a}{GA}+D1=\frac{R\left(\frac{H}{b}-1\right)a}{GA}+D2 \tag{19}$$

$D1 := 0$:

$D2 = solve(ws1 = ws2, D2)$;

$$D2=-\frac{R\,H\,a}{b\,GA} \tag{20}$$

$D3 := \frac{R \cdot H}{GA}$:

$D2 := -\frac{R \cdot a \cdot H}{b \cdot GA}$:

$unassign('x')$:

The shear deformation equations now become:

ws;

$$\begin{cases} -\frac{R\,x}{GA} & 0 < x \text{ and } x < a \\ \frac{R\left(\frac{H}{b}-1\right)x}{GA}-\frac{R\,H\,a}{b\,GA} & a < x \text{ and } x < c \\ -\frac{R\,x}{GA}+\frac{R\,H}{GA} & c < x \text{ and } x < H \end{cases} \tag{21}$$

Defining the variables:

$a := 1595$:

$b := 410$:

$c := a + b$:

$H := 2 \cdot a + b$:

$R := 23600$:

$EI := 36471000000000$:

$GA := 123264000$:

One can plot the shear rotation and deformation:

$plot(g \cdot 1000, x = 0..3600)$;

$plot(ws, x = 0..3600)$;

Figure E.8: Maple worksheet page 8

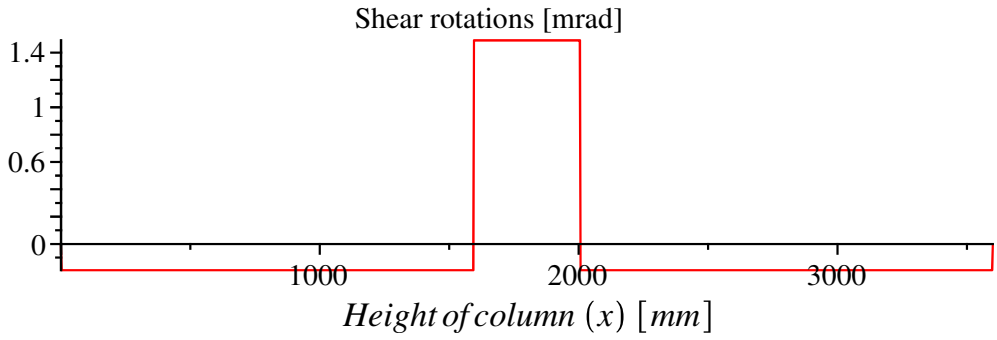

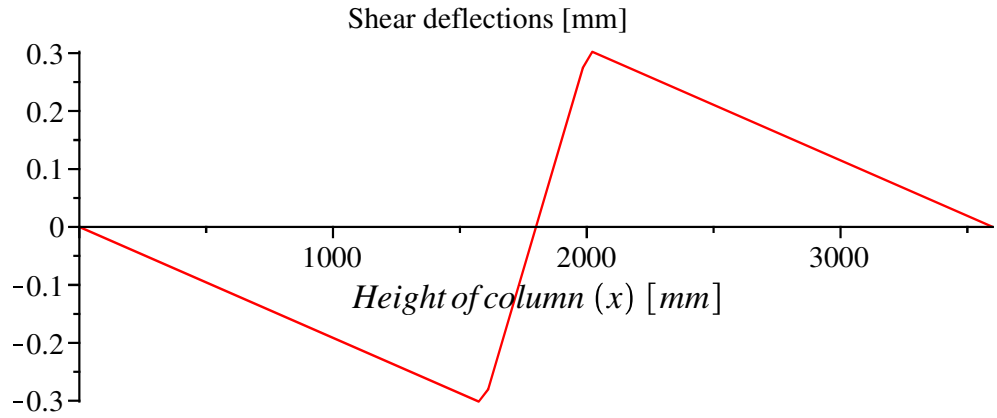

Total rotations and deformations now become:

$rot1 := t1 + g1$:
$rot2 := t2 + g2$:
$rot3 := t3 + g3$:
$rot := piecewise(0 < x < a, rot1, a < x < c, rot2, c < x < H, rot3)$:
$plot(rot \cdot 1000, x = 0..3600)$;
$w1 := wb1 + ws1$:
$w2 := wb2 + ws2$:
$w3 := wb3 + ws3$:
$w := piecewise(0 < x < a, w1, a < x < c, w2, c < x < H, w3)$:
$plot(w, x = 0..3600)$;

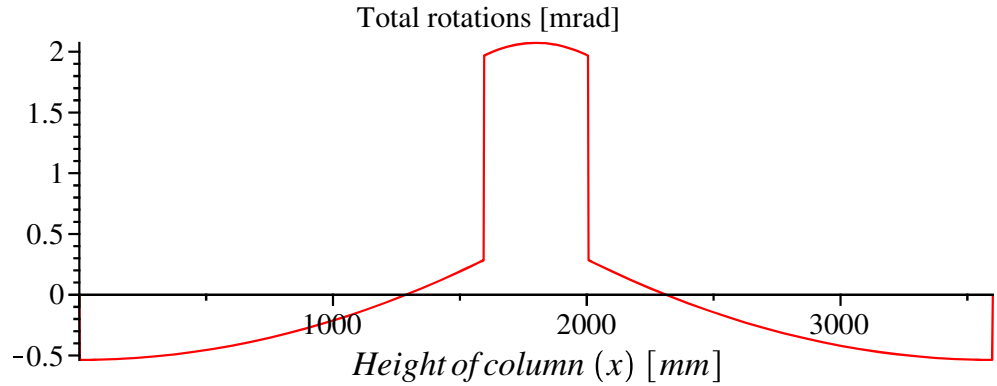

Figure E.9: Maple worksheet page 9

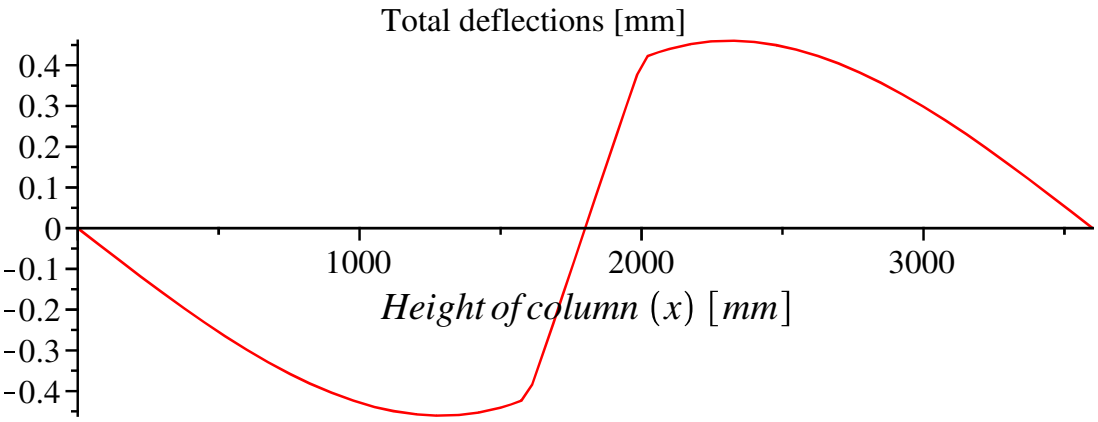

Figure E.10: Maple worksheet page 10

E.2 MMBA after yielding for gravity system

This section shows the derivation of the MMBA for gravity frames after yielding. This is an extension of the MMBA for gravity frames before yielding which has been derived in Section 8.6. Yield rotation only applies to concrete, as reinforcement can yield before ultimate strength is reached. Therefore this section does not apply for timber, but the procedure has been further developed for concrete gravity systems. In the case of concrete systems shear deformation is much less significant than for timber systems, and therefore this term has been left out of the equations.

Yielding of steel can only happen in the monolithic case. Displacements of the jointed ductile connection stay the same as before yield rotation and are given by Equation 8.55. Displacements for the monolithic case are now split into two parts, yield displacement and plastic displacements. Yield displacements are given in Equation E.9.

$$\Delta_y = \phi_y \frac{L_b^2}{32} \tag{E.9}$$

Plastic rotations are defined in Equation E.10, where L_p is the length of the plastic hinge region, as shown in Figure E.11.

$$\theta_p = (\phi - \phi_y) L_p \tag{E.10}$$

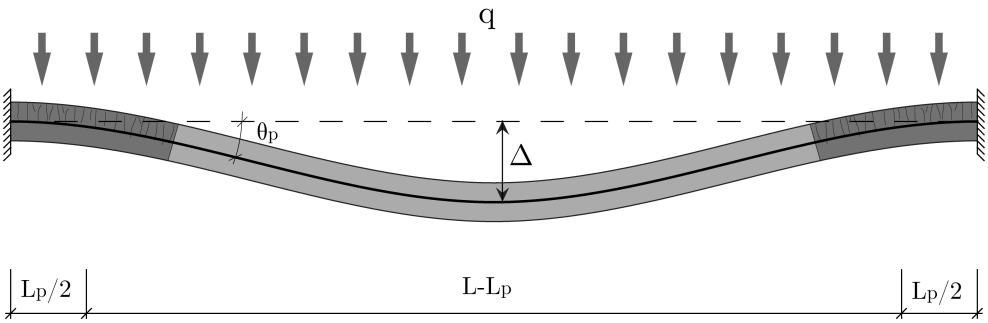

Figure E.11: Schematics of gravity MMBA for concrete systems after yielding

The mid-span displacements due to rotation in the plastic hinge zones are given by Equation E.11. This equation is very similar to Equation 8.54, where

mid-span displacements due to gap opening are calculated.

$$\Delta = \frac{5}{16}\theta_p(L_b - L_p) \tag{E.11}$$

Combining Equations E.10 and E.11 and adding the plastic displacement to the yield displacement (Equation E.9) gives a new formula for the monolithic displacements, shown in Equation E.12.

$$\Delta_{mon} = \Delta_y + \Delta = \phi_y\frac{L_b^2}{32} + \frac{5}{16}(\phi - \phi_y)L_p(L_b - L_p) \tag{E.12}$$

The member compatibility can be applied again and rewritten to define the curvature, as shown in Equation E.13.

$$\begin{aligned}
\Delta_{mon} &= \Delta_{imp} \\
\phi_y\frac{L_b^2}{32} + \frac{5}{16}(\phi - \phi_y)L_p(L_b - L_p) &= \frac{5}{16}\theta_{imp}L_b + \frac{L_b^2}{32}\phi_{dec} \\
10(\phi - \phi_y)\frac{L_p}{L_b}\left(1 - \frac{L_p}{L}\right) &= 10\frac{\theta_{imp}}{L_b} + \phi_{dec} - \phi_y \\
(\phi - \phi_y) &= \frac{10\frac{\theta_{imp}}{L_b} - (\phi_y - \phi_{dec})}{10\frac{L_p}{L_b}\left(1 - \frac{L_p}{L_b}\right)} \\
\phi &= \frac{10\frac{\theta_{imp}}{L_b} - (\phi_y - \phi_{dec})}{10\frac{L_p}{L_b}\left(1 - \frac{L_p}{L_b}\right)} + \phi_y
\end{aligned} \tag{E.13}$$

The form of this equation is again very similar to the seismic MMBA, but the cantilever length has been replaced by the full beam length with different factors.

E.3 MMBA for seismic cantilever system

This section shows the derivation for the seismic MMBA (cantilever system as shown in Figure E.12) with the inclusion of shear.

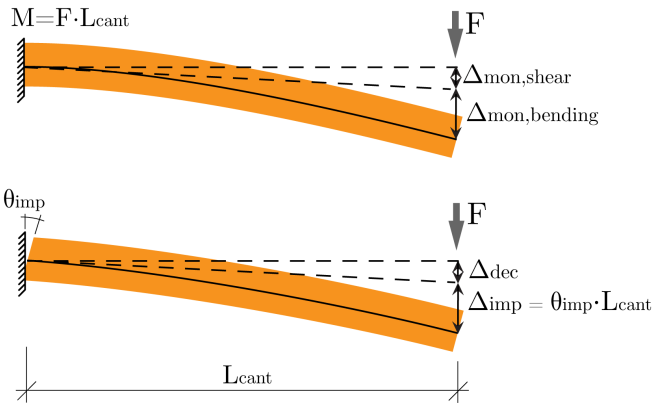

Figure E.12: Comparison of displacements for monolithic and rocking connection of cantilever beam

Before decompression the displacement of a cantilever is given by Equation E.14.

$$\begin{aligned}
\Delta_{mon} &= \Delta_{mon,bending} + \Delta_{mon,shear} = \frac{FL_{cant}^3}{3EI} + \frac{FL_{cant}}{GA_s} \\
\Delta_{mon} &= \frac{ML_{cant}^2}{3EI} + \frac{M}{GA_s} = \frac{M}{EI} \cdot \left(\frac{L_{cant}^2}{3} + \frac{EI}{GA_s} \right) \\
\Delta_{mon} &= \phi \cdot \left(\frac{L_{cant}^2}{3} + \frac{EI}{GA_s} \right)
\end{aligned} \tag{E.14}$$

At decompression the curvature is given by Equation E.15.

$$\Delta_{dec} = \phi_{dec} \cdot \left(\frac{L_{cant}^2}{3} + \frac{EI}{GA_s} \right) \tag{E.15}$$

After decompression the imposed deformation of the cantilever is given by Equation E.16.

$$\Delta_{imp} = \theta_{imp} L_{cant} + \Delta_{dec} = \theta_{imp} L_{cant} + \phi_{dec} \cdot \left(\frac{L_{cant}^2}{3} + \frac{EI}{GA_s} \right) \tag{E.16}$$

Equating the displacements of a monolithic system with the jointed ductile system results in a formula for the curvature, as shown in Equation E.17.

$$\begin{aligned} \Delta_{mon} &= \Delta_{imp} \\ \phi \cdot \left(\frac{L_{cant}^2}{3} + \frac{EI}{GA_s} \right) &= \theta_{imp} L_{cant} + \phi_{dec} \cdot \left(\frac{L_{cant}^2}{3} + \frac{EI}{GA_s} \right) \\ \phi &= \frac{L_{cant}}{\frac{L_{cant}^2}{3} + \frac{EI}{GA_s}} \cdot \theta_{imp} + \phi_{dec} \\ \phi &= \frac{3}{L_{cant} + \frac{3EI}{L_{cant} GA_s}} \cdot \theta_{imp} + \phi_{dec} \end{aligned} \tag{E.17}$$

For a rectangular section the following assumptions can be made:

- $I = bh^3/12$
- $A_s = 2/3bh$
- $G = E/20$

Applying these equations to Equation E.17 results in Equation E.18.

$$\phi = \frac{3}{L_{cant} + \frac{15h^2}{2L_{cant}}} \cdot \theta_{imp} + \phi_{dec} \tag{E.18}$$

Appendix F

Analysis of frames

This appendix presents additional information which belongs to the analysis of post-tensioned timber frames, Chapter 9. Firstly the derivation of the analytical model for calculation of bending moments in a post-tensioned timber frame are presented in Section F.1. Section F.2 presents the loading data, material properties, strength reduction factors and design checks according to Australian / New Zealand design standards.

Section F.3 shows calculation of the moment-rotation behaviour due to gap opening of a beam-column connection in a post-tensioned timber frame. The final section, Section F.4, presents an overview of the output of the framework analysis program for the full frame design. Deflections, rotations, bending moments, shear forces and axial forces are presented. Each output is shown for different load cases and different levels of post-tensioning.

F.1 Analytical derivation of beam model

Four components contribute to connection rotation:

1. Distributed load (q)
2. Post-tensioning force at deviator ($F_{pt,v}$)
3. External connection moment ($M_{con,ext}$)
4. Internal connection moment ($M_{con,int}$)

Each of these components lead to external connection rotation as shown in Table F.1.

Table F.1: Equations to calculate rotation components for a beam in a post-tensioned timber frame

Deflection component	Schematics	Equation
Distributed load	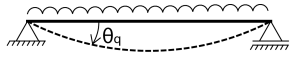	$\theta_q = \frac{q \cdot L^3}{24EI}$
Deviator uplift	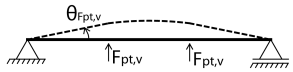	$\theta_{Fpt,v} = \frac{F_{pt,v} \cdot L^2}{9EI}$
Int. conn. moment	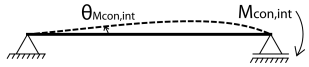	$\theta_{Mcon,int} = \frac{M_{con,int} \cdot L}{6EI}$
Ext. conn. moment	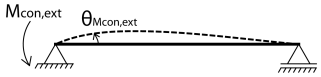	$\theta_{Mcon,ext} = \frac{M_{con,ext} \cdot L}{3EI}$

Assuming downwards rotations as positive and upwards rotations as negative, the total external connection rotation of one connection can be described by Equation F.1.

$$\theta_{con,ext} = \theta_q - \theta_{Fpt,v} - \theta_{Mcon,int} - \theta_{Mcon,ext} \tag{F.1}$$

The total external connection rotation can be written in terms of the external connection moment and connection stiffness, as shown in Equation F.2.

$$\theta_{con,ext} = \frac{M_{con,ext}}{k_{external}} \tag{F.2}$$

Combining the three equations above, results in Equation F.3, whereby two parameters are introduced for simplification, as shown in Equation F.4.

$$\frac{M_{con,ext}}{k_{external}} = \frac{q \cdot L^3}{24EI} - \frac{F_{pt,v} \cdot L^2}{9EI} - \frac{M_{con,int} \cdot L}{6EI} - \frac{M_{con,ext} \cdot L}{3EI}$$
$$\frac{M_{con,ext}}{k_{external}} = a - b \cdot M_{con,int} - 2b \cdot M_{con,ext} \tag{F.3}$$

$$a = \frac{q \cdot L^3}{24EI} - \frac{F_{pt,v} \cdot L^2}{9EI}$$
$$b = \frac{L}{6EI} \tag{F.4}$$

Equation F.3 can be rewritten to find an expression for $M_{con,ext}$ and a similar derivation can be performed for $M_{con,int}$. The resulting two equations are shown in Equation F.5.

$$M_{con,ext} = \frac{a - b \cdot M_{con,int}}{1/k_{external} + 2b}$$
$$M_{con,int} = \frac{a - b \cdot M_{con,ext}}{1/k_{internal} + 2b} \tag{F.5}$$

These two expressions can be used to solve for one of the connection moments, which is performed using Maple. The result is shown in Equation F.6.

$$M_{con,ext} = \frac{a(1 + b \cdot k_{internal})k_{external}}{1 + 2b \cdot k_{external} + 2b \cdot k_{internal} + 3b^2 \cdot k_{external} \cdot k_{internal}} \tag{F.6}$$

The resulting external connection moment can be used in Equation F.5 to calculate the internal connection moment.

F.2 Code based design

The Australian / New Zealand design codes (Standards New Zealand, 2002a,b, 1993) are used to perform a full design including strength and deflection checks. This section presents the loading data, material properties, strength reduction factors and design checks.

Loads A timber-concrete floor spanning 8m is assumed to be placed on the main floor beams, similar to used in the design of post-tensioned timber beams in Section 7.6. The dead weight of the floor, including a provision for partitions is taken as $G = 8 \times 3.7 = 29.6 kN/m$. The building is assumed to be an office building (Figure F.1), which should be designed for a live load of $Q = 8 \times 3.0 = 24 kN/m$.

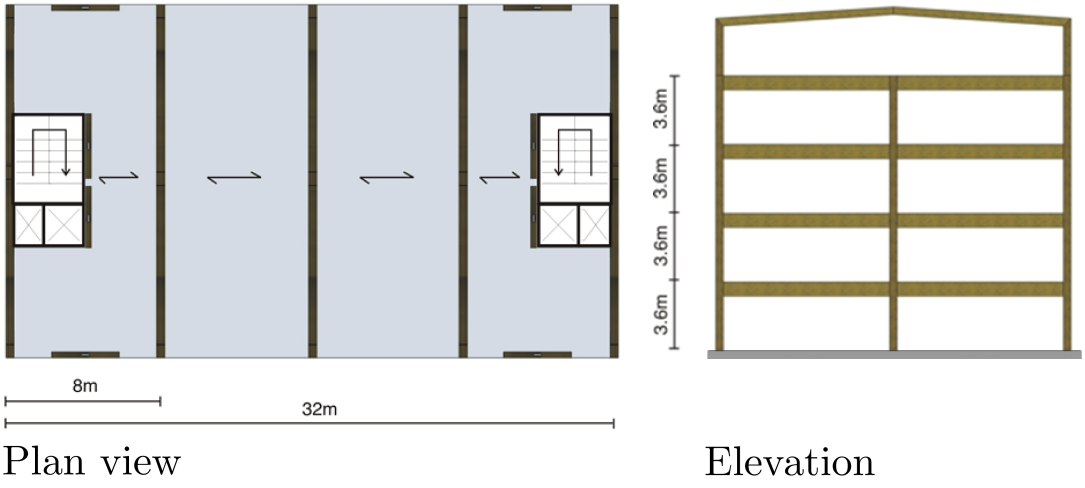

Figure F.1: Plan and elevation of prototype building used for frame design

Load combinations The design standard specified several load combinations which should be taken into account for serviceability limit state design (SLS) and ultimate limit state design (ULS). For gravity beams (no lateral loads involved) the following load-combinations are applicable:

- ULS 1: ψ_{to}PT
- ULS 2: 1.35G + ψ_{te}PT
- ULS 3: 1.2G + 1.5Q + ψ_{te}PT

- ULS 4: 1.2G + 1.5ψ_1Q + ψ_{te}PT
- SLS 1: PT only
- SLS 2: G + ψ_sQ + ψ_{ts}PT
- SLS 3: G + ψ_lQ + ψ_{tl}PT

Where:

- ψ_{to} = Factor for increase in tendon force due to over-stressing
- ψ_{te} = Factor for increase in tendon force under ULS load
- ψ_{ts} = Factor for increase in tendon force under short-term SLS load
- ψ_{tl} = Reduction factor for tendon force under long-term SLS load
- ψ_s = Combination factor for short-term imposed action
- ψ_l = Combination factor for long-term imposed action

Combination factors for short-term and long-term imposed action are given in Table 4.1 of AS/NZS 1170.0:2002 (Standards New Zealand, 2002a). In most cases these factors are 0.7 and 0.4 for short-term and long-term, respectively.

The first ULS check is for the situation when the beam is getting post-tensioned. The beam will be overstressed to compensate for instantaneous losses. Experimental testing has shown that these losses are in the order of 10%. Therefore the factor ψ_{to} can be taken as 1.1. For highly stressed beams this design check could become governing.

The second ULS check is for a heavy permanent action with a small imposed action. For office buildings this check is usually not governing the design, therefore this has not been evaluated in this chapter.

The third ULS check is for the maximum combination of dead and imposed action. Under this load the beam will deflect significantly and as a result the post-tensioning force will increase. For a quick design the amount tendon elongation, and thus increase in post-tensioning force can be estimated at 20%. This should be checked in a final design. For this load-combination a load duration factor for medium term loading, $k_{1,M} = 0.8$, should be used.

The fourth ULS check is a long-term strength check, based on a reduced imposed load and the long-term post-tensioning load. For this load-combination a load duration factor for long-term loading, $k_{1,L} = 0.57$ (or 0.6 for NZS3603), should be used.

The first SLS check is for the precamber only. The precamber is limited for construction purposes. In this chapter the limit of span over 300 is used. This limit also allows for a good first estimate of required post-tensioning force.

The second SLS check is for short-term deflections under permanent action and a factor of imposed action. This factor is given by AS/NZS 1170.0:2002 and for residential, office and retail buildings this factor $\psi_s = 0.7$. The tendon force under this load will be lower than the initial post-tensioning force due to post-tensioning losses over time, but an increase will occur due to tendon elongation. These effects approximately balance each other and thus the factor ψ_{ts} can be taken as 1.0.

The third SLS check is for long-term deflections under permanent action and a factor of imposed action. This factor is given by AS/NZS 1170.0:2002 and for residential, office and retail buildings this factor $\psi_l = 0.4$. The tendon force under this load will be lower than the initial post-tensioning force due to post-tensioning losses over time. The maximum expected post-tensioning loss for parallel to grain loading is about 15% and for frames 25% (Davies and Fragiacomo, 2007). Therefore the factor ψ_{tl} can be taken as 0.85 for the design of beams and 0.75 for the design of frames. A creep factor of 2.0 has been assumed for timber in an indoor environment.

Material properties A generic LVL11 material is used throughout this chapter. Material properties are listed in Table F.2. Notably the design procedure herein described can be extended and applied to other engineered wood materials with different mechanical properties

Table F.2: Material properties for generic LVL11

Property	Symbol	Magnitude
Bending strength	f_b	48MPa
Compression strength parallel to grain	f_c	45MPa
Tension strength parallel to grain	f_t	30MPa
Compression strength perpendicular to grain	f_p	12MPa
Modulus of elasticity	E	11GPa
Shear modulus	G	550MPa

A size effect is applicable to members over 150mm in tension and members over 300mm in bending. The equations to calculate the allowable bending and tensile strength are shown in Equation F.7, where d is the larger cross-sectional dimension of the bending/tension member.

$$\begin{aligned} f'_b &= (300/d)^{0.167} f_b \\ f'_t &= (150/d)^{0.167} f_t \end{aligned} \tag{F.7}$$

Post-tensioning For the design of the post-tensioning system a range of post-tensioning forces was evaluated. The post-tensioning force was based on the initial timber compressive stress due to post-tensioning. For beams (Section 7.6), this range was taken as 0 to 10MPa. For frames, the post-tensioning force is more effective as it creates semi-rigid connections and the angle of tendons at the deviator is larger, resulting in an increase of uplift forces. Therefore the post-tensioning force in frames can be lower than in beams. The lower post-tensioning force also helps with the design of the connection, as the strength of the column perpendicular to grain is much lower than the strength of the beam. The range taken for the design of post-tensioned timber frames was from 0 to 5MPa. The corresponding force and number of tendons (15.2mm diameter) are presented in Table F.3. Also shown are the maximum design forces ($F_{d,max}$), which are based on 70% of yield strength and the ultimate design forces (F_{ult}), which are 90% of yield strength.

Table F.3: Design of post-tensioning system for timber frame

PT stress (MPa)	F_{pt} (kN)	No. of tendons (-)	Tendon area (mm^2)	$F_{d,max}$ (kN)	F_{ult} (kN)
1	184	2	286	304	392
2	368	3	429	456	588
3	552	4	572	608	784
4	736	5	715	760	980
5	920	6	858	912	1176

Strength and stiffness modification factors For evaluation of the section capacity one needs to determine several factors, according to the timber design Standards AS 1720.1:2010 (Standards Australia, 2010) and NZS 3603:1993 (Standards New Zealand, 1993). Table F.4 shows typical factors, which are used in this chapter, for the design of an office building.

Table F.4: Values for strength and stiffness reduction factors according to Australian and New Zealand timber design standards (Standards Australia, 2010; Standards New Zealand, 1993)

Description	Value	Assumption
Strength reduction factor	$\phi = 0.9$	LVL
Load duration factor	$k_{1,L} = 0.57$	Permanent load
	$k_{1,M} = 0.8$	Medium duration load
	$k_2 = 2.0$	(j_2 in AS)
Partial seasoning factor	$k_4 = 1.0$	Moisture content $< 15\%$
	$k_5 = 1.0$	Moisture content $< 15\%$
Temperature factor	$k_6 = 1.0$	Covered timber under ambient cond.
Load sharing factor	$k_9 = 1.0$	Does not apply for LVL
Stability factor	k_{12}	evaluated in calculations

Design checks The formulas provided in Equation F.8 are used for the calculation of bending, compression and shear strength of a section.

$$\begin{aligned} M_d &= \phi \cdot k_1 \cdot f'_b \cdot Z \\ N_d &= \phi \cdot k_1 \cdot f'_c \cdot A \\ V_d &= \phi \cdot k_1 \cdot f'_s \cdot A_s \end{aligned} \tag{F.8}$$

The design check for bending and compression is given in Equation F.9 and the design check for shear in Equation F.10.

$$\frac{N^*}{N_d} + \frac{M^*}{M_d} < 1 \tag{F.9}$$

$$V^* < \phi V_d \tag{F.10}$$

Furthermore, as described in Section 7.5, for beams with low post-tensioning force, the tensile strength of the bottom flange should be checked according to design checks in EN 1995:2004 (CEN, 2004b).

An extra design check has been implemented to check the compressive strength of the beam at the connection. After gap opening the full compressive force due to post-tensioning has to be transferred through the bottom flange. The design check as presented in Equation F.11 has been used.

$$F_{pt,uls} < \phi N_n = \phi \cdot k_1 \cdot f_c \cdot 0.5 A_{flange} \tag{F.11}$$

In this design a deflection limit (w_{lim}) of span over 300 has been used, as recommended for floor beams by Appendix C of AS/NZS 1170.0 (Standards New Zealand, 2002a).

F.3 Connection design

This section shows calculation of the moment-rotation behaviour due to gap opening of a beam-column connection in a post-tensioned timber frame as shown in Figure F.2. The moment-rotation behaviour is used for the framework model, as described in Section 9.2. The influence of joint panel shear rotation and interface compression are also described in that section.

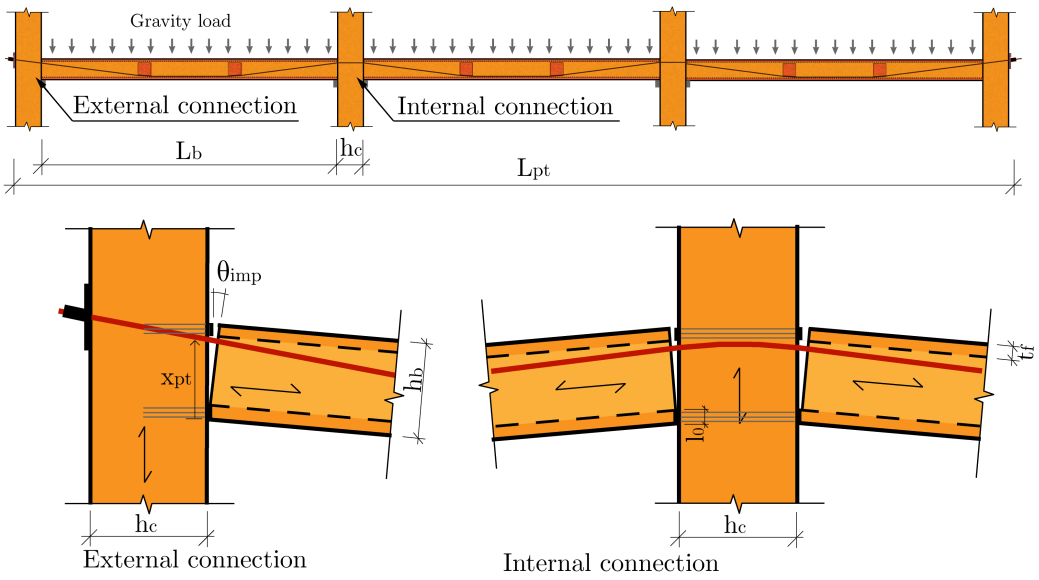

Figure F.2: Overview of frame with external and internal connections

A list of constants used in the connection design is given in Table F.5.

Reduction factors for tendon elongation The reduction factors for tendon elongation (ω) are calculated as in Equations F.12 to F.17.

$$k_{beam} = \frac{E_t \cdot A_b}{L_b} = \frac{11000 \cdot 183600}{10000} = 202kN/mm \tag{F.12}$$

$$k_{col} = k_{scr} \cdot \frac{2E_{90} \cdot w_c}{ln\left(\frac{h_c}{l_0} + 1\right)} = 1.7 \cdot \frac{2500 \cdot 400}{ln\left(\frac{600}{90} + 1\right)} = 334kN/mm \tag{F.13}$$

Table F.5: Constant values used for simplified procedure for calculating gap opening for framework model

Parameter	Symbol	Frame
Number of beams	n	3
Beam length	L_b	10mm
Beam height	h_b	800mm
Beam width	b	400mm
Flange thickness	t_f	90mm
Web thickness	t_w	90mm
Timber area	A	183600mm^2
Shear area	A_s	106600mm^2
Moment of Inertia	I	12.7×10^9 mm^4
Modulus of Elasticity	E	11000MPa
Shear modulus	G	550MPa
Position of tendon	x_{pt}	680mm
Tendon length	L_{pt}	32.4m
MoE of tendons	E_{pt}	200000MPa
Screw reinforcing stiffness factor	k_{scr}	1.7

$$k_{pt} = \frac{E_{pt} \cdot A_{pt}}{L_{pt}} = \frac{200000 \cdot 858}{32400} = 5.30 kN/mm \tag{F.14}$$

$$\omega_{beam} = \frac{n \cdot k_{pt}}{k_{beam}} = \frac{3 \cdot 5.30}{202} = 0.079 \tag{F.15}$$

$$\omega_{col} = \frac{2 \cdot 3 \cdot 5.30}{334} = 0.095 \tag{F.16}$$

$$\omega_{dev} = 0.10 \tag{F.17}$$

The value for ω_{dev} was assumed to be 10%, based on recommendations in Section 8.6.3. Adding the three reduction factors gives a total reduction in tendon elongation of 27.4% due to frame shortening and deviator uplift. This calculation has been performed for the five different levels of post-tensioning, each with a different number of tendons and thus a different area of post-tensioning. The results are shown in Table F.6.

Table F.6: Reduction factors for tendon elongation

PT stress (MPa)	Tendon area (mm^2)	ω_{beam}	ω_{col}	ω_{dev}	ω_{total}
1	286	2.6	3.2	10	15.8
2	429	3.9	4.8	10	18.7
3	572	5.2	6.3	10	21.5
4	715	6.6	7.9	10	24.5
5	858	7.9	9.5	10	27.4

Decompression Decompression is calculated for a compressive stress in the beam due to post-tensioning of 3MPa. This gives an initial post-tensioning force of 550kN. At decompression the post-tensioning force is larger than the initial post-tensioning force as a result of tendon elongation due to deviator deflections. An iterative procedure to calculate the post-tensioning force at decompression was performed and the resulting force was 604kN, an increase of 10% compared to the initial post-tensioning force. This post-tensioning force gave an uplift force at the deviators of 102kN.

The assumption was made that only the flanges were touching the column. The post-tensioning force at decompression resulted in a compressive stress at the top and bottom flanges of 15.3MPa. The resulting decompression moment is calculated in Equation F.18.

$$\begin{aligned} M_{dec} &= 0.5 F_{pt,dec} \left(h_b - 2t_f + \frac{4t_f^2}{3h_b} \right) \\ M_{dec} &= 0.5 \cdot 604000 \left(800 - 2 \cdot 90 + \frac{4 \cdot 90^2}{3 \cdot 800} \right) = 192 kNm \end{aligned} \tag{F.18}$$

The curvature at decompression is calculated in Equation F.19.

$$\phi_{dec} = \frac{M_{dec}}{EI} = \frac{192 \cdot 10^6}{11000 \cdot 12.7 \cdot 10^9} = 1.37 \cdot 10^{-6} \tag{F.19}$$

Deviator deflections are the summation of the initial precamber of beam deflections, as shown in Equation F.20

$$\Delta_{dev,dec} = \phi_{dec} \cdot \left(\frac{2}{81}L_b^2 + \frac{4EI}{3GA_s}\right) + \frac{4}{648}\frac{F_v L_b^3}{EI} + \frac{F_v L_b}{3GA_s}$$
$$\Delta_{dev,dec} = 1.37 \cdot 10^{-6} \cdot \left(\frac{2}{81}10000^2 + \frac{4 \cdot 11000 \cdot 12.7 \cdot 10^9}{3 \cdot 550 \cdot 106600}\right) + \dots$$
$$\dots \frac{4}{648}\frac{102000 \cdot 10000^3}{11000 \cdot 12.7 \cdot 10^9} + \frac{102000 \cdot 10000}{3 \cdot 550 \cdot 106600}$$
$$\Delta_{dev,dec} = 7.74 + 4.49 + 5.77 = 18.0mm \tag{F.20}$$

This deviator deflection leads to tendon elongation as shown in Equation F.21.

$$\Delta l_{pt,dev} = 2 \cdot n \left(\sqrt{\left(\frac{L_b}{3}\right)^2 + (\Delta_{imp,dev} + x_{pt})^2} - \sqrt{\left(\frac{L_b}{3}\right)^2 + x_{pt}^2}\right)$$
$$\Delta l_{pt,dev} = 2 \cdot 3 \left(\sqrt{\left(\frac{10000}{3}\right)^2 + (18.0 + 680)^2} - \sqrt{\left(\frac{10000}{3}\right)^2 + 680^2}\right)$$
$$\Delta l_{pt,dev} = 18.2mm \tag{F.21}$$

Due to frame shortening, the resulting tendon elongation is presented in Equation F.22, and the post-tensioning force is shown in Equation F.23.

$$\Delta l_{pt} = \frac{\Delta l_{pt,dev}}{1 + \omega_{beam} + \omega_{col} + \omega_{dev}}$$
$$\Delta l_{pt} = \frac{18.2}{1 + 0.053 + 0.065 + 0.1} = \frac{17.7}{1.218} = 14.9mm \tag{F.22}$$

$$F_{pt,dec} = \left(\epsilon_{pt,i} + \frac{\Delta l_{pt}}{L_{pt}}\right) \cdot E_{pt} A_{pt}$$
$$F_{pt,dec} = \left(0.48\% + \frac{14.9}{32400}\right) \cdot 200000 \cdot 572 = 604kN \tag{F.23}$$

It can be seen that this result matches the post-tensioning force at decompression which was given at the start of this section.

Gap opening It is assumed that the gap is fully opened at 2mrad rotation (end of transition phase), based on comparisons with experimental data from frame testing as presented in Section 8.6.6. At this level of rotation the compressive force is acting only at the bottom flange, where there is a triangular stress block. The design follows the procedure as presented in Figure 8.22 with the change that the neutral axis depth is known, namely the height of the bottom flange. Therefore the iterative part is no longer necessary. It should be noted that for low levels of post-tensioning the neutral axis depth might be smaller than the bottom flange, but this is not taken into account here. The results of the procedure are shown in Equations F.24 to F.30.

$$\theta_{imp} = 2mrad \tag{F.24}$$

$$\begin{aligned}
\Delta_{imp,dev} &= \Delta_{dev} + \Delta_{dev,dec} \\
\Delta_{imp,dev} &= \left(\frac{22 \cdot 10000}{81} + \frac{8EI}{3GA_s \cdot L_b}\right)\theta_{imp} + \Delta_{dev,dec} \\
\Delta_{imp,dev} &= \left(\frac{22L_b}{81} + \frac{8 \cdot 11000 \cdot 12.7 \cdot 10^9}{3 \cdot 550 \cdot 106600 \cdot 10000}\right) \cdot 0.002 + 18.0 \\
\Delta_{imp,dev} &= 6.7 + 18.0 = 24.7mm
\end{aligned} \tag{F.25}$$

$$\begin{aligned}
\Delta l_{pt,dev} &= 2 \cdot n \left(\sqrt{\left(\frac{L_b}{3}\right)^2 + (\Delta_{imp,dev} + x_{pt})^2} - \sqrt{\left(\frac{L_b}{3}\right)^2 + x_{pt}^2}\right) \\
\Delta l_{pt,dev} &= 2 \cdot 3 \left(\sqrt{\left(\frac{10000}{3}\right)^2 + (24.7 + 680)^2} - \sqrt{\left(\frac{10000}{3}\right)^2 + 680^2}\right) \\
\Delta l_{pt,dev} &= 25.1mm
\end{aligned} \tag{F.26}$$

$$\Delta l_{pt,gap} = 2 \cdot n \cdot \theta_{imp}(x_{pt} - c) = 2 \cdot 3 \cdot 0.002(680 - 90) = 7.1mm \tag{F.27}$$

$$\Delta l_{pt} = \frac{\Delta l_{pt,dev} + \Delta l_{pt,gap}}{1 + \omega_{beam} + \omega_{col} + \omega_{dev}}$$
$$\Delta l_{pt} = \frac{25.1 + 7.1}{1 + 0.053 + 0.065 + 0.1} = \frac{32.2}{1.218} = 26.4mm \tag{F.28}$$

$$F_{pt,dec} = \left(\epsilon_{pt,i} + \frac{\Delta l_{pt}}{L_{pt}}\right) \cdot E_{pt} A_{pt}$$
$$F_{pt,dec} = \left(0.48\% + \frac{26.4}{32400}\right) \cdot 200000 \cdot 572 = 646kN \tag{F.29}$$

$$M_{con} = F_{pt}\left(\frac{h_b}{2} - \frac{t_f}{3}\right) = 646000\left(\frac{800}{2} - \frac{90}{3}\right) = 239kNm \tag{F.30}$$

This sequence of calculations can be repeated for a range of connection rotations and a range of initial levels of post-tensioning. The resulting connection moment rotation behaviour for gap opening is shown in Figure F.3.

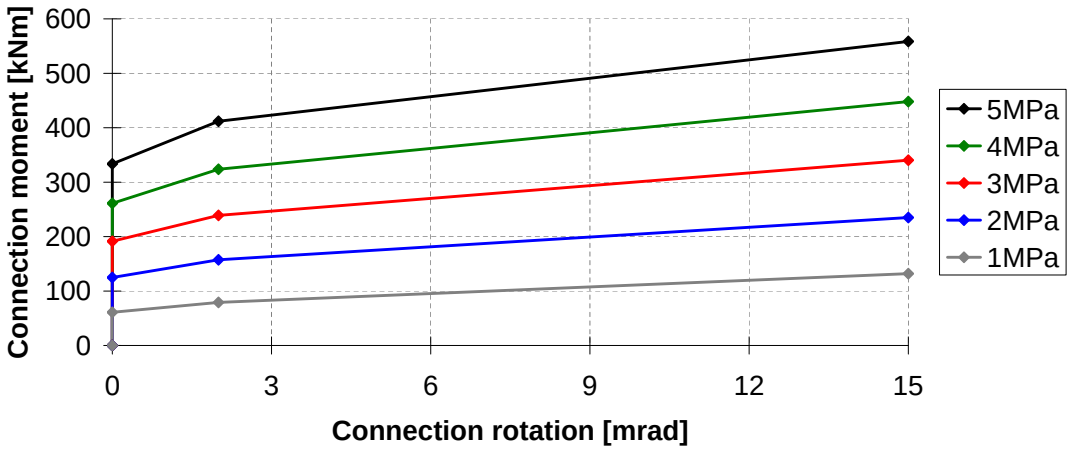

Figure F.3: Connection moment-rotation behaviour due to gap opening

F.4 Framework analysis results

A framework model, as described in Section 9.2 was made in a framework analysis program. For this the program Scia Engineer (Nemetschek, 2011) was used. An overview of half of the model is shown in Figure F.4. The rotational spring for joint panel shear deformation and interface compression and the rotational spring for gap opening were placed at 10mm apart in order to get output for every individual rotational component.

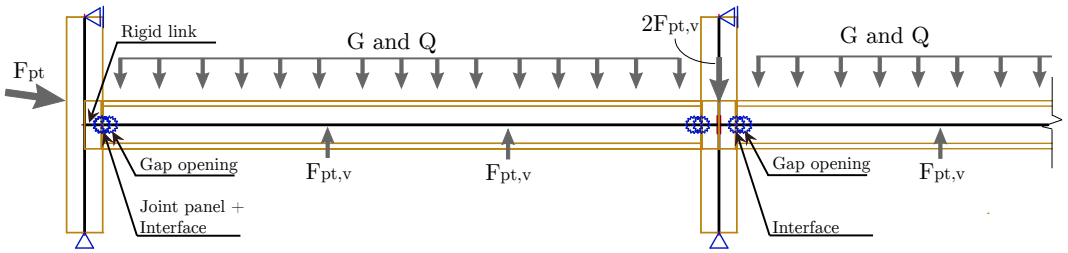

Figure F.4: Structural system of framework model

This section gives an overview of the output of the program. Deflections, rotations, bending moments, shear forces and axial forces are presented. Each output is shown for different load cases and different levels of post-tensioning. Two models without post-tensioning, one with pinned beam-column connections and the other with fully fixed beam-column connections, are also included for comparison.

The following load-combinations have been analysed, where G = 30kN/m and Q = 24kN/m. Values of post-tensioning (F_{pt} and $F_{pt,v}$) and tendon elongation (ψ_{te}) are given in Table F.7.

- PT Only: 1.1PT
- SLS - Long-term: G + 0.4Q + 0.75PT
- SLS - Short-term: G + 0.7Q + PT
- ULS: 1.2G + 1.5Q + ψ_{te}PT

Table F.7: Loading and tendon elongation for framework model

PT stress (MPa)	F_{pt} (kN)	$F_{pt,v}$ (kN)	ψ_{te} (-)
1	184	31	1.71
2	368	62	1.33
3	552	93	1.20
4	736	124	1.16
5	920	155	1.15

The following results are shown for the five different levels of post-tensioning and for pinned and fully fixed connections:

1. Deflections
    - PT Only
    - SLS - Long-term
    - SLS - Short-term
    - ULS
2. Rotations
    - PT Only
    - SLS - Long-term
    - SLS - Short-term
    - ULS
3. Bending moments
    - PT Only
    - ULS
4. Shear forces
    - PT Only
    - ULS
5. Axial forces
    - PT Only
    - ULS

F.4.1 Deflections

PT Only: 1.1PT

No output for this load case

(a) Pinned

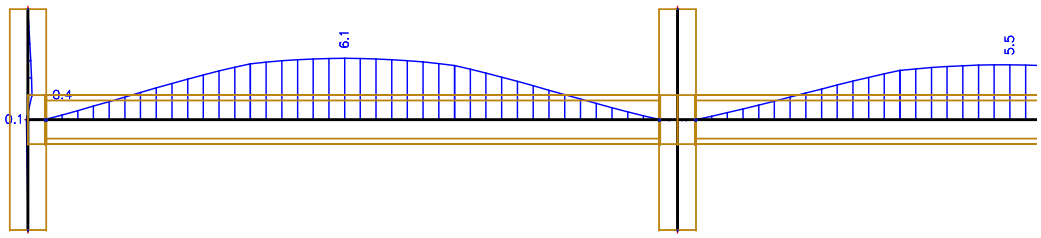

(b) 1MPa

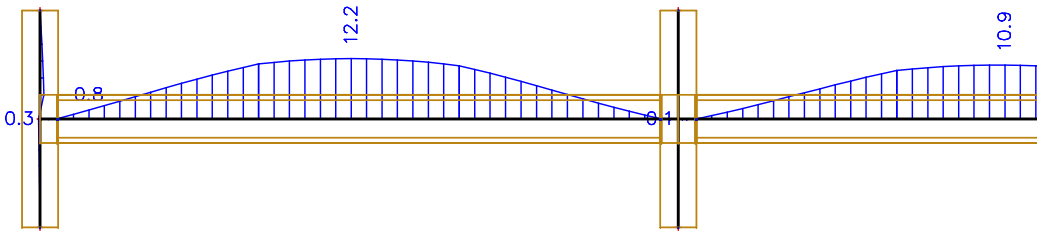

(c) 2MPa

Figure F.5: Post-tensioning only - Deflections (mm)

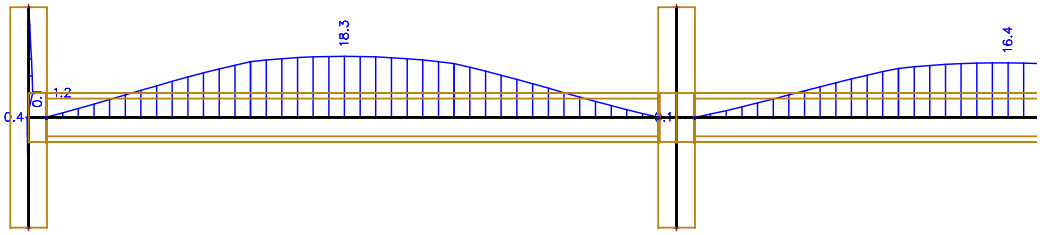

(a) 3MPa

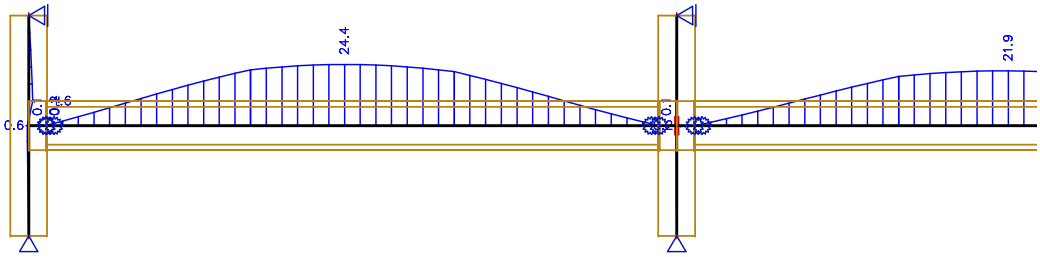

(b) 4MPa

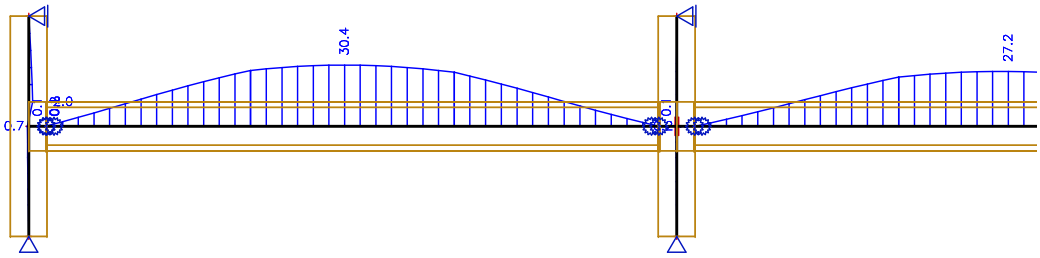

(c) 5MPa

No output for this load case

(d) Fixed

Figure F.6: Post-tensioning only - Deflections (mm) (continued)

SLS - Long-term: G + 0.4Q + 0.75PT

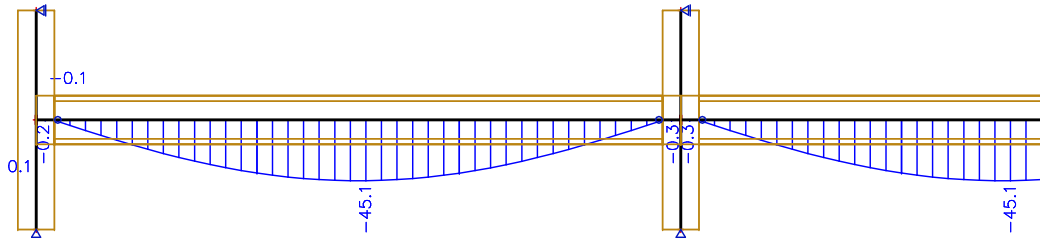

(a) Pinned

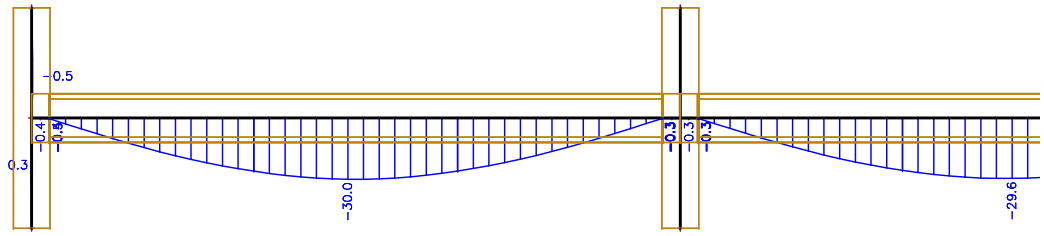

(b) 1MPa

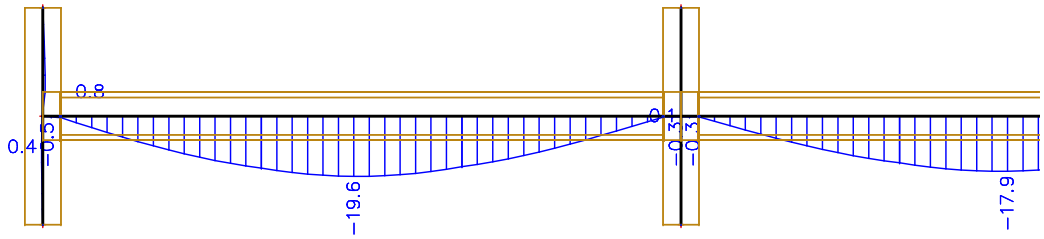

(c) 2MPa

Figure F.7: Long-term SLS - Deflections (mm)

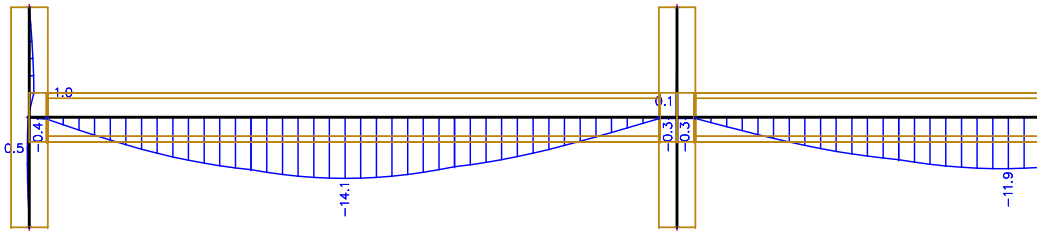

(a) 3MPa

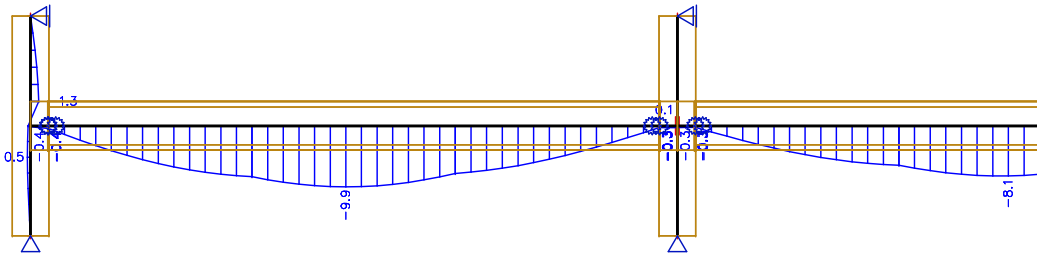

(b) 4MPa

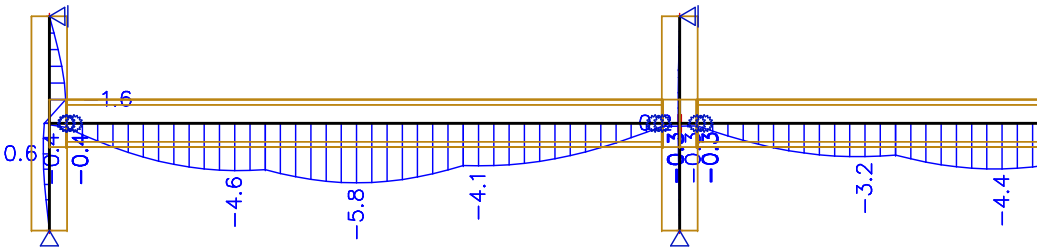

(c) 5MPa

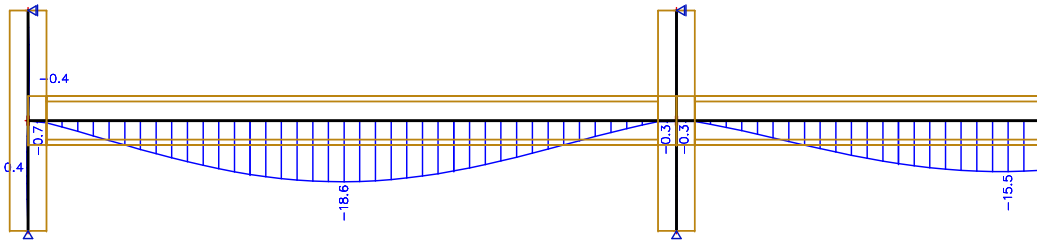

(d) Fixed

Figure F.8: Long-term SLS - Deflections (mm) (continued)

SLS - Short-term: G + 0.7Q + PT

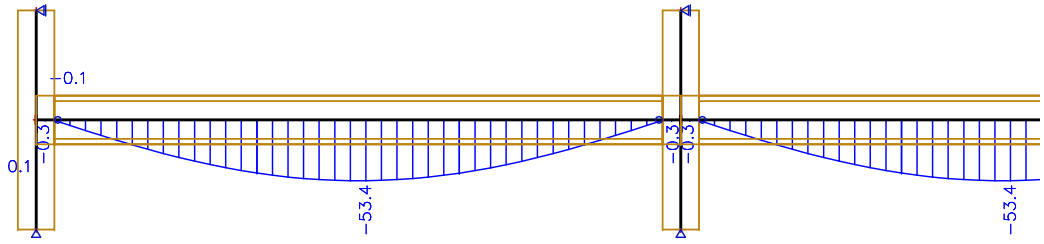

(a) Pinned

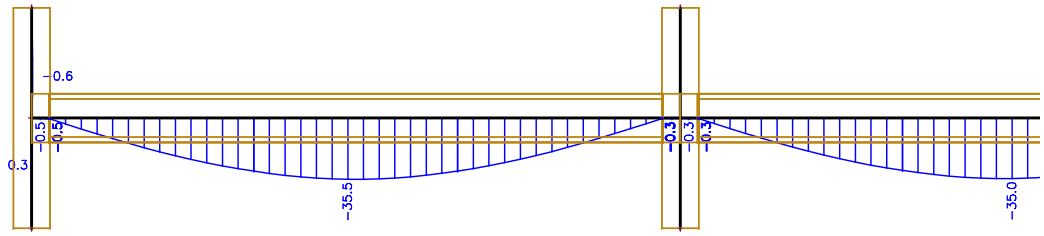

(b) 1MPa

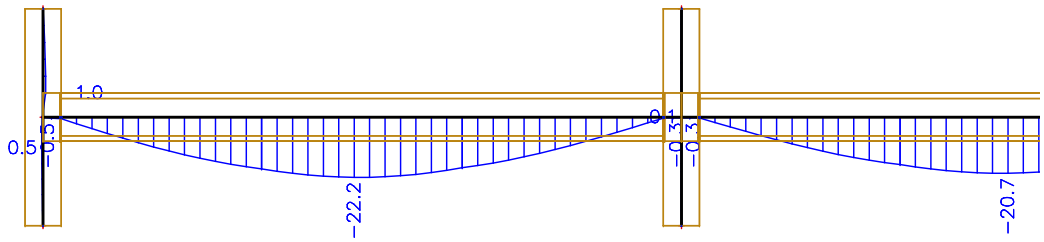

(c) 2MPa

Figure F.9: Short-term SLS - Deflections (mm)

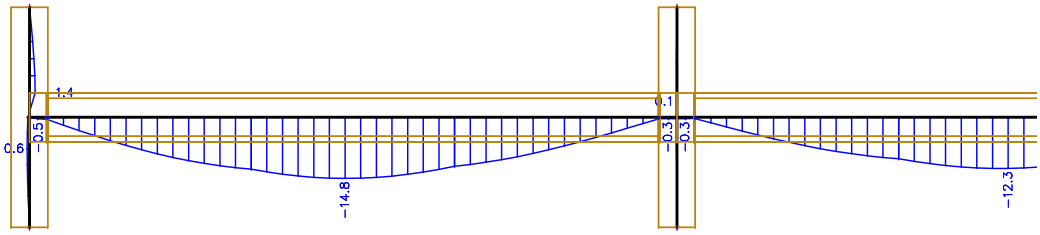

(a) 3MPa

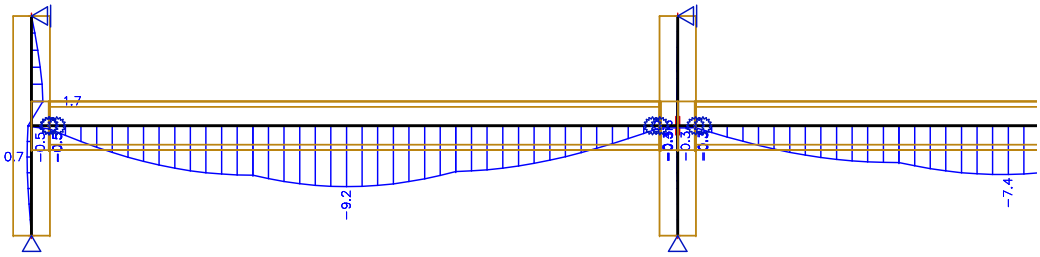

(b) 4MPa

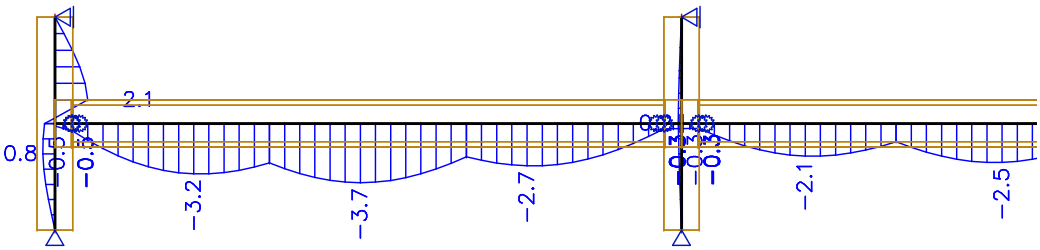

(c) 5MPa

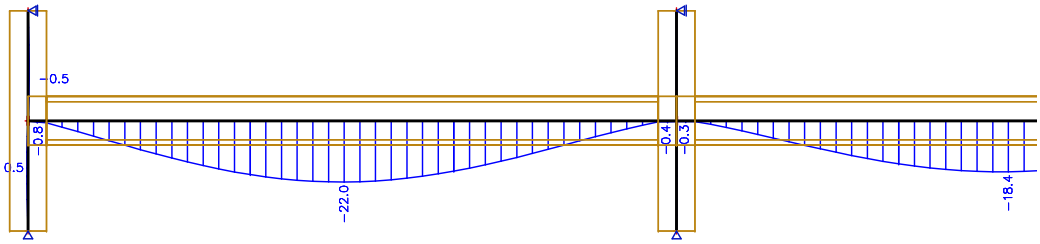

(d) Fixed

Figure F.10: Short-term SLS - Deflections (mm) (continued)

ULS: 1.2G + 1.5Q + ψ_{te}PT

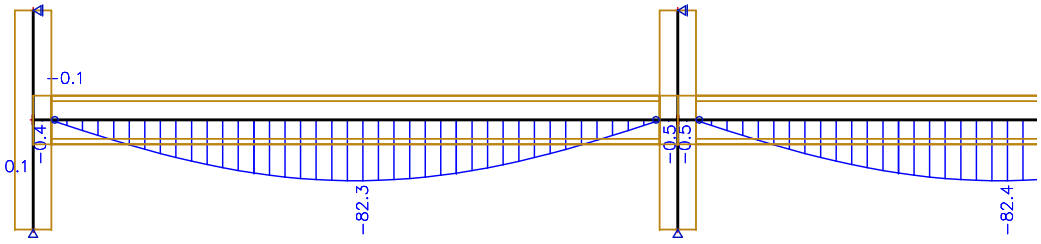

(a) Pinned

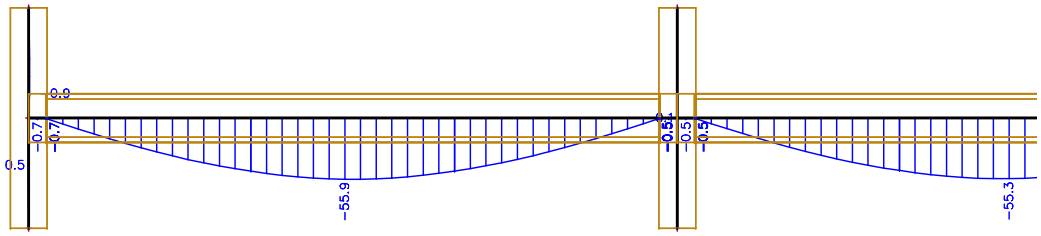

(b) 1MPa

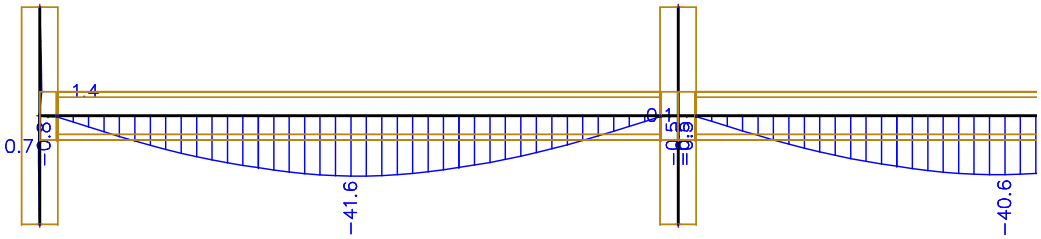

(c) 2MPa

Figure F.11: ULS - Deflections (mm)

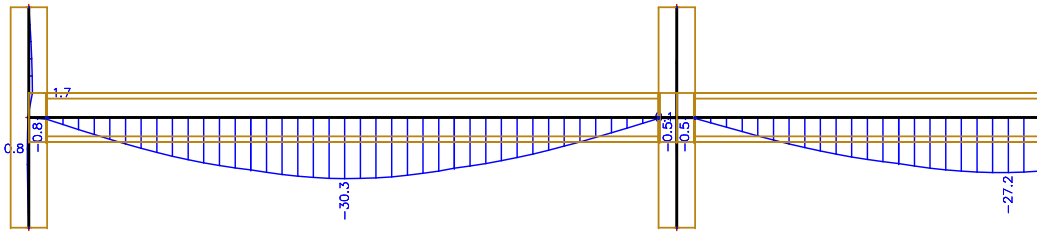

(a) 3MPa

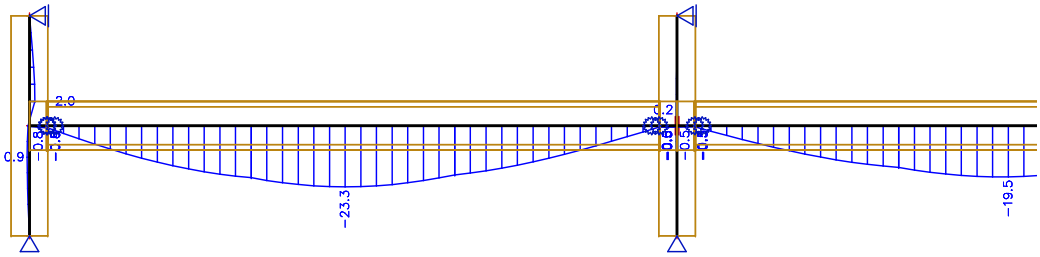

(b) 4MPa

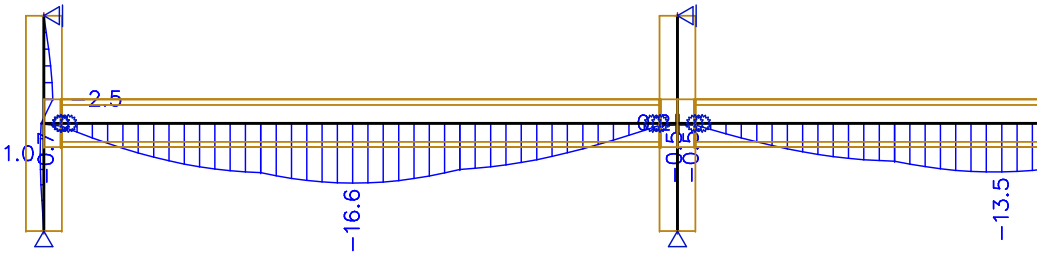

(c) 5MPa

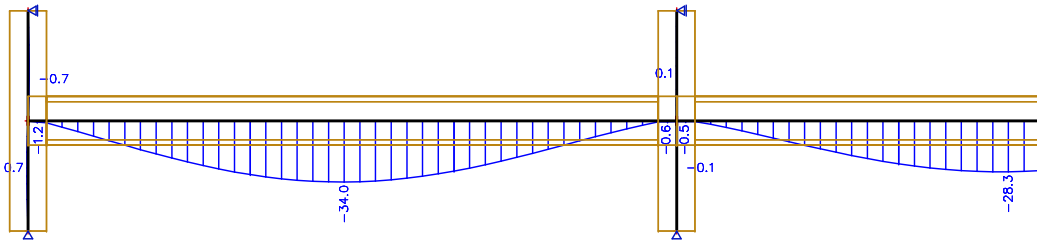

(d) Fixed

Figure F.12: ULS - Deflections (mm) (continued)

F.4.2 Rotations

PT Only: 1.1PT

No output for this load case

(a) Pinned

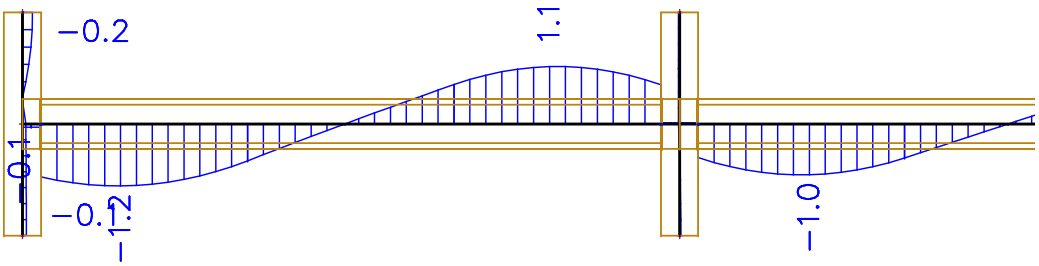

(b) 1MPa

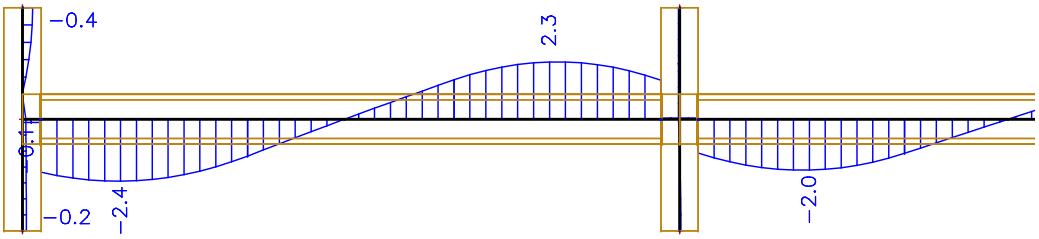

(c) 2MPa

Figure F.13: Post-tensioning only - Rotations (mrad)

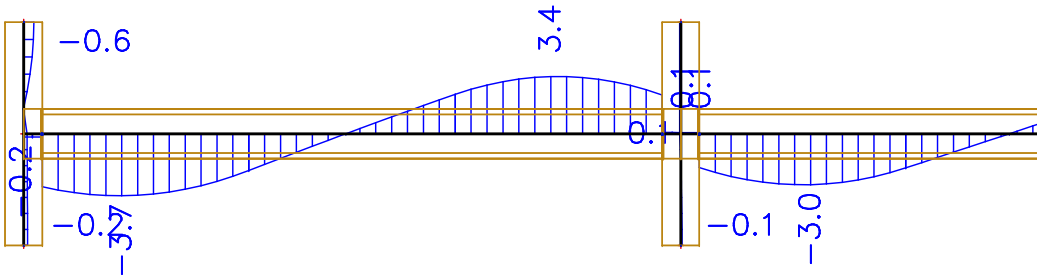

(a) 3MPa

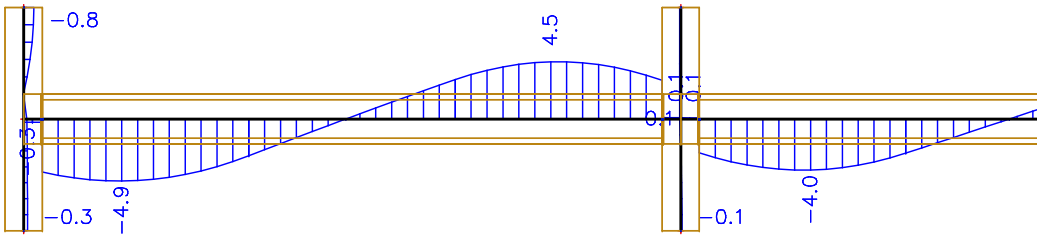

(b) 4MPa

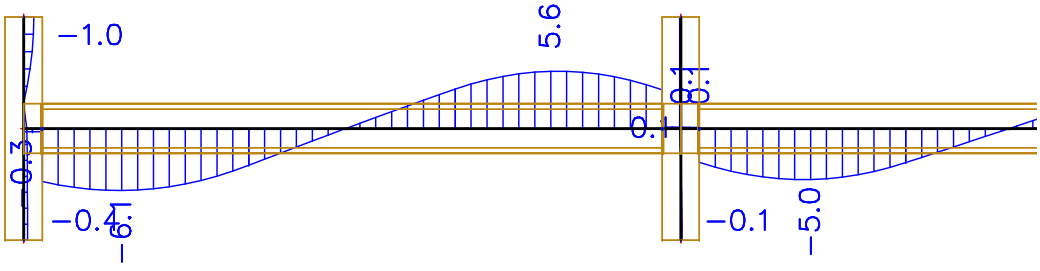

(c) 5MPa

No output for this load case

(d) Fixed

Figure F.14: Post-tensioning only - Rotations (mrad) (continued)

SLS - Long-term: G + 0.4Q + 0.75PT

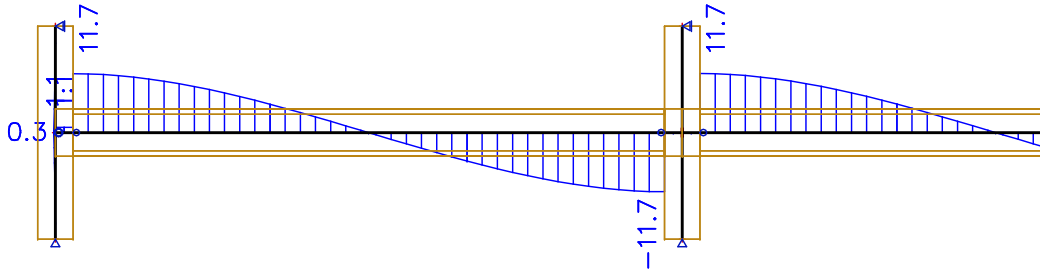

(a) Pinned

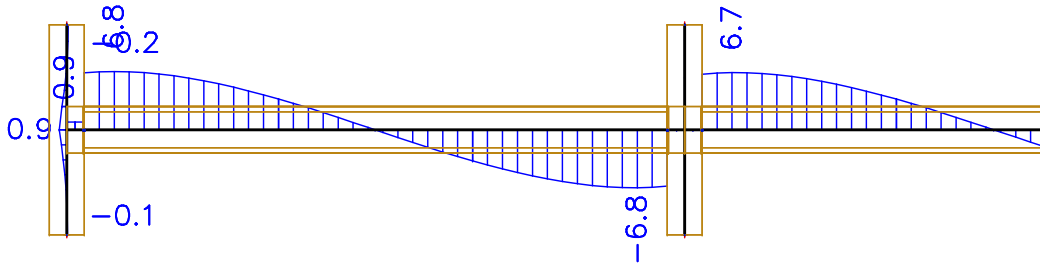

(b) 1MPa

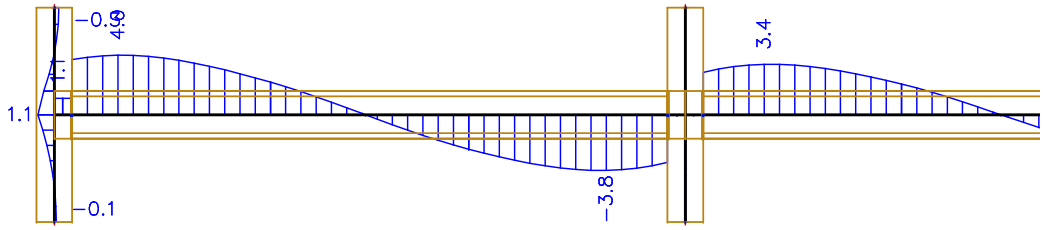

(c) 2MPa

Figure F.15: Long-term SLS - Rotations (mrad)

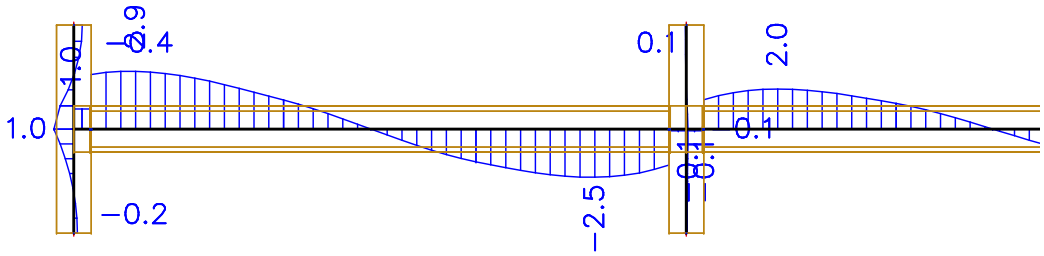

(a) 3MPa

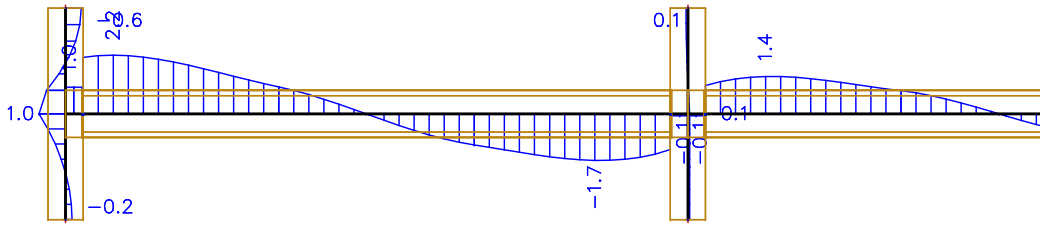

(b) 4MPa

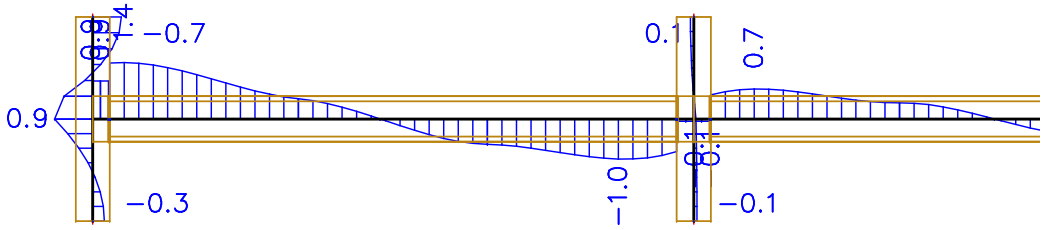

(c) 5MPa

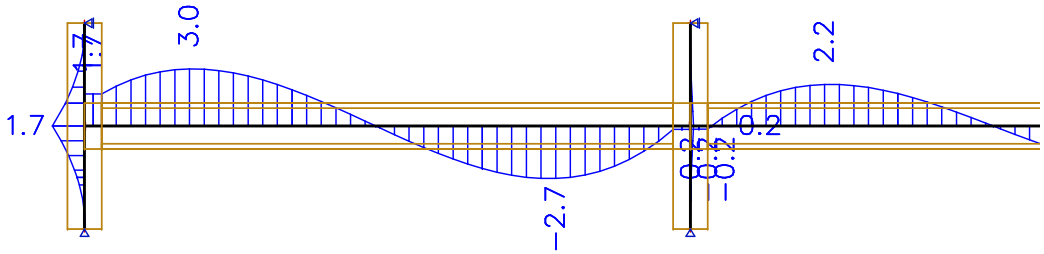

(d) Fixed

Figure F.16: Long-term SLS - Rotations (mrad) (continued)

SLS - Short-term: G + 0.7Q + PT

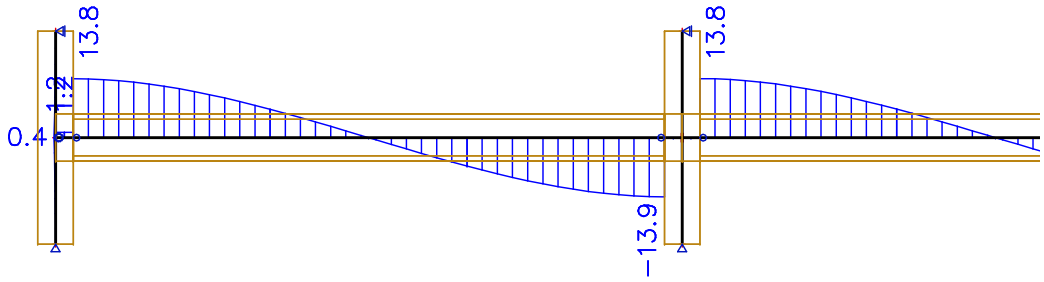

(a) Pinned

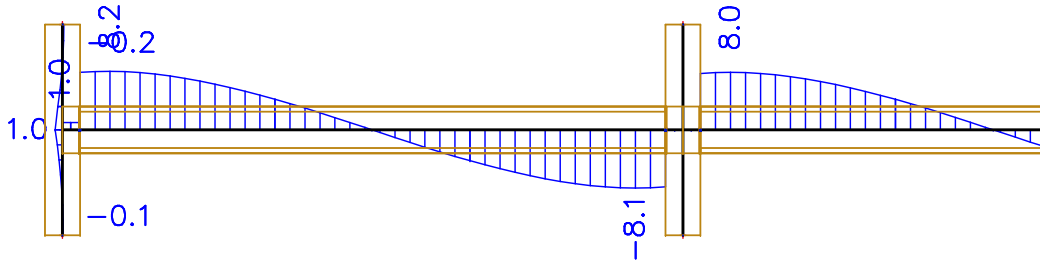

(b) 1MPa

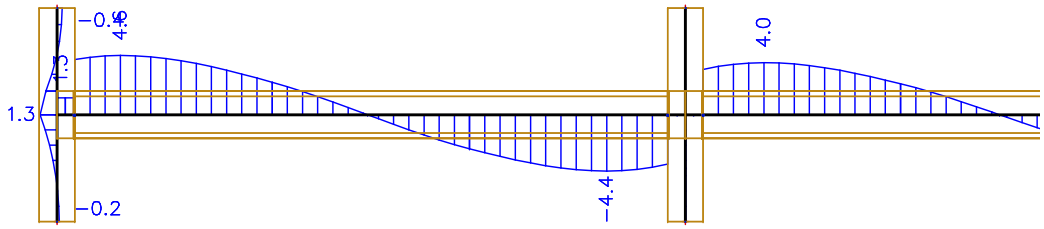

(c) 2MPa

Figure F.17: Short-term SLS - Rotations (mrad)

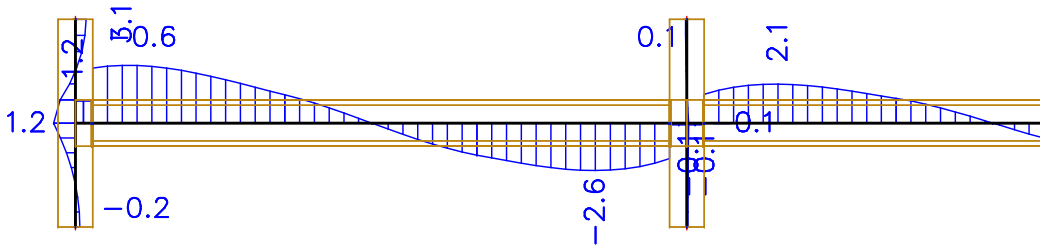

(a) 3MPa

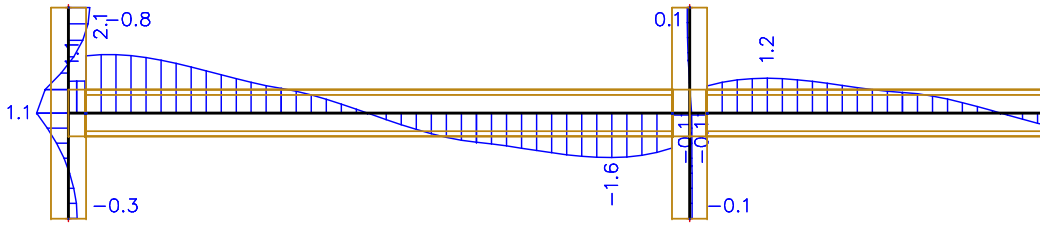

(b) 4MPa

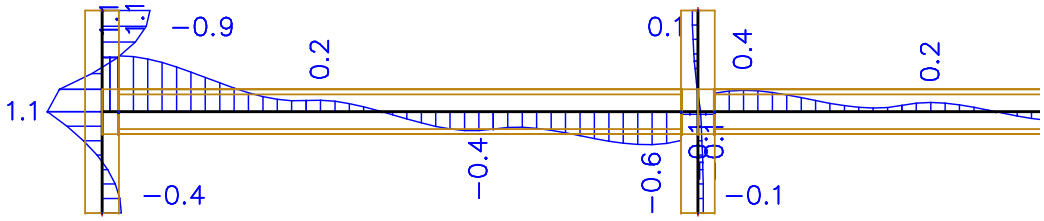

(c) 5MPa

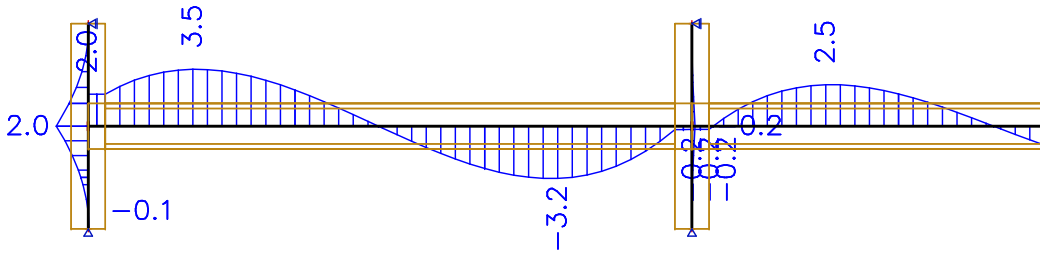

(d) Fixed

Figure F.18: Short-term SLS - Rotations (mrad) (continued)

ULS: 1.2G + 1.5Q + ψ_{te}PT

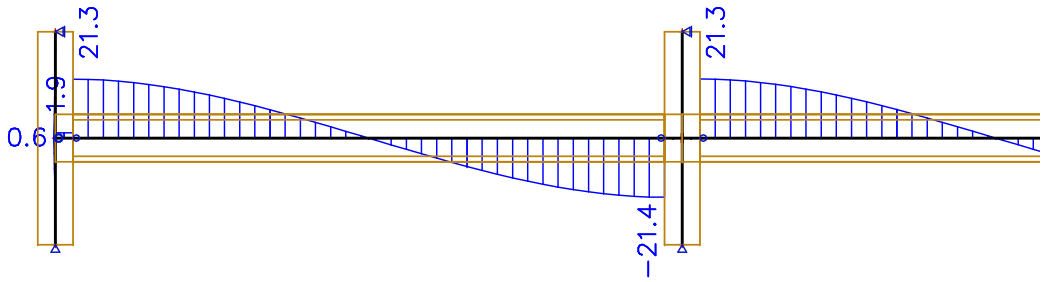

(a) Pinned

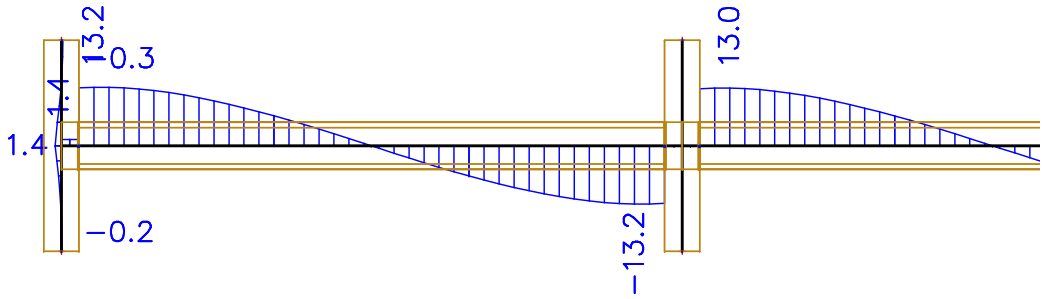

(b) 1MPa

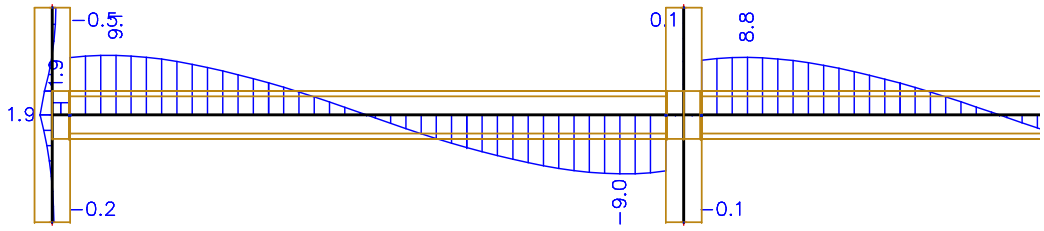

(c) 2MPa

Figure F.19: ULS - Rotations (mrad)

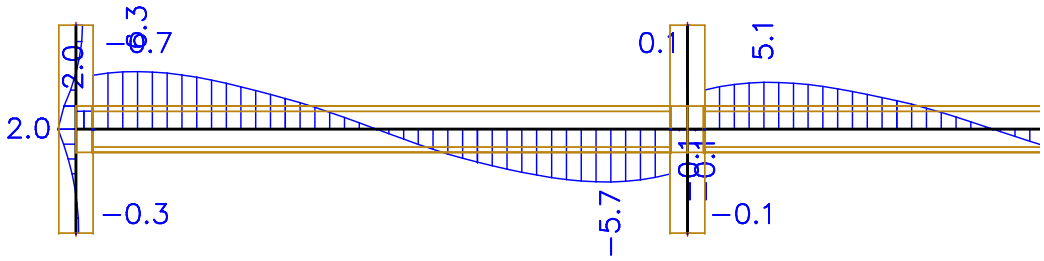

(a) 3MPa

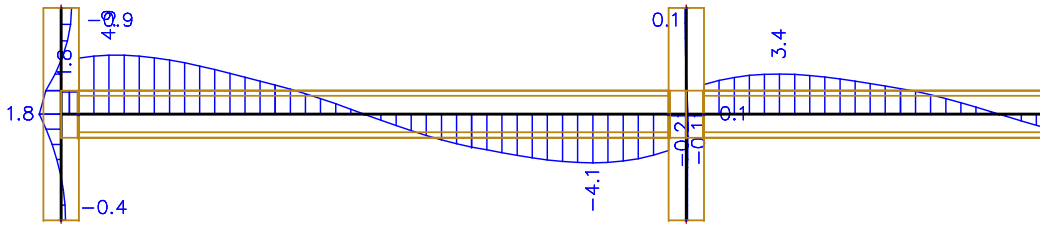

(b) 4MPa

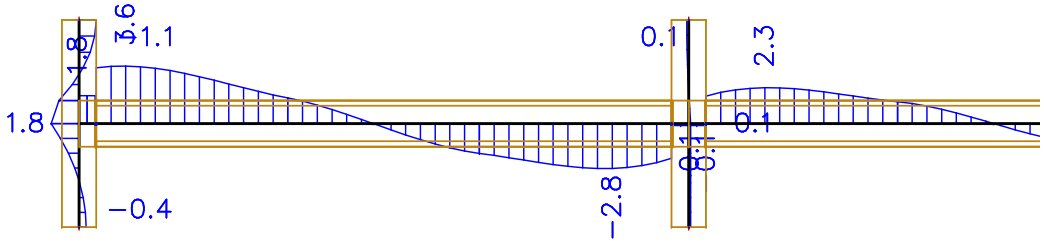

(c) 5MPa

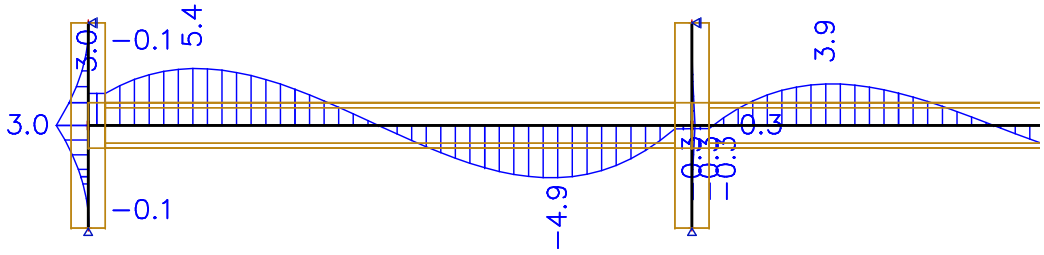

(d) Fixed

Figure F.20: ULS - Rotations (mrad) (continued)

F.4.3 Bending moments

PT Only: 1.1PT

No output for this load case

(a) Pinned

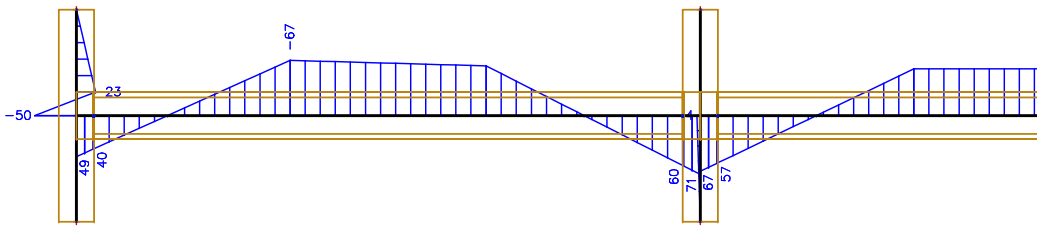

(b) 1MPa

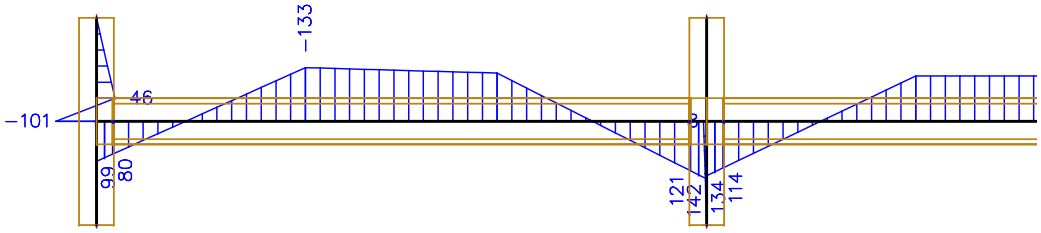

(c) 2MPa

Figure F.21: Post-tensioning only - Bending moments (kNm)

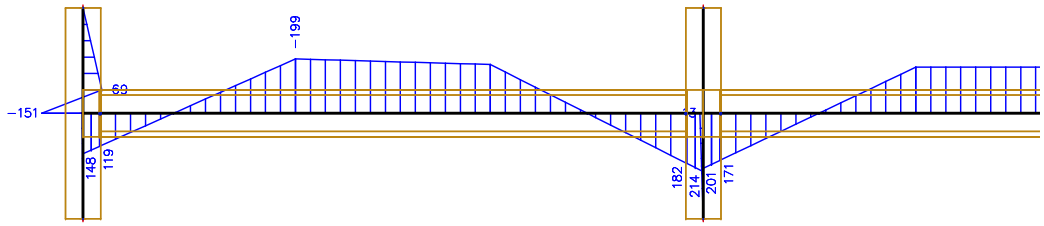

(a) 3MPa

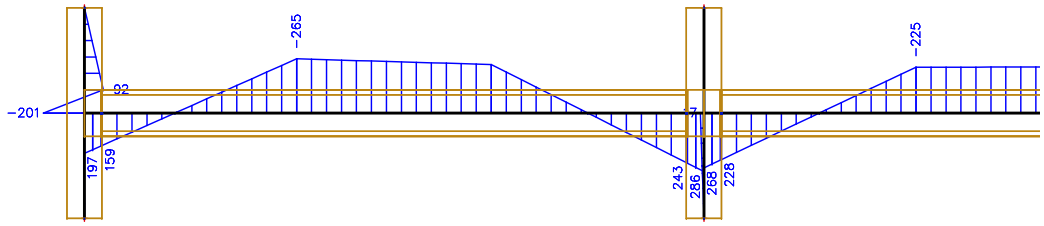

(b) 4MPa

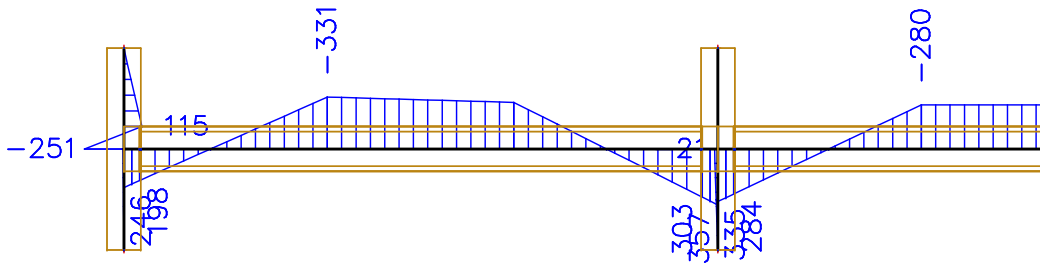

(c) 5MPa

No output for this load case

(d) Fixed

Figure F.22: Post-tensioning only - Bending moments (kNm) (continued)

ULS: 1.2G + 1.5Q + ψ_{te}PT

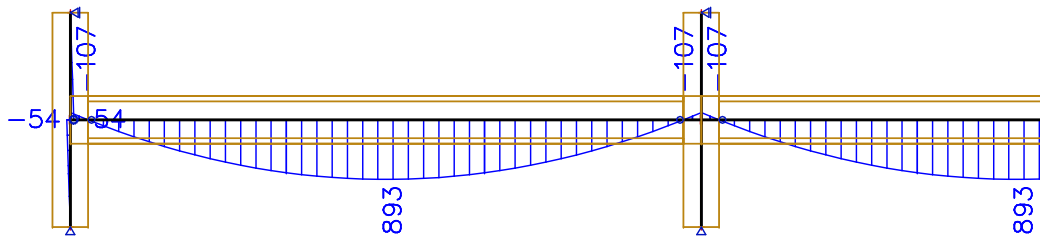

(a) Pinned

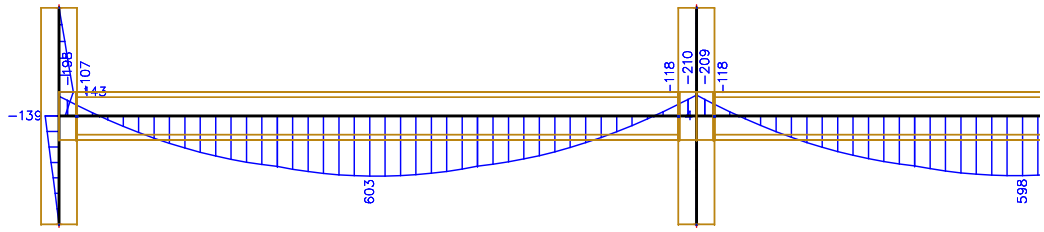

(b) 1MPa

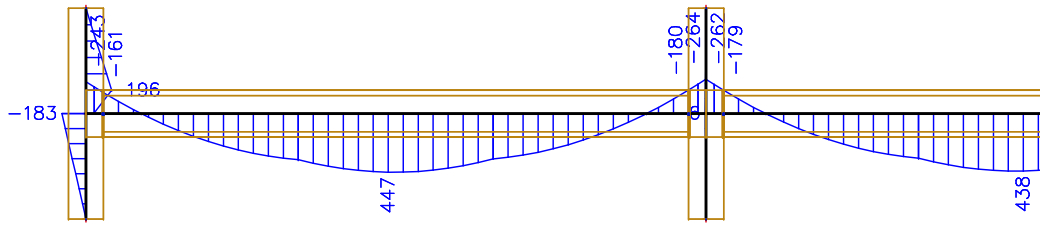

(c) 2MPa

Figure F.23: ULS - Bending moments (kNm)

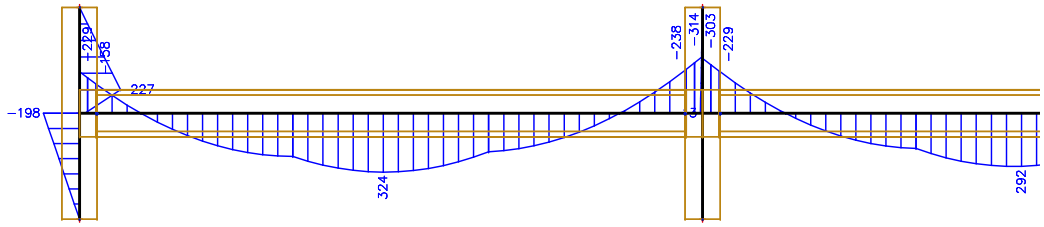

(a) 3MPa

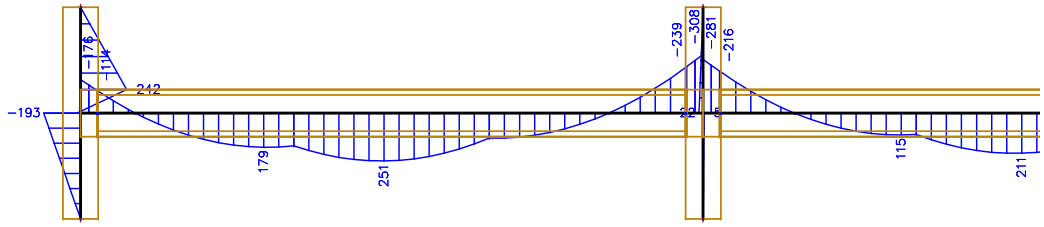

(b) 4MPa

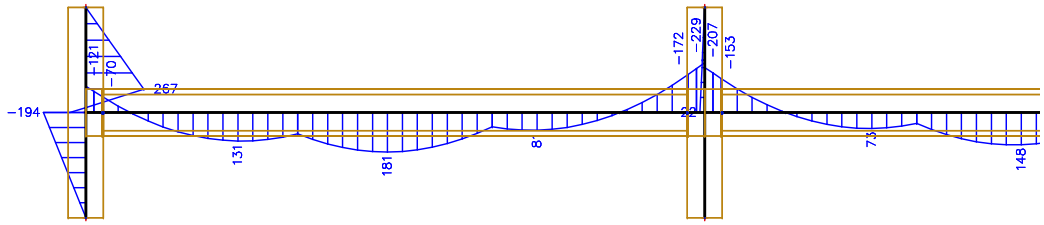

(c) 5MPa

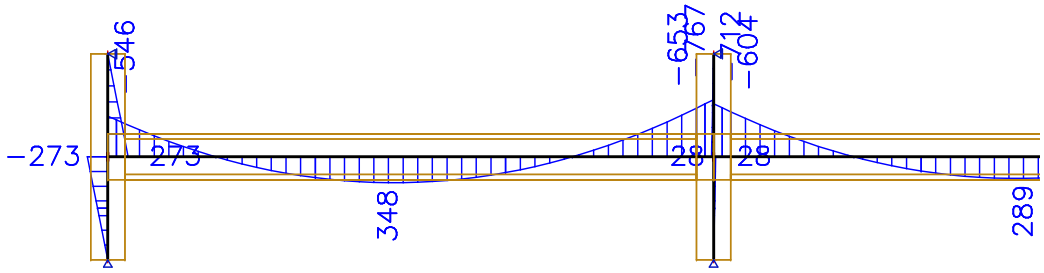

(d) Fixed

Figure F.24: ULS - Bending moments (kNm) (continued)

F.4.4 Shear forces

PT Only: 1.1PT

No output for this load case

(a) Pinned

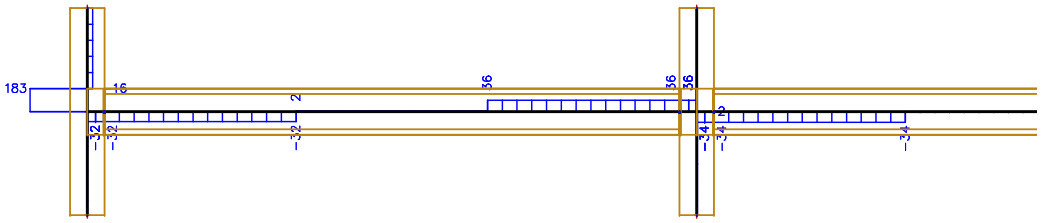

(b) 1MPa

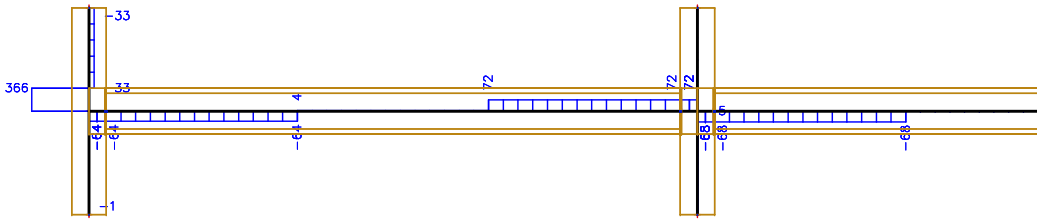

(c) 2MPa

Figure F.25: Post-tensioning only - Shear forces (kN)

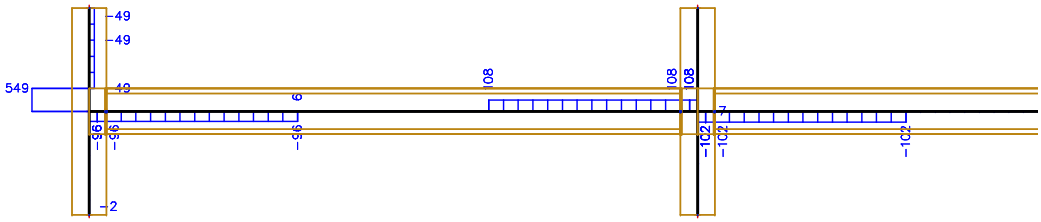

(a) 3MPa

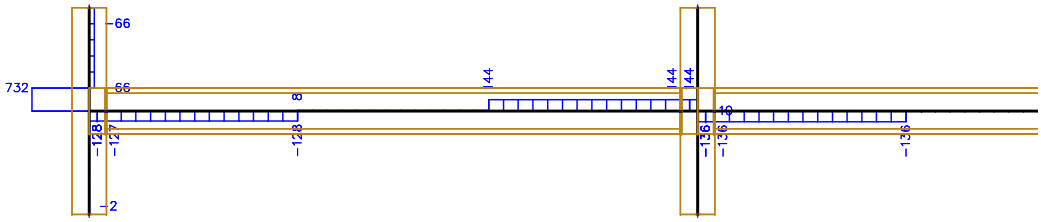

(b) 4MPa

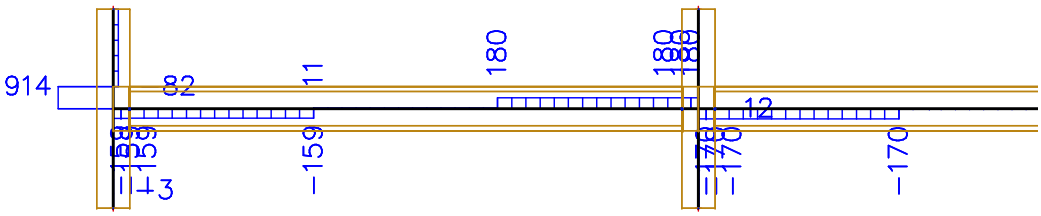

(c) 5MPa

No output for this load case

(d) Fixed

Figure F.26: Post-tensioning only - Shear forces (kN) (continued)

ULS: 1.2G + 1.5Q + ψ_{te}PT

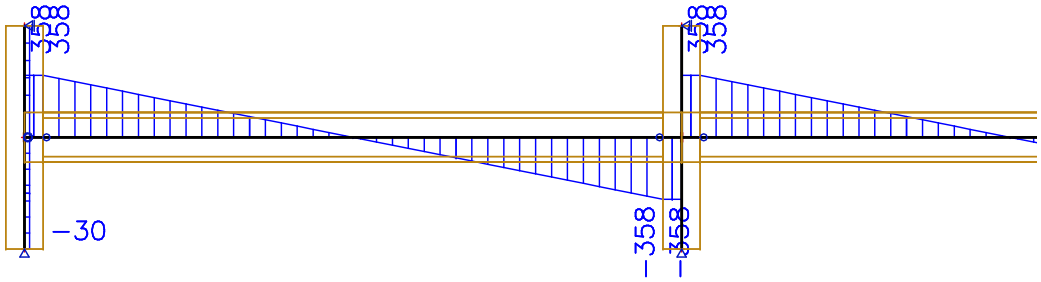

(a) Pinned

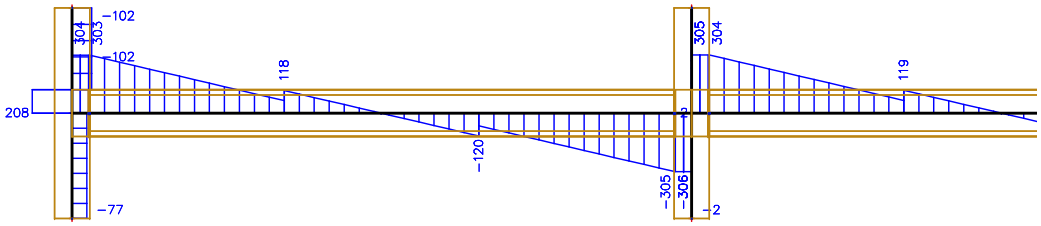

(b) 1MPa

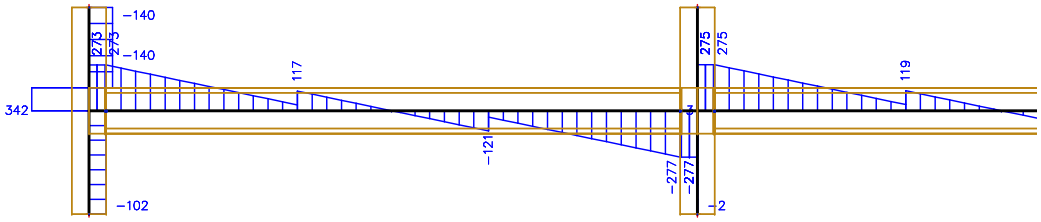

(c) 2MPa

Figure F.27: ULS - Shear forces (kN)

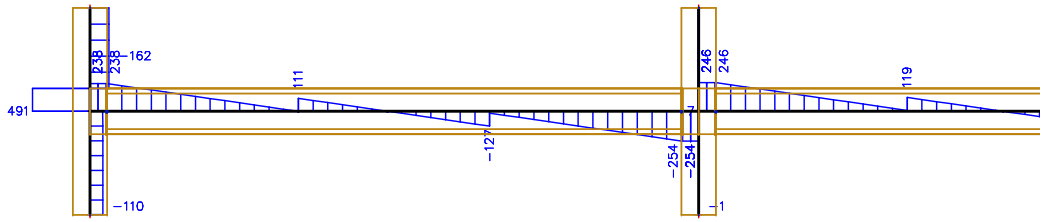

(a) 3MPa

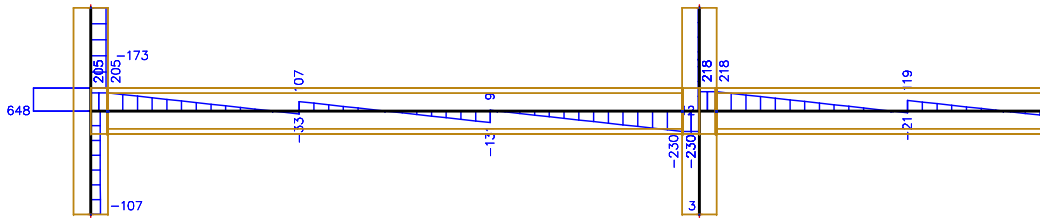

(b) 4MPa

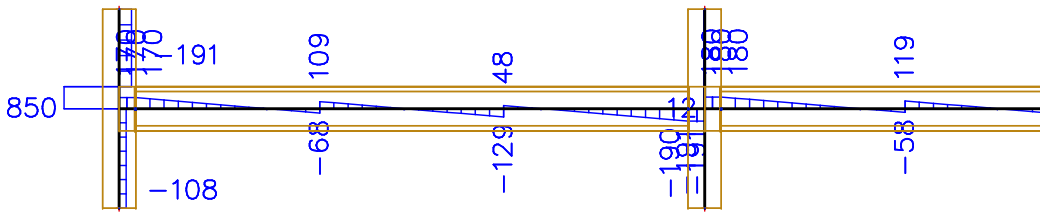

(c) 5MPa

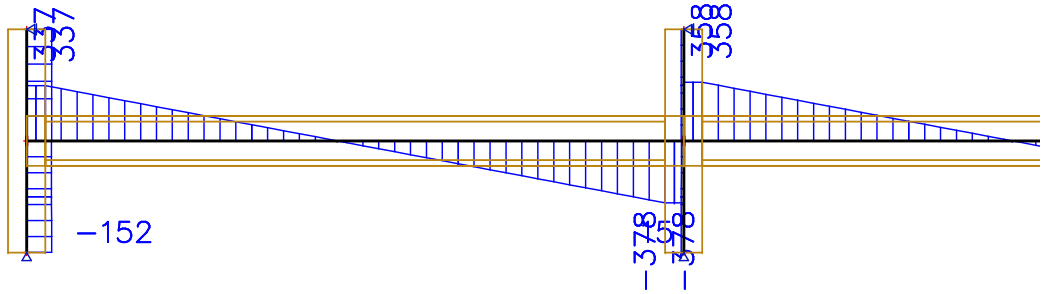

(d) Fixed

Figure F.28: ULS - Shear forces (kN) (continued)

F.4.5 Axial forces

PT Only: 1.1PT

No output for this load case

(a) Pinned

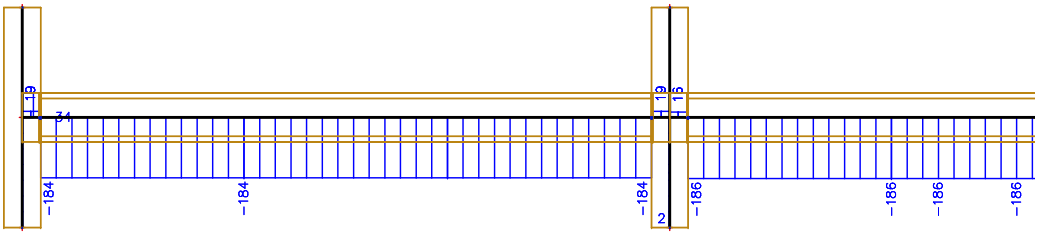

(b) 1MPa

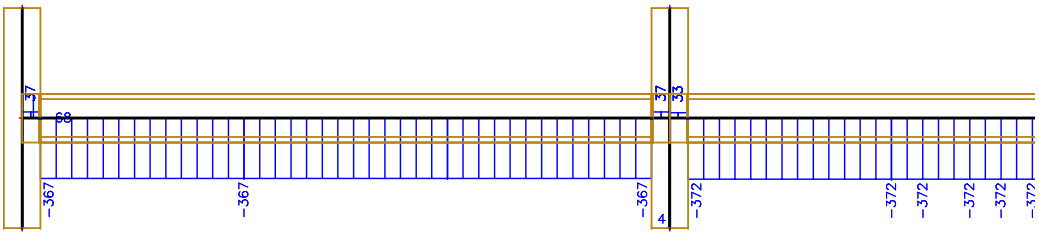

(c) 2MPa

Figure F.29: Post-tensioning only - Axial forces (kN)

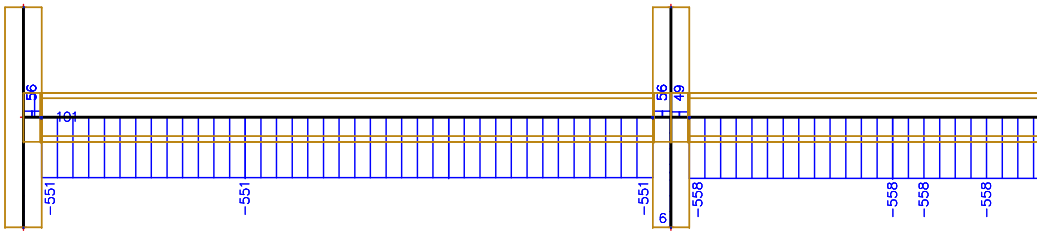

(a) 3MPa

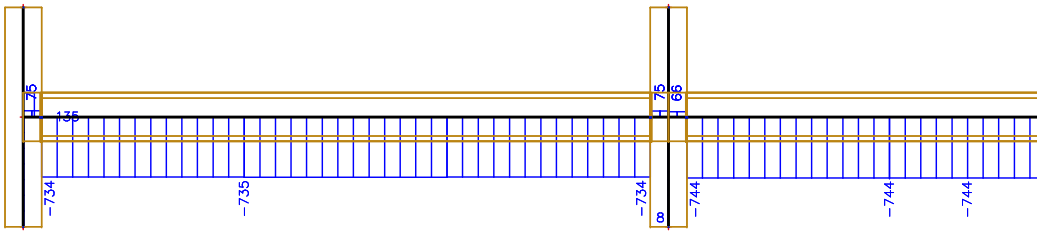

(b) 4MPa

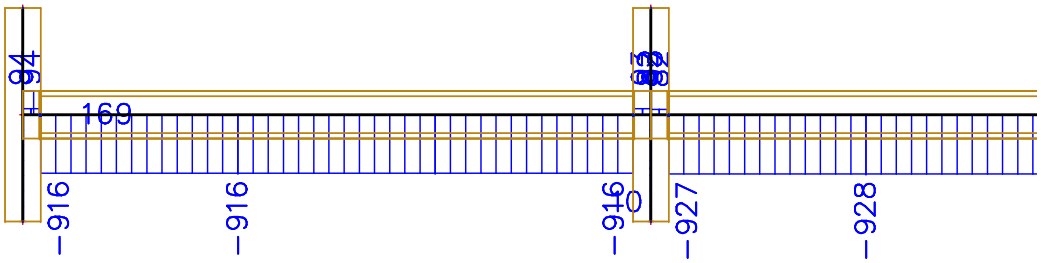

(c) 5MPa

No output for this load case

(d) Fixed

Figure F.30: Post-tensioning only - Axial forces (kN) (continued)

ULS: 1.2G + 1.5Q + ψ_{te}PT

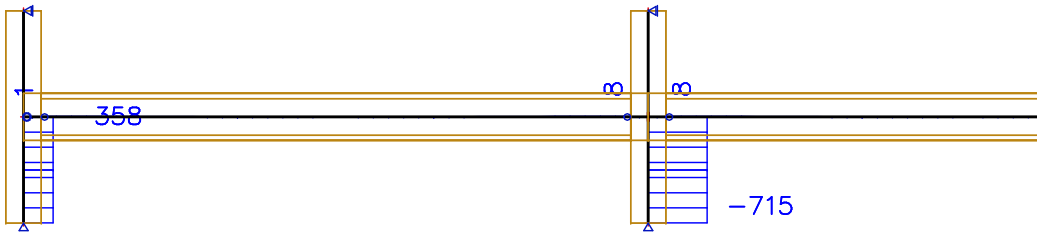

(a) Pinned

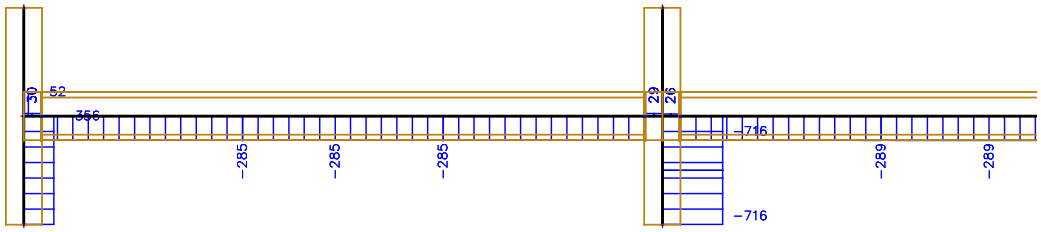

(b) 1MPa

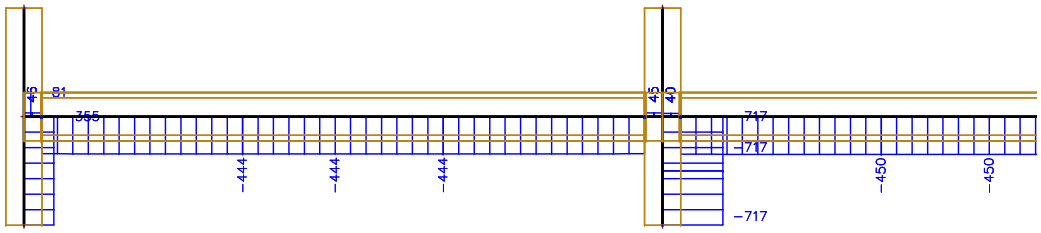

(c) 2MPa

Figure F.31: ULS - Normal forces (kN)

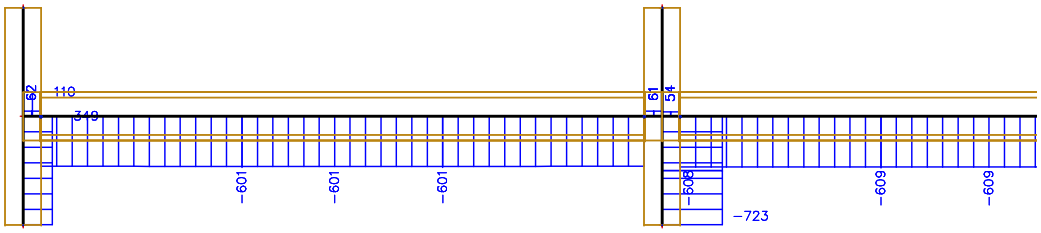

(a) 3MPa

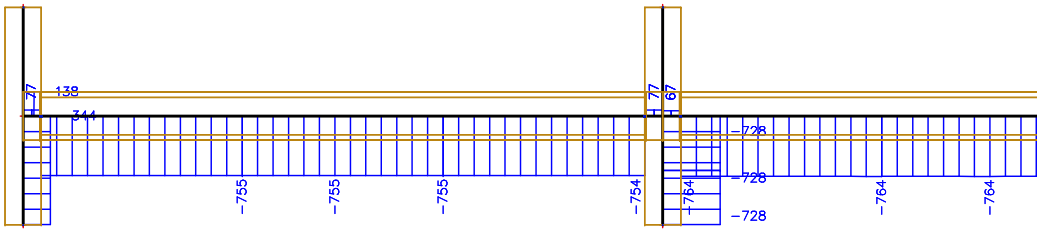

(b) 4MPa

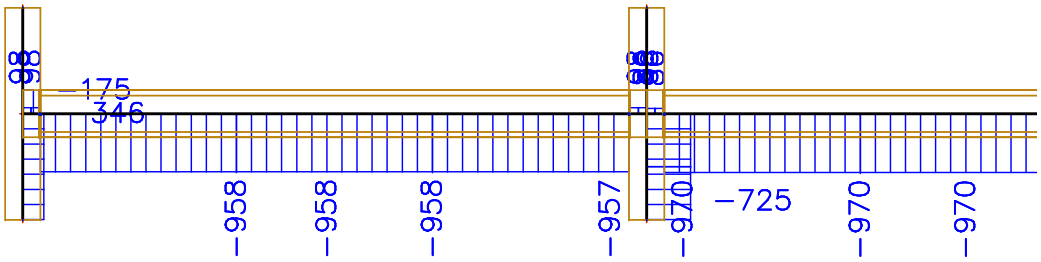

(c) 5MPa

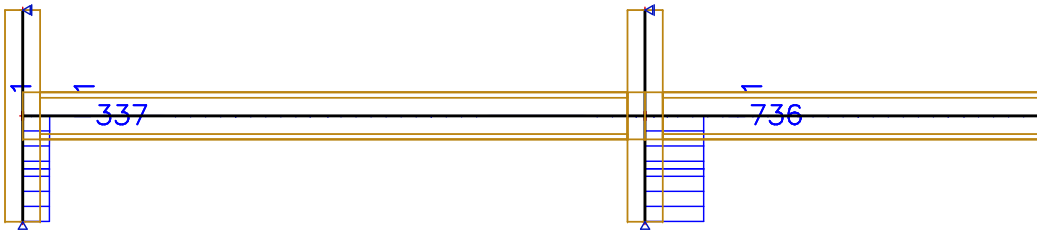

(d) Fixed

Figure F.32: ULS - Normal forces (kN) (continued)

Appendix G

Technical drawings

This Appendix contains a list of drawings used for experimental testing.

Beam testing

1. Beam 1 - Benchmark
2. Beam 2 - Straight PT
3. Beam 3 - Draped PT
4. Beam 4 - Draped PT (2)
5. Instrumentation

Connection testing

1. Beam-column test setup
2. Column 1 (LVL11)
3. Column 2 (Cross-banded LVL)
4. Beam
5. Instrumentation full test setup
6. Instrumentation joint panel region

Frame testing

1. Test setup and instrumentation for one-bay frame testing
2. Test setup and instrumentation for two-bay frame testing
3. Order for external column for frame (Type 1)
4. Order for internal column for frame (Type 2)
5. Order for beam for one-bay frame
6. Order for beam for two-bay frame
7. Corbel manufacturing

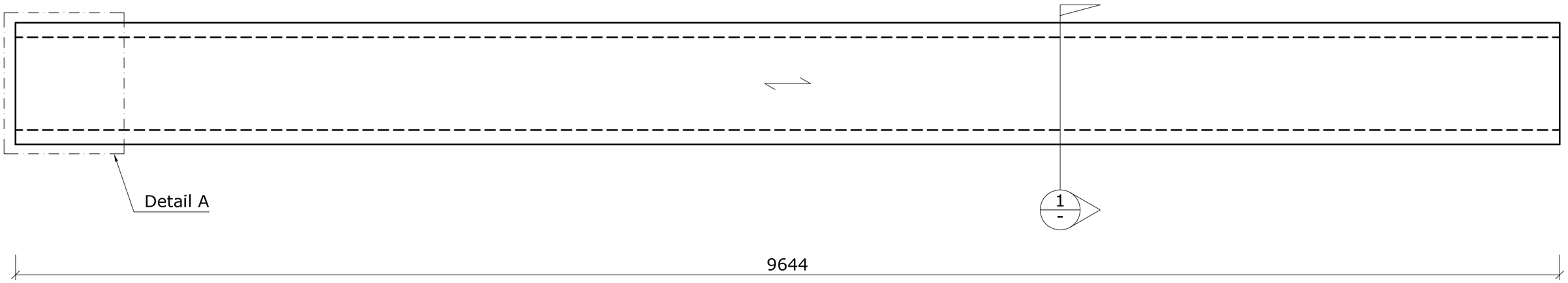

Side View

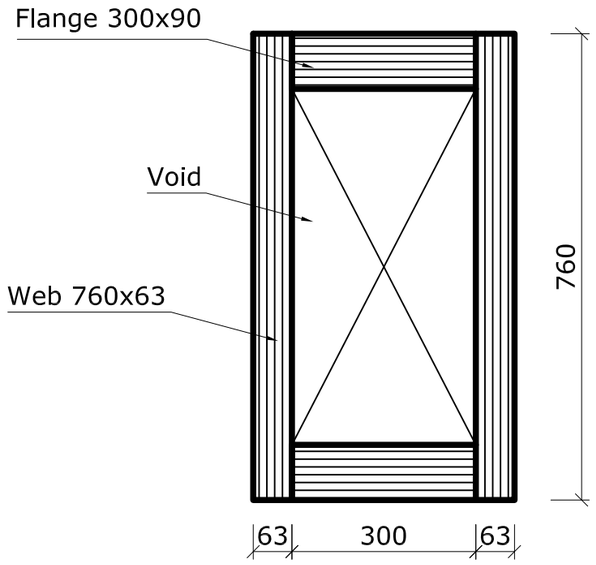

Section 1

(scale 1:10)

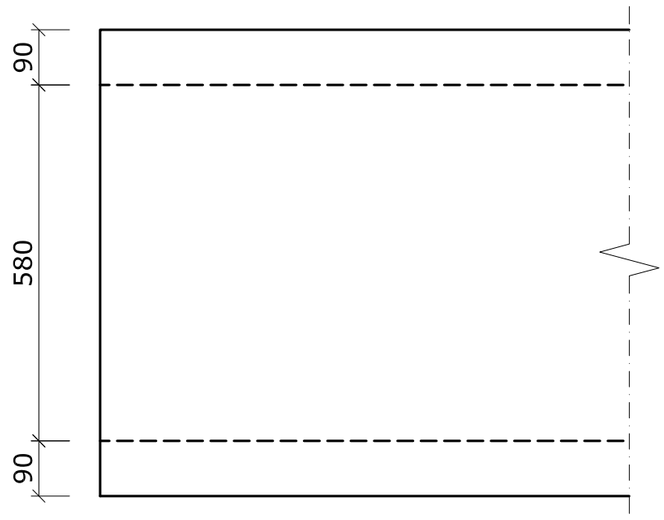

Detail A

(scale 1:10)

Notes:

- All timber Nelson Pine LVL11

UNIVERSITY OF CANTERBURY
Te Whare Wānanga o Waitaha
CHRISTCHURCH NEW ZEALAND

Title	Beam 1	
By	Wouter van Beerschoten	
Rev.	0	First draft
	1	Order
Date: 13-12-2011		Scale: 1:25
Units: mm		Drawing no.: 1/4

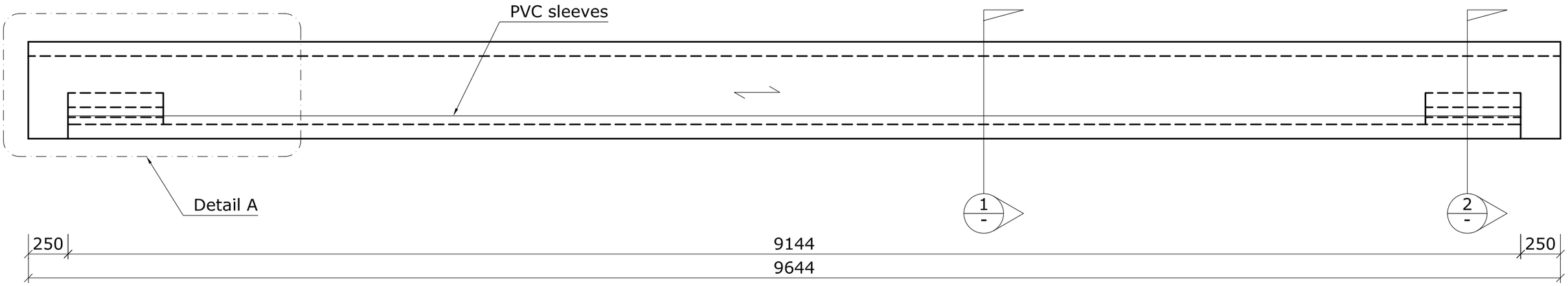

Side View

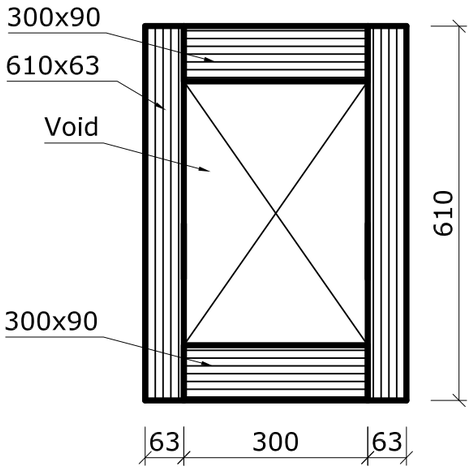

Section 1

(scale 1:10)

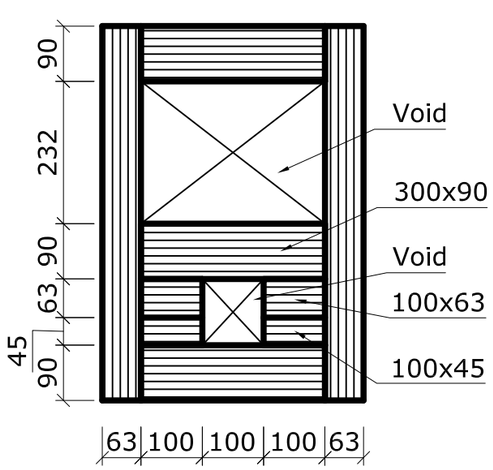

Section 2

(scale 1:10)

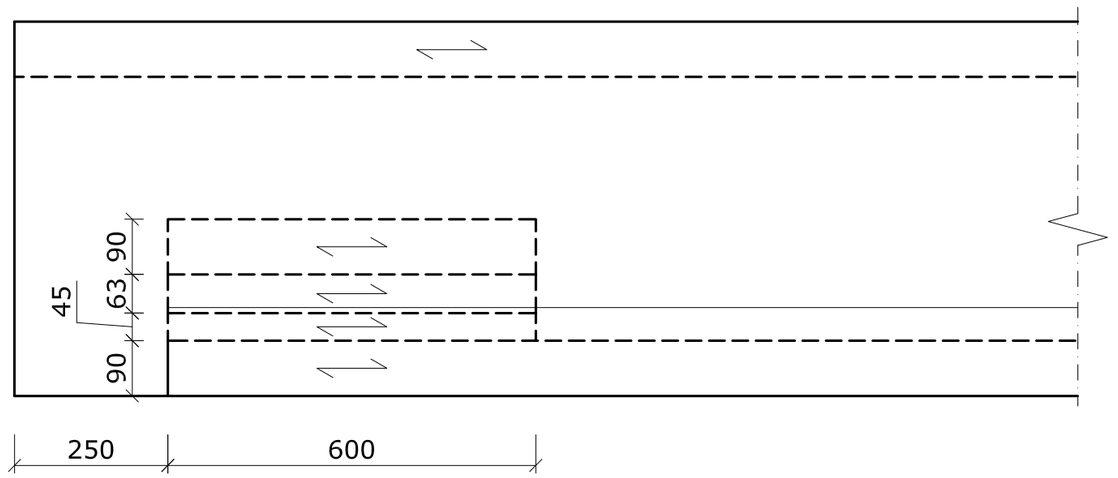

Detail A

(scale 1:10)

Notes:

- All timber Nelson Pine LVL11
- Anchorage sheets glued in
- Supply with 7 PVC sleeves installed (Ø22mm), length 9044mm

UNIVERSITY OF CANTERBURY
Te Whare Wānanga o Waitaha
CHRISTCHURCH NEW ZEALAND

Title	Beam 2	
By	Wouter van Beerschoten	
Rev.	0	First draft
	1	Order
Date: 13-12-2011		Scale: 1:25
Units: mm		Drawing no.: 2/4

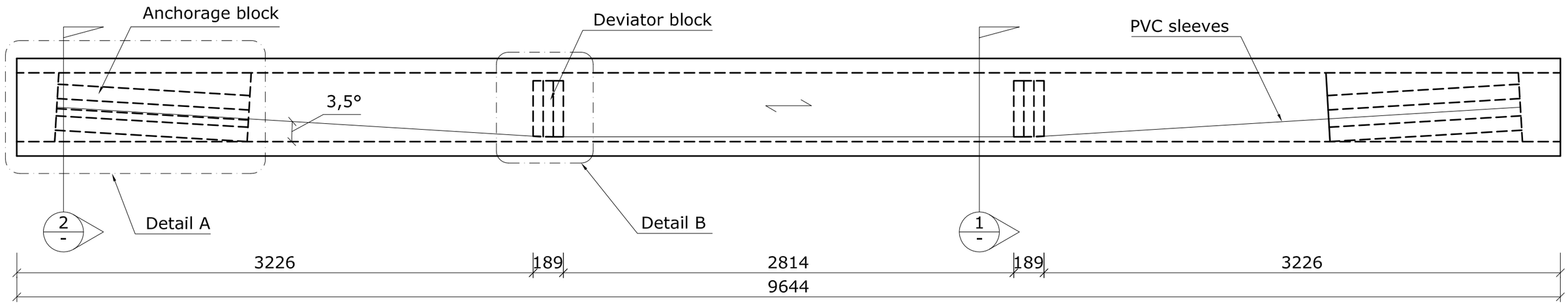

Side View (scale 1:25)

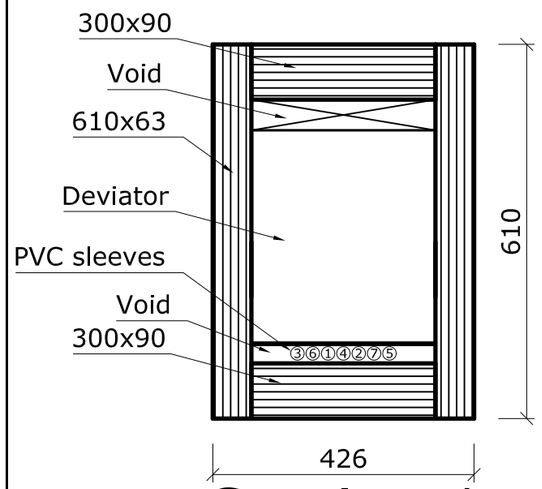

Section 1

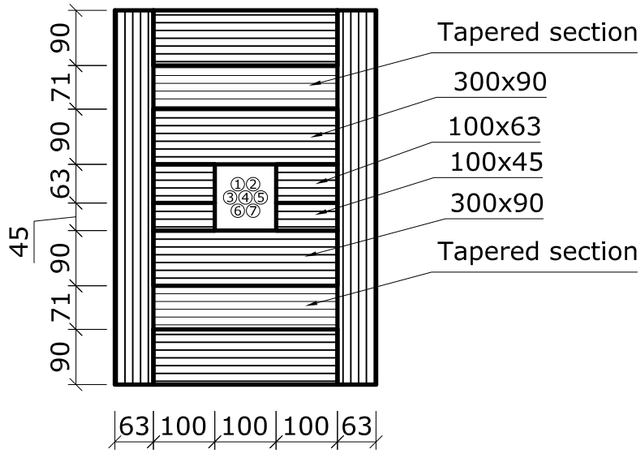

Section 2

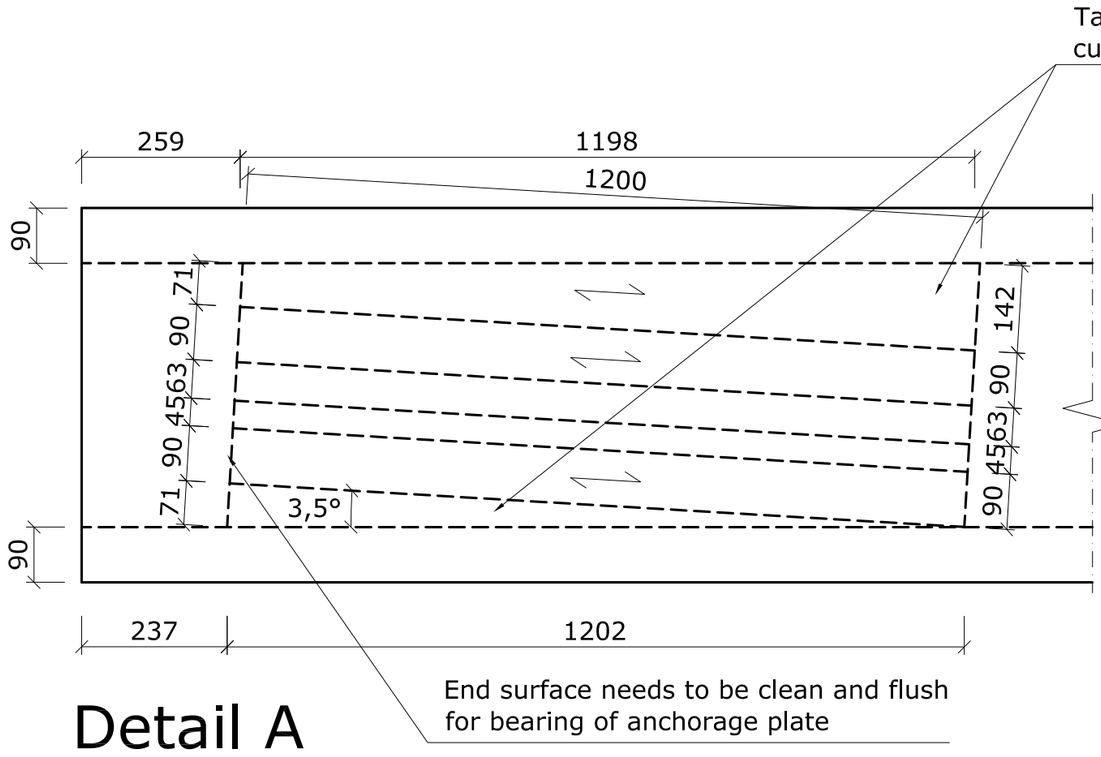

Detail A

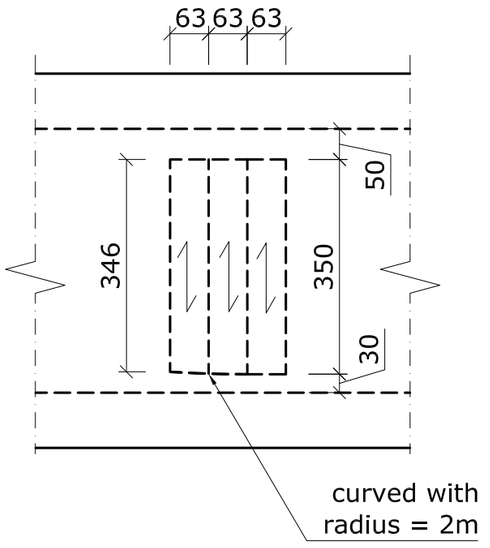

Detail B

Notes:

- All timber Nelson Pine LVL11
- Glue connections on anchorage block are critical! Ensure proper glue bond on all sides.
- Anchorage blocks and deviator first glued together and next glued into beam.
- Supply with 7 PVC sleeves installed (Ø22mm), length 9m, number the ends and position in order as specified (fix position by taping sleeves together). Ensure no twisting of the sleeves.

UNIVERSITY OF CANTERBURY
Te Whare Wānanga o Waitaha
CHRISTCHURCH NEW ZEALAND

Title	Beam 3	
By	Wouter van Beerschoten	
Rev.	1	Order
	2	Updated dimensions
	3	Revised anchorage block
Date: 16-5-2012		Scale: 1:10
Units: mm		Drawing no.: 1/2

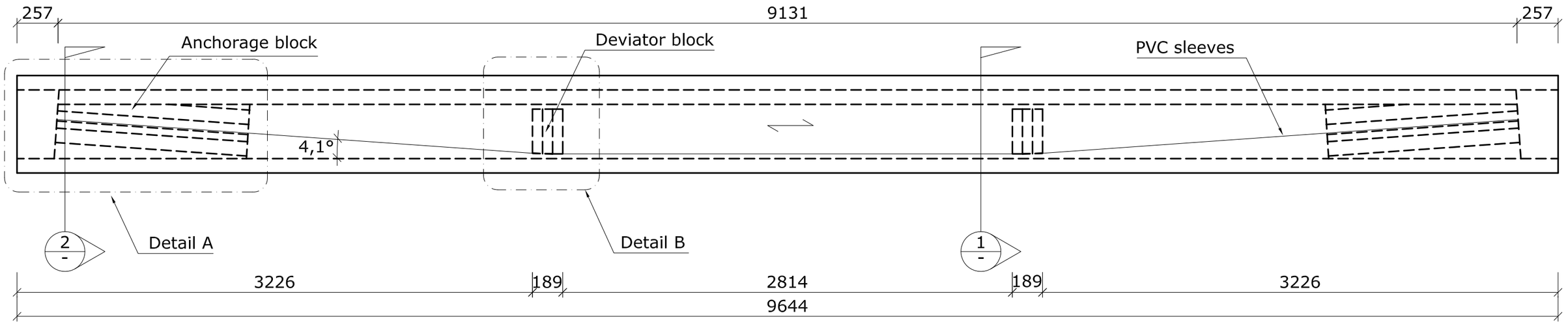

Side View (scale 1:25)

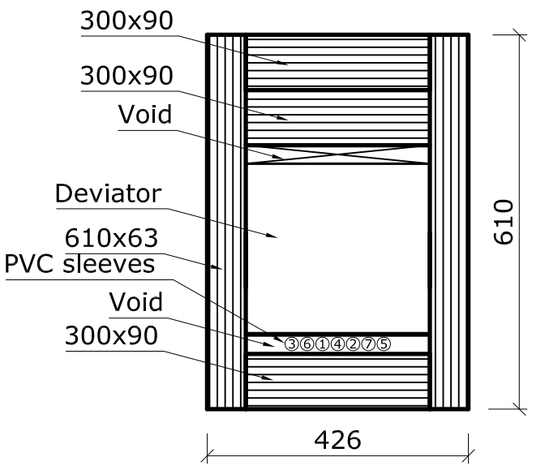

Section 1

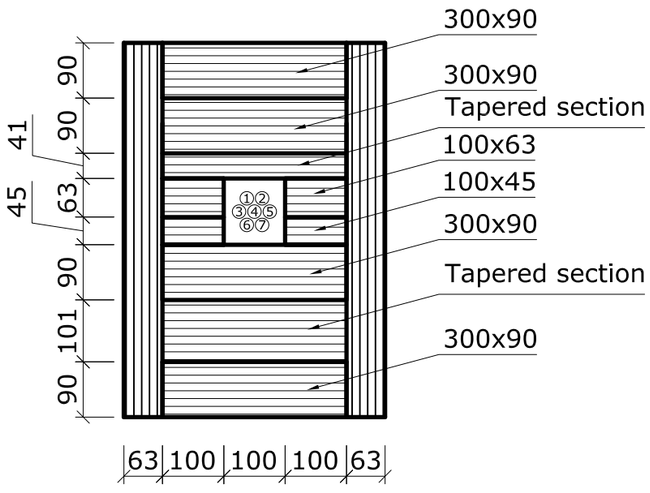

Section 2

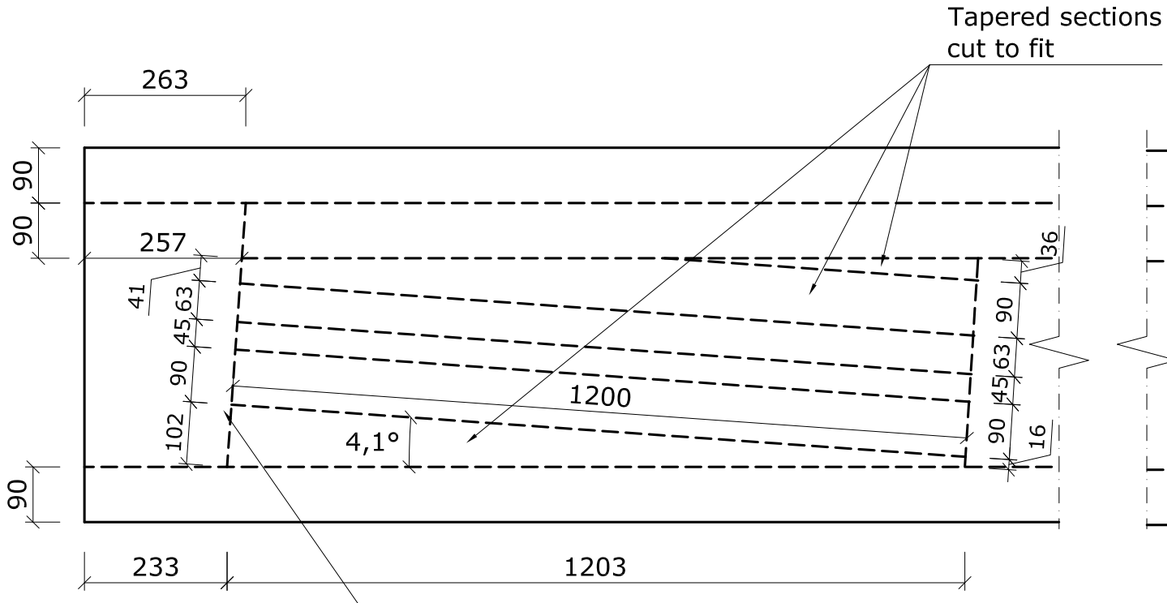

Detail A

End surface needs to be clean and flush for bearing of anchorage plate

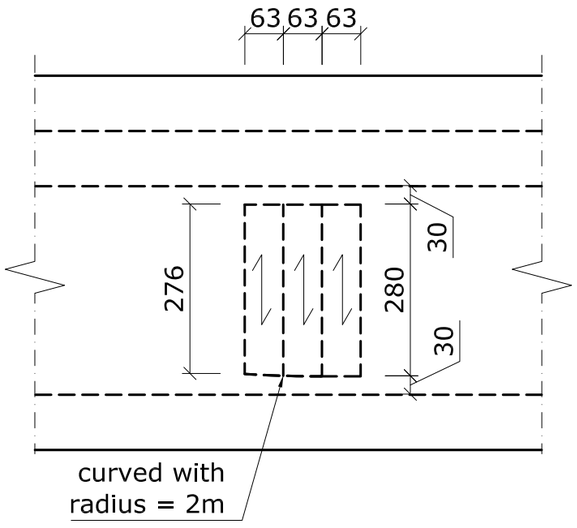

Detail B

Notes:

- All timber Nelson Pine LVL11
- Glue connections on anchorage block are critical! Ensure proper glue bond on all sides.
- Anchorage blocks and deviator first glued together and next glued into beam.
- Supply with 7 PVC sleeves installed (Ø22mm), length 9m, number the ends and position in order as specified (fix position by taping sleeves together). Ensure no twisting of the sleeves.

UNIVERSITY OF CANTERBURY
Te Whare Wānanga o Waitaha
CHRISTCHURCH NEW ZEALAND

Title	Beam 4	
By	Wouter van Beerschoten	
Rev.	1	Order
	2	Updated dimensions
	3	Revised anchorage block
Date: 16-5-2012		Scale: 1:10
Units: mm		Drawing no.: 2/2

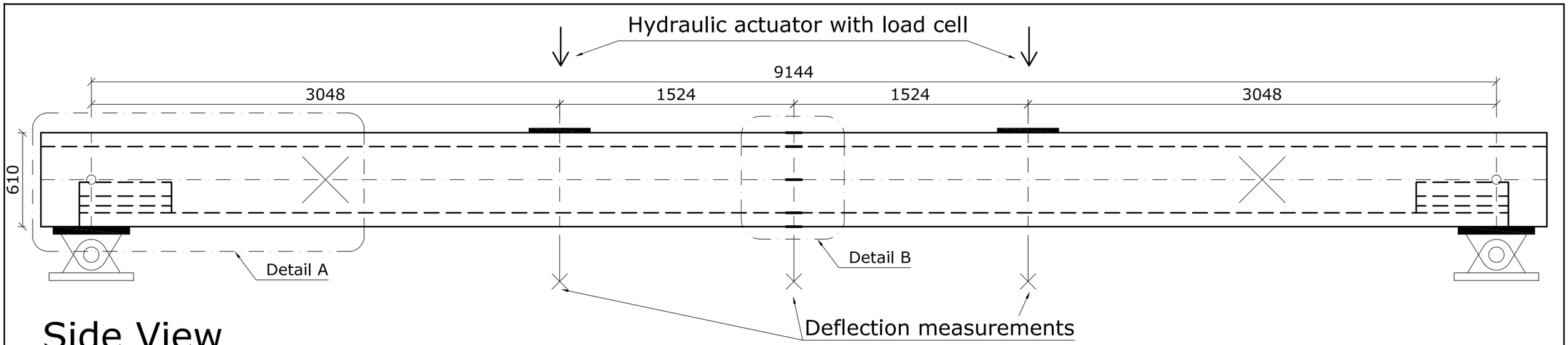

Side View

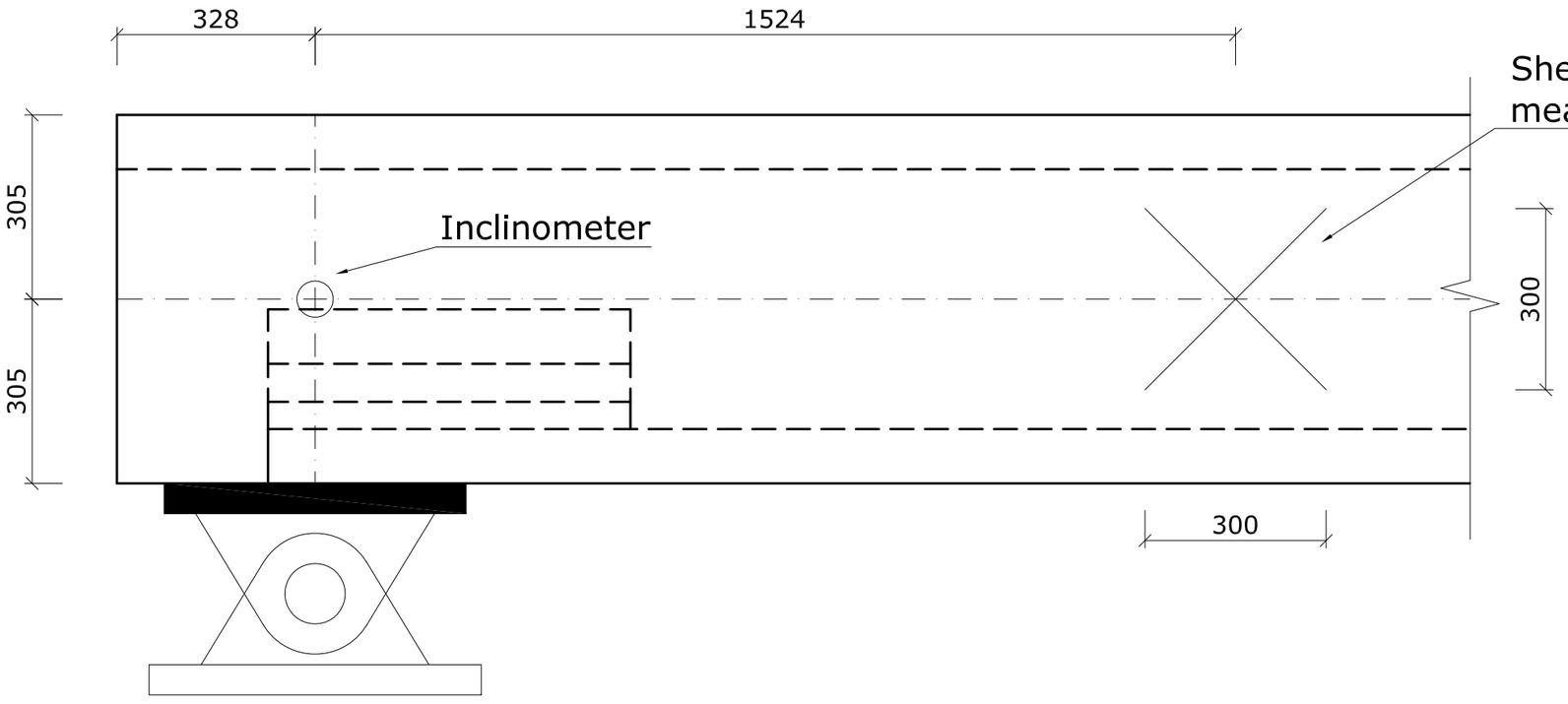

Detail A

(scale 1:10)

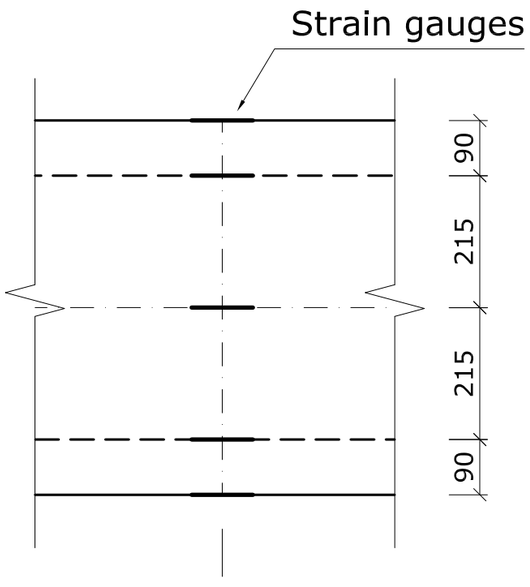

Detail B

(scale 1:10)

UNIVERSITY OF CANTERBURY
Te Whare Wānanga o Waitaha
CHRISTCHURCH NEW ZEALAND

Title	Beam 2 - Instrumentation	
By	Wouter van Beerschoten	
Rev.	0 Final	
Date: 13-12-2011		Scale: 1:25
Units: mm		Drawing no.: 1/1

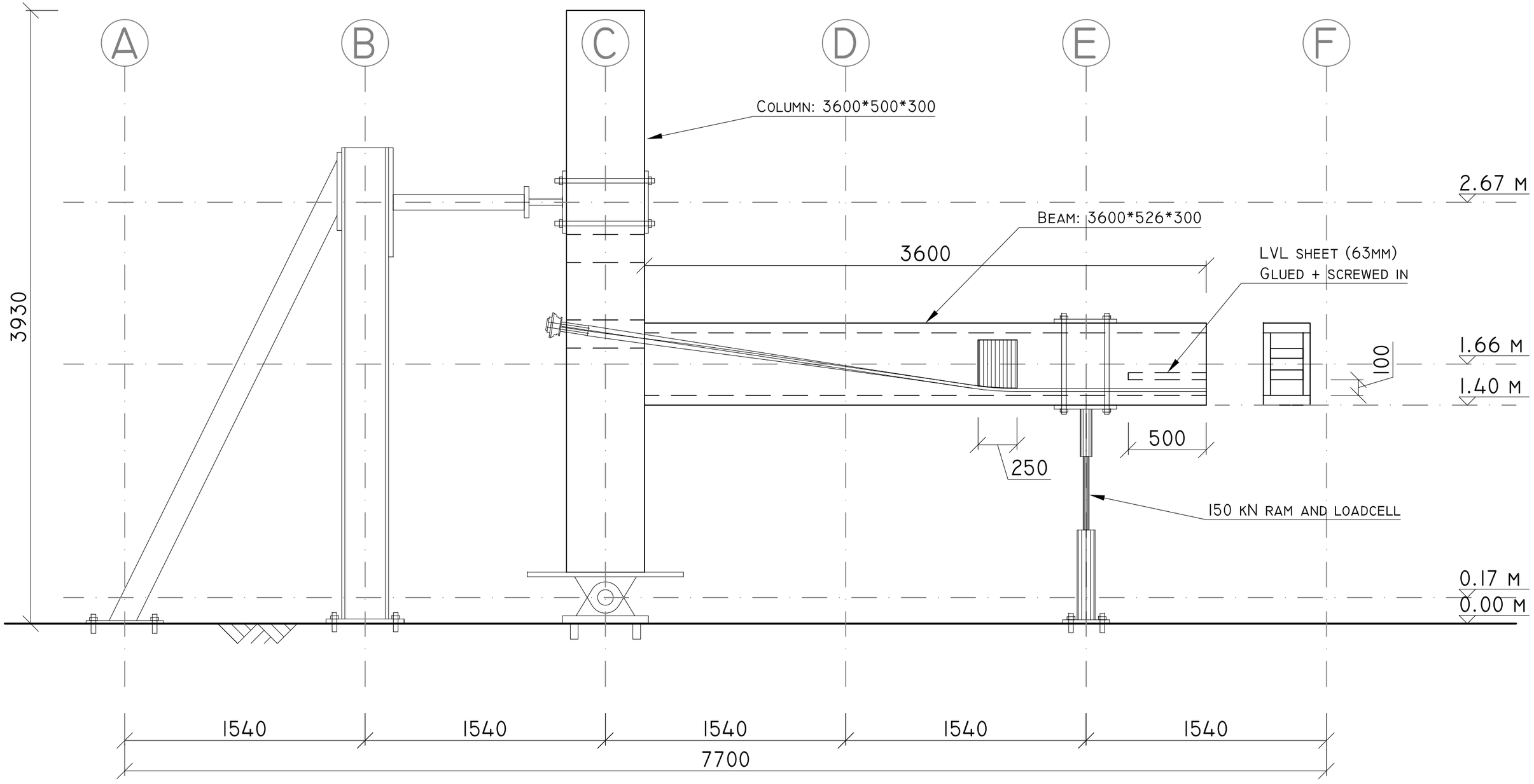

TEST SETUP

UNIVERSITY OF CANTERBURY
Te Whare Wānanga o Waitaha
CHRISTCHURCH NEW ZEALAND

TITLE	EXTERNAL CONNECTION TESTING	
BY	WOUTER VAN BEERSCHOTEN	
REV.	0	ORIGINAL
DATE: 13-10-2010		SCALE: 1:25
UNITS: MM		DRAWING NO.: 1/4

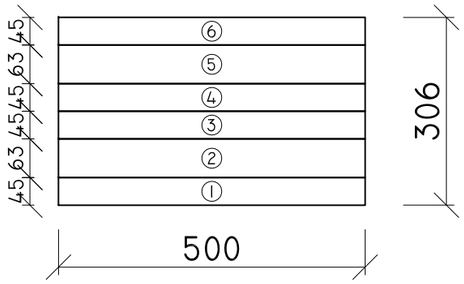

COLUMN 1 - LAYERS
(SCALE 1:10)

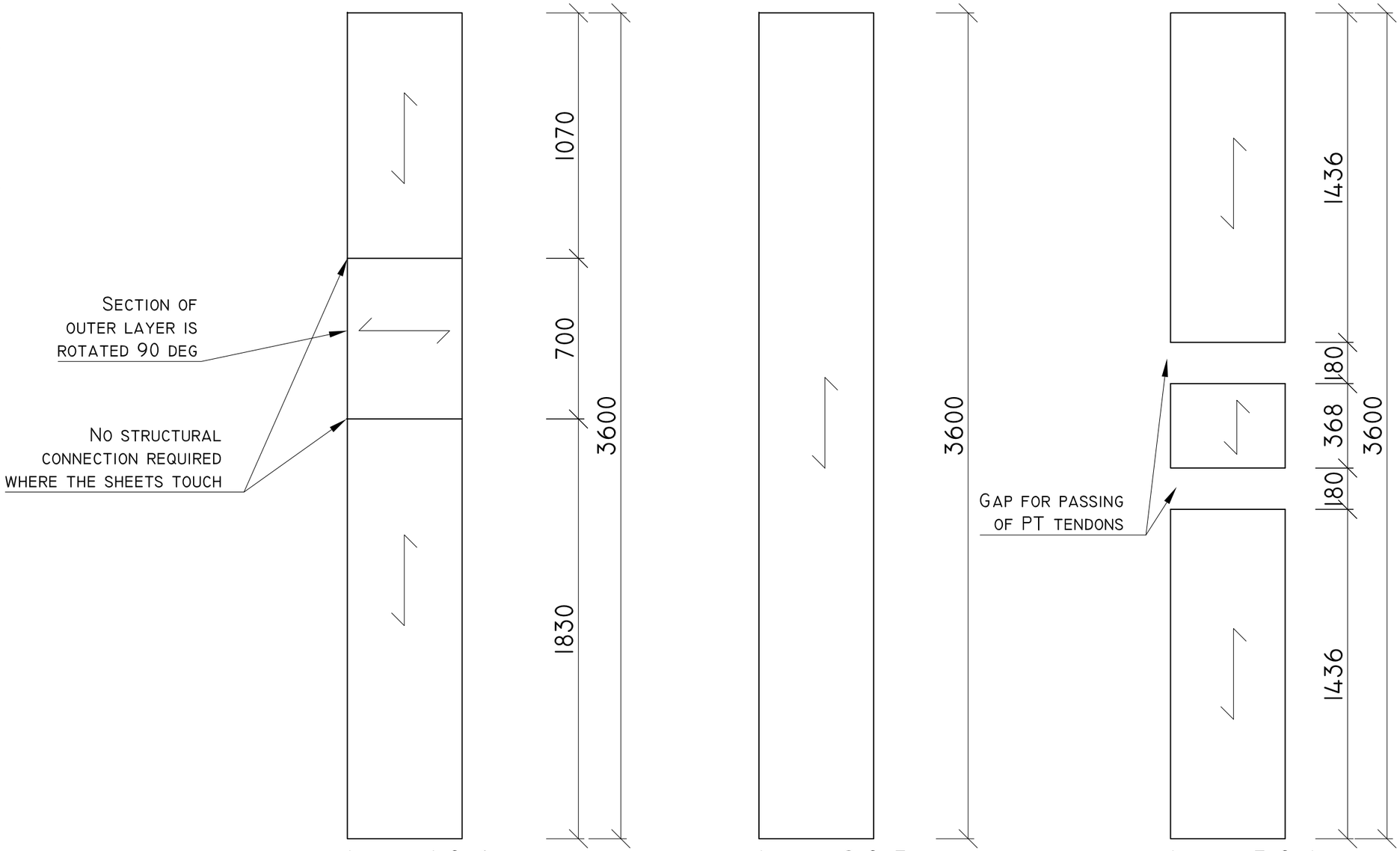

LAYER 1 & 6
(45MM)

LAYER 2 & 5
(63MM)

LAYER 3 & 4
(45MM)

NOTES:

- ALL NP LVL11
- CUT OUT OF 610MM WIDE SHEETS
- ANY CUT OFFS WILL BE USED FOR MATERIAL TESTING. SO PLEASE SAVE THEM AND SHIP THEM OVER

UNIVERSITY OF CANTERBURY
Te Whare Wānanga o Waitaha
CHRISTCHURCH NEW ZEALAND

TITLE	COLUMN 1	
BY	WOUTER VAN BEERSCHOTEN	
REV.	0	ORIGINAL
DATE: 13-10-2010		SCALE: 1:20
UNITS: MM		DRAWING NO.: 2/4

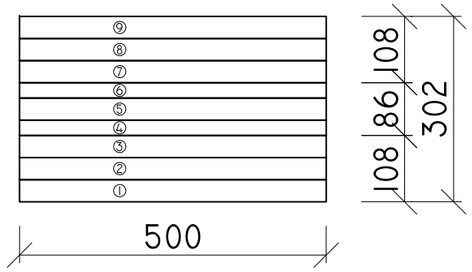

9 = 36MM
8 = 36MM
7 = 36MM
6 = 25MM
5 = 36MM
4 = 25MM
3 = 36MM
2 = 36MM
1 = 36MM

COLUMN LAYERS

(SCALE 1:10)

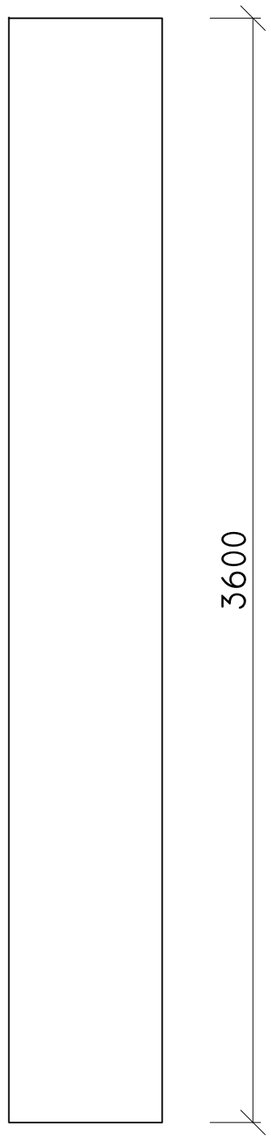

LAYER 1,2,3,7,8,9

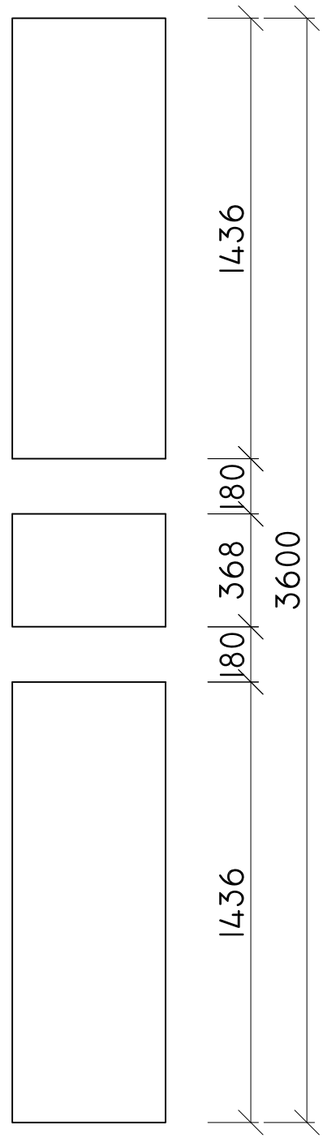

LAYER 4,5,6

NOTES:

- ALL NP CROSSLAM (E9)
- ANY CUT OFFS WILL BE USED FOR MATERIAL TESTING. SO PLEASE SAVE THEM AND SHIP THEM OVER
- 25MM CROSSLAM HAS 3 ROTATED VENEERS (4 NORMAL ONES)
- 36MM CROSSLAM HAS 2 ROTATED VENEERS (8 NORMAL ONES)

UNIVERSITY OF CANTERBURY
Te Whare Wānanga o Waitaha
CHRISTCHURCH NEW ZEALAND

TITLE	COLUMN 2	
BY	WOUTER VAN BEERSCHOTEN	
REV.	0	ORIGINAL
DATE: 13-10-2010		SCALE: 1:20
UNITS: MM		DRAWING NO.: 3/4

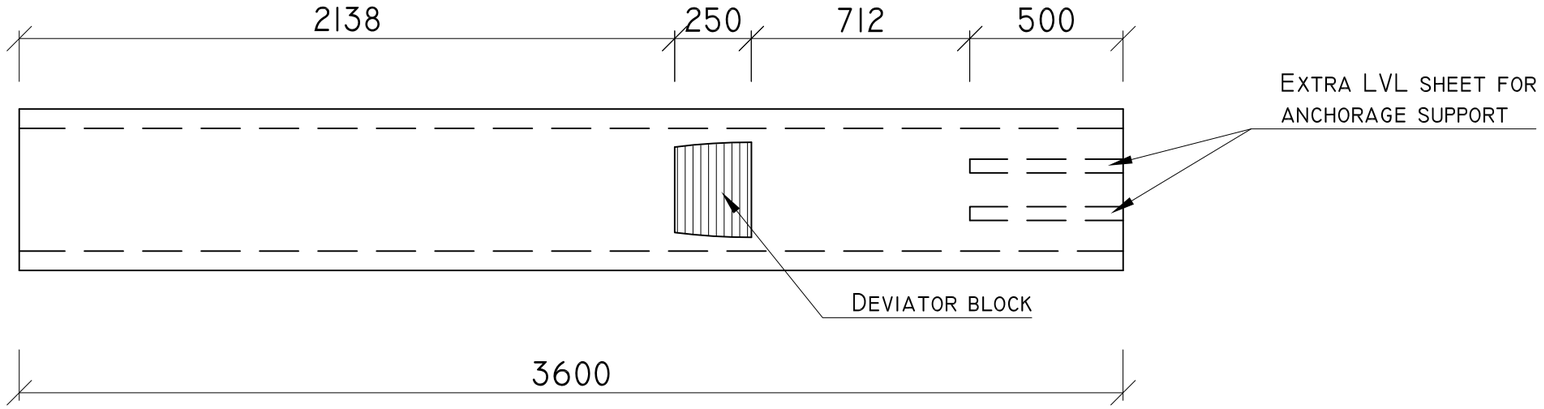

SIDE VIEW

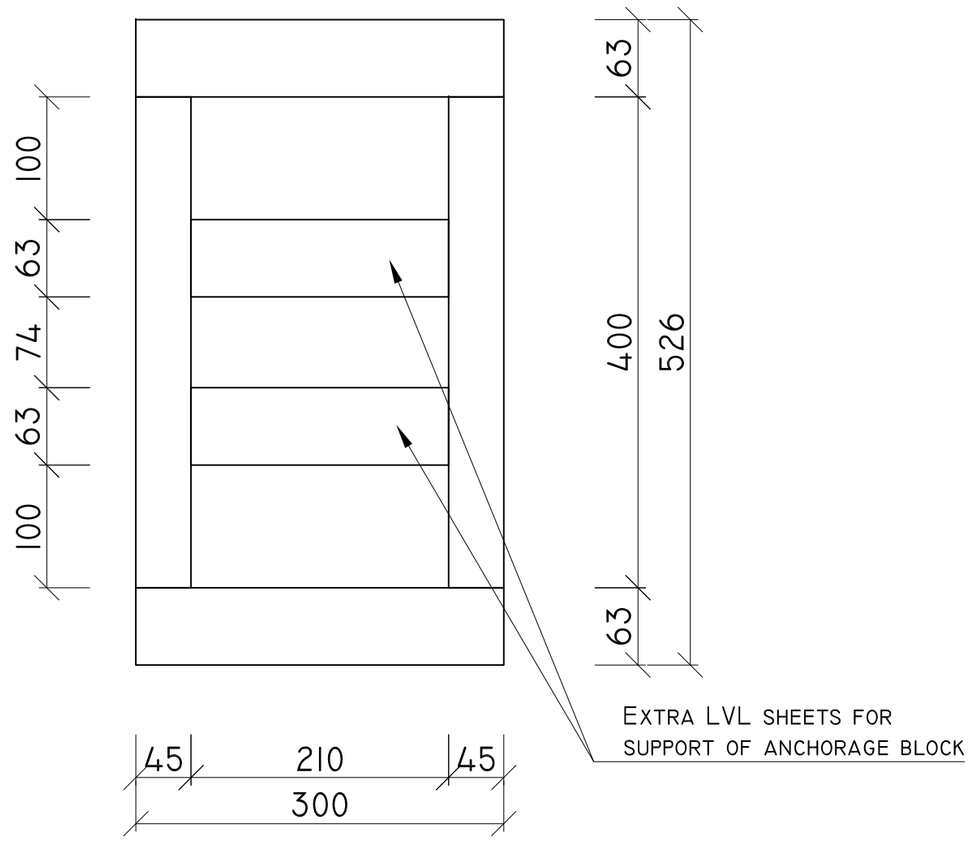

FRONT VIEW (1:5)

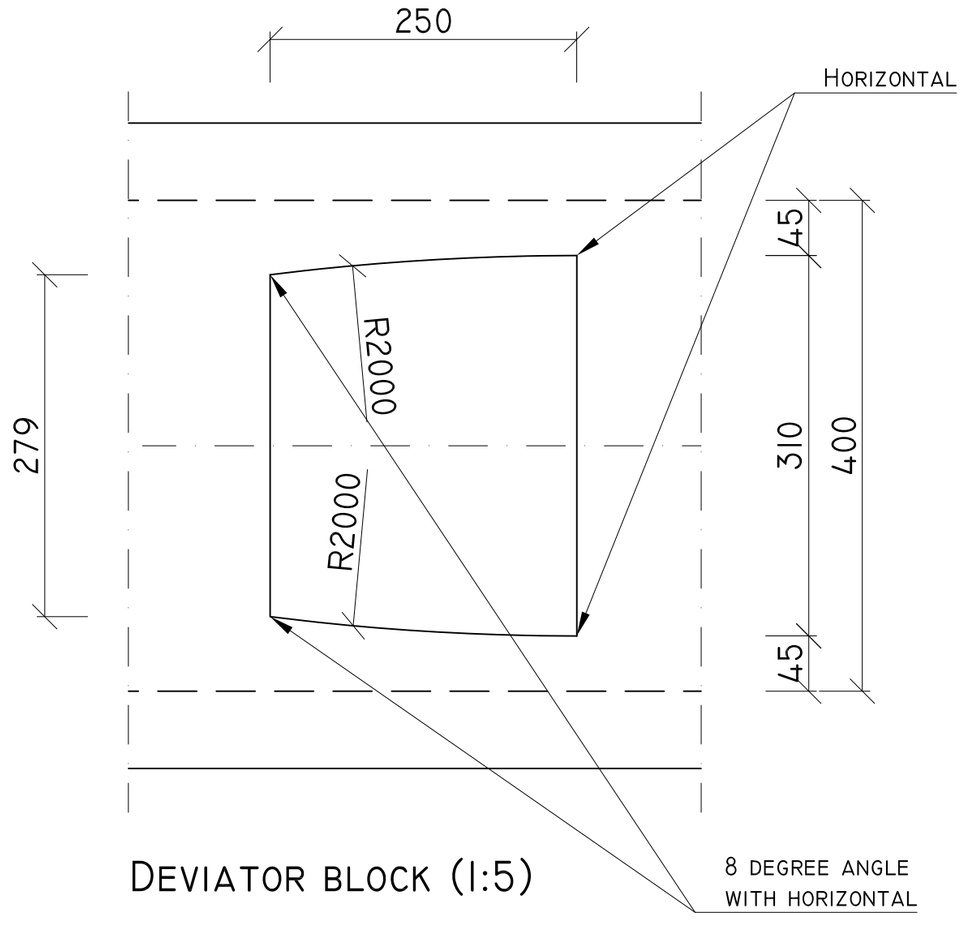

DEVIATOR BLOCK (1:5)

NOTES:

- ALL NP LVL11
- ANY CUT OFFS WILL BE USED FOR MATERIAL TESTING. SO PLEASE SAVE THEM AND SHIP THEM OVER
- DEVIATOR BLOCK CAN BE MADE UP OF 2 * 63MM AND 2 * 45MM (=216MM) AND PLANED DOWN TO FIT
- PLEASE SUPPLY ONE EXTRA LVL SHEET OF THE SAME DIMENSIONS AS THE EXTRA ANCHORAGE SUPPORT (500 * 210 * 63MM)
- NO NEED TO INSTALL PVC DUCTS FOR PT TENDONS

UNIVERSITY OF CANTERBURY
Te Whare Wānanga o Waitaha
CHRISTCHURCH NEW ZEALAND

TITLE	BEAM	
BY	WOUTER VAN BEERSCHOTEN	
REV.	0	ORIGINAL
DATE: 13-10-2010		SCALE: 1:20
UNITS: MM		DRAWING NO.: 4/4

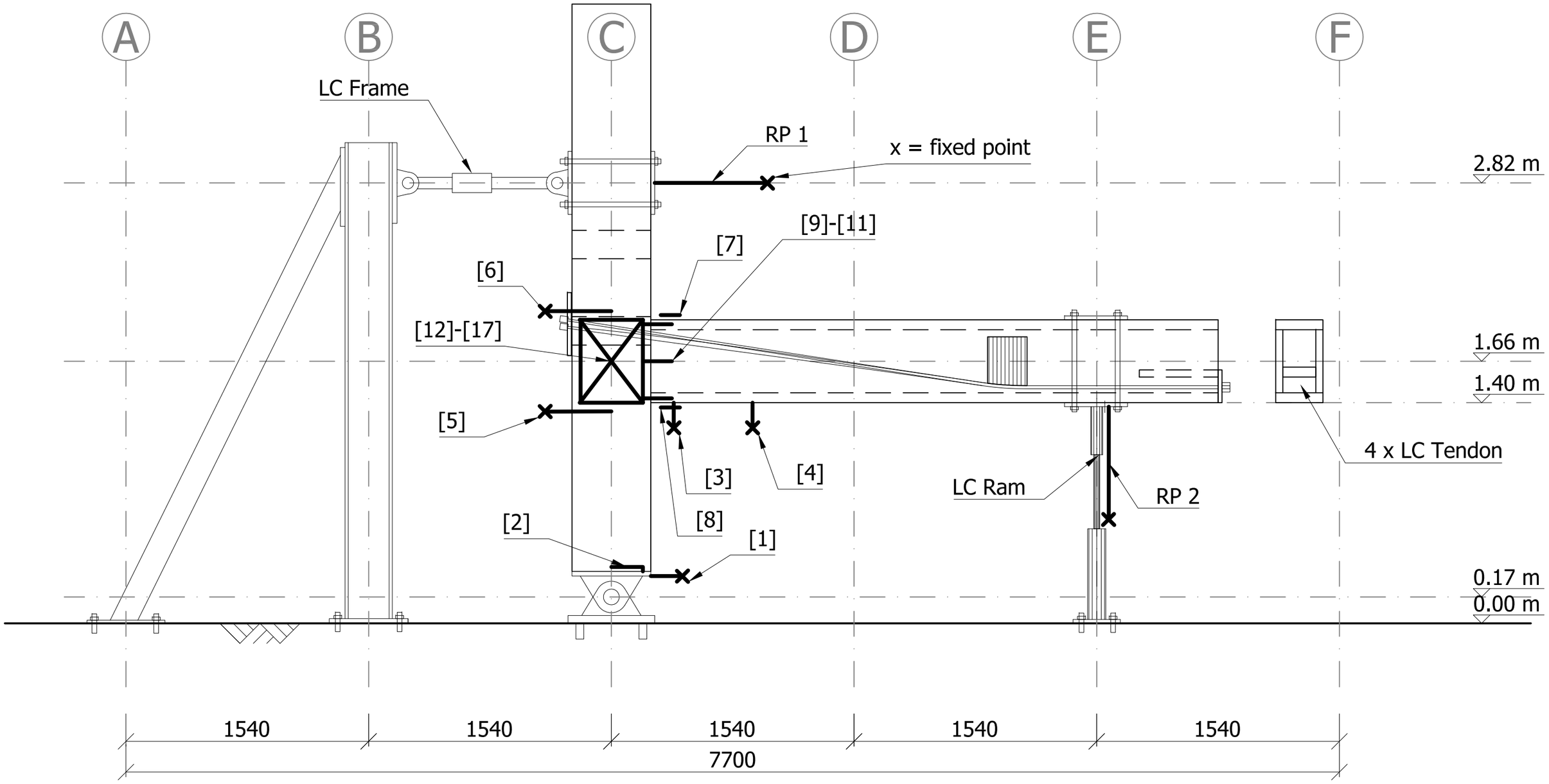

Instrumentation

[1]	30mm	Displacement of base plate
[2]	30mm	Displacement of column on base plate
[3]	50mm	Rotation of beam
[4]	50mm	Rotation of beam
[5]	30mm	Rotation of column interface
[6]	30mm	Rotation of column interface
[7]	30mm spring	Indentation of column
[8]	30mm spring	Indentation of column
[9]-[11]	50mm	gap opening
[12]-[17]	30mm	Joint panel deformation

UNIVERSITY OF CANTERBURY
Te Whare Wānanga o Waitaha
CHRISTCHURCH NEW ZEALAND

Title	External connection testing	
By	Wouter van Beerschoten	
Rev.	0	Original
	1	Deleted strain gauges
Date: 10-05-2011		Scale: 1:25
Units: mm		Drawing no.: 1/1

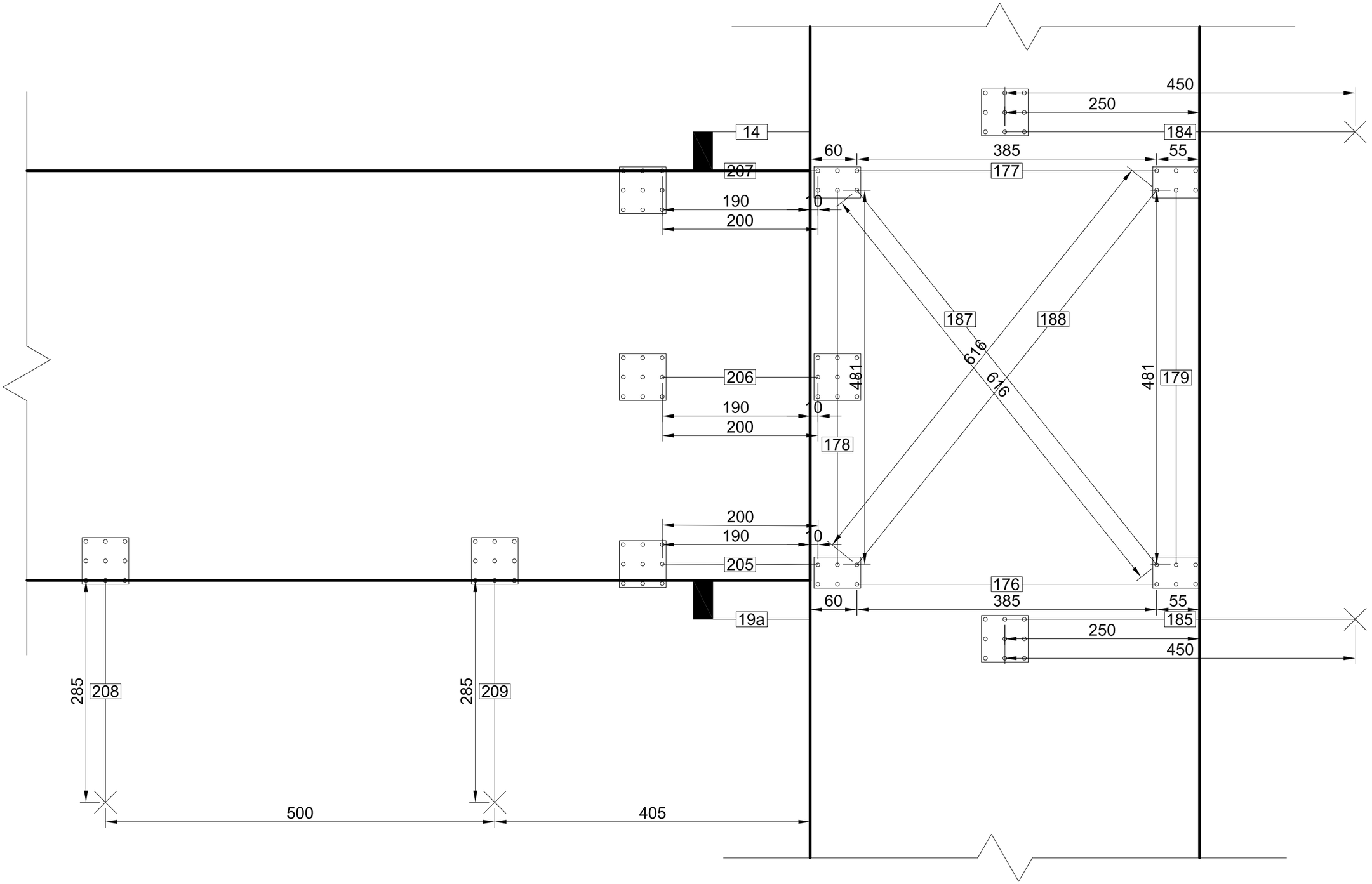

Instrumentation

Joint region

UNIVERSITY OF CANTERBURY
Te Whare Wānanga o Waitaha
CHRISTCHURCH NEW ZEALAND

TITLE	EXTERNAL CONNECTION TESTING	
BY	WOUTER VAN BEERSCHOTEN	
REV.	0	ORIGINAL
DATE: 12-05-2011		SCALE: 1:5
UNITS: MM		DRAWING NO.: 2/2

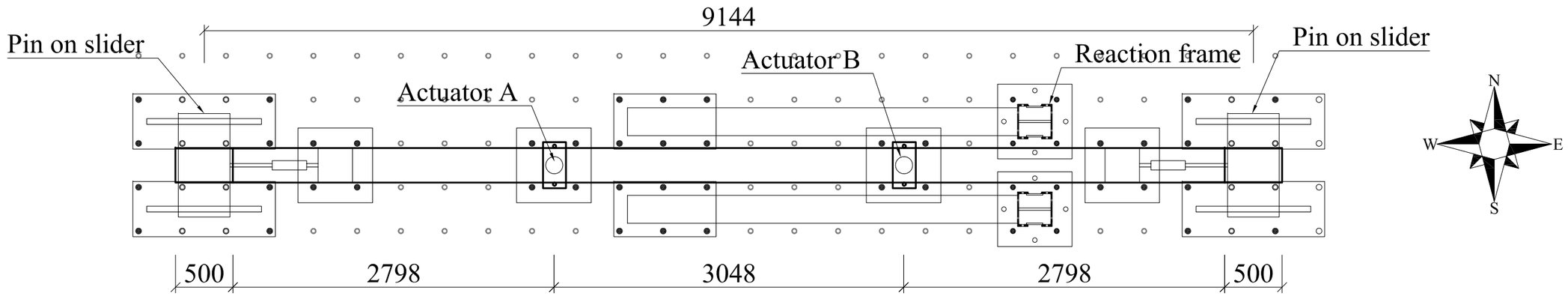

Top view

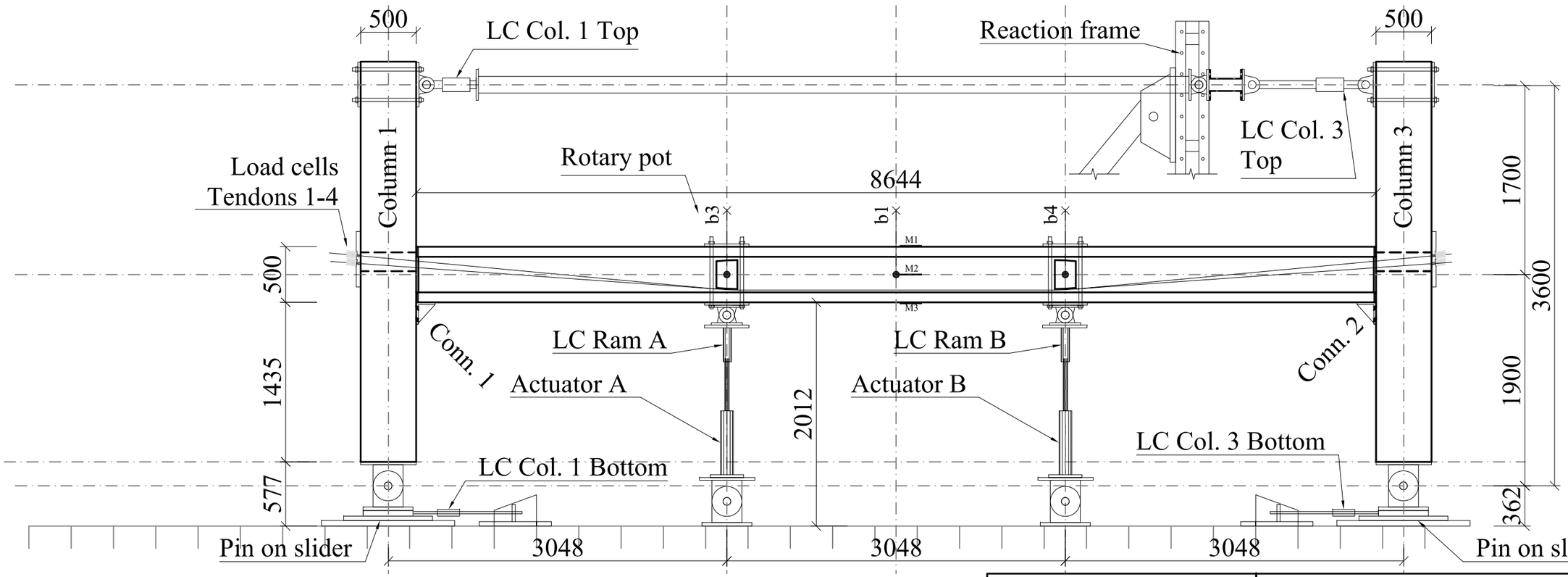

Front view

UNIVERSITY OF CANTERBURY
Te Whare Wānanga o Waitaha
CHRISTCHURCH NEW ZEALAND

TITLE	TEST SETUP - STAGE 3	
BY	WOUTER VAN BEERSCHOTEN	
REV.	0	ORIGINAL
	1	UPDATED REACTION FRAME AND DIMENSIONS
DATE: 12-10-2012		SCALE: 1:40
UNITS: MM		DRAWING NO.: 1/3

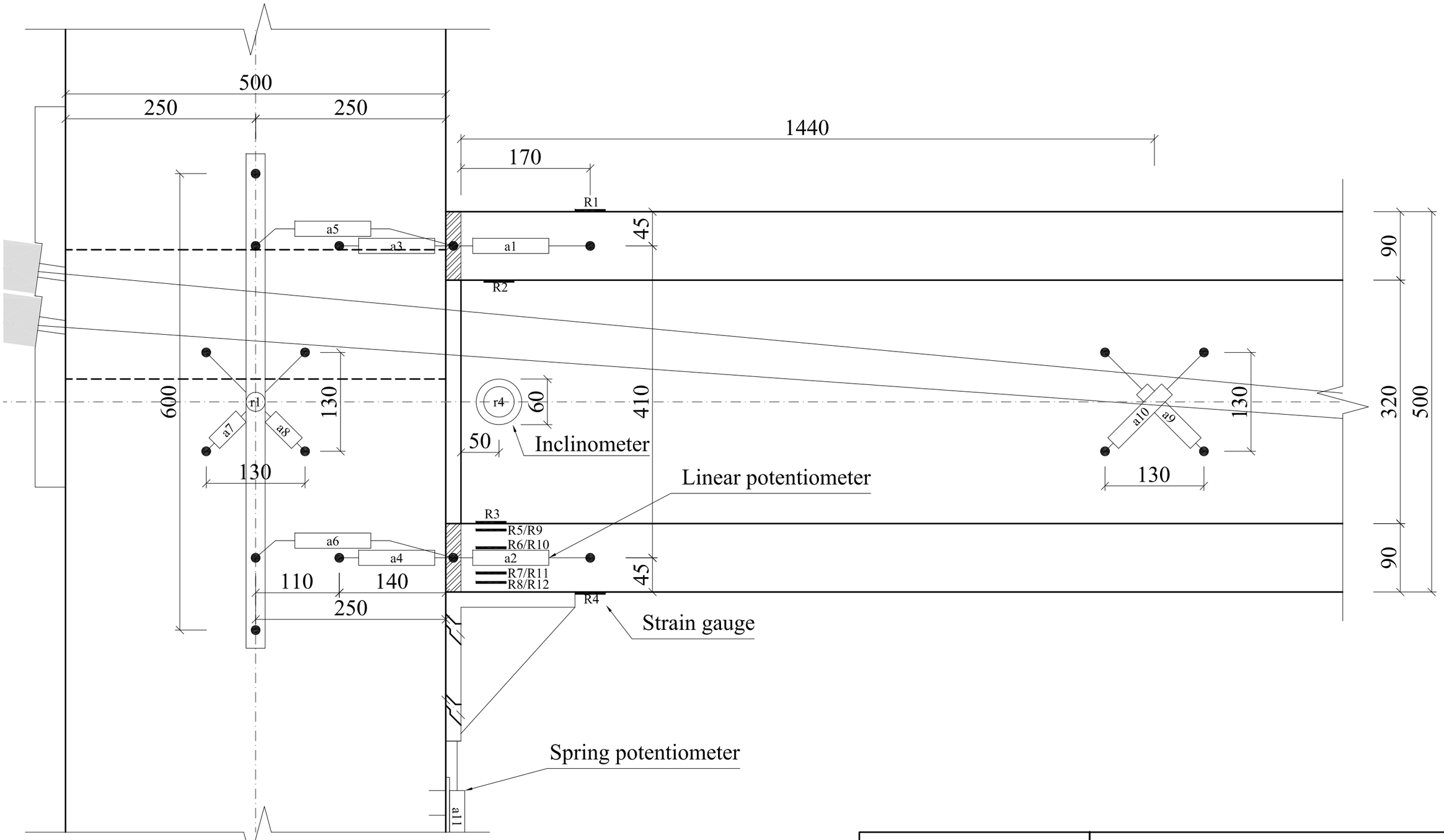

Connection 1

UNIVERSITY OF CANTERBURY
Te Whare Wānanga o Waitaha
CHRISTCHURCH NEW ZEALAND

TITLE	FRAME INSTRUMENTATION	
BY	WOUTER VAN BEERSCHOTEN	
REV.	0 ORIGINAL	
DATE: 23-07-2012		SCALE: 1:5
UNITS: MM		DRAWING NO.: 2/3

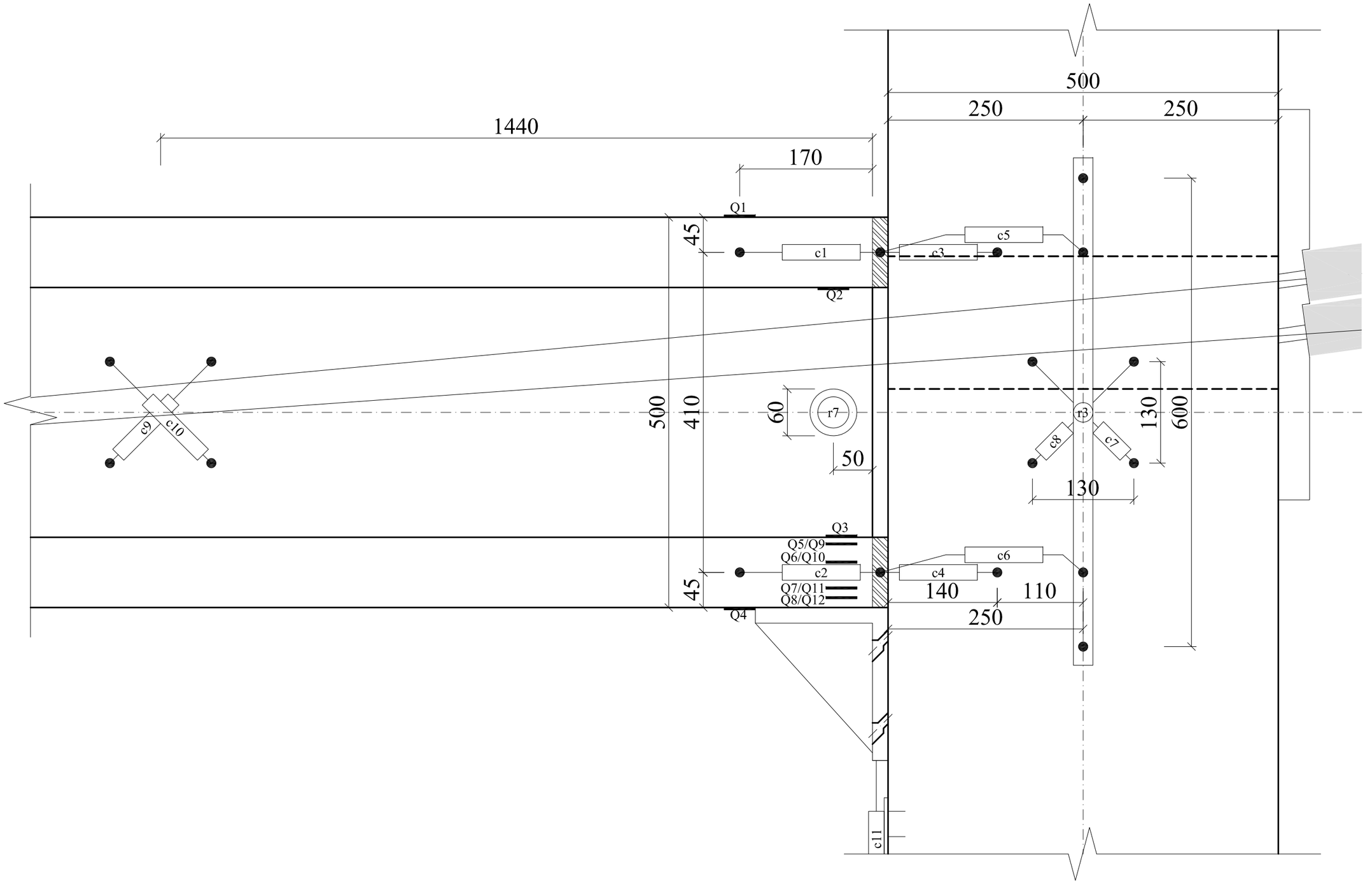

Connection 2

UNIVERSITY OF CANTERBURY
Te Whare Wānanga o Waitaha
CHRISTCHURCH NEW ZEALAND

TITLE	FRAME INSTRUMENTATION	
BY	WOUTER VAN BEERSCHOTEN	
REV.	0	ORIGINAL
DATE: 23-07-2012		SCALE: 1:5
UNITS: MM		DRAWING NO.: 3/3

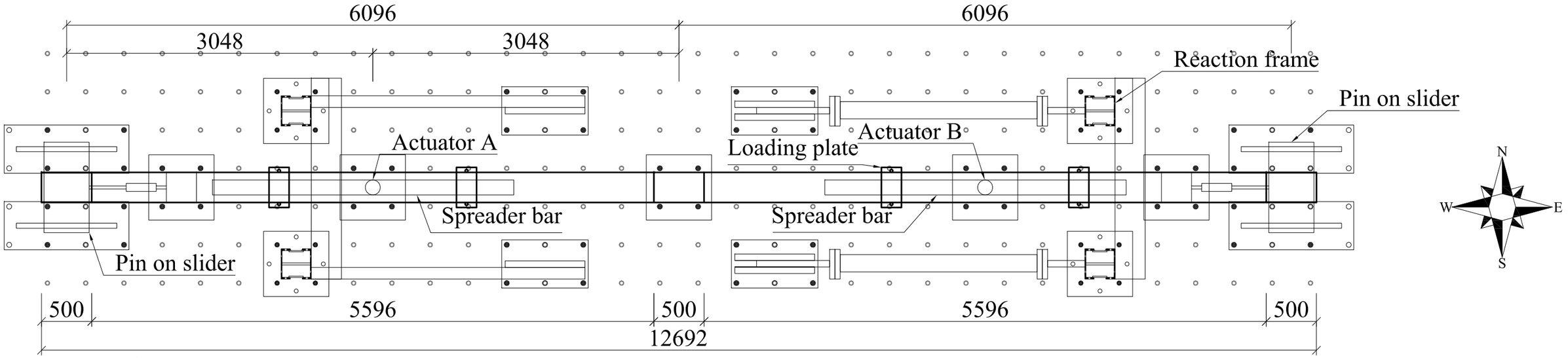

Top view

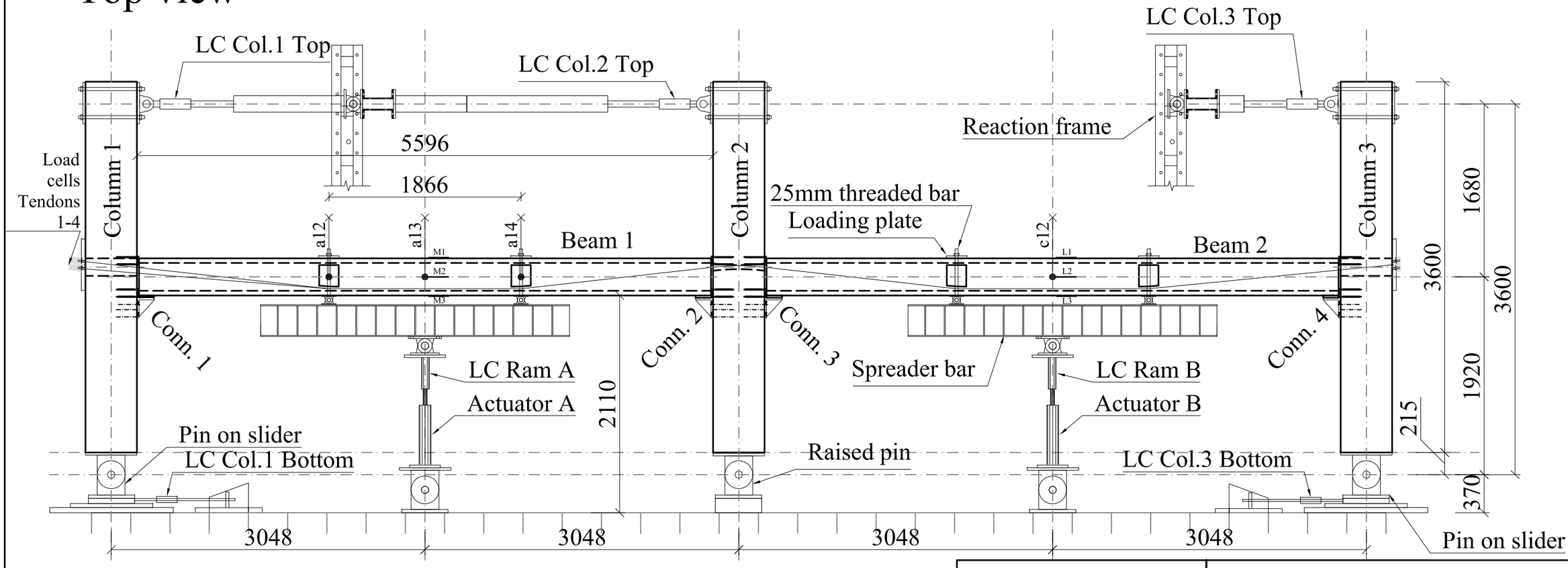

Front view

UNIVERSITY OF CANTERBURY
Te Whare Wānanga o Waitaha
CHRISTCHURCH NEW ZEALAND

TITLE	TEST SETUP - STAGE 4	
BY	WOUTER VAN BEERSCHOTEN	
REV.	0	ORIGINAL
DATE: 24-04-2012		SCALE: 1:40
UNITS: MM		DRAWING NO.: 1/4

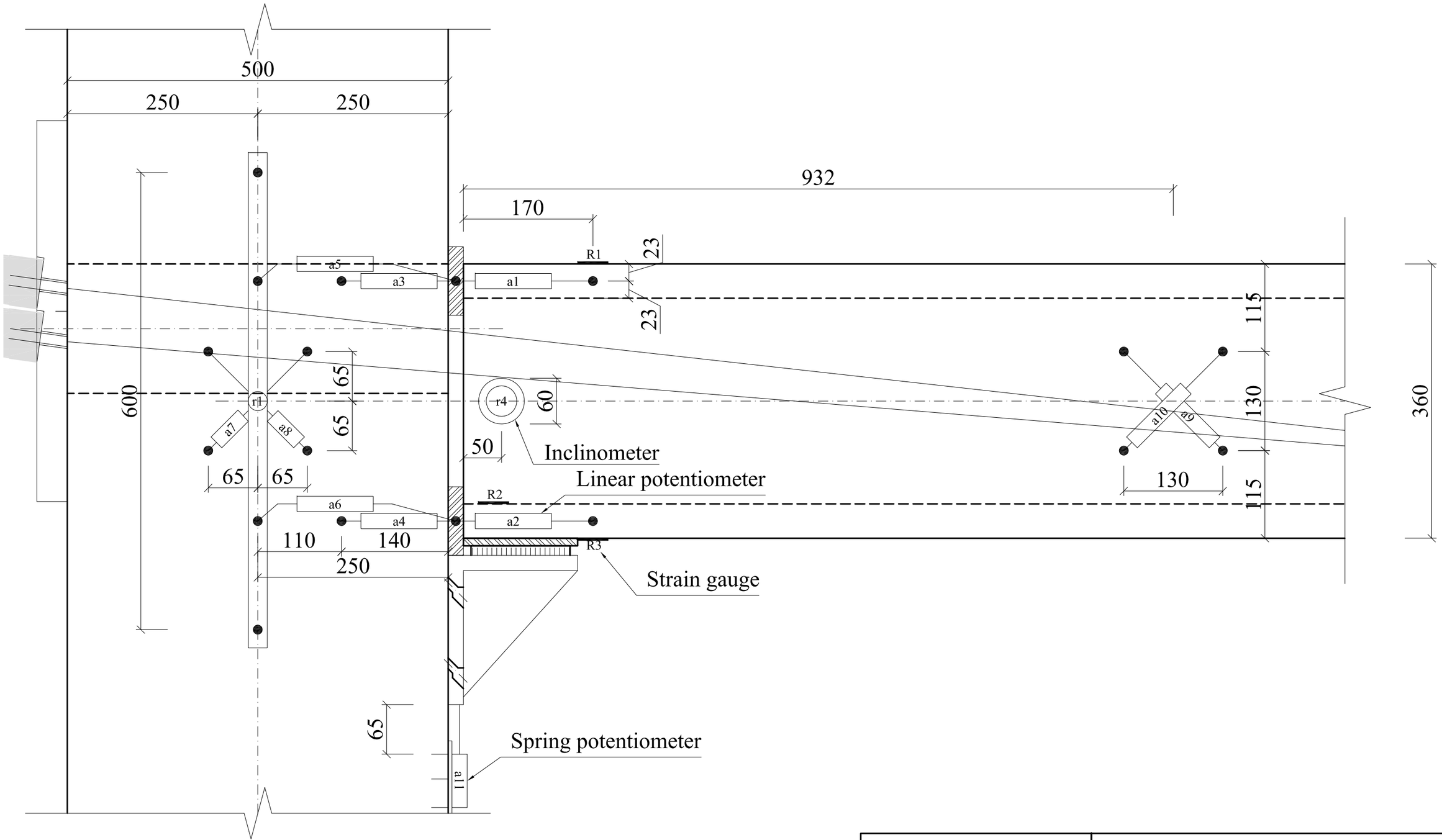

Connection 1

UNIVERSITY OF CANTERBURY
Te Whare Wānanga o Waitaha
CHRISTCHURCH NEW ZEALAND

TITLE	FRAME INSTRUMENTATION	
BY	WOUTER VAN BEERSCHOTEN	
REV.	0	ORIGINAL
DATE: 23-07-2012		SCALE: 1:5
UNITS: MM		DRAWING NO.: 2/4

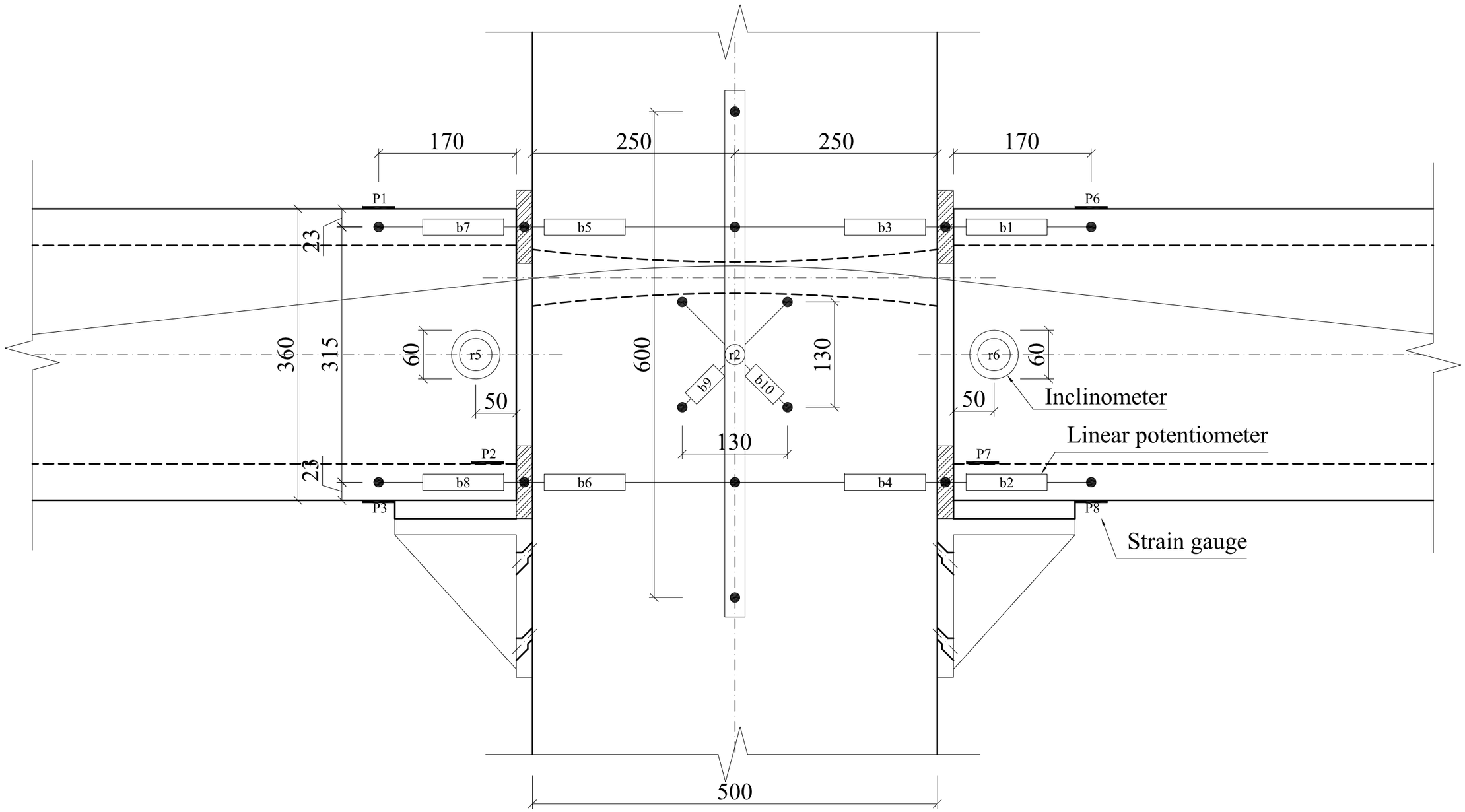

Connection 2 & 3

UNIVERSITY OF CANTERBURY
Te Whare Wānanga o Waitaha
CHRISTCHURCH NEW ZEALAND

TITLE	INSTRUMENTATION - STAGE 4	
BY	WOUTER VAN BEERSCHOTEN	
REV.	0	ORIGINAL
DATE: 23-07-2012		SCALE: 1:5
UNITS: MM		DRAWING NO.: 3/4

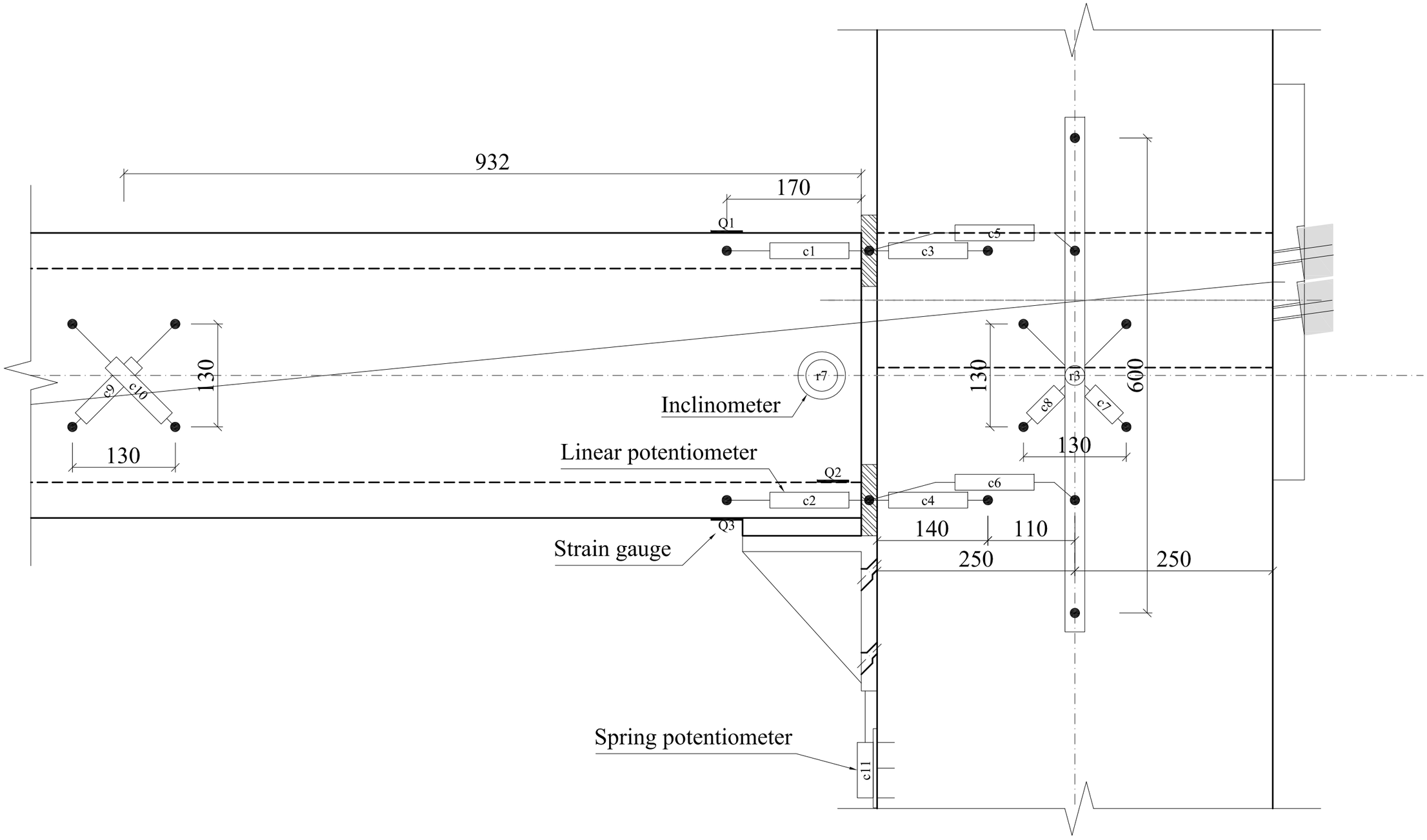

Connection 4

UNIVERSITY OF CANTERBURY
Te Whare Wānanga o Waitaha
CHRISTCHURCH NEW ZEALAND

TITLE	INSTRUMENTATION - STAGE 4	
BY	WOUTER VAN BEERSCHOTEN	
REV.	0 ORIGINAL	
DATE: 23-07-2012		SCALE: 1:5
UNITS: MM		DRAWING NO.: 4/4

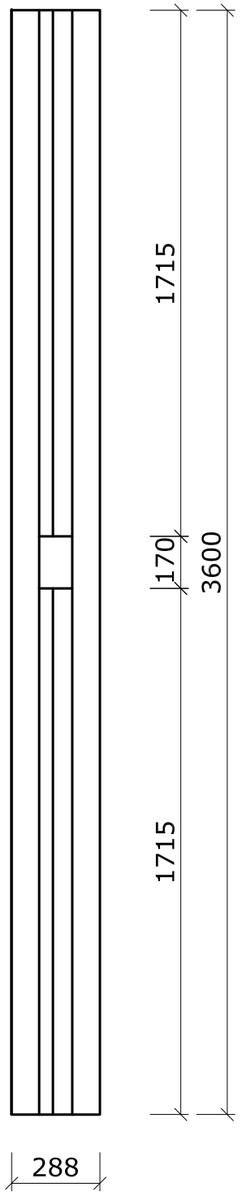

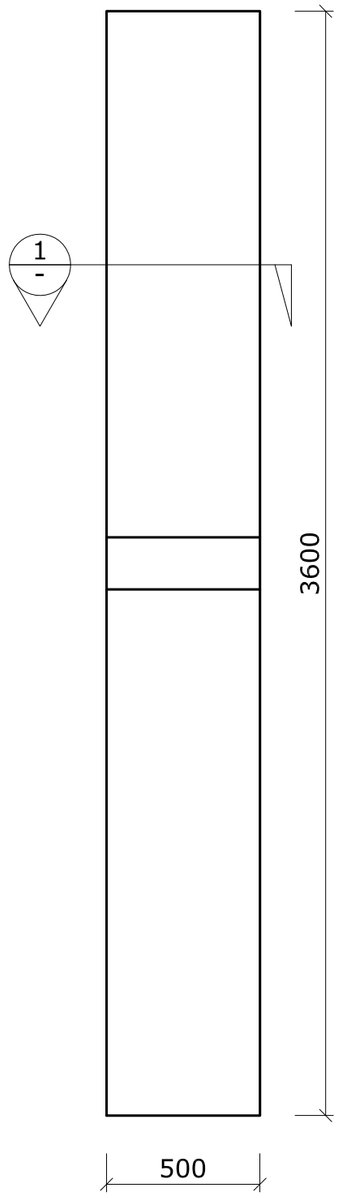

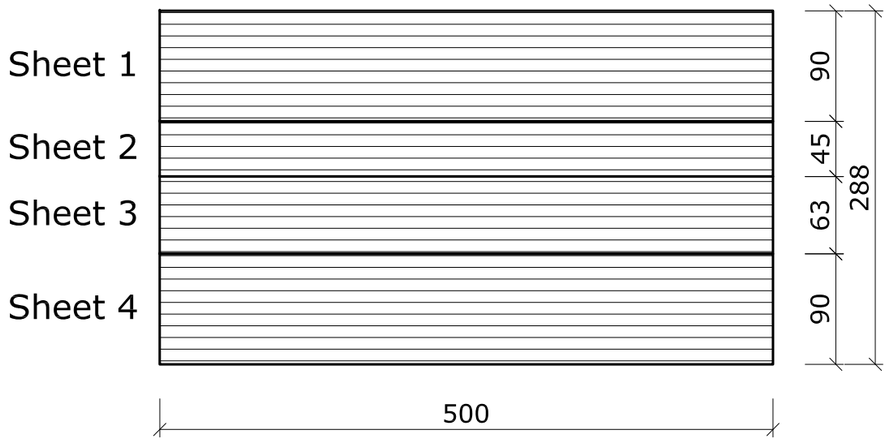

Section 1
(scale 1:5)

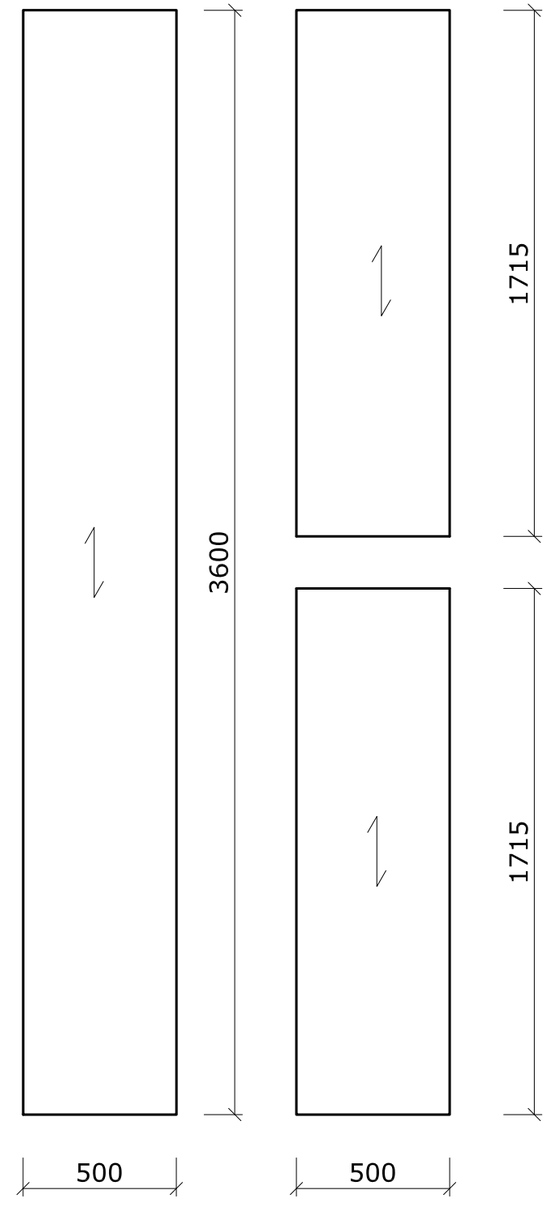

Sheet 1 & 4

Sheet 2 & 3

Front View

Side View

Notes:

- All timber Nelson Pine LVL11
- Manufacture 2 Columns Type 1
- 90mm sheet can be 2 x 45mm, if final column size (288mm) is still achieved

UNIVERSITY OF CANTERBURY
Te Whare Wānanga o Waitaha
CHRISTCHURCH NEW ZEALAND

Title	Column Type 1	
By	Wouter van Beerschoten	
Rev.	0	Internal Revision
	1	Order
Date: 24-04-2012		Scale: 1:20
Units: mm		Drawing no.: 3/4

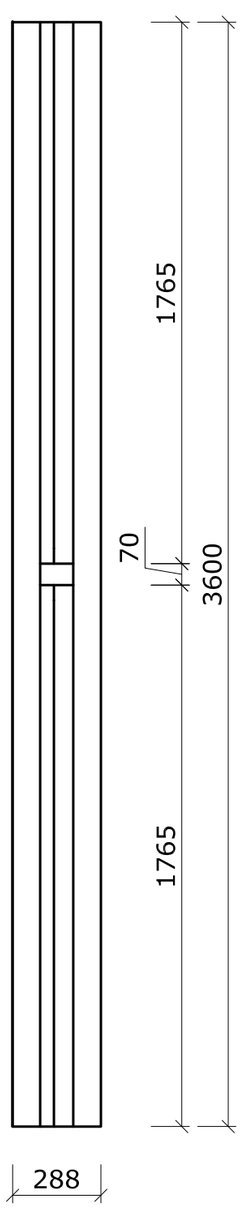

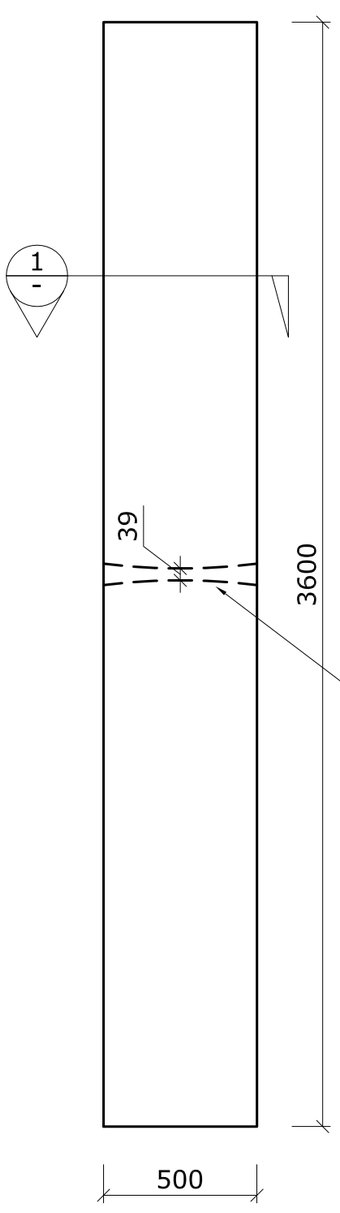

Front View

Side View

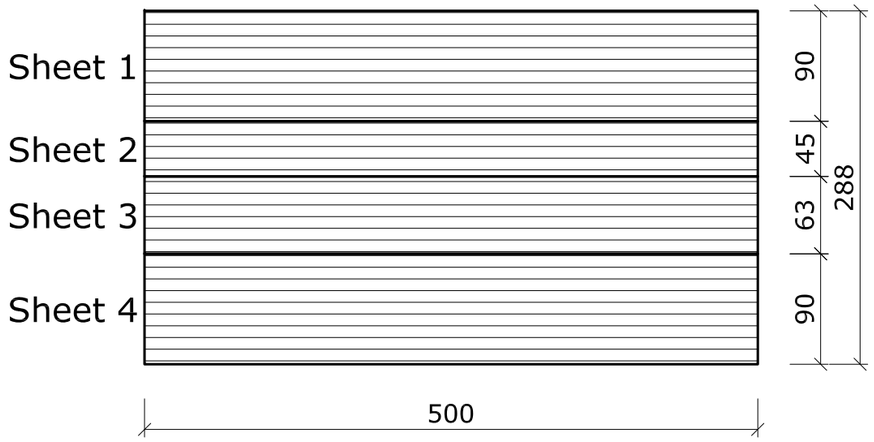

Section 1
(scale 1:5)

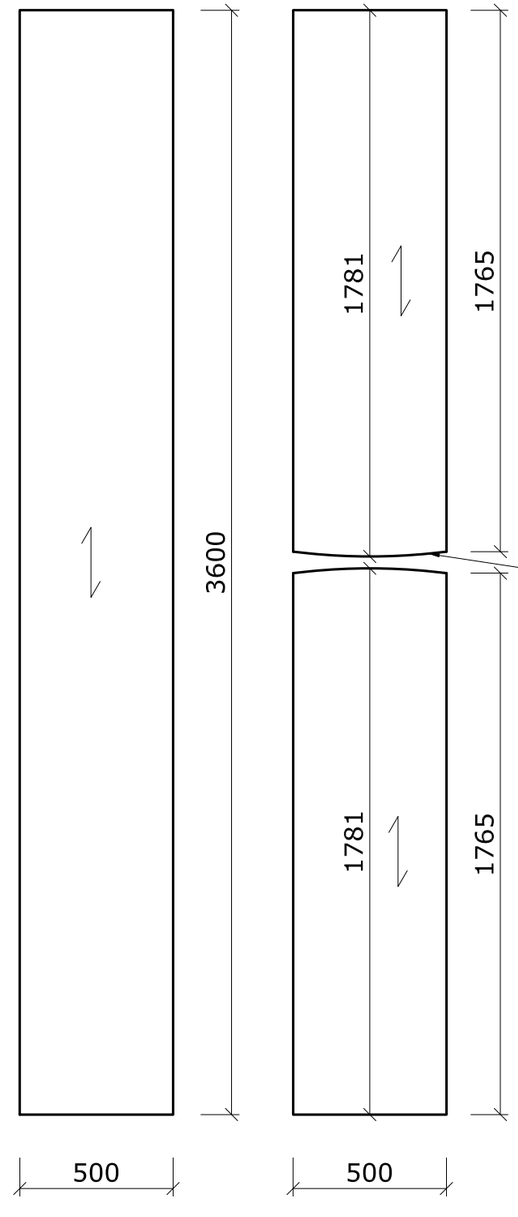

Sheet 1 & 4

Sheet 2 & 3

Notes:

- All timber Nelson Pine LVL11
- Manufacture 1 Columns Type 1
- 90mm sheet can be 2 x 45mm, if final column size (288mm) is still achieved

UNIVERSITY OF CANTERBURY
Te Whare Wānanga o Waitaha
CHRISTCHURCH NEW ZEALAND

Title	Column Type 2	
By	Wouter van Beerschoten	
Rev.	0	Internal Revision
	1	Order
Date: 24-04-2012		Scale: 1:20
Units: mm		Drawing no.: 4/4

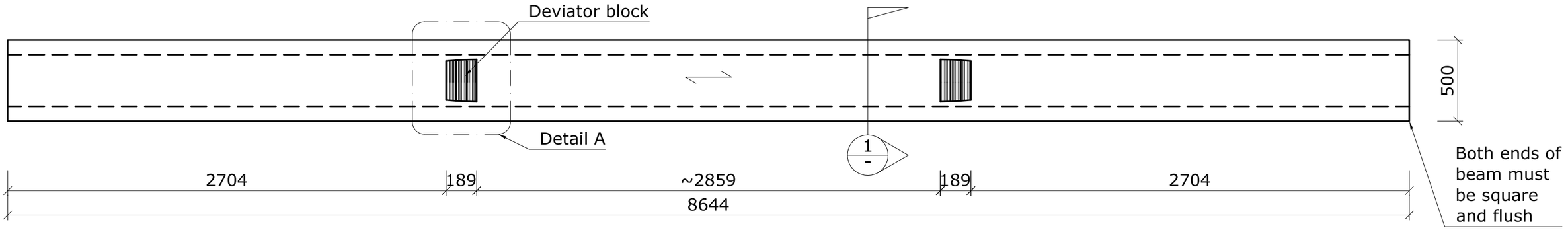

Side View

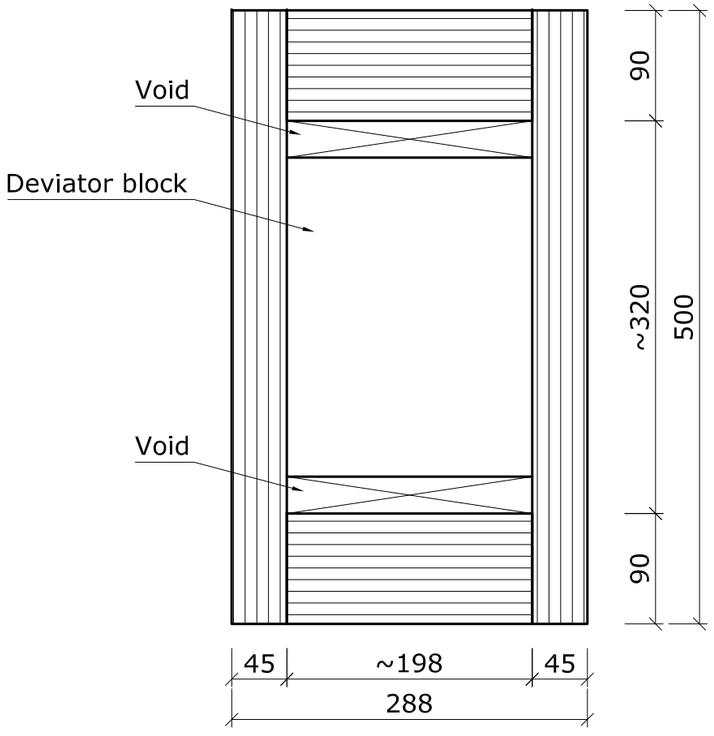

Section 1
(scale 1:5)

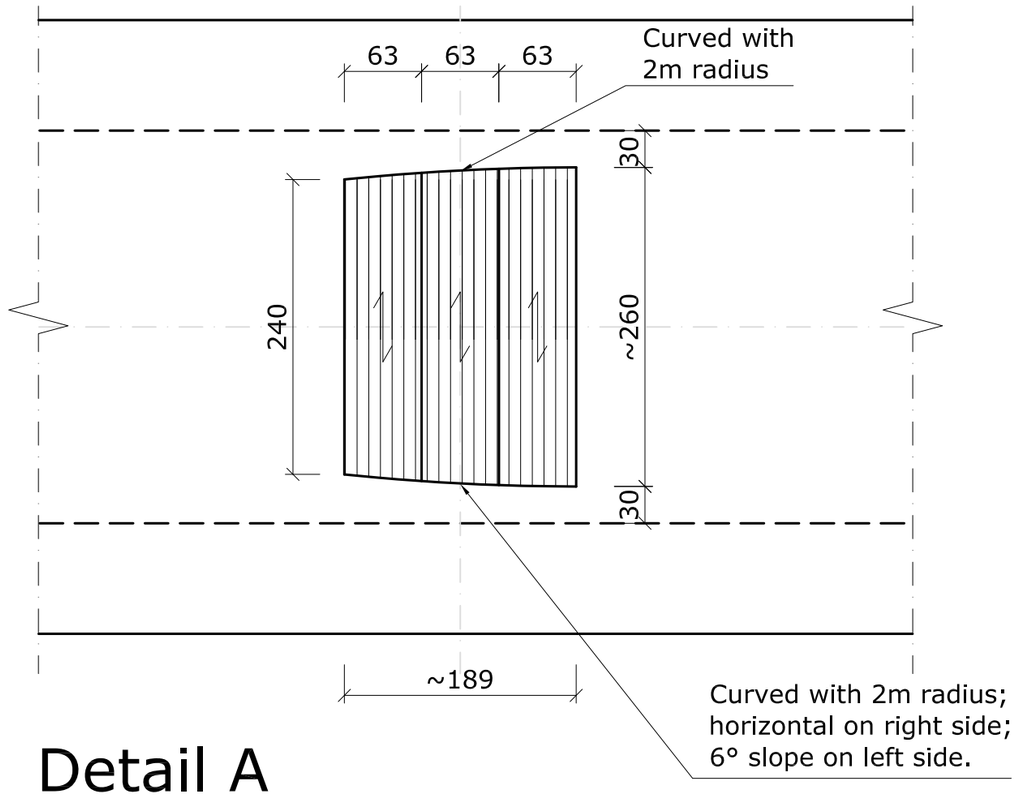

Detail A
(scale 1:5)

Notes:

- All timber Nelson Pine LVL11
- Manufacture 2 Beams Type 2
- Approximate sizes have been marked with '~'
- Width of beam has to match width of column, 200mm top and bottom flange can vary slightly to achieve this

UNIVERSITY OF CANTERBURY
Te Whare Wānanga o Waitaha
CHRISTCHURCH NEW ZEALAND

Title	Beam Type 1	
By	Wouter van Beerschoten	
Rev.	0	Internal revision
	1	Order
Date: 24-04-2012		Scale: 1:25
Units: mm		Drawing no.: 1/4

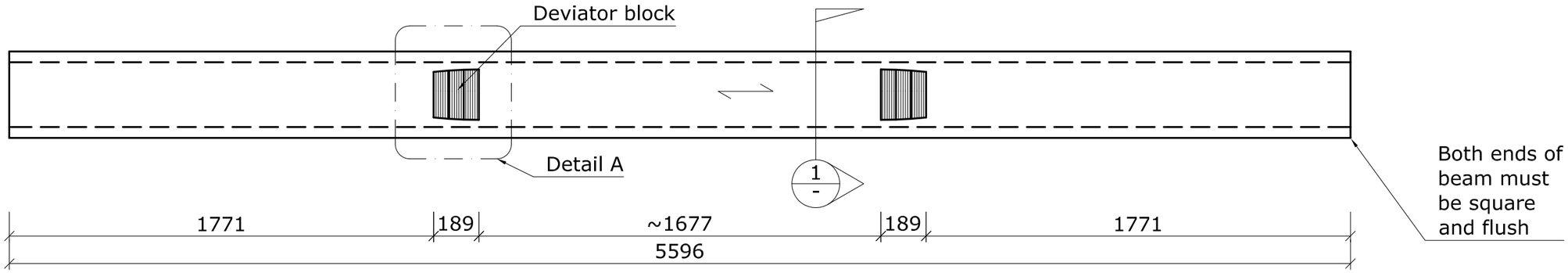

Side View

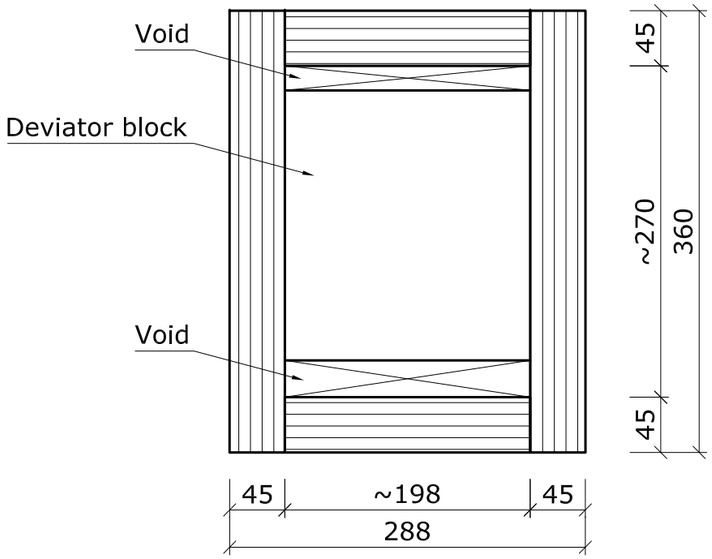

Section 1
(scale 1:5)

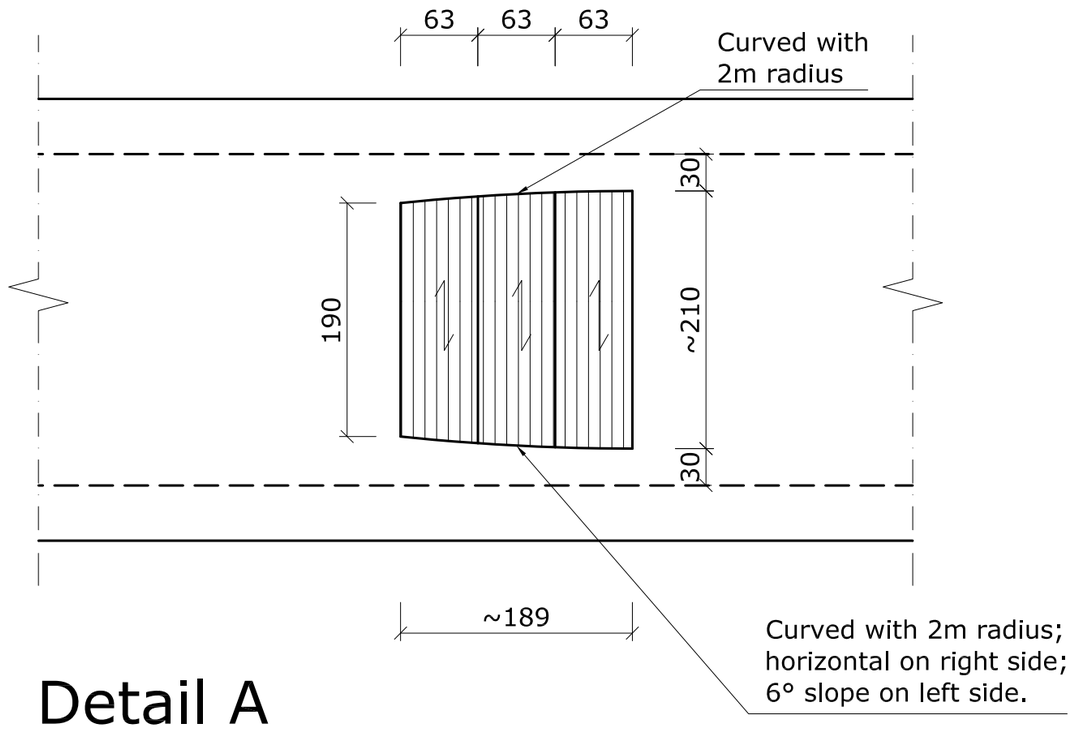

Detail A
(scale 1:5)

Notes:
- All timber Nelson Pine LVL11
- Manufacture 2 Beams Type 2
- Approximate sizes have been marked with '~'
- Width of beam has to match width of column, 200mm top and bottom flange can vary slightly to achieve this

UNIVERSITY OF CANTERBURY
Te Whare Wānanga o Waitaha
CHRISTCHURCH NEW ZEALAND

Title	Beam Type 2	
By	Wouter van Beerschoten	
Rev.	0	Internal revision
	1	Order
Date: 24-04-2012		Scale: 1:20
Units: mm		Drawing no.: 2/4

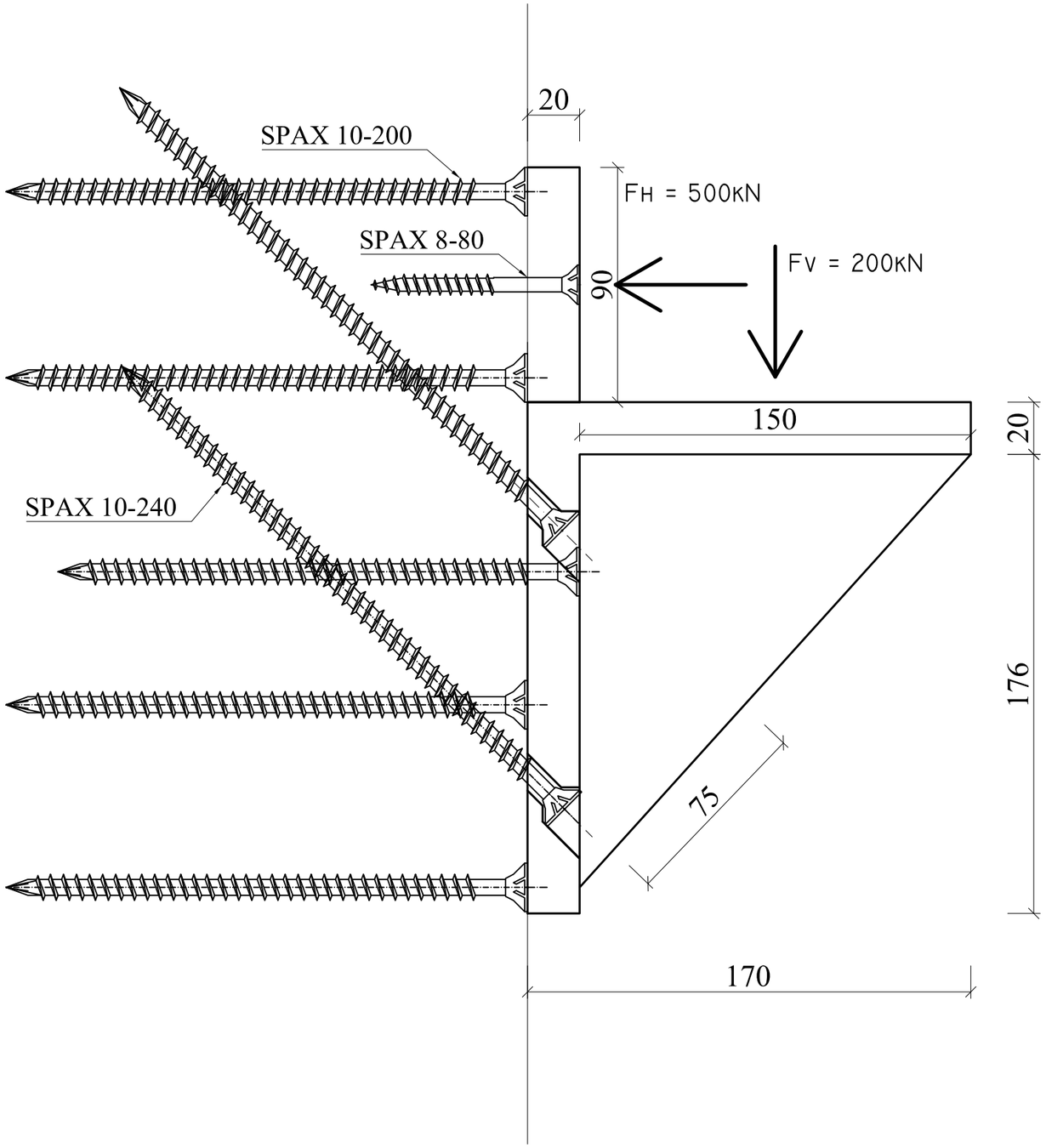

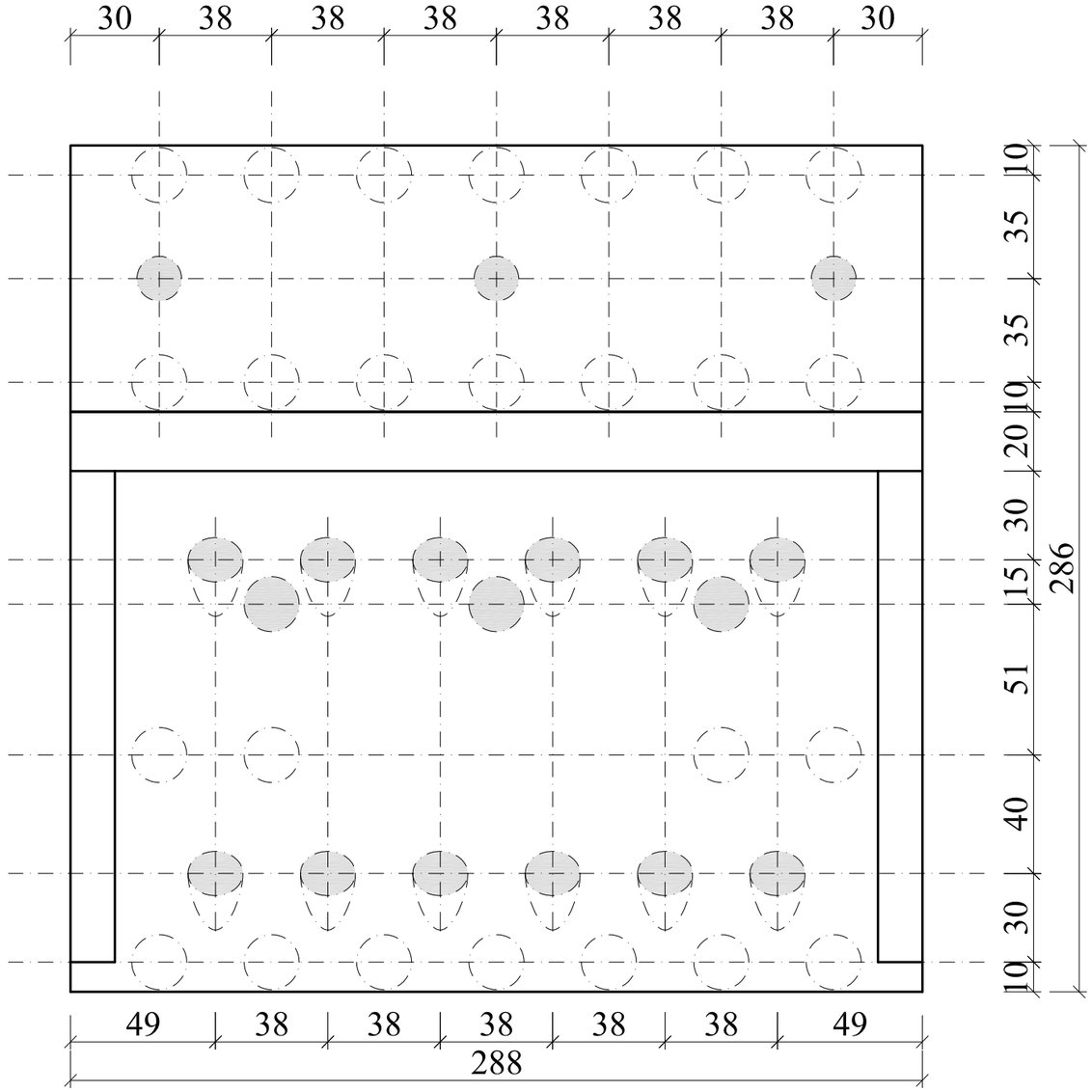

TOTAL NUMBER OF SCREWS:
- 12 x SPAX 10-240
- 3 x SPAX 8-80
- 25 x SPAX 10-200

UNIVERSITY OF CANTERBURY
Te Whare Wānanga o Waitaha
CHRISTCHURCH NEW ZEALAND

TITLE	STEEL CORBEL	
BY	WOUTER VAN BEERSCHOTEN	
REV.	0	ORIGINAL
DATE: 26-06-2012		SCALE: 1:2
UNITS: MM		DRAWING NO.: 1/1